Transactions of the ASME®

Transactions of the ASME, Journal of Turbomachinery (ISSN 0889-504X) is published quarterly (Jan., Apr., July, Oct.) for $125.00 per year by The American Society of Mechanical Engineers, 345 East 47th Street, New York, NY 10017. Second class postage paid at New York, NY and additional mailing offices. POSTMASTER: Send address change to Transactions of the ASME, Journal of Turbomachinery, c/o THE AMERICAN SOCIETY OF MECHANICAL ENGINEERS, 22 Law Drive, Box 2300, Fairfield, NJ 07007-2300.

CHANGES OF ADDRESS must be received at Society headquarters seven weeks before they are to be effective. Please send old label and new address.

PRICES: To members, $36.00, annually; to nonmembers, $125.00.
Add $15.00 for postage to countries outside the United States and Canada.

INDEXED by Applied Mechanics Reviews and Engineering Information, Inc.

Journal of Turbomachinery

Published Quarterly by The American Society of Mechanical Engineers

VOLUME 113 • NUMBER 2 • APRIL 1991

TECHNICAL PAPERS

(Contents Continued on p. 160)

(Contents Continued)

ANNOUNCEMENTS

Mixing in Axial-Flow Compressors: Conclusions Drawn From Three-Dimensional Navier-Stokes Analyses and Experiments

J. H. Leylek
Engineer,
Computational Turbomachinery
Aerodynamics.

D. C. Wisler
Manager,
Aerodynamics Research Laboratory.

General Electric Aircraft Engines,
Cincinnati, OH 45215

Extensive numerical analyses and experiments have been conducted to understand mixing phenomena in multistage, axial-flow compressors. For the first time in the literature the following are documented: Detailed three-dimensional Navier–Stokes solutions, with high order turbulence modeling, are presented for flow through a compressor vane row at both design and off-design (increased) loading; comparison of these computations with detailed experimental data show excellent agreement at both loading levels; the results are then used to explain important aspects of mixing in compressors. The three-dimensional analyses show the development of spanwise (radial) and circumferential flows in the stator and the change in location and extent of separated flow regions as loading increases. The numerical solutions support previous interpretations of experimental data obtained on the same blading using the ethylene tracer-gas technique and hot-wire anemometry. These results, plus new tracer-gas data, show that both secondary flow and turbulent diffusion are mechanisms responsible for both spanwise and circumferential mixing in axial-flow compressors. The relative importance of the two mechanisms depends upon the configuration and loading levels. It appears that using the correct spanwise distributions of time-averaged inlet boundary conditions for three-dimensional Navier–Stokes computations enables one to explain much of the flow physics for this stator.

1.0 Introduction

The relative importance of convection by secondary flows and diffusion by turbulence as mechanisms responsible for mixing in multistage, axialflow compressors has been the subject of considerable research and discussion recently. This was highlighted in the paper and discussions of Wisler et al. (1987), where those authors presented research that moved the mixing focus to consideration of the total mixing process involving both circumferential and spanwise convection, diffusion and their interaction. They concluded from their tests and analyses that both secondary flow and turbulent diffusion can play important roles in the mixing process.

Based on their data, Wisler et al. proposed a total mixing picture that included: convection of fluid near endwalls and along airfoil surfaces by secondary flow, diffusion by turbulence everywhere, the effects of the rotor tip-clearance vortex and endwall boundary layer skew, turbulence levels and unsteadiness, wake chopping, the circumferential transport of fluid by wake dispersion, and centrifugation of fluid in the rotor wakes. The relative importance of these mechanisms was configuration and loading dependent.

Historically, this research followed the earlier work of Adkins and Smith (1982), who put forward the concept that secondary flows were responsible for spanwise mixing, and the work of Gallimore and Cumpsty (1986), who concluded that random turbulent diffusion, not secondary flow, was the dominant mechanism of spanwise mixing.

There were many Discussions submitted about the Wisler et al. (1987) paper. Among them was the well-reasoned Discussion of Gallimore and Cumpsty, who had reservations about data interpretation. They concluded from the data of Wisler et al. that spanwise secondary flows are small, are restricted to localized regions near the blade surface–endwall corners, and therefore do not contribute significantly to spanwise mixing. They maintained that the overwhelming contributor to radial mixing is turbulent diffusion.

Resolving these issuses and obtaining the correct physical mechanisms for mixing in compressors are important to understanding and computing the aerodynamic flowfields. This has become increasingly apparent in light of the trend toward higher stage loadings, higher solidities, and lower aspect ratios.

2.0 Definitions and Objectives

2.1 Definitions. The following definitions will be helpful.

Secondary Flow. The flow deviation between the real three-

Contributed by the International Gas Turbine Institute and presented at the 35th International Gas Turbine and Aeroengine Congress and Exposition, Brussels, Belgium, June 11–14, 1990. Manuscript received by the International Gas Turbine Institute January 18, 1990. Paper No. 90-GT-352.

dimensional flow and the "so-called" primary flow (streamtubes) computed using axisymmetric, two-dimensional, blade-to-blade, etc. models is called secondary flow. These flows are associated with all components of streamwise vorticity. Strong secondary flows can be produced by turning of the mean flow, pressure gradients, boundary layer skew, blockage, tip leakage, and wake effects to name a few. Although they can also be produced by turbulence gradients, such secondary flows are generally very weak. Secondary flows are deterministic and can produce bulk mixing. They can be computed by three-dimensional Navier–Stokes and Euler methods.

Turbulent Diffusion. This, on the other hand, is a fundamentally different mixing mechanism that is characterized by disorder and irregular fluctuations (randomness). Often there is a broad spectrum of turbulence velocity and length scales.

Turbulence and Unsteadiness. For turbomachinery, one can distinguish phenomena that correlate with shaft speed. Turbulence is any random unsteadiness that does not correlate with shaft speed (time-unresolved unsteadiness). Deterministic unsteadiness is any unsteadiness that correlates with shaft speed, like rotor wakes (time-resolved unsteadiness). Both types of unsteadiness can produce mixing.

For simplicity and consistency with past literature, we use the word "secondary flow" to describe the deterministic, axisymmetric and nonaxisymmetric flows described in the definition above. This mechanism for spanwise mixing is in dispute. We use "turbulent diffusion" to define the time-resolved and unresolved unsteady features of the flowfield that produce mixing by turbulence. That this is an important contributor to mixing is, to our knowledge, not in dispute.

We are striving for a physically correct view of mixing. In that regard, we ask the following: Are there secondary flows in a compressor sufficiently large to transport enough fluid out of and into primary flow streamtubes to contribute to mixing?

2.2 Objectives. There were two primary objectives of this work. The first was to describe by both computations and experiments the three-dimensional, complex flow through the stator of an axial-flow compressor showing the development of any radial and tangential aerodynamic flows and the diffusion levels. This includes describing the effects of increased loading on the flowfield. The second was to use these results to clarify the issue of the relative importance of convection by secondary flows and diffusion by turbulence as mechanisms responsible for radial and tangential mixing in multistage, axial-flow compressors.

3.0 Technical Approach

The overall technical approach used to achieve the objectives described earlier is presented.

3.1 Computational Program. A three-dimensional Navier–Stokes system was used to compute the flowfield in a stator passage within an imbedded stage of a multistage compressor. A highly refined computational grid mesh was generated to make large-scale simulations of aerodynamic flowfields for two loading levels. Extensive comparisons with experiment were made to validate the computations. The results were used to understand secondary flow aspects of the mixing process in compressors.

3.2 Experimental Program. A test program was set up in the General Electric Low-Speed Research Compressor (LSRC) to measure the flowfields and diffusion rates in an imbedded stage of a multistage compressor. High-quality blading, representative of current compressor design practice, was tested in a facility large enough to make detailed measurements.

The ethylene tracer-gas technique, three-dimensional hot-wire anemometry, along with conventional pressure and flow-angle instrumentation were used to measure the aerodynamic flows, fluid migration, diffusion rates, and unsteadiness for two loading levels.

4.0 Three-Dimensional Navier–Stokes System

The three-dimensional Navier–Stokes system used to obtain the computational results presented in this paper is described briefly.

This system was developed by the first author to provide a user-friendly, practical-analysis tool that designers with little CFD experience can use to simulate complex, three-dimensional viscous flows in turbomachinery components. It is comprised of the following major modules: preprocessor, CRAY JCL generator, solver, and postprocessor. The solver resides on the CRAY X/MP supercomputer. All other modules are installed on various frontend VAX computers. Each interactive module is completely menu-driven with "expert rules" embodied to improve accuracy and efficiency. This system is linked to the existing turbomachinery design methodology and three-dimensional graphics programs.

4.1 Integration Into Design Methodology. In order to conduct a three-dimensional, viscous flow analysis and compare it with design intent or test data, designers use the two-way link between the three-dimensional Navier–Stokes system and the existing turbomachinery design methodology (TDM) as shown in Fig. 1. Geometry and flow information are passed from the TDM, through the grid generator, to the three-dimensional system via the forward link. The aft links are used to superimpose the computational results onto original design or test data.

4.2 Computational Elements

Preprocessor. The preprocessor program bridges the gap

Nomenclature

C = tangential distance measured from SS to PS in percent stator pitch
c = chord
DP = design point
F = percent of peak ethylene concentration
h = annulus height $= r_c - r_H$
I = radial immersion measured from casing
ibid. = refers to reference Wisler, Bauer, and Okiishi (1987)
IL = increased loading
k = turbulence kinetic energy
LE = leading edge
N–S = Navier–Stokes
PS = pressure surface
P_s = static pressure
P_T = total pressure
r_c = radius of casing
r_H = radius of hub
r, θ, Z = radial (spanwise), tangential (circumferential), and axial directions in cylindrical coordinates
SS = suction surface
TE = trailing edge
U_p = pitchline rotor speed
α = swirl angle
ϵ = dissipation rate of turbulence kinetic energy
λ = blockage parameter
ϕ = meridional angle
$\bar{\omega}$ = loss coefficient $= \left[\frac{P_{T\text{inlet}} - P_{T\text{exit}}}{P_{T\text{inlet}} - P_{S\text{inlet}}}\right]$

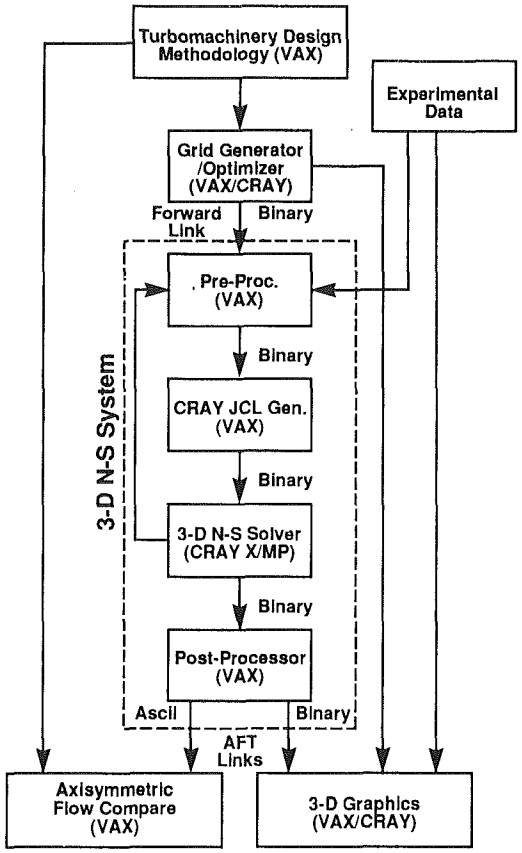

Fig. 1 Integration of the three-dimensional Navier-Stokes computational system, shown inside the dashed box, into the turbomachinery design methodology

between the existing turbomachinery design methodology and the complex three-dimensional Navier–Stokes solver, thus providing a practical analysis tool for designers who are not necessarily experts in CFD.

Some features of the preprocessor include: "expert rules" to activate options; ability to draw initial distributions of field variables from various sources; transparent solver-specific operations like grid staggering, coordinate transformations, and unit system conversions; extensive error detection and cures; and full restart capability.

CRAY JCL Generator. This module generates a Job Control Language deck for the CRAY X/MP computer through a series of menus. One can extract a tightly dimensioned solver for each simulation from the source code residing on the CRAY.

Three-Dimensional Navier–Stokes Solver. The flow code sequentially solves the Reynolds-averaged Navier–Stokes equations on completely generalized, nonorthogonal, curvilinear coordinates. It can simulate three-dimensional, subsonic, viscous, compressible, and turbulent flows in the complex geometries encountered in turbomachinery bladerows. The solver was originally developed by Hah (1987).

The computational methodology is based on a pressure-correction scheme, which includes the concept of the pressure-implicit split operator, developed by Issa (1982), to improve the rate of convergence. A three-point, central-difference discretization is used for all diffusion terms in the governing equations. Convective terms are discretized using a modified version of the original quadratic upwinding (QUICK) scheme of Leonard (1979). This scheme, based on three points in upwind direction, is third-order accurate. The current solver does not require explicit addition of any type of artificial dissipation. It is highly vectorized on the CRAY X/MP supercomputer and is capable of running out-of-core solutions by utilizing the CRAY Solid-State-Disk (SSD) storage device. This is essential for economical operation.

No slip and no-flux boundary conditions are imposed on all solid surfaces. Profiles of total pressure, total temperature, swirl angle, meridional angle, turbulence kinetic energy, and turbulence dissipation rate are fixed at the inlet plane. At the exit plane, the static pressure is fixed at one location and asymptotic conditions are used for all other variables. Finally, repeating conditions are imposed for all variables on all planes upstream, downstream, and at tip clearance regions of a bladerow.

Details of the solver and sample applications are given by Hah and Leylek (1987).

Turbulence Model. Mainstream turbulence intensity and length scale effects play important roles in turbulent flow simulations. The two-equation k–ϵ turbulence models incorporated into the current solver, unlike zero or one-equation models of turbulence, account for both of these effects.

A standard (or high Reynolds number) k–ϵ turbulence model, used in conjunction with wall function formulations, is the default model used to attain closure for transport equations in turbulent flow simulations. Optionally, a low Reynolds number k–ϵ model developed by Chien (1982) may be switched on for computations involving extremely fine grid meshes.

Inlet conditions for k and ϵ are established using total velocity, turbulence intensity, and length-scale data and equilibrium assumptions. The length scale is assumed equal to some fraction of the airfoil span when, as is often the case, there are no data available for this parameter.

It is our understanding that within the current state of the art, better practical (economical) turbulence modeling in turbomachinery, especially for large-scale turbulence, is not possible at present.

Postprocessor. This code transfers data from the staggered to the main grid making all differences between the solver and the current design system transparent to users. It prepares output consistent with the existing graphics system and the turbomachinery design methodology.

4.3 Validation of the Computational System. The three-dimensional Navier–Stokes system has undergone extensive validation using both classical and turbomachinery flows for which high-density, high-quality data exist. One example, important to the discussion in Section 6.3, is given.

Flow Over a Cylinder. This complex, challenging flowfield has become a standard test case for CFD code validation. Because geometry, compressibility, turbulence modeling, and other complicating factors are nonexistent for this simulation, any numerical problems in flow solvers can be isolated. Moreover, many high-quality experimental data exist for this well-understood flow.

Computationally, this problem was modeled as a flow in a cascade of cylinders. It was set up very much like a three-dimensional turbomachinery problem except that airfoils were replaced by cylinders. A fine, computational grid mesh with 99 tangential, 5 radial, and 125 streamwise nodes was used to simulate a Reynolds number 30 case. Pitchwise and spanwise extent of the computation domain were both equal to five diameters.

The computed velocity-vector field downstream of the cylinder in Fig. 2 shows a steady, attached, symmetric, closed wake with two counterrotating vortices. The geometric parameters of the closed wake are seen to be in excellent agreement with the experimental data of Coutanceau and Bouard (1977) in Table 1.

Other examples are given by Hah and Leylek (1987).

5.0 Test Vehicle Apparatus

5.1 Low-Speed Research Compressor (LSRC). The LSRC

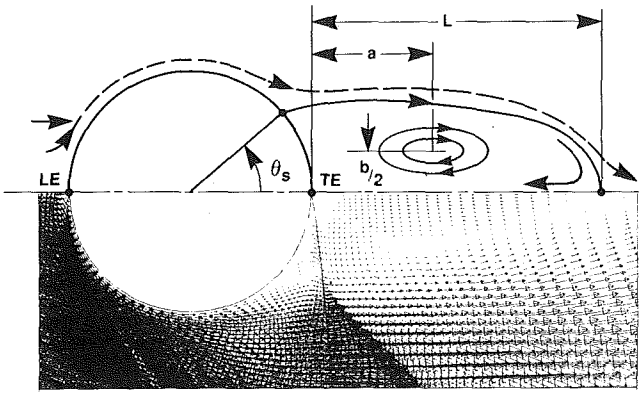

Fig. 2 Three-dimensional Navier-Stokes computation of flow over a cylinder shows region of separated flow and a steady, attached, symmetric, closed wake with two counterrotating vortices

Table 1 Comparison of the geometric parameters defining the closed wake for flow around a cylinder, Reynolds number = 30; experimental data from Coutanceau and Bouard (1977)

Experiment $\lambda = 0.12$	3-D Navier Stokes System
L 1.17	1.18
a 0.42	0.49
b 0.47	0.49
θ_s 48°	47°

is an experimental facility that duplicates the essential features of smaller, high-speed compressor flowfields in a large, low-speed machine where very detailed investigations of the flow can be made. The facility, which has a constant casing diameter of 1.524 m (60.0 in.), is described by Wisler (1985). The LSRC was set up in four identical stages to simulate the repeating stage environment. The third stage was the test stage.

Blading. Two compressor configurations were tested. Compressor I, having performance characteristics typical of compressors in some current engines, had high hub/tip ratio, low-aspect-ratio, high-solidity blading with shrouded stators and inlet guide vanes. The blading was a low-speed, aerodynamic model of stages 4–9 of a highly loaded, high-reaction, nine-stage compressor. A meridional view of the 0.85 radius-ratio geometry of the test stage is given in Fig. 3 and some blading parameters are given in Table 2.

Compressor II had blading designed with about 20 percent higher loading levels, higher spanwise gradients in circulation and swirl angles, lower-aspect ratios, higher solidities, and more advanced techniques than that for Compressor I, although the number of airfoils and radius ratio were the same. Some parameters for Stator II are also given in Table 2.

Performance. The overall performance and test results for Compressor I, which are used in this paper, can be found from Wisler et al. (1987). Tests were conducted at two loading levels. For the design-point loading, the flow coefficient was 0.525, the pressure coefficient was 0.639, and the efficiency was 90.2 percent. At increased loading these values were 0.458, 0.690, and 89.0 percent, respectively. Performance data were obtained at 850 rpm.

Tests for Compressor II were conducted at its design point. Overall performance was good and the stator, across which the ethylene tracer-gas measurements were made, also performed well.

5.2 Instrumentation

Ethylene Tracer-Gas. The details of the ethylene tracer-gas technique were previously reported (ibid). The same techniques were used for the tests on Compressor II. Ethylene was

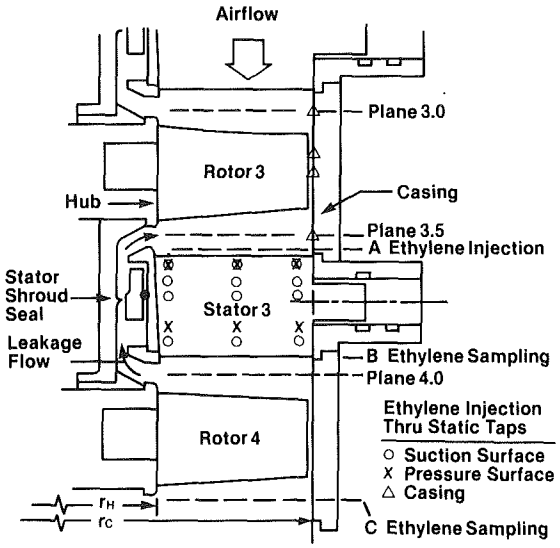

Fig. 3 *Cross section of compressor test stage*

Table 2 Pitchline blading parameters

	Rotor I	Stator I	Rotor II	Stator II
Solidity	1.11	1.32	1.64	1.61
Aspect Ratio	1.25	1.45	0.85	1.18
Chord, cm (in)	9.12 (3.59)	7.90 (3.11)	13.5 (5.31)	9.65 (3.80)
Stagger, Deg.	49.1	20.3	40.0	18.1
Camber, Deg.	32.3	53.4	—	—
No. of Airfoils	54	74	54	74
Axial Spacing, cm (in)	2.79 (1.10)		2.79	

injected upstream of the stator at location A, shown in Fig. 3, and sampled downstream at location B. For reference, the equivalent injection location A is marked in the sampling plane B with an "X" in later figures.

As before, the word "core" refers to the region of peak ethylene concentration found in the sampling plane B. The locations of the cores are marked with an "O" in later figures. Generally, cores move in response to pressure gradients under the combined influence of primary and secondary flows. The word "contour" refers to all of the isoconcentration lines surrounding the core. Symmetric contours imply isotropic turbulence. Distorted contours can result from secondary flows and gradients in turbulence and velocity.

Hot-Wire Anemometry. The details of this technique were likewise previously reported (ibid). In addition, three-wire, fully three-dimensional hot-wire measurements were taken in Compressor II. The total size of the probe head was 3.5 mm.

6.0 Computed Three-Dimensional Flowfield

Simulation details and comparisons of the computed stator flowfield with experiment are presented in this section.

The computational simulations for both the design point and increased loading conditions were carried out on the same high-pressure compressor Stator I as reported by Wisler et al. (1987). No special handling, tuning, or adjustments of any kind were made to the previously validated Navier–Stokes system to "match" experimental data in the present study. The computational model was found to be very close to its experimental counterpart; consequently, meaningful comparisons could be made and conclusions drawn, especially about secondary flows, with considerable confidence.

6.1 Grid, Boundary Conditions, and Convergence

Grid. The computational grid mesh represents the largest

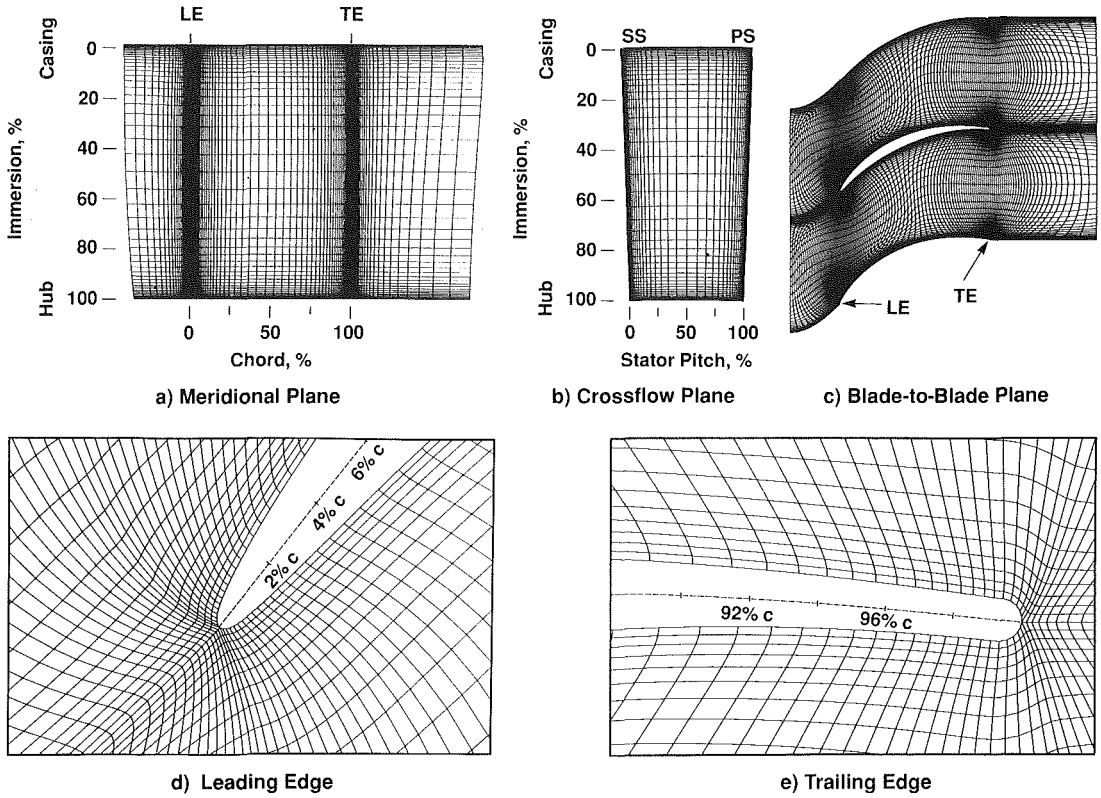

Fig. 4 Computational grid for the stator passage: 236,160 total grid nodes with 40 tangential, 48 radial, and 123 axial nodes

scale simulation carried out using our three-dimensional Navier–Stokes system to date. To our knowledge, it is one of the finest grid-size cases documented in the literature for turbomachinery CFD. A total of 236,160 grid nodes were used, in staggered form, with 40 nodes in the tangential, 48 nodes in the radial, and 123 nodes in the axial directions. Meridional, crossflow, and blade-to-blade plane view of the H-type grid mesh are shown in Figs. 4(*a–c*). Highly enlarged views of the leading and trailing edges in Figs. 4(*d, e*) indicate the resolution in the computational representations of these regions.

Boundary Conditions. Inlet and exit boundary conditions, for both design point (*DP*) and increased loading (*IL*) cases, were derived from actual LSRC measurements. These inlet profiles are a time average of unsteady flow conditions. The implications of this feature of the boundary conditions will be highlighted in Section 8.0. The *DP* and *IL* boundary conditions resulted in vastly different solutions, demonstrating the influence of the inlet boundary conditions on the predicted flowfield.

Radial distributions of mass-averaged inlet total pressure, average swirl angle from the tufts, and meridional angle for the *DP* and *IL* cases are presented in Figs. 5(*a–c*), respectively. Computed profiles are superimposed upon experimental data. The high degree of precision in our ability to impose the exact measurements is clear. In other words, we matched the time-averaged inlet vorticity. In addition, we matched average turbulence kinetic energy at the inlet plane.

Constant inlet total temperature was imposed during computations since its spanwise variation was estimated to be within 1.5 R and therefore negligible. This plus the adiabatic wall boundary condition allow one to specify the inlet total enthalpy everywhere in the computation domain and thus turn off the energy equation. A significant cost savings resulted.

At the exit plane, measured static pressure was matched near the hub endwall, and asymptotic conditions were imposed for all other variables. Overall mass flow rates were matched identically.

Convergence. Starting from a uniform distribution for all field variables, one iterates until each transport equation satisfies a built-in convergence criterion. A solution is declared "fully converged" when the normalized residuals of each governing equation are no greater than 1 percent. Normalized residual is computed by adding the absolute values of a residual for all the control volumes in the whole domain and dividing this sum by the total inlet flux of a relevant quantity for each equation (i.e., inlet mass flux for continuity).

Computational results presented in this paper were fully converged, requiring approximately 1700 iterations and about 11 hours of CRAY X/MP cpu-time. About 4 megawords of core memory and 12 megawords of out-of-core storage (SSD) were needed to contain the problem.

6.2 Computed Flowfield at Stator Exit. In this section we will demonstrate, in most cases, excellent agreement between computed and measured quantities for both loading levels, thus giving credibility to the computed results.

Total Pressure. Radial distributions of mass-weighted, circumferentially averaged total pressure at the stator exit for *DP* and *IL* simulations are presented in Fig. 6*a*. Agreement between measured and computed data is excellent. Magnitudes and distributions are correct across the span. Note that the measured weakening of the profiles near the hub is successfully predicted by analysis.

Computed and measured total-pressure contours on crossflow planes at the stator exit for both *DP* and *IL* cases are presented in Fig. 7. Overall agreement between predictions and data is remarkably good. At the design point in Fig. 7(*a, b*), the small separated flow regions near the suction surface at both endwalls are captured. The quite small differences in the pitchwise extent of loss pockets at the suction surface/casing junction are probably due to the small vane tip-clearance-related leakage present in the experiments but not modeled in the computations.

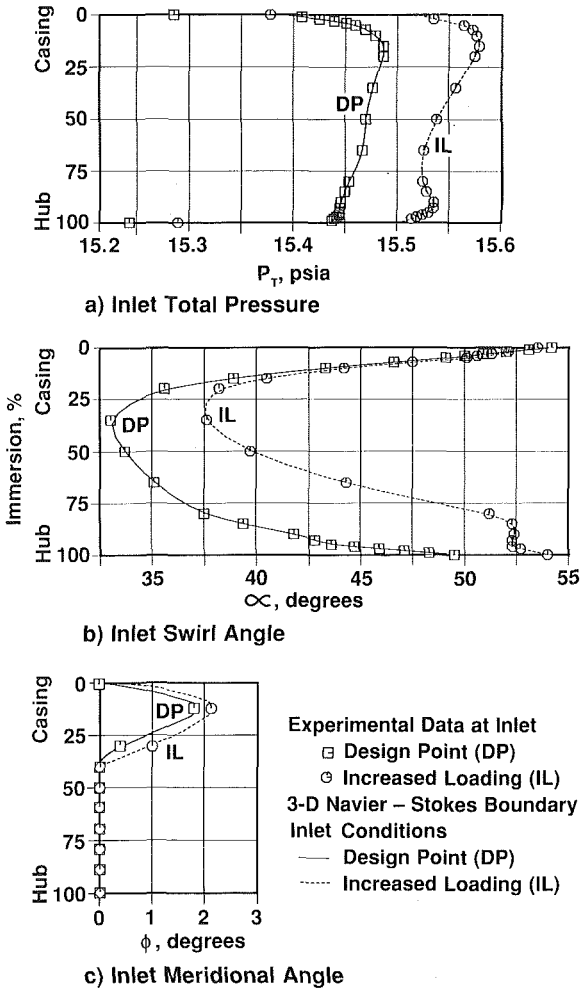

Fig. 5 Experimental data used for the inlet boundary conditions for the three-dimensional computations at both the design point and increased loading

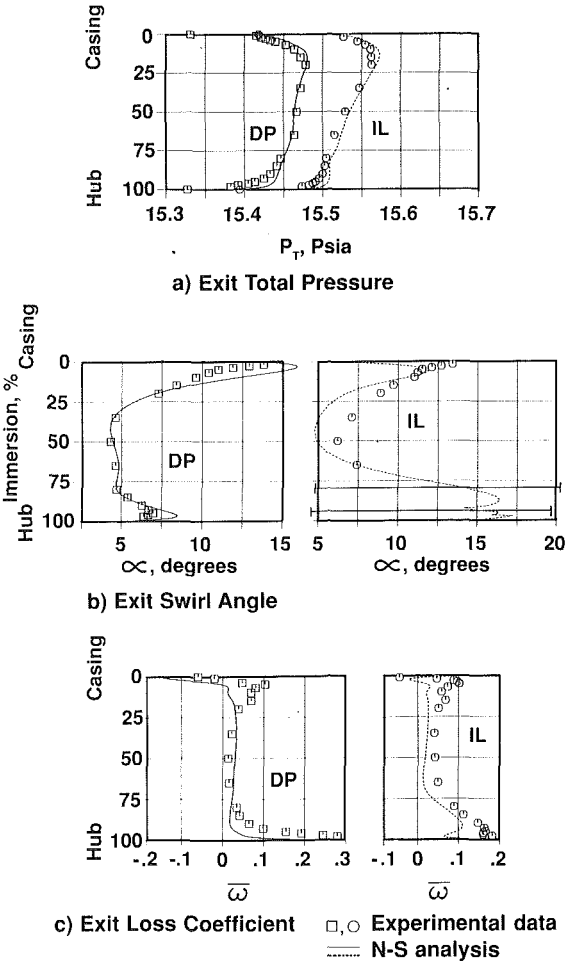

Fig. 6 Comparison of the computed and measured flowfield at the stator exit for design point (DP) and increased loading (IL); symbols are experimental; lines are three-dimensional computations

The prediction of a larger-than-measured region of flow separation near the hub at increased loading in Figs. 7(*c*, *d*) probably results for the following two reasons: the pumping effects of the downstream rotor, which could shrink the region of separation, was not modeled; and there was a greater uncertainty in inlet swirl data. Also, hub shroud leakage was not modeled. These impact swirl, loss and surface pressure.

Flow (swirl) Angles. Computed, circumferentially averaged, exit flow angles for *DP* and *IL* cases are compared with similar LSRC data in Fig. 6(*b*). At the design point, agreement is excellent all across the span. The measured underturning near both endwalls is well predicted. At increased loading, agreement in the midspan region is reasonably good. Note that large fluctuations were encountered in the increased loading experiments especially near the hub endwall where a large separated flow region was found. The actual spreads in the experimental flow angles are indicated where it was not practical to give a single value.

Loss Coefficients. The level and distribution of losses represent perhaps the most difficult consequence of a viscous flow to predict by three-dimensional Navier–Stokes codes. Losses are extremely sensitive to many effects present in the experiments, which may not be duplicated in the computations. Upstream rotor tip vortex, wake chopping and transport, and shroud leakage flow are but a few examples of mechanisms affecting losses. Therefore, in the turbomachinery CFD literature, there is often only an order-of-magnitude type comparison or no mention at all of predicted loss levels.

The radial distribution of loss coefficients at the stator exit is shown in Fig. 6(*c*) for *DP* and *IL* cases. Although there are some differences between measured and computed losses, we found acceptable agreement between them. Loss trends near the hub and casing endwalls are predicted well. What is most encouraging is the negative loss predictions near the casing surface as indicated by LSRC data. The negative loss phenomenon is often observed in experiments and is explained in terms of radially outward migration of relatively high-total-pressure fluid.

6.3 Airfoil-Surface Pressure Distributions. Computed vane-surface static pressures are compared with experimental data at four spanwise locations (5, 20, 80, and 95 percent immersions) for both design point and increased loading in Figs. 8(*a–h*). Since pitchline results were similar to 20 percent immersion results, they are not shown.

Design point computations in Figs. 8(*a–d*) are in excellent agreement with measurements. Leading edge and overall loading levels and diffusion rates on the suction surface are well predicted. Note that a small separation region is predicted for the 5 percent immersion case at about 80 percent chord (Fig. 8*a*). Apparently the very small leakage flow at the stator o.d. in the experiment was successful in preventing this corner flow separation. This was confirmed by other experiments. At 95 percent immersion, measurements are influenced by hub shroud leakage.

Increased loading computations (Figs. 8*e–h*) show higher loadings, in general, compared with experimental data. This

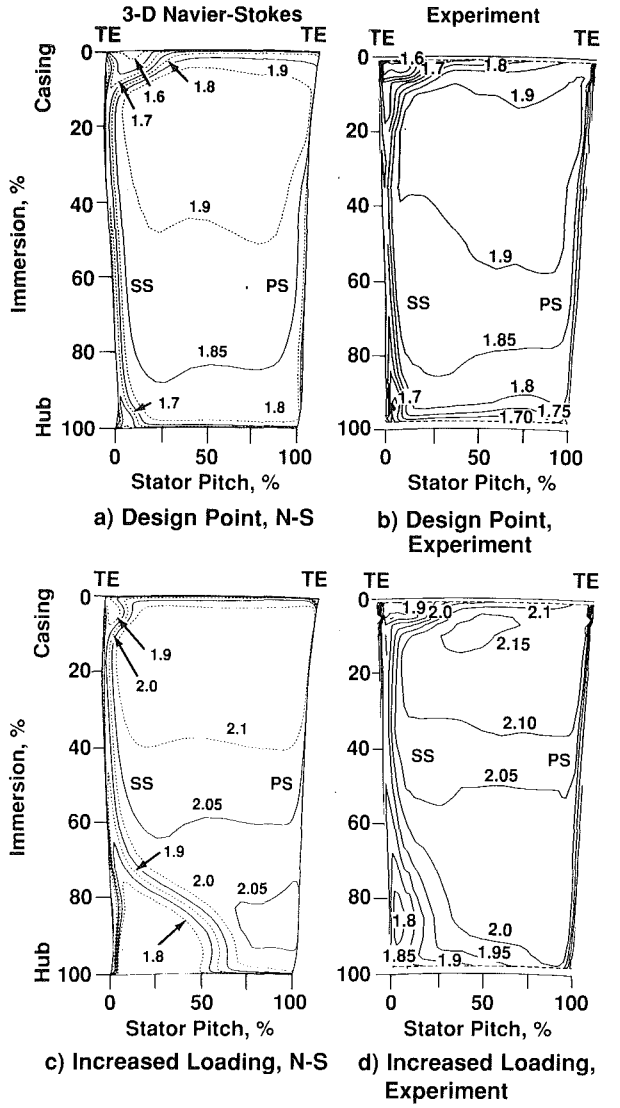

Fig. 7 Comparison of computed and measured contours of constant pressure coefficient at stator 3 exit

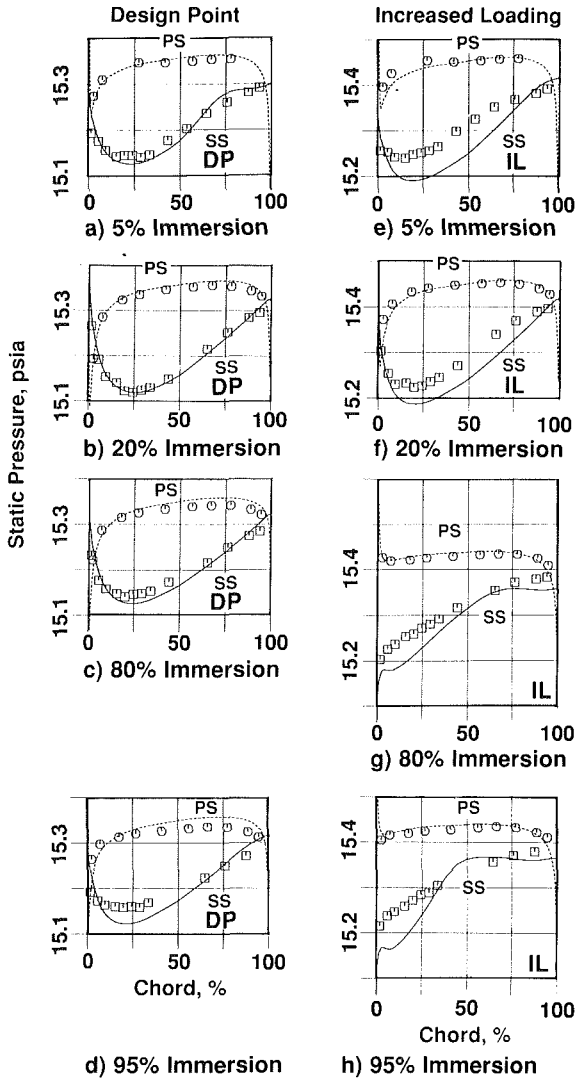

Fig. 8 Airfoil surface pressure distributions at design point and increased loading; computations compared with experiment; (*a–d*) design point (DP); (*e–h*) increased loading (IL)

is consistent with the increased turning found in Fig. 6(*b*). However, midspan leading edge loading and the diffusion rates, reflected by the slope of the static pressure on the suction surface, are in good agreement with measured data. One important consequence of increased loading, according to experimental data, is the large separation region on the airfoils near the hub. This, too, is predicted well as indicated by the flat portions of the static pressure curves on the suction surface (Figs. 8*g*, *h*).

The local spike in static pressure very near the trailing edges is caused by the standard wall functions used in the turbulence model and not by the Navier–Stokes numerics. Since the Navier–Stokes system successfully resolved the separated flow over a cylinder (Section 4.3), the numerical aspects of the solver are sound.

6.4 Development of Three-Dimensional Flowfield Through Stator Passage

Limiting Streamlines. Computed streamlines near suction, pressure, casing, and hub surfaces of the vane are presented in Fig. 9 for *DP* and *IL* cases. Flow information on grid nodes immediately adjacent to solid surfaces is used.

Suction surface streamlines for the design point indicate a relatively strong region of spanwise flow near the casing and a weaker one near the hub (Fig. 9*a*). At increased loading in Fig. 9(*b*), a smaller region of spanwise flow appears near the casing surface while a large region occupies the hub endwall. These are caused by the separated flow described earlier.

Computed streamlines near the pressure surface for the design point (Fig. 9*c*) and increased loading (Fig. 9*d*) reveal radially inward and outward flow regions coexisting along much of the span. The large radial shifts in streamlines near the casing in Fig. 9(*c*, *d*) and near the hub in Fig. 9(*d*) are caused mostly by classical secondary flows.

Near the casing endwall (Figs. 9*e*, *f*) the first streamline off the pressure surface shifts toward the suction surface. This shift is exaggerated at increased loading in Fig. 9(*f*). The first design-point streamline near the suction surface reveals the streamwise and pitchwise extent of the separation bubble.

Hub endwall streamlines show relatively weak secondary flow at the design point (Fig. 9*g*). However at increased loading in Fig. 9(*h*) the large region of separation is seen.

Separated Flow Near Endwalls. Regions of flow separation, identified by the limiting streamlines, were found in the vane passage. Enlarged views of velocity vectors in Fig. 10 indicate the strength and the extent of flow separation. Blade-to-blade and meridional plane views are shown.

Near the suction surface/casing corner at the design point

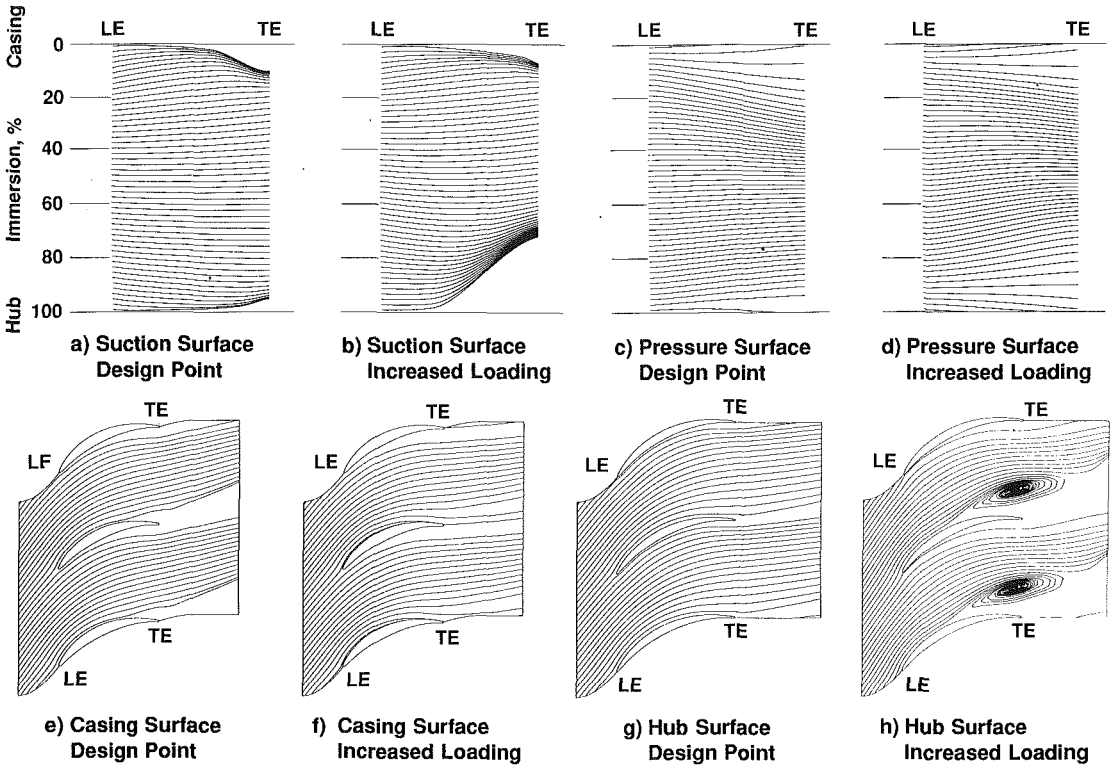

Fig. 9 Computed streamlines near vane and endwall surfaces

(Figs. 10*a*, *b*),the separated flow begins at about 70 percent axial chord and occupies a region from 0 to 13 percent pitch and 0 to 7.5 percent immersion. At increased loading in Figs. 10(*c*, *d*), this separation is nearly eliminated as flow is pushed outward by the hub blockage and the dynamic head increases.

The trend is opposite near the suction surface/hub corner. At the design point in Figs. 10(*e*, *f*), only a small separation bubble is found near the trailing edge. It starts at 86 percent chord, and is confined within 3 percent pitch and 4 percent span. At increased loading in Figs. 10(*g*, *h*), a large separated flow region, starting at 36 percent chord, occupies a region extending to 40 percent pitch and 30 percent span (70–100 percent immersion).

Radial and Circumferential Velocity Vectors. The complex nature of these flow vectors at the design point and increased loading levels is shown in Fig. 11. Projections of total velocity vectors onto crossflow planes at 95 percent axial chord location are shown. Both views are aft-looking-forward, with through-flow velocity vectors pointing mostly out of the page everywhere except within the separation regions described above. There is still a small amount of swirl in the fluid so midpitch, midspan tangential vectors are still present.

At design-point loading (Fig. 11*a*), a complex secondary flow pattern exists with radially outward and inward flow clearly visible from 0 to 42 percent immersion, especially near the vane surfaces. Increased tangential velocities (skew) are seen from 0 to 25 percent immersion. These would transport fluid and thus ethylene tracer-gas cores toward the pressure surface. Along the suction and pressure surface, there are three stagnation points across which radial velocity components change direction.

A different flow pattern develops at increased loading as the large region of flow separation near the hub promotes spanwise secondary flow (Fig. 11*b*). Radially outward flow, especially below the pitchline, is much stronger here than anywhere at the design point. Only one stagnation point is present on the suction surface. There are three stagnation points on the pressure surface, as before, except that radial velocities are stronger here, as well. The secondary flow features near the pressure surface from 0 to 40 percent immersion remain unchanged.

The radial and tangential velocities are strongly influenced by the location, strength, and extent of secondary flows and separated regions.

Radial Velocities Near Vane Surfaces. Streamwise development of radial velocities along the stator span between leading and trailing edges is presented in Fig. 12. Contours of radial velocity on grid nodes right next to the vane surfaces are projected on meridional planes for the *DP* and *IL* cases.

Significant radial velocities are developed as far upstream as 10 percent axial chord. There are multiple cells, each one containing positive or negative radial velocity contours, along both suction and pressure surfaces. At the design point, peak radial velocities on the pressure surface are found at about 20 percent immersion (Fig. 12*b*). At increased loading, peak radial velocities are above the large separation bubble at about 85 percent immersion and 70 percent axial chord near the suction surface (Fig. 12*c*).

Development of Radial Velocities Through the Stator Passage. The three-dimensional Navier–Stokes computations predict sizable radial velocities in the stator passage, as shown in Fig. 13 for the two loading levels. Both radially inward and outward velocities are present and appear in large pocket areas in the vicinity of the airfoil surfaces. These pockets are well away from the passage corners.

At the design point in Figs. 13(*a–e*), the radial velocities are mostly caused by the more classical secondary flows (compare with Fig. 11).

At increased loading in Figs. 13(*f–i*), a pocket of radially outward flow in the suction-surface hub region is seen to grow along the span. This results from the boundary layer separation found at increased loading and discussed in Section 6.4. The size of this blockage region and the magnitude of the radially outward flow may be somewhat overpredicted by the three-dimensional computations, but this does not change the principal flow features.

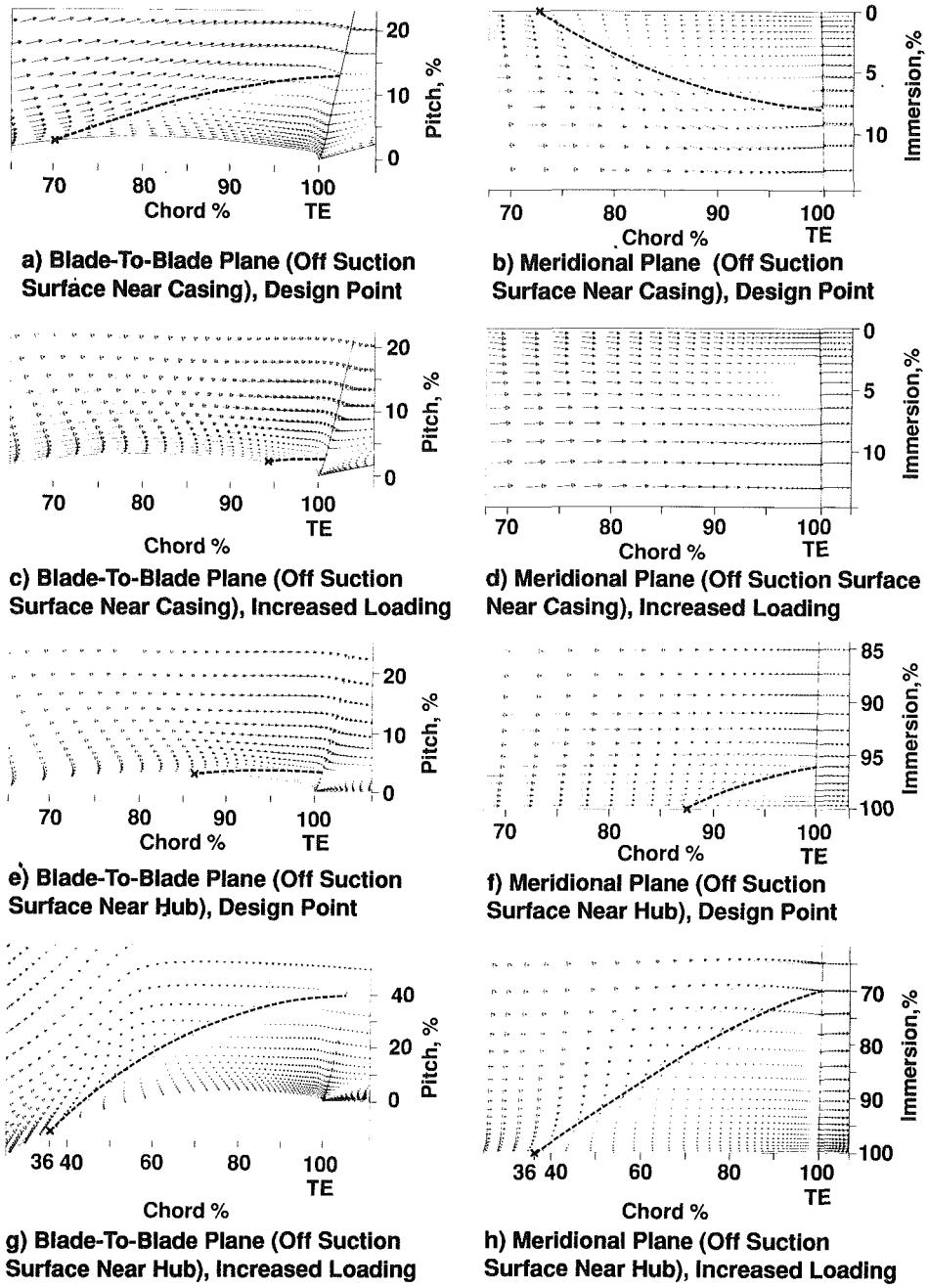

a) Blade-To-Blade Plane (Off Suction Surface Near Casing), Design Point

b) Meridional Plane (Off Suction Surface Near Casing), Design Point

c) Blade-To-Blade Plane (Off Suction Surface Near Casing), Increased Loading

d) Meridional Plane (Off Suction Surface Near Casing), Increased Loading

e) Blade-To-Blade Plane (Off Suction Surface Near Hub), Design Point

f) Meridional Plane (Off Suction Surface Near Hub), Design Point

g) Blade-To-Blade Plane (Off Suction Surface Near Hub), Increased Loading

h) Meridional Plane (Off Suction Surface Near Hub), Increased Loading

Fig. 10 Separated flow near endwalls; boundaries of separated flow regions are marked by dashed lines; "X" marks the point of separation

Some pockets have radial velocities that are quite large. Peak values at the design point are +20 and −16 ft/sec (+ is radially outward). These values are +10 and −8 percent of the rotor pitch velocity. At increased loading, the peak values are +39 and −16 ft/sec or +18 and −8 percent of U_p.

7.0 Mixing in Axial Compressors—Conclusions From Three-Dimensional Computations and Experiment

In this section, we will show that both secondary flow and turbulent diffusion can contribute significantly to both spanwise (radial) and tangential mixing in an axial-flow compressor. The picture presented will be one of convective and diffusive fluxes interacting, in some areas augmenting each other and in other areas opposing each other.

7.1 The Identification Problem. Although the identification of secondary flows by ethylene core motion is straightforward, the identification of secondary flows and turbulent diffusion by contour distortion is more open to question. This identification problem is illustrated in Fig. 14 where, in the extreme, fluid injected at 7 percent immersion and 51 percent pitch upstream of the stator at the "X" ends up at 35 percent immersion, 98 percent pitch downstream at the furthermost extent of the contour. The motion of Core 4 from "X" to "O" in the tangential direction toward the pressure surface and in the radially outward direction is reasonably attributed to secondary flow. But what causes the large radially inward contour distortion along the pressure surface?

In their Discussion of the Wisler et al. (1987) paper, Gallimore and Cumpsty attributed the radial distortion of Contour 4 to local anisotropic turbulent diffusion very near the pressure surface. They noticed that the radial motion of Core 4 was

small and radially outward while the contour distortion was radially inward. They also noticed that another contour, oblong Contour 29 (see Fig. 16*e*) on the pressure surface, had little radial core motion. From this, they reasoned that secondary flows were too small and in the wrong direction to cause contour distortion and radial mixing.

Likewise, Vittal and Sehra in their Discussion (ibid.) concluded that the skewed contours were probably due to nonuniform gradients in turbulent diffusion.

In their Authors' Closure, Wisler et al. attributed the spanwise shape of Contour 4 to the combined effects of secondary flow and turbulent diffusion. They reasoned from their data

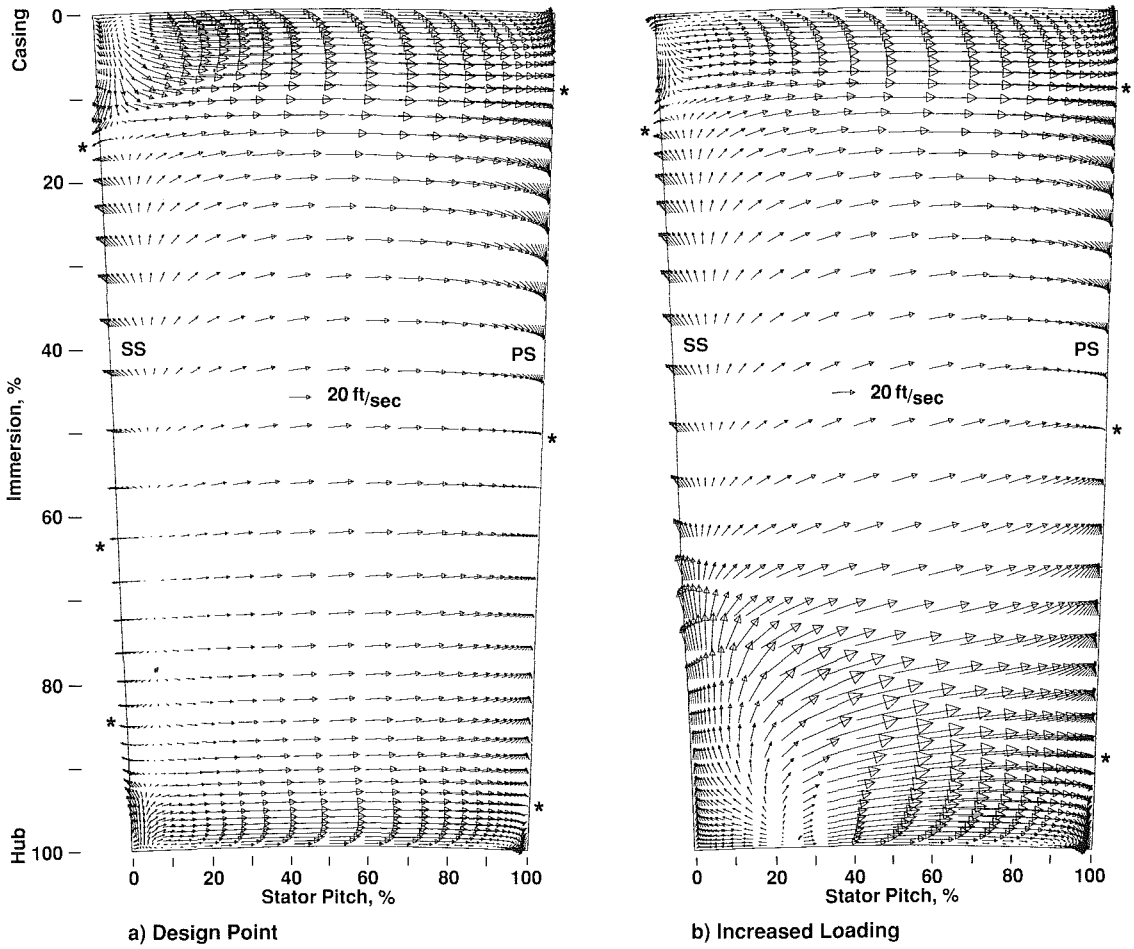

Fig. 11 Computed velocity vectors (resultant of radial and tangential components) show secondary flowfield in crossflow plane at 95 percent chord; view is aft looking forward; throughflow velocity (not shown) is mostly out of page. Because this projection is not a true Trefftz plane, a small contribution of throughflow velocity to swirl exists. * indicates a stagnation point in the *r*, θ plane.

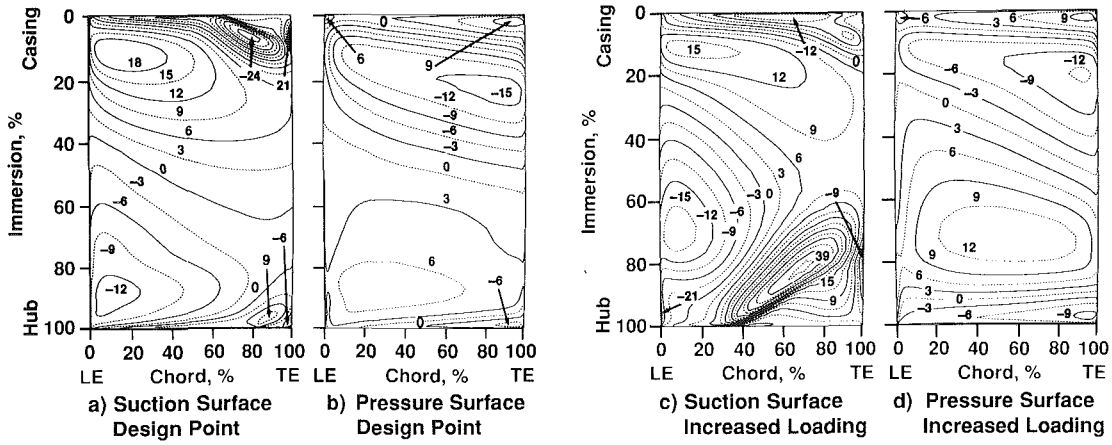

Fig. 12 Computed radial velocities near vane surfaces in meridional plane, contours of constant V_r, + = outward, − = inward, Δ = 0.91 m/s (3 ft/sec)

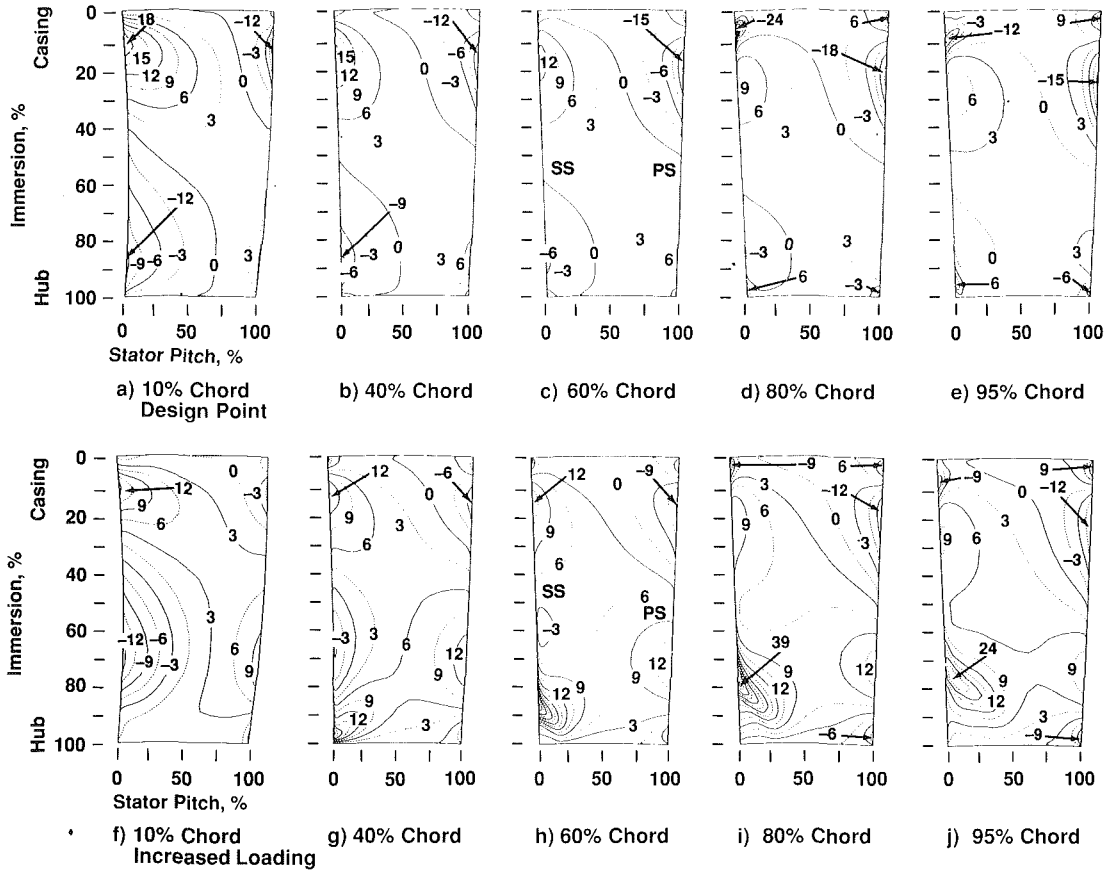

Fig. 13 Development of radial velocities through stator passage in crossflow plane, contours of constant V_r, + = outward, − = inward, Δ = 0.91 m/s (3 ft/sec), (*a–e*) design point, (*f–j*) increased loading

that turbulent diffusion could account for only about one-half of the radially inward spreading of Contour 4. The rest was attributed to the radial secondary flow probably resulting from the strong tangential motion impinging on the vane pressure surface. This would create a "type of stagnation point at (about) 10 percent immersion" (ibid.) with radial spreading around it, thus explaining the lack of aforementioned Core 29 motion and the oblong symmetrical spreading of its Contours.

Furthermore they reasoned that a core, like Core 4 in Fig. 14, could be entrained in one area of secondary flow and thus travel in a direction different from its diffusing contours, which could become entrained in and distorted by another area of secondary flow.

This is a difficult issue. However, three-dimensional Navier–Stokes analyses and new experimental data enable us now to understand better the cause of these distorted contours.

7.2 Mixing in Compressors—Confirmation of Previous Results. The three-dimensional Navier–Stokes solutions are compared with the experimental results for Compressor I. A consistent picture of mixing emerges that confirms previous interpretations of ethylene data and provides new insight into the complex fluid motion through the stator as loading increases.

Addressing the Identification Problem. The experimental and computational comparisons made in Fig. 15 allow us to explain the identification problem. The tracer-gas results were taken from Wisler et al. (1987), Figs. 5 and 6. The computations are from Figs. 13(*d*, *i*) of the present paper.

For the design point (Fig. 15*a*), we first compare the N–S computed contours of radial velocity to the experimental core motion (X's to O's) along the midpitch radial injection line

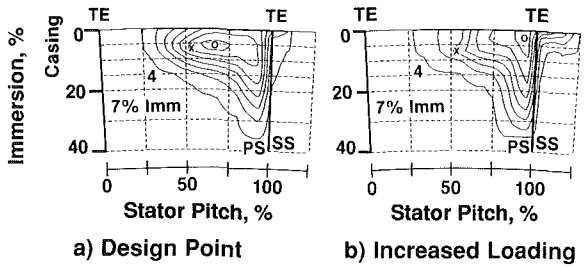

Fig. 14 Ethylene tracer-gas Contour 4 from Wisler et al. (1987) illustrates the identification problem, injection upstream of stator 3 at "x", sampling downstream; see Fig. 3. Contours surrounding core of max = 95 percent, min = 5 percent, Δ = 15 percent

C–H. It becomes immediately clear that the tracer gas was injected all across the span into a midpitch region having no radial velocity. Even as the cores near the casing are transported circumferentially toward the pressure surface by the tangential secondary flow previously shown in Fig. 11(*a*), they are transported into a region of little radial velocity as shown by the N–S computations. Only those cores very near the casing that get transported circumferentially to a region near the pressure surface experience the outward radial flow in the corner and move accordingly. This explains why there is little radial core motion for these points.

Near the hub, the cross-passage secondary flow from the boundary layer skew (see Fig. 11*a*) transports the cores a small amount toward the pressure surface. Very near the hub, the stator shroud leakage (not modeled) transports that core toward the suction surface.

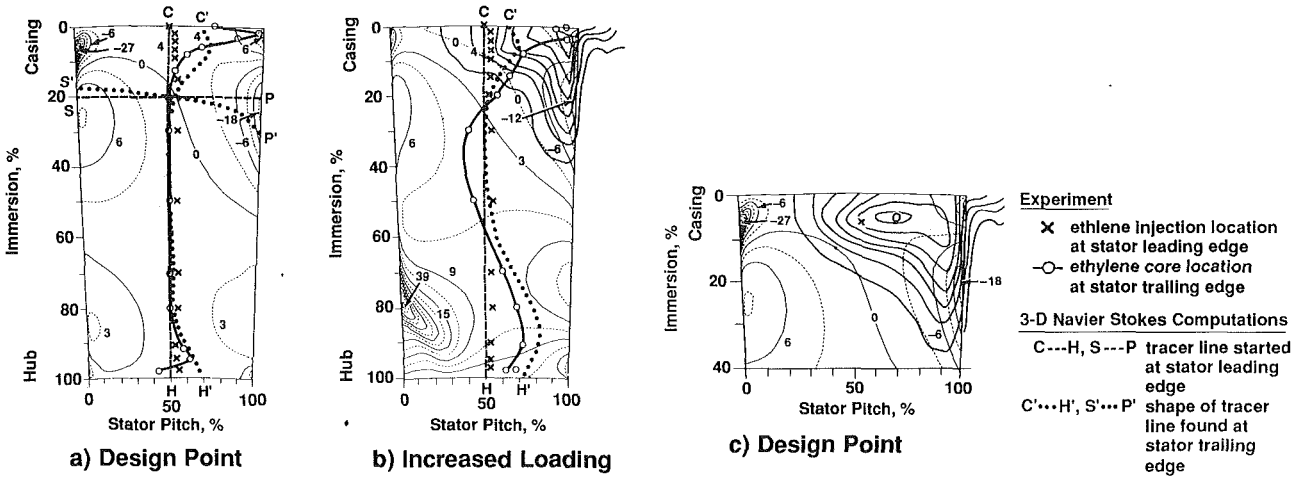

Fig. 15 Comparisons of three-dimensional N-S computations and experiment show the effects of spanwise and circumferential secondary flows as mechanisms for distorting tracer lines and contours. Computations of contours of constant radial velocity from Fig. 13 (*d, i*). + = outward, − = inward. Experimental values from Wisler et al. (1987), Figs. 5 and 6.

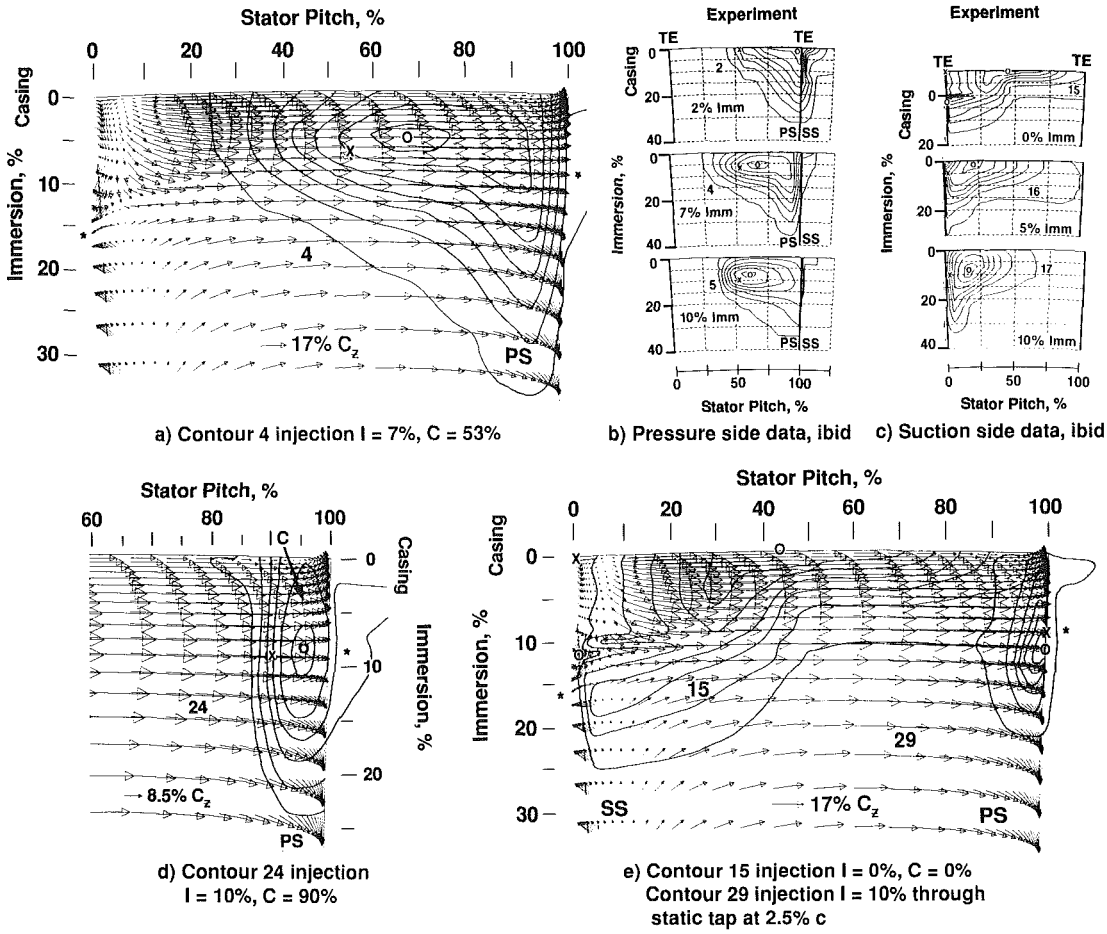

Fig. 16 Design point comparison of the three-dimensional N-S computations and experiment for the outer annulus region. Computed vectors (arrows) at 95 percent chord; superimposed experimental tracer-gas contours of 95 percent max, 5 percent min, Δ = 15 percent, x = injection *at stator 3 leading edge, 0 = sampling at trailing edge; * indicates a* stagnation point.

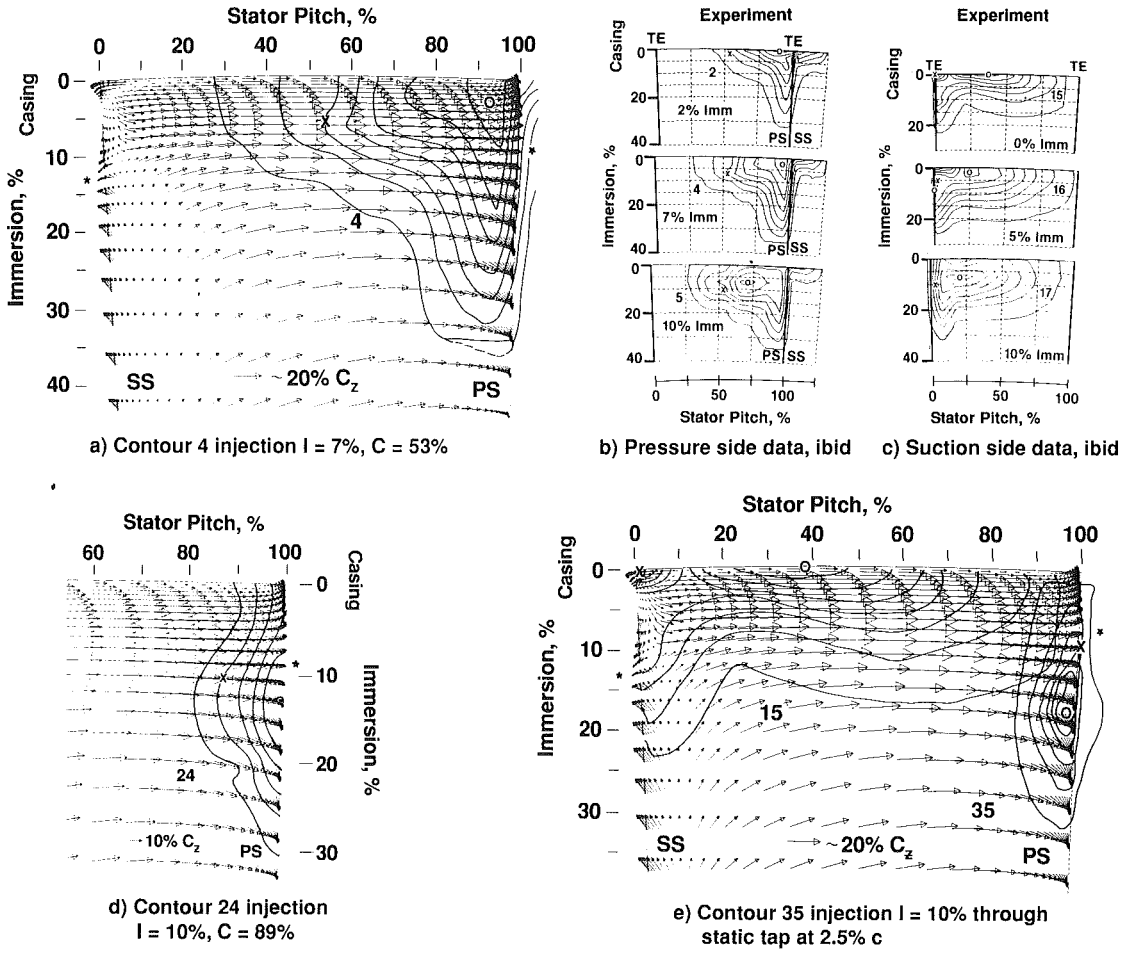

Fig. 17 Increased loading comparison of three-dimensional N–S computations and experiment for the outer annulus region, computed vectors (arrows) at 95 percent chord, superimposed experimental tracer-gas contours of 95 percent max, 5 percent min, Δ = 15 percent, x = injection at stator 3 leading edge, 0 = sampling at trailing edge; * indicates a stagnation point.

A midpitch radial tracer line was also computed using the three-dimensional Navier–Stokes analysis (line C–H to C'–H' in Figs. 15*a*, *b*). It is in reasonable agreement with experiment except locally very near both endwalls. Very near the casing the measured boundary layer skew effects are larger than computed. The small clearance between the stator o.d. and the casing (not modeled) allows leakage flow through that region. This would give more circumferential core motion toward the pressure surface. Very near the hub the shroud leakage effects explain the differences.

We next turn our attention in Fig. 15(*a*) to tracking computationally a tangential line through the stator passage. A straight line S–P from the suction-to-pressure surface at a constant 20 percent immersion was started at the leading edge. At 95 percent chord it has distorted from line S–P to line S'–P', showing that fluid particles near the pressure surface can be transported radially by secondary flow a distance equal to 10 percent of span. This occurs well away from the airfoil/endwall corner regions and leads to an explanation of spanwise contour distortion.

Finally, tracer gas Contour 4 is superimposed on the computations in Figs. 15(*b*, *c*). The motion of Contour 4 is clear. As the fluid near the casing diffuses about the circumferentially transported core, it becomes entrained in the pocket of secondary flow along the pressure surface, shown by the N–S computations. This pulls the contours radially inward. Experimental Contour 4 shows radially inward distortion exactly where the computed, radially inward, secondary flow is located. The contribution of classical-type secondary flow to the distortion of Contour 4 near the pressure surface is confirmed. Turbulent diffusion also contributes to the contour distortion, but this is agreed upon by all.

At increased loading in Fig. 15(*b*), the same overall picture is present near the casing. In the hub area, the large region of separated flow pushes the injection line toward the pressure surface. Predicted radial velocities that are larger than measured in the midpitch region are probably caused by the overprediction of the separated region in the hub, as explained in Section 6.2.

Pressure Surface/Casing Region. The flow in this region was the subject of much discussion and controversy in the Wisler et al. (1987) paper. This discussion centered around the Identification Problem already described in Section 7.1 above. Now however, the three-dimensional Navier–Stokes solution provides additional insight for resolving this controversy.

Comparisons of the computations and experiments are made in Figs. 16 and 17 for the design point and increased loading conditions. The computations in this corner region show a strong cross-passage motion impinging on the pressure surface with a stagnation point at about 10 percent immersion. The

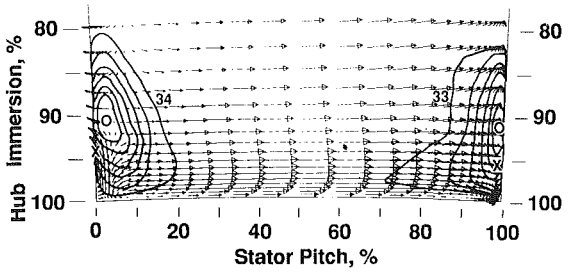

a) Contour 34 injection though static tap 2.5% c, I = 95%
Contour 33 injection through static tap 2.5% c, I = 95%

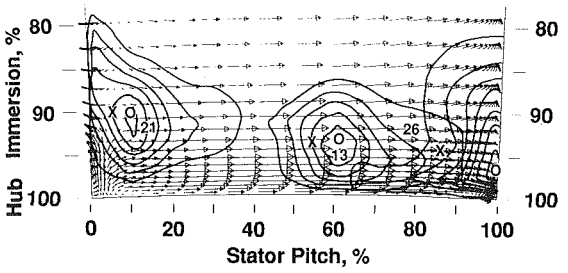

b) Contour 21 injection I = 90%, C = 3%
Contour 13 injection I = 95%, C = 53%
Contour 26 injection I = 95%, C = 89%

Fig. 18 Design point comparison of three-dimensional N-S computations and experiment for the inner annulus region. Computed vectors at 95 percent chord, experimental tracer-gas contours of 95 percent max, 5 percent min, Δ = 15 percent, x = injection at stator 3 leading edge, 0 = sampling at trailing edge.

flow proceeds radially outward toward the casing and radially inward toward the hub around this stagnation point.

The fluid motion predicted by the three-dimensional Navier–Stokes computations is in complete agreement with the experimental data. In Figs. 16(*a*) and 17(*a*), experimental Cores 4 injected at 7 percent immersion move circumferentially. At increased loading in Fig. 17(*a*), Core 4 gets transported near the pressure surface where it is then pushed outwardly into the corner. The motion of Cores 2 and 5 in Figs. 16(*b*) and 17(*b*) is also explained by the computations.

For both loading levels, the distorted shapes of Contours 4 in Figs. 16(*a*) and 17(*a*) are also predicted by the computations. Diffusing Contours 4 get transported circumferentially by the cross-passage flow. Once they diffuse beyond 10 percent immersion, they enter the region of radially inward secondary flow predicted near the pressure surface. The major areas of radially inward distortion of experimental Contours 4 occur where the predicted radially inward secondary flows occur. These computed spanwise velocities persist until about 40 percent immersion. In this case, the tangential secondary flow (mixing) is important because it sets up the radial secondary flow as it impinges on the pressure surface. Consequently, the arrows in Figs. 5 and 6 of Wisler et al. (1987) are not misleading.

The magnitude of these computed radially inward, secondary flow velocities is about 8 percent of the pitchline wheel speed. This would transport the fluid a distance equal to about 9–10 percent of the span in a region well away from the endwall corner region. These magnitudes are the same as those estimated experimentally by Wisler et al. (1987), as needed to explain at least half of the radial distortion of the contours. Consequently, both secondary flow and diffusion act to create the final contour shapes.

The motions of experimental Cores and Contours 24, 29, and 35 in Figs. 16(*d*, *e*) and 17(*d*, *e*) are also explained for both loading levels. Cores 24 were injected at 90 percent pitch and Cores 29 and 35 were injected through a static tap on the pressure surface near the leading edge at 10 percent immersion. For the design point in Figs. 16(*d*, *e*), this ethylene injection is just at the location of the stagnation point on the pressure surface as shown by the computations. Thus the cores remain trapped in the stagnation region. The contours, while being flattened by the cross-passage flow pushing toward the pressure surface, are spread radially inward by secondary flow. Anisotropic turbulence very near the pressure surface would also contribute to this spreading.

A pronounced outward stretching of Contour 24 is marked by the letter "C" in Fig. 16(*d*). We think this stretching results primarily from the pressure-surface-to-suction-surface leakage through the clearance over the stator o.d. and not primarily by anisotropic turbulence. As seen in the figure, ethylene was found in the suction-surface region. Anisotropic turbulence would go to zero in both directions in this corner and therefore not cause the contour to appear to disappear into the casing. A similar observation is made for Contours 29, 24, and 35 in Figs. 16(*e*), 17(*d*), and 17(*e*), respectively.

At increased loading in Figs. 17(*d*) and 17(*e*), the same general description applies. Cores 24 and 35 become more entrained in the radially inward flow and move accordingly.

Suction Surface/Casing Region. The flow in this region is presented in Figs. 16(*e*) and 17(*e*) for the two loading levels.

The three-dimensional computations at the design point (Fig. 16*e*) show flow moving both circumferentially and radially from the corner region. This explains the motion of experimental split-Core 15, which is marked on the computation plot. In the radial direction, Core 15 is seen to stop at about 12 percent immersion. This is just about where the three-dimensional computations predict that the flow would be stopped by the radially outward secondary flow pushing up from below. These two flows then merge and move circumferentially.

As loading increases in Fig. 17(*e*), the stagnation point on the suction surface moves from 16 percent immersion to 13 percent immersion. As a result, the radially inward motions of Contour 15 and split-Core 15 are now contained at about 10 percent immersion by the radially outward secondary flow from below.

Note that at both loading levels in Figs. 16(*e*) and 17(*e*) (except very near the suction surface), the experimental Contours appear to be prevented from diffusing past 20 percent immersion by the radially outward flow pushing up from below. The strong cross-passage flow gives large circumferential distortion to the contours.

The development of the flowfield in this suction-surface/casing-corner region is more complex than indicated by looking only at Figs. 16 and 17. The reader should examine Figs. 12 and 13 to see the strong radially outward flow over the first 60 percent chord, followed by the radially inward flow around the local corner separation near the trailing edge. This causes the cores to move a small amount radially outward as they are carried circumferentially.

Pressure Surface/Hub Region. This flow is shown in Figs. 18(*a*, *b*) and 19(*a*, *b*). The three-dimensional computations for both loading levels predict circumferential motion toward the pressure surface forming stagnation points at 95 percent immersion for the design point and 89 percent immersion for increased loading.

At the design point in Fig. 18(*a*), test point 33 is injected through a static tap at 95 percent immersion, very near the stagnation point. Its core moves radially outward a small amount and its contour is pressed into an oblong shape. Contour 26 is also pressed into an oblong shape. Radial flows are weak.

At increased loading in Fig. 19(*a*), the stagnation point has moved to 89 percent immersion. The strong cross-passage flow, produced by the separated region on the suction surface, causes

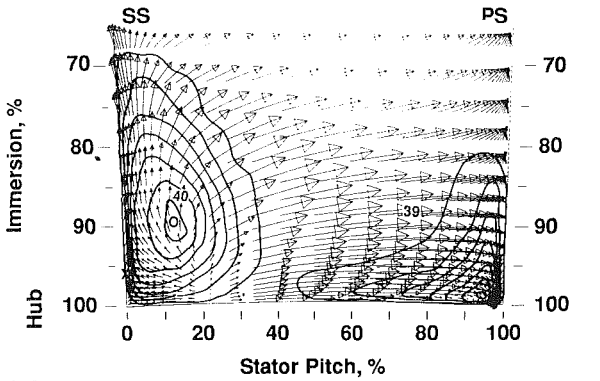

a) Contour 40 injection through static tap 2.5%c, I = 95%
Contour 39 injection through static tap 2.5%c, I = 95%

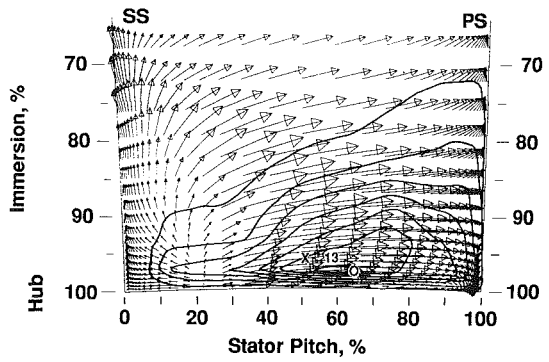

b) Contour 13 injections I = 95%, C = 53%

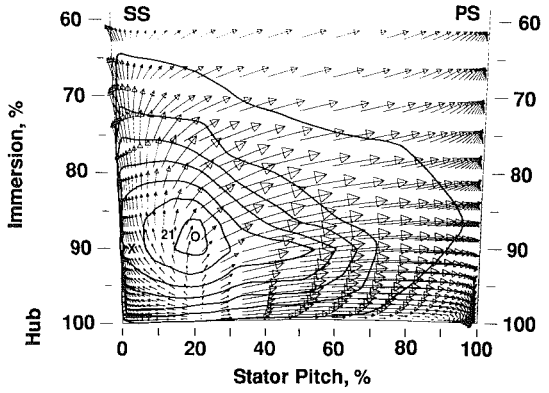

c) Contour 21 injection I = 90%, C = 3%

Fig. 19 Increased loading comparison of three-dimensional N-S computations and experiment for the inner annulus region. Computed vectors at 95 percent chord, experimental tracer-gas contours of 95 percent max, 5 percent min, Δ = 15 percent, x = injection at stator 3 leading edge, 0 = sampling at trailing edge.

strong radially inward and outward flow about the stagnation point at 89 percent immersion. The Core 39 moves to the hub. The contour is pressed into a boomerang shape by the secondary flow and any anisotropic turbulence present. The contour diffuses and is transported radially inward and then toward the suction surface as the computational arrows show. Since stator hub–shroud leakage was not modeled computationally, the full magnitude of this measured, reverse cross-passage flow is not predicted. In addition, Contour 39 diffuses radially outward, and after passing about 89 percent immersion, encounters significant outward secondary flow.

Contour 13, in Fig. 19(*b*), shows large distortion. The computed cross-passage and radially outward velocity vectors can explain much of the distortion.

Suction Surface/Hub Region. This flow is shown in Figs. 18(*a*, *b*) and 19(*a*, *c*) for the two loading levels. Again, the reader should refer to Figs. 12 and 13 for a complete description of the development of this complex velocity field at increased loading.

The three-dimensional Navier–Stokes computations predict radially outward flow from the corner along the suction surface. For the design point in Figs. 18(*a*, *b*) this outward flow is quite weak. It proceeds to about 88 percent immersion where it is stopped by inward flow from above.

At increased loading in Figs. 19(*a*, *c*), there is a drastic difference with very strong radially outward and circumferential flow. The distortion of diffusing Contours 40 and 21 and their Core motion are readily explained by examining the computed vectors.

7.3 Spanwise Mixing by BOTH Secondary Flow and Turbulent Diffusion: New Data. Ethylene tracer-gas measurements were made across Stator 3 in Compressor II at the design point. Compressor II had more discernible spanwise secondary flows than Compressor I. This has given more insight into the identification problem for Compressor II and allowed an explanation of virtually all of the contour patterns in terms of combined secondary flow and turbulent diffusion.

For ease of description, Contours having elliptical-type shapes will be referred to as having a major axis along the direction of stretching and a minor axis normal to it. It is assumed that motion of the Core is the final arbiter for the existence of secondary flow.

Secondary Flow. In this section, we deal with evidence of secondary flow as demonstrated by core motion. Ethylene was injected very near the pressure surface at 10 percent, 15 percent, and 20 percent radial immersion. The results are presented in Fig. 20(*a–c*). Large spanwise core motion, clearly indicating secondary flow, and large contour stretching are evident at each immersion.

For injection at 10 percent immersion in Fig. 20(*a*), Core A moves both radially outward from 10 percent to 0 percent immersion and tangentially toward the suction surface. Contour A spreads radially inward and along the casing.

The motion of Cores B and C and the spanwise stretching of their Contours into elliptical shapes in Figs. 20(*b*, *c*) are particularly instructive. These injection points at 15 percent and 20 percent immersion are well away from the endwall/airfoil-corner region. Cores B and C are transported inwardly along the pressure surface with Core C moving a distance along the major axis equal to 10–11 percent of the annulus height. This is clearly directional and results from deterministic secondary flow.

The shape of Contour C about the core in Fig. 20(*c*) is not symmetrical. We reason that, along the major axis in the inward direction, secondary flow (shown by core motion) acts to distort the contour. In the outward direction, ethylene diffusing from the "X" injection point eventually becomes entrained in the region of secondary flow shown in Fig. 20(*a*). This adds to the stretching in the region marked "C1."

In Figs. 20(*a*, *d*), ethylene injection at 10 percent immersion and 99 percent and 80 percent stator pitch respectively gives patterns very similar to those described in Fig. 14 for Compressor I; i.e., a contour at the endwall/airfoil corner with stretching in both directions and outward core motion in the direction opposite to inward contour stretching along the pressure surface. However, the interpretation of the data for Compressor II is now more straightforward. The motion of Cores A and E in Figs. 20(*a*, *d*) is self-evident. Their contours diffuse into the secondary flow region described in Figs. 20(*b*, *c*) and are stretched inwardly along the pressure surface. Near the casing, diffusing Contour E in Fig. 20(*d*) is stretched toward the suction surface as it becomes entrained in the cross-passage secondary flow shown by the motion of Core F in the figure.

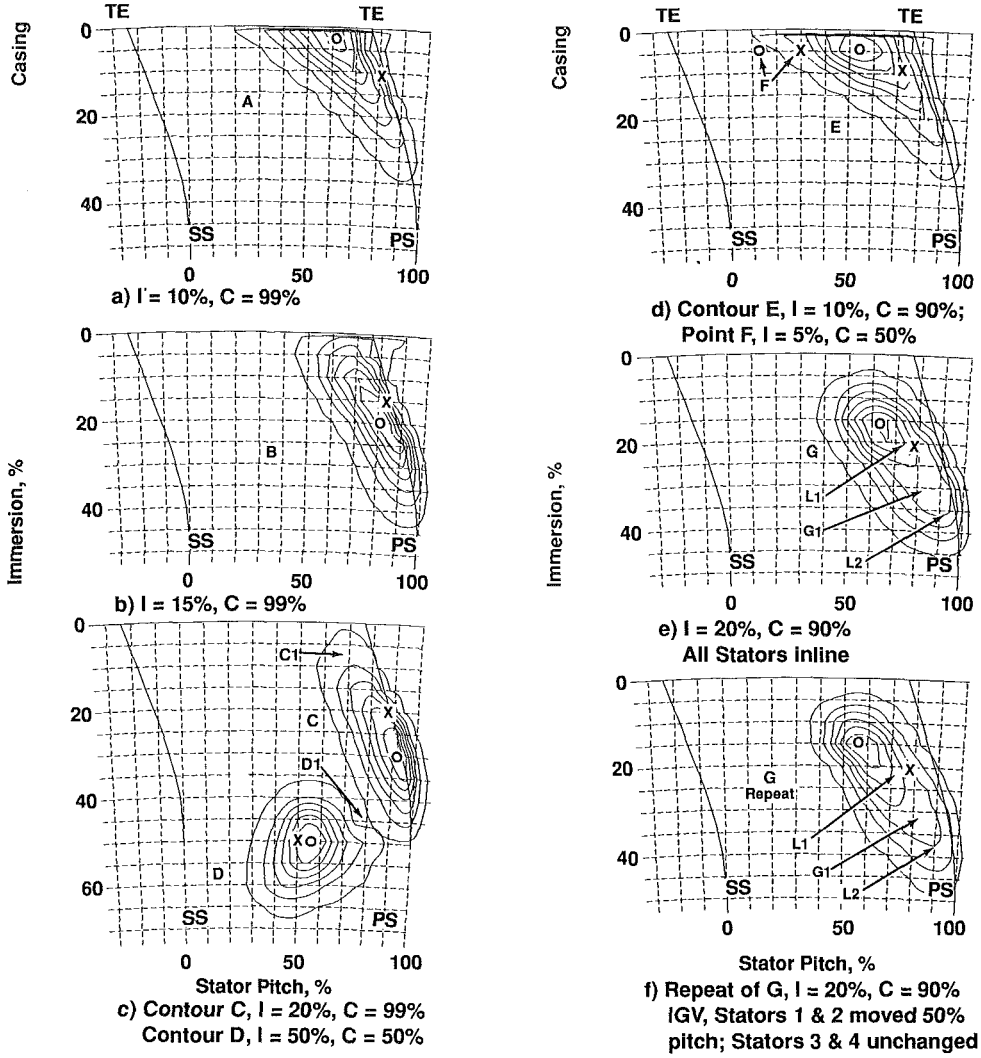

Fig. 20 Ethylene tracer-gas measurements for Compressor II show spanwise mixing by combined effects of secondary flow and turbulent diffusion; injection at stator 3 leading edge at "X," sampling downstream at "O," contours of max = 95 percent, min = 5 percent, Δ = 15 percent

Test point G in Fig. 2(*e*) was injected at 20 percent immersion and 80 percent stator pitch. Along the major axis, we have another example of outward core motion and inward contour distortion. The outward core motion is clear evidence of secondary flow. We think that in the inward direction the diffusing Contour G becomes entrained in the inward region of secondary flow shown in Figs. 20(*b*, *c*) and is transported inward. The large region between L1 and L2, annotated as G1 in Fig. 20(*e*) dominates the distortion. It is well away from the endwall/airfoil corner region and reasonably away from the pressure surface.

Test point G was repeated to evaluate any effects of upstream stator wakes as the direct cause of Contour G stretching. The IGV's and Stators 1 and 2 were moved circumferentially 50 percent of the stator pitch while Stators 3 and 4 were unchanged. The results, presented in Fig. 20(*f*), are nearly identical to those in Fig. 20(*e*), indicating that time-resolved unsteadiness in the upstream stator wakes was not responsible for Contour G stretching in region G1.

Turbulent Diffusion. The ethylene tracer-gas results from Compressor II in Fig. 20 show diffusion effects everywhere, as evidenced by the enlarging contours. This is similar to the results for Compressor I. Clearly turbulent diffusion is an important mixing mechanism.

Ethylene injection point D at midpitch and midspan in Fig. 20(*c*) shows almost no core motion, indicating that diffusion dominates in this region. The depression at D1 in the nearly symmetric Contour D probably results from the secondary flow seen by test point C.

Diffusion also dominates along the minor axis of each of the contours B, C, G, and G-repeat in Fig. 20(*b*, *c*, *e*, *f*), respectively. For these contours, it is observed that the distances along the minor axis from the "X" injection point to the 5 percent contour line are nearly equal to each other and to the radius of Contour D in Fig. 20c. This implies nearly equal, average unsteadiness velocities in these directions throughout the stator passage.

Fully three-dimensional hot-wire measurements were made in Compressor II at the trailing edge plane of Stator 3 in a grid covering the contour regions in Fig. 20. Away from airfoil and endwall surfaces, rms radial and tangential total unsteadiness (periodic and random) velocities were found to be nearly equal for this highly loaded compressor. This is consistent with the abovementioned observation that spreading distances along the minor axis are nearly equal to the spreading distance for symmetric Contour D in Fig. 20(*c*). The probe was too large to make meaningful measurements of any anisotropic turbulence very near the pressure surface.

Mixing. Both secondary flow and turbulent diffusion were

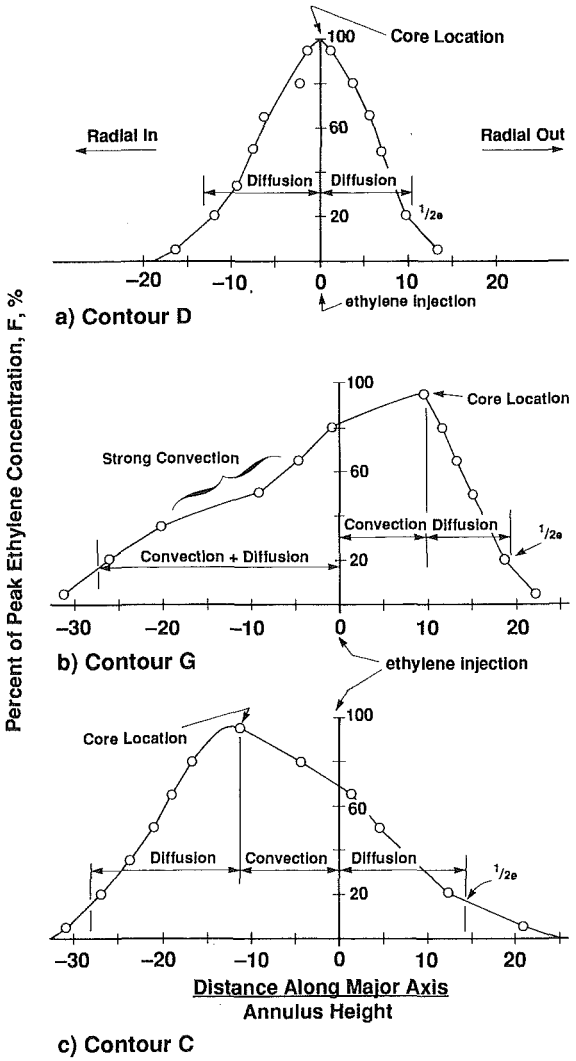

Fig. 21 Ethylene concentration as a function of distance from injection location shows regions of spanwise (radial) convection and diffusion

shown to be present in Compressor II. Their relative contributions to mixing can now be estimated from the data in Fig. 20. Contours C, D, and G are replotted in Fig. 21 as distribution functions of ethylene concentration to show the extent of the mixing.

In Fig. 21(*a*), the shapes of the experimental distribution functions for Contour D reasonably approximate those for classical-type turbulent diffusion. This means that along these directions diffusion dominates.

In Fig. 21(*b*), we first examine the data along the major axis on the radially outward side of the injection point for Contour G. The areas of convection and diffusion are clearly shown to be of the same order of magnitude. Most of the mixing is complete by the 1/2*e* point.

Next we examine the data in Fig. 21(*b*) on the radially inward side of the injection point where large contour distortion occurs. This could be caused by either convective or diffusive effects, or both. We think that both are acting and that diffusing Contour G becomes entrained in the region of secondary flow previously shown in Figs. 20(*b*, *c*) and is transported inward as it diffuses. Although taken at the trailing edge plane, hot-wire data do provide some evidence for nearly isotropic unsteadiness away from solid surfaces. If true through the blade passage, this would imply diffusion rates along the major axis that are more like those along the minor axis.

The distribution function showing the spanwise extent of mixing for Contour C in Fig. 21(*c*) also has large convective and diffusive effects.

8.0 Discussion

This discussion focuses on the degree of three dimensionality of the flow, the role of convection and diffusion in the mixing process, the adequacy of time-averaged unsteady measurements as boundary conditions in certain CFD simulations, and the enormous potential of combining the use of CFD and LSRC-type facilities.

Flow in the modern stator blading shown in this paper can be highly three-dimensional even for design point loading levels. This three-dimensionality is magnified significantly and spread further into the passage with increased loading. The mixing process that results is likewise complex.

Mixing has previously been described as though it is dominated exclusively by either turbulent diffusion or secondary flow. Although this may be convenient for limited modeling, we feel that both mechanisms are important and need to be included to simulate the detailed flow physics.

Certainly there are diffusion and unsteady effects, tip vortex effects, wake effects, large-scale turbulence effects, and shock wave effects in supersonic flow that contribute to mixing. Certainly, there is anisotropic diffusion very near surfaces. But certainly too, it has been shown that secondary flows can contribute to mixing in a significant way, in both the cross-passage and spanwise directions.

Diffusion is always present in turbulent flow and is naturally anisotropic in the immediate vicinity of solid surfaces. Convective fluxes, when present, may be larger or smaller than their diffusive counterparts, and may be in the same or opposing directions. The magnitude and direction of these fluxes depend on many parameters including airfoil geometry, loading level, and particular location within a passage. This, after all, is the essence of solving the Navier–Stokes equations in CFD codes where the convective and diffusive fluxes are considered across each control surface of every finite volume within a computation domain.

We feel that to abandon, permanently, the radial and tangential convective flux terms, in the belief that diffusive ones suffice, is an oversimplification. Our analyses and experiments indicate, clearly, that such a simplification cannot be justified.

With regard to the boundary conditions for the CFD analysis, recall that the experiments are conducted in a multistage environment whereas the computational simulation resembles an isolated stator in a cascade. Our results suggest that it is possible to capture much of the relevant physics for Navier–Stokes simulations by specifying correct boundary conditions. Our use of experimental data for boundary conditions has apparently provided the correct profile of incoming vorticity and the average turbulence kinetic energy. We suspect that this plus the correct vorticity generated by viscous effects has allowed us to get the excellent data match and correct secondary flows. For a more complete simulation of multistage influences in a turbomachinery blade row, the reader is referred to a procedure proposed by Adamczyk (1985).

Finally, we see an enormous potential for the use of CFD in conjunction with an LSRC-type facility to address issues of current interest in turbomachinery. As we have demonstrated here, results from this combination give insight into complex phenomena that would otherwise be lost. This can be of immediate use to the design community, especially in understanding the effects of loading in compressor blade and vane rows.

9.0 Conclusions

The following conclusions about mixing in axial-flow compressors are drawn from the three-dimensional Navier–Stokes computations and experiments.

- Both secondary flows and turbulent diffusion were shown to play important roles in the mixing process and can contribute to both spanwise and cross-passage mixing. The relative importance of each of these two mechanisms is configuration and loading dependent.
- In the endwall region and along airfoil surfaces, secondary flow was found to be of the same order of magnitude as turbulent diffusion for the compressors evaluated. Other compressors may not exhibit this same proportion.
- Diffusion is an important mixing mechanism everywhere.
- Large pockets of spanwise secondary flow were found computationally along the vane surface, well away from the endwall-corner regions. Small pockets were found in the endwall corners. These locations agreed with experiment. Even at design conditions, the flow can be highly three dimensional.
- The three-dimensional Navier–Stokes computations support previous interpretations of ethylene tracer-gas measurements.
- The strong spanwise (radial) secondary flows in the outer pressure-surface region of Compressor I resulted from the tangential secondary flows (skew) impinging on the pressure surface. This is fundamentally convective flow physics that would be present without diffusive and large-scale turbulence effects.
- To abandon radial convective flux terms in the belief that diffusive ones suffice is an oversimplification not supported by our data.
- A potent role for CFD in turbomachinery has been demonstrated as follows: CFD validation by careful benchmark experiments, like those from the LSRC, leads to more confidence in the code and mutual reinforcement of CFD and experimental results. This leads to a fundamental joining of CFD and experiment to explain aspects of difficult fluid mechanics phenomena of current interest—in this case mixing.
- From the designer's perspective, the success of our off-design (increased loading) CFD computations has far-reaching implications. It means that designers may be able to locate and correct undesirable features of a design as loading varies before hardware is manufactured.
- Using correct profiles of time-averaged inlet boundary conditions for three-dimensional Navier–Stokes computations enables one to explain much of the flow physics for this stator.

Acknowledgments

The authors are indebted to Dr. Mikio Suo for his constant support and encouragement during the development of the Navier–Stokes system, to Mrs. Rosanna Heins for the extensive programming contributions, and to Mr. Randall Bauer for carrying out ethylene trace-gas measurements for Compressor II. The authors also wish to thank General Electric Aircraft Engines for permission to publish this paper.

References

Adamczyk, J. J., 1985, "Model Equation for Simulating Flows in Multistage Turbomachinery," ASME Paper No. 85-GT-226.

Adkins, G. G., Jr., and Smith, L. H., Jr., 1982, "Spanwise Mixing in Axial-Flow Turbomachines," ASME *Journal of Engineering for Power*, Vol. 104, pp. 97–110.

Chien, K. Y., 1982, "Predictions of Channel and Boundary-Layer Flows With a Low-Reynolds-Number Turbulence Model," *AIAA Journal*, Vol. 20, No. 1, pp. 33–38.

Coutanceau, M., and Bouard, R., 1977, "Experimental Determination of the Main Features of the Viscous Flow in the Wake of a Circular Cylinder in Uniform Translations. Part 1. Steady Flow," *Journal of Fluid Mechanics*, Vol. 79, Part 2, pp. 231–256.

Gallimore, S. J., and Cumpsty, N. A., 1986, "Spanwise Mixing in Multistage Axial Flow Compressors: Part I—Experimental Investigations; Part II—Throughflow Calculations Including Mixing," ASME JOURNAL OF TURBOMACHINERY, Vol. 108, pp. 2–16.

Hah, C., 1987, "Calculation of Three-Dimensional Viscous Flows in Turbomachinery With an Implicit Relaxation Method," *Journal of Propulsion*, Vol. 3, No. 5, pp. 415–522.

Hah, C., and Leylek, J. H., 1987, "Numerical Solution of Three-Dimensional Turbulent Flows for Modern Gas Turbine Components," ASME Paper No. 87-GT-84.

Issa, R. I., 1982, "Solution of Implicitly Discretized Fluid Flow Equations by Operator-Splitting," Int. Rep., Dept. Min. Resources Engrg., Imperial College, London, United Kingdom.

Leonard, B. P., 1979, "A Stable and Accurate Convective Modeling Procedure Based on Quadratic Upstream Interpolation," *Computer Methods in Applied Mechanics and Engineering*, Vol. 19, pp. 59–98.

Wisler, D. C., 1985, "Loss Reduction in Axial-Flow Compressors Through Low-Speed Model Testing," ASME *Journal of Engineering for Gas Turbines and Power*, Vol. 107, pp. 354–363.

Wisler, D. C., Bauer, R. C., and Okiishi, T. H., 1987, "Secondary Flow, Turbulent Diffusion, and Mixing in Axial-Flow Compressors," ASME JOURNAL OF TURBOMACHINERY, Vol. 109, pp. 455–482.

- Both secondary flows and turbulent diffusion were shown to play important roles in the mixing process and can contribute to both spanwise and cross-passage mixing. The relative importance of each of these two mechanisms is configuration and loading dependent.
- In the endwall region and along airfoil surfaces, secondary flow was found to be of the same order of magnitude as turbulent diffusion for the compressors evaluated. Other compressors may not exhibit this same proportion.
- Diffusion is an important mixing mechanism everywhere.
- Large pockets of spanwise secondary flow were found computationally along the vane surface, well away from the endwall-corner regions. Small pockets were found in the endwall corners. These locations agreed with experiment. Even at design conditions, the flow can be highly three dimensional.
- The three-dimensional Navier–Stokes computations support previous interpretations of ethylene tracer-gas measurements.
- The strong spanwise (radial) secondary flows in the outer pressure-surface region of Compressor I resulted from the tangential secondary flows (skew) impinging on the pressure surface. This is fundamentally convective flow physics that would be present without diffusive and large-scale turbulence effects.
- To abandon radial convective flux terms in the belief that diffusive ones suffice is an oversimplification not supported by our data.
- A potent role for CFD in turbomachinery has been demonstrated as follows: CFD validation by careful benchmark experiments, like those from the LSRC, leads to more confidence in the code and mutual reinforcement of CFD and experimental results. This leads to a fundamental joining of CFD and experiment to explain aspects of difficult fluid mechanics phenomena of current interest—in this case mixing.
- From the designer's perspective, the success of our off-design (increased loading) CFD computations has far-reaching implications. It means that designers may be able to locate and correct undesirable features of a design as loading varies before hardware is manufactured.
- Using correct profiles of time-averaged inlet boundary conditions for three-dimensional Navier–Stokes computations enables one to explain much of the flow physics for this stator.

Acknowledgments

The authors are indebted to Dr. Mikio Suo for his constant support and encouragement during the development of the Navier–Stokes system, to Mrs. Rosanna Heins for the extensive programming contributions, and to Mr. Randall Bauer for carrying out ethylene trace-gas measurements for Compressor II. The authors also wish to thank General Electric Aircraft Engines for permission to publish this paper.

References

Adamczyk, J. J., 1985, "Model Equation for Simulating Flows in Multistage Turbomachinery," ASME Paper No. 85-GT-226.

Adkins, G. G., Jr., and Smith, L. H., Jr., 1982, "Spanwise Mixing in Axial-Flow Turbomachines," ASME *Journal of Engineering for Power*, Vol. 104, pp. 97–110.

Chien, K. Y., 1982, "Predictions of Channel and Boundary-Layer Flows With a Low-Reynolds-Number Turbulence Model," *AIAA Journal*, Vol. 20, No. 1, pp. 33–38.

Coutanceau, M., and Bouard, R., 1977, "Experimental Determination of the Main Features of the Viscous Flow in the Wake of a Circular Cylinder in Uniform Translations. Part 1. Steady Flow," *Journal of Fluid Mechanics*, Vol. 79, Part 2, pp. 231–256.

Gallimore, S. J., and Cumpsty, N. A., 1986, "Spanwise Mixing in Multistage Axial Flow Compressors: Part I—Experimental Investigations; Part II—Throughflow Calculations Including Mixing," ASME JOURNAL OF TURBOMACHINERY, Vol. 108, pp. 2–16.

Hah, C., 1987, "Calculation of Three-Dimensional Viscous Flows in Turbomachinery With an Implicit Relaxation Method," *Journal of Propulsion*, Vol. 3, No. 5, pp. 415–522.

Hah, C., and Leylek, J. H., 1987, "Numerical Solution of Three-Dimensional Turbulent Flows for Modern Gas Turbine Components," ASME Paper No. 87-GT-84.

Issa, R. I., 1982, "Solution of Implicitly Discretized Fluid Flow Equations by Operator-Splitting," Int. Rep., Dept. Min. Resources Engrg., Imperial College, London, United Kingdom.

Leonard, B. P., 1979, "A Stable and Accurate Convective Modeling Procedure Based on Quadratic Upstream Interpolation," *Computer Methods in Applied Mechanics and Engineering*, Vol. 19, pp. 59–98.

Wisler, D. C., 1985, "Loss Reduction in Axial-Flow Compressors Through Low-Speed Model Testing," ASME *Journal of Engineering for Gas Turbines and Power*, Vol. 107, pp. 354–363.

Wisler, D. C., Bauer, R. C., and Okiishi, T. H., 1987, "Secondary Flow, Turbulent Diffusion, and Mixing in Axial-Flow Compressors," ASME JOURNAL OF TURBOMACHINERY, Vol. 109, pp. 455–482.

DISCUSSION

S. J. Gallimore[1]

The authors are to be congratulated on a significant contribution to the literature on mixing in multistage axial flow compressors. The care and attention to detail both in the computation, experiments, and the analysis of the results is evident throughout the paper. In particular the new experimental results reported in Fig. 20 show without doubt radial or spanwise mixing caused by a combination of secondary flow and turbulent diffusion, a conclusion that was not easily drawn from the earlier work of Wisler et al. (1987). It is clear that some, though not necessarily all, of the contour distortion in these results is caused by secondary flow. Perhaps the one part missing is a simulation of these results using the Navier–Stokes solution. A scalar could be introduced into the computed flowfield and allowed to be both convected and diffused downstream to produce contours analogous to the ethylene. This would be a most convincing demonstration of the secondary flow and turbulent diffusion contributions to spanwise mixing and it is difficult to see what else could be done after that to clarify the situation further on a fundamental level. Are the authors considering such a series of calculations?

N. A. Cumpsty[2]

This represents a fine piece of work and the authors are to be congratulated on the thought and care that have gone into it. Quite apart from its importance for mixing, it demonstrates how powerful experiment and three-dimensional calculation can be when used together.

One of the things that the calculations show is that three-dimensional flows are important and can be quite large. It is perhaps overdue to change the terminology and stop using the term secondary flow, but instead to refer to three-dimensional flow. If these three-dimensional convective effects play a large or dominant part in the spread of contours and the redistribution of momentum and enthalpy it does seem to me to be eccentric to refer to the process as mixing when it can be calculated; to me the term mixing should be left for the unpredictable effects, such as turbulence, and not used for those effects like the three-dimensional flow, which was clearly calculated here with considerable precision. Terminology has confused us in another way, because Adkins and Smith, Gallimore and Cumpsty, and now Li and Cumpsty (1990a and 1990b) considered only *spanwise* mixing, whereas Wisler, Bauer, and

[1]Rolls-Royce plc, P. O. Box 31, Derby DE2 8BJ United Kingdom.
[2]Whittle Laboratory, University of Cambridge, Madingley Rd., Cambridge CB3 ODY United Kingdom.

Okiishi considered mixing in the circumferential direction as well.

I am of the opinion that there is now more agreement than disagreement about the effects at work. In Fig. 20, which shows contours in Compressor II, there does seem to me to be clear evidence that convective effects are spreading the contours radially: In case B it does seem that small diffusive movements are enough to move the tracer gas into the regions where the core was shifted in case A. For compressor I, however, I am not fully convinced that convective effects, which are deterministic features of the main flow, are responsible for the majority of *radial* spreading, despite the quality of the results shown. It is clear that they can be responsible for a large part of the circumferential spread, as is also shown recently by Li and Cumpsty (1990a and 1990b). One should be struck that for Compressor I most of the results show very little radial movement of the core, the most significant exception being Fig. 17(*c*): In most cases the radial position of the core is substantially unchanged, despite significant radial spread, and it seems too much of a coincidence that the core should usually miss the major regions of radial velocity. That anisotropic spreading does take place is, I believe, reasonably well established by the results of Li and Cumpsty, and it might be useful if the authors would look at their data from this point of view.

The availability of the calculation opens up possibilities for processing computed results to reveal more about the flow. It would, for example, be possible to consider how a scalar variable present in the flow at an injection point would be altered as the flow progresses downstream, thereby simulating the mixing experiments. For this the estimated diffusive processes would need to be included. More easily, it should be possible with very little work to find the streaklines, assuming that the flow is steady and ignoring any diffusive effects. If these were calculated for a ring of points around the injection points one could see whether they spread out to adopt shapes similar to those of the measured contours. Alternatively, and potentially, more convincingly, one could equally well trace back from positions around a contour—if the convective effects dominate the streaklines should congregate closely around the actual injection point. The contours shown by the authors in Figs. 16(*a*) and 16(*b*) would be good ones to choose for this.

I think that it is now incontrovertible that turbulence (in the loosest sense) plays a major part in the spanwise mixing; the three-dimensional flow also has some part in the spanwise direction and often dominates in the circumferential direction. The mixing is affected by the design of the compressor in many ways and tip clearance has been shown by Li and Cumpsty to play an important role in fixing this in the region near the casing. Just as the loss and blockage tend to rise as tip clearance is increased above a very small optimum value, the mixing also rises and this makes possible the repeating stage at different levels of tip clearance.

Gallimore and Cumpsty (1986) showed that the level of mixing coefficient had a weak effect on throughflow calculations, though the presence of some mixing was very important. This led to the very simple assumption that a uniform level across the span is adequate; this is not a statement based on physics but on the wish for simplicity. From the point of view of the designer it does not matter very greatly how the mixing is produced provided the level can be estimated within a factor of two or three. The method for estimating mixing given by Gallimore and Cumpsty is not in any sense a model, but is a simple empirical scaling sufficient to give estimates of adequate accuracy.

Mixing in axial compressors has attracted a great deal of attention in the last few years and there are now a large number of tracer-gas measurements in the open literature. I cannot see that very much additional insight will come from gathering more until our ideas are clearer. For the time being I think that more progress will come from careful thought and the utilization of numerical methods together with the existing measurements. Nevertheless I do think that there is some reason for looking at mixing in axial turbines, where the balance between three-dimensional flow and turbulent effects is likely to be very different; it may well be that the insights gained from the turbine will allow us to be more categorical in the future with regard to mixing in compressors.

References

Li, Y. S., and Cumpsty, N. A., 1990a, "Mixing in Axial Flow Compressors: Part 1—Test Facilities and Measurements in a Four Stage Compressor," ASME Paper No. 90-GT-38; JOURNAL OF TURBOMACHINERY, this issue.

Li, Y. S., and Cumpsty, N. A., 1990b, "Mixing in Axial Flow Compressors: Part 2—Measurements in a Single-Stage Compressor and Duct," ASME Paper No. 90-GT-39; JOURNAL OF TURBOMACHINERY, this issue.

T. H. Okiishi[3]

I think that Jim Leylek and Dave Wisler have provided sufficient evidence to persuade us to believe that the conclusions of Wisler et al. (1987) are correct. Their thoughtful comparison of CFD simulation and low-speed research compressor data compels me to conclude still that secondary flows and turbulent diffusion are important drivers of the spanwise and crosswise mixing that occurs in low aspect ratio, high solidity stator rows in the subsonic stages of modern multistage, axial-flow compressors.

Their paper has reinforced my confidence in using ethylene as a tracer gas for determining the extent of secondary flows and turbulent diffusion in turbomachines and other flow devices. The tracer gas technique is an important tool that ought to be used more in observing fluid flows.

I support the authors in their suggestion that combining CFD simulation with benchmark quality laboratory experiments can lead to significant benefits and I am encouraged by the recent increase in such collaboration.

The details of mixing in compressor rotor rows have not yet been studied to the extent that mixing in stator rows has. It is likely that secondary flows and turbulent diffusion are important in rotor rows; however, mechanism details remain to be discovered. Eventually, these phenomena must be better understood. The measurement challenges involved are substantial.

For clarification I would appreciate having the authors elaborate on any blade-to-blade variations in the stator 3 inlet data set. For example, were the stator 2 wake avenues discernible at the stator 3 inlet? If there were circumferential variations in flow at the stator 3 inlet, how would placement of these variations relative to the stator 3 vanes affect the secondary flows generated?

A. J. Strazisar[4]

I would like to congratulate the authors for completing such a detailed investigation of the mixing phenomena in multistage axial-flow compressors. I believe that the approach they used in this investigation is noteworthy for a number of reasons. First, the authors have developed graphic analysis tools, which allow them to plot the results of numerical predictions and

[3]Professor and Chair, Department of Mechanical Engineering, Iowa State University, Ames, IA 50011.

[4]Internal Fluid Mechanics Division, NASA Lewis Research Center, Cleveland, OH 44135.

experimental measurements on the same plot, as demonstrated in Figs. 16–19. This is a powerful capability, which enhances our ability to understand the flow physics information contained in both the numerical and experimental results. Second, the authors have used a minimal amount of experimentally measured information obtained upstream of the stator as input to a three-dimensional flowfield analysis, which in turn predicts a wealth of flow physical information within the stator. This exercise demonstrates the powerful capabilities of three-dimensional Navier–Stokes analysis. It raises the possibility that we can use interstage data in existing compressors, coupled with three-dimensional analysis of a particular blade row, to assess the impact of design changes in that blade row without having to calculate the flowfield through the entire machine. Finally, the authors have used the numerical solution inside the stator blade row to provide an understanding of how ethylene traces injected upstream of the stator develop the characteristics they display downstream of the stator. Without the numerical solution, the stator blade was simply a "black box" with an unknown transfer function that somewhat modified the ethylene traces into the shape they display at the blade exit, where they can first be measured. In summary, the authors have demonstrated how a tightly coupled CFD and experimental effort can be used to complement one another in explaining important flow physics.

This paper plus that of Li and Cumpsty (1991) [see References in Cumpsty's Discussion] represent the latest volley in an on-going match between the Whittle Labs (Gallimore, 1985; Gallimore and Cumpsty, 1986) and General Electric (Wisler et al., 1987) to understand the mixing that takes place in multistage compressors. The most recent contributions from Whittle and G.E. have elevated the acquisition and interpretation of ethylene traces to new levels. The big winner in the friendly duel between the Cambridge and Cincinnati teams is the turbomachinery community at large, for these two teams have greatly increased our understanding of multistage flow physics in the course of their investigations. The efforts of these two research groups have complemented one another over the last five years. I think that it's fair to say at this point that the Leylek and Wisler paper has shown us that both turbulent diffusion and secondary flow are important contributors to mixing in multistage compressors, and that neither can be ignored in analyses that aim to predict multistage compressor performance accurately.

I would like to ask the authors to clarify a few points in the present paper. First, the authors used a very dense mesh, which yields impressive resolution of the leading and trailing edges as well as the airfoil and endwall surfaces. However, the authors do not mention whether or not a grid refinement study was done. I assume that the solution is grid-independent in the sense that using an even finer mesh would not markedly change the solution. But in the interest of saving CPU time, I wonder how rapidly the quality of this CFD solution would deteriorate if fewer grid points were used.

Second, the authors mention that they have matched the average turbulent kinetic energy at the inlet plane of the computation by using the k–ϵ turbulence model. It is my understanding that the level of the k parameter is determined from hot-wire measurements of the turbulence intensity in the rig. This raises questions as to how sensitive the solution is to the value of k, and also how good would the solution have been if hot-wire information were not available. I think this is important when considering the application of the authors' approach to a high-speed compressor. In a high-speed research compressor, pressure, temperature, and angle information might be readily available while hot-wire measurements might be difficult to obtain.

In comparing Figs. 3 and 4, it seems that the upstream boundary of the CFD mesh extends beyond measurement plane 3.5, which is where upstream boundary conditions were measured in the rig. This leads to a question relative to Fig. 5, in which the experimental measurements are compared to the CFD result at plane 3.5. If the CFD grid actually does extend upstream of Plane 3.5, then were the actual CFD boundary conditions changed slightly so that the computed conditions matched the experimental measurements at Plane 3.5?

My final questions and comments have to do with the use of the CFD solution to interpret the ethylene contours. First, why are the CFD results in Figs. 14–19 displayed at 95 percent chord when the ethylene contours were measured somewhere downstream of 100 percent chord? Second, in Figs. 16–19 the authors use computed velocity vectors at 95 percent chord to help explain the ethylene contour distortions. While I do not question their interpretations I would like to point out a word of caution here. The ethylene contours at the stator exit plane result from the effects of diffusion and secondary flow *integrated along the entire stator chord* while the velocity vector plots only display the local secondary flow field. There may be cases in other compressors in which the ethylene contour is shaped by a strong secondary flow that exists near the stator leading edge but does not persist all the way to the stator trailing edge. In such cases, a comparison between the secondary velocity field and the ethylene contour at the stator exit plane might not display as good an agreement as that shown in the present work. Finally, the authors marked a gapwise and spanwise line of particles in the stator inlet plane and then traced them through the CFD solution to the stator exit plane, with the results being shown in Fig. 15. This demonstrates that they have the postprocessing ability to trace fluid particles through the CFD solution. I therefore find myself wondering why the authors did not mark a small ring of fluid particles at the stator inlet plane to simulate an ethylene injection jet and then trace this ring of particles downstream to predict the distortion of the ring numerically. This exercise would account for the integrated effects of secondary flow all along the stator chord. Also, since the numerical solution does not model turbulent diffusion, it would seem to me that this exercise would have yielded numerical predictions of the amount of ethylene contour distortion due solely to secondary flow, and would have shed further light on the split between turbulent diffusion effects and secondary flow effects.

References

Gallimore, S. J., 1985, "Spanwise Mixing in Multi-stage Axial Compressors," Ph.D. Dissertation, Dept. of Engineering, Cambridge University, United Kingdom, Sept.

Authors' Closure

We greatly appreciate the time, effort, and thought expended by those technical experts who provided written discussions of our paper. Furthermore, the enthusiastic, thoughtful and lengthy oral discussion following the formal presentation of the paper at the 35th International Gas Turbine Conference in Brussels was both useful and gratifying because general agreement and closure was reached on the mixing controversy. We are indebted to the session organizers, Prof. Nick Cumpsty and Dr. Simon Gallimore, who encouraged and facilitated this discussion. We thank all discussers for their kind remarks.

Having studied the four Discussions carefully, we have organized our closure into nine topics. Each of these is presented below.

1 General Agreement and Resolution of the Controversy. Since the appearance of the Adkins and Smith paper on spanwise mixing in axial turbomachines in 1982, much serious research and healthy, but friendly, discussion and controversy has ensued to understand the physical mechanisms

involved in mixing. The core papers that address this international quest have already been listed.

It is now clear that the controversy has been resolved and that there is general agreement with the conclusions of Leylek and Wisler (present paper) that both secondary flow (three-dimensional convective effects) and turbulent diffusion can play important roles in the mixing process. This is based on comments made in the written Discussions of the paper and in the oral discussion following its formal presentation. This consensus is also summarized in one section called "Resolution of the Debate" that is contained in Dr. Arthur Wennerstrom's 1991 Review paper on the subject (this issue).

2 Change in Terminology. Professor Cumpsty suggests that "it is perhaps overdue to change the terminology and stop using the term secondary flow, but instead to refer to three-dimensional flow." We, too, are in favor of using terminology that clarifies things. In fact when we wrote the paper, we discussed dropping the term secondary flow and substituting the term three-dimensional convective effects. But as we stated in Section 2.1, we chose instead to stick with the original terminology for "simplicity and consistency with past literature."

In general however, we do not think that the ASME readership is actually confused by the present terminology, for the basic issues are clear: namely, convective versus diffusive processes as the cause for redistributing (mixing) mass, momentum and enthalpy. If we change terminology, we must be careful that we clarify and don't bury real differences in semantics.

3 Lack of Radial Core Motion for Compressor I Implying That Anisotropic Turbulent Diffusion Is Responsible for Radial Contour Spreading. In the second half of the third paragraph of Prof. Cumpsty's Discussion, he indicates that for Compressor I he is not fully convinced that convective effects are responsible for the majority of the radial spreading of the ethylene contours, since most of the cores show little radial motion. He asks us to look at our contour spreading from the viewpoint that its cause is anisotropic turbulent diffusion as seen in his tests in a long, straight, rectangular duct.

What is so striking about the Leylek and Wisler (present paper) results for Compressor I is that: (1) The lack of radial core movement is so perfectly explained by the N-S calculations, and (2) the radial and tangential secondary flows computed by the N-S analysis are in just the directions needed, with just the magnitude needed to explain the major contribution that secondary flow plays in every single contour distortion and every single core motion of every single one of the many injection locations (except very near the hub where stator shroud leakage wasn't modeled) at both loading levels. We cannot see how this massive agreement between experiment and analysis is coincidence.

Our story would be open to significant criticism if we *had* gotten radial core motion in the experiment when the N-S analysis didn't predict it. Therefore we view the fact that we got no radial core motion at those locations where the N-S analysis predicted no radial secondary flow as a *strong* point, not a weakness. When we injected ethylene into regions where radial secondary flows were predicted, e.g., Cores 15, 29, 35, and 40 in Figs. 16(*c*), 17(*c*), and 19(*a*), we got large, experimental, radial core motion.

With respect to anisotropic turbulent diffusion, the results from tests conducted in a long, straight rectangular duct reported in Fig. 8 of Li and Cumpsty (Part II, 1991) do show contour spreading (distortion) in the corner of a duct having no secondary flow present. The shape of their contours so obtained is classical and predictable. That the cause of the contour distortion in this case is anisotropic turbulence and that this cause, in some part, operates in compressors *very* near solid surfaces is not disputed.

However, the flow in the corner of a long, straight duct is very much different from that in an embedded stage of a highly loaded HP compressor, especially when significant boundary layer skew exists. Thus mere general similarity of shapes of ethylene contours does not prove similarity of causes.

That radial and tangential secondary flows are present in Compressor I and that they are in the location and direction to distort diffusing ethylene contours is convincingly shown in Section 7.2 and not even questioned for Compressor II in Section 7.3 of Leylek and Wisler (present paper).

4 Blade-to-Blade Variations. Professor Okiishi asked us to elaborate on any blade-to-blade variations in the stator 3 inlet data set. We have circumferential traverse data in both the absolute and relative frames that allow us to discern wake profiles. These time-averaged data were mass-averaged circumferentially to obtain the radial distributions shown in Fig. 5 of the paper. Other than this, any attempt to incorporate Stator 2 wake avenues further would require an unsteady, three-dimensional, N-S code simulating rotor-stator interaction.

We did attempt to find experimentally the effects of the placement of Stator 2 wake avenues on ethylene contour distortion across Stator 3. These results are reported in Fig. 20(*f*) where the upstream IGV and stators were moved circumferentially 50 percent of a stator pitch and Stators 3 and 4 were unchanged. The resulting ethylene contours were nearly identical to those taken for all stators in line. This means that these wake avenues did not alter our basic conclusions.

5 Gridding and Grid Refinement. We consider this question by Dr. Strazisar to be an extremely important and serious issue. Overall quality of computational results is very sensitive to the quality of the grid. We did not discuss our gridding technique in the paper (because of length) but hoped someone would raise the question.

A great deal of care was taken in selecting the grid. The following parameters were considered: (*a*) grid density and independence, (*b*) orthogonality, (*c*) stretching and aspect ratios, and (*d*) y^+ requirements.

5(a) Grid Density and Independence. We know from past experience that we could have used fewer grid nodes, say 160,000, but chose to go with the finest mesh we could afford, about 236,000 nodes, in order to generate a grid-independent computed flow field with high resolution near all metal surfaces. This practice, we thought, would better compliment our high-density, high-quality experimental data. The grid independence issue was further resolved by imposing strict convergence criteria on the residuals of every dependent variable as described in Section 6.1.

5(b) Orthogonality. A special grid optimizer was used to orthogonalize the grid, especially in the high gradient regions near the stator surfaces (Fig. 4*d*, *e*).

5(c) Stretching and Aspect Ratios. Stretching was tightly controlled and kept to ≤ 20 percent in all three directions. Aspect ratio was well within 10 in most of the computation domain.

5(d) y^+ Requirements. Placement of the first grid nodes near all metal surfaces was consistent with y^+ requirements of wall functions. A good representative y^+ value of 40 was computed near stator surfaces. Near the endwalls the average y^+ was 60.

These values of grid density, stretching, aspect ratio, and y^+ that we chose are recognized by the CFD community as conservative.

6 Sensitivity to Inlet Turbulent Kinetic Energy. Overall results, especially the secondary flow features, are not very sensitive to inlet turbulent kinetic energy, k, as long as a rea-

sonable value is used for this parameter. Previous numerical experiments on engine blading indicate that things were not too dependent on the exact level at the inlet. Similar observations were made on another blading when inlet turbulence intensity was varied between 8, 10, and 12 percent. However, when the same simulation was repeated with 0 percent intensity, laminarlike separation regions appeared around the leading edge.

This means that as long as inlet turbulent kinetic energy is reasonably close to measured values, our conclusions about mixing would not be affected.

7 Location of Computational and Experimental Inlet Planes. We placed the computational inlet plane a small distance upstream of its experimental counterpart. This was done to prevent numerical problems in subsonic flow due to interactions between leading edge disturbances and inlet boundary conditions. The present simulation represents the closest placement of the inlet plane to the leading edge that we have ever done. Since there is almost no change in profiles between the CFD inlet plane and the actual location where the experimental data were taken, we used the experimentally determined boundary conditions at the CFD inlet plane without any modifications.

8 Data Comparisons at 95 percent Chord. Although the ethylene data were taken at 99 percent chord, we chose to make the comparisons with computational results at 95 percent chord. This gave the closest computational picture to a Trefftz plane, thereby avoiding perceived distortions due to viewing angle (e.g., high airfoil curvature especially very near the trailing edge).

We agree with Dr. Strazisar that the distortions of the ethylene contours are an integrated effect along the entire stator passage. This is why we devoted our entire Section 6.4 to the development of the three-dimensional flowfield through the stator passage. In particular the data in Figs. 12 and 13 show the history of the developing secondary flows that cause contour distortion.

After carefully examining dozens of vector and contour plots, a small portion of which are shown in Figs. 11 and 13, we concluded that the chordwise position chosen for comparison with data was one of many that was representative of this integrated effect. A different choice of chordwise position (see Fig. 13*c–e*) would not have changed our conclusions.

9 Use of CFD Solution to Interpret Ethylene Contours. Suggestions are made by Dr. Gallimore, Dr. Cumpsty (his paragraph 4), and Dr. Strazisar (his paragraph 6) about expanding our CFD capability to compute ethylene contours to aid further in the interpretation of experimental data. We agree, in general, that such a capability would be useful and bring even more realism into computational simulation of ethylene tracer experiments. We would like to point out, however, that development of this capability would require considerable time and effort in CFD coding and validation.

The ethylene injection and tracking process involves the diffusion and convection of a scalar in a flowfield. Computationally, the best approach to handle this is through a species conservation equation for ethylene, which could be added to our CFD code. This would make it possible to make direct comparisons between computationally and experimentally obtained ethylene contours. We do not currently possess this capability.

However, we do possess the capability of tracing the trajectory (due to convection only) of massless particles started along a computational *grid line* in a crossflow plane. We used this capability in Fig. 15 to show the radial and tangential distorting effects of the secondary flow. At the time we felt that this was sufficient. We are now evaluating the merits of extending our capability to also trace a *circle* of massless particles, a feature not available at the time of publication.

General Comments In summary, we have shown beyond reasonable doubt that both secondary flow and turbulent diffusion play major roles in mixing in axial-flow compressors. This was our original premise.

We are indebted to the American Society of Mechanical Engineers for providing the international forum in which the paper, discussions, and our closure can be presented.

References

Wennerstrom, A. J., 1991, "A Review of Predictive Efforts for Transport Phenomena in Axial Flow Compressors," ASME JOURNAL OF TURBOMACHINERY, this issue.

Mixing in Axial Flow Compressors: Part I—Test Facilities and Measurements in a Four-Stage Compressor

Y. S. Li

N. A. Cumpsty

Whittle Laboratory,
Cambridge University,
United Kingdom

The mechanism of mixing in axial flow compressors has been investigated in two low-speed machines. For reasons of length this is described in two parts. Results in a four-stage compressor are described here in Part I and show that the mixing coefficients across the first and the third stators are of similar magnitude. Part I also describes the background and experimental facilities and techniques used in both parts together with the nomenclature and all the references. Part II describes the results from a large single-stage compressor. It also presents measurements of mixing in a simple two-dimensional duct, and presents conclusions for the whole investigation.

1 Introduction

The importance of mixing in axial flow compressors was first demonstrated by Adkins and Smith (1982). Mixing implies both the diffusion of temperature and the existence of shear stresses. It is a good approximation to assume the same magnitude for all the diffusion processes, including the diffusion of foreign gas. As a means to studying mixing, the diffusion of a foreign gas, deduced from the spreading of a tracer gas, has been very helpful. Adkins and Smith (1982) and Gallimore (1986) showed that including mixing effects in the throughflow calculation program could improve the predictions significantly, although the mechanisms they envisage for mixing were fundamentally different.

The mechanism postulated for mixing by Adkins and Smith (1982) is a spanwise convection process established by secondary flows. On this basis they established a mixing model and incorporated it into their throughflow calculation program by relating their mixing coefficients to the calculated radial secondary flow velocities from empirical models. Their predictions showed much better agreements with experimental data than those that ignored mixing.

Gallimore and Cumpsty (1986) investigated mixing in two four-stage compressors by using a tracer gas technique. They concluded that it was a turbulent-type diffusion that was the dominant mechanism of mixing, rather than a deterministic radial convection process set up by secondary flows. They found that the mixing level was comparatively uniform across the span and for simplicity they therefore treated it as constant along the span in their mixing model.

Wisler et al. (1987) took detailed measurements on a large-scale, low-speed four-stage research compressor. They concluded that both secondary flow and turbulent diffusion could play important roles in the mixing process, with the secondary flow contribution being of the same order of magnitude as, and in some cases greater than, the diffusive effects from turbulence near endwalls and along airfoil surfaces. There is no dispute that secondary flow is dominant for the *circumferential* spread of the tracer gas in the endwall region, but controversy has remained regarding its contribution to spanwise mixing. There is also controversy about the interpretation by Wisler et al. of experimental results in the end-wall and blade surface corners where the tracer gas concentration contours were distorted. This distortion was explained by Wisler et al. in terms of secondary flow but, as stated in the discussion of the paper, anisotropic turbulent diffusion could have the same effect, and it was not very clear which was the dominant mechanism in these areas. Wisler et al. also found that the mixing levels differed considerably across the span: lower in the free-stream region and much higher in the end-wall regions, in particular near the casing at design condition.

At the inception of the current research it was confidently envisaged that away from the end walls the principal mechanism of mixing would be associated with the blade wakes, with the unsteady motions in them referred to hereafter as turbulence. It was intended that by using three-sensor hot wires the turbulent stresses (and therefore the mixing) could be measured in the wakes and end-wall regions. In the event this was impossible because the small-scale, high-frequency turbulent eddies in the flow could not be resolved by the smallest three-sensor probe that could be made.

Both secondary flow and anisotropic inhomogeneous turbulent diffusion could cause nonuniform mixing, especially in the blade surface and end-wall corners, for it is known that

Contributed by the International Gas Turbine Institute and presented at the 35th International Gas Turbine and Aeroengine Congress and Exposition, Brussels, Belgium, June 11-14, 1990. Manuscript received by the International Gas Turbine Institute December 20, 1989. Paper No. 90-GT-38.

close to solid surfaces a turbulent flow field may be anisotropic and inhomogeneous. It is however extremely difficult to measure the characteristics of anisotropic turbulence in compressors due to instrumentation limitations. Therefore, as well as tests using low-speed compressors, mixing tests were conducted in a duct corner and these were able to give a clear view of the physics of mixing where secondary flow of the type defined in compressors was excluded.

The primary objectives of the present research can be summarized as:

1 to find out what causes the mixing and to determine the relative importance of turbulent diffusion and secondary flows on mixing in axial flow compressors, in particular, in the endwall regions;

2 to find out how the mixing developed through multistage compressors: It had been assumed that the level of mixing would be low in the first stage and would rise through the machine, but this proved not to be the case and it was possible to use a single-stage machine for some of the mixing investigations.

2 Experimental Facilities

The principal research facility for this work was a four-stage compressor, the C106, with inlet guide vanes (IGV) and four identical stages. It has a constant casing diameter of 508 mm (20 in.) and hub-to-casing ratio of 0.75. The blades, designed by Rolls-Royce in 1986, have modified controlled-diffusion type airfoil sections, designed to eliminate separation near the trailing edge. The design rotational speed is 3500 rpm, but in the experiments it was operated at about 3000 rpm due to the excessive vibration level at higher speeds. Most tests were carried out at the design flow coefficient $\phi = 0.55$, at which the axial velocity was uniform across the span outside the endwall region, and the Reynolds number was 1.67×10^5 based on the rotor blade chord and the mean inlet velocity at midspan. Details of the design parameters are given in Table 1. The stator blades were unshrouded at the hub, and tip clearances for the rotor and stator were about 1.2 percent chord.

Additional tests were also performed on a large single-stage compressor, the Deverson rig. This has a casing diameter of 1.524 m (60 in.), a hub-to-casing ratio of 0.8, no IGVs, and a design flow coefficient of 0.55. The blades have C4 sections and free vortex design with axial discharge flow downstream of the stator. Tests were performed at a rotational speed of 500 rpm, which, for a flow coefficient of 0.51, gives the Reynolds number as 3.1×10^5. Details of the design parameters are shown in Table 2. The rotor tip clearance for most tests described here was 3 percent chord and the stators were sealed to a stationary hub. Some tests were also made at a reduced rotor tip clearance of 0.7 percent chord. This compressor and its performance have been described by McDougall (1990).

The tracer gas technique has been well established and the system used in this experimental work is that used by Gallimore (1985), but slightly modified so that the response time is halved. Very small quantities of ethylene are introduced into the flow at a point upstream and the spatially varying concentrations of ethylene are measured downstream. The concentrations are measured in a flame ionization detector (FID) system: The output voltage from the FID is proportional to the amount of ethylene sampled at a constant flow rate. In the experiments on the two compressors, ethylene was injected at a constant rate of 80 cc/min by an L-shaped probe with 0.5 mm o.d. and 5 mm arm length. The same injection probe was used in the duct flow with ethylene injected at a constant rate of 60 cc/min. For the tracer gas test on the four-stage compressor the mixture of air and ethylene was sampled through the central hole of a cobra probe with the two side holes used to align the probe to flow direction. For the test on the single-stage compressor a Kiel probe was used for sampling, while in the duct measurements a pitot tube with 1.64 mm o.d. was used.

The general unsteadiness and phase-lock-ensemble averaged turbulence were measured by a single straight hot-wire probe on the two compressors. The output signals from the hot-wire anemometers were fed into a data logging and processing system, which had a maximum sample frequency of 125 kHz and could allow multichannel simultaneous samples.

In trying to understand the mixing process (particularly the relative importance of secondary flow and anisotropic turbulence) and in trying to obtain three-dimensional shear stress

Table 1 C106 four-stage compressor midheight blading parameters

	Rotor	Stator
Solidity	1.47	1.56
Aspect Ratio	1.75	1.75
Chord (mm)	35.5	36.0
Stagger(deg.)	44.2	23.2
Camber(deg.)	20.0	40.6
No. of Airfoils	58	60
Axial Spacing(mm)	13.0	

Table 2 Deverson single-stage compressor midheight blading parameters

	Rotor	Stator
Solidity	1.31	0.95
Aspect Ratio	1.37	1.34
Chord(mm)	111.0	114.0
Stagger(deg.)	47.9	14.3
Camber(deg.)	26.5	42.9
No. of Airfoils	51	36
Axial Spacing(mm)	50.0	

Nomenclature

C = relative concentration of ethylene
c = chord length
L_s = stage length
r = radius of contours
t = blade thickness
U = blade speed
V_z = axial velocity
W = relative velocity
W_{dm} = maximum relative velocity defect in rotor blade wake
Δy = circumferential distance
Z = axial distance of ethylene convection
β = relative flow angle
ϵ = turbulent diffusion
ρ = density
ϕ = flow coefficient $= V_z/U$, where V_z is mass averaged and U is the blade speed at midspan
ψ_{T-T} = total-to-total pressure rise coefficient $= (P_{o2} - P_{o1})/\rho U^2$
ψ_{T-S} = total-to-static pressure rise coefficient $= (P_{s2} - P_{o1})/\rho U^2$
ω = stage loss coefficient

Subscripts

1 = inlet
2 = exit
z = axial

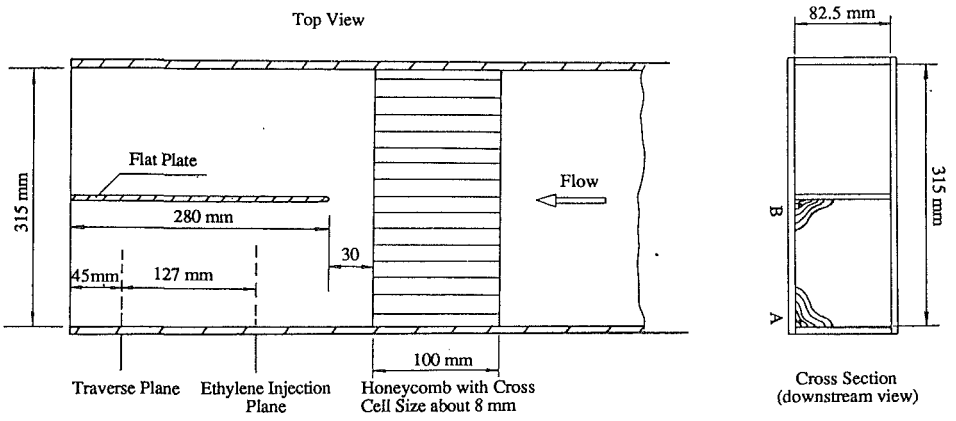

Fig. 1 Rectangular duct for tracer gas tests in corners

measurements with a three-sensor hot-wire probe it became clear that understanding was hampered by the inherent complexity of the flow in a compressor. It also seemed probable that some effects would be present in a much simpler geometry. A long rectangular duct with a 315 mm × 82.5 mm cross section was therefore used. The working section of the duct is shown in Fig. 1. This was at the downstream end of the duct and a screen was placed over the outlet of the duct to prevent atmospheric disturbances from affecting the flow. The average velocity of the air was about 30 m/s, comparable to that in the single-stage compressor. A honeycomb section 100 mm thick with cells about 8 mm across was placed just upstream of the working section to remove all secondary flow at entry. A turbulent boundary layer about 15 mm thick existed on all the walls at entry to the working section. To simulate the thinner boundary layer on a blade compared with on end wall, a plate was positioned along the center of the duct downstream of the honeycomb.

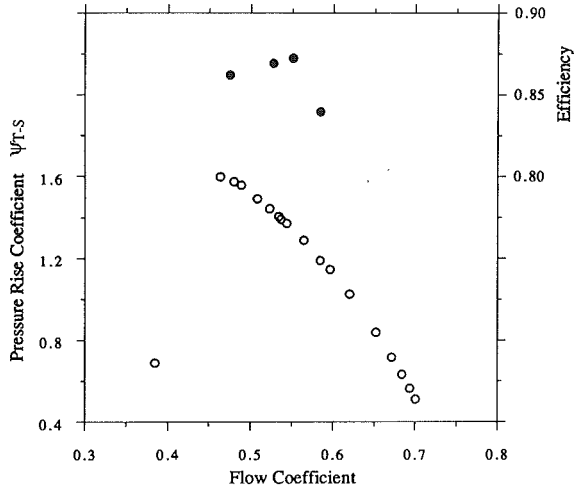

Fig. 2 C106 four-stage compressor performance

3 C106 Four-Stage Compressor Results

Figure 2 shows the compressor performance versus mass-averaged flow coefficient. The compressor pressure rise coefficient is the difference between compressor exit casing static and inlet total pressures, nondimensionalized by ρU^2, where U is the blade rotational speed at midspan. The overall adiabatic efficiency of the compressor is also shown, though this could only be measured to the accuracy of ± 1.5 percent from the temperature rise. The peak efficiency was at the design condition ($\phi = 0.55$) and was about 87 percent, which is acceptable bearing in mind the modest Reynolds number of 1.67×10^5. Measurements of velocities and flow angles from hub to casing made with a yaw probe were almost identical downstream of the third and fourth rotors, showing that the repeating stage condition had been well simulated.

For the tracer gas tests in the stators ethylene was injected at 24 percent of stator blade axial chord upstream of the stator blade leading edge and sampled at 15 percent of axial chord downstream of the trailing edge. These injection and sample planes were also the ones at which hot-wire measurements were made, and the hot-wire probe was located at about the midpitch of the stator blade passage at both upstream and downstream planes.

Figure 3(*a*) shows the ethylene tracer gas contours downstream of the third stator with the compressor operating at the design flow coefficient. Ethylene was injected upstream of the third stator at midpitch at 10, 50, and 90 percent span, respectively. The contours show relative concentration (i.e., they are each nondimensionalized by the peak concentration value). The local mixing magnitude is inferred from the *spread* of the contours. The bulk convection is inferred from the migration of the core (peak concentration point). For all three sets of contours in Fig. 3(*a*) the spanwise shifts of the peak concentration relative to the corresponding injection positions are very small across this stator, except near the casing. Estimates of the average radial velocity over the chord can be made from the radial shift of the peak concentration relative to the spanwise position of injection, and the maximum radial velocity calculated in this way is about 6 percent of axial velocity.

Ethylene was also injected at midpitch upstream of the third stator at only 2.5 percent span from the hub and casing and sampled downstream of the same row. These ethylene contours are shown in Fig. 3(*b*). There is a little radial shift of the peak concentration point close to the casing. Near the hub there is a large tangential shift of the peak concentration point from midpitch to the blade pressure surface, and a radial shift out from 2.5 percent span to about 9 percent span. The movement near the hub was believed to be caused by the rotating hub and unshrouded stators, which resulted in very large hub boundary layer skew in the rotational direction. The ethylene contours were also slightly distorted along the hub due to the leakage flow, but most contours were fairly circular despite the large migration of the whole.

Figure 3(*c*) shows contours across the *first* stator at conditions corresponding to those in Fig. 3(*a*), which were across the *third* stator. Radial migration of the cores was everywhere small here, even near the casing. For injection at 90 percent span the core migrated tangentially about 16 percent pitch across the first stator and about 10 percent of pitch across the third stator, in both cases toward the suction surface. The overturning causing this might be due to the combined effects

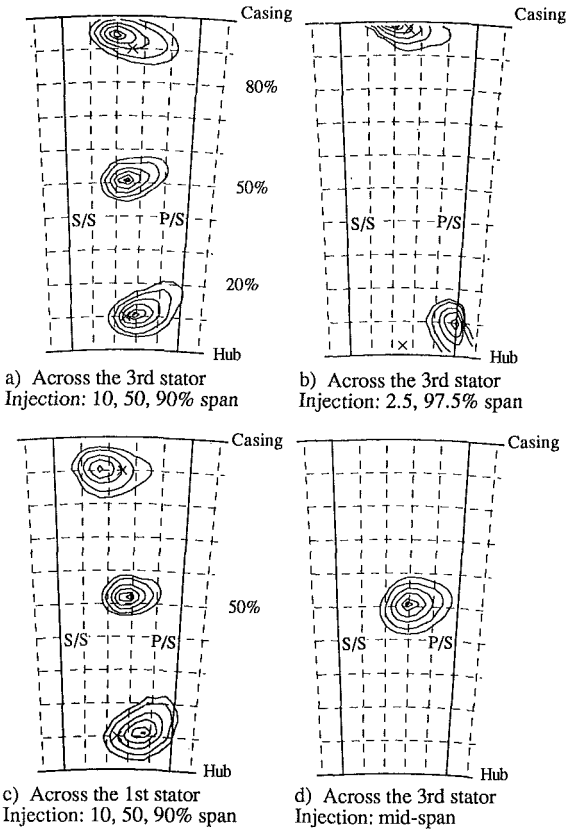

Fig. 3 Ethylene contour spreading across the first and third stators of the C106 four-stage compressor. Contour = 0.1, 0.2, 0.4, 0.6, 0.8, 0.9, 0.95. Ethylene injection at midpitch and upstream of corresponding stators. (*a*), (*b*), (*c*) at design condition $\phi = 0.55$; (*d*) compressor near stall $\phi = 0.48$. Injection at position ×.

of the cross-passage secondary flow generated within the stator blade passage and variations in flow direction at inlet to the stators. At 10 percent span from the hub there were core migrations toward the pressure surface of the stator blade (underturning): about 23 percent of pitch across the first stator and 10 percent of pitch across the third stator. These were a result of the skewed hub wall boundary layer at inlet to and across the stators, largely because of the rotating hub.

Since the radial movement of the contour peaks attributable to secondary flow was small, the ethylene spreads in spanwise direction were mainly caused by a form of turbulent diffusion. The difference between the ethylene spreads in the tangential and radial directions is the stretching in the tangential direction and, on the assumption that away from solid walls the turbulence is roughly isotropic and homogeneous, this must have been contributed by some other mechanisms. The relative motion of fluid inside the wake, the so-called wake transportation effect, was described by Kerrebrock and Mikolajczak (1970). When the rotor wake is passing through a stator blade row, there will be a relative motion inside the wake toward the stator blade pressure surface. The maximum velocity defect inside the wake can be denoted by W_{dm} relative to the flow with relative velocity W outside the wake; the relative flow direction β_2 is assumed the same inside and outside the wake. After traveling an axial distance Z across the stator the maximum tangential distance convected by this kind of relative motion will be given by the formula

$$\frac{\Delta y}{Z} = \frac{W_{dm}}{W} \tan \beta_2 \qquad (1)$$

This was used to estimate the maximum tangential transportation of tracer gases near midspan across the third stator blade

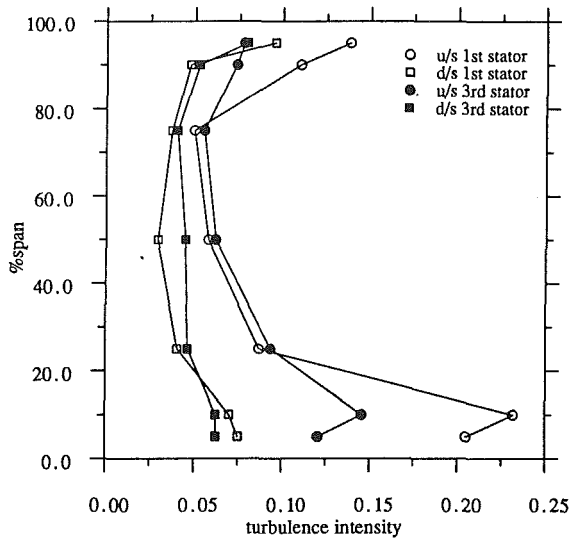

Fig. 4 C106 four-stage compressor single hot-wire measurements showing the general unsteadiness at design condition upstream (u/s) and downstream (d/s) of stator rows

row. The maximum axial velocity defect was taken from the phase-lock-ensemble average measurements obtained with a single hot-wire probe downstream of the third rotor at midspan and was about 17 percent of the free-stream axial velocity. The flow angle was obtained from conventional performance tests and was 42.5 deg. The estimated maximum circumferential transportation by the relative motion at midspan was 27 percent of stator pitch. The tangential stretching of the 5 percent contour at midspan, the difference in the tangential and radial extent of the contours, was measured to be 24 percent of stator pitch, similar to the level predicted by the simple method.

It should be pointed out that this larger tangential spreading of ethylene contours was caused by the flows in the periodic upstream rotor blade wakes and is different from the secondary flow in the end-wall boundary layers. In the casing wall boundary layer region the peak concentration point (core) moved toward the suction surface under the action of the time mean secondary flow, but the contours were elongated toward the pressure surface, as a result of this unsteady flow associated with the rotor blade wakes.

Compared with the third stator, the ethylene contours through the first stator look more isotropic (i.e., more uniform) with slightly larger spreading in spanwise direction in the end-wall regions and less elongation toward the pressure surface. The larger spanwise mixing for the first stage is consistent with hot-wire measurements: Fig. 4 shows general unsteadiness, commonly referred to as turbulence intensities, in the meridional plane upstream and downstream of the first and third stators. These were measured by a single hot-wire probe with the sensing wire in the tangential direction. The general unsteadiness in the first stator was higher than that across the third stator, particularly in the end-wall regions, so larger spanwise diffusion across the first stator is to be expected. It should also be noted from Fig. 4 that the unsteadiness level falls quite strongly across the stators, reflecting the decay of the rotor wakes.

In spite of the small differences mentioned above, the general spreads of ethylene across the first stator were almost the same as those across the third stator, indicating that the mixing levels were of similar magnitude. This was a surprise because it had been assumed that turbulence would build up through the stages and that the mixing would not reach its maximum until the repeating stage condition had been achieved. The mixing coefficients were estimated from the measured ethylene diffusion by using Hinze's (1959) mixing model, as modified by Gallimore and Cumpsty (1986)

Table 3 Normalized spanwise mixing coefficients across the first and third stators of the C106 compressor at design flow coefficient ($\phi = 0.55$)

Spanwise Position(%span)	1st Stator Mixing Coeff.	3rd Stator Mixing Coeff.
2.5	–	5.1×10^{-4}
10.0	7.5×10^{-4}	5.8×10^{-4}
50.0	4.4×10^{-4}	4.6×10^{-4}
90.0	6.4×10^{-4}	4.6×10^{-4}
97.5	–	4.6×10^{-4}

$$\frac{\epsilon}{V_z L_s} = \frac{\left(\frac{r}{L_s}\right)^2}{-4\,\frac{Z}{L_s}\ln C} \tag{2}$$

The spanwise mixing coefficients across the first and the third stators are given in Table 3. (These and the results for the other compressors will be discussed in Part II.) The spanwise mixing coefficient for the C106 is almost uniform along the span across the third stator; the spanwise mixing coefficient across the first stator was almost the same as that across the third stator at midspan region, but slightly higher in the two end-wall regions. This is consistent with Fig. 4, which shows that the unsteadiness into the first stator was also noticeably higher near the end walls. The higher unsteadiness (turbulence) and mixing of the first stage presumably point to slightly higher loading and are aspects of the difference between the first and the repeating stages.

One tracer gas test was performed across the third stator of the C106 at midspan near stall at a flow coefficient of 0.48. The results, shown in Fig. 3(*d*), indicate a very small radial shift of peak concentration with almost circular contours. The mixing coefficient was, however, increased by 75 percent compared to design flow coefficient.

4 Conclusions

For the C106 four-stage compressor the mixing level at midspan was substantially increased at a flow coefficient below that for peak efficiency as found by Wisler et al. For the operation at design conditions it is concluded that:

1 There are substantial *circumferential* fluid motions in the compressor end-wall regions due to the effects of end-wall boundary layer skew and secondary flows. However, there was little *spanwise* motion attributable to the radial secondary flows in the C106 four-stage compressor tested.

2 The relative fluid motion inside the rotor blade wakes is mainly responsible for the larger tangential mixing across the stator in the mainstream region by transporting low-momentum fluid toward the pressure surface of the stator blades.

3 For multistage compressors with inlet guide vanes, the spanwise mixing coefficients through the compressor were found to be of similar magnitude for the first stage and for a later repeating stage. The mixing levels in the end-wall regions were slightly higher in the first stage.

4 In the repeating stage the magnitude of spanwise mixing was found to be substantially uniform across the whole span for the C106 compressor with moderate blade loadings and small tip clearances.

More general conclusions besides those based on the C106 are given in Part II.

Acknowledgments

The support of Rolls-Royce and the Ministry of Defence for this work is gratefully acknowledged. Y. S. Li also acknowledges the support of the British Council.

References

Adkins, G. G., and Smith, L. H., Jr., 1982, "Spanwise Mixing in Axial Flow Turbomachines," ASME *Journal of Engineering for Power*, Vol. 104, pp. 97–110.

Bragg, G. M., 1969, "The Turbulent Boundary Layer in a Corner," *J. Fluid Mech.*, Vol. 36, part 3, pp. 485–503.

Gallimore, S. J., 1985, "Spanwise Mixing in Multi-stage Axial Compressors," Ph.D. Thesis, University of Cambridge, United Kingdom.

Gallimore, S. J., and Cumpsty, N. A., 1986, "Spanwise Mixing in Multistage Axial Flow Compressors: Part I—Experimental Investigation," ASME JOURNAL OF TURBOMACHINERY, Vol. 108, pp. 2–9.

Gallimore, S J., 1986, "Spanwise Mixing in Multistage Axial Flow Compressors: Part 2—Throughflow Calculations Including Mixing," ASME JOURNAL OF TURBOMACHINERY, Vol. 108, pp. 10–16.

Gessner, F. B., and Jones, J. B., 1961, "A Preliminary Study of Turbulence Characteristics of Flow Along a Corner," ASME *Journal of Basic Engineering*, Vol. 83.

Gessner, F. B., 1973, "The Origin of Secondary Flow in Turbulent Flow Along a Corner," *Journal Fluid Mech.*, Vol. 58, part 1, pp. 1–25.

Hinze, J. O., 1959, *Turbulence, An Introduction to Its Mechanism and Theory*, McGraw-Hill, New York, Chap. 5.

Hoagland, L. C., 1960, "Fully Developed Turbulent Flow in Straight Rectangular Ducts—Secondary Flow, Its Cause and Effect on the Primary Flow," MIT Tech. Report No. 2.

Hunter, I. H., and Cumpsty, N. A., 1982, "Casing Wall Boundary-Layer Development Through an Isolated Compressor Rotor," ASME *Journal of Engineering for Power*, Vol. 104, pp. 805–817.

Kerrebrock, J. L., and Mikolajczak, A. A., 1970, "Intrastator Transport of Rotor Wakes and Its Effect on Compressor Performance," ASME *Journal of Engineering for Power*, Vol. 92, pp. 359–368.

Kotidis, P. A., 1988, "Unsteady Radial Transport in a Transonic Compressor Stage," Ph.D. Thesis, MIT, Cambridge, MA.

Lockhart, R. C., and Walker, G. J., 1974, "The Influence of Viscous Interactions on the Flow Downstream of an Axial Compressor Stage," *Proc. 2nd Int. Symposium on Air-Breathing Engines*, Sheffield, United Kingdom.

McDougall, N. M., 1990, "A Comparison Between the Design Point and Near-Stall Performance of an Axial Compressor," ASME JOURNAL OF TURBOMACHINERY, Vol. 112, pp. 109–115.

Perkins, H. J., 1970, "The Formation of Streamwise Vorticity in Turbulent Flow," *J. Fluid Mech.*, Vol. 44, part 4, pp. 721–740.

Prandtl, L., 1952, *The Essentials of Fluid Dynamics*, Blackie, United Kingdom.

Smith, L. H., Jr., 1966, "Wake Dispersion in Turbomachines," ASME *Journal of Basic Engineering*, Vol. 88, pp. 688–690.

Smith, L. H., Jr., 1970, "Casing Boundary Layers in Multi-stage Axial Flow Compressors," *Flow Research on Blading*, L. S. Dzung, ed., Elsevier, Amsterdam.

Walker, G. J., 1987, Discussion for the paper by Wisler et al. (1987).

Wisler, D. C., Bauer, R. C., and Okiishi, T. H., 1987, "Secondary Flow, Turbulent Diffusion, and Mixing in Axial Flow Compressors," ASME JOURNAL OF TURBOMACHINERY, Vol. 109, pp. 455–482.

Mixing in Axial Flow Compressors: Part II—Measurements in a Single-Stage Compressor and a Duct

Y. S. Li

N. A. Cumpsty
Whittle Laboratory,
Cambridge University,
Cambridge, United Kingdom

This paper follows directly from Part I, which contains not only the description of the facilities and the results for the C106 four-stage compressor, but also the background, list of nomenclature, acknowledgments, and references. The discussion and conclusions for Parts I and II are given here. The single-stage compressor results show the significant effects of inlet guide vane (IGV) wakes on mixing across the stage in the so-called "free-stream" region; in the casing region tip clearance flow is shown to play an important role in mixing. Explanations for these results are given. Investigations were also carried out in a two-dimensional rectangular duct flow to reveal the mixing mechanism in the corner region similar to those formed by blade surfaces and endwalls in a compressor. Turbulent diffusion has been found to be the dominant mechanism in spanwise mixing; anisotropic inhomogeneous turbulent diffusion is mainly responsible for the nonuniform mixing in the corner region. The larger spread of tracer gas in the tangential direction than in the radial direction is mainly caused by the wake dispersion and relative flow motions within the blade wakes as well as secondary flow contributions in the end-wall regions.

1 Experimental Results

1.1 Deverson Single-Stage Compressor Results: Rotor Tip Clearance 3 Percent Chord. The similarity in mixing level across the first and the third stages of the C106 four-stage compressor (reported in Part I) suggested that the low-speed single-stage Deverson compressor could be used effectively to study mixing. Because of its greater size this made accurate measurements much easier. Unlike the four-stage compressor, the Deverson compressor was designed to operate without inlet guide vanes. Figure 1 shows the pressure rise characteristics. All the tracer gas tests were carried out at the peak total pressure rise position, where the mass-averaged flow coefficient was 0.51, marked by a vertical line in the figure. The inlet boundary layer was tripped well upstream of the rotor to simulate thick end-wall boundary layers in a multistage machine; measurements of flow angle and magnitude showed that the hub and casing wall boundary layers entering the stator each occupied about 20 percent span.

For tracer gas tests in the stator ethylene was injected at 20 percent of stator blade axial chord upstream of the leading edge of the stator and sampled at 62 percent of axial chord downstream of the trailing edge. For tracer gas spreading across the rotor, ethylene was injected at 67 percent of rotor blade axial chord upstream of the rotor leading edge and sampled at 42 percent of axial chord downstream of the trailing edge; this sample plane was also the plane at which hot-wire measurements were made downstream of the rotor.

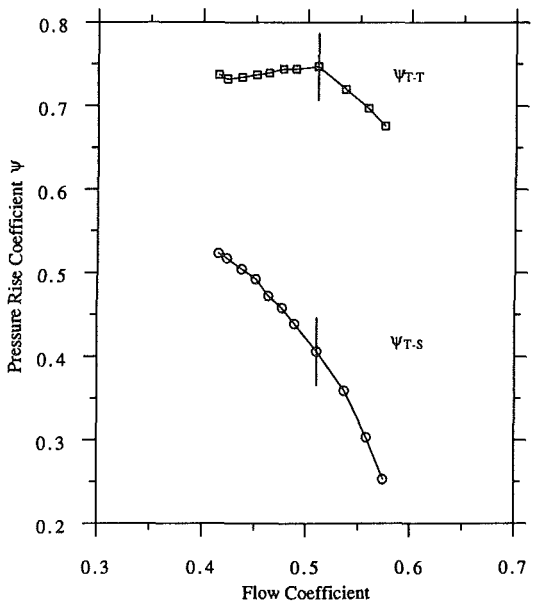

Fig. 1 Deverson single-stage compressor characteristics

Contributed by the International Gas Turbine Institute and presented at the 35th International Gas Turbine and Aeroengine Congress and Exposition, Brussels, Belgium, June 11-14, 1990. Manuscript received by the International Gas Turbine Institute December 20, 1989. Paper No. 90-GT-39.

Mixing Across the Stator Without "IGV" Wakes. The contours in Fig. 2 show the ethylene spreading and the core migration across the stator blade row. In Fig. 2(*a*) the ethylene contours were obtained downstream of the stator with injection upstream of the row at 10, 50, and 90 percent span, all at midpitch. In Fig. 2(*b*) for contour 4 ethylene was injected upstream of the leading edge of the stator at 2 mm (1.3 percent span) from the hub and 22 percent pitch in the adjacent blade passage (the passage to the right in Fig. 2*b*). For contour 5 ethylene was injected at midpitch of the stator blade passage and 2 mm from the casing.

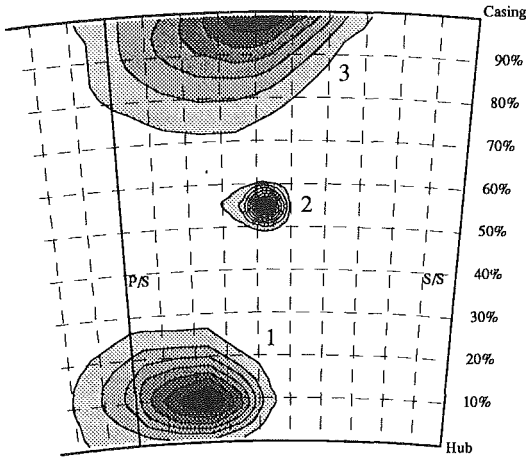

a) Injection: u/s stator at 10%,50%,90% span & at mid-pitch
Contours: min=0.10 interval=0.10

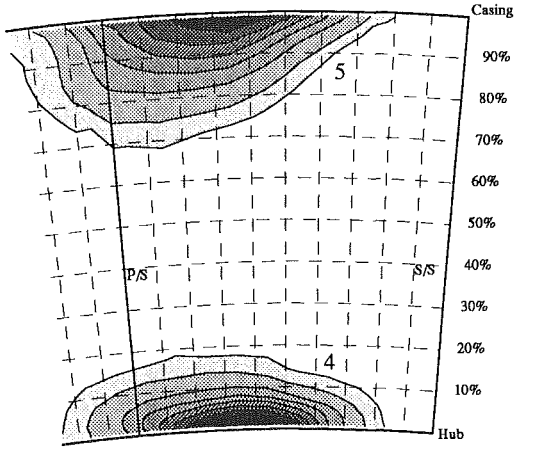

b) Injection: u/s stator 2mm from hub at 1.22 pitch and 2mm from casing at mid-pitch; Contours: 5,10,20,30,40,50,60,70,80%

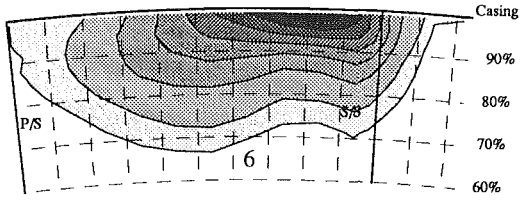

c) Injection:u/s stator 2mm from casing near s/s corner
Contours: 5,10,20,30,40,50,60,70%

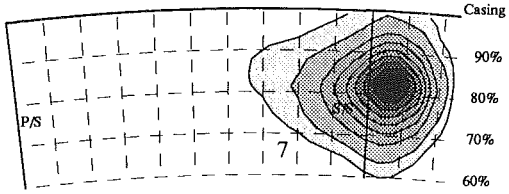

d) Injection: u/s stator at 75% span & near leading edge
Contours: 5,10,20,30,40,50,60,70,80%

Fig. 2 Ethylene contours downstream of stator showing mixing across the Deverson single-stage compressor stator at $\phi = 0.51$, $t/c = 0.03$ (no inlet guide vanes)

As described in Part I, movement of the core (position of peak concentration) is used to infer bulk movement of the flow, whereas spreading of the contours is used to infer local mixing. For contour 2, injection at 50 percent span, and contour 3, injection at 90 percent span, the core migrated about 5 percent span and 8 percent span in the spanwise direction, respectively. This was due to the blockage from a large separation in the suction surface and hub corner extending on the blade surface out to about midspan near the trailing edge, as shown by McDougall (1989). Measurements showed that the radial shift of the peak ethylene concentration could be reduced significantly by introducing a small clearance at the stator blade hub, because this eliminated the corner separation, thereby reducing the blockage and the outward deflection of the flow. Since the flow through the whole stator blade passage had been shifted toward the casing and the pressure surface by the corner separation, these migrations of the peak concentration points will not be treated here as a mixing effect although they do bring about overall redistribution of the flow.

The large core migration in the direction of rotation (i.e., toward the pressure surface) near the hub, about 88 percent stator blade pitch for contour 4 and about 25 percent stator pitch for contour 1, result from highly skewed inlet flow and also from the suction surface and hub corner separation. Furthermore all the contours in Fig. 2 were stretched in the circumferential direction toward the pressure surface of the stator blade, resulting from the effect of the incoming rotor wakes on the flow across the stator, as pointed out in Part I for the four-stage compressor results.

The spanwise spreading of ethylene was increased in the corner formed by the pressure surface and casing, contours 3

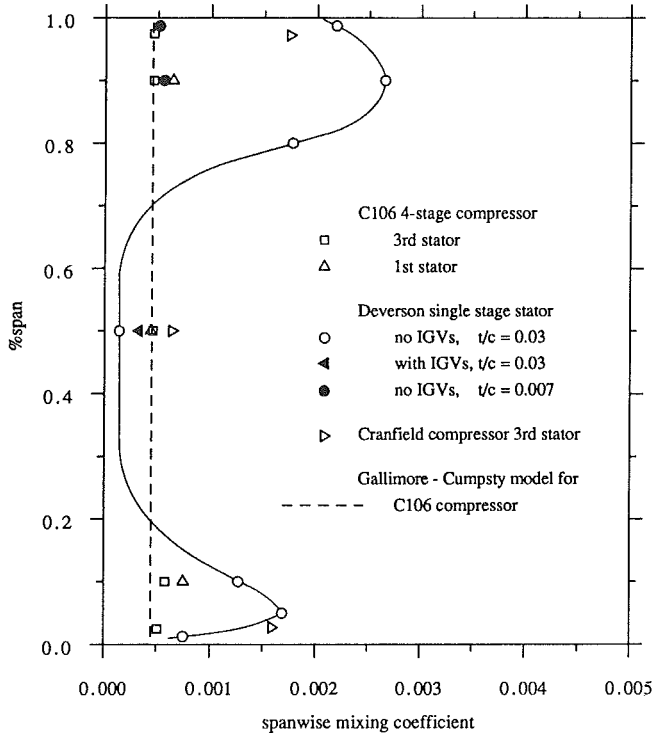

Fig. 3 Normalized spanwise mixing coefficients through stators of different machines at about peak efficiency

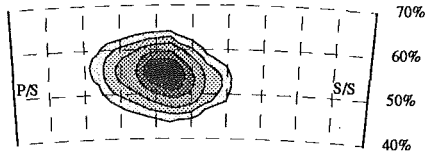

a) Ethylene spreading across the stator with IGV wakes
Injection: u/s stator at mid-span & mid-pitch; Sample: d/s stator

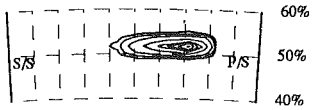

b) Ethylene spreading across the rotor without IGV wakes
Injection: u/s rotor at mid-span; Sample: d/s rotor

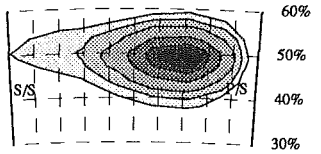

c) Ethylene spreading across the rotor within an IGV wake
Injection: u/s rotor at mid-span & inside the wake; Sample: d/s rotor

Fig. 4 Ethylene contour spreading across the single-stage compressor rotor and stator showing the effect of IGV wake dispersion by rotor on mixing across the stage at $\phi = 0.51$; contours = 5, 10, 20, 40, 60, 70, 80, and 90 percent

and 5. This might be due to turbulence gradients across the blade boundary layer, to anisotropic turbulence close to the corner, to secondary flow (inlet skew to stator), or to all of these. The distinct spanwise elongation of contours along the pressure surface found by Wisler et al. (1987) was not found in this machine at the positions examined. Contour distortion just became evident with injection near suction surface and 2 mm (1.3 percent span) from the casing, as shown in Fig. 2(*c*). The core here was shifted toward the pressure surface along the casing and the contours were strongly elongated in that direction as well. The contours in Fig. 2(*c*) were also stretched radially inward along the suction surface, though the bulk of the flow in the passage was moved toward the casing, as shown by the radially outward shift of peak concentration for contour 3 in Fig. 2(*a*). Even close to the blade surface in Fig. 2(*d*), the flow was shifted toward the casing by a similar amount to that in contour 3. However in Fig. 2(*d*), the tracer gas spread radially outward and inward relative to the peak concentration point along the blade surface with about equal magnitude; the radial spread was, however, larger than that normal to the blade on the pressure surface side. All the contours near the wall supported the idea that inhomogeneity and anisotropy of turbulence were responsible for the tendency for the tracer gas to spread further along the blade surfaces, the hub, and the casing. Contour 4 in Fig. 2 (*b*), with injection close to the hub, provides a good example. The contour spreading along the hub was almost symmetric about the peak, but spreading in this direction was much greater than that along the span. This gave clear evidence of anisotropic turbulent diffusion rather than the systematic motion as an explanation for the increased spreading parallel to surface. The role of anisotropic and inhomogeneous turbulence in the mixing mechanism will be shown more clearly in the duct corner flow.

The ethylene spreading across the span for the Deverson stage was substantially different from that found in the C106 four-stage compressor: Most noticeably it was very small in the mainstream region and large in the end-wall boundary layers. The spanwise mixing coefficients estimated from the ethylene contours are plotted together with the mixing coefficients on the four-stage C106 compressor in Fig. 3. The value near midspan for the Deverson stage without IGV is about a third of that obtained in the C106 or a quarter of that in the Cranfield compressor used by Gallimore (1985). Near the casing the mixing coefficients are very high for the Deverson compressor compared with the C106 compressor. The loading of the Deverson stage is not significantly different from the other machines. The most obvious difference near midspan is the absence of any blades ahead of the Deverson rotor, while near the casing the Deverson rotor had high values of tip clearance.

The Effect of IGVs on Mixing. In order to see the influence of inlet guide vane (IGV) wakes on mixing across the rotor and the stator, radial rods were placed upstream of the rotor spanning the annulus. The rods were circular in cross section, so that no turning would be introduced and the mean flow conditions into the stage should not be substantially altered. The rods were 4 mm in diameter, to give about the same momentum thickness as the stator blade wake at midspan region, and were put upstream of the rotor at an axial distance equal to the rotor and stator axial gap. The rods had the same pitch as the stator.

Figure 4 shows the ethylene spreading across the stator and rotor for injection at midpitch and midspan, all at the peak total pressure rise point, $\phi = 0.51$. With the simulated IGV wakes upstream of the rotor, tracer gas contours measured downstream of the stator with injection upstream of it are shown in Fig. 4(*a*). Compared with Contour 2 in Fig. 2(*a*) (obtained with no IGV wakes), the ethylene spreading was increased by 44 percent in the spanwise direction and 67 percent in the tangential direction. For Fig. 4(*a*) the rods were displaced circumferentially about half a stator pitch so as not to be aligned with the stator blades. However the increase in ethylene spreading was also about the same when the rods were circumferentially aligned with the stator blades. Although the mixing rate across the stator was increased significantly in the free-stream region with the rods to simulate IGVs, the mixing rates inside the hub and casing boundary layers remained essentially unaltered and these results are therefore not shown.

Across the rotor the mixing rate without IGVs was very small outside the end-wall region. As shown in Fig. 4(*b*), the radial spread was only about 5 percent span, with the tangential elongation of the contours being caused by the rotor rotation. With rods to simulate IGVs, the mixing across the rotor was much larger, shown in Fig. 4(*c*): Spanwise spreading across the rotor was then about 20 percent span, while the circumferential spreading almost covered a complete rotor blade pitch. The peak concentration core downstream of the rotor remained at midspan position. The flow within the rod wake was highly turbulent and the significant ethylene spreading in spanwise direction is explainable in terms of turbulent diffusion of the wake flow. However, the large ethylene spreading in the circumferential direction was a combined effect of turbulent diffusion and wake dispersion.

The dispersion of the stator wake by downstream rotor blades had been known for many years (e.g., Smith, 1966; Lockhart and Walker, 1974; Walker, 1987). The IGV wake is chopped into segments, terminated by rotor blades or their wakes, because each segment is transported at different speeds on the pressure and suction sides of the rotor blade passage. Downstream of the rotor the IGV wake fluid is spread over an avenue of discontinuous segments terminated by rotor wakes, and these segments move in the tangential direction at the same speed as rotor blade. Using Walker's (1987) analysis the circumferential extent of the wake dispersion was estimated to be 0.46 of rotor pitch downstream of the rotor. The experimentally observed maximum dispersion of the wake was obtained by using the 5 percent ethylene concentration contour,

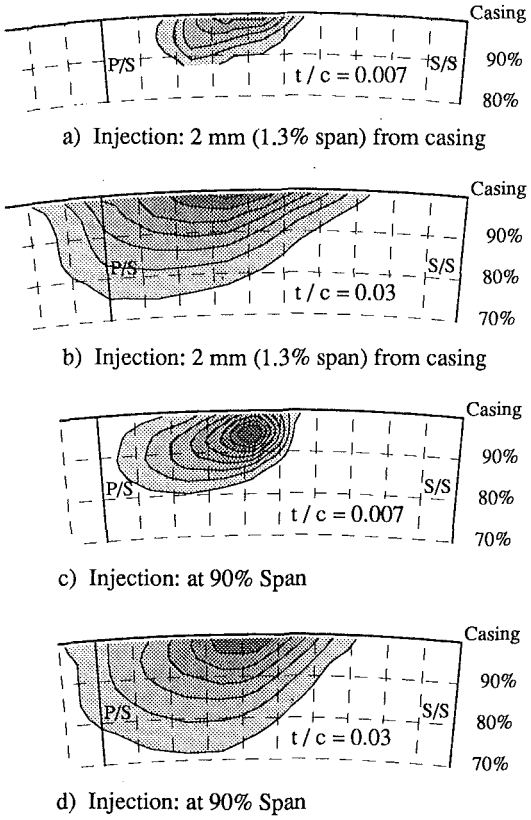

Fig. 5 Ethylene contour spreading across the Deverson single-stage comrpessor stator at small and large rotor tip clearances with injection upstream of the stator at midpitch; contours: min. = 0.1, interval = 0.1 (no IGVs)

shown in Fig. 4(*c*). Assuming isotropic mixing well away from solid surfaces, the spanwise spreading distance of the tracer gas was subtracted from the circumferential spreading to give the measured dispersion. The resulting dispersion due to the wake chopping was 0.50 of rotor pitch, which is in satisfactory agreement with the estimate of 0.46 obtained above. Walker (1987) also found good agreement between such predictions and the tracer gas results from Wisler et al. (1987).

Midspan circumferential traverses downstream of the rotor with a single hot-wire probe showed that phase-lock ensemble-averaged turbulence intensities (the total unsteadiness after removing the periodic unsteadiness of the rotor) were increased significantly with rods upstream of the rotor to simulate IGVs compared with tests without IGVs. Across the rotor the peak concentration point of the tracer gas remained almost at the same position as injection, indicating that the radial secondary flow was small in the mainstream. It is therefore believed that the significant increase in turbulence intensities caused by the IGV wakes was primarily responsible for the larger spanwise mixing across the stator. The spanwise mixing coefficient across the stator with IGV wakes is shown in Fig. 3 at midspan and is close to the values obtained in multistage compressors.

1.2 Deverson Single-Stage Compressor Results: Rotor Tip Clearance 0.7 Percent Chord. Apart from the absence of IGVs, the major difference between the build of the Deverson single-stage compressor used for the results presented so far and the other compressors is the larger rotor tip clearance: 3 percent of chord compared to about 1.2 percent for the C106 four-stage compressor. Tracer gas measurements were subsequently taken across the stator of the Deverson compressor with the rotor blade tip clearance reduced to 0.7 percent of chord. Ethylene was injected at midpitch upstream of the stator at 98.7 percent span (2 mm from the casing) and 90 percent span and was sampled downstream of the stator. The positions

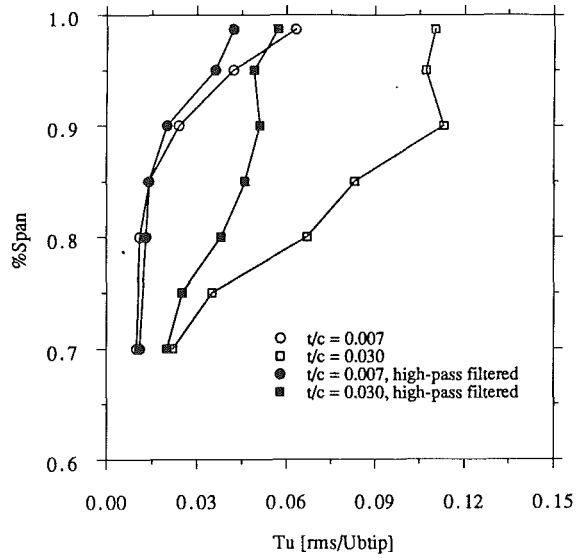

Fig. 6 Ensemble-averaged time mean turbulence intensities downstream of Deverson rotor at $\phi = 0.51$ (no IGVs)

of injection and sample planes were the same as those for the 3 percent tip clearance tests.

The tracer gas contours measured downstream of the stator with small rotor tip clearance are shown in Fig. 5(*a*) for the injection close to casing and in Fig. 5(*c*) with injection at 90 percent span. Their counterparts at the large tip clearance case are shown in Fig. 5(*b*) and Fig. 5(*d*) for comparison. The tracer gas spreading across the stator was significantly reduced in both radial and circumferential directions when the rotor tip clearance was decreased.

The spanwise mixing coefficients for the 0.7 percent tip clearance case were deduced from the tracer gas spreading shown in Fig. 5 and are plotted in Fig. 3 as solid circles. With the tip clearance to blade chord ratio reduced the spanwise mixing coefficients across the single-stage compressor stator were about the same as those in the C106 four-stage compressor; clearly tip clearance has an extremely strong effect on mixing near endwalls even in the rows downstream of that with clearance.

Detailed measurements of the velocity field have been made downstream of the Deverson rotor by Dr. A. Goto at rotor tip clearances equal to 0.7 and 3.0 percent of chord. At a flow coefficient of 0.51 the average casing boundary layer thicknesses are about 20 mm and 40 mm, respectively. These thicknesses are very similar to the overall spanwise spread found for the contours with injection close to the casing wall shown in Fig. 5. The measurements of flow downstream of the rotor show much larger regions of disturbed flow near the casing with large clearance, there being a strong tip leakage flow across the pitch from suction surface to pressure surface. The 3 percent tip clearance produced a spanwise migration of the peak concentration location of about 8 percent span, nearly twice that of the 0.7 percent chord tip clearance, as shown by Figs. 5(*c*) and 5(*d*). This extra migration is, however, toward the casing, and does not help to explain the significant contour spreading in the radially inward direction at the larger tip clearance. The extra tip clearance flow is, however, very important in producing a thick casing boundary layer, a well-established effect (Smith, 1970; Hunter and Cumpsty, 1982). The thick boundary layer and the large turbulent region associated with the clearance jet then cause the much greater spread of tracer gas and correspondingly higher mixing coefficient.

The extra tip clearance flow generates higher turbulence in the tip region. Figure 6 shows the turbulence intensity distribution across the casing boundary layer downstream of the

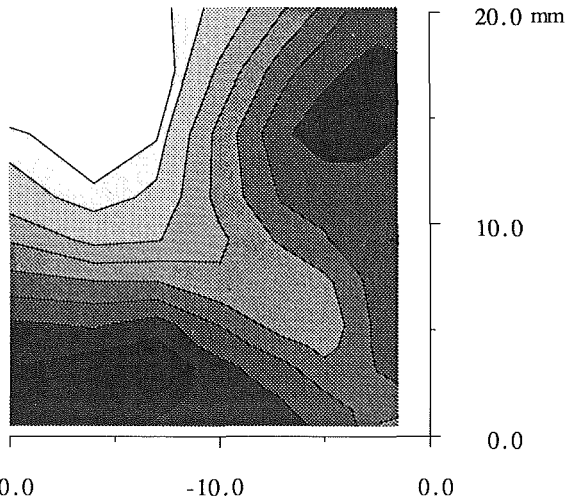

Fig. 7 Turbulence intensities in duct flow, corner A; contours: 2.8, 3.0, 3.5, 4.0, 4.5, 5.0, 5.5, 5.8, 6.0, and 6.1 percent, respectively

rotor at tip clearances of 0.7 and 3.0 percent of chord at the same flow coefficient used for the tracer gas tests, 0.51. They were measured by a single hot-wire probe with the sensing wire perpendicular to the time-mean streamwise velocity. What is actually shown in Fig. 6 is the ensemble average of the unsteadiness, specifically the root mean square of the difference between instantaneous velocity and ensemble average velocity. The open symbols in Fig. 6 show the entire signal with a frequency range from blade passing frequency upward. Clearly the unsteadiness is very much higher at the larger tip clearance. It was noticed that the signals contain large amplitudes at relatively low frequencies comparable to the blade passing frequency; this is not turbulence in the normal meaning of the word, but differences in the rotor passage flow from one realization to another. The low-frequency components up to twice blade passing frequency were removed digitally to give the points shown in Fig. 6 with solid symbols. (A test showed that virtually identical results would be obtained with filtering at three times blade passing frequency, so this choice is not critical.) With the low-frequency unsteadiness removed the levels of what is more realistically described as turbulence are much lower. Nevertheless with 3 percent tip clearance the turbulence intensity is about twice that at smaller clearance.

The rotor tip clearance can have little direct effect on the mixing level near the stator hub and cannot explain the higher levels of mixing there, which is evident in Fig. 3. The explanation is probably the poor local aerodynamics since the stator suction surface hub corner showed clear evidence of separation even at $\phi = 0.55$ (McDougall, 1989). At the same flow coefficient there is also slight evidence of a small separated region near the rotor hub. These can be expected to give the raised levels of mixing near the hub shown in Fig. 3.

1.3 Duct Flow Results. As indicated in the introduction, both secondary flow and anisotropic turbulence can cause nonuniform mixing in particular directions. The experimental work by Wisler et al. (1987) had shown greater ethylene contour spread along the blade surface and along the end-wall than normal to the solid boundaries, particularly in the end-wall corner region. They attributed this to a combination of secondary flow and turbulent diffusion. In fact, turbulence is well known to be anisotropic close to solid surfaces, with larger velocity fluctuations parallel than normal to the surface. There are also turbulence gradients near solid surfaces and in the corner regions; the turbulence is inhomogeneous. In an experiment with foreign gas injection, larger spreading would therefore be expected to occur along the surface than normal to the surface even without any secondary flow effect. The corner flow in a rectangular duct is ideal for demonstrating

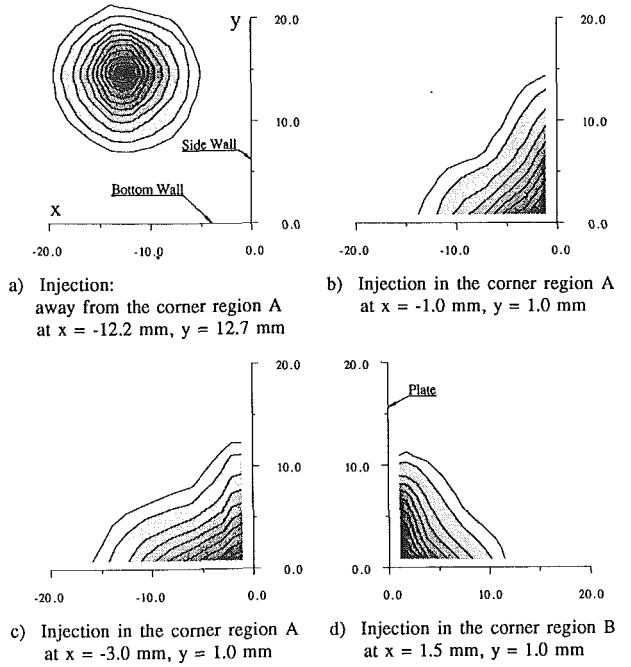

a) Injection: away from the corner region A at x = -12.2 mm, y = 12.7 mm

b) Injection in the corner region A at x = -1.0 mm, y = 1.0 mm

c) Injection in the corner region A at x = -3.0 mm, y = 1.0 mm

d) Injection in the corner region B at x = 1.5 mm, y = 1.0 mm

Fig. 8 Ethylene contour spreading in a turbulent duct flow; contours = 5, 10, 20, 30, 40, 50, 60, 70, 80, and 90 percent

the significant effect of anisotropic and inhomogeneous turbulent diffusion on mixing, provided any secondary flow is suppressed. However, even the corner flow in a rectangular duct can be complicated because of the mechanism of secondary flow of the so-called *second* type. Secondary flow of the second type is driven by turbulent stress gradients, whereas secondary flow of the first type, conventional secondary flow, is generated by the turning of mean flow having nonuniform stagnation pressures. Both experimental and theoretical investigations for the second type of secondary flow are described in the literature (e.g., Prandtl, 1952; Hoagland, 1960; Bragg, 1969; Gessner, 1961, 1973; Perkins, 1970; Nakamura et al., 1982). Secondary flow of the second type develops slowly and is usually of small magnitude; see Perkins (1970).

The contours of turbulence intensities in the duct corner region A (see Fig. 1 in Part I) are shown in Fig. 7. They were measured by a single straight hot-wire probe. The peak levels were about 6 percent of the free-stream velocity and decreased toward the duct corner bisector, with regions of higher turbulence on each side. The field is clearly inhomogeneous. The turbulence close to the walls would also be anisotropic, as has been measured by others, although it could not be measured by a single straight hot-wire probe during these experiments.

Figure 8 shows the ethylene contour spreading in the turbulent duct flow. For all the tests the injection was 127 mm upstream of the sampling plane. At the injection plane it can be assumed that there will be no secondary flow because of the proximity to the honeycomb. The ethylene contours at the sample plane in corner A, with ethylene injected at 12.2 mm from the side wall and 12.7 mm from the bottom wall, are shown in Fig. 8(*a*). The contours are almost circular, but with slightly greater spreading toward the bottom and the side-wall surfaces caused by the higher turbulence intensity there. When the injection was close to the corner, however, the contours were significantly distorted, with larger spreading along the two solid surfaces. With injection at 1 mm from each wall surface, Fig. 8(*b*), the contours were no longer circular relative to the peak concentration point and the spreading along the two wall surfaces was about 59 percent larger than along the corner bisector direction. The contour distortion was even more clear when the ethylene was injected at 3 mm from the

side wall and 1 mm from the bottom wall, as shown in Fig. 8(*c*). Significant contour distortion occurred along the side wall in an area about 3 mm from the wall, a region of very high turbulence as shown in Fig. 7. There was a small shift of about 1.5 mm in peak concentration point toward the side wall. The ethylene spreading along the bottom surface was in the direction opposite to the peak concentration point shift, and was much larger than that along the corner bisector direction. The contours shown in Fig. 8(*c*) are similar to those obtained by Wisler et al. (1987) in the blade pressure surface–casing wall corner of the third stator of their four-stage research compressor.

The core migration in Fig. 8 indicates that secondary flow (of the second type) existed in the corner region. Flow angle measurements (by rotating a single straight hot-wire probe) showed that the maximum flow angle deviation from that at the center of the duct occurred close to the wall: 1.75 deg at 10 mm from the side wall. The maximum possible secondary flow velocity (of the second type) calculated from the highest flow angle measured close to the wall was less than 2 percent of the mainstream velocity. The core migration by this secondary flow was compared with the amount by which contour spreading along the wall surface exceeded that along the corner bisector. The core migration attributable to secondary flow accounted for about 25 percent of the larger contour spreading near the surface. The remainder of the spreading along the surface must be contributed by the anisotropic, inhomogeneous turbulent diffusion. Since, however, the secondary velocity of the second type is created directly by turbulence, it is not inappropriate to attribute all of this spreading to the effect of turbulence.

For flows in compressors, the boundary layer along the blade surface would be normally thinner than on the endwall. To simulate this, a thin flat plate (280 mm long) was fitted in the middle of the duct and the ethylene was injected in corner B formed by the plate and the duct bottom wall. The contours are shown in Fig. 8(*d*). Significant contour distortion again occurred along the solid surfaces, in particular along the flat plate. Farther away from the corner region the contours were less distorted, as shown by the lower concentration contours. The behavior of mixing with the plate was generally very similar to that in corner A.

The mixing coefficients in the corner flow derived from the tracer gas contours in Fig. 8 were all very similar and the mean normalized mixing coefficient was 5.7×10^{-4}, comparable to values in the end-wall regions of the C106 four-stage compressor shown in Fig. 3.

2 Discussion

The mixing coefficients for the single-stage compressor without inlet guide vanes were significantly different from those of the C106 four-stage compressor: much higher in the end-wall regions and significantly lower in the mainstream region; see Fig. 3. In the mainstream region the difference between mixing coefficients observed for these two machines was clearly shown to be the absence of any upstream blade rows in the single-stage compressor.

The effect of compressor blade loading on mixing had been demonstrated by Wisler et al. (1987). This was believed to be another influential factor for the different mixing levels observed in the present experimental results. The C106 four-stage compressor stator blades were designed with a diffusion factor of 0.4, almost uniform across the span. For the single-stage compressor, however, the stator blades were more heavily loaded with an almost constant design diffusion factor of about 0.5 outside the end wall boundary layer. Previous oil dye visualization studies by McDougall (1989), and those taken by the present authors, had shown separations in the corners formed by the end-walls and the stator blade suction surface even at design and near design conditions. Separation in the suction surface–casing corner was much smaller than the separation in the suction–surface hub-corner. With separation present in the end-wall regions, increased mixing would be expected.

In Fig. 3 the spanwise mixing coefficients across the third stator of the Cranfield four-stage compressor, referred to as compressor A by Gallimore and Cumpsty (1986), are also shown for comparison with the C106 four-stage and the Deverson single-stage compressor results. The design parameters for the stators of the Cranfield and the single-stage compressors were similar: Both compressors have shrouded stators but the Cranfield compressor rotors had a tip clearance of 1.5 percent chord. In the mainstream all the mixing coefficients were similar to each other, except for that of the Deverson compressor without IGVs. Near the hub the spanwise mixing coefficients for the third stator of the Cranfield compressor and the stator of the single-stage compressor were very similar, but larger than those of the C106 four-stage compressor, which was unshrouded. Near casing the value of the mixing coefficient for the Cranfield compressor was noticeably lower than that of the Deverson single stage with a tip clearance-to-chord ratio of 3 percent, but larger than those of the C106 four-stage and the single stage at small tip clearance.

An empirical model for the prediction of spanwise mixing coefficients in a multistage compressor was given by Gallimore and Cumpsty (1986) and was expressed as

$$\frac{\epsilon}{V_z L_s} = A \frac{t}{L_s} \left[\frac{2\omega(t/L_s)}{3\phi^2} \right]^{1/3} \tag{1}$$

This was used to calculate the normalized mixing coefficient $\epsilon / V_z L_s$ for the C106 compressor using the measured stage loss coefficient ω and flow coefficient ϕ, the blade trailing edge thickness t and $A = 0.4$, as used by Gallimore and Cumpsty. Since the C106 four-stage compressor blades have controlled diffusion airfoils with relatively thick trailing edges and the blades were designed to have attached flow at the trailing edge, it was thought that the blade trailing edge thickness would be more representative of the typical length scale of turbulent eddies in this compressor. A normalized mixing coefficient of 4.5×10^{-4} was estimated for design point operation and this is shown in Fig. 3 by the dashed line. It is very close to the values derived from tracer gas tests for the four-stage compressor.

Kotidis (1988) studied mixing across a transonic rotor and found significant diffusion of tracer gas across the entire span. His instrumentation was sufficiently fast that the concentration of the tracer gas in the wake of the rotor was rather apparent. High-frequency instrumentation also revealed the presence of strong spanwise vortices in the wakes and it is believed that substantial radial flows take place along the cores of these vortices. If this is also the mechanism dominating mixing away from the endwalls in the compressors used for the present study, as well as those used by Gallimore and Cumpsty (1986) and Wisler et al. (1987), it is inappropriate to refer to it as turbulence, though this catch-all term is retained here. One can, nevertheless, see why high levels of turbulence and high rates of mixing would be found in the same regions even when mixing is produced by motion inside large eddies: The shed vortices can be random and unsteady, and the flow in the blade wake is inevitably turbulent.

3 Conclusions

The following conclusions are drawn based on the experimental observations reported and discussed in this two-part paper:

1 There are substantial circumferential fluid motions in the compressor end-wall regions attributable to end-wall boundary layer skew and secondary flows. However, there was

little spanwise motion attributable to this in the C106 four-stage compressor. The fluid migration toward the casing over most of the stator blade passage of the single-stage compressor was caused by the blockage arising from a separation in the stator suction surface–hub wall corner.

Despite the large skew of the hub wall boundary layer through the single-stage compressor stator, no significant ethylene contour distortion onto or along the pressure surface was observed in the hub corner. In the corner formed by the casing wall and suction surface of the single stage there was elongation of ethylene contours radially inward along the blade surface, but without any sign of the core being moved radially inward by the flow.

2 The substantial mixing away from the end-walls in the tangential direction, particularly across the rotor, is mainly due to flow dispersion or chopping of wakes from upstream by the rotating blades.

3 The dispersion by the rotating blade row of wakes from a stationary upstream row can cause a significant increase in the mixing coefficient in the mainstream across the subsequent stator row by generating periodic patches of random unsteadiness.

4 The relative fluid motion inside the rotor blade wakes is mainly responsible for the larger tangential mixing across the stator in the mainstream region. Low-momentum fluid is transported toward the pressure surface of the stator blade by the relative motion in the rotor wakes.

5 For the Deverson single-stage compressor the mixing coefficient around midspan in the stator was low without IGVs upstream of the rotor; the mixing level was increased significantly with IGVs upstream and was then close to the value in a multistage machine. For the C106 four-stage compressor (with inlet guide vanes), the spanwise mixing coefficients were found to be of similar magnitude for the different stages; the mixing coefficient in the mainstream was about the same, while in the end-wall regions it was slightly higher in the first stage. The effect of wakes on mixing is not additive and it is concluded that this is because the blade wakes decay rapidly through succeeding blade rows.

6 Tip clearance flows play an important role in the mixing process by thickening the endwall boundary layer and by creating high levels of turbulent diffusion in the endwall region. The radial distribution of spanwise mixing coefficients can be approximately uniform or can vary significantly: Large casing tip clearance and hub corner separation have been found to lead to locally increased mixing levels near the endwall.

7 Tests with a simple flow in a duct confirmed that anisotropic turbulence can produce tracer gas contours in corners distorted in ways similar to that sometimes previously found in compressors. Anisotropic turbulence contributes to the greater diffusion parallel to solid walls than normal to them.

8 Mixing in the tangential direction, particularly along the end-walls, is usually larger than the radial mixing because of the combined effects of secondary flow convection, periodic transportation by the rotor blade wakes, and anisotropic inhomogeneous turbulent diffusion.

little spanwise motion attributable to this in the C106 four-stage compressor. The fluid migration toward the casing over most of the stator blade passage of the single-stage compressor was caused by the blockage arising from a separation in the stator suction surface–hub wall corner.

Despite the large skew of the hub wall boundary layer through the single-stage compressor stator, no significant ethylene contour distortion onto or along the pressure surface was observed in the hub corner. In the corner formed by the casing wall and suction surface of the single stage there was elongation of ethylene contours radially inward along the blade surface, but without any sign of the core being moved radially inward by the flow.

2 The substantial mixing away from the end-walls in the tangential direction, particularly across the rotor, is mainly due to flow dispersion or chopping of wakes from upstream by the rotating blades.

3 The dispersion by the rotating blade row of wakes from a stationary upstream row can cause a significant increase in the mixing coefficient in the mainstream across the subsequent stator row by generating periodic patches of random unsteadiness.

4 The relative fluid motion inside the rotor blade wakes is mainly responsible for the larger tangential mixing across the stator in the mainstream region. Low-momentum fluid is transported toward the pressure surface of the stator blade by the relative motion in the rotor wakes.

5 For the Deverson single-stage compressor the mixing coefficient around midspan in the stator was low without IGVs upstream of the rotor; the mixing level was increased significantly with IGVs upstream and was then close to the value in a multistage machine. For the C106 four-stage compressor (with inlet guide vanes), the spanwise mixing coefficients were found to be of similar magnitude for the different stages; the mixing coefficient in the mainstream was about the same, while in the end-wall regions it was slightly higher in the first stage. The effect of wakes on mixing is not additive and it is concluded that this is because the blade wakes decay rapidly through succeeding blade rows.

6 Tip clearance flows play an important role in the mixing process by thickening the endwall boundary layer and by creating high levels of turbulent diffusion in the endwall region. The radial distribution of spanwise mixing coefficients can be approximately uniform or can vary significantly: Large casing tip clearance and hub corner separation have been found to lead to locally increased mixing levels near the endwall.

7 Tests with a simple flow in a duct confirmed that anisotropic turbulence can produce tracer gas contours in corners distorted in ways similar to that sometimes previously found in compressors. Anisotropic turbulence contributes to the greater diffusion parallel to solid walls than normal to them.

8 Mixing in the tangential direction, particularly along the end-walls, is usually larger than the radial mixing because of the combined effects of secondary flow convection, periodic transportation by the rotor blade wakes, and anisotropic inhomogeneous turbulent diffusion.

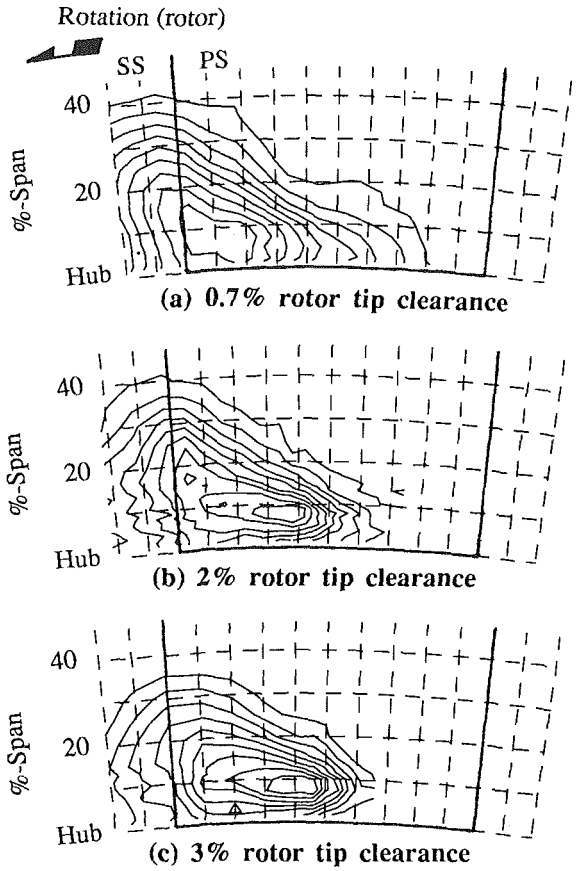

Fig. 9 Ethylene contour downstream of stator of Deverson compressor at different rotor tip clearances ($\phi = 0.51$, contour interval = 0.1, minimum contour = 0.1, injection: upstream stator at 10 percent span and midpitch)

DISCUSSION

A. Goto[1]

Since I had an opportunity to work on the same compressor as that used by Li and Cumpsty, I would like to add a few points to this paper.

Additional measurements were carried out at 0.7, 2, and 3 percent rotor tip clearances and the dominant effect of the small-scale turbulence, generated within the rotor, on mixing across the downstream stator was confirmed. The maximum value of the mixing coefficient in the casing region was found to increase linearly with the rotor tip clearance, starting from the value at midspan, because of turbulent-type small-scale unsteadiness due to the diffusion of the tip leakage vortex.

Figure 9 compares the ethylene tracer-gas spreading in the hub region between three different rotor tip clearances. In every case, a radial contour distortion is observed in the hub–pressure surface corner region. Although the cause of the difference between the present results and Li and Cumpsty's result (compare Fig. 9(*c*) with contour 1 in Fig. 2) is as yet unexplained, the distortion is identical with that found in duct flow measurements (Fig. 8), by which Li and Cumpsty pointed out the possibility of anisotropic turbulence as the mechanism of contour distortion.

What I have commented here will be the subject of a paper to be submitted to the 1991 International Gas Turbine and Aeroengine Congress and Exposition.

D. C. Wisler[2]

Professor Cumpsty and his students continue to make im-

[1]Ebara Research Co., Ltd., 4-2-1 Honfujisawa, Fujisawa-shi 251, Japan.

[2]GE Aircraft Engines, Cincinnati, OH, USA.

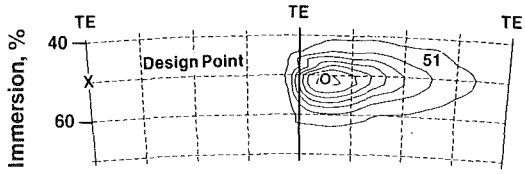

a) Spreading across Rotor 4, X = Stator 3 suction surface at 80% chord, O = downstream of Rotor 4 at Plane C

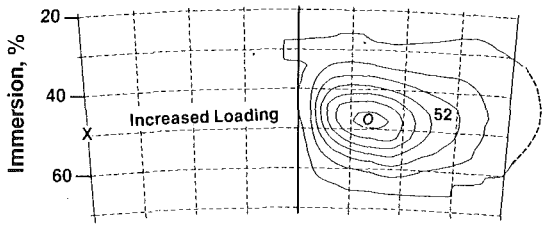

b) Spreading across Rotor 4, X = Stator 3 suction surface at 80% chord, O = downstream of Rotor 4 at Plane C

Fig. 10 Ethylene contour spreading showing enhancement of circumferential spreading and mixing by rotor action; X = injection location, O = sampling plane

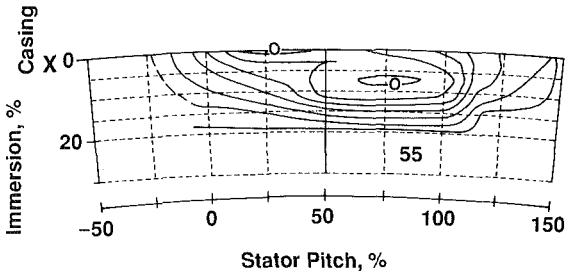

Fig. 11 Ethylene contours and split cores showing mixing action of the rotor: X = casing injection at 25 percent Rotor 3 chord, 0 = downstream of Rotor 3 at plane 3.5

portant contributions to the understanding of mixing in axial-flow compressors. Of particular interest in this paper are the effects of the IGVs and rotor tip clearance on mixing. I would like to discuss these effects first, noting similarities with our data. An assessment of the relevance of the duct flow results is given at the end.

I believe that there is now considerable agreement about the mechanisms causing mixing in axial compressors. That both convective and diffusive effects can and do operate in the mixing process is no longer disputed. This became apparent during the discussion at the end of the Mixing session in Brussels.

The effects of the IGVs on mixing are very interesting and I agree with the analysis of Li and Cumpsty. In fact Wisler et al. (1987) presented ethylene trace-gas data across the rotor that can be directly compared with those of Li and Cumpsty. The Wisler et al. (1987) results in their Fig. 19(*a*), also included here as Fig. 10(*a*), give spreading across the fourth rotor when ethylene was injected into the wake of the upstream imbedded stator at 50 percent immersion. The Li and Cumpsty (1991) Part II data in their Fig. 4(*c*) show similar spreading across the first rotor when ethylene was injected into the wakes of rods that simulate IGVs, also at 50 percent immersion. The agreement in the shapes of these fourth and first rotor contours in both the circumferential and radial directions is striking. Both Wisler et al. and Li and Cumpsty attribute this spreading at 50 percent immersion to turbulent diffusion and wake dispersion. Increasing the turbulence level increases the spreading as shown by Li and Cumpsty (1991) in Figs. 4(*b*, *c*) and Wisler et al. (1987) in Figs. 10(*a*, *b*). These results are important in developing wake dispersion models, such as that of Walker.

Do the authors have similar data across the rotor but taken in the tip clearance region at the casing? This would complement their tip clearance results in Fig. 5 and would allow further comparison with Wisler et al.'s Fig. 25, shown here as Fig. 11, where not only diffusion but circumferential and radial convection are seen as well.

The new results of Li and Cumpsty in Fig. 5, showing the effects of tip clearance on spreading levels, are dramatic. It does seem to me that there is much less boundary layer skew in these results than in those of Wisler et al. (1987). Perhaps this difference in the compressors is partly responsible for the lack of distinctive distortion in the Fig. 5 contours near the pressure surface.

The duct flow results in Fig. 8 of Li and Cumpsty, Part II, require further consideration. The idea here is that a simple, rectangular duct, having no secondary flow, is used to demonstrate how anisotropic and inhomogeneous turbulent diffusion distort ethylene contours. These distorted contours from the duct are then compared to those from the compressor of Wisler et al. (1987), and similarities in shapes are noted. Based on these similarities, one is then to conclude that anisotropic turbulence is the dominant mechanism responsible for the mixing in the endwall and corner regions of a compressor.

In response to this, I believe that the shapes of the contours in the duct are accurate, classical, and predictable data. That anisotropic turbulence is responsible for distorting these duct contours and that this mechanism, in some measure, also operates very near surfaces in compressors are both correct.

However, there are very significant differences between the flow in the corner of a long, straight, rectangular duct and that in the end-wall region of an imbedded stage of a highly loaded HP compressor, particularly with respect to boundary layer skew. I think that these differences must be taken into account when diagnosing causes of contour distortion (mixing). After all, both convection and diffusion can distort contours.

Mere general similarity of the shapes of ethylene contours between the duct and the compressor does not mean similarity of causes. Both diffusion and convection have been shown by Leylek and Wisler (1991) to operate in the endwall region in question in compressors. It seems only logical to conclude that both of these mechanisms operate to cause the mixing.

References

Leylek, J. H., and Wisler, D. C., 1991, "Mixing in Axial-Flow Compressors; Conclusions Drawn From Three-Dimensional Navier-Stokes Analyses and Experiments," ASME JOURNAL OF TURBOMACHINERY, Vol. 113, this issue.

Authors' Closure

Response to Discussion by Dr. A. Goto

We greatly appreciate the additional information about the mixing phenomenon obtained by Dr. Goto in the single-stage compressor. Dr. Goto points out quite correctly that his measurements on the same machine show much more radial distortion of the tracer gas contours. One possible reason for the difference between the contours in Fig. 9(*c*) obtained by Dr. Goto and contour 1 in Fig. 2 of our paper is that the flow coefficients may have been slightly different in the two cases. Furthermore the rotor had been stripped and rebuilt many times and there may have been some slight difference in stagger. The difference between the shape of the contours is, nevertheless, significant and worth pointing out.

It is also worth noting that the radial distortion of the contours found by Dr. Goto is more pronounced at the two smaller tip clearances, shown in his discussion as Figs. 9(*a*, *b*). Our

measurements were made only at 3 percent clearance, which corresponds to his Fig. 9(*c*), and for this case the contour distortion is rather less. The spreading of the contours near the hub must be altered because the flow field in the hub region is altered. The principal alteration in the flow field attributable to reduction in tip clearance is that the blockage produced near the casing is smaller and this means that the static pressure rise is larger across the rotor. This does not, however, explain why the contours should be more radially distorted when the tip clearance is small.

Response to Discussion by Dr. D. C. Wisler

The authors would like to thank Dr. Wisler for his kind remarks and for his considered response to their papers. There is a large measure of agreement between us and it is encouraging that both the scope and the need for further investigation seem to be disappearing.

Dr. Wisler asks whether there are any measurements across the rotor tip with and without the wakes of the inlet guide vanes. One example of this is available and is shown in Fig. 12. These tests were performed near peak efficiency with the rather large tip clearance equal to 3 percent of chord. Although there is some increase in the spreading when the wakes are present, this is very much less than the results at midspan, shown in Fig. 4 of Part II of our original paper. This is because the flow in the tip region is already highly turbulent and the addition of the extra wake turbulence is relatively insignificant.

We agree with Dr. Wisler that the effect of tip clearance on mixing is dramatic. On reflection it can be realized that this increase in mixing with tip clearance is necessary if a repeating stage is to be possible at a range of tip clearances. The loss and blockage rise locally as the tip clearance is increased; to spread this across the annulus, in order to preserve the profile into the next stage, the mixing level must increase in step. Clearly these tests identified a very important variable in determining the level of mixing. More careful and detailed measurements of the variation in mixing with tip clearance have been obtained by Dr. A. Goto on the same Deverson compressor and these will be presented at the ASME Gas Turbine and Aeroengine Congress and Symposium to be held in Orlando in 1991.

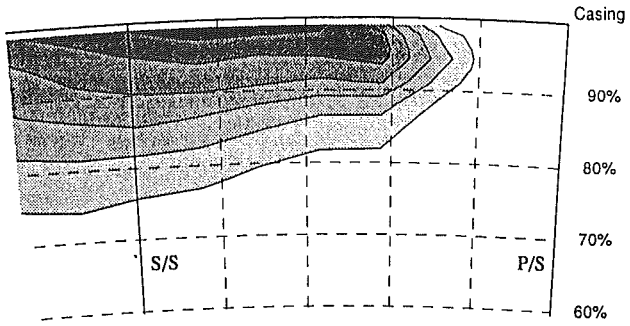

a) Without IGV upstream; Injection: 2mm from the casing u/s of rotor; Sampling: d/s of the rotor

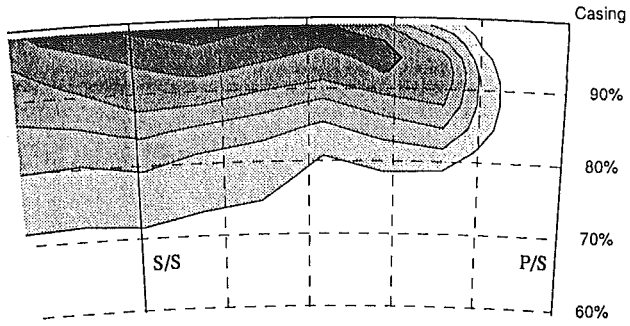

b) With IGVs upstream; Injection: 2mm from the casing inside IGV wake u/s of rotor; Sampling: d/s of the rotor

Fig. 12 Tracer gas spreads across the Deverson rotor, showing the enhancement of mixing by the IGV wakes and by the action of rotation; $\phi = 0.51$; contours: minimum = 0.1, interval = 0.1

The experiments in the straight duct were performed to substantiate a hypothesis that the distortion of the contours seen near corners in compressors *could* be produced by the anisotropic and inhomogeneous turbulence that exists near solid walls. Although the results confirm this they do not show that this is the *only* way in which the contours can be distorted.

A Review of Predictive Efforts for Transport Phenomena in Axial Flow Compressors

A. J. Wennerstrom
Aero Propulsion & Power Laboratory,
Wright Research & Development Center,
Wright-Patterson Air Force Base,
OH 45433-6563

Transport phenomena as they apply to throughflow calculations in axial-flow compressors are reviewed. An historical background is presented. Then the debate raised by the Adkins and Smith versus the Gallimore and Cumpsty approaches to radial transport is discussed. This debate was resolved in that it was finally concluded that both turbulent transport and convective secondary flows play a role in spanwise transport. Other major related efforts mentioned are those of Hirsch and his colleagues and Papailiou and his colleagues. Readers are encouraged to reconsider exploitation of the work of Kerrebrock and Mikolajczak concerning circumferential transport. Comments on future trends are offered.

Introduction

The most common approach for designing turbomachinery since at least the 1950's has been to compute the flow field using an axisymmetric computation in which the flow is confined to concentric stream tubes. This reduces the calculations to a mathematically two-dimensional problem. It has traditionally been assumed that no mass, momentum, or energy is transported across the concentric stream surfaces. Parameter variations in the circumferential (blade-to-blade) direction have either been ignored by posing the problem initially as two dimensional as did Wennerstrom (1974), or have been included by averaging these terms in the three-dimensional equations as did Smith (1966) and Jennions and Stow (1985).

This idealization ignores what are generally termed "secondary flows." Sir William Hawthorne has defined secondary flows as those flows associated with all components of streamwise vorticity. L. H. Smith, Jr. chose to define secondary flow as resulting from those velocities generated by streamwise vorticity in the real flow in excess of the streamwise vorticity associated with an axisymmetric rotational flow through closely spaced blades. Although there was originally some debate on the difference between these definitions, Horlock pointed out in a discussion of a paper by Dixon in Lakshminarayana et al. (1974), p. 196, that there was no inconsistency between the two definitions. These points were reviewed again by Horlock (1977).

Another more intuitive way of defining secondary flow is to say that it encompasses all real flow features that tend to violate the assumption of steady flow confined to axisymmetric concentric stream tubes. This includes stream surface warp due to inviscid secondary flow and also other features such as tip leakage flows, boundary layer and wake centrifugation, and turbulent diffusion. Most early efforts to analyze secondary flows were relatively academic and were seldom, if ever, applied to correct or improve the design of a real piece of hardware.

The first really practical approaches to secondary flow analysis were those that treated the subject as a transport phenomenon. I have chosen to call these hybrid solutions because they are not truly two dimensional nor are they three dimensional. Rather, they took the approach of superimposing semi-empirical models of secondary flow features as corrections to an otherwise classical axisymmetric solution. Since the most commonly employed axisymmetric solution process is the streamline curvature method, which is inherently iterative, this was relatively straightforward.

Early Solutions for Radial Transport

The first such hybrid method published was by Tipton (1968). In it he attempted to take into account the effect of the non-equilibrium in the radial direction between the free stream and the boundary layer and wake fluid. He then employed this to predict the change in the spanwise total pressure loss distribution relative to a purely axisymmetric prediction. His solution, presented nondimensionally, took the form

$$\frac{\omega_p}{\omega_{p_t}} = f(\omega, r, C_u, T_{2_{bl}}, T_2) \tag{1}$$

where ω_p = loss coefficient at any radius
ω_{p_t} = loss coefficient at reference radius
ω = rotor angular velocity
r = radius
C_u = exit whirl velocity
$T_{2_{bl}}$ = exit mean boundary layer temperature
T_2 = exit free stream static temperature

He further assumed that the area-integrated overall loss was equal to the value predicted using axisymmetric cascade plane methods. In this way he obtained absolute values for the revised

Contributed by the International Gas Turbine Institute. This paper is a revised and updated version of a keynote paper presented at the Third International Symposium on Transport Phenomena and Dynamics of Rotating Machinery, Honolulu, Hawaii, April 1-4, 1990. Manuscript received at ASME Headquarters December 1990.

spanwise distribution. No additional losses due to any secondary flow features were included and no adjustments to the deviation angles were made. Tipton acknowledged that his highly simplified analysis had limitations (one of which was it did not recognize strong shocks) but he was nevertheless able to show some very encouraging correlations with available data.

A few years later, Hearsey (1975) explored the implementation of Tipton's approach but decided to go another route. Hearsey agreed with Tipton that one of the major secondary flow mechanisms was spanwise transport of boundary layer and wake fluid due to its radial nonequilibrium with the free stream. However, his approach was to determine the ratio of radial shear stress to axial shear stress on an element of the blade surface boundary layer. He then assumed that the extent of radial movement of the boundary layer/wake fluid was proportional to the force ratio. From this, he derived the angular difference between the free-stream direction and the direction of boundary layer/wake motion, which, coupled with an axial distance, gave a radial displacement. This shift was computed at a great many radii and summed in the trailing edge plane of each blade row to predict a new spanwise distribution of loss coefficient, defined as a revision of a distribution originally defined by two-dimensional blade element predictions. One empirical constant was associated with this prediction in addition to the many simplifying assumptions.

The above analysis, like Tipton's, only resulted in a spanwise redistribution of the relative total pressure loss coefficient. It did not introduce any spanwise transport of mass or energy across axisymmetric stream tubes, which would result from secondary flow. To remedy this, Hearsey (1975) also introduced a model to deal with turbulent transport and mixing phenomena. He approached this by assuming that the flow might be described by the Navier–Stokes equations for laminar flow, with the molecular kinematic viscosity replaced by an appropriate eddy viscosity. The flow was assumed to be contained by frictionless walls so the result would be the effects of mixing without regard for annulus wall boundary layers. To determine the effect of turbulence on total enthalpy, the energy equation for laminar flow was used, neglecting streamwise conduction. Changes were computed in the distributions of entropy, total enthalpy, and angular momentum. The eddy viscosity was presumed uniform throughout the flowfield and was the only empirical constant incorporated.

Hearsey presented only a very limited evaluation of this work using the NACA five-stage compressor as a test case. It could be concluded that the general trends exhibited were correct, although more cases would have to be examined in order to evaluate its reliability better and to define better appropriate values for the two empirical constants required. A substantial increase in computational time also resulted, on the order of one order of magnitude. As a result, little use was ever made of this work, although one gas turbine manufacturer is known to have employed it for the design of a multistage compressor with reasonably good success.

The First Comprehensive Radial Transport Solutions

The first effort along these lines that could be called both comprehensive and successful was that published by Adkins and Smith (1982). They included five secondary flow effects: (1) mainstream, non-free-vortex flow; (2) end-wall boundary layers; (3) blade end-wall clearances; (4) blade end shrouding; and (5) blade boundary layer and wake centrifugation. The approach was roughly as follows. An inviscid secondary flow model was developed for each of the five effects identified. This restricts application to design-point or near-peak-efficiency operation of machines having good performance. Losses specified at the trailing edge of each blade row are comprised of a cascade-type profile loss and an end-wall loss, which is a function of clearance, passage aspect ratio, and proximity to stall. The model of each secondary flow effect provides a prediction of cross-passage and spanwise secondary velocities. The cross-passage velocities influence the mainstream flow solution through their effect on blade row exit flow angles. The spanwise secondary velocities are summed and used in a mixing analysis, which is an inviscid phenomenon resulting from the convection of fluid properties by the secondary flow field. The following expression is derived to describe how any fluid property, e.g., stagnation enthalpy, changes in the streamwise direction:

$$\frac{\partial \bar{P}}{\partial z} = \epsilon \frac{\partial^2 \bar{P}}{\partial y^2} \tag{2}$$

where $\bar{P}$ is a cross-passage averaged parameter value
z is the streamwise direction
y is the spanwise direction
ϵ is mixing coefficient

The mixing coefficient is a function of span, increases linearly in the streamwise direction, and tends to have higher values near end walls due to the nature of secondary flow. The mixing coefficient at any streamwise location is taken to be the sum of the contributions of all upstream blade rows. However, because the analysis did not allow for viscous dissipation of the secondary flow field nor did it allow for interactions with end walls and succeeding blade rows, empirical adjustments were made to the mixing coefficient formulation. The quantities eventually mixed are stagnation temperature, stagnation pressure, and angular momentum. Because the meridional plane and secondary flow solutions are mutually dependent, three or four iterative loops through the mixing calculation were typically required to achieve convergence.

Before showing sample results for the Adkins and Smith approach, it is worth describing a second comprehensive and successful hybrid approach introduced by Gallimore and Cumpsty (1986) and Gallimore (1986). Then a comparison will be shown using both methods to analyze the same compressors. Gallimore and Cumpsty noted that an aspect of the flow neglected by Adkins and Smith was that of turbulent or random mixing. Considering that there are a great many sources of turbulence in a multistage turbomachine, random fluctuations in the radial direction could give rise to turbulent diffusion of the flow properties across the span. In an effort to sort out whether the most probable mechanism for fluid mixing was spanwise convection or turbulent diffusion, they performed ethylene tracer experiments in two low-speed multistage compressors. From these they concluded that the dominant mechanism causing spanwise mixing in the latter stages of multistage compressors was a random, turbulent-type diffusion process rather than diffusion caused by convective secondary flows.

Gallimore then constructed a spanwise mixing model, which represented the physical process of the radial mixing of momentum and heat by turbulent diffusion. He employed the axial, radial, and tangential momentum equations and the energy equation to calculate the streamwise changes of stagnation enthalpy, entropy, and tangential momentum. The mixing model modifies the traditional adiabatic and inviscid assumptions by introducing heat transfer in the radial direction, and the radial transfer of momentum implies the presence of axial and tangential shear stresses. The equations used in his axisymmetric streamline curvature solution were modified as follows.

The entropy change in the streamwise direction was now calculated from an energy equation of the form

$$\frac{\partial s}{\partial m} = \frac{1}{r\rho T V_m} \frac{\partial}{\partial r}\left(rk_t \frac{\partial T}{\partial r}\right) + \frac{\phi}{\rho T V_m} + \frac{\partial s_e}{\partial m} \tag{3}$$

The last term in this equation is defined by the traditional empirical loss coefficients derived from cascade plane and end-wall effects. The other terms are new and involve k_t, the eddy

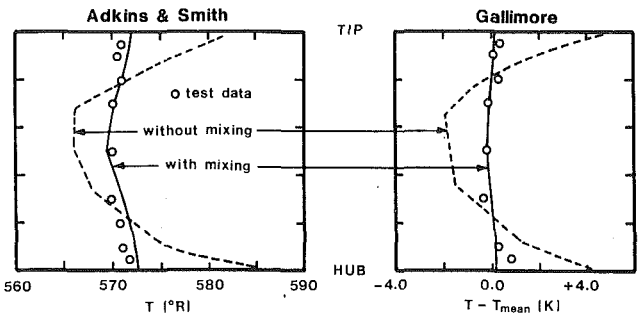

Fig. 1

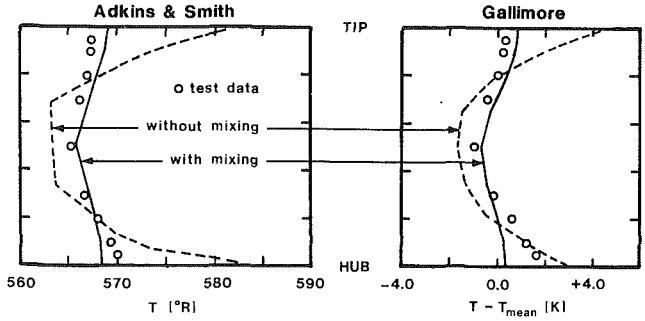

Fig. 2

thermal conductivity, and ϕ, the dissipation function. The dissipation function is computed from

$$\phi = \mu_t \left[\left(\frac{\partial V_z}{\partial r} \right)^2 + \left(\frac{\partial V_\theta}{\partial r} - \frac{V_\theta}{r} \right)^2 \right] \tag{4}$$

in which μ_t is the eddy viscosity. All other undefined variables are readily available in any streamline curvature throughflow computation.

The tangential momentum equation is modified to include a tangential shear stress term, E_θ, which is simply added to the tangential blade force term, F_θ. This is defined as

$$E_\theta = \frac{\partial}{\partial r} \left[\mu_t \left(\frac{\partial V_\theta}{\partial r} - \frac{V_\theta}{r} \right) \right] + \frac{2\mu_t}{r} \left(\frac{\partial V_\theta}{\partial r} - \frac{V_\theta}{r} \right) \tag{5}$$

The streamwise momentum equation is similarly modified to include a streamwise shear stress term added to the streamwise blade force term F_z. The axial component of this term, E_z, is defined as

$$E_z = \frac{1}{r} \frac{\partial}{\partial r} \left(\mu_y r \frac{\partial Vz}{\partial r} \right) \tag{6}$$

Again, the only new variable introduced is μ_t, the eddy viscosity; all other variables are readily available in any streamline curvature throughflow computation.

Now it is instructive to compare the results of using each spanwise mixing model on the same test cases, keeping in mind that the models were conceived from totally different physical principles. The only common comparison convenient to make is the total temperature distribution behind two three-stage compressors of different aspect ratio. Figure 1 compares the two methods for the lower aspect ratio compressor; Fig. 2 for the higher aspect ratio. These figures were adjusted to have a common vertical scale. However, they were taken unmodified from the cited references, so the horizontal scales are slightly different. The important thing to note is that both methods show a remarkable improvement relative to the unmixed case; also, one method does about as well as the other.

The Great Debate

The fact that two totally different concepts for estimating the mixing coefficient would lead to such similar results aroused considerable interest and controversy. A serious attempt to resolve this was made by Wisler et al. (1987) in which further experiments were conducted using the ethylene tracer technique, hot-wire measurements, and conventional methods. Wisler et al. concluded that both mechanisms of transport and diffusion are important. However, an extensive discussion published with this paper by ten distinguished workers, including the original authors of this controversy, left the question somewhat unresolved. In some respects, from the designer's point of view who simply wants a useful end result, the difference may be largely academic. As L. H. Smith, Jr. pointed out in his discussion of the paper,

> the secondary flows calculated by Adkins and Smith, while not always correct in detail, do spring from phenomena that are bound to agitate the flow and cause turbulent mixing, and that these agitations should be more or less proportional to the strengths of the secondary flows calculated. With this view, it doesn't really matter much how the mixing is divided between secondary flow convection and turbulent diffusion; the end result is the same, and that end result has been found to be a satisfactory representation of the circumferential-average properties of the flow.

Accepting this statement makes Gallimore's approach more attractive, regardless of one's opinion of the mechanism, simply because it is far easier to implement in a streamline curvature computational scheme.

Resolution of the Debate

Since this lecture was first given, the major area of disagreement in this debate was resolved through a paper by Leylek and Wisler (1991). There never was any disagreement concerning the importance of turbulent diffusion. Rather the controversy revolved around what importance, if any, convective secondary flow phenomena had in the overall context of mixing. The Leylek and Wisler paper showed conclusively that spanwise mixing is caused by a *combination* of secondary flow and turbulent diffusion. Gallimore acknowledged this in a discussion following presentation of the paper.

A second even more recent paper by Kirtley et al. (1990) further substantiates this conclusion. In this paper the "average-passage" approach of Adamczyk was used to analyze secondary flow in a two-stage turbine. A conclusion presented on p. 8 states,

> therefore, while diffusion models may work extremely well, they are fundamentally incorrect in regions of large secondary flows. We expect turbulent diffusion models to under-predict spanwise mixing near end walls and in low aspect ratio machines where secondary flows are substantial.

A significant feature of the Leylek and Wisler (1991) paper was the use of a three-dimensional viscous computational fluid dynamic (CFD) code to support the experimental observations. The question was posed to Adamczyk (1990): Why should a CFD code with a state-of-the-art κ–ϵ turbulence model do so well at predicting a flow containing significant convective flows and turbulent diffusion inasmuch as the model was largely derived with turbulent boundary layers in mind? The answer was deceptively simple. In working with the "average-passage" model, which considers the contribution of nonsteady terms, it had been observed that a formulation could be derived that was mathematically similar to a steady formulation with a k–ϵ turbulence model. Thus, given appropriate values for the constants, which would be different from those appropriate for just a turbulent boundary layer, the influence of large-scale turbulence could be effectively incorporated. This is consistent with statements of Leylek and Wisler, who concluded:

> our use of experimental data for boundary conditions has apparently provided the correct profile of incoming vorticity and the average turbulence kinetic energy. We suspect that this plus the correct vorticity generated by viscous effects has allowed us to get the excellent data match and correct secondary flows.

Transonic and Supersonic Compressors

All of the foregoing comparisons, those of Adkins and Smith, Gallimore and Cumpsty, Wisler et al., and Leylek and Wisler, were made with relatively low-speed multistage compressors. Although Reynolds numbers and loading levels were fully simulated, in such machines operating near peak performance, the boundary layers are relatively unseparated. In transonic and supersonic stages, the situation may be very different. Here, the suction surface boundary layer on rotor blades frequently separates at the shock impingement line and it may or may not reattach. Kerrebrock (1981) observed that

> time-resolved measurements of both radial and tangential flow angle, as well as of static pressure and stagnation pressure, in the MIT Blowdown Compressor have shown that the rotor blade wakes just downstream of the blade trailing edges have radial velocities of the same order as the axial or tangential velocities.

This remark referred to a transonic compressor. He further went on to note that while these radial velocity components average nearly to zero in the peripheral mean, they can lead to very strong radial coupling in the flow because of radial disequilibrium caused by the difference between tangential velocities in the wake and in the inviscid flow. Also, this phenomenon is quite capable of being important in a single stage; it does not have to be the result of passage through several upstream stages.

Thus, accepting the fact that both turbulent diffusion and convective secondary flows play a significant role at low Mach numbers, at transonic and supersonic Mach numbers and possibly under some other circumstances convective secondary flows may achieve even greater importance. Some interesting further concepts related to spanwise transport in transonic compressors were recently presented in a thesis by Kotidis (1989). His main theme was to evaluate the transport potential of vortices shed from the blading. In his conclusions, he finds that the shed vortices can explain the magnitude of mass transport toward the hub; however, the vortex model underestimates by a factor of about five the transport measured toward the tip. On the other hand, earlier in his thesis he examines other mechanisms of radial transport, one of which is "spanwise flows in regions of separation." This approach predicted the correct magnitude of flow toward the tip to reasonable accuracy. Therefore, much like the Adkins and Smith model, which includes five different mechanisms of convective transport, one could imagine a model applicable to supersonic Mach numbers, which included convective transport in regions of separation as well as that due to strong vortex shedding.

One other item has been left unresolved by this debate. The Adkins and Smith model uses the cross-passage velocities computed to correct the exit flow angles from each blade row in addition to using the spanwise velocities in combination with a diffusion equation. The comparisons shown of predicted versus measured flow angles are rather good. No such data were presented by Gallimore. Thus, while it is known that Gallimore's solution will influence the exit flow angles, it is not known by this writer whether the adjustments will be of the right sign or magnitude.

Other Recent Work on Radial Transport

A review of efforts to predict spanwise transport in axial flow compressors would not be complete without mentioning the efforts of two other investigators: specifically C. Hirsch and his colleagues and K. D. Papailiou and his colleagues.

De Ruyck et al. (1989) have presented an approach that combines some of the concepts of the Adkins and Smith approach and some from the Gallimore and Cumpsty approach. It is not a simple amalgamation, however; it differs in a number of important respects. Rather than use inviscid secondary flow theory like Adkins and Smith, an integral approach is employed. However, the diffusion-type equation of Adkins and Smith is used and a turbulent diffusion coefficient is added to the mixing coefficient computed from secondary flows.

The computational strategy is roughly as follows. As with all hybrid methods, a conventional throughflow computation is accomplished without mixing. The non-free-vortex contribution to secondary flow can then be directly computed. End-wall boundary layers are predicted using a three-dimensional integral method wherein end-wall secondary flows and clearance effects are introduced. Profile boundary layers and wakes are computed allowing blade surfaces to be treated separately such that wakes may be asymmetric and radial flows may have opposite signs. Finally, a full computation of the transport equation including secondary flows and turbulent diffusion delivers the radial redistributions. With this approach, and including many assumptions of course, the number of empirical free parameters can be reduced solely to the turbulent diffusion coefficient. General observations to date have been that turbulent diffusion is the dominant but not sole mechanism for mixing. However, once again, all the examples studied have been subsonic and the relative importance of the mechanisms could change as the Mach number increases to transonic or supersonic levels.

Kaldellis et al. (1989) have followed an approach differing in several significant ways from all others so far. Like the model of DeRuyck et al. (1989), the flow is divided into an inviscid core flow and viscous zones and uses an integral approach to define longitudinal velocities in viscous regions. However, turbulent transport is not directly incorporated in the sense introduced by Gallimore (1986) and a total kinetic energy integral equation is substituted for an entrainment equation. An equation is used for streamwise transport of the meridional components of vorticity including viscous terms; the corresponding peripheral velocity profile is deduced from this and the concept of a peripheral blockage is introduced. Another novel feature of the analysis is a model for shock/secondary-flow interaction aimed at dealing with this effect on the outer casing. Also, unlike most of the other recent efforts to date, the two sample cases presented by Kaldellis et al. (1989) were transonic single stages, which both had supersonic relative Mach numbers at the tip. The predictions shown looked reasonably encouraging. The fact that they were without a model of random turbulent diffusion may lend some further credence to the supposition that turbulent diffusion may be much more important at subsonic Mach numbers and particularly in multistage turbomachinery.

Circumferential Transport

One of the most difficult tasks that any designer of turbomachinery faces is comparing data from a test that is almost always three dimensional with design information that is most frequently derived from an axisymmetric calculation. It is often not possible to "reverse engineer" the results adequately to understand where certain losses originated, and this is usually one of the major objectives of the development process.

Everything that has been discussed to this point in this paper has dealt with radial transport effects superimposed on an axisymmetric solution. This is where the majority of effort has been spent because it is vital to the design of multistage turbomachinery and is potentially useful for the design of even highly loaded single stages such as fans. Also, a very practical consideration is that when analyzing data from a multistage turbomachine, the only interstage data likely to be available are circumferentially averaged total pressures and temperatures measured at stator leading edges. Regardless of their validity, these data are at least compatible with axisymmetric or hybrid throughflow calculations.

However, for analyzing the behavior of single stages, a classic paper by Kerrebrock and Mikolajczak (1970) dealing with circumferential transport has considerable relevance. The main

concept conveyed by this paper can be described as follows. Consider a compressor stage comprised of a rotor followed by a stator. The boundary layer fluid shearing off the rotor will normally have a greater angular momentum than the free stream; therefore, a higher stagnation temperature because more work was done on it by the rotor. This fluid, comprising the rotor wake, will tend to pile up on the pressure surface of the following stator because it has a higher angular velocity and also a lower meridional velocity than the free stream. In the exit plane, this appears as a circumferentially periodic total temperature gradient showing peak temperatures in the fluid nearest the pressure surface of the stator blades. Kerrbrock and Mikolajczak showed that it was possible to make a reasonably accurate prediction of rotor viscous losses from the circumferential total temperature distribution at the exit of the following stator. This effect could also be seen in the results of Wisler et al. (1987).

Now, all of the previous discussion in this paper focused on spanwise transport phenomena. Even in a single stage, and most particularly in high-Mach-number stages, it is clear that spanwise transport phenomena can and often will cause a major rearrangement of the fluid between the rotor exit and any downstream measuring planes. Therefore, the question is posed that if spanwise transport phenomena (of whatever sort are considered most relevant) are combined with the circumferential transport as described by Kerrebrock and Mikolajczak, could we not do a better job of identifying the source of losses in a single rotor–stator combination? It is my opinion that for transonic and supersonic stages where the temperature rise is significant, the combination of convective and turbulent spanwise transport mechanisms with the circumferential rectification of rotor wakes could contribute a great deal toward understanding the full significance of comprehensive measurements in the exit planes of highly loaded single stages.

Future Trends

There seems little doubt that hybrid computation schemes such as described in this paper will be the design tool of choice for multistage compressors for many years to come. Although computational fluid dynamics (CFD) has made great strides through both software and hardware improvements, it is still a long way from realistic to imagine the extensive use of it for the design of multistage turbomachinery. At the present time, considering the need for dealing with three-dimensional and nonsteady effects, CFD is too time consuming and expensive to use for routine multistage design and is likely to remain so in the foreseeable future. However, as illustrated by Leylek and Wisler (1991) and Kirtley et al. (1990), CFD can contribute significantly to our ability to sort out conceptually what is really going on in a complex three-dimensional flow field.

With the resolution of the debate indicating that both turbulent diffusion and convective flows should be included in a comprehensive hybrid computation scheme, future work on these models should incorporate both effects. Also the presence of shock waves in transonic and supersonic stages is likely to introduce strong convective effects, which may not yet have been well modeled. CFD may again contribute to defining the magnitude of these effects and further experimental work is warranted to illuminate the transport properties of transonic and supersonic relative flows.

In the short term, the Gallimore model may be the most attractive scheme with which to upgrade a traditional throughflow code not currently incorporating any mixing effects. This is because of its relative simplicity and because, as shown in Figs. 1 and 2, it does produce greatly improved results for some range of cases. However, as with any model that omits one or more important elements of the physics, the farther one strays from a familiar and proven data base, the more erroneous and misleading the results may become.

Multistage turbine design is another fertile area for the application of hybrid methods incorporating transport phenomena. The first published application of these methods to turbine design was recently presented by Bernard and Falchetti (1989). Although the secondary flows in turbines differ in many respects from those in compressors, the concept of developing an analogous hybrid method for turbine design is entirely reasonable.

Finally, I would like to encourage those working in this area to reconsider the work of Kerrebrock and Mikolajczak (1970) with respect to circumferential transport. These concepts combined with some of the recent work in radial transport could shed a great deal of light on the behavior of highly loaded transonic and supersonic single stages.

Acknowledgments

The conference organizers of the International Gas Turbine Institute of ASME are to be commended for encouraging the "great debate" referenced in this paper. They recognized the potential for this debate in 1986, took extraordinary steps to encourage spoken and written discussion in 1987, and have supported its continuation through the 1990 conference.

References

Adamczyk, J. J., 1990, Private Communication.

Adkins, G. G., Jr., and Smith, L. H., Jr., 1982, "Spanwise Mixing in Axial-Flow Turbomachines," ASME *Journal of Engineering for Power*, Vol. 104, No. 1, pp. 97–110.

Bernard, J., and Falchetti, F., 1989, "Calcul des Ecoulements Secondaires dans une Turbine Axiale," *Secondary Flows in Turbomachines*, AGARD-CP-469.

DeRuyck, J., Hirsch, C., and Segaert, P., 1989, "Secondary Flows and Radial Mixing Prediction in Axial Compressors," *Secondary Flows in Turbomachines*, AGARD-CP-469.

Gallimore, S. J., and Cumpsty, N. A., 1986, "Spanwise Mixing in Multistage Axial Flow Compressors: Part I—Experimental Investigation," ASME JOURNAL OF TURBOMACHINERY, Vol. 108, No. 1, pp. 2–9.

Gallimore, S. J., 1986, "Spanwise Mixing in Multistage Axial Flow Compressors: Part II—Throughflow Calculations Including Mixing," ASME JOURNAL OF TURBOMACHINERY, Vol. 108, No. 1, pp. 10–16.

Hearsey, R. M., 1975, "A Revised Computer Program for Axial Compressor Design," ARL-TR-75-0001, Aerospace Research Laboratories, Wright-Patterson Air Force Base, OH.

Horlock, J. H., 1977, "Recent Developments in Secondary Flow," *Secondary Flows in Turbomachines*, AGARD-CP-214, pp. 1/1–1/18.

Jennions, K., and Stow, P., 1985, "A Quasi-Three-Dimensional Blade Design System," ASME *Journal of Engineering for Gas Turbines and Power*, Vol. 107, No. 2, pp. 301–316.

Kaldellis, J., Douvikas, D., Falchetti, F., and Papailiou, K. D., 1990, "A Secondary Flow Calculation Method for Single-Stage Axial Transonic Flow Compressors, Including Shock-Secondary Flow Interaction," ASME JOURNAL OF TURBOMACHINERY, Vol. 112, pp. 652–668.

Kerrebrock, J. L., 1981, "Flow in Transonic Compressors," *AIAA Journal*, Vol. 19, No. 1, pp. 4–19.

Kerrebrock, J. L., and Mikolajczak, A. A., 1970, "Intra-stator Transport of Rotor Wakes and Its Effect on Compressor Performance," ASME *Journal of Engineering for Power*, Vol. 92, No. 4, pp. 359–368.

Kirtley, K. R., Beach, T. R., and Adamczyk, J. J., 1990, "Numerical Analysis of Secondary Flow in a Two-Stage Turbine," AIAA Paper No. AIAA-90-2356.

Kotidis, P. A., 1989, "Unsteady Radial Transport in a Transonic Compressor Stage," GTL Report No. 199, Gas Turbine Laboratory, Massachusetts Institute of Technology, Cambridge, MA.

Lakshminarayana, B., Britsch, W. R., and Gearhart, W. S., 1974, "The Fluid Mechanics, Acoustics, and Design of Turbomachines (Part I)," NASA-SP-304.

Leylek, J. H., and Wisler, D. C., 1991, "Mixing in Axial-Flow Compressors: Conclusions Drawn From 3-D Navier–Stokes Analyses and Experiments," ASME JOURNAL OF TURBOMACHINERY, Vol. 113, this issue.

Smith, L. H., Jr., 1966, "The Radial Equilibrium Equation of Turbomachinery," ASME *Journal of Engineering for Power*, Vol. 88, No. 1, pp. 1–12.

Tipton, D. L., 1968, "Improved Techniques for Compressor Loss Calculation," *Advanced Components for Turbojet Engines*, AGARD-CP-34, pp. 7/1–7/23.

Wennerstrom, A. J., 1974, "On the Treatment of Body Forces in the Radial Equilibrium Equation of Turbomachinery," *Traupel-Festschrift*, Juris Verlag, Zurich, pp. 351–367.

Wisler, D. C., Bauer, R. C., and Okiishi, T. H., 1987, "Secondary Flow, Turbulent Diffusion, and Mixing in Axial-Flow Compressors," ASME JOURNAL OF TURBOMACHINERY, Vol. 109, No. 4, pp. 455–482.

Three-Dimensional Wake Decay Inside of a Compressor Cascade and Its Influence on the Downstream Unsteady Flow Field: Part I—Wake Decay Characteristics in the Flow Passage

C. Poensgen

H. E. Gallus

Institut für Strahlantriebe und
Turboarbeitsmaschinen,
RWTH Aachen,
5100 Aachen, Federal Republic of Germany

A measuring technique based on multisensor hot-wire anemometry has been developed to determine the unsteady three-dimensional velocity vector and the structure of turbulent flows. It has then been applied to the passage and the exit flow of an annular compressor cascade, which is periodically disturbed by the wakes of a cylinder rotor, located about 50 percent of blade chord upstream. In part I of this paper the decay of the rotor wakes will be described first without stator and secondly through a stator passage. The time-dependent turbulent flow field downstream of this stator is discussed in Part II. The rotor wakes have a major influence on the development of three-dimensional separated regions inside the compressor cascade, and this interaction will be addressed in both parts of this paper.

Introduction

The flow in modern multistage compressors is three-dimensional, viscous, and unsteady. Separated regions with partly reversed flows, combined with rotor–stator interactions, make the flow pattern even more complex. Although methods of flow analysis made progress in recent years, the modeling of turbulence remains difficult, mainly because of the lack of experimental data. There is a significant influence on the efficiency of a compressor in all points of operation due to:

1 Convection velocity defect of wakes into a cascade located downstream
2 Potential rotor–stator interactions
3 The process of turbulence convection and turbulence production in the wake itself
4 Turbulence production in the downstream passage flow
5 Interaction of separated regions, leakage flows, and boundary layers with incoming unsteady wake flow

In recent years, progress had been made in understanding the three-dimensional unsteady flow field in rotors and stators of axial compressors. Flow visualization techniques, measurements on blade surfaces, and probe measurements in the axial gaps have added to the understanding of complex flow phenomena.

Because it is difficult to obtain data on the outgoing flow of a rotor, most of these investigations were addressed to stator cascades. In a research program carried out by R. P. Dring and his co-workers in a two-stage large-scale compressor (Dring et al., 1982; Joslyn and Dring, 1985), the nature and the extent of wall separation in stators and in rotors were investigated at design and off-design conditions. Dong et al. (1987) determined the influence of the hub corner separation. They found a reduction of the overall losses due to the presence of the hub gap leakage flow. Suder et al. (1987) determined the two-dimensional kinematics of rotor wakes during their passage through the downstream stator in unseparated flow using laser fringe anemometry. The three-dimensional unsteady stator–rotor interaction inside the rotor passage has been investigated by Adachi and Matsuuchi (1983) using triple hot-wire anemometry.

Investigations by Schulz and Gallus (1988) and Schulz et al. (1990) were carried out in order to get a better comprehension of the flow in an annular compressor cascade. They found a corner stall at the hub of the stator blade, and determined the growth of this separated region for several operating points of the cascade in steady-state flow. In a second step, they investigated the stator flow pattern in a flow field,

Contributed by the International Gas Turbine Institute and presented at the 35th International Gas Turbine and Aeroengine Congress and Exposition, Brussels, Belgium, June 11–14, 1990. Manuscript received by the International Gas Turbine Institute January 31, 1990. Paper No. 90-GT-21.

Table 1 Design parameters of the annular cascade

Number of blades	24
Outer diameter	428 mm
Inner diameter	321 mm
Tip clearance	0.55 mm
Blade chord	62.6 mm
Stagger angle	61.0 deg
Inlet metal angle	44.2 deg
Outlet metal angle	15.0 deg
Aspect ratio	0.84
Solidity at midspan	0.78
Number of rotor rods	24
Inlet Mach number	0.299
Rotor speed	3000 rpm

which was disturbed by a rotor with rotating cylinders. The obtained data were compared to those of the steady-state stator investigation. It was found that the losses of the compressor cascade decrease, and the structures of the boundary layers change their characteristics.

Due to progress in data acquisition and data reduction techniques, a full digital operating measuring technique based on multiple hot-wire sensors was built up, in order to determine the unsteady flow field downstream of rotors, by a nonrotating stationary fixed probe. Using this technique, it is possible to get an insight into the time-dependent three-dimensional flow field in the stator and into the reaction of the separated flow regions to unsteady disturbances. In addition to previous investigations, the present paper addresses some detailed flow structure analysis:

1 Downstream flow field of the rotor
2 Transport of rotor wakes in the stator passage
3 Interaction of secondary flows in the stator with incoming wakes
4 Influence of unsteady wake flow on the hub corner stall.

Transport and decay characteristics of velocity and turbulence are determined, and regions of turbulence production were found. Because of the four dimensions of the herein described investigations (three-dimensional velocity vector and one dimension in time space) the amount of data acquired is very high, and only some characteristic results are shown. All contour plots and secondary flow plots in this part of the paper are viewed in the downstream direction.

Experimental Facility and Test Program

The measurements were carried out in an annular compressor cascade described in detail by Schulz and Gallus (1988, 1990). The cascade consists of 24 untwisted blades, mounted on the hub. Table 1 shows its most significant parameters.

Figure 1 displays some further geometric parameters and the locations where the measurements were taken for this study. The inlet flow angle to the stator was set by an adjustable IGV. The wakes of the IGV blades are leveled out and they could not be measured in a plane 20 mm upstream of the stator. Therefore, the wakes of the IGV blades do not have any influence on the flow patterns in the stator.

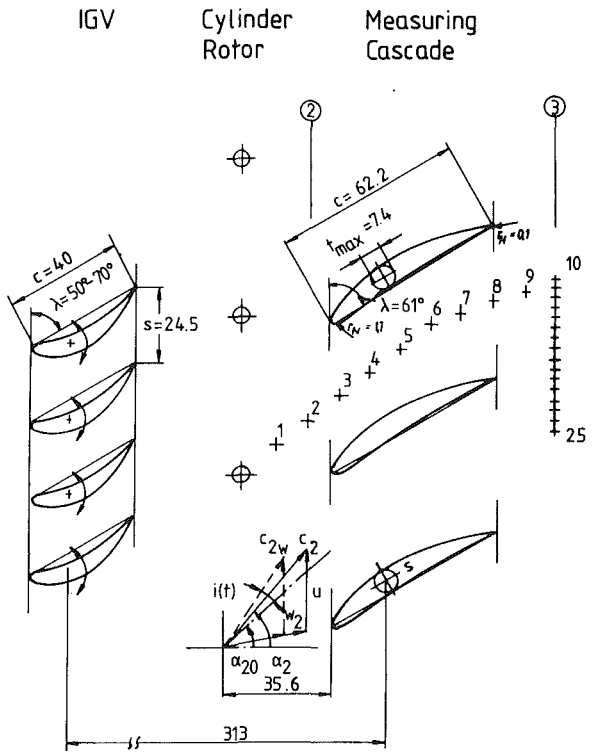

Fig. 1 Cascade geometry at midspan and locations of measurement

In order to stay compatible with former investigations, a rotor with cylindrical spokes was used, and the operation conditions were identical to those reported by Schulz et al. (1990). Since the aim of these investigations was to determine the influence of unsteady wake flow on the flow field inside the stator passage, and its influence on separated zones inside the stator, only the incidence angle to the stator blades was varied; the wake parameters, i.e., wake width, wake depth, and reduced frequency, have been kept constant. In order to avoid the risk of flow separation in a rotor blading due to throttling the flow, a rotor with cylindrical spokes was used. Comparing the wake profiles measured by the authors with results published by Ravindranath and Lakshminarayana (1979), the wake produced by a cylinder rotor is similar to those produced by a compressor rotor blade. As the cylinder Reynolds number is on the order of 25,000 the von Karman vortices shed off the rods no longer have a well-defined frequency (Schlichting, 1951), and the cores of the vortices move parallel to the wake center line. As data acquisition is based on the time-average method triggered by the rotor rods, the von Karman vortices

Nomenclature

a = coefficient for sensor calibration
c = velocity
h = calibration coefficient for the hot-wire sensor
i = incidence angle to the stator
k = calibration coefficient for the hot-wire sensor
L = dimension of polynomial fit
l = mixing length
M = number of points per time window dimension of polynomial fit
N = number of time window dimension of polynomial fit
p = pressure
t = time
u = reference inlet velocity to the stator at midspan
w = relative velocity
α = yaw angle/flow angle in the absolute frame of reference
β = pitch angle/flow angle in the relative frame of reference
ρ = density
ω = total pressure loss

Subscripts

eff = effective velocity measured by a hot-wire sensor
r = radial direction
z = axial direction
φ = circumferential direction
2 = stator inlet
3 = stator exit plane

Superscripts

$\bar{}$ = averaged value
$\tilde{}$ = periodic value
$'$ = instantaneous value

Table 2 Coordinates of measurement locations for the test cases 1–3

No.	Axial position, mm	Circumferential angle, deg	
		with stator	without stator
1	19.2	-4.60	0.0
2	29.2	-2.08	0.0
3	39.2	0.16	0.0
4	49.2	2.46	0.0
5	59.2	4.89	0.0
6	69.2	5.92	0.0
7	80.0	7.14	0.0
8	90.2	8.00	0.0
9	100.2	9.29	0.0
10	112.2	10.84	0.0

Table 3 Coordinates of measurement locations for the test cases 4 and 5

No.	Axial position, mm	Circumferential angle, deg
11	112.2	10.84
12	112.2	9.84
13	112.2	8.84
14	112.2	7.84
:	:	:
25	112.2	−4.16

shed off will be regarded as turbulent distortions. Nevertheless, the vortices were detected in the hot-wire real time data.

According to Fig. 1, Tables 2 and 3 list the locations of probe measurement for the five test series described in this paper. All axial positions are referred to the centerline of the cylindrical rotor rods.

Five test cases have been investigated:

1 The stator blading was removed, and the wake flow was measured at 10 different axial locations downstream of the rotor. At each axial position, 18 radial measurements were carried out in order to get the spanwise characteristics of the unsteady flow. During this investigation, the characteristics of wake decay, which is not influenced by any blading, are obtained. The IGV's (see Fig. 1) were set, so that the flow angle corresponds to the stator inlet condition of the second test case.

2 In this test case, the measurements are repeated at the same axial locations but on the centerline of the stator passage. The inlet flow angle to the stator was 44.2 deg, which corresponds to an incidence angle of 2 deg. The change of the wake decay characteristics due to the presence of the stator is observed and compared to the first test case.

3 In order to determine the influence of a higher loaded stator on the wake, measurements have been carried out for an incidence angle to the stator of 7 deg. The study of the interactions of the separated zones inside the stator passage with the incoming wakes was the goal of this investigation.

4 The next step was to determine the full three-dimensional unsteady flow field downstream of the stator at 16 circumferential and 18 radial locations about 22.2 mm downstream of the stator trailing edge for the same inlet conditions as reported in test case 2.

5 Increasing the incidence angle to 7 deg will result in a downstream flow field, which is mainly influenced by the hub corner stall of the stator. Its unsteady nature was determined in this test case.

In order to get the full steady thermodynamic state of the flow of all test cases and to get the full three-dimensional unsteady velocity vectors, all measurements have been carried out with five-hole probes and with triple hot-wire sensors. The mean-average velocities obtained with both probe types are compared. These measurements were carried out far enough downstream of the rotor. Thus the mean-average velocity at one arbitrary location should be the same detected either by the five-hole pneumatic probe or by hot-wire anemometry. This procedure provides a control mechanism of the sensor contamination effects by dust and other small particles.

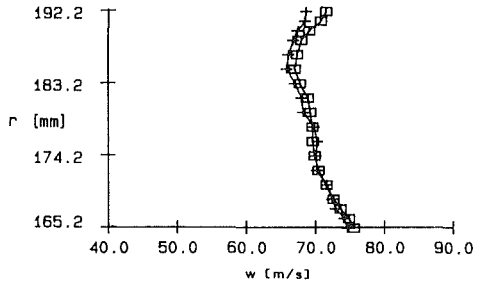

Fig. 2(*a*) Outlet conditions of the rotor relative velocity

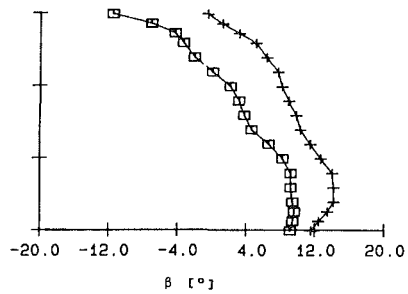

Fig. 2(*b*) Outlet conditions of the rotor relative inlet flow angle

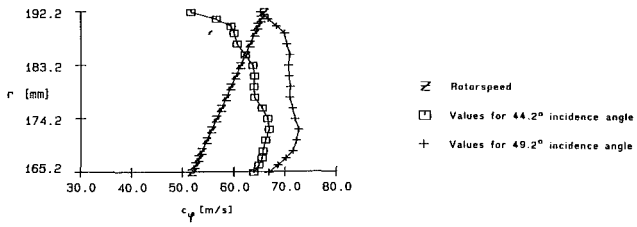

Fig. 2(*c*) Circumferential inlet velocity compared to the rotor speed

Table 4 Variation of hot-wire calibration parameters

	Min	Max	Step
Mach number	0.05	0.05	0.05
Yaw angle, deg	-25	25	5
Pitch angle, deg	-25	25	5

The results of the test cases 1–3 are reported to this part of the paper, while the other test cases are reported in part II.

The rotational speed of the rotor remains constant in all test cases, a fact that is of importance to the spanwise distribution of the wake trajectory as it is discussed later.

The outlet flow conditions of the rotor are summarized in Fig. 2. The relative velocity from the rotor rods becomes minimal at about 70 percent span, and reaches the maximum of 75 m/s near the hub. For rotors with cylinders, the inlet flow angles and the exit flow angles to the rods are about the same. Regarding the radial distribution of the relative exit flow angle β in Fig. 2, there is a greater spanwise variation of the rotor exit flow angle for $\alpha_2 = 44.2$ deg than for the higher incidence case. The relative exit flow angle of the rotor is responsible

for the direction of the traveling wake front. Therefore, the relative exit flow angle has a major influence on the spanwise distribution of the wake in the stator. It is expected that the rotor wakes for the lower incidence case will get a greater spanwise twist during their passage through the stator.

Data Acquisition and Data Reduction

For the investigations described herein five-hole probes and three-sensor hot-wire probes were used. The cone diameter of the five-hole probe is 2.6 mm, and the hot-wire sensors have a length of 3 mm using 9 μm tungsten wire. The data acquisition method is based on the triggered time-average procedure. Using this method, frequencies lower than a fourth of the blade passage frequency cannot be detected. To check the presence and influence of acoustic waves or other lower frequent periodicities of the flow, a two-channel spectrum analyzer was installed in On-Line control. For all test cases no periodic disturbances not related to the blade passage frequency were found.

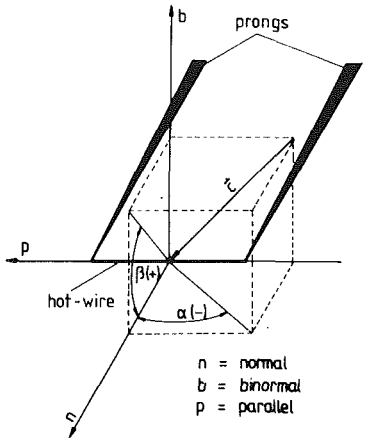

Fig. 3 Coordinate system bounded to the hot-wire sensor

The data from the five-hole probe were received by a scanivalve transducer system and recorded by a digital multimeter, which is connected to the processing computer. A description of the probe and its calibration procedure is given by Bohn and Simon (1975).

The data from the hot-wire anemometers were recorded by a digital multimeter (d-c signal) and an eight-channel transient recorder (a-c signal). The input range of the transient recorder was adapted to the output intensity of the hot-wire anemometers for a better resolution of the signals. Both signals were superimposed in the data reduction process.

This procedure guarantees a high accuracy in data acquisition. Each channel of the transient recorder has a sampling frequency of up to 1000 kHz and a storage buffer of 128,000 data words. The data acquisition was triggered by a photocell located at the hub of the rotor, so that four wakes were sampled in one time window with a digital resolution of 256 points at a sampling frequency of 71 kHz. After one rotor revolution, the next time window was recorded, until 256 of these time windows were stored in the transient recorder. These *real-time* data were transferred to an IBM compatible controlling computer and stored. Through an On-Line control the probe was always aligned to the mean flow direction, before starting the unsteady measurements. This procedure is necessary in order to minimize errors in determining the turbulence quantities. The statistical evaluation of the turbulence quantities is based

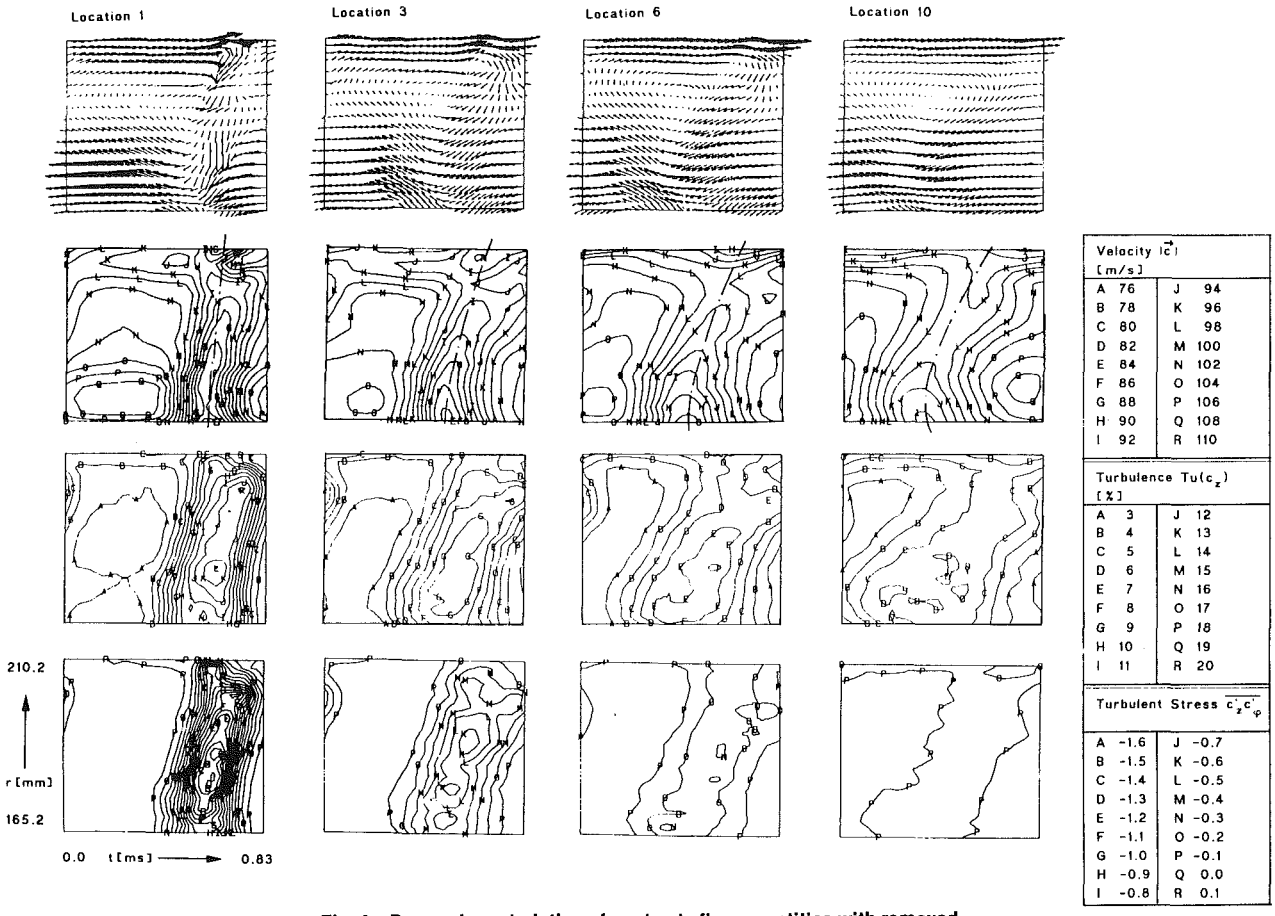

Fig. 4 Decay characteristics of unsteady flow quantities with removed stator blades (test case 1)

on the instantaneous velocity vectors, which should be within the calibrational cone of the triple hot-wire sensors. The recorded time-dependent signals were filtered by a digital low-pass Blackman filter, which is implemented in the data reduction procedure to eliminate high-frequency noise. The Channon factor, which describes the relation between the cut-off frequency of the filter process and the sampling frequency, is about 0.4. The calibration procedure of the triple hot-wire probe is based on a polynomial least-square fit method. This method yields to linear Gauss matrices, from which the calibration coefficients are obtained. The calibration procedure is described by Poensgen and Gallus (1989). Applying this to the real-time data, the real-time velocity vector was found, and all three-dimensional turbulence intensities and the turbulence correlations could be calculated.

It is noted by the authors that the least-square fit method for calibrating triple hot-wire sensors achieves an accuracy in velocity measurement of 0.5 m/s, and the mean deviation of the pitch and yaw angles is less than 0.2 deg in a free jet calibration flow. The range of Mach number and flow angles in the calibration procedure is shown in Table 4. This accuracy of measurement cannot be achieved using signal linearization procedures and reducing the data according to equations (1) and (2). (Figure 3 displays the geometric coordinate system that equations (1) and (2) are based on.)

$$c_{\text{eff}}^2 = c_n^2 + k^2 c_b^2 + h^2 c_p^2 \tag{1}$$

$$c_{\text{eff}}^2 = c^2(\cos^2\alpha + k^2 \sin^2\alpha) \tag{2}$$

It was not possible to find factors k and h. They have been found to be dependent on flow angle and on the flow velocity. A basic study on this effect has been published by Joergensen (1971). Comparing the least-square fit method to the conventional methods, an improvement in accuracy of at least 20 Db was obtained. This improvement in accuracy encourages the authors to give quantitative results on the turbulence correlation quantities. But we also know that there is a need for a second measuring technique, which is able to evaluate the turbulence correlation quantities in order to get the correct uncertainty band. The investigations of Bartenwerfer (1981) showed that the error in determining the turbulence and the turbulence correlation quantities is dependent on the overall turbulence level of the flow and on the turbulence distribution, which is either normally or Gauss distributed. He also showed that the accuracy in determining the turbulence quantities depends on the data reduction routines. Linearized signal processing leads to larger errors with increasing turbulence level, then to nonlinear signal processing.

Finally a remark on turbulence correlations should be made. The turbulence correlation integrals, which analytically have to be integrated over an infinite range, are discretized and a summation range naturally is finite. This leads to two problems:

1 The convergence of these *finite* series was found to be dependent on the flow turbulence level and on the turbulence intensity distribution

2 It is impossible to evaluate isotropic turbulence using *finite* series in data reduction. Therefore, isotropic turbulence has to be defined by a margin. We feel that the turbulence structure is nearly isotropic when the turbulence intensity is one order higher than the correlation terms.

The real-time velocity vector is split up into the instantaneous velocity (equations (3)–(5)), the periodically averaged velocity (equation (6)), and the mean velocity vector (equation (7)). The instantaneous velocity vector is given by its spherical coordinate:

$$\rho c'_{ij} = \sum_{l}^{L}\sum_{m}^{M}\sum_{n}^{N} a_{c\ l,m,n}\ u_{i,j}^{lmn}\delta_{l,m,n} \tag{3}$$

$$\alpha'_{,j} = \sum_{l}^{L}\sum_{m}^{M}\sum_{n}^{N} a_{\alpha\ l,m,n}\ u_{i,j}^{lmn}\delta_{l,m,n} \tag{4}$$

$$\beta'_{i,j} = \sum_{l}^{L}\sum_{m}^{M}\sum_{n}^{N} a_{\beta\ l,m,n}\ u_{i,j}^{lmn}\delta_{l,m,n} \tag{5}$$

$$\delta_{l,m,n} = \begin{cases} 1 \text{ for } l+m+n \le \max\{L, M, N\} \\ 0 \text{ for } l+m+n > \max\{L, M, N\} \end{cases}$$

where i denotes the time location of the velocity vector in one time window, j labels the number of the time window, and a represents the polynomial coefficients. The mean velocity vector and the periodic velocity vector are obtained by simple summation as follows:

$$\tilde{\mathbf{c}}_i = \frac{1}{M}\sum_{i}^{M}\mathbf{c}_{i,j} \tag{6}$$

$$\bar{\mathbf{c}} = \frac{1}{MN}\sum_{i}^{M}\sum_{i}^{N}\mathbf{c}_{i,j} \tag{7}$$

The turbulence intensities are split into the main coordinate directions defined by equations (8)–(10). The turbulence correlations are calculated following equations (11)–(13)

$$Tu(c_{\varphi,i}) = \frac{\sqrt{\frac{1}{N}\sum_{j}^{N}(c'_{\varphi i,j} - \tilde{c}_{\varphi i})^2}}{\bar{\mathbf{C}}} * 100 \text{ [percent]} \tag{8}$$

$$Tu(c_{r,i}) = \frac{\sqrt{\frac{1}{N}\sum_{j}^{N}(c'_{ri,j} - \tilde{c}_{ri})^2}}{\bar{\mathbf{C}}} * 100 \text{ [percent]} \tag{9}$$

$$Tu(c_{z,i}) = \frac{\sqrt{\frac{1}{N}\sum_{j}^{N}(c'_{zi,j} - \tilde{c}_{zi})^2}}{\bar{\mathbf{C}}} * 100 \text{ [percent]} \tag{10}$$

$$\overline{c'_z c'_{\varphi i}} = \frac{1}{N}\sum_{j}^{N}(c'_{zi,j} - \tilde{c}_{zi})(c'_{\varphi i,j} - \tilde{c}_{\varphi i}) \tag{11}$$

$$\overline{c'_z c'_r} = \frac{1}{N}\sum_{j}^{N}(c'_{zi,j} - \tilde{c}_{zi})(c'_{ri,j} - \tilde{c}_{ri}) \tag{12}$$

$$\overline{c'_r c'_{\varphi i}} = \frac{1}{N}\sum_{j}^{N}(c'_{ri,j} - \tilde{c}_{ri})(c'_{\varphi i,j} - \tilde{c}_{\varphi i}) \tag{13}$$

The overall periodic turbulence intensity is defined by equation (14) and the mean (time-independent) turbulence is defined by equation (15):

$$Tu(|\mathbf{c}|_i) = \sqrt{\frac{1}{3}(Tu^2(c_{\varphi i}) + Tu^2(c_{ri}) + Tu^2(c_{zi}))} \tag{14}$$

$$Tu(|\mathbf{c}|) = \frac{1}{N}\sum_{i}^{N} Tu(|\mathbf{c}|_i) \tag{15}$$

The total pressure loss coefficient is defined by equation (16):

$$\omega(r,\varphi) = \frac{p_{t2}(r) - p_{t3}(r,\varphi)}{\frac{\rho(r)}{2}u^2(r)} \tag{16}$$

Since the investigation has taken place in a stator cascade, all quantities in the following figures are given in the absolute coordinate system with respect to the cascade coordinates shown in Fig. 1. All figures with turbulence correlations presented in

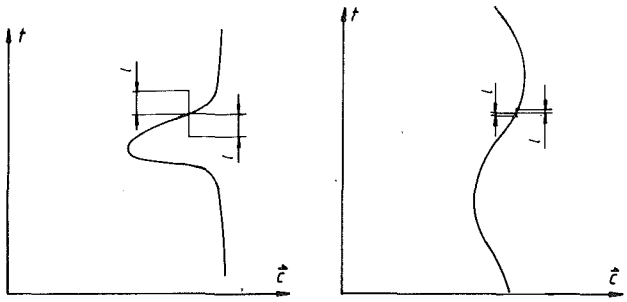

Fig. 5 Sketch of turbulent mixing procedure near to the rotor and far downstream

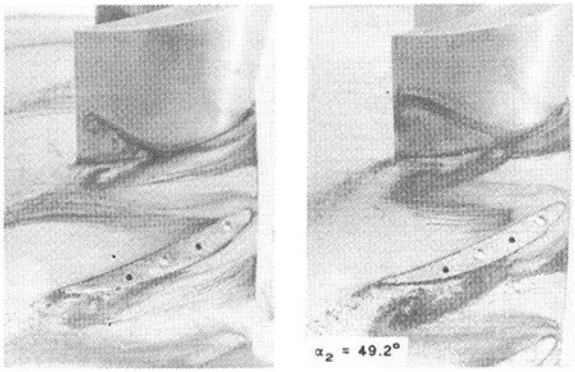

Fig. 6 Development of hub corner stall with incidence (Schulz, 1990)

this paper are referred to the square of the mean velocity at the measurement location.

The great amount of data leads to the numeric problem to reduce all the recorded data in an appropriate time. The calibration procedure following equations (3)–(5) has to be carried out at each location of measurement about 65,000 times, and in addition the time-averaging and correlation procedures using equations (8)–(13) have to be done. This has to be multiplied by the number of measurement locations, which is 180 for test cases 1–3 and 270 for test cases 4 and 5. Doing this data reduction using an IBM compatible computer (8 MHz with floating point processor 80,287) requires a computation time of several days. Therefore, this problem could only be solved using a four-processor transputer inboard card in the processing computer, which reduces the computation time by a factor of about 120.

Results and Discussion

Natural Wake Decay (Test Case 1). In order to get a basic understanding of the natural wake decay dependent on axial distance and spanwise distribution, the stator blades were removed (first test series). The unsteady flow was determined at 10 axial locations with 18 spanwise positions each. In Fig. 4, the secondary flow plot as well as the contour diagrams of the velocity, the axial turbulence intensity, and the turbulence correlation in the circumferential plane are shown. They are plotted as a function of time and radius in the relative frame of reference. The relative velocity to the rotor is exactly the same compared to the later-described test case 2, with a stator inlet flow angle of 44.2 deg.

In the first measurement location downstream of the rotor, the wake has a strong radial velocity component (Fig. 4, No. 1). Near the tip of the rotor, the flow pattern is very complex. Leakage flow, horseshoe vortex, and irregular shed von Karman vortices (Re = 25,000) are superimposed. Near the hub, a vortexlike distortion was detected. Because no unsteady boundary layer measurements of the sidewalls were carried out, no details about the flow structures in the casing and hub boundary layers near the rotor are determined. One channel vortex is induced due to the spanwise distribution of the difference between the circumferential velocity component of the flow in the absolute frame of reference and the velocity of the rotor rods. The spanwise distribution of the circumferential velocity in the absolute frame of reference and the rotor speed is shown in Fig. 2(*c*).

While being convected downstream, the channel vortex and the tip-flow structures decay continuously. The distortion near the hub, though, is amplified up to measurement location 3, and then decays. The authors believe that the flow structure near the hub is amplified due to the changing from the rotating hub to the stationary frame of reference of the stator. This takes place between measurement locations 2 and 3.

There are significant differences in the decay characteristics of velocity, turbulence intensities, and turbulence correlations. While the velocity defect decreases to about half its value, the turbulence inside the wake decays faster due to mixing effects (from about 14 percent turbulence intensity to about 6 percent). The turbulence correlation contour plots at position 1 show nearly isotropic turbulence outside of the wake, and anisotropic turbulence in the wake region. The turbulence correlation decreases very fast, and downstream of point 6 the overall turbulence structure becomes nearly isotropic.

The wake contour profiles of velocity, flow angles, and turbulence intensities tend toward a sinusoidal shape. Close to the rotor the anisotropic characteristic of turbulence in the wake is clearly visible (high-turbulence correlations).

Based on the Prandtl mixing length theory and observation of the *real-time* data (which cannot be shown in the paper), some conclusions on turbulence structure can be made. Close to the rotor the velocity gradients normal to the wake are large (Fig. 5). The turbulent eddies are strong and their kinetic energy is high. The mixing length of a turbulent eddy generated in the shear flow (Fig. 5) is large enough to cover a considerable portion of the sheared flow inside the wake. This will result in a turbulence correlation that is not equal to zero. Convected downstream, the turbulence will mix out. The turbulent eddies become smaller and their kinetic energy is also lower. Far downstream of the rotor, the velocity defect of the rotor wake decreases (Fig. 4), and in addition, the velocity profiles tend to have a sinusoidal shape (Fig. 5). This causes lower velocity gradients normal to the wake. Therefore the turbulence production in the wake decreases in locations further downstream of the rotor. Here the movement of the eddies normal to the wake shear flow is not large enough to generate significant turbulence correlations (Fig. 5).

With respect to Fig. 4 some observation about the spanwise structure of the wake can be made:

1 The spanwise distribution of the relative velocity has a significant influence on the wake depth and on the Reynolds number to the cylindrical rods.

2 The solidity of the cylindrical rods decreases from hub to tip. Therefore, the velocity defect of the rotor wake reaches a maximum near the hub, and the velocity outside the wake also becomes maximal. This effect is shown in the contour plot of the velocity in Fig. 4, plot 1.

3 The angle between the tangent of the wake trajectory and the axis of the annular cascade corresponds to the relative exit flow angle of the rotor. As this angle β is not constant in the spanwise direction (Fig. 2*b*), the wake will spread out and becomes spanwise skewed while convected downstream (Fig. 10).

The secondary flow pattern in location 1 is similar to the flow structures found in test case 1 without stator. The channel vortex and the disturbances near the hub have about the same intensity. It can be seen that the flow structures downstream

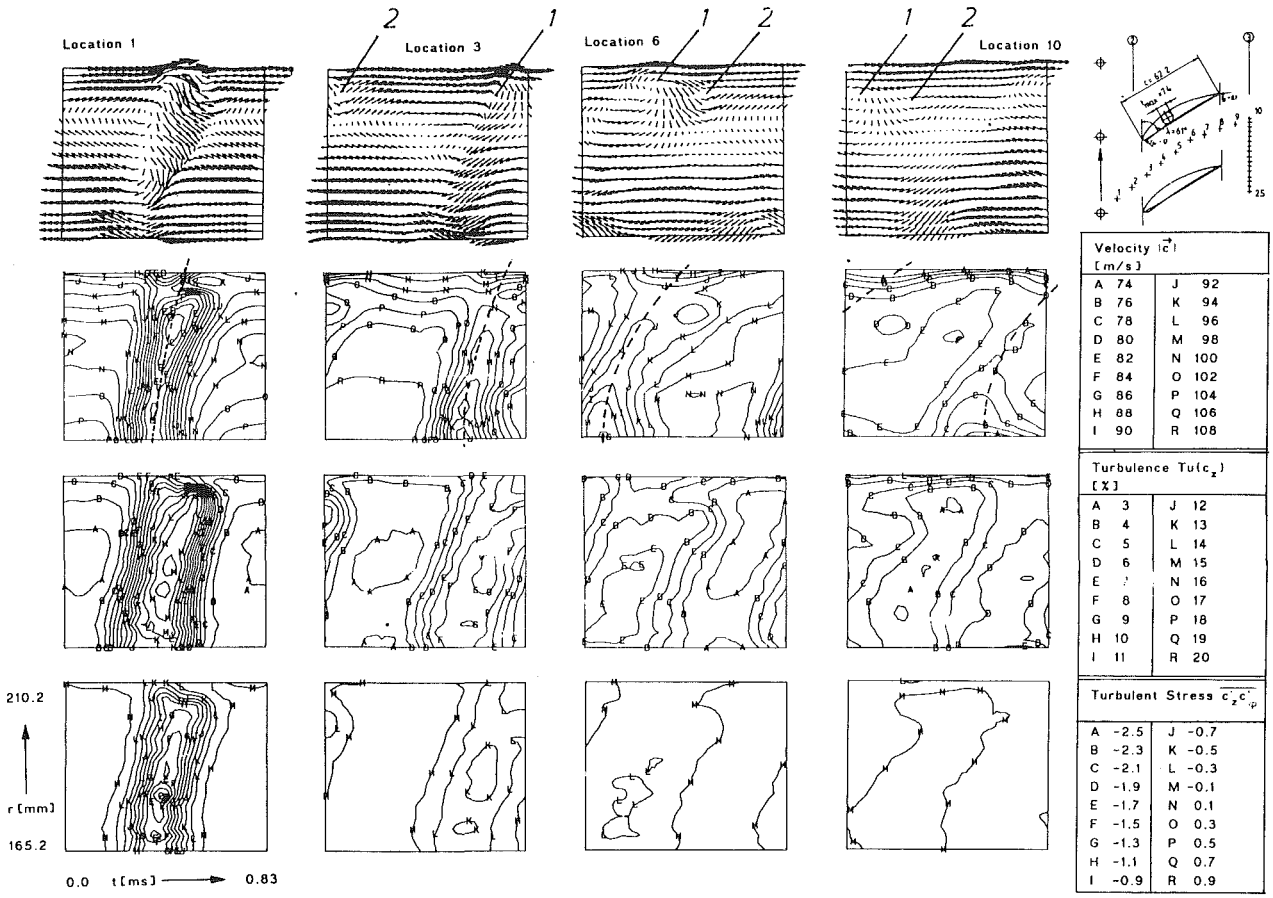

Fig. 7 Decay characteristics of unsteady flow quantities $\alpha_2 = 44.2$ deg (test case 2)

of the rotor tip region become stronger. While passing the stator blade row this tip flow rolls up into two vortices (labeled No. 1 and 2). They reach their maximum of intensity near location 7 (not shown here), and from then on they decay. Regarding the rotational sense of the upper vortex (No. 1), this amplification can be related to the secondary flow at the casing of the stator channel.

Wake Decay Throughout the Stator Passage (Test Cases 2 and 3)

Moderate Blade Loading. In a second step, the wake decay was determined along the centerline between two stator blades. The surface of measurements corresponds to an S2M surface as it is known from quasi-three-dimensional calculations. The investigations were carried out for slightly loaded blades with 2 deg incidence angle, which corresponds to an inlet flow angle of 44.2 deg and also for a higher loading (7 deg incidence) to get an interaction of the quite severe hub corner stall with wake flow.

The suction side and hub surface flow have been visualized by means of dye injection (Schulz et al., 1988) at two different angles of attack. The extent of the hub corner stall with increasing incidence angle is clearly visible and reported in more detail by Schulz and Gallus (1988) and Schulz et al. (1990).

Some representative data for the second test case (2 deg incidence angle) are shown in Fig. 7. According to Fig. 4, the secondary flow plots, the contour plots of the velocity, circumferential turbulence intensity, and the turbulence correlation in the crossflow plane at 4 locations downstream of the rotor are shown.

The secondary flow was detected by the hot-wire sensors as an overturning of flow, which is combined with a larger deceleration of the mean velocity as can also be seen in the velocity contour plots of Fig. 7 near the casing. It has to be noted that the radial velocity gradients in Fig. 7 at location 3 outside the wake are related to the wake itself and not to the casing boundary layer. The solidity of the rotor rods becomes maximum at the hub because the diameter of the rods is constant versus span. This causes a high displacement of the rotor passage flow near the hub due to the cylinders, so that the wake is sharp and deep. The passage flow between two cylinders here reaches its maximal values. As the radius is increased, the solidity of the cylindrical rods increases and the velocity defect of the rotor wake decreases. The inverse effect occurs to the flow outside the wake. This will cause the velocity gradient observed at location 3. The region of secondary flow near the casing is first seen in the velocity contour plot for location 5 (not shown here).

Comparing the velocity defect in the stator passage with the case where the stator blades are removed (test case 1), it was found that the wakes have been smoothed by the presence of the stator. The wake depth decreases at location 10 from 13 m/s to about 7 m/s at 30 percent midspan. When the rotor wake enters the stator passage, the flow velocity is accelerated 96 m/s at location 2 to a mean velocity of about 108 m/s at location 4. Between these locations the velocity defect of the wake at 30 percent span decreases from 18 m/s to 12 m/s. From there on the wake decay is influenced by two different effects. The adverse pressure gradient will lead to an amplification (Hill et al., 1963) of the wake, but stronger mixing effects cause further wake decay.

Turbulence intensities and turbulence correlations of the rotor wake are less affected by the presence of the stator.

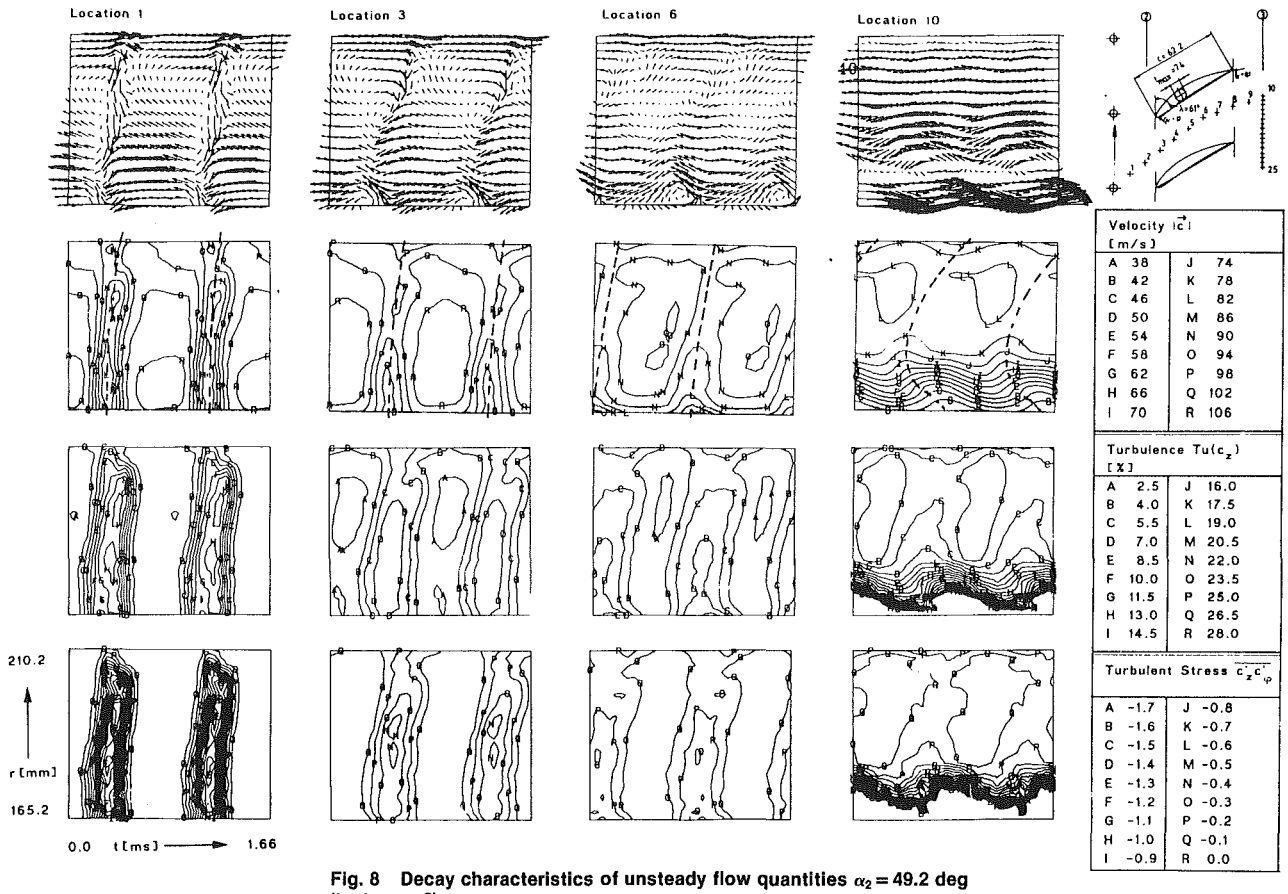

Fig. 8 Decay characteristics of unsteady flow quantities $\alpha_2 = 49.2$ deg (test case 3)

Downstream of measurement location 5 the turbulence correlations diminish (Fig. 7).

The spanwise distribution of the wake trajectories frozen at an instant of time is shown schematically in Fig. 10. The relative flow to the rotor and the spanwise deviation of the flow in the stator are responsible for the spanwise twisting of the wake trajectories. The wake flow near the casing is decelerated with respect to the midspan flow. This effect is visible regarding the contour plot of velocity in Fig. 7. The dotted line indicates the spanwise center of the wake.

High Blade Loading. Some data for the higher loaded test case (case No. 3) are shown in Fig. 8. Comparing these results with those shown in Fig. 7, the velocity gradients near the casing are less distinct for the higher loaded case. This is due to the growing hub corner separation in the stator, which causes the pressure gradients to have a more radial orientation. The secondary flow at the casing decreases and the casing boundary layer becomes thinner. This effect has been reported by Joslyn and Dring (1985), Dong et al. (1987), and Schulz and Gallus 1988). Therefore, in this test case vortices produced in the tip region of the rotor, while passing the stator blades, cannot get a significant amplification by the casing secondary flow in the passage, as was found for the lower incidence test case. Accordingly, the secondary flow plots (Fig. 8) show only minor vortex like distortions near the casing.

On the other hand, the disturbance at the hub of the rotor is amplified while transported downstream through the stator passage. This disturbance rolls up into a vortex and the center of this vortex moves into the stator passage. The rotational sense of the vortex is the same as one of the hub (lower) passage vortices generated by secondary flow.

A dramatic increase of turbulence between the hub and 30 percent span was found downstream of location 6. Here the hot-wire sensors are located close to the boundary of the corner stall region. Hot-wire probes and the five-hole probe measurement showed that the mean flow velocity in this region is greater than 40 m/s, and both probes give the same values. Therefore, the flow is unidirectional and not separated. This has been confirmed by Schulz et al. (1990) using flow visualization techniques (Fig. 6). From this fact follows that this high turbulence is not caused by the corner stall but by the secondary flow. This turbulence, to a large extent, must be generated in the secondary flow region due to its deceleration when it enters the corner stall region.

The turbulence structure in the secondary flow region near the corner stall separation is not isotropic, as can be seen in the turbulence and turbulence stress contour plots of Fig. 8. In this region, the turbulence intensities reach values of over 30 percent. The level of the turbulence intensities and of the turbulence correlations is periodic and in phase with the periodic velocity fluctuation. In the rotor wake flow turbulence intensities reach their maximum in the wake at times when the velocities are low. The turbulence fluctuation waves and the periodic velocity waves are *out of phase* by 180 deg. Close to the boundaries of the hub corner stall the periodic turbulence waves and the periodic velocity waves are in phase. The hub corner stall has a periodic motion with respect to time. So do the velocity gradients in the boundary of the hub corner stall. In instances of time when the velocities at the measuring location are high, the velocity gradients at the boundary of the hub corner stall are large, because the stall region reaches its minimum in spatial extent. High velocity gradients will subsequently produce high turbulence intensities. The motion of the hub corner stall is described in further detail in part II of this paper.

In addition to the turbulence intensity, the wake itself is amplified in the region close to the corner stall. The wake

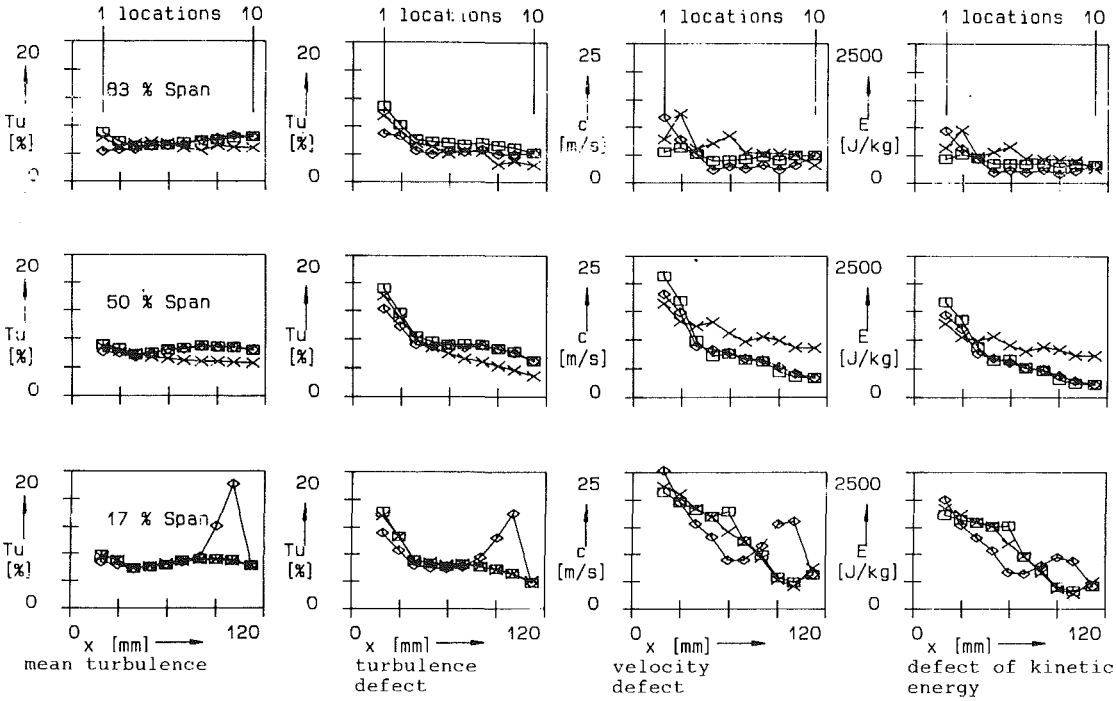

Fig. 9 Wake decay of mean turbulence intensity, turbulence defect, velocity defect, and defect of kinetic energy

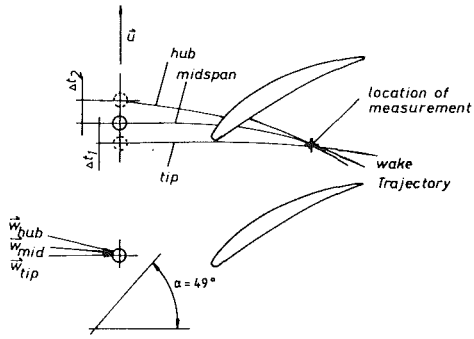

Fig. 10 Wake trajectories for a frozen instance of time in the rotor passage

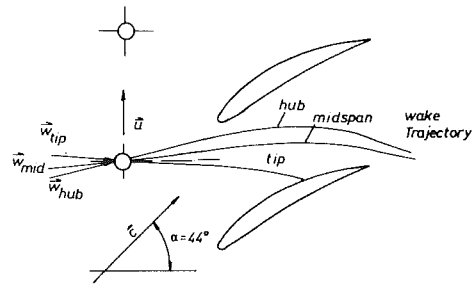

Fig. 11 History of wake trajectories; different spanwise positions at one measuring location

depth increases from 10 m/s at location 5 to about 18 m/s at location 9 (at 17 percent span), and thus the wake depth is nearly doubled (Fig. 9).

As the hot-wire probe is close to the hub corner stall, there are large velocity gradients due to the influence of the stalled region at these locations.The separation region at the hub is influenced by rotor wakes, so the separation has a motion in time. Therefore, the velocity field at the boundary of the hub corner stall is also moving, and due to the large velocity gradients, the probe will experience large velocity differences during one time period.

The white areas near the hub are regions of turbulence levels beyond 30 percent, where all hot-wire measurements suffer from greater systematic errors. This leads to a more qualitative character of the obtained results.

Downstream of measurement location 5, an increasing time delay of the wake centerline is detected while moving the hot-wire sensors toward the hub. This time delay results from a greater deceleration of the flow between the hub and about 30 percent of span, and also from the higher deviation (secondary flow) of the flow in this region. The wakes detected one radial line of measuring points that are produced at different rotor positions as sketched in Fig. 11. Further measurements in the stator passage will clarify this problem.

The overall mean turbulence intensities and the differences between the turbulence intensity in the wake and in the core flow for all three test cases at three spanwise locations are shown in Fig. 9. In the third and fourth column the velocity defect of the wake and the corresponding defect of kinetic energy are given for test case 3. For the case with removed stator, the overall turbulence intensity decreases monotonously.

For the other two test cases, the turbulence intensity decreases from the rotor to the inlet plane of the stator, and from here on the turbulence intensity increases until there is a difference in turbulence intensity of about 3 percent in the stator exit plane compared to test case 1. Further downstream the turbulence intensity decreases along the investigated S2M surface. Close to the hub an amplification of the velocity defect is determined. Calculating the corresponding defect of kinematic energy, an increase was found. This effect is related to the periodic motion of the hub corner stall.

It was found that the total pressure losses of the compressor cascade decreased in unsteady flow compared to those obtained in an undisturbed flow field (without rotor). This tendency was observed for various incidence angles and quantitative results are given by Schulz at al. (1990). They found that although the losses at midspan increase due to the earlier onset of transition of boundary layers in the rotor case, the overall losses decrease. This can be related to the significant loss re-

duction due to a smaller hub corner stall region. Intensive turbulent mixing, the hub vortex coming out of the rotor and its amplification while it is convected downstream, and also the periodic fluctuations of secondary flow, are believed to diminish the hub corner stall.

The unsteady inlet flow to the stator will result in an unsteady blade loading, and this among others will result in a periodic secondary flow. Since the secondary flow rolls up inside the corner stall region into a vortex system, it is believed that this might also contribute to the periodic motion of the corner stall. This was the motivation and the objective of the investigations described in Part II of this paper.

Conclusions

1 The turbulence structure of the wake in the first measurement location is not isotropic. The axial and circumferential turbulence intensities are larger than the radial ones. The turbulence intensities in the rotor wake reach values of 17 percent. Outside the wake, the turbulence is isotropic with a turbulence intensity of about 3 percent.

2 Turbulent eddies generated in the wake near the rotor are large and they have high kinetic energy. The mixing length is large enough to generate turbulent correlations. Farther downstream the wake velocity gradients are small, and the turbulence production is weak. Turbulent eddies no longer have the mixing length sufficient to produce significant turbulent correlations.

3 The wake decays without stator and in the stator passage have totally different characteristics. Due to the acceleration of the flow at the inlet of the stator and due to mixing effects in the diverging parts of the stator passage, the wake velocity defects decrease twice as fast. The overall turbulence intensity increases while the wake is passing through the stator blades. The decay of the turbulence correlations is one order faster than the decay of the velocity defect, and the Reynolds stresses generated are nearly mixed out already at the inlet of the stator. Therefore they do not have a significant influence on flow separations occurring in the stator. The isotropic turbulence seems to be the only turbulence quantity of importance.

4 For a low incidence angle to the stator, a significant secondary flow exists at the casing. Flow structures generated by the tip leakage flow of the rotor are highly affected by this secondary flow inside the passage and roll up into two vortices.

5 The wake flow induces an unsteady loading to the stator blades. This causes an unsteady pressure field, which generates an unsteady secondary flow at the hub. This secondary flow may amplify vortices shed near the hub of the rotor. In our investigations, one vortex was found, and it is believed that this vortex re-energizes the hub boundary layers, and thus reduces the stator hub corner stall.

6 For the higher loaded case, a significant amplification of the rotor wake between the hub and about 30 percent span was observed inside the stator passage near the boundaries of the hub corner separation. This effect has been also found by Schulz at al. (1990). Here the velocity defect doubles its size.

7 The flow pattern found close to the hub corner separation inside the stator passage was at all times positive and nonreversed. This was observed by flow visualization, pneumatic measurement, and hot-wire anemometry. The high turbulence intensities in this region indicate that the secondary flow near the corner separation is a highly active center of turbulence production. This can also be seen by the dramatic increase in turbulence correlations.

8 It has been demonstrated by the measurements that separated zones in the stator flow may be forced into unsteady periodic motion due to incoming wakes. This effect, in turn, amplifies the wake information, which therefore will be transported farther downstream. For this reason the effect of wake amplification might be even more important in a multistage environment.

Acknowledgments

The authors are indebted to Dr. H. D. Schulz for his contribution to this paper. Basic studies for the calibration procedures of multisensor hot-wire probes were carried out by B. Banken and D. Steinebach, who are gratefully acknowledged by the authors. The assistance of PARSYTEC PARACOM GmbH in programming the transputer is also acknowledged.

References

Adachi, T., and Matsuuchi, K., 1983, "Measurement of the Three-Dimensional Unsteady Flow Inside a Rotor Blade Passage of an Axial-Flow Fan," ASME Paper No. 83-TOKYO-IGTC-67.

Bartenwerfer, M., 1981, "Zur Analyse von Hitzdrahtsignalen turbulenter Strömungen," Ph. D. Thesis, University of Berlin.

Bohn, D., and Simon, H., 1975, "Mehrparametrige Approximation der Eichräume und Eichflächen von Unterschall-5Loch-Sonden," *ATM Messtechnische Praxis*, Lieferung 470.

Dong, Y., Gallimore, S. J., and Hodson, H. P., 1987, "Three-Dimensional Flows and Loss Reduction in Axial Compressors," ASME JOURNAL OF TURBOMACHINERY, Vol. 109.

Dring, R. P., Joslyn, H. D., and Hardin, L. W., 1982, "An Investigation of Axial Compressor Rotor Aerodynamics," ASME *Journal of Engineering for Power*, Vol. 104, pp. 84–96.

Hill, P. G., Schwab, U. W., and Senoo, Y., 1963, "Turbulent Wakes in Pressure Gradients," ASME *Journal of Applied Mechanics*, Vol. 30, p. 518.

Joergenson, F. E., 1971, "Directional Sensitivity of Wire and Fiber-Film Probes," *DISA Information*, No. 11, May.

Joslyn, H. D., and Dring, R. P., 1985, "Axial Compressor Stator Aerodynamics," ASME *Journal of Engineering for Gas Turbines and Power*, Vol. 107.

Poensgen, C. A., and Gallus, H. E., 1989, "Ein Verfahren zur Vermessung der instationären dreidimensionalen Geschwindigkeitsvektoren in Turbomaschinen," Internal Technical Report No. 89–1, RWTH Aachen, Federal Republic of Germany.

Ravindranath, A., and Lakshminarayana, B., 1979, "Mean Velocity and Decay Characteristics of the Near- and Far-Wake of a Compressor Rotor Blade of Moderate Loading," ASME Paper No. 79-GT-202.

Schlichting, H., 1951, *Boundary Layer Theory*, McGraw-Hill Series in Mechanical Engineering, New York.

Schulz, H. D., and Gallus, H. E., 1988, "Experimental Investigation of the Three-Dimensional Flow in an Annular Compressor Cascade," ASME JOURNAL OF TURBOMACHINERY, Vol. 110.

Schulz, H. D., Gallus, H. E., and Lakshminarayana, B., 1990, "Three-Dimensional Separated Flow Field in the Endwall Region of an Annular Compressor Cascade in the Presence of Rotor-Stator Interaction: Part 1—Quasi-Steady Flow Field and Comparison With Steady-State Data; Part 2—Unsteady Flow and Pressure Field," ASME JOURNAL OF TURBOMACHINERY, Vol. 112, pp. 669–690.

Suder, K. L., Hathaway, M. D., Okiishi, T. H., Strazisar, A. J., and Adamczyk, J. J., 1987, "Measurements of the Unsteady Flow Field Within the Stator Row of a Transonic Axial-Flow Fan—Part I: Measurement and Analysis Techniques," ASME Paper No. 87-GT-226; "Part II: Results and Discussion," ASME Paper No. 87-GT-227.

Three-Dimensional Wake Decay Inside of a Compressor Cascade and Its Influence on the Downstream Unsteady Flow Field: Part II—Unsteady Flow Field Downstream of the Stator

C. Poensgen

H. E. Gallus

Institut für Strählantriebe und
Turboarbeitsmaschinen,
RWTH Aachen,
5100 Aachen, Federal Republic of Germany

A measuring technique based on multisensor hot-wire anemometry has been developed to determine the unsteady three-dimensional velocity vector and the structure of turbulent flows. It then has been applied to the passage and the exit flow of an annular compressor cascade, which is periodically disturbed by the wakes of a cylinder rotor, located about 50 percent of blade chord upstream. In Part I of this paper the decay of the rotor wakes has been described first without stator and secondly through a stator passage. The time-dependent turbulent flow field downstream of this stator is discussed in Part II of this paper. The rotor wakes have a major influence on the development of three-dimensional separated regions inside the compressor cascade, and this interaction will be addressed in both parts of the paper.

Introduction

Most of the present analysis and design methods in turbomachinery are based on steady aerodynamics. The unsteady flow associated with blade row interaction has a major influence on the flow field, boundary layers, turbulence intensities, separation, vibration, and noise. The demand for higher performance in aircraft engine design results in a closer spacing of the blade rows. This requires more sophisticated design methods including the possibility to calibrate numerical schemes and their turbulence modeling. There is a need to get a better understanding of the three-dimensional unsteady flow in a blade row including the influence of rotor–stator interactions.

This paper is addressed to the rotor–stator interaction and its influence on the flow field downstream of an annular compressor cascade. The development of losses, wake-induced vortices, and the influence of the unsteady flow on the hub corner separation, as well as on the tip leakage flow is discussed. The wake transport through the blades and its effect on the corner separation inside the passage are discussed in Part I of this paper.

It is found that the tip leakage flow has a major influence on the loss development of the stator for low incidence angles. Basic investigations on tip leakage flow have been carried out by Dishart and Moore (1990), Bindon (1989), and Yaras and Sjolander (1989) using rectangular, large-scale turbine cascades. They found that the tip leakage flow is inseparably combined with secondary flow aspects, but they did not look to the influence of blade loading on the tip leakage flow.

The investigation of the flow field downstream of a compressor cascade by pneumatic probes is a very common technique, and results are reported in a large number of papers. The major objective of this paper is to shed light on the influence of unsteady inlet flow on the exit flow of an annular compressor blading. Therefore triple hot-wire probes have been used in addition to pneumatic probes in order to get the high resolution in time required. Investigations have been performed at two different incidence angles to the stator blading, i.e., $i=2$ deg and $i=7$ deg. The interaction of both the tip leakage flow and the hub corner separation with the incoming wake flow is determined.

The test facility and the test program are described in Part I of this paper; the description will not be repeated here.

Steady-State Data and Loss Analysis

The data were taken 22.2 mm downstream of the trailing edge of the compressor cascade. The measurement grid is dimensioned by 18 points in radial and by 16 points in circumferential direction. The test series have been carried out for

Contributed by the International Gas Turbine Institute and presented at the 35th International Gas Turbine and Aeroengine Congress and Exposition, Brussels, Belgium, June 11–14, 1990. Manuscript received by the International Gas Turbine Institute January 12, 1990. Paper No. 90-GT-22.

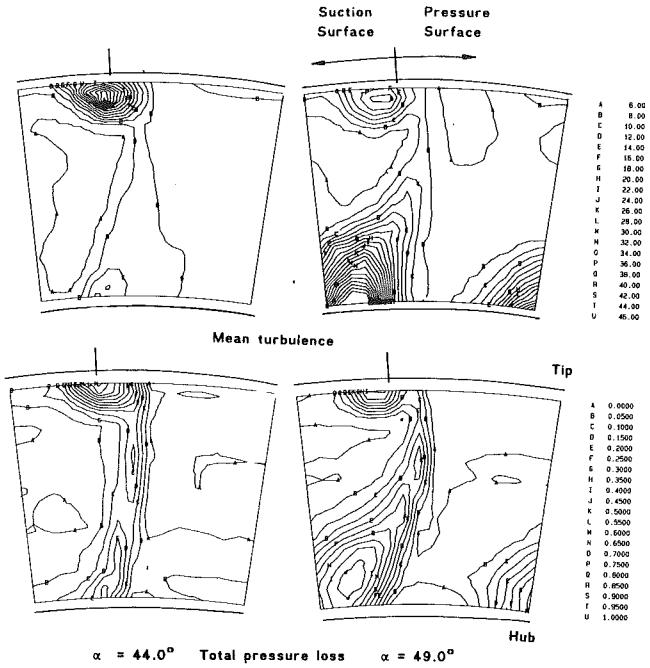

Fig. 1 Loss and mean-turbulence contour plots

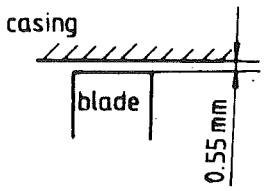

Fig. 2 Tip gap geometry

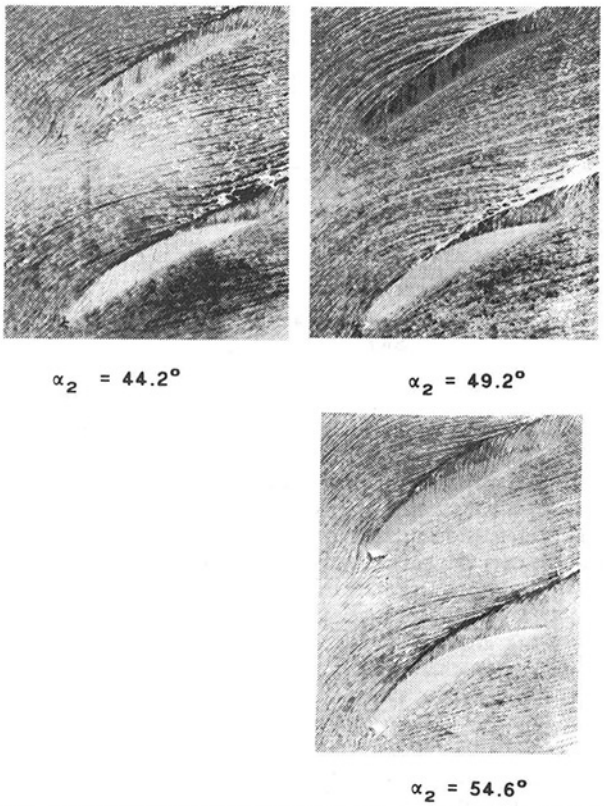

Fig. 3 Oil flow visualization of tip leakage flow with incidence (Schulz, 1990)

two different incidence angles: $i=2$ deg and $i=7$ deg, respectively. The data were acquired with five-hole and with triple hot-wire probes. By doing this, the total pressure loss distribution was determined, along with the mean average velocity, turbulence, and turbulence correlation intensities and their time-dependent characteristics.

The total pressure loss contours determined by five-hole probe measurements and the steady mean turbulence intensities detected by hot-wire anemometry are shown in Fig. 1. Figure 2 shows schematically the geometry of the tip clearance. The gap has a width of about 0.55 mm and the edges of the tip of the stator blade are sharp. For the lower incidence case ($\alpha_2=44.2$ deg), the tip leakage flow of the stator is dominant and the highest losses occur in this region. For the other incidence, the total pressure losses generated by the tip leakage flow decrease, but the total pressure losses as well as the mean-average turbulence due to the stator hub corner stall rise in intensity. The increase of the hub corner separation with incidence in uniform flow and in unsteady flow is reported in more detail by Schulz et al. (1990). They also found a decrease of the casing losses with incidence, even though flow visualizations (Fig. 3) showed a higher penetration of the passage flow by the tip clearance vortex with loading. This might lead to the assumption that the tip clearance flow increases with incidence, and thus the losses produced in the region will do the same. However, the opposite effect was found (Fig. 1). The question remains whether in the measuring plane all losses are detected, or whether there exist losses due to secondary kinetic energies, which are not mixed out at this location. These would mix out farther downstream.

To estimate mixing losses generated by secondary flow, the values of the secondary energy coefficients have to be determined by integration. The definitions of these coefficients are given according to Dishart and Moore (1990):

Total Kinetic Energy Coefficient

$$\mathrm{TKEC}=\frac{\int_A \rho c_z \frac{c^2}{2}\,dA}{\dot{m}\frac{u^2}{2}} \tag{1}$$

Nomenclature

A = area
c = velocity
i = incidence angle to the stator
$\dot{m}$ = mass flow
u = reference inlet velocity to the stator at midspan
α = flow angle in the absolute frame of reference
ρ = density
TKEC = Total Kinetic Energy Coefficient
SKEC = Streamwise Kinetic Energy Coefficient
NKEC = Normal Kinetic Energy Coefficient

Subscripts

n = normal direction to the streamline
s = streamwise direction
z = axial direction
2 = stator inlet
3 = stator exit

Table 1 Kinetic energy coefficients of the stator for test cases 4 and 5

Inlet flow angle to the stator	44.2 deg	49.2 deg
Outlet flow angle	22.2 deg	23.9 deg
Total kinetic energy for the entire cascade	0.6103	0.6011
Streamline kinetic energy for the entire cascade	0.6076	0.5964
Normal kinetic energy for the entire cascade	0.0027	0.0047
Total kinetic energy for the tip leakage flow	0.0544	0.0701
Streamline kinetic energy for the tip leakage flow	0.0536	0.0693
Normal kinetic energy for the tip leakage flow	0.0008	0.0008

Normal Kinetic Energy Coefficient

$$\mathrm{NKEC} = \frac{\int_A \rho c_z \frac{c_n^2}{2}\, dA}{\dot{m}\frac{u^2}{2}} \tag{2}$$

Streamwise Kinetic Energy Coefficient

$$\mathrm{SKEC} = \frac{\int_A \rho c_z \frac{c_s^2}{2}\, dA}{\dot{m}\frac{u^2}{2}} \tag{3}$$

The total kinetic energy is split into the normal and streamwise kinetic energy and referred to the total kinetic energy at stator inlet. The normal kinetic energy of the flow in the measuring plane then is assumed to dissipate farther downstream.

The integration according to equations (1)–(3) has been carried out over the entire cascade and over the area covered by the tip leakage vortex. Thus the normal kinetic energy coefficient for the tip leakage flow was obtained separately. The results are given in Table 1. It was found that the normal kinetic energy coefficient of the tip leakage flow is about the same for both test cases investigated. Thus circulation and rotational energy are assumed not to be affected by incidence. The observed significant reduction in loss in the tip leakage flow region is also valid for the fully mixed-out losses.

The question still remains, why even though the leakage flow vortex increases in size with increasing incidence angle, the total pressure losses and the turbulence production rate in the vortex decrease.

The losses generated by a tip leakage flow are augmented by:

- viscous stress and separation bubbles inside the gap
- sudden expansion as the flow emerges from the gap
- intensive turbulent mixing of leakage flow with the tip corner passage flow on the suction side
- counterrotation of the leakage flow vortex (labeled No. 1 in Fig. 5) and the top passage vortex (labeled No. 2 in Fig. 5)
- adverse pressure gradients in a compressor flow field
- interaction of the tip leakage flow with the tip corner boundary layers and the tip corner separation

While increasing the incidence angle to the stator, the pressure difference between suction side and pressure side rises and this causes a higher mass flow through the tip gap. By the flow visualization shown in Fig. 3 it can be seen that the tip leakage vortex starts at 50 percent chord for $\alpha_2 = 44.2$ deg. With increasing incidence, the initialization point of the vortex moves upstream. For the inlet flow angle of $\alpha_2 = 49.2$ deg, the tip leakage vortex is first visible at about 30 percent chord. Thus only the pressure gradients on the rear part of the blade surface will have a significant influence on the mixing and the convection process of the tip leakage vortex. Schulz et al. (1990) showed that in the rear part of the suction side (Fig. 4), close to the tip, the pressure gradients remains constant with incidence. Thus the tip leakage flow is not influenced by the pressure gradient in the rear part of the suction side.

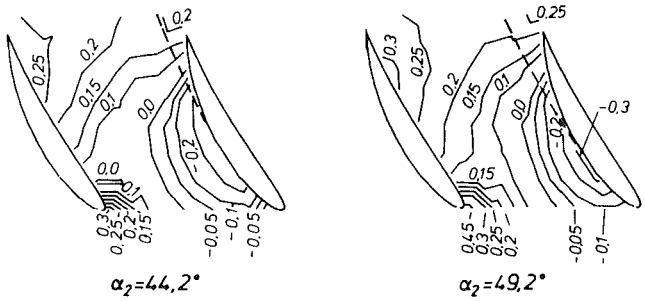

Fig. 4 Static pressure distribution at the casing (Schulz, 1990)

With incidence the axis of the tip leakage vortex moves into the stator passage (Fig. 3). For the lower incidence test case, the tip leakage vortex is attached on the blade suction side, but for the other test case, the leakage flow separates from the blade surface. This effect can also be seen by comparing the velocity contour plots of Figs. 6 and 10.

Thus the leakage flow interacts with the blade boundary layer and the tip corner flow for $\alpha_2 = 44.2$ deg, which tends to separate. This flow has low kinetic energy.

Because the leakage flow vortex moves farther into the passage for the higher incidence case ($i = 7$ deg), there will be an increased interaction with the passage flow. As the flow in the passage has a larger kinetic energy closer to the suction side, the tip leakage flow will be more accelerated in the main streamwise direction. The axial velocity of the vortex center rises from 33 m/s for the lower incidence case to 45 m/s for $i = 7$ deg. Thus the velocity gradients in the vortex are smaller with incidence. The lower sheared flow will subsequently produce less turbulence. Thus the turbulence intensity in the center of the leakage vortex decreases from 35 to 18 percent, and the total pressure losses decrease from $\rho = 0.6$ to $\rho = 0.4$ with incidence.

The static pressure contour plots of the casing, shown in Fig. 4, were taken from Schulz et al. (1990). The dotted lines represent the assumed trajectory of the tip leakage vortex center. The isobar lines diverge from the suction side toward the midpassage. Therefore, the adverse pressure gradients along the centerline of the tip leakage vortex for the higher incidence test case ($i = 7$ deg) are lower compared to the other incidence test case ($i = 2$ deg).

As has already been discussed, the mass flow through the gap increases with incidence. This causes higher discharging losses due to the internal gap flow. However, the reduction of the overall losses of the leakage flow with incidence indicates that the losses produced in the gap are of lower importance compared to the mixing losses. Similar effects have been found by Yaras and Sjolander (1989).

Comparing the normal energy coefficient for the entire cascade with the corresponding values for the region affected by the tip leakage flow, one third of the transported secondary energy is formed by the tip leakage vortex in the lower incidence case. For the higher incidence test case the normal energy coefficient for the cascade has nearly doubled. This amount of secondary energy is mainly brought about by the increase in hub corner separation.

As the blade loading of the stator blade profile losses is increased, the total pressure losses generated by the hub corner separation rise. Comparing the mean-average turbulence intensity for both test cases at midspan (Fig. 1), there is a slight increase of the mean-average turbulence intensity from 9 percent to about 10 percent at $\alpha_2 = 44.2$ deg, but in the flow field downstream of the corner stall the turbulence level rises from 10 percent for the lower incidence case to a value of over 40 percent for the higher loaded case. This turbulence level indicates that intermittent reversed flow due to turbulent eddies of high amplitude occurs.

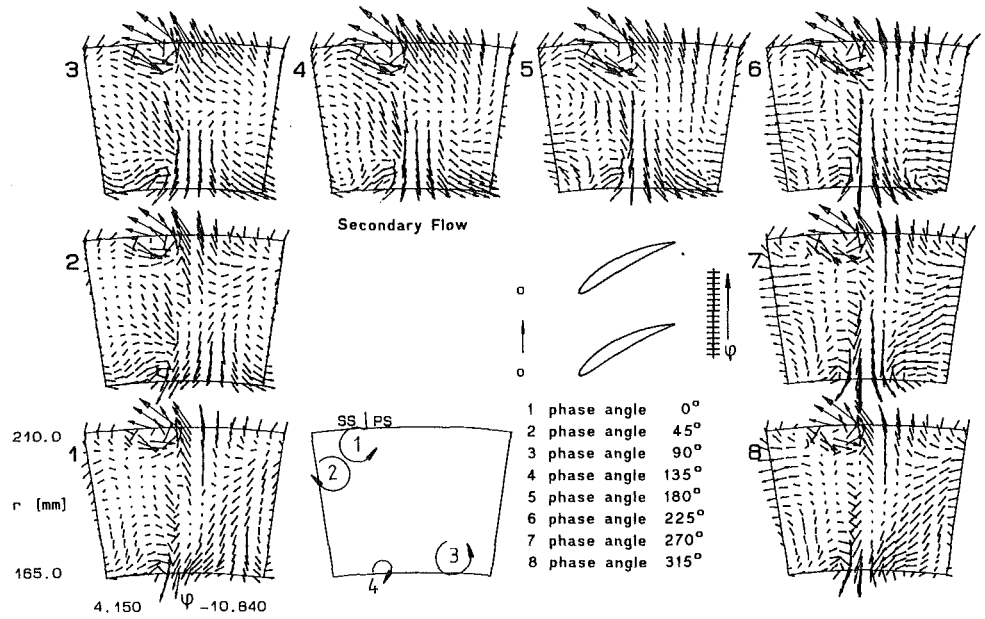

Fig. 5 Secondary flow vectors downstream of the stator $\alpha_2 = 44.2$ deg

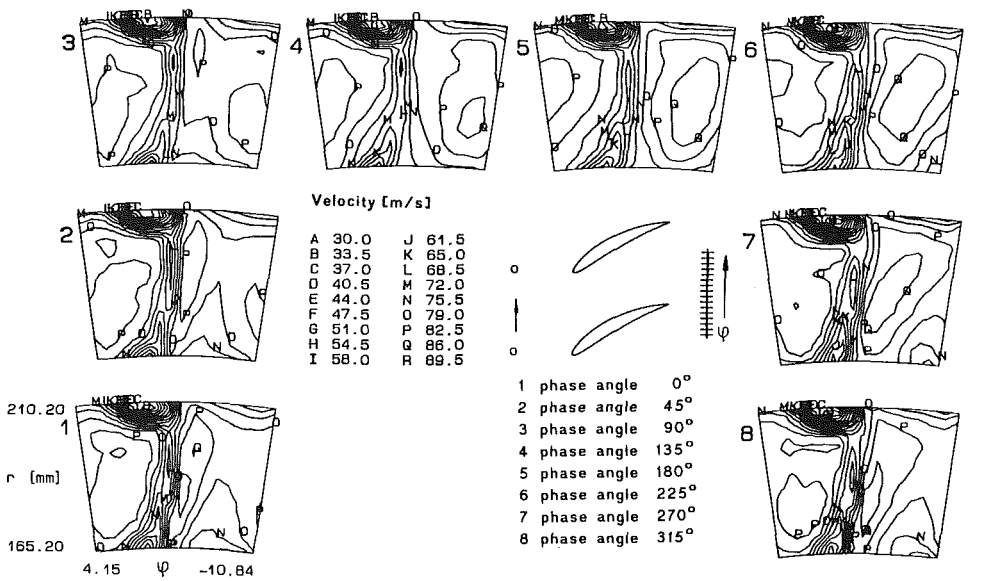

Fig. 6 Velocity contour plots downstream of the stator $\alpha_2 = 44.2$ deg

It is noted by the authors that values of turbulence intensities over 30 percent determined by hot-wire anemometry are inaccurate. The determination of turbulence will lead to systematic errors dependent on the structure of turbulence (Bartenwerfer, 1981). If the turbulence intensity distribution follows the Gauss distribution, turbulent spots of high amplitude will result in a temporal reversed flow with respect to the hot-wire sensors, and the flow direction is not in the range of the sensor calibration. Therefore, the calibration equations (equations (3)–(5) in Part I) will give incorrect results.

Unsteady Flow Field

The flow downstream of the annular compressor cascade is dominated by several vortices, produced either in the stator passage or transported vortices generated by the rotor. The interaction of rotor-produced vortices and the passage vortices of the stator can be classified by two different phenomena. If the circulation of the stator passage vortex is larger than the circulation of a rotor-generated vortex, the passage vortex will capture the rotor-induced vortex. The superposition will lead to one vortex, which fluctuates periodically in size. If the stator passage vortices are weak, there will be a superposition of rotor-generated and passage vortex for an instance of time, but the rotor-generated vortices can be observed in the stator exit plane traveling in the circumferential direction.

In order to demonstrate the unsteady behavior of the downstream flow field, the secondary flow plots and the contour plots of velocity for one turbulence intensity and one turbulence correlation are shown for eight different phase angles with respect to the wake distortion. The results for the fourth test case, $\alpha_2 = 44.2$ deg, are shown in Figs. 5–8. Data for the higher blade loading $\alpha_2 = 49.2$ deg are presented in Figs. 9–12. There exist similar flow plots for other quantities like velocity amplitudes, flow angles, etc., but since it is not possible to present all results in this paper, only representative quantities are selected. All contour plots and secondary flow plots are viewed in the downstream direction. Traces of the rotor wake

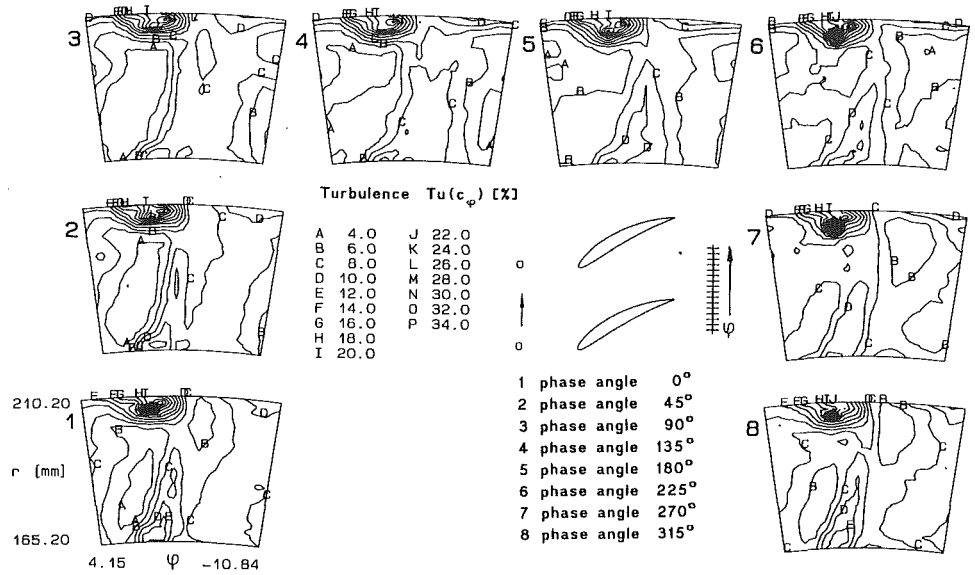

Fig. 7 Turbulence contour plots downstream of the stator $\alpha_2 = 44.2$ deg

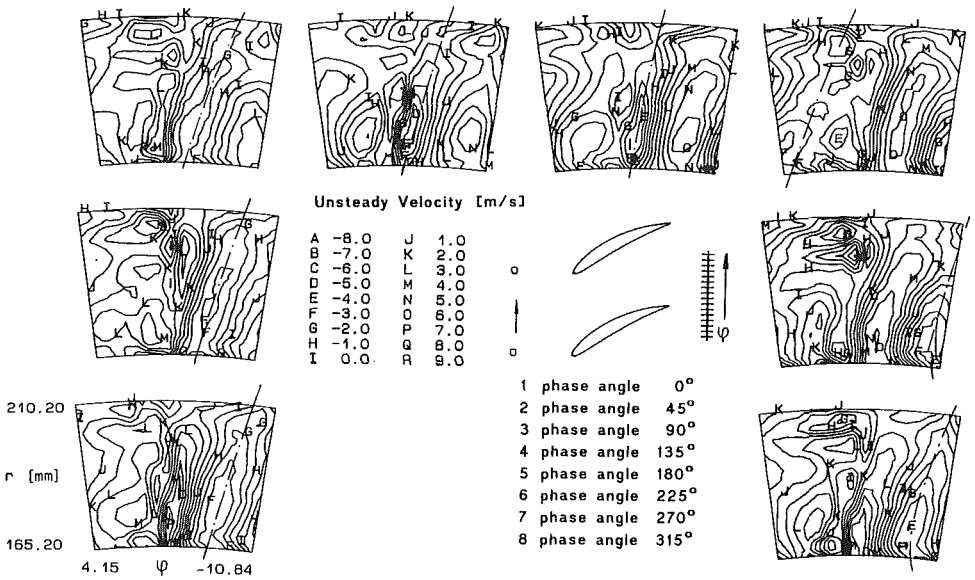

Fig. 8 Unsteady velocity contour plots downstream of the stator $\alpha_2 = 44.2$ deg

move in the secondary flow figures from right to left with respect to time.

Regarding first the test case for the lower blade loading, the influence of the rotor on the stator wake at midspan was found to be small. The periodic velocity amplitude is about 3 m/s. Close to the pressure side, at 30 percent span, the highest fluctuations of the velocity were detected, having an amplitude of 12 m/s. The periodic velocity at the suction side rises to 8 m/s. The flow downstream of the hub corner stall shows only small velocity fluctuations. They are comparable to those found in the stator profile wake at midspan.

The periodic velocity fluctuations near the axis of the tip leakage flow vortex are low. Nevertheless, the turbulence production in this vortex system is periodic with an amplitude of about 10 percent of turbulence intensity (Fig. 7).

According to Fig. 6, the rotor wake is located at the trailing edge of the stator at phase angles from 135 through 180 deg. At these time intervals, the velocity gradients inside the stator wake flow, as well as inside the leakage vortex and at the border of the hub corner separation, reach their minimum. So do the turbulence intensities and the turbulence correlations. This indicates low turbulence production and therefore low losses due to mixing. The inverse effects are observed at phase angles from 270 to 315 deg. The highest turbulence intensities and turbulence correlations are found in the tip leakage vortex and close to the hub of the stator at time intervals when the free-stream flow passes the stator blade surfaces and not, as one might have expected, the wake flow. The unsteady turbulence intensities downstream of the stator depend significantly on unsteady turbulence production in the stator and not on convected turbulent eddies shed off the rotor. Convected turbulence produced by the rotor wake is of minor significance. In contrast to the wake flow, where the highest turbulence intensities are located in region of the lowest velocities, downstream of the stator, the periodic turbulence intensities are in phase with the velocity fluctuations.

At the lower loading ($\alpha_2 = 44.2$ deg) the passage vortices are weak (Fig. 5). For this case, disturbances generated at the hub and near the tip of the rotor, which roll up into vortices while passing through the stator, have a major influence on the stator

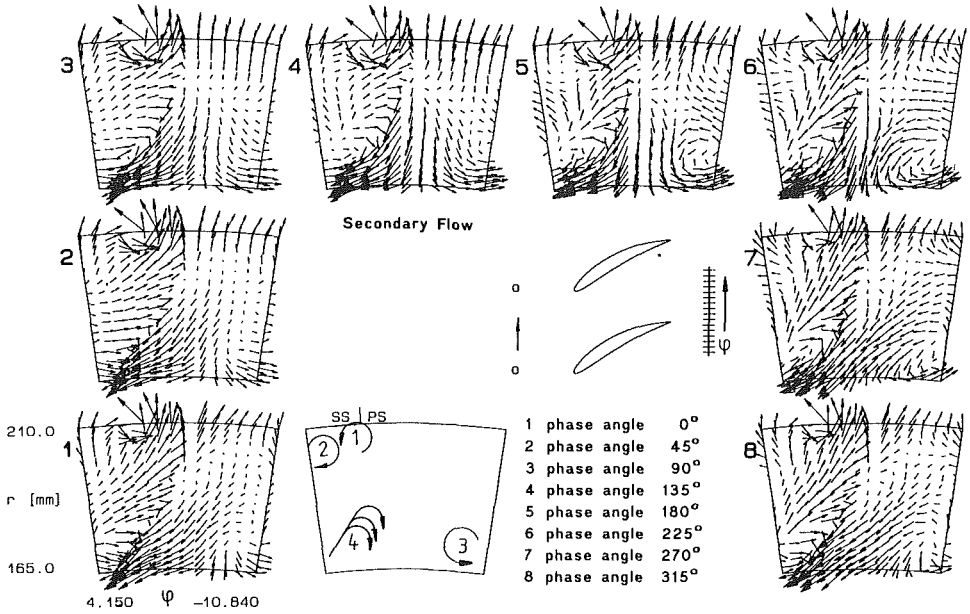

Fig. 9 Secondary flow vectors downstream of the stator $\alpha_2 = 49.2$ deg

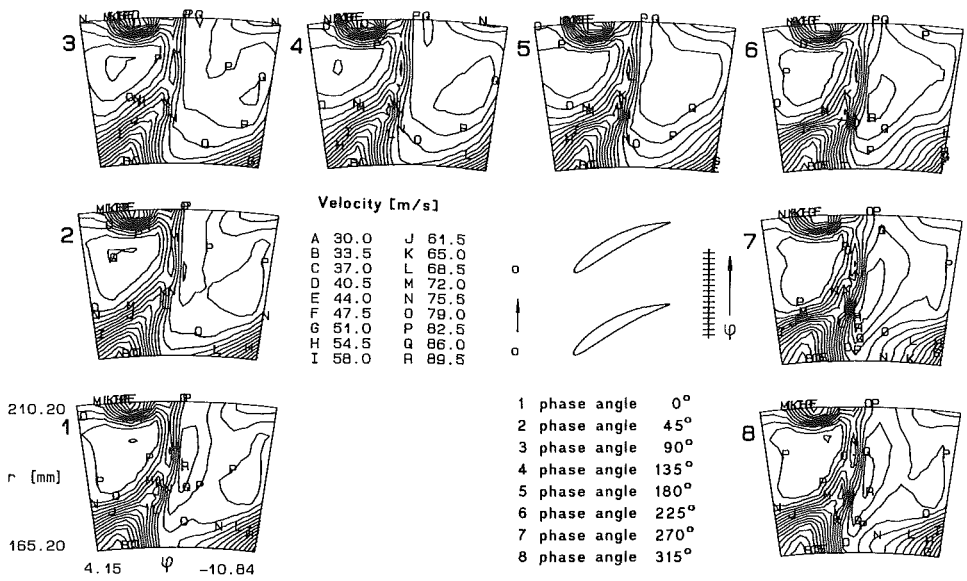

Fig. 10 Velocity contour plots downstream of the stator $\alpha_2 = 49.2$ deg

passage vortices. As is discussed in Part I of this paper, the rotor-generated disturbances at the rotor tip are amplified while being convected downstream through the stator passage (Part I, Fig. 8). In Fig. 5, a sketch of the vortices, which will be addressed in the following discussion, is shown. The influence of the rotor-generated hub vortex (labeled No. 4) is first visible in the secondary flow plot taken at a phase angle of 135 deg (Fig. 5, plot No. 4) near the stator hub corner separation. This vortex moves toward the hub corner of the neighboring blade, where it disappears. At this time interval, the lower passage vortex (labeled No. 3) is not affected by the wake shed off the rotor, and its center is located at about 35 percent span at midpassage. At phase angles from 180 to 225 deg (Fig. 5, plots No. 5 and 6) a counterrotating vortex (labeled No. 2) in addition to the stator tip leakage vortex (labeled No. 1) is generated. Probably this vortex is a superposition of the top stator passage vortex and the rotor-generated tip vortex. At the phase angle of 315 deg (plot No. 8), this vortex diminishes. The vortex generated by the hub corner stall (labeled No. 4) is not affected in any significant way by the rotor wakes.

Figure 8 displays the contour plots of the periodic unsteady velocity. The midspan of the rotor wake through the measuring plane can be observed clearly. The center of the rotor wake, where the unsteady velocities reach their minimum, is marked by dotted lines. Near the pressure side of the stator blade, the velocity fluctuations caused by the rotor wakes have maximal amplitudes. When passing the stator blade from pressure side to suction side, the rotor wake will be smoothed and its wake width will increase. This might be a "shadow effect" caused by the stator, which inhibits rotor wake material from reaching the stator trailing edge at the suction side.

The radial shape of the centerline of the rotor wake is twisted, as is discussed in Part I of this paper, so there is a radial phase lag, but the wake can be observed continuously. The leakage flow vortex is not affected very much by the unsteadiness due to the rotor. The highest velocity fluctuations around the leakage flow vortex have an amplitude of 3 m/s.

As the inlet flow angle to the stator $\alpha_2 = 49.2$ is increased, the stator exit flow field is dominated by the influence of the hub corner stall (Figs. 9–12). The lower passage vortex (labeled

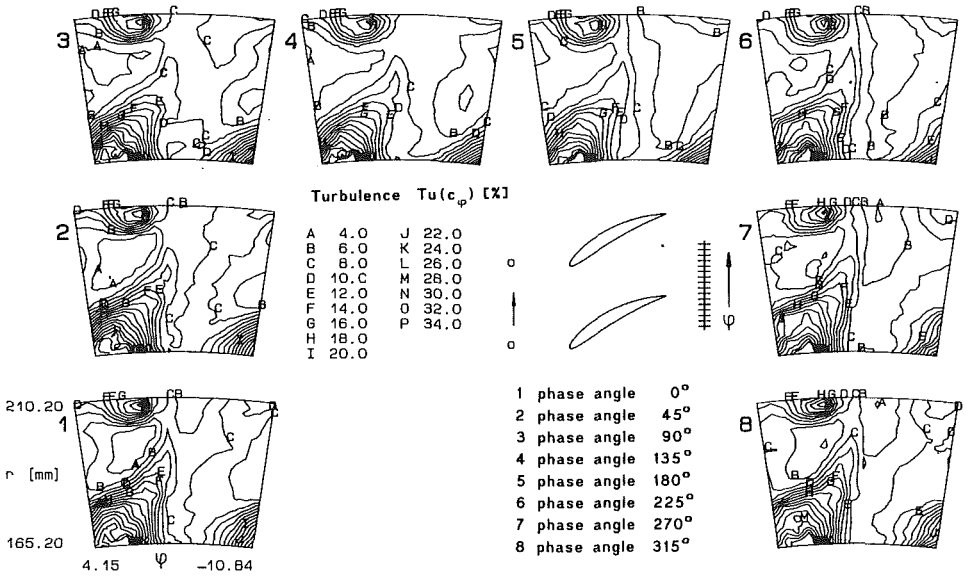

Fig. 11 Turbulence contour plots downstream of the stator $\alpha_2 = 49.2$ deg

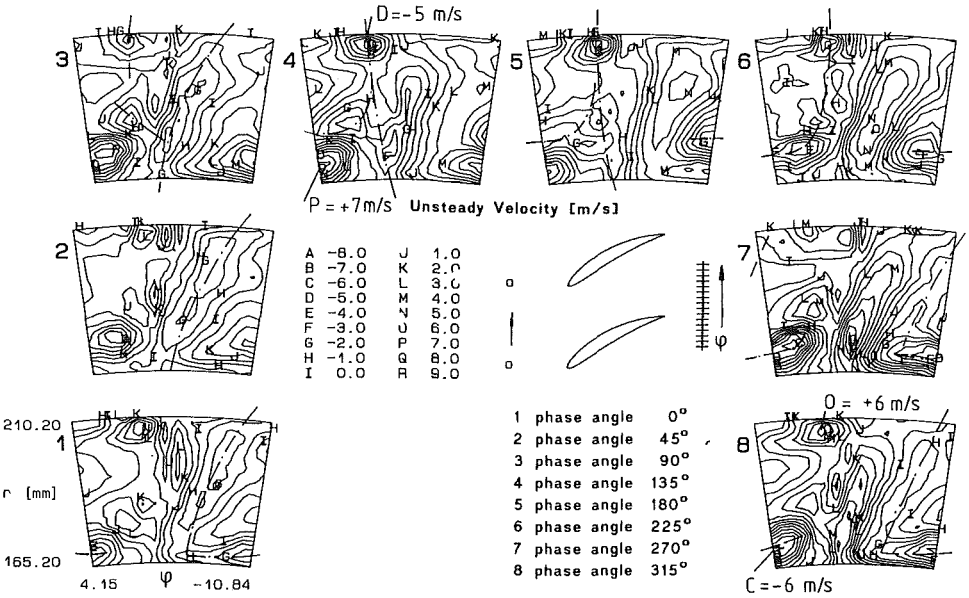

Fig. 12 Unsteady velocity contour plots downstream of the stator $\alpha_2 = 49.2$ deg

No. 3 in Fig. 9) and the vortex generated by the hub corner separation (labeled No. 4) both show significant changes in size with respect to time (Fig. 9). These vortices are counter-rotating, and their periodic circulation is in phase. The lower passage vortex is affected by the vortex generated at the hub of the rotor in a similar way, as it was found for $\alpha_2 = 44.2$ deg. The extent of the hub corner stall changes periodically with the rotor wake flow. Comparing the velocity contour plots of Fig. 10, Plots No. 3–7, the changing of the velocity contour lines at the boundary of the hub corner stall is visible. Here the velocity gradients have a large fluctuation. This effect generates large amplitudes of velocity (up to 16 m/s, Fig. 10) and turbulence intensities (Fig. 11) at the boundary of the hub corner stall, but in its center the flow is nearly steady. The detected turbulence fluctuation downstream of the hub corner stall region is in phase with the velocity fluctuation. The turbulence production at the boundary of the hub corner stall is related to the velocity gradients located in this region. Therefore, the determined turbulence fluctuations in the measuring plane are produced inside the stator passage (compare also Part I of this paper). The consequence of the periodic motion of the hub corner stall is a nonlinear amplification of the rotor wake signal in the region around the hub corner stall. It is nonlinear, because the periodic turbulence quantities and the velocity fluctuations are in phase as opposed to the rotor wakes. The amplification of the rotor wakes in the abovedescribed manner can be very important in a multistage environment.

There is a phase lag in the exit plane between the velocity amplitude at the boundary of the hub corner stall and the core flow of nearly 180 deg. Simultaneously with high velocities in the free-stream flow, there are low velocities downstream of the hub corner stall region, which leads to a pulsating character of the total flow. Comparing contour plot No. 3 in Fig. 10 (90 deg phase angle) to plot No. 7 in Fig. 10 (270 deg phase angle), the maximum velocity moves from midpassage to near the pressure side, and in addition its maximum increases from 85 m/s to 92 m/s. At the same time, the boundary of the hub corner stall moves toward midpassage and the velocity gradients in this region become smaller, while the velocity gradients in the stator wake close to the pressure side increase.

Therefore, the turbulence production and subsequently the loss production are pulsating in the exit plane as well.

As there is a phase lag of 180 deg between the overall motion of the hub corner stall and the core flow, this motion can be compared to a vibration system in the state of overcritical excitation.

Due to the unsteady blade loading, the tip leakage vortex chances a periodic change in intensity. The turbulence production in the tip leakage vortex system is found to be periodic as well, as can be seen in Figs. 8 and 12. Regarding the unsteady velocity contour plots (Fig. 12), it can be seen that the boundaries of the tip leakage vortex have a periodic unsteady velocity amplitude of about 6 m/s. This velocity fluctuation is 180 deg out of phase with respect to the velocity fluctuation near the boundary of the hub corner stall (Fig. 12). This indicates that the periodic change in blockage due to the pulsating corner stall results in an unsteady loading of the flow near the tip of the stator. This subsequently influences the leakage flow. At instances of time where the hub corner separation is contracted, there is a higher loading of the stator blade near the tip, and therefore the leakage flow vortex increases. The adverse effect appears when the hub corner stall reaches its maximum extent. Regarding the secondary flow plot (Fig. 9), the unsteady periodic velocity fluctuation also results in an unsteady periodic strength of the vortex circulation (compare Plots 4 and 8).

For the higher incidence test case, the rotor wake cannot be detected as clearly as for the lower incidence test case. There appears to be a superposition of the rotor wakes themselves while they are being transported through the cascade and the way the tip leakage flow and the hub corner stall respond to the rotor wakes. Therefore, when combining, the maxima in velocity show up as a result of the countermotion of the core flow and the hub corner stall. These lines are also strongly curved (Fig. 12). The more dominant unsteady effect is no longer the transported rotor wake throughout the stator, as has been found for the lower incidence test case, but there is a significant interaction of separated zones inside the stator and incoming periodic unsteadiness.

Conclusions

1 Losses generated by the tip leakage flow were found to decrease with increasing loading of the cascade. The reasons for this unexpected behavior are believed to be two effects: As the tip leakage vortex moves into the passage with incidence, the adverse pressure gradient affecting the vortex flow decreases. In addition, the vortex detaches from the suction side of the stator blade with increasing inlet flow angle. For low incidence angles, the tip leakage flow interacts with the suction side boundary layers and the suction side tip corner flow, which has a slight separation near the trailing edge. Therefore the main streamwise velocities in the tip leakage vortex increase with incidence. Lower velocity gradients will subsequently result in lower shear stresses and reduced turbulence production.

2 Increasing the incidence angle results in a large amount of turbulence production in the hub corner stall region. The mean-averaged turbulence intensities rise to more than a factor of 3. Here the levels of turbulence correlation and high Reynolds stresses are also high.

3 At lower blade loading, vortices shed off the rotor are observed to move in the circumferential direction downstream of the stator. They have a significant influence on the passage vortices generated in the stator passage, giving them a periodic motion.

4 Downstream of the stator the fluctuations of the turbulence intensities are in phase with the periodic velocities for both test cases. The situation is just the opposite in wake flows. The periodic variation of turbulence production rate in the stator passage is large compared to the convected turbulence, generated by the rotor wake.

5 The influence of the unsteady flow field on the stator wake, as well as on the center of the tip leakage vortex and the center of the stator hub corner separation, is small. However, large amplitudes of velocity and turbulence quantities are found in the boundary of these structures, in particular at the boundary of the hub corner separation. The largest velocity amplitudes occur near the blade pressure side at about 30 percent span.

6 The intensity of the lower passage vortex rises with increasing incidence angle, but the top passage vortex loses its influence. The lower passage vortex captures the hub vortex shed off the rotor, and this results in a strong periodic motion of the lower passage vortex. A strong vortex generated by the hub corner separation is found. This vortex is counterrotating to the lower passage vortex and has a highly periodic circulation, which is in phase with the periodicity of the lower passage vortex.

7 For the higher incidence test case, due to the delays in wake transport and wake amplification close to the hub, the stator separation has a periodic motion in size. This motion is out of phase compared to the wake flow in the main passage. This effect represents a nonlinear amplification of the rotor wake and will convect rotor wake information further downstream. This is very important for multistage axial compressors.

Acknowledgments

The authors are indebted to Prof. John Moore, Senior Professor of the Virginia Polytechnic Institute and State University, and to Dr. H. D. Schulz for their contribution and discussions to this paper.

References

Bartenwerfer, M., 1981, "Zur Analyse von Hitzdrahtsignalen turbulenter Strömungen," Ph.D. Thesis, Berlin, Germany.

Bindon, J. P., 1989, "The Measurement and Formation of Tip Clearance Loss," ASME JOURNAL OF TURBOMACHINERY, Vol. 111, No. 3, pp. 257–263.

Dishart, P. T., and Moore, J., 1990, "Tip Leakage Losses in a Linear Turbine Cascade," ASME JOURNAL OF TURBOMACHINERY, Vol. 112, pp. 599–608.

Schulz, H. D., and Gallus, H. E., 1988, "Experimental Investigation of the Three-Dimensional Flow in an Annular Compressor Cascade," ASME JOURNAL OF TURBOMACHINERY, Vol. 110.

Schulz, H. D., 1989, "Experimentelle Untersuchung der drei-dimensionalen abgelösten Strömung in einem Axialverdichter-ringgitter," Ph.D. Thesis, RWTH Aachen, Germany.

Schulz, H. D., Gallus, H. E., and Lakshminarayana, B., 1990, "Three-Dimensional Separated Flow Field in the Endwall Region of an Annular Compressor Cascade in the Presence of Rotor-Stator Interaction: Part I—Quasi-Steady Flow Field and Comparison With Steady-State Data; Part II—Unsteady Flow and Pressure Field," ASME JOURNAL OF TURBOMACHINERY, Vol. 112, pp. 669–690.

Yaras, M. I., and Sjolander, S. A., 1989, "Losses in the Tip-Leakage Flow of a Planar Cascade of Turbine Blades,"AGARD-CPP-468.

Experimental and Numerical Investigation of Three-Dimensional Viscous Flows and Vortex Motion Inside an Annular Compressor Blade Row

H. E. Gallus
Institut für Strahlantriebe und Turboarbeitsmaschinen, RWTH Aachen, Federal Republic of Germany

C. Hah
GE Research & Development Center, Schenectady, NY

H. D. Schulz
Institut für Strahlantriebe und Turboarbeitsmaschinen, RWTH Aachen, Federal Republic of Germany

A detailed experimental and numerical investigation was carried out to examine the three-dimensional flow field, secondary flows, and vortex motion in an annular compressor cascade. Various flow visualizations near the blade surface and endwalls, wall static pressure and loss measurements, as well as hot-film and hot-wire measurements inside the blade boundary layers were performed at various flow rates to understand the complex flow phenomena. A Reynolds-averaged Navier–Stokes equation was solved to investigate the flow numerically. The detailed comparison between measurement and numerical prediction indicates that the complex three-dimensional flow phenomena (corner stall, vortex motion, radial mixing, etc.) are very well predicted with the numerical method.

Introduction

The flow in modern multistage compressors with high blade loading, low-aspect-ratio blading, and reduced blade row spacing is extremely complex. In many instances, separated regions exist both on the blade and on the hub wall region (corner stall) (Joslyn and Dring, 1985; Dong et al., 1987; Wisler et al., 1987). This feature generates highly viscous, three-dimensional and unsteady flow, which has a profound effect upon the performance of the blade row. In particular, the exit static pressures, flow angles, and losses show large spanwise and circumferential variations, and flow calculations based on axisymmetric flow are barely adequate to predict these highly three-dimensional flows (Dring and Joslyn, 1986, 1987).

In order to gain a basic understanding of the extent and nature of flow separation in stators, Schulz and Gallus (1988) carried out a detailed measurement of the flow and the pressure field in a stator-alone configuration. In a continuation of this investigation they performed the same measurements in the presence of rotating cylinders upstream of the measuring cascade (Schulz et al., 1990a, 1990b) and thus isolated the effect of rotor–stator interaction on the separated flow inside the stator. At both test conditions, i.e., steady incoming flow and with a rotor upstream, the following measurements were taken:

1 visualization of the flow on the blades, hub, and casing (dye injection and oil flow technique)
2 wall static pressure measurements
3 steady and unsteady blade pressure measurements
4 blade boundary layer investigations with hot-wire and hot-film probes
- time-averaged and time-resolved boundary layer profiles
- transition behavior
- location of boundary layer separation

5 five-hole probe measurements at the cascade exit

This extensive and comprehensive data base is very well suited to verifying computational codes, capable of predicting large regions of separation.

With the development of flow calculation methods, various three-dimensional viscous flow codes (e.g., Moore and Moore, 1985; Briley and McDonald, 1979; Hah, 1984; Denton, 1974; Dawes, 1988) have been proposed for turbomachinery application. These codes have been successfully applied for various flow problems in turbomachinery. However, most flow prediction capabilities have been tested near the design operating condition. One of the goals of applying viscous flow computation is to predict flow separation properly. The main objective of this paper is to evaluate a numerical procedure for the calculation of corner stall in a compressor stator using the above-described experimental work.

A three-dimensional viscous flow code, which has been developed for turbomachinery component design, is used for the present study. The code has been successfully applied to the flows inside a turbine stator (Hah, 1984), a turbine rotor (Hah, 1987), centrifugal compressor (Hah et al., 1988; Hah and Krain, 1990), various inlet and outlet guide vanes, etc. In turbulent

Contributed by the International Gas Turbine Institute and presented at the 35th International Gas Turbine and Aeroengine Congress and Exposition, Brussels, Belgium, June 11–14, 1990. Manuscript received by the International Gas Turbine Institute January 26, 1990. Paper No. 90-GT-155.

flows with large regions of separation, the streamline curvature and the rotation alter the mean velocity field as well as the local turbulence structure, and the conventional mixing-length-type turbulence model or standard two-equation model does not predict the separated region accurately. For most separated flows, the flow separation is significantly underpredicted. A two-equation turbulence model with a low Reynolds number near-wall modification, which also allows for curvature and rotation effects on turbulence and which has been used for a variety of internal flows, has been applied for the present study.

The purpose of this paper is to compare the results from the numerical calculation with the experimental data. The accuracy of the prediction, its limitations, and the approach for further improvements will be discussed. Some of the numerical results also will be used to shed some insight into the complex separated flow structure and the vortex motion inside the compressor cascade.

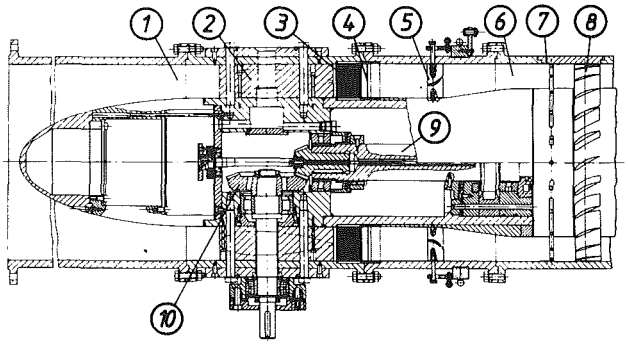

Fig. 1 Annular cascade test facility

Experimental Facility and Inlet Conditions

The experiments were performed in the annular cascade of the Institut für Strahlantriebe und Turboarbeitsmaschinen, shown in Fig. 1.

A turbocompressor set provides a continuous airflow to the test rig. The swirl angle of the flow is varied by means of 48 adjustable inlet guide vanes (IGV (5)). Angular momentum is conserved while the flow passes through a channel contraction to level out the wakes of the IGV. The test cascade (8) consists of 24 untwisted blades, mounted on the hub (tip clearance 0.8 percent of blade height), with a hub-to-tip ratio of 0.75 and a tip diameter of 428 mm. The aspect ratio is 0.86 and the solidity at midspan is 0.78. The blade profiles are radially stacked at their center of gravity and the blade metal angles at inlet and exit are 44 and 15 deg, respectively (measured from axial); other geometric parameters are shown in Fig. 2.

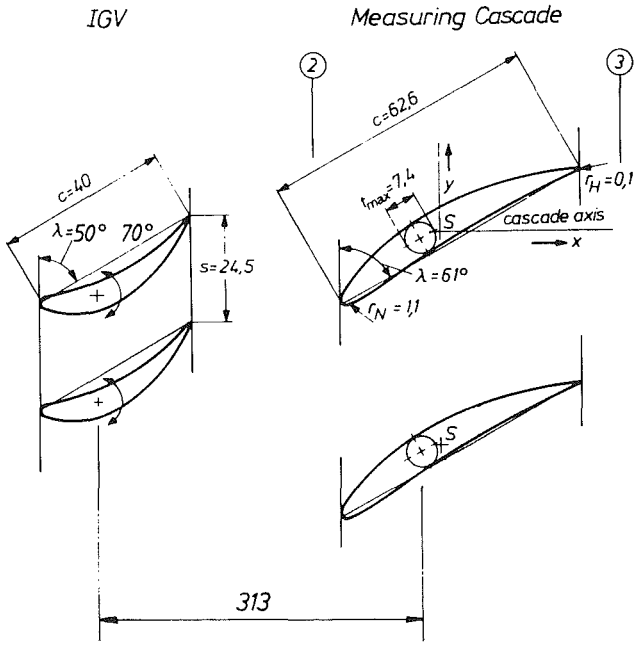

Fig. 2 Midspan cascade geometry

For the investigation described in this paper, the results of the computation are compared with steady-state data. For these tests the rotor (labeled (7) in Fig. 1) has been removed. The properties of the incoming flow have been surveyed with pneumatic five-hole and boundary layer probes 56 percent of blade chord upstream of the stator leading edge, and the inlet conditions have been specified there for the code as well. The inlet angle to the stator and therefore the blade loading have been varied, and measurements were taken at five different points of operations, identified by the inlet angles at midspan, namely α_2 = 40.0 deg, α_2 = 44.2 deg, α_2 = 49.2 deg, α_2 = 54.6 deg, and α_2 = 57.6 deg. These angles are measured from axial, and zero incidence is at α_2 = 42.0 deg. The spanwise distributions of inlet velocity, total pressure and inlet angle for α_2 = 44.2

Nomenclature

c = blade chord
C = absolute velocity
C_1, C_2, C_3, C_4, C_μ, σ_k, σ_ϵ = constants in turbulence closure model
Cp = pressure coefficient = $(P_{loc} - P_{2m})/(P_{t2} - P_2)_m$
C_v = specific heat
e = total energy
i = incidence
F_i = additional body force in equation (2)
k = turbulent kinetic energy
LE = leading edge
p = static pressure
PS = pressure side
r_N = leading edge radius
r_H = trailing edge radius
R = gas constant
s = blade spacing
S = center of gravity
SS = suction side
t = blade thickness
T = temperature
TE = trailing edge
x = axial direction
z = spanwise direction
α = flow angle (measured from axial direction)
δ_{ij} = Kronecker delta
ϵ_{ijk} = permutation tensor
λ = stagger angle
μ = dynamic viscosity
ν = kinematic viscosity
ρ = density
$\bar{\omega}$ = circumferentially mass-averaged loss coefficient = $(\bar{P}_{t2} - \bar{P}_{t3})/(\bar{P}_{t2} - \bar{P}_2)$
Ω_1 = angular velocity

Subscripts

0 = design flow angle
2 = upstream of the cascade (56 percent of chord)
3 = downstream of the cascade (35 percent of chord)
loc = local
m = blade midspan height
t = total

Superscripts

$\bar{(\ )}$ = circumferentially mass averaged

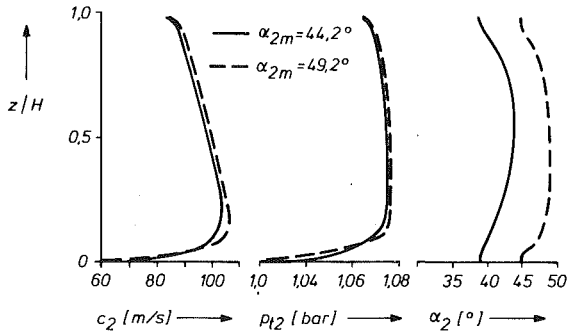

Fig. 3 Flow properties at cascade inlet

deg and $\alpha_2 = 49.2$ deg are shown in Fig. 3. The displacement thickness δ_1 of the inlet boundary layer and its momentum thickness δ_2 were 1.77 percent and 1.28 percent of blade height, respectively, for $\alpha_2 = 44.2$ deg and 1.87 percent and 1.23 percent, respectively, for $\alpha_2 = 49.2$ deg. The circumferential uniformity of the flow has been checked and found acceptable (the variations in velocity and flow angle were less than 1 percent). The instrumentation and the accuracy of the measurements are described in more detail by Schulz and Gallus (1988).

Governing Equations and Turbulence Modeling

The following Reynolds-averaged Navier–Stokes equations are solved for the current problem:

$$\frac{\partial}{\partial x_i}(\rho U_i) = 0 \tag{1}$$

$$\frac{\partial}{\partial X_j}(\rho U_i U_j) + 2\rho\,\epsilon_{ijk}\Omega_j U_K = -\frac{\partial p}{\partial x_i} + \frac{\partial}{\partial x_j}\left[\mu\left(\frac{\partial U_i}{\partial x_j} + \frac{\partial U_j}{\partial x_i} - \frac{2}{3}\frac{\partial U_k}{\partial x_k}\delta_{ij}\right) - \rho\overline{u_i u_j}\right] + F_i \tag{2}$$

$$\frac{\partial}{\partial x_j}(\rho U_j e) = \frac{\partial}{\partial x_j}\left(\left(\frac{\mu}{\mathrm{Pr}}\right)_{\mathrm{eff}}\frac{\partial T}{\partial x_j}\right) - \frac{\partial}{\partial x_j}(pU_j) + U_i F_i + \frac{\partial}{\partial x_j}\left[U_i\mu\left(\frac{\partial U_i}{\partial x_j} + \frac{\partial U_j}{\partial x_i} - \frac{2}{3}\frac{\partial U_k}{\partial x_k}\delta_{ij}\right)\right] \tag{3}$$

$$P = \rho RT \tag{4}$$

where U_i = mean velocity, u_i = fluctuating velocity, e = total energy, Ω_i = angular velocity,

$$\left(\frac{\mu}{\mathrm{Pr}}\right)_{\mathrm{eff}} = \left(\frac{\mu}{\mathrm{Pr}}\right)_{\mathrm{laminar}} + \left(\frac{\mu}{\mathrm{PR}}\right)_{\mathrm{turbulent}}$$

and

$$e = C_v T + \frac{1}{2}U_i U_i$$

A modified k–ϵ, two-equation model is used to estimate Reynolds stresses. The turbulence model is extended to the solid wall following the studies of Chien (1982). The following additional transport equations are solved to calculate turbulent stress terms:

$$\frac{\partial(\rho U_i k)}{\partial x_i} = \frac{\partial}{\partial x_i}\left(\frac{\mu_{\mathrm{eff}}}{\sigma_K}\frac{\partial k}{\partial x_i}\right) - \rho\,\overline{u_i u_j}U_{i,j} - \rho\epsilon - \frac{2\mu k}{l^2} \tag{5}$$

$$\frac{\partial(\rho U_i \epsilon)}{\partial x_i} = \frac{\partial}{\partial x_i}\left(\frac{\mu_{\mathrm{eff}}}{\sigma_\epsilon}\frac{\partial \epsilon}{\partial x_i}\right) + C_1\frac{\rho\epsilon}{k}(\overline{u_i u_j}U_{i,j}) - \frac{\rho\epsilon}{k}\left[c_2 f\epsilon + \frac{2\nu k e^{-c_4 u^* l/\nu}}{l^2}\right] \tag{6}$$

where

$$\mu_{\mathrm{eff}} = \mu + C_\mu(k^2/\epsilon)[1 - \exp(-c_3 u^* l/\nu)]$$

and

$$f = 1 - \frac{0.4}{1.8}e^{-(k^2/6\nu\epsilon)^2}$$

Various previous studies indicate that this modified two-equation turbulence model improves separated flow prediction significantly when the proper computational grid is used. No attempt was made to optimize constants of the turbulence modeling equations for this study. Therefore, standard values of various constants of the turbulence model are used; the values are

$$C_\mu = 0.09, \quad C_1 = 1.35, \quad C_2 = 1.8, \quad \sigma_k = 1.0,$$
$$\sigma_\epsilon = 1.3, \quad C_3 = 0.0115, \quad C_4 = 0.5$$

Numerical Procedure and Boundary Conditions

Equations (1)–(6) are solved numerically with a fully conservative control volume approach. The finite difference equations are formulated in terms of Cartesian momentum (ρU_i), static pressure (p), total internal energy (e), turbulent kinetic energy (k), and turbulent energy dissipation rate (ϵ). The numerical fluxes through control volume surfaces are estimated with a quadratic upwinding scheme, and so the formal spatial accuracy is third order on smoothly varying meshes. The steady-state solution is obtained through the elliptic relaxation of the finite difference equations, and each relaxation consists of one semi-implicit prediction and two implicit correction steps. During each iteration, pressure-based correction equations are used to ensure global conservation. The detailed numerical procedure is explained by Hah (1987).

The computations were carried out on standard H-type grids (Fig. 4).

34 nodes in blade-to-blade, 39 nodes in spanwise direction, and 99 nodes in streamwise direction are used for the solution. As the stator has a tip clearance (0.767 percent of the chord), six computational nodes in the spanwise direction are used to describe the tip clearance.

At the inflow boundary, the measured distributions of total pressure, total temperature, and inlet flow angles are fixed. At the outflow boundary, the static pressure is fixed at the shroud and all other flow variables are extrapolated. Standard periodicity conditions are applied upstream and downstream of the blade as well as inside the tip-clearance regions. For the turbulence, the experimental value of the turbulent kinetic energy is prescribed at the inflow boundary (the measured value $k = 1.44\ \mathrm{m^2/s^2}$ at midspan was taken constant across the span), and standard equilibrium condition is used to estimate the length scale for turbulence dissipation. Residuals of each finite difference equation are integrated over the entire domain. When the total integrated *residuals* of all the equations are reduced by four orders of magnitude from the *initial value*, the solution is considered to be converged. For the current flow with large flow separation regions, the overall computational work is about 10–15 percent more than at attached flows. Typical computing time was about 1/2–3/4 hours on a Cray-XMP with SSD storage.

Analysis of Experimental and Numerical Results

Since the main objective of this paper is to evaluate the capability of the numerical code to predict flows with larger regions of separation, it was applied to the cascade flow at three different loadings of the blade, corresponding to three different inlet angles, namely $\alpha_2 = 44.2$ deg, $\alpha_2 = 49.2$ deg, and $\alpha_2 = 54.6$ deg. At $\alpha_2 = 44.2$ deg the cascade already shows a considerable corner stall at the hub region (Fig. 5).

The flow along the blade starts to separate at the hub after

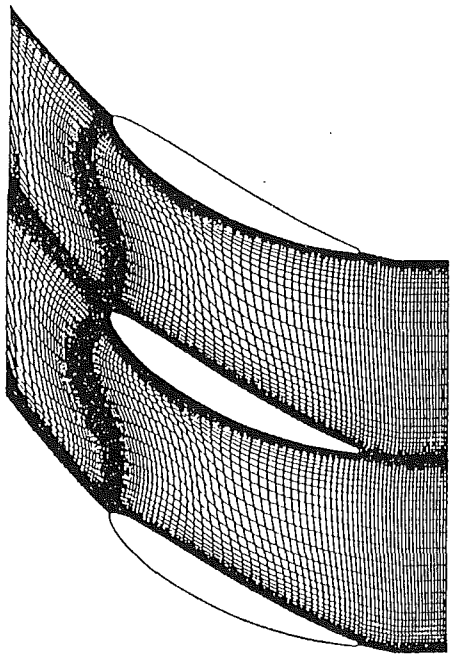

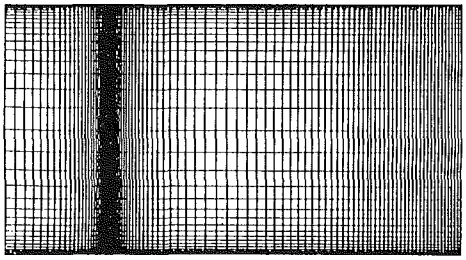

Fig. 4 Computational grid (34 × 39 × 99 nodes)

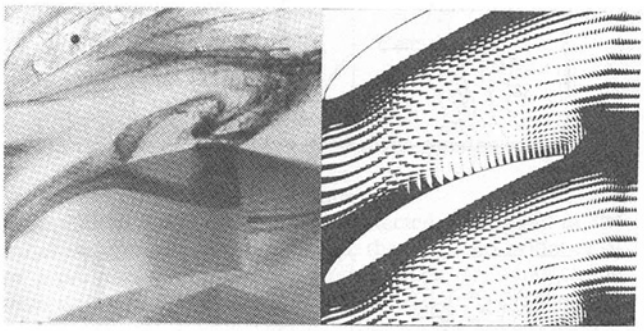

Fig. 5 Measured and calculated surface flow at the hub (α_2 = 44.2 deg, flow visualized by dye injection)

60 percent of chord, and the corner stall region extends at the trailing edge to about 40 percent of span. This hub corner stall grows in size with increasing loading (Schulz and Gallus, 1988), and at α_2 = 54.6 deg the flow already starts to separate at the hub after about 20 deg of chord and up to 60 percent of span at the trailing edge (Fig. 6). The prediction of these highly three-dimensional flows is an enormous task for numerical methods.

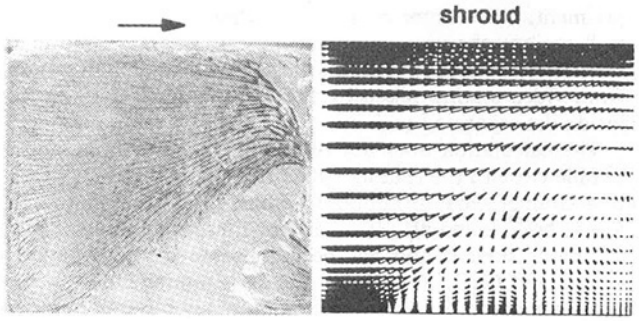

Fig. 6 Measured and calculated flow along the blade section side (α_2 = 54.6 deg, flow visualized by an oil flow method)

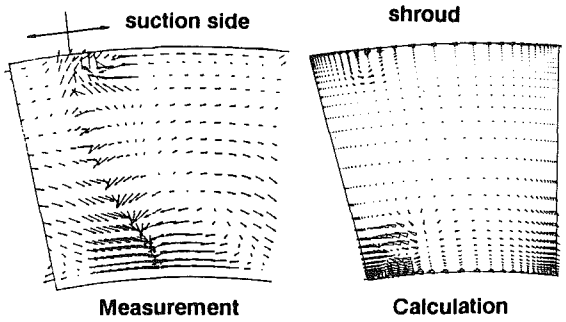

Fig. 7 Measured and calculated secondary flow vectors in the cascade exit plane (looking upstream, α_2 = 49.2 deg)

Flow Field Along the Walls and in the Exit Plane. A comparison of the measured and predicted flow along the hub, the blade suction side, and in the exit plane of the cascade is shown in Figs. 5, 6, and 7. To condense the large amount of data, the results are not shown for all blade loadings, and only representative comparisons are given in this paper.

Figure 5 shows the flow along the hub at the lower loading (α_2 = 44.2 deg), visualized by dye injection. The flow separates on the blade suction side at about 60 percent of chord, forming a vortex with a clockwise orientation. Secondary flows (cross-passage flow) as well as back flow, which originates at the blade pressure side and turns around the trailing edge, feed low-momentum fluid into this vortex system.

This complex flow structure is very well represented by the numerical calculation (Fig. 5). It shows the main features: the separated region, the vortex system, the cross-passage flow, and the back flow around the trailing edge. The latter, though, seems to penetrate a little bit farther into the passage, before it turns back into the vortex. The nearly vanishing flow vectors represent the low-momentum fluid inside the separated flow region.

Figure 6 shows a comparison of the flow along the blade suction side at the highest loading investigated in this study (α_2 = 54.6 deg). As mentioned before, the flow separates at the hub already after 20 percent of chord, and the separation line goes up to about 60 percent of span at the trailing edge. This is also well predicted in the calculation. Here the calculation shows a better resolution of the flow structure than the flow visualization. In the experiments, the viscosity of the oil has to be chosen such that the traces of the mean flow remain visible, and features such as boundary layer transition or laminar separation bubbles can be resolved. Inside the separated zone, the flow velocities are much smaller, and for example the back flow only shows traces if its velocity is higher than 30 m/s (core flow velocities are about 100 m/s). Therefore only traces of the vortex close to the trailing edge, where the velocity of the back flow is still high, can be seen in the ex-

periment. The vortex in the leading edge part of the corner stall region, shown by the calculation, is not visible in the experiment presented here, but this phenomenon is also known from video studies taken by the authors from dye injection inside the separated region.

The calculation does not represent the laminar separation bubble close to the leading edge of the blade. The occurrence of a laminar separation bubble, which is barely visible in Fig. 6, has been found also through hot-film measurements along the blade surface and has been reported in more detail by Schulz and Gallus (1989). At steady incoming flow (without upstream rotor), a laminar separation bubble was observed, which moves upstream on the blade suction side with increasing loading. Inside the laminar separation bubble the flow undergoes transition and reattaches as turbulent downstream. Therefore, for a considerable portion of the blade the flow is laminar (at $\alpha_2 = 44.2$ deg the laminar separation bubble is located on the suction side between 40 and 55 percent of blade chord). This feature cannot be captured by the calculation, since the numerical grid used here was too coarse to pick up boundary layer transition. In the calculation, the flow was considered to be already turbulent at the blade leading edge. This might be one of the reasons for the deviation between measurement and calculation discussed in the further parts of this paper. Therefore, proper modeling of the boundary layer transition on the blade profiles will add to the further improvement of the calculation method, but this of course is a very ambitious objective and would require a much finer computational grid.

A comparison of the measured and calculated flow fields at the cascade exit is given in Fig. 7 (looking upstream).

Here the secondary flow vectors deduced from pneumatic five-hole probe measurements and from the calculation are shown at medium loading, i.e., at $\alpha_2 = 49.2$ deg. As discussed in more detail by Schulz et al. (1990a), the striking feature is the deflection of the flow even in the main stream. The separated region cannot be sustained downstream of the cascade, and hence it closes off slightly upstream of the plane where the flow has been traversed. The flow perceives the corner stall as a solid obstruction. The data indicate large flow turning around the trailing edge of the separated region from both sides. Imbalance between the radial pressure gradient and centrifugal forces results in downward flow downstream of the corner stall region. These features have been recently confirmed by triple hot-wire measurement and will be presented by Poensgen and Gallus (1991).

The tip clearance vortex and the secondary flow on the shroud can be clearly seen in both the measurement and the calculation, and one can notice a very good agreement between measurement and prediction in the upper part of the stator passage. In the lower part, the secondary vectors look quite different. While the calculation predicts the deviation of the core flow due to the blockage caused by the corner stall reasonably well, it does not quite show the closing of the flow downstream of the separated region in the above-described manner.

Wall Static Pressure Field in the Stator Passage. Since the static pressure remains constant downstream of the location where the flow separates, flow separation inside a flow passage generally can be detected by the static pressure distribution. The severe distortion of the static pressure field in the experiment due to the occurrence of hub corner stall has been discussed in more detail by Schulz and Gallus (1988). This distortion can be considered to be an inviscid effect, in the sense that it is mostly brought about by the blockage of the flow rather than viscous interactions. As discussed above, the blockage is generated by the corner stall, which is perceived by the main flow somewhat like a solid obstruction. Therefore, if one would know the effective area of the flow channel or could model the displacement caused by the corner stall, even an inviscid calculation would give the correct pressure distribution. But of course, to know the effective area one has to predict the occurrence and the extent of separated regions, and this fact brings up the necessity for a Navier–Stokes solution.

Figures 8(*a–c*) show the measured and predicted wall static pressure contours for all inlet angles investigated in this study. The measured pressure contours are derived from 56 pressure taps at the shroud and 114 pressure taps at the hub. The blade pressures are measured by 19 pressure taps along the blade suction side and 15 taps along the blade pressure side. These measurements are taken at 11 different spanwise positions to give an acceptable resolution for the blade static pressure contours. The measurements are very well reproduced and the standard deviation is about 1 percent of the measured value.

As the code predicts the extent of the separated regions at the hub fairly well (compare Figs. 5 and 6), the measured static

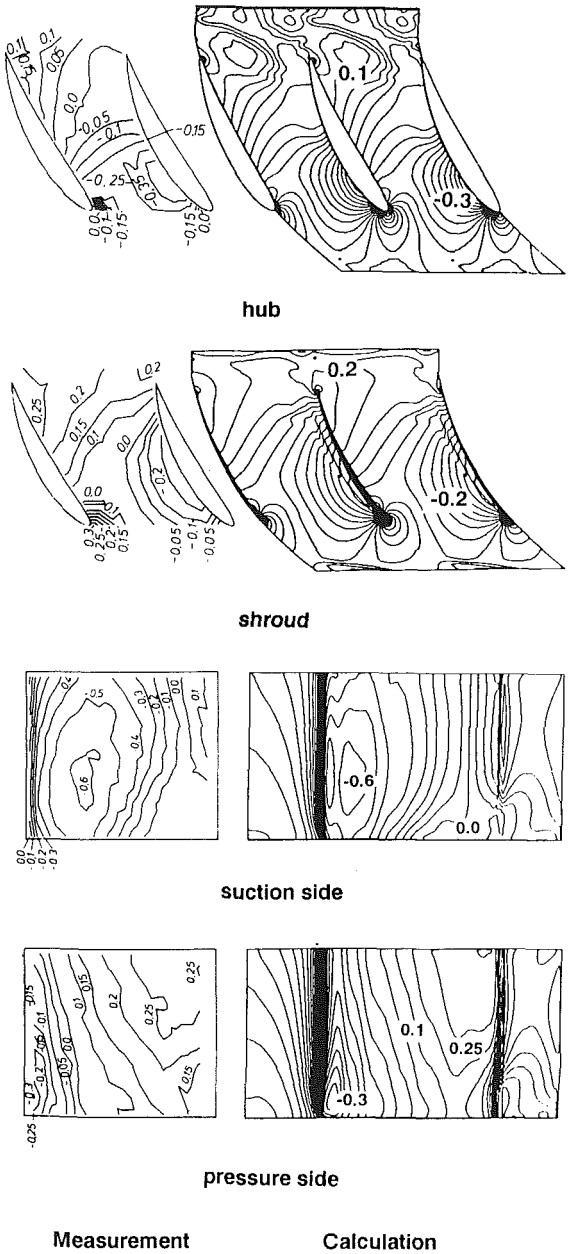

Fig. 8(*a*) Measured and calculated static pressure contours

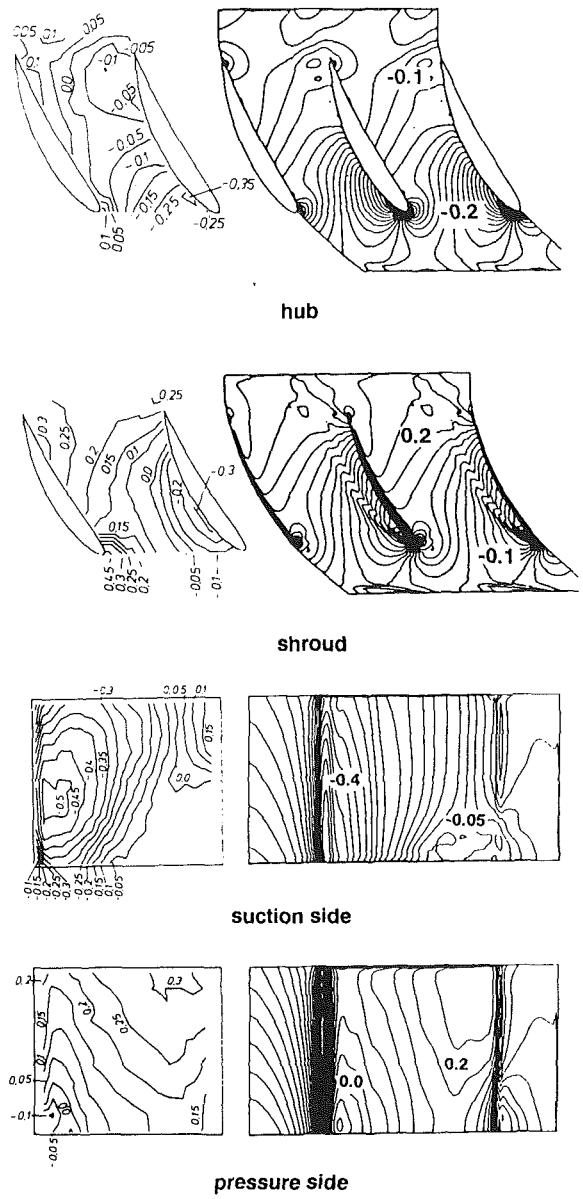

Fig. 8(*b*) Measured and calculated static pressure contours

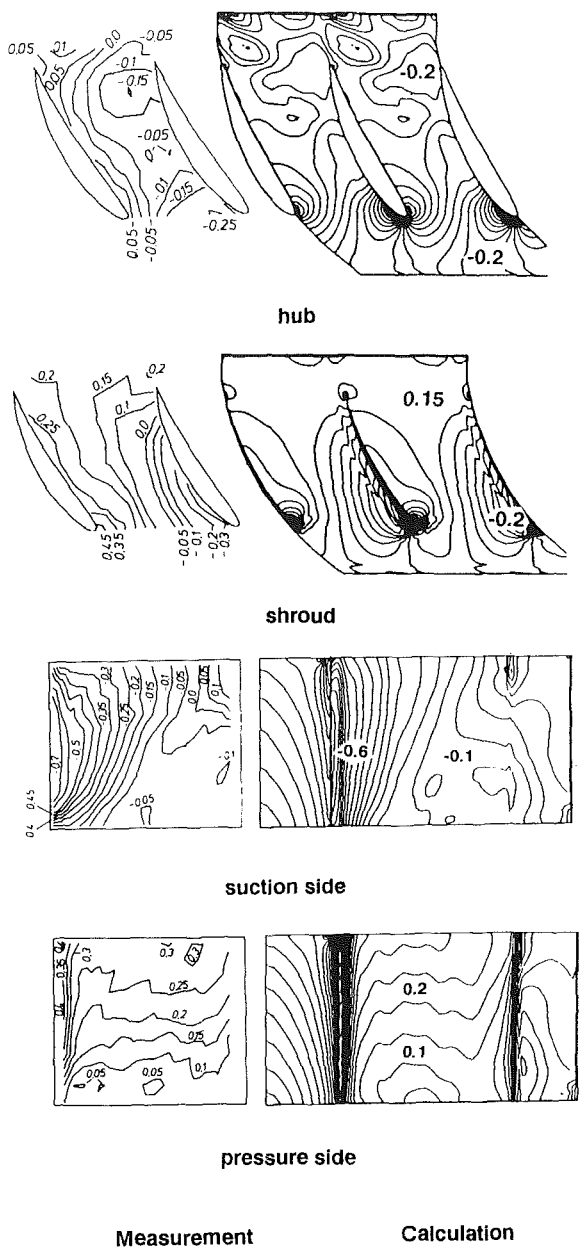

Fig. 8(*c*) Measured and calculated static pressure contours

pressure distribution is very well predicted, especially at the shroud and the pressure side, where there was no evidence of flow separation found in the experiment (the very small casing corner stall seen in the flow visualization did not have an effect on the measured pressure distribution (Schulz and Gallus, 1988)). At low (α_2 = 44.2 deg, Fig. 8*a*) and medium loadings (α_2 = 49.2 deg, Fig. 8*b*), the extent of the hub corner stall and its impact on the static pressure distribution is slightly underpredicted. This becomes evident by comparing the pressure contours at the blade suction side. Generally flow separation is largely underpredicted by numerical methods. It was attempted to overcome this shortcoming by incorporating a near wall correction. The underprediction of the separated region in this case is therefore thought to be a result of a too-coarse grid and the lack of modeling boundary layer transition. Since in the calculation the boundary layer is basically turbulent from near the blade leading edge, the turbulence generated in the boundary layer might postpone flow separation. This is particularly true for the low and medium loading, since here the blade boundary layer is laminar over a considerable portion of the blade suction side (Schulz and Gallus, 1989). At the high loading (α_2 = 54.6 deg, Fig. 8*c*), the boundary layer undergoes transition very early (compare Fig. 6), and here the predicted pressure distribution at the blade suction side is excellent.

The influence of turbulence on the development of the hub corner stall has been reported by Schulz et al. (1990a). In order to improve the calculation, a much finer grid has to be used, and boundary layer transition has to be modeled correctly.

Losses and Flow Angles in the Exit Plane. The losses deduced from measurements and the calculated losses in the exit plane, 35 percent of chord downstream of the stator trailing edge, are shown in Fig. 9 (looking upstream). The exit flow field

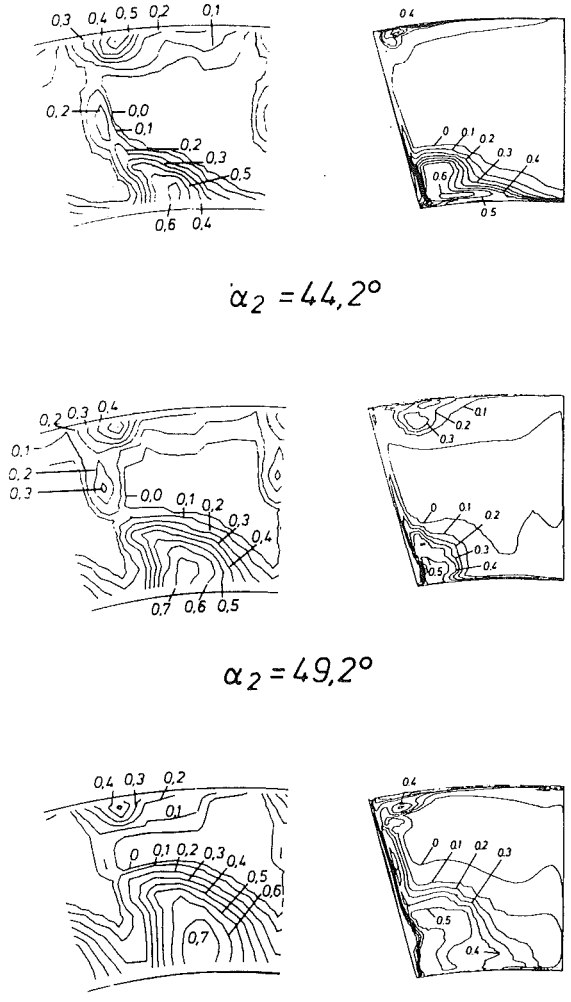

Fig. 9 Measured and calculated loss contours in the cascade exit plane (looking upstream)

has been measured with pneumatic five-hole probes on 22 circumferential and 19 radial positions. Because of large variations of the flow angle in the measuring plane, the probe has been yawed in every measuring location to assure that the flow vectors are within the range the probe is calibrated for. There still might be some errors in flow angle in regions of large total pressure gradients due to the finite dimension of the probe head (probe head diameter was 2.6 mm). The total pressure measurements, though, are considered to be reasonably accurate, and most errors occur due to the unsteady nature of the flow. The uncertainty of the probe measurements is estimated to be about ±0.1 percent of the measured total pressure and ±1 deg in flow angle.

Figure 9 shows the contour plots of the loss coefficient for all inlet angles investigated in this study. As defined in the nomenclature, the loss coefficients are deduced from the difference of the local total pressure in the exit plane and the midspan total pressure at cascade inlet, nondimensionalized by the midspan dynamic head at inlet.

Increasing the inlet angle results in a pitchwise and spanwise growth of the hub corner stall, and subsequently the losses in this region increase as well. This trend is also reproduced by the numerical method, and particularly at the low (α_2 = 44.2 deg) and at the high loading (α_2 = 54.6 deg), the agreement between measurements and calculations is reasonably good. At medium loading (α_2 = 49.2 deg), the numerical solution shows large losses at the tip. These losses are not caused by a casing corner stall, rather than by the developing tip leakage vortex, which can be deduced from the flow vectors in this region (Fig. 7). The center of the loss also moves away from the suction surface, which is a further indication for the appearance of a strong tip leakage vortex. The development of the tip leakage vortex is more suppressed at the high inlet angle (α_2 = 54.6 deg), since here the massive hub corner stall and the subsequent displacement of the flow result in a re-energization of the upper passage flow. This has been discussed in great detail by Poensgen and Gallus (1991). The agreement between the measured and the calculated losses at α_2 = 49.2 deg is rather poor in the lower part of the passage. As mentioned before, the extent of the hub corner stall is underpredicted by the code and consequently so are the losses. However, one has to keep in mind that flows with large separation are very hard to predict, and to the knowledge of the authors flow calculations like this have not been performed before. The numerical solution is quantitatively not always correct, but generally represents the same trends.

The spanwise distribution of pitchwise mass-averaged flow turning is compared in Fig. 10.

Due to the displacement of the flow by the growing hub corner stall, the flow is considerably underturned in the lower part of the flow passage. This will result in a severe deviation from the designed exit flow angle and consequently, in multistage compressors, in a mismatch of the following blade row. The determination of the correct exit flow angle is therefore very important to the turbomachinery design procedure.

The spanwise distribution of the exit flow angle, and consequently the flow turning, is very well predicted by the numerical method. In the way it has been used in this study, it is a very powerful tool for the design of first-stage compressor rotors or any blade row with steady incoming flow.

For a multistage environment though, somehow rotor–stator interaction has to be taken into account, since the wakes shed off the upstream blade row might alter the flow field inside a compressor cascade considerably. As reported by Schulz et al. (1990a, 1990b), this is particularly valid for separated regions inside a blade row, which decrease due to unsteady effects and higher turbulence generated by the rotor. Subsequently the exit flow angles, which are largely effected by corner stall regions, change as well. This can be seen in Fig. 10 by the measured distribution of flow turning in the presence of an upstream rotor (from Schulz et al., 1990a). For this kind of flow, though, the time derivatives of the Navier–Stokes equations have to be considered as well, and the turbulence closure models have to be modified to account for large-scale turbulence effects.

Topological Structure of Three-Dimensional Separation. Since the comparison of the measured and the calculated results provides sufficient evidence that the numerical method predicts the separated flow reasonably well, an attempt was made to use the numerical results to shed some new light into the complex flow structure inside the separated flow region. Here measured data are not available, since at these relatively high flow velocities (core flow velocities of about 100 m/s), flow visualization is restricted to surface flows, and probe measurements exhibit large errors and disturb the flow itself to an intolerable extent.

Calculated velocity vectors in planes parallel to the hub have been plotted to deduce from these "slices" the flow structure inside the separated region. In Fig. 11 the velocity vectors calculated at the hub and at 5, 10, 15, and 20 percent of span are shown.

Looking at these sections, one can distinguish two domains. Close to the hub (i.e., at the hub and at 5 percent span), the

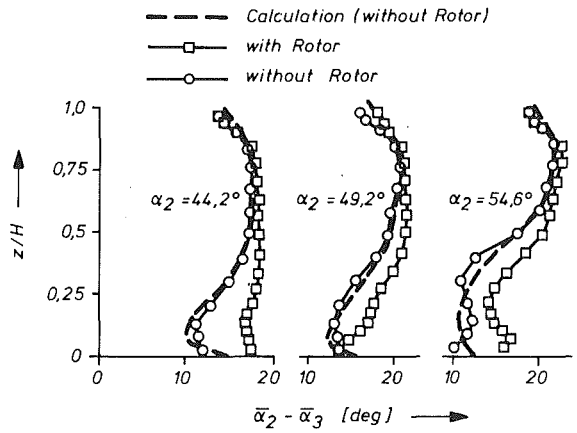

Fig. 10 Flow turning throughout the compressor cascade

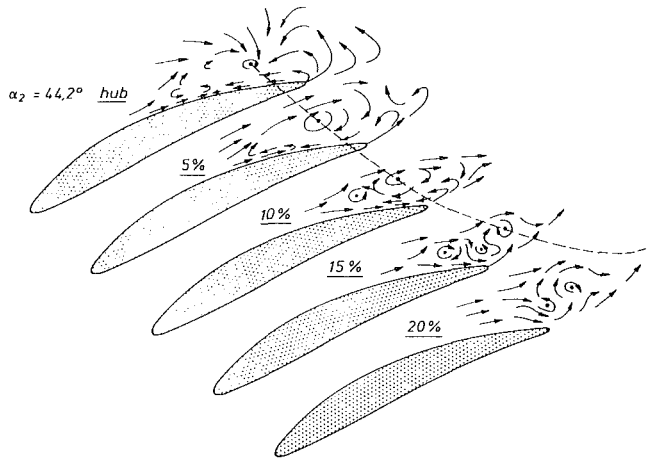

Fig. 11 Velocity vectors inside the hub corner stall at various spanwise positions (from numerical calculations)

pattern resembles the flow structure found in endwall corner stall regions (compare Fig. 5). From 10 percent span through 20 percent span, however, the pattern looks very much like a blade stall with a typical vortex pairing sequence. There might be two explanations for these flow patterns with respect to steady or unsteady aerodynamic phenomena. If one considers all vortices as stationary, it can be deduced from Fig. 11 that the strong vortex developing at the hub has been convected downstream and its axis will bend 90 deg toward the cascade axis (as indicated in Fig. 11). In this case, the vortex would connect with the passage vortex, since they would have the same sense of rotation.

If the vortex pairing, starting at 10 percent of span, is an unsteady phenomenon in the sense of a von Karman vortex street (which would be a common physical phenomenon for a blade stall), the hub vortex (which is stationary in any case, as proven by measurements) has to connect to these convecting vortices, and its axis at certain instances of time always has to switch back to the new developing vortex. This interpretation is purely heuristic and cannot be proven or even corroborated by any measurements taken so far by the authors, but it might aid in the interpretation of some other experimental results.

The calculated velocity vectors in Fig. 11 show that the separated region lifts off the blade surface, and underneath the separation bubble, a thin layer of flow in the mainstream direction can be seen. This process starts at 5 percent of span, and already at 15 percent span, the flow right at the blade suction side seems to be attached all the way down to the trailing edge. This lifting off the blade surface of the separation bubble, which could also be interpreted as a spanwise blade stall recovery, has not been seen in the measurements (compare Fig. 5). Here there is a distinct separation line from 60 percent of chord at the hub up to 40 percent of span at the trailing edge.

Concluding Remarks

The three-dimensional flow fields inside an annular compressor cascade at various blade loadings have been studied experimentally and numerically. The suction surface hub endwall corner separation was the primary three-dimensional feature of the flow. Its extent as well as its impact on the static pressure distribution inside the stator passage could be reasonably well predicted by the three-dimensional viscous flow code used in this study. It also resolves the vortex motion on the walls inside the separated flow regions, which has been evaluated by flow visualization in the experiments.

Flows with extensive separated regions are very hard to predict, and the numerical solution is quantitatively not always correct but shows the same trends.

At low and medium blade loadings, the extent of the hub corner stall was slightly underpredicted. This might be due to the too-coarse grid used in this study, which does not allow us to resolve the boundary layer transition on the blade suction side. For further improvement it is necessary to use a more refined grid and to have more grid points inside the boundary layer.

The exit flow angle was very well predicted by the numerical method. Since the flow parameters in the exit plane determine the incoming flow to the downstream blade row, they are very important in multistage environments, and this numerical code is a very useful tool for the design of the first blade row in a multistage compressor. For subsequent blade rows though, somehow rotor–stator interactions have to be taken into account. For this even more complex numerical problem the code has to be extended to unsteady flows, and the turbulence closure models have to be modified to account for large-scale turbulence effects.

Acknowledgments

The always valuable discussion on the matter of this paper with C. Poensgen is gratefully acknowledged by the authors.

References

Briley, N. R., and McDonald, H., 1979, "Analysis and Computation of Viscous Subsonic Primary and Secondary Flows," presented at the Fourth AIAA Computational Fluid Dynamics Conference, Williamsburg, VA.

Chien, K. Y., 1982, "Predictions of Channel and Boundary Layer Flows With a Low Reynolds Number Turbulence Model," *AIAA Journal*, Vol. 20, No. 1, pp. 33–38.

Dawes, W. N., 1988, "Development of a 3D Navier–Stokes Solver for Application to All Types of Turbomachinery," ASME Paper No. 88-GT-70.

Denton, J. D., 1974, "A Time-Marching Method for Two- and Three-Dimensional Blade to Blade Flows," Aeronautical Research Council, R and M No. 3775, London.

Dong, Y., Gallimore, S. J., and Hodson, H. P., 1987, "Three-Dimensional Flows and Loss Reduction in Axial Compressors," ASME JOURNAL OF TURBOMACHINERY, Vol. 109, pp. 354–361.

Dring, R. P., and Joslyn, H. D., 1986, "Through-Flow Analysis of a Multistage Compressor: Part II—Analytical-Experimental Comparisons," ASME JOURNAL OF TURBOMACHINERY, Vol. 108, pp. 23–31.

Dring, R. P., and Joslyn, H. D., 1987, "Throughflow Analysis of a Multistage Compressor Operating at Near-Stall Condition," ASME JOURNAL OF TURBOMACHINERY, Vol. 109, pp. 483–491.

Hah, C., 1984, "A Navier–Stokes Analysis of Three-Dimensional Turbulent Flows Inside Turbine Blade Rows at Design and Off-Design Conditions," ASME *Journal of Engineering for Gas Turbines and Power*, Vol. 106, pp. 421–429.

Hah, C., 1987, "Calculation of Three-Dimensional Viscous Flows in Turbomachinery With an Implicit Relaxation Method," *AIAA Journal of Propulsion and Power*, Vol. 3, No. 5, pp. 415–422.

Hah, C., Bryans, A. G., Moussa, Z., and Tomsho, M. E., 1988, "Application of Viscous Flow Computations for the Aerodynamic Performance of a Back-

swept Impeller at Various Operating Conditions," ASME JOURNAL OF TURBOMACHINERY, Vol. 110, No. 3, pp. 303–311.

Hah, C., and Krain, H., 1990, "Secondary Flows and Vortex Motion in a High-Efficiency Backswept Impeller at Design and Off-Design Conditions," ASME JOURNAL OF TURBOMACHINERY, Vol. 112, pp. 7–13.

Joslyn, H. D., and Dring, R. P., 1985, "Axial Compressor Stator Aerodynamics," ASME *Journal of Engineering for Gas Turbines and Power*, Vol. 107, pp. 485–493.

Moore, J., and Moore, J. G., 1985, "Performance Evaluation of Linear Turbine Cascades Using Three-Dimensional Viscous Flow Calculations," ASME *Journal of Engineering for Gas Turbines and Power*, Vol. 107, pp. 967–975.

Poensgen, C., and Gallus, H. E., 1991, "Three-Dimensional Wake Decay Inside of a Compressor Cascade and Its Influence on the Downstream Unsteady Flow Field: Part II—Unsteady Flow Field Downstream of the Stator," ASME JOURNAL OF TURBOMACHINERY, Vol. 113, this issue.

Schulz, H. D., and Gallus, H. E., 1988, "Experimental Investigations of the Three-Dimensional Flow in an Annular Compressor Cascade," ASME JOURNAL OF TURBOMACHINERY, Vol. 110, p. 467.

Schulz, H. D., and Gallus, H. E., 1989, "Experimental Investigation of the Influence of Rotor Wakes on the Development of the Profile Boundary Layer and the Performance of an Annular Compressor Cascade," AGARD CPP-468/469, presented at the Conference on Unsteady Aerodynamic Phenomena in Turbomachines, Luxembourg.

Schulz, H. D., Gallus, H. E., and Lakshminarayana, B., 1990a, "Three-Dimensional Separated Flow Field in the Endwall Region of an Annular Compressor Cascade in the Presence of Rotor–Stator Interaction: Part 1—Quasi-Steady Flow Field and Comparison With Steady-State Data," ASME JOURNAL OF TURBOMACHINERY, Vol. 112, pp. 669–678.

Schulz, H. D., Gallus, H. E., and Lakshminarayana, B., 1990b, "Three-Dimensional Separated Flow Field in the Endwall Region of an Annular Compressor Cascade in the Presence of Rotor–Stator Interaction: Part 2—Unsteady Flow and Pressure Field," ASME JOURNAL OF TURBOMACHINERY, Vol. 112, pp. 679–690.

Wisler, D. C., Bauer, R. C., and Okiishi, T. H., 1987, "Secondary Flow, Turbulent Diffusion, and Mixing in Axial-Flow Compressor," ASME JOURNAL OF TURBOMACHINERY, Vol. 109, pp. 455–482.

Unsteady Radial Transport in a Transonic Compressor Stage

P. A. Kotidis[1]

A. H. Epstein

Gas Turbine Laboratory,
Massachusetts Institute of Technology,
Cambridge, MA 02139

Time-resolved radial transport has been measured in a transonic compressor rotor by injecting a thin sheet of tracer gas upstream of the rotor and then surveying the tracer concentration at the rotor exit. The simultaneous, co-located, high-frequency response measurements of local tracer gas concentration, total temperature, and total pressure made downstream of the rotor showed that most of the fluid transported radially appears in the blade wakes and that this fluid has considerably higher entropy than the circumferential mean. Both inward and outward fluid transport along the span was observed (3.5 percent of the total throughflow moved toward the tip while 1.6 percent moved toward the hub). Tracer concentration and fluid total temperature and pressure varied considerably from wake to wake, even on multiple samplings of the same blade. The time mean spreading rate inferred from these measurements is in general agreement with previously reported studies on multistage low-speed compressors and is well predicted by the method of Gallimore and Cumpsty. It is suggested that a vortex street in the blade wakes could be responsible for both the observed radial transport and the large wake-to-wake variability. A quasi-three-dimensional model of a vortex street wake was developed and shown to be consistent with the data. The model predicts all of the inward transport but only 20 percent of the outward transport. It is hypothesized that outflow in separated regions on the blade suction surface is responsible for the remainder of the transport toward the rotor tip. Since the entropy, as well as the mass of the fluid transported radially, was measured, an estimate of the redistribution of loss in rotor due to radial fluid transport could be made. This showed that the effect of radial transport in this rotor was to move substantial loss from the rotor hub to tip, implying that a conventionally measured spanwise efficiency survey may not accurately represent the performance of individual blade sections.

Introduction

Traditionally, axial compressors have been designed on a primarily two-dimensional basis, using streamline curvature techniques to ensure radial equilibrium. The mean streamsurfaces were designed, the blade-to-blade flows calculated, and then the spanwise variations taken into account. The advent of three-dimensional Euler calculational procedures has permitted more detailed looks at the three-dimensional inviscid flow structure. Stages are designed for the most part to minimize radial flows. It has long been known, however, that some spanwise transport does occur across the nominal steady-state two-dimensional streamsurfaces. This three-dimensional mixing is clearly important in multistage compressors and has been accounted for in the design process by empirically based models of spanwise mixing such as that proposed by Adkins and Smith (1982).

Radial transport may also be of concern in single-stage compressors as well. Kerrebrock (1980) noted that although the total loss in transonic rotors may be well predicted, the spanwise loss distribution often is not. It is puzzling in that the rotor efficiency is much lower near the tip and higher near the hub than could be explained by strictly two-dimensional shock and viscous loss models, including tip clearance losses. Accounting for the three-dimensional shock structures as proposed by Prince (1980) does not help here since the shock leaning predicts reduced rather than increased loss in the supersonic tip region and has no direct influence in the subsonic region near the hub. Kerrebrock speculated that the high tip and low hub efficiencies might be caused by radial flows, which would serve to redistribute losses radially without necessarily generating much loss themselves. Thompkins and Usab (1982) examined the radial flow on a transonic fan rotor blade using a quasi-three-dimensional boundary layer code and concluded that centrifuging of the attached boundary layer would not transport much loss radially. Given a sufficiently large separated region, however, a considerable amount of lossy fluid could be moved radially.

At this point some additional data were clearly needed to delineate clearly the physical processes at work in these machines. Gallimore and Cumpsty (1986a) and Wisler et al. (1987) have measured radial mixing in multistage low-speed com-

[1]Current address: Avco Research Laboratory-Textron, Everett, MA 02149.

Contributed by the International Gas Turbine Institute and presented at the 35th International Gas Turbine and Aeroengine Congress and Exposition, Brussels, Belgium, June 11–14, 1990. Manuscript received by the International Gas Turbine Institute January 6, 1990. Paper No. 90-GT-133.

pressors. Their data, however, were measured in the time average only so that the mechanisms and structure of the radial mixing remained in some debate. Furthermore, although many flow phenomena are well modeled in low-speed machines, some are not. Given the degree of uncertainty in the detailed fluid mechanics of compressor radial flows and the lack of data on loss redistribution (if any), measurements on high-speed compressors seemed in order.

The objective of the research described herein was to make quantitative measurements of the radial transport in a modern transonic rotor with sufficient spatial and temporal resolution so as to establish the magnitude of the radial flows and to elucidate mechanisms responsible. In the next sections, we describe the experimental apparatus, present the data, develop an analytical model of the flow field to explain the observations, and finally comment on the importance of radial flows in transonic fans and compressors.

Experimental Apparatus

The conceptual basis of the experiment was to inject a thin sheet of tracer gas upstream of the rotor (the sheet is oriented normal to the radial direction) and then map the tracer gas distribution downstream of the rotor with instrumentation whose frequency response is large compared to blade passing (Fig. 1). The frequency response of the laboratory frame instrument translates into spatial resolution in the rotor relative frame and also yields information on the rotor relative unsteadiness of the flow. The instrument chosen also measures time-resolved total temperature and pressure and thus entropy so that the instantaneous loss distribution can be determined simultaneously with tracer distribution.

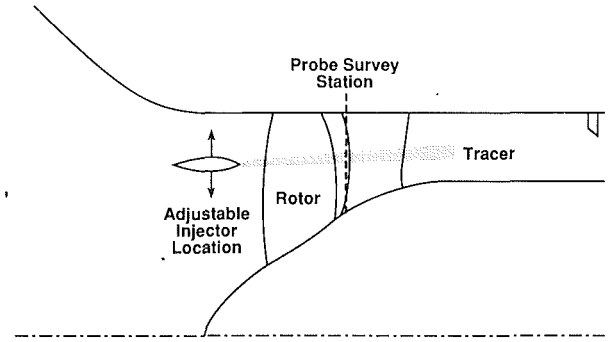

Fig. 1 Experimental arrangement in high throughflow compressor showing upstream tracer gas injector and probe survey station

The test compressor selected was a low aspect ratio, high throughflow, transonic machine designed by Wennerstrom (1984). With a design stage pressure ratio of 2.1 and peak efficiency of 90 percent, this 0.43 m-diameter, 427 m/s tip speed machine is the prototype for a current generation of military compressors now under development. The compressor was operated in the MIT Blowdown Compressor Facility (Kerrebrock et al., 1974), which provides steady-state running conditions for approximately 50 ms in an argon-Freon 12 atmosphere. Previous measurements on this high throughflow stage in the blowdown facility were reported by Ng and Epstein (1985).

The tracer gas was injected through the hollow trailing edge of a NACA 65-021 airfoil located approximately 0.2 chord upstream of the rotor. (This section was chosen because it

Nomenclature

a = longitudinal spacing between vortices
c_p = constant pressure specific heat
$C_{\max}$ = maximum tracer gas concentration (mass Fraction)
C_p = static pressure coefficient
C_{rel} = $C(X, Y)/C_{\max}$
$C(X, Y)$ = tracer gas concentration (mass fraction) at point X, Y
d = maximum blade thickness
F = strength of line source of tracer gas injection per unit length
h = lateral spacing at the two rows of vortices in vortex street
k = vortex circulation outside the vortex
K_o = modified Bessel function of the second kind, zero order
L = axial chord
M = Mach number
p = static pressure
P_T = total (stagnation) pressure
r = radial distance from vortex center
r_o = radius of vortex core edge
$\mathfrak{R}$ = gas constant
R = radial (spanwise) distance, measured from the rotor centerline
Re = vortex Reynolds number = k/ν
R_t = tip radius of the rotor
Δs = specific entropy change
t = time
T_T = total (stagnation) temperature
U = free-stream velocity
$\mathbf{w}(R, \theta, z)$ = velocity in vortex core in the blade relative frame
$\mathbf{W}(R, \theta, z)$ = free-stream velocity in blade relative frame
W_i = velocity induced by vortex street
W_p = peripheral velocity at vortex core edge
α = empirical eddy viscosity constant
ϵ = mixing coefficient
γ = ratio of specific heats
ν = kinematic viscosity
ν_t = eddy kinematic viscosity
ρ = static density
ϕ = flow coefficient
$\bar{\omega}$ = relative total pressure loss coefficient
Ω = rotor angular velocity
$\langle\ \rangle$ = averaged over vortex core circumference

Subscripts

c = within vortex core
core = isolated vortex core
pot = isolated potential vortex
row = single row of potential vortices
R = spanwise direction
x = vortex streamwise direction
y = direction orthogonal to vortex streamwise
z = rotor axial direction
θ = rotor tangential direction
∞ = free stream, outside vortex core

Superscripts

$\bar{}$ = nondimensional
$'$ = frame moving with vortices with origin along vortex centerline
$''$ = frame moving with vortices with origin at vortex center

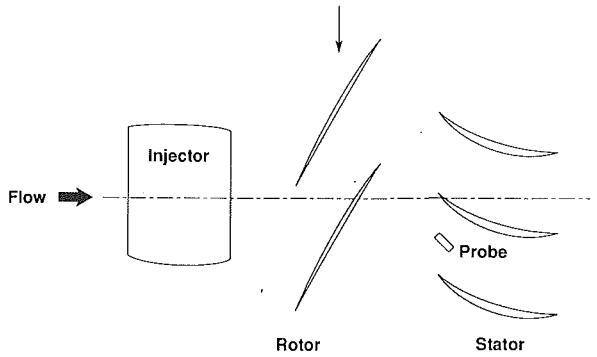

Fig. 2 Scale drawing of compressor near tip section showing relative scale of injector and concentration probe

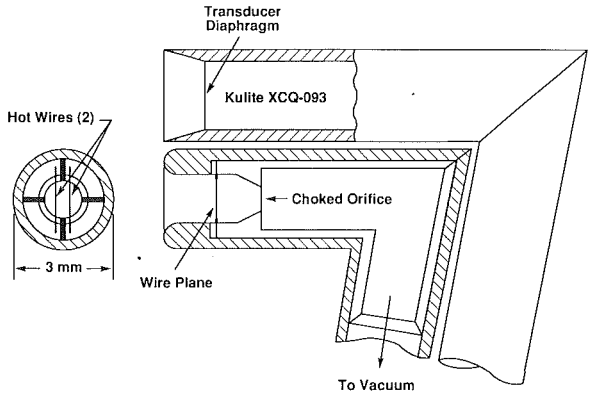

Fig. 3 High frequency response concentration, temperature, and pressure probe

remained subcritical at the rotor inlet Mach number, while having sufficient cross-sectional area to pass the tracer mass flow at low loss.) The airfoil was hollow with a thin (0.75 mm) slot along the trailing edge and oriented so as to inject the thin sheet of tracer tangent to the circumference at one radial location spanning approximately two rotor blade pitches (Fig. 2). The airfoil was supported on two radial struts (also NACA 65-021) such that its spanwise position could be varied between tests. The struts were hollow and supplied the gas to the injector. In order for the sheet of injectant gas to suffer the minimum dispersion, it is important that the velocity at the injection slot exit match that of the freestream. In a blowndown tunnel the Mach numbers are constant, however, the freestream temperature and thus velocity decay with time. Therefore, the injectant was also blown down from its own supply tank whose volume was adjusted so that its decay rate matched that of the main flow. A miniature, high frequency response pressure transducer was mounted within the injector to monitor the pressure during the blowdown test.

Instrumentation

The principal instrumentation for this experiment was a dual hot-wire aspirating probe first reported by Ng and Epstein (1983). This probe (Fig. 3) consists of two co-planar, 6.25-μm-dia hot wires at different temperatures, mounted in a constant-area channel with a choked exit. When operated in constant-temperature anemometer loops, the hot wires respond to the total temperature (T_T) of the gas and the mass flux (ρU) by the wires. The mass flux through the choked channel of fixed geometry is a function of the free-stream total pressure (P_T) and total temperature (T_T). Thus, there are only two unknowns (P_T) and T_T) and two measurements (the voltage from each hot wire). Nonuniform gas composition influences both the mass flux by the wires and the heat transfer from the wires and thus introduces a third variable, which requires a third measurement. This was provided by "piggybacking" a high-frequency response pressure transducer (Kulite XCQ-093) on the aspirating probe to measure pressure directly. The two signals from the hot wires are then used to determine temperature and gas composition. The spatial resolution of the measurement is limited by the size of the probe (3 mm circumferentially and 6 mm radially). The frequency response was established through shocktube testing and calculation to be approximately 20 kHz (4–5 times blade passing frequency). More details on the probe are given by Kotidis and Epstein (1991) and Kotidis (1989).

The probe sensitivity is dependent on the chemical composition of the fluid. The criteria for tracer selection were that it match the density of the main flow in order to follow flow accelerations properly within the rotor and that it give maximum sensitivity and thus signal output from the probe. After considering many tracers, including CO_2 and a He–Xe mix, a mixture of helium and Freon-12 was selected. This 57 percent weight fraction He mixture matched the 54.5 molecular weight of the mainflow argon–Freon-12 mixture in the blowdown facility while having the high thermal conductivity necessary for good probe sensitivity. Since we were unable to calculate the properties of a quaternary gas mixture accurately, the probe response was established by steady-state parametric testing at various temperatures, pressures, and concentrations to establish calibration curves. These curves were then dynamically checked at a few points in a shocktube. Kotidis gives details of the data reduction procedure.

The principal sources of measurement error were noise in the anemometers and drift between calibrations. The exact magnitude was a nonlinear function of the instantaneous concentration, temperature, and pressure, and this error was calculated for each time point for each test. The average total uncertainty was 0.08 percent in total pressure and 0.21 percent in total temperature as a percentage of instantaneous value; and 0.33 percent of full scale in mass fraction of the tracer gas.

The rotor and stator are closely coupled in this stage and the stator sweeps forward from midspan to both the hub and tip. Thus, the probe was traversed at constant velocity from tip to hub during each test at a station located just ahead of the midspan stator leading edge at mid stator pitch. (The traverse velocity is less than 1 percent of that of the free stream.)

Proof of Concept Tests

There were two criteria that were critical for the success of these measurements. The first was that the presence of the upstream injector and injectant not influence the operation or performance of the compressor stage. The second was that the sheet of tracer gas not mix excessively due to factors other than the influence of the rotor flowfield during the transit from the injector to the survey station at the stator leading edge.

The influence of the injector on the rotor performance was assessed by examining radial traverses of the time-averaged rotor outflow. Since the distribution of rotor exit total pressure, temperature, and flow angle were the same with and without the injector present, we concluded that the influence of the injector on the rotor flow was not a concern.

The degree of radial spreading of the jet, which is independent of the rotor flowfield, was assessed by blowdown tests with the rotor and stators replaced by casing fairings. Figure 4 shows a measurement of the time-averaged tracer distribution measured at the same axial station as it would be with the stage in place. The measured jet thickness (0.9 cm) is small compared with the passage height at this station (10 cm) and is consistent with estimates of spreading from turbulent jets. (The inflow turbulence intensity level was measured as 0.6 percent.) This amount of spreading is sufficiently small for our purposes.

Another concern was to insure that the total amount of tracer

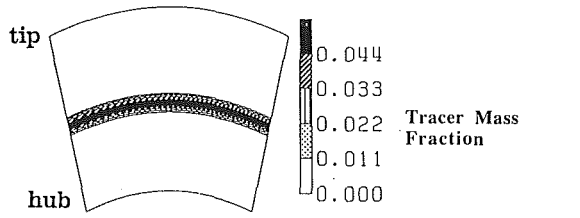

Fig. 4 Time-averaged survey of tracer distribution with blading removed

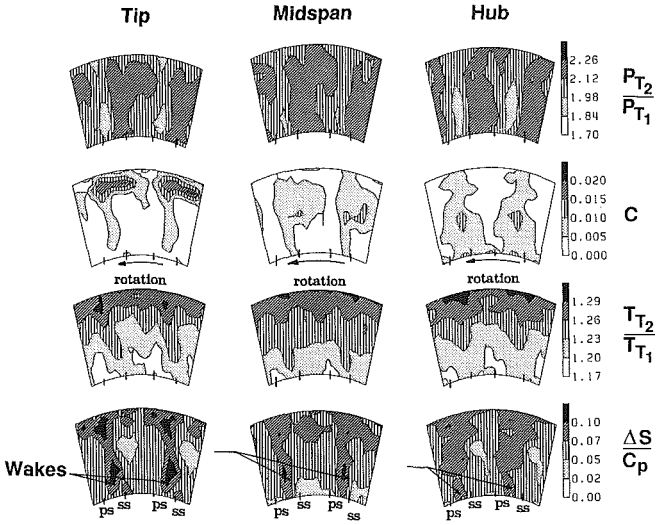

Fig. 5 Ten blade ensemble averaged contour plots of total pressure ratio, tracer concentration (*C*), total temperature ratio, and entropy measured near the stator leading edge for various injector locations; two blade pitches of data are shown

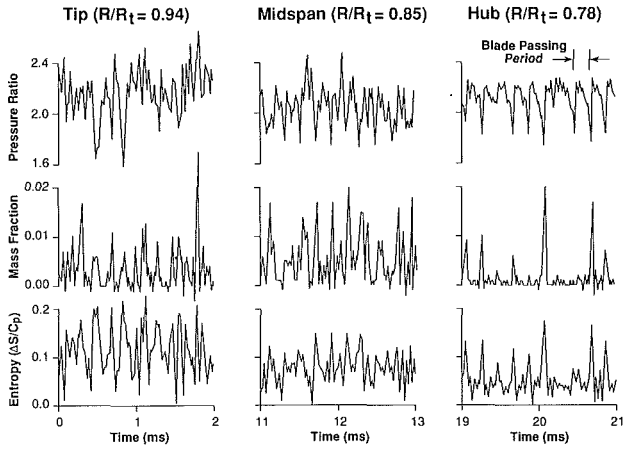

Fig. 6 Instantaneous measurements of total pressure, tracer concentration, and entropy measured at different radii with the injector located near midspan

gas detected by the probe was consistent with the amount injected. This checked both that the probe d-c calibration was valid and that the injector flow was mainly two dimensional. The total mass of gas measured by the probe was 80 percent of that injected, based upon the assumption that the flow from the injector is only two dimensional. Again, this agreement was sufficient for our purposes. Thus, we conclude from these consistency and proof of concept checks that we understand the nature of the experiment and that the artifacts introduced in the data by nonideal behavior were small.

Data Presentation

The data reported herein were all obtained at design point operation of the compressor. The experiments were performed with the injector positioned at three spanwise locations, which we will refer-to as tip (R/R_t = 0.95), midspan (R/R_t = 0.86), and hub (R/R_t = 0.81). All data were taken as instantaneous values of concentration, pressure, and temperature as the probe was slowly traversed from tip to hub. The entropy change of the fluid was calculated from the temperature, pressure, and concentration. The instantaneous data were then ensemble averaged or time averaged in post-test processing, depending on the use.

We present the ensemble-averaged data first in Fig. 5, which shows 10 blade ensemble averages of the concentration, temperature, pressure, and entropy assembled into contour plots as viewed looking upstream over two blade pitches. The blade wake positions as indicated on the figures are judged from the location of the total pressure defects (or excesses depending on the local velocity triangles). Comparing the total pressure and temperature plots, we see some variation with injector location of these flow quantities whose spanwise time-averaged distributions are unaffected by the presence of the injector (see Proof of Concept Tests, above). This variation is not due to the injector presence but rather is a result of the relatively small number of blade passages averaged to make the contour plots in this highly unsteady flowfield (dictated by the short running time of the facility). Here, we are concerned mainly with the average flow features, which are reproduced from test to test.

In the case of near-tip injection in Fig. 5, while most of the tracer remains near the tip, some does travel inward all the way to the hub. The fluid that migrates inward does so in the blade wakes. When the tracer is injected near midspan, the tracer actually moves both radially inward and outward. The inward transport is again confined to the wake region. When the injection is done closer to the hub, the tracer moves outward toward the tip, mostly in the wake region. By comparing the contours of the three tests, we note that there is relatively less radial transport with tip injection than with midspan or hub injection. Note that these contours do not extend all the way to the tip and hub surfaces so that details of the endwall flows are not seen. In particular, the edge of the tip vortex may just be at the top of the contours.

While the contour plots are effective in conveying large amounts of data quickly, the ensemble-averaging process can filter information from the data. Figure 6 shows a short segment of time-resolved data taken with midspan (r/r_t = 0.86) tracer injection for measurements made at three spanwise positions. (Note that the tip, midspan, and hub measurements are not taken simultaneously since the probe is traversed from tip to hub during a test.) In the hub region, the downspikes in total pressure are the blade wakes. In the tip region, the velocity triangles are such that the wakes have a total pressure excess. Note that all quantities show the flow to be highly unsteady and a periodic. There are very significant blade-to-blade differences. These are much larger than can be explained by minor geometry differences between blades or turbulent fluctuation (Epstein et al., 1988). (It is this high level of fluctuation that causes the variation in the contour plots of Fig. 5.) The tracer concentration at each spanwise position is not uniform across the blade pitch but rather all of the tracer gas is concentrated in a relatively few "spikes," which appear only in the blade wakes. Not all wakes contain tracer, however. It is important to note that those wakes with tracer concentration spikes also contain high entropy. A more complete presentation of these time-resolved measurements can be found from Kotidis (1989).

The measurements thus show that most of the fluid transported along the span in this transonic compressor rotor appears in the blade wakes but does not appear in every wake sampled. Furthermore, the fluid that is transported radially has high entropy relative to the mean. The implication is thus

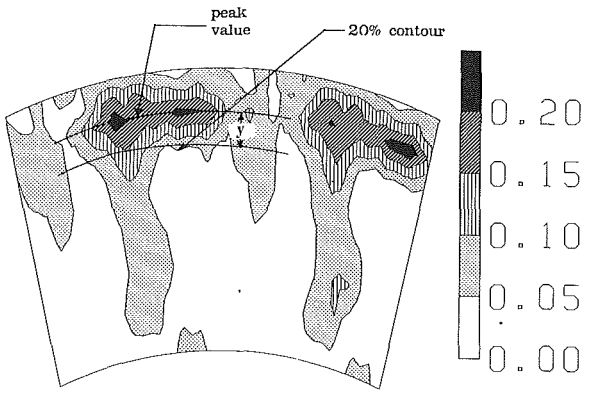

Fig. 7 The 20 percent concentration contours were used to derive an average mixing coefficient for equation (3)

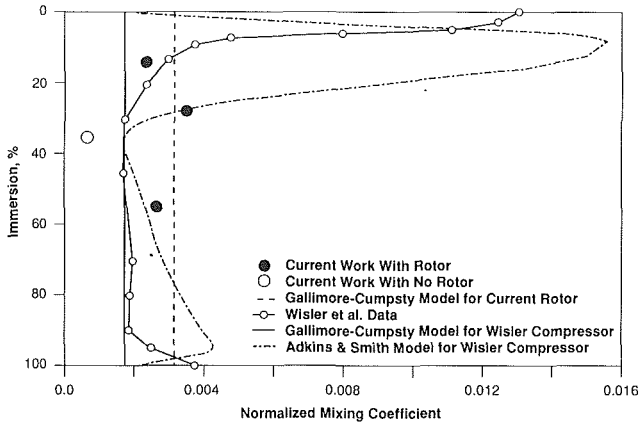

Fig. 8 Normalized spanwise mixing coefficients for this single-stage transonic compressor compared to low-speed multistage data from the literature

that the radial transport may modify the spanwise efficiency distribution of the rotor.

Comparison of Time-Averaged Mixing Rates

While our interest here is more toward elucidating the details of the radial flow in a transonic compressor than deducing empirical spanwise mixing rates for a designer, it is useful as a first step to compare our time averaged results with published data such as those of Gallimore and Cumpsty (1986), and Adkins and Smith (1982), if for no other reason than as an additional validity check on our measurements and data reduction procedure. The goal here is to derive a diffusion constant, ϵ, from the experimental data in a manner consistent with previous work. The only difference is that, in this case, the tracer is introduced as a line source rather than the point source as used by Gallimore and Cumpsty. The solution of the diffusion equation for a line source of strength F per unit length is given by Hinze (1959) as

$$C(X, Y) = \frac{F}{2\pi\epsilon} K_o \left[\frac{U(X^2 + Y^2)^{1/2}}{2\epsilon} \right] \exp\left(\frac{UX}{2\epsilon}\right) \quad (1)$$

where C is the concentration at X and Y, X is the flow direction, Y the radial (spanwise) direction, U the free-stream velocity, and K_o the modified Bessel function of the second kind, zero order. This can be simplified for small values of ϵ/UX and small values of Y/X as

$$C(X, Y) = \frac{F}{2(\pi\epsilon U|X|)^{1/2}} \exp\left[-\frac{UY^2}{4\epsilon|X|} \right] \quad (2)$$

Following the procedure of Gallimore and Cumpsty, we then derive an expression for spanwise spreading rate, Y/L (where L is chosen as the rotor axial chord), as a function of normalized mixing coefficient ϵ/UL, and $C_{rel} = C(X, Y)/C_{max}$,

$$\frac{Y}{L} = \left[-4\frac{\epsilon}{UL}\frac{|X|}{L} \ln C_{rel} \right] \quad (3)$$

C_{max} is assumed to occur along the X axis.

Given the measured concentration distributions (Fig. 5), the mixing coefficient can now be estimated with equation (3). The crossflow dimension, Y, was derived from the contour plots in a manner consistent with that of Wisler et al. (1987), which was concerned with only the turbulent diffusion contribution to the mixing; specifically, the cross-stream dimension, Y, is taken as the point at which the concentration is 20 percent of the maximum value. This is illustrated in Fig. 7. Note that the tracer in the wakes has been ignored in this analysis.

The results of this fit to the data are shown in Fig. 8, along with some data reported in the literature for multistage compressors. The values from this work fall within the range of values expected from the literature. Single-stage low-speed compressors with high inflow turbulence exhibit comparable mixing rates, but those with low inflow turbulence levels (the case here) show considerably reduced mixing (Cumpsty). The high level observed in this compressor could be due either to a higher level of inherent flow unsteadiness within the transonic machine due to such phenomena as shock oscillations (Ng and Epstein, 1985), or to some interaction between the injection process and rotor flowfield that doesn't appear in the time-averaged rotor performance. (Note though that the no-rotor data point in Fig. 8 is a factor of 5 below the with-rotor mixing coefficient, implying that most of the mixing is due to the rotor.)

Gallimore and Cumpsty proposed that the turbulent mixing coefficient can be estimated as

$$\frac{\epsilon}{UL} = A\frac{d}{L}\left[\frac{2\bar{\omega}(d/L)}{3\phi^2} \right]^{1/3} \quad (4)$$

where d is the blade thickness, L the compressor length, ϕ the flow coefficient, ω the loss coefficient, and A a property of turbulent flow with a proposed value of about 0.4. Applying equation (4) to this compressor yields the dashed straight line on Fig. 8, which is in quite good agreement with the data. Note that the measured relative total pressure loss coefficient (about one half of which is shock loss in this transonic compressor) was used here.

From these comparisons we concluded two things: first, that the data reported herein are in fact consistent with previously reported multistage measurements; second, that the techniques of Gallimore and Cumpsty, derived from low-speed multistage data, do a quite reasonable job in predicting the time-averaged mixing in a transonic compressor rotor.

Radial Transport by Spanwise Wake Vortices

The measurements show that the fluid in the wakes at the measurement station has undergone considerable radial transport, both radially in and out. Wake outward centrifuging has long been observed on low-speed compressors and, although some experimenters have reported measurements of inward flows, they have not been explained. An order-of-magnitude analysis of such classical mechanisms as secondary flow and tip leakage vortices does not account for this degree of transport (Kotidis, 1989). Radial flow in the rotor blade boundary layers can account for much of the radial outflow if the boundary layers are separated (Thompkins and Usab, 1982), but does not explain the inward radial migration of the tracer. One physical phenomenon that may account for much of this transport is the spanwise vortex street structure within the blade wakes. In the following sections, we shall present some back-

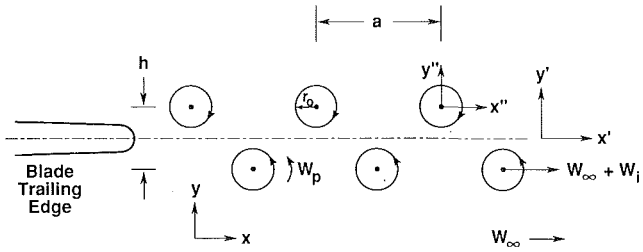

Fig. 9 Schematic of two-dimensional vortex street wake behind rotor blade

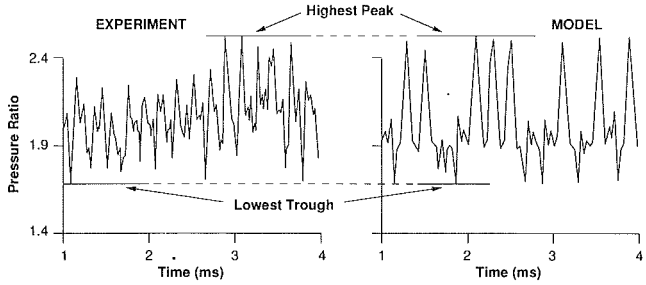

Fig. 10 Comparison of experimental data and model prediction; the peak-to-peak amplitude and relative number of up and down spikes are matched to derive vortex strength and spacing ratio

ground on this phenomenon, develop a very simple three-dimensional vortex street model, and compare the radial fluid transport predicted by the model with the measurement.

The presence of vortex streets has long been recognized in the wakes of high Reynolds number, transonic flat plates and turbine airfoils in steady flow (Paterson and Weingold, 1984; Heinemann et al., 1976; Greenway and Wood, 1973). More recently, Gertz (1986) identified vortex streets in the wakes of highly loaded transonic compressor rotor blades. The flow in these vortex street wakes can explain several of the more puzzling aspects of the high frequency response measurements, including the large wake-to-wake variability (Epstein et al., 1988) and also, as we shall see, some of the spanwise fluid transport. The large blade-to-blade variation in wake total temperature, pressure, and concentration (Fig. 6, for example) can be seen as an artifact of the pseudo-random sampling of the vortex street (which is periodic in the blade relative frame) by instrumentation fixed in the laboratory frame. Thus, the wake total temperature (for example) may appear to vary by $\pm 20°C$, depending upon whether a vortex core happens to be sampled by the probe.

Gertz constructed a simple, two-dimensional model of the vortex street wake, details of which are given in the Appendix. The wake is modeled as two staggered rectilinear rows of Rankine vortices of opposite sign in a uniform free stream. The vortices consist of an inner region with a forced-vortex core and an outer region following the irrotational flowfield of the classic von Karman vortex street. The wake is characterized by the vortex size (r_o) and strength and the ratio of streamwise vortex spacing (a) to the distance between vortex rows (h) (Fig. 9). This is sufficient to describe the vortex street completely with such parameters as vortex convection velocity, shedding frequency, and wake average temperature and pressure defect yielded directly by the model. These parameters were derived by Gertz by fitting the model to experimental data as measured at one spanwise and axial station. As such, the model describes the wake only at that position and offers information neither on the temporal evolution of the wake nor on its three-dimensional structure. We have extended this model in a simple fashion to provide this information. The approach taken is to fit a two-dimensional vortex street model at several radial positions, establish consistency between the two-dimensional layers, and then to stack the two-dimensional models to yield the spanwise static pressure gradient from which the radial transport can be calculated. We realize that this approach is neither rigorous nor complete but rather is presented as a first estimate of the role that wake vortices may play in spanwise fluid transport in a high speed compressor.

The first step in constructing this quasi-three-dimensional model is to fit the two-dimensional model at various spanwise locations; $R/R_{tip} = 0.95$, 0.88, 0.81, and 0.75 were chosen. Gertz fit his model to laser anemometer data, inferring the vortex strength from the wake velocity defect and the vortex spacing ratio (h/a) from the statistical distribution of velocities. Since we did not have laser anemometry data available for this stage, we developed a procedure based on the wave forms of the high frequency response probe data. Basically, the vortex street model was fit to the data by guessing the values for the vortex strength and spacing ratio, predicting the time-resolved total pressure in the laboratory frame, and comparing the model prediction with the measurement. (Other information was needed to establish the flow geometries, namely wheel speed, flow angle, Mach number, and wake-to-pitch ratio, which came from time-resolved measurements on this stage reported by Ng and Epstein.) In particular, the maximum peak-to-peak pressure excursion (related to vortex strength, k) and the relative number of up spikes and down spikes about the mean (related to the vortex spacing) were compared (Fig. 10). The guess of vortex strength and spacing ratio was then modified and the procedure repeated until the model prediction and data agreed. This procedure was less tedious than it might appear, quickly converging to seemingly unique values of vortex strength and spacing. An uncertainty analysis was performed in which the uncertainties of the individual measurement quantities input to the model were assessed (total pressure, wheel speed, flow angle, Mach number, and wake-to-pitch ratio), and then fed in the worst case through the procedure. The net result was a uncertainty of approximately 5 percent in vortex strength and spacing. More detail on this procedure may be found from Kotidis (1989).

The vortex model was then used to predict the shedding frequency of the vortex street at the specified radii. This is shown in Table 1 along with a Strouhal number based on wake momentum thickness at the blade trailing edge (estimated by the method of Koch and Smith, 1976). The frequencies are about the same at each radius within the experimental error (as discussed above). This condition is absolutely necessary for the vortices to be coherent along the blade span. The relative phase coherence of the shedding among the radii (the other necessary condition) could not be assessed from these data. It seems likely to us, however, that natural processes evident, for example, in cylinders in shear flow (Gaster, 1969; Gerrard, 1966) tend to enforce coherence over at least part of the span. We predicate the remainder of the analysis, then, on the assumption that the shed vortices in the wake are coherent over much of the blade span.

Also of interest are the numerical values of the shedding frequency (about three times blade passing) and the Strouhal number. These are consistent with the findings of Gertz on a different transonic rotor. The Strouhal numbers are within the general range of universal wake Strouhal numbers, St*, based on wake width that would be expected for a cylinder or bluff body at this Reynolds number (Griffin, 1980).

Flow Along the Vortex Cores

The two-dimensional vortex models (equations (A10) and (A12)) show a strong spanwise gradient of static pressure (Fig. 11) and we will use this information to calculate the resultant fluid transport along the core. To simplify the process, we will

Table 1 Vortex shedding frequency from two-dimensional vortex model fit

Radius Ratio (R/R_t)	Frequency (kHz)	Strouhal Number
0.95	16.9 ±1.5	0.155
0.88	16.7 ±1.5	0.151
0.81	17.3 ±1.5	0.164
0.75	16.4 ±1.5	0.180

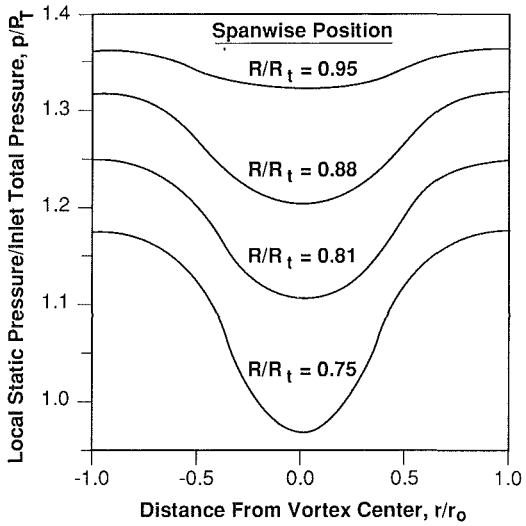

Fig. 11 Static pressure distribution through the vortex cores as predicted by the two-dimensional model at four spanwise locations

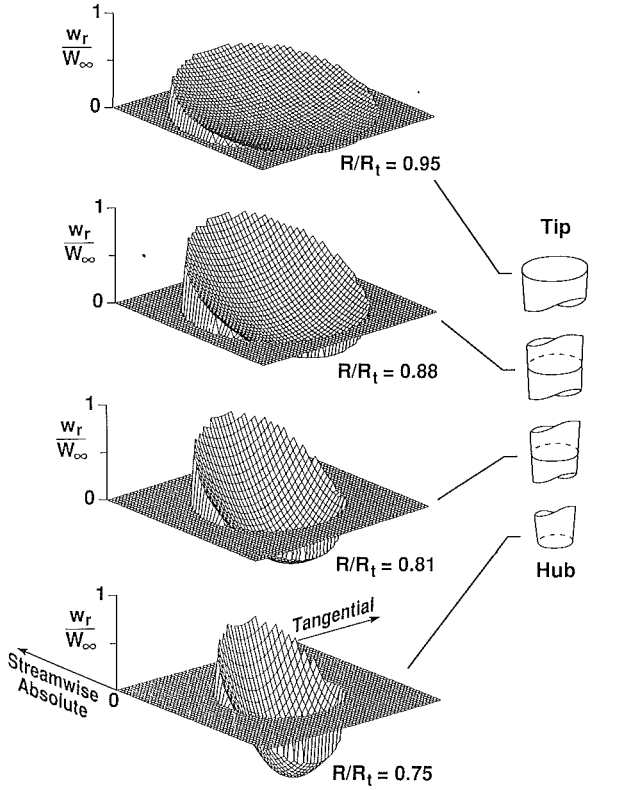

Fig. 12 Perspective of radial velocity distribution within the vortex cores as predicted by the model at the probe survey station

neglect: (*a*) any tilting or distorting of the vortex, and (*b*) any influence the endwalls may have on the vortex formation and development, since the radial pressure gradient should be a predominant influence. We justify these assumptions on the basis that this vortex model is basically empirical and descriptive rather than predictive.

We write the equation of motion for the vortex core region in rotor relative frame (neglecting viscous stresses) as

$$\frac{D\mathbf{w}}{Dt}+2\Omega\times\mathbf{w}=\Omega^2\mathbf{R}-\frac{\nabla p_c}{\rho_c} \tag{5}$$

where D/Dt denotes the substantial derivative, Ω is the angular velocity of the rotor, $\mathbf{w}$ the velocity in the core, $\mathbf{R}$ the radial (spanwise) location, and p_c and ρ_c the vortex core fluid static pressure and density. Similarly, in the free stream,

$$\frac{D\mathbf{W}}{Dt}+2\Omega\times\mathbf{W}\ =\ \Omega^2\mathbf{R}-\frac{\nabla p_\infty}{\rho_\infty} \tag{6}$$

where p_∞ and ρ_∞ are the freestream static pressure and density, and $\mathbf{W}$ is the free-stream velocity. When the vortex core and the free-stream are at the same spanwise location, we can subtract equation (6) from equation (5), yielding

$$\frac{D\mathbf{w}}{Dt}=\frac{D\mathbf{W}}{Dt}+2\Omega\times(\mathbf{W}-\mathbf{w})+\frac{\nabla p_\infty}{\rho_\infty}\ -\ \frac{\nabla p_c}{\rho_c} \tag{7}$$

The radial (spanwise) velocity in the vortex, ∇w_R, can be derived from equation (7) by vector manipulation (the radial velocity in the free-stream is assumed to be small compared to that in the vortex cores):

$$\Delta w_R=-\Delta t\left[(W_\theta-w_\theta)\left(\frac{W_\theta+w_\theta}{R}+2\Omega\right)-\frac{1}{\rho_\infty}\frac{\partial p_\infty}{\partial R}+\frac{1}{\rho_c}\frac{\partial p_c}{\partial R}\right] \tag{8}$$

This can then be translated into the laboratory frame, since the wheel speed and vortex geometry are known. We estimate the quantities in equation (8) in the following manner. The time interval, Δt, is calculated as the particle convection time from the blade trailing edge to the probe survey location using the calculated distribution of axial velocity in the vortex cores. The vortex model fit to the data at each spanwise station yields w_θ (the θ component of equation (A9)), while W_θ is taken from the direct measurement on this rotor by Ng and Epstein (1983). The density is calculated with the state equation

$$\rho_\infty=\frac{p_\infty}{\Re T_\infty}=\frac{\gamma p_\infty}{W_\infty}\mathrm{M}_\infty^2 \tag{9}$$

and assuming the static temperature is uniform

$$\rho_c=\frac{\gamma p_c}{W_\infty}\mathrm{M}_\infty^2 \tag{10}$$

where M_∞ is the blade relative free-stream Mach number. M_∞ and p_∞ were measured by Ng and Epstein (1985). The spanwise static pressure gradients ($\partial p_\infty/\partial R$ and $\partial p_c/\partial R$) are estimated from the vortex model results in Fig. 11. Note that p_c and ρ_c are functions of r/r_o.

We now have a snapshot of the three-dimensional vortex structure at the probe survey location. The radial velocity distribution calculated with equation (8) is shown in Fig. 12. The spanwise vortex core shape resulting from the model tapers by 80 percent from tip to hub (the diameter varies from 2.9 to 1.6 percent of the rotor tip chord) and contains both inward and outward flow along the blade at each spanwise location. The substantial outward flow in the core is a result of the rotor tangential velocity component introduced by the noninertial frame of vortices. (If the vortex were in the laboratory frame, the flow would be entirely inward along the span, given the same static pressure gradients.) The net fluid motion is essentially zero at the three outer spanwise locations indicated on the figure, and about 40 percent of the free-stream velocity toward the hub at $R/R_t = 0.75$. The ratio of peak spanwise to free-stream total velocity, 0.6–0.7, is similar to that observed by Koochesfahani (1989) in vortices in the wake of a pitching airfoil (a somewhat different flow), implying that this model and data fitting procedure give physically realizable values.

Table 2 Wake vortex growth estimate

Spanwise Location, R/R_{tip}	$r_o(0)$* Near Trailing Edge	$r_o(t)$* at Probe Location
0.95	2.7%	2.9%
0.88	2.1%	2.4%
0.81	1.5%	1.9%
0.75	1.1%	1.6%

* As percent of rotor tangential tip chord.

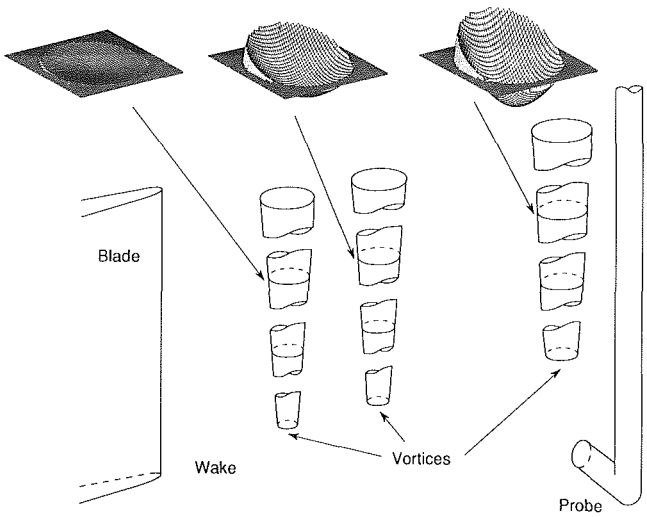

Fig. 13 An example of the streamwise evolution of the radial velocity distribution within the vortex cores

Estimating Vortex Evolution

In order to estimate the total spanwise transport of fluid in the compressor, we must establish the time history of the shed vortices in the wake. We would, in general, expect both their size and strength to change with time as they are convected from the blade trailing edge to the probe measurement station. Unfortunately, we do not have measurements of this process but here must rely on modelling. We will make an analogy between the wake vortex evolution and that of wing trailing edge vortices (of which much more is known), noting differences between the two such as the noninertial frame of the wake and the streamwise orientation of the trailing edge vortices.

Lamb (1945) estimated the growth of a vortex in laminar flow, giving the circumferential velocity, $|w''|$, as

$$|w''| = \frac{k}{2\pi r}\left(1 - e^{(-r^2/4\nu t)}\right) \tag{11}$$

where r is the radius of the vortex core, ν the kinematic viscosity, and k the circulation outside the vortex. Squire (1965) extended this to turbulent flow by simply replacing ν with an eddy viscosity, ν_t,

$$\nu_t = \alpha K \tag{12}$$

where α is an empirical constant. Govindaraju and Saffman (1971) reported values for α ranging from 5×10^{-5} to 7.6×10^{-3}, depending on the vortex Reynolds number. For our vortices, Re = 10^5, so that $\alpha = 4\times10^{-4}$. Following Squire's suggestion of defining the radius of the edge of the vortex core, r_o, as the distance at which the vorticity is 5 percent of that at the center, we can write the vortex edge radius at any time (t) as

$$r_o(t) = (12\nu_t t)^{1/2} \tag{13}$$

We must include the effects of the initial vortex size when it is formed, so equation (13) can be rewritten as

$$r_o(t) = (r_o(t=0)^2 + 12\nu_t \Delta t)^{1/2} \tag{14}$$

Table 3 Spanwise transport behind rotor

	Vortex Model	Measurement
% of Compressor Mass Flow Moving From:		
Hub to Tip	0.6%	3.5%
Tip to Hub	1.3%	1.6%
Extent of Spanwise Fluid Motion as Fraction of Span:		
Hub to Tip	0.58	0.40
Tip to Hub	0.44	0.40

where $r_o\,(t=0)$ is the core size near the blade trailing edge where the vortex can first be considered fully formed. The location of this vortex origin point has not been rigorously determined. For simplicity, we will adopt the findings of Cantwell and Coles (1983) who found the vortex to be fully formed approximately three diameters downstream of right circular cylinders. Since the characteristic of length scale for the compressor blade shedding is the boundary layer momentum thicknesses, we will assume that the vortices are fully formed three momentum thicknesses downstream of the blade trailing edge. For the vortex convection velocities derived from the data fit, this formation period (the end of which is now defined as $t=0$) is 20 percent of the total flow time from the trailing edge to the probe sampling location. Thus, the Δt in equation (14) is 80 percent of the flow time. The vortex evolution can now be estimated by marching downstream in small time steps, starting at the vortex formation location. At each time step, the vortex core radius, r_o, is calculated with equation (14). Gertz's two-dimensional vortex model is then fit to the new r_o at each spanwise station, assuming the vortex strength is constant. (The only role that viscosity plays in this modeling is to diffuse the vortex.) Numerical values are presented in Table 2. Overall, the vortex size does not change greatly, implying that the accuracy of growth rate estimate may not be critical. Figure 13 illustrates the vortex evolution as it is convected downstream.

Using this description of vortex growth, we can then calculate the total spanwise transport numerically. At each streamwise station, the Gertz model is refit to yield the velocity and density distributions within the core, from which the instantaneous radial velocity distribution is calculated with equation (8). This procedure is repeated for each time step as we march downstream to the probe survey station. Integration of the spatial distribution of the radial velocities then directly yields the total spanwise transport.

Comparison of Vortex Model and Data

A comparison between the vortex model estimate above and the measured spanwise transport is summarized in Table 3. The model predicts about 85 percent of the total mass transport from tip to hub but only 15 percent of that from hub to tip. The spanwise extent of the motion is in reasonable agreement.

We infer from this comparison that a spanwise coherent vortex street in the wake is the principal physical mechanism for inward radial transport in the transonic compressor rotor studied, but that a different mechanism may account for the major portion of the outward transport. A likely candidate for the outward transport is motion within separated regions of the blade boundary layers. A previous two-dimensional numerical study (Epstein et al., 1988) showed that vortex shedding was itself tied to boundary layer separation in that the larger the region of separation on the blade, the stronger (and larger) the vortices in the wakes (since the vorticity in the boundary layer can end up as vorticity in the wake vortices). When there was little separation, the vortex shedding was very weak. An unpublished experimental investigation of two transonic fans with similar relative Mach numbers and pressure ratios, but different blading, showed that the blades with suc-

tion surface separation (as inferred from deviation measurements) shed strong vortices (as inferred from laser anemometer statistics), while the unseparated (or at least less separated) blades did not. Thus, some separation would seem to be necessary for strong vortex shedding in the blade wake. It is quite likely that very highly loaded blading such as the rotor studied here have some regions of boundary layer separation, even though the overall rotor performance is very good. Thus, we believe that the vortex transport described in this paper is not necessarily present in all rotors but is a function of individual blade design. Furthermore, this phenomenon should be of more importance for transonic and supersonic blading since the shock wave boundary layer interaction often results in regions of separated flow, especially at higher Mach numbers. To the degree to which such two-dimensional thinking can be extended to three dimensions, we believe that the less the separation, the less the radial transport. Verification of this hypothesis will require further experimental evidence and would greatly benefit from more sophisticated modeling of the three-dimensional separation and vortex structure.

Influence of Spanwise Fluid Transport on Apparent Rotor Spanwise Performance

We have presented measurements of spanwise fluid transport in a transonic compressor rotor. A key feature of these data is that most of the transport is within the blade wakes and the measured entropy of this fluid is quite high compared to the mean. Thus, the transport serves to redistribute entropy as well as fluid along the span. We wish here to assess the impact of this fluid motion on the apparent spanwise distribution of rotor efficiency. The question we ask is whether the efficiency as measured at (for example) the stator leading edge plane represents the true loss incurred along the nominal two-dimensional design streamsurfaces through the rotor, or does the spanwise entropy transport significantly alter the apparent loss of each blade element? We will base this calculation on the information from the experimental measurements rather than the analytical model.

The distribution of rotor adiabatic efficiency in the absence of radial flow was estimated in the following manner. The rotor flowfield was divided into four streamtubes centered at the spanwise locations of Fig. 12 with the quantitative mass exchange among the streamtubes inferred from the measured tracer concentration and the fluid state from the temperature and pressure measurements. The results of the vortex model were then used to establish the fraction of the mass exchange occurring downstream of the blade trailing edge (85 percent of the inward flow and 15 percent of the outward). The remaining mass exchange was assumed to occur within the blade passage (presumably in the blade boundary layers or separated regions). The total temperature change due to the work done on the fluid displaced radially within the rotor passage was calculated with Euler's turbine equation. This fluid was then mixed out assuming a constant-area mixing process, thus incurring a total pressure loss. Because the transit time from the blade trailing edge to the probe survey station is so short compared to turbulent mixing times, the fluid transported radially downstream of the rotor trailing edge was assumed not to be mixed at the measurement station and thus was not debited with a mixing loss. We now have a quantitative measure of the change in total temperature and pressure in each streamtube due to the spanwise fluid transport. Subtracting this change from the measurements along the span then yields an estimate of what the efficiency distribution would be were there no spanwise fluid exchange. (The turbulent mixing, as in Figs. 7 and 8, has a significantly lesser spanwise extent that the processes of importance here.) The exact magnitude of the entropy change proved sensitive to the fraction of the mass transport assumed to occur within the blade passage, since only this mass was debited with mixing losses. (Other than in providing this information by way of the model, wake vortices do not enter into this calculation. The results would be the same should some other physical mechanism be responsible for the measured spanwise transport.)

The results of this calculation are presented in Fig. 14, which shows the rotor adiabatic efficiency distribution (1) as measured, (2) as it would be without spanwise entropy transport (the above calculation), and (3) as estimated by Kerrebrock as the sum of two-dimensional viscous plus normal shock losses. In the first and second cases, the efficiency integrated over the span is similar. We wish to emphasize the general trend of these calculations (which are based on several layers of approximate models) rather than make a strictly quantitative comparison. It is clear that a principal effect of this spanwise transport is to move a substantial amount of loss from the rotor hub to tip, making the hub performance appear quite good and the tip quite bad. This quantitatively bears out Kerrebrock's (1980) original conjecture on the loss distribution in transonic rotors.

To generalize, we would infer from these measurements and calculations that the performance of the hub sections of high pressure ratio transonic rotors can be much worse than generally realized, with much of their loss mistakenly attributed to the tip sections. (This should not be surprising since these hub sections have quite large turning and diffusion while tending to exhibit (apparently) extremely low loss.) It may make sense, therefore, to revisit the design of the hub region in transonic rotors in an attempt to improve overall efficiency. There may be more loss there than meets the eye.

Summary and Conclusions

This paper describes a set of time-resolved measurements of spanwise fluid transport in a high pressure ratio transonic compressor stage. The measurements show spanwise transport of several percent of the total mass flow. This transport is both radially inward and outward and is concentrated mainly in the blade wakes. The fluid that moves along the span has considerably higher entropy than the mean and this can redistribute the loss without necessarily altering the overall efficiency of the machine.

A quasi-three-dimensional vortex street wake model is presented. When fit to the data to derive the vortex characteristics, the model predicts most of the inward fluid transport along the span and about 15 percent of the outward motion. It is hypothesized that most of the outward transport is in separated

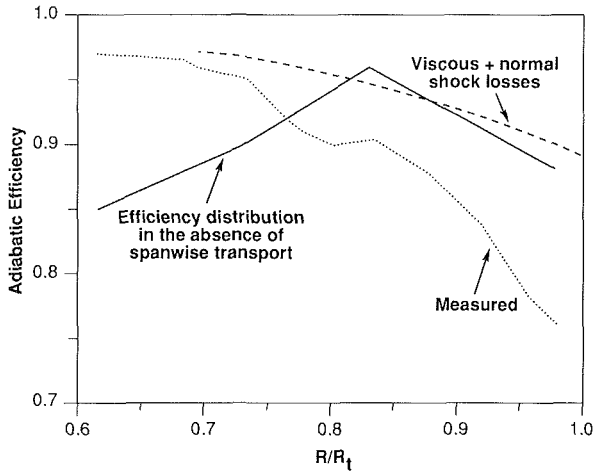

Fig. 14 Comparison of the measured spanwise efficiency distribution as it would be without spanwise entropy transport, and as the sum of two-dimensional shock and viscous losses as estimated by Kerrebrock (1980)

regions within the blade boundary layers. The net effect of the spanwise fluid transport is to move some of the loss incurred in the blade passage near the hub toward the rotor tip, making the hub section performance appear better than it actually is and the tip section performance concomitantly worse.

Future work in this area could include more sophisticated three-dimensional modeling of the boundary layer separation, vortex formation, and vortex evolution processes. Experimental information on the steady and unsteady boundary layer behavior of full-scale compressors is required here. (Flow visualization would be very helpful.) Also the question of loss generation (rather than just loss migration) in these processes should be studied.

Acknowledgments

This work was supported by the US Air Force Office of Scientific Research, Capt. H. Helin, technical monitor. The authors would like to thank Professors E. M. Greitzer and J. L. Kerrebrock for many useful discussions.

References

Adkins, G. G., Jr., and Smith, L. H., Jr., 1982, "Spanwise Mixing in Axial-Flow Turbomachines," ASME *Journal of Engineering for Power*, Vol. 104, No. 1.

Batchelor, G. K., 1964, "Axial Flow in Trailing Line Vortices," *Journal of Fluid Mechanics*, Vol. 20, Part 4, pp. 645–658.

Cantwell, B., and Coles, D., 1983, "An Experimental Study of Entrainment and Transport in the Turbulent Near Wake of a Circular Cylinder," *Journal of Fluid Mechanics*, Vol. 136, pp. 321–374.

Cumpsty, N. A., 1989, Private Communication.

Epstein, A. H., Gertz, J. B., Owen, P. R., and Giles, M. B., 1988, "Vortex Shedding in High Speed Compressor Blade Wakes," AIAA *Journal of Propulsion and Power*, Vol. 4, No. 3.

Gallimore, S. J., and Cumpsty, N. A., 1986a, "Spanwise Mixing in Multistage Axial Flow Compressors: Part I—Experimental Investigation," ASME JOURNAL OF TURBOMACHINERY, Vol. 108, pp. 2–9.

Gallimore, S. J., and Cumpsty, N. A., 1986b, "Spanwise Mixing in Multistage Axial Flow Compressors: Part II—Throughflow Calculations Including Mixing," ASME JOURNAL OF TURBOMACHINERY, Vol. 108, pp. 10–16.

Gaster, M., 1969, "Vortex Shedding From Slender Cones at Low Reynolds Numbers," *Journal of Fluid Mechanics*, Vol. 38, Part 3, pp. 565–576.

Gerrard, J. H., 1966, "The Three-Dimensional Structure of the Wake of a Circular Cylinder," *Journal of Fluid Mechanics*, Vol. 25, Part 1, pp. 143–164.

Gertz, J. B., 1986, "Unsteady Design Point Flow Phenomena in Transonic Compressors," Ph.D. Thesis, Dept. of Aeronautics and Astronautics, MIT; also MIT GTL Report No. 188.

Govindaraju, S. P., and Saffman, P. G., 1971, "Flow in a Turbulent Trailing Vortex," *The Physics of Fluids*, Vol. 14, No. 10, pp. 2074–2000.

Greenway, M. E., and Wood, C. J., 1973, "The Effect of a Bevelled Trailing Edge on Vortex Shedding and Vibration," *Journal of Fluid Mechanics*, Vol. 61, Part 2.

Griffin, O. M., 1980, "Universal Similarity in the Wakes of Stationary and Vibrating Bluff Structures," ASME Paper No. 80-WA/FE-4.

Heinemann, H. J., Lawaczeck, O., and Butefisch, K. A., 1976, "Von Karman Vortices and Their Frequency Determination in the Wakes of Profiles in the Sub- and Transonic Regimes," *IUTAM Symposium*, pp. 75–82.

Hinze, J. O., 1959, *Turbulence*, McGraw-Hill, New York.

Kerrebrock, J. L., et al., 1974, "The MIT Blowdown Compressor Facility," ASME *Journal of Engineering for Power*, Vol. 96, No. 4.

Kerrebrock, J. L., 1980, "Flow in Transonic Compressors," Paper No. AIAA-80-0124, Dryden Lectureship in Research, Pasadena, CA.

Koch, C. C., and Smith, L. H., 1976, "Loss Sources and Magnitudes in Axial Flow Compressors," ASME *Journal of Engineering for Power*, Vol. 98, No. 3.

Koochesfahani, M. M., 1989, "Vortical Patterns in the Wake of An Oscillating Airfoil," *AIAA Journal*, Vol. 27, No. 9, pp. 1200–1205.

Kotidis, P. A., 1989, "Unsteady Radial Transport in a Transonic Compressor Stage," Ph.D. Thesis, Department of Aeronautics and Astronautics, MIT, Cambridge, MA.

Kotidis, P. A., and Epstein, A. H., 1991, "High Frequency Response Concentration, Temperature, and Pressure Probe for Compressible Flows," submitted to *Rev. of Sci. Inst.*

Lamb, H. L., 1945, *Hydrodynamics*, Dover Publications, New York.

Ng, W. G., and Epstein, A. H., 1983, "High Frequency Temperature and Pressure Probe for Unsteady Compressible Flows," *Review of Scientific Instruments*, Vol. 54, No. 12.

Ng, W. G., and Epstein, A. H., 1985, "Unsteady Losses in Transonic Compressors," ASME *Journal of Engineering for Gas Turbines and Power*, Vol. 107, No. 2.

Owen, P. R., 1986, "Computational Simulation of Unsteady Flow in a Transonic Compressor Rotor," MIT GTL Report No. 189.

Paterson, R. W., and Weingold, H. P., 1984, "Experimental Investigation of a Simulated Compressor Airfoil Trailing Edge Flowfield," Paper No. AIAA-84-0101.

Prince, D. C., Jr., 1980, "Three-Dimensional Shock Structures for Transonic/Supersonic Compressor Rotors," *Journal of Aircraft*, Vol. 17, No. 1.

Squire, H. B., 1965, "The Growth of a Vortex in Turbulent Flow," *The Aeronautical Quarterly*, Vol. XVI, pp. 302–306.

Thompkins, W. T., Jr., and Usab, W. J., Jr., 1982, "A Quasi-Three-Dimensional Blade Surface Boundary Layer Analysis for Rotating Blade Rows," ASME *Journal of Engineering for Power*, Vol. 104, No. 2.

Wennerstrom, A. J., 1984, "Experimental Study of a High-Throughflow Transonic Axial Compressor Stage," ASME *Journal of Engineering for Gas Turbines and Power*, Vol. 106, pp. 553–560.

Wisler, D. C., Bauer, R. C., and Okiishi, T. H., 1987, "Secondary Flow, Turbulent Diffusion, and Mixing in Axial-Flow Compressors," ASME JOURNAL OF TURBOMACHINERY, Vol. 109, pp. 455–482.

APPENDIX

Two-Dimensional Vortex Wake Model

The rotor blade wakes have been modeled as modified ideal Karman vortex streets consisting of two staggered rectilinear rows of Rankine vortices of opposite sign in a uniform free-stream. The analysis is performed in the reference frame moving with the vortex cores, and a coordinate transformation is used to compute the flowfield, as would appear to a stationary probe.

The vortex street is modeled by summing the contributions of the two staggered rows of Rankine vortice. Each vortex consists of an inner and an outer region, the boundary of which is denoted as the core radius, r_o. The inner region consists of forced-vortex flow, while the outer region follows the irrotational flowfield of a classical Karman vortex street of point vortices. The addition of finite vortex cores is considered a more realistic assumption, since it avoids infinite velocities at the vortex centers and also allows for smoothly varying averaged wake profiles, as seen in the experimental data. Following Lamb, the complex velocity of single infinite row of equally spaced vortices of strength k and spaced a distance a can be written as

$$w(\zeta)'' = w_x'' - iw_y'' = \frac{-ik}{2a} \cot \frac{\pi z}{a} \tag{A1}$$

where $\zeta = x'' + iy''$. Here the (x'', y'') frame moves with the vortex cores and is fixed to the center of a vortex in either the upper or lower row. In this frame, the velocity components parallel and perpendicular to the direction of motion of the vortices are w_x'' and w_y'', respectively. The (x', y') frame also moves with the vortex cores, but is positioned at the centerline between the two rows of vortices. A third reference frame, (x, y), is fixed to the rotor blade trailing edge. The velocity components in the (x', y') and (x, y) frames are (w_x', w_y') and (w_x, w_y), respectively.

These components will be nondimensionalized with respect to the pressure-defect velocity W_p, which represents the velocity at the edge of an isolated vortex core and is related to the pressure drop from the free stream to the edge of an isolated core

$$W_p = k/2\pi r_o \tag{A2}$$

All lengths will be expressed with respect to the vortex spacing a, and the equations describing the velocity components of a single isolated row in the (x'', y'') frame are then

$$\bar{w}_{x_{\text{row}}}'' = \bar{k} \frac{\sinh 2\pi\bar{y}''}{\cosh 2\pi\bar{y}'' - \cos 2\pi\bar{x}''} \tag{A3a}$$

$$\bar{w}_{y_{\text{row}}}'' = \bar{k} \frac{\sinh 2\pi\bar{y}''}{\cosh 2\pi\bar{y}'' - \cos 2\pi\bar{x}''} \tag{A3b}$$

where we nondimensionalize as

$$\bar{w}_x'' = \frac{\bar{w}_x''}{W_p}, \quad \bar{w}_y'' = \frac{\bar{w}_y''}{W_p}, \quad \bar{x}'' = \frac{x''}{a}, \quad \bar{y}'' = \frac{y''}{a},$$

$$\bar{k} = \frac{k}{2aW_p}, \quad \bar{W}_i = \frac{W_i}{W_p}, \quad \bar{r} = \frac{r}{a}, \quad \bar{r}_o = \frac{r_o}{a}, \quad \bar{W}_\infty = \frac{W_\infty}{W_p}$$

To ensure that the velocity decays smoothly from the edge to the center of the vortex core, the velocity in the vortex core is obtained by subtracting the contributions of an isolated potential vortex from the velocity field of the row of vortices and adding the contributions of an isolated viscous core. The velocity components in a vortex core of positive circulation (lower row) are then

$$\bar{w}_x'' = \left[\bar{w}_{x_{\text{row}}}'' - \bar{w}_{x_{\text{pot}}}'' \right] + \bar{w}_{x_{\text{core}}}'' \tag{A4a}$$

$$\bar{w}_y'' = \left[\bar{w}_{y_{\text{row}}}'' - \bar{w}_{y_{\text{pot}}}'' \right] + \bar{w}_{y_{\text{core}}}'' \tag{A4b}$$

where

$$\bar{w}_{x_{\text{pot}}}'' = -\left(\frac{\bar{r}_o}{r}\right)\left(\frac{\bar{y}''}{\bar{r}}\right), \quad \bar{w}_{x_{\text{core}}}'' = -\left(\frac{\bar{y}''}{\bar{r}_o}\right)$$

$$\bar{w}_{y_{\text{pot}}}'' = -\left(\frac{\bar{r}_o}{\bar{r}}\right)\left(\frac{(\bar{x}'')_{\min}}{\bar{r}}\right), \quad \bar{w}_{y_{\text{core}}}'' = \left(\frac{(\bar{x}'')_{\min}}{\bar{r}_o}\right)$$

Here $(\bar{x}'')_{\min}$ is the axial distance to the center of the nearest vortex core. For a vortex core of negative circulation (upper row), the direction of the contributions due to the isolated vortex must be reversed.

The flowfield of the complete vortex street is now found by summing the velocity components of two isolated rows spaced h apart and staggered by $a/2$. Each row induces a motion in the opposite row, which results in motion of the entire vortex street. This motion, the induced velocity W_i, is found by solving for the velocity induced at the center of a vortex by the opposing row

$$\bar{W}_i = -\bar{k} \tanh\left(\pi \frac{h}{a}\right) \tag{A5}$$

If the vortex street is formed in a freestream of velocity, W_∞, then in the frame of reference fixed to the blades (x, y) the vortex street moves with velocity equal to $W_\infty + W_i$. In the (x', y') frames, the free-stream velocity is simply $(-W_i)$. The velocity components in the primed frame are then

$$\bar{w}_x' = \bar{w}_{x_{\text{upper row}}}'' + \bar{w}_{x_{\text{lower row}}}'' - \bar{W}_i \tag{A6a}$$

$$\bar{w}_y' = \bar{w}''_{\text{upper row}} + \bar{w}_{y_{\text{lower row}}}''$$

The velocity $|\bar{w}'|$ is then

$$|\bar{w}'| = \sqrt{(\bar{w}_x')^2 + (\bar{w}_y')^2} \tag{A7}$$

Given a location in the (x', y') frame, the upper and lower velocity components can be calculated from equation (A3) by a simple coordinate transformation and by noting that the sign of k changes. For the upper row,

$$\bar{x}' = \bar{x}' - \frac{1}{2}, \quad \bar{y}'' = \bar{y}' - \frac{h}{2a}$$

and, for the lower row,

$$\bar{x}'' = \bar{x}', \quad \bar{y}'' = \bar{y}' + \frac{h}{2a}$$

Since the vortex cores move at a velocity of $(W_\infty + W_i)$, the parallel and perpendicular velocity components in the frame relative to the rotor blades (x, y) are then

$$\bar{w}_x = \bar{w}_x' + (\bar{W}_\infty + \bar{W}_i) \tag{A8a}$$

$$\bar{w}_y = \bar{w}_y' \tag{A8b}$$

The blade relative velocity is then

$$|\bar{w}| = \sqrt{(\bar{w}_x)^2 + (\bar{w}_y)^2} \tag{A9}$$

In the frame of reference moving with the vortices (x', y') the flow is steady and the free-stream velocity is equal to $(-W_i)$. For the cases considered herein, it is sufficient to assume constant density since the maximum Mach number in this frame of reference is approximately 0.10. The pressure is expressed in terms of a pressure coefficient based on the pressure-defect velocity W_p,

$$\bar{C}_p \equiv \frac{(p - p_\infty)}{\rho_\infty W_p^2} \tag{A10}$$

Thus, in the irrotational, inviscid regions outside of a vortex core, $r > r_o$, the pressure is found from Bernouilli's equation

$$\bar{C}_p = -\frac{1}{2}\left[(|\bar{w}'|)^2 - \bar{W}_i^2\right] \tag{A11}$$

Within a vortex core, the radial momentum equation is integrated across the core. The inner-and outer-pressure solutions are matched at r_o with the variation in velocity accounted for by the average of the velocity squared around the circumference. The pressure at the center of the vortex is then expressed in terms of this average velocity, $\langle |\bar{w}_o^2| \rangle$, and the pressure coefficient inside the vortex cores, $r < r_o$,

$$\bar{C}_p = -\frac{1}{2}\left\langle |\bar{w}_o^2| \right\rangle \left[2 - \left(\frac{r}{r_o}\right)^2 \left(2 - \frac{|\bar{w}_o^2|}{\left\langle |\bar{w}_o^2| \right\rangle} \right) \right] + \frac{\bar{W}_p^2}{2} \tag{A12}$$

The average of the velocity squared at the vortex core, $r = r_o$, can be found numerically given the vortex street geometry. For a typical von Karman-like street ($h/a = 0.28$), $\langle |\bar{w}_o^2| \rangle$ is nearly equal to unity (1.002). For values of $r = r_o$, $|\bar{w}_o|$ is evaluated at a point on the circumference ($r = r_o$) where a ray from the center of the vortex through the point in question intersects the edge of the core at $r = r_o$.

Using the Model

The two-dimensional vortex model was utilized in the following manner. To begin with, h/a and W_p/W_∞ were guessed (classic von Karman vortex street values could be used to start). The ratio r_o/h was set constant and equal to 0.5 following the arguments of Gertz (1986).

Now, the nondimensional vortex strength, k, can be calculated using the nondimensional version of equation (A2). The induced velocity of the vortex street W_i is then calculated with equation (A5). Equations (A3) now give the velocity components, $(\bar{w}_x'')_{\text{row}}$ and $(\bar{w}_y'')_{\text{row}}$, of an isolated row of vortices, which are then used in equations (A4) to calculate the velocity distribution in the vortex core frame, $\bar{w}_x''$ and $\bar{w}_y''$. This is then transformed into the frame of the vortex street with equation (A6), which is in turn transformed into the blade relative frame using equations (A8). We now have the velocity field everywhere in the blade relative frame. $|\bar{w}_o|$ can be calculated with equation (A9) at $r = r_o$, the square of which can then be averaged about the circumference of the vortex to yield $\langle |\bar{w}_o^2| \rangle$. The pressure coefficient, C_p, is now calculated with equation (A12).

W_∞ can be calculated from the measured M_∞ and T_∞; therefore, since W_p/W_∞ is known (it was guessed), the static pressure, p is given by equation (A9) (p_∞ was measured). Alternately, W_∞ can be calculated from a standard data match (streamline curvature fit) to the time averaged measurements. (These two approaches yielded similar answers.)

We now have a complete description of the flowfield and can calculate the laboratory frame total pressure history. This is then compared to the measurement (Fig. 10) and the guesses for h/a and W_p/W_∞ revised until the model prediction and measurements agree. The values that best fit the data are presented in Table A.1.

Table A.1 Two-dimensional vortex model parameters that fit data

Spanwise Position, R/R_t	0.95	0.88	0.81	0.75
h/a (±0.03)	0.66	0.57	0.48	0.40
W_p/W_∞ (±0.02)	0.15	0.30	0.38	0.52

In the body of the paper, $w(x, y)$—the two-dimensional model blade relative velocity derived in this appendix—is referred to as $\mathbf{w}(R, \theta, z)$ inside the vortex cores (r/r_o) and as $\mathbf{W}(R, \theta, z)$ outside the cores $(r > r_o)$.

Table A.1 Two-dimensional vortex model parameters that fit data

Spanwise Position, R/R_t	0.95	0.88	0.81	0.75
h/a (±0.03)	0.66	0.57	0.48	0.40
W_D/W_∞ (±0.02)	0.15	0.30	0.38	0.52

In the body of the paper, $w(x, y)$—the two-dimensional model blade relative velocity derived in this appendix—is referred to as $\mathbf{w}(R, \theta, z)$ inside the vortex cores (r/r_o) and as $\mathbf{W}(R, \theta, z)$ outside the cores $(r > r_o)$.

DISCUSSION

N. A. Cumpsty[2]

The authors are to be congratulated on a very nice paper based on some most impressive measurements. The success of the high response concentration probe in obtaining information about the spread of tracer gas at blade passing frequency is quite extraordinary. The vortex model is extremely elegant and appealing, which may make people attribute more of the mixing to it than it actually produces. It needs to be remembered that only about 15 percent of the spread radially outward is attributable to the mechanism of radial transport along the vortex core.

Apart from wishing to compliment the authors, one of my principal objects is to express surprise that the level of mixing across their transonic rotor is so similar to that measured across the stator in a multistage compressor. Li and Cumpsty (1991a, 1991b) show that for a subsonic compressor rotor the mixing across the rotor near midspan is much lower when there are no upstream blades than when there are; when there are upstream blades the level of mixing is similar to that across stators in multistage compressors. The high level of mixing across the isolated transonic rotor row may be related to an important aspect of transonic rotors and, although it is mentioned in the text, this should, I believe, be stressed in the conclusions.

Although it is always nice to see one's name in print when results agree with what one proposed, it is not really correct to refer to the Gallimore-Cumpsty *model*. All that was put forward was a simple empirical scaling with the subsidiary assumptions that a uniform level of mixing coefficient across the span seemed as precise as one could specify, based on the data then available. (It has also been shown that adequate prediction of the flow can be obtained when a spanwise uniform level is introduced.)

Figure 14 shows the distribution of measured efficiency compared with the estimates obtained by assuming two-dimensional shock losses and viscous losses. There are good reasons for suspecting that this method of estimating losses is seriously flawed since the principal mechanism of loss is probably the shock boundary layer interaction (Hah and Wennerstrom, 1991). Very much higher losses can be generated at supersonic inlet velocities than can be accounted for in terms of even a normal shock (Freeman and Cumpsty, 1989).

[2]Whittle Laboratory, University of Cambridge, Cambridge CB3 ODY, United Kingdom.

References

Freeman, C., and Cumpsty, N. A., 1989, "A Method for the Prediction of Supersonic Compressor Blade Performance," ASME Paper No. 89-GT-326; to be published in the *AIAA Journal of Propulsion and Power*.

Hah, C., and Wennerstrom, A. J., 1991, "Three-Dimensional Flow Fields Inside a Transonic Compressor With Swept Blades." ASME JOURNAL OF TURBOMACHINERY, Vol. 113, this issue.

Li, Y. S., and Cumpsty, N. A., 1991a, "Mixing in Axial Flow Compressors: Part 1—Test facilities and Measurements in a Four-Stage Compressor," ASME JOURNAL OF TURBOMACHINERY, Vol. 113, this issue.

Li, Y. S., and Cumpsty, N. A., 1991b, "Mixing in Axial Flow Compressors: Part 2—Measurements in a Single Stage Compressor and Duct," ASME JOURNAL OF TURBOMACHINERY, Vol. 113, this issue.

Authors' Closure

The authors would like to thank Professor Cumpsty for his kind remarks. In regard to the relatively high mixing rates observed in our transonic rotor compared to the low-speed compressor of Li and Cumpsty, we agree with Professor Cumpsty that the difference may be important and was somewhat surprising. We offer the following observations. The turbulence level measured one blade span upstream of this rotor was 0.02 percent (using Li and Cumpsty's definition), which is quite low. However, the level of high-frequency unsteadiness within transonic rotor passages has been shown to be quite high (Gertz, 1986) and this level may quite likely be responsible for the larger mixing rates observed in a transonic compressor relative to low-speed machines. A major point that we have tried to make is that much of the unsteadiness usually regarded as turbulence can in fact consist of deterministic phenomena, including shock wave motion (Ng and Epstein, 1985) and vortex shedding (Epstein et al., 1988). Vortex shedding seems to be particularly sensitive to boundary layer separation, which is less likely on well-designed low-speed blading than for transonic equivalents, since shock-induced separation is not a concern. We believe that vortex shedding and flow in separated regions were important mechanisms for radial transport in the stage we measured.

In regard to the spanwise loss distribution: Certainly the approach of Kerrebrock (1980) is the simplest possible one and, as Dr. Cumpsty points out, more accurate techniques exist. While these other approaches may predict higher losses better in the supersonic tip sections, they do not simultaneously predict lower losses near the supersonic hub. Our principal point here is only that spanwise mixing can redistribute entropy along the span, altering the efficiency distribution. We hope this point is not lost due to the first-order nature of Kerrebrock's original estimate.

Temporally and Spatially Resolved Flow in a Two-Stage Axial Compressor: Part 1—Experiment

R. C. Stauter

R. P. Dring

F. O. Carta

United Technologies Research Center,
East Hartford, CT 06108

The fluid dynamics of turbomachines are extremely complex, due in part to the aerodynamic interactions between rotors and stators. It is necessary to acquire fluid dynamic data that reflect the interactive nature of a turbomachine to correlate with the fluid dynamics predicted from modern analyses. The temporal and spatial variations in the midspan aerodynamics of the second stage of a two-stage compressor have been studied with a two-component LDV system. Spatial variations were examined by traversing the LDV probe volume through a dense matrix of both axial and circumferential positions, while temporal resolution was achieved by acquiring all data as a function of the instantaneous rotor position. Hence, the data set reveals rotor and stator wake structure and decay in both the stationary and rotating frames of reference. The data also compared very favorably with extensive pneumatic measurements previously acquired in this compressor. In Part 2 of the paper, the data are used in the assessment of a prediction of the flow in the compressor using a time-accurate, thin-layer, two-dimensional Navier–Stokes analysis.

Introduction

The flow field within the airfoil rows of a multistage axial compressor is influenced by many different aerodynamic phenomena, both inviscid and viscous, interacting in a very complex fashion. The throughflow has significant spatial variations; additionally there are tip clearance flows, secondary flows, endwall and airfoil surface boundary layers, and impinging wakes. Furthermore, the relative motion between the rotors and stators means that these are all fundamentally unsteady phenomena.

Historically, turbomachine flow fields have been measured as if they were steady flow fields (e.g., Dring et al., 1982, 1983; Joslyn and Dring, 1985; Cyrus, 1986, 1988; Dong et al., 1987; Wisler et al., 1987), which was adequate for earlier designs. However, increasing demands on gas turbine engine performance, weight, and size have necessitated the use of higher airfoil loading, lower aspect ratios, and closer axial airfoil row spacings. These trends have amplified the unsteady effects of interaction because the higher loading causes the strength of airfoil wakes impinging on succeeding airfoil rows to increase. Closer airfoil row spacing means that these stronger airfoil wakes are not able to decay as much before encountering the succeeding airfoil row, and that the potential field effect of the succeeding row extends farther into the preceding row (and vice versa); hence, the unsteady interaction effects between the rotor and stator potential fields are much stronger. In addition to their effect on compressor aerodynamic performance, these unsteady effects also induce significant fluctuating forces on the airfoils, which may cause or accelerate airfoil structural failure.

The compressor designer must have accurate predictive analyses to design compressors that satisfy current and future demands for performance and durability. Various computer algorithms are being proposed to satisfy this need. Some of these methods attempt to compute the fundamental, large-scale unsteadiness and nonuniformity of a turbomachine flow field, e.g., Rai (1987), Rai and Madavan (1988), and Gundy-Burlet and Rai (1989). Other methods attempt to extend the Reynolds averaging and correlation strategy, used to model the small-scale (turbulent) unsteadiness in any method, to all larger-scale fluctuations and nonuniformities, e.g., Adamczyk (1985) and Adamczyk et al. (1986). In any case, corresponding time-accurate data with high spatial resolution are required to assess the predictive performance of such computer codes. Such data must represent accurately the time-varying nature of the flow field and they should be consistent with previous data acquired under a steady-flow assumption, when reduced to a time-averaged basis. The acquisition and evaluation of such data, and their comparison with earlier time-average measurements, are the subject of Part 1 of this paper. In Part 2, Gundy-Burlet et al. (1991) use the data in the assessment of a prediction of the flow in the compressor, which uses a time-accurate, thin-layer, two-dimensional, Navier–Stokes analysis.

Experimental Facility and Instrumentation

The experiment was conducted using a two-stage axial compressor model installed in the United Technologies Research

Contributed by the International Gas Turbine Institute and presented at the 35th International Gas Turbine and Aeroengine Congress and Exposition, Brussels, Belgium, June 11–14, 1990. Manuscript received by the International Gas Turbine Institute, January 15, 1990. Paper No. 90-GT-259.

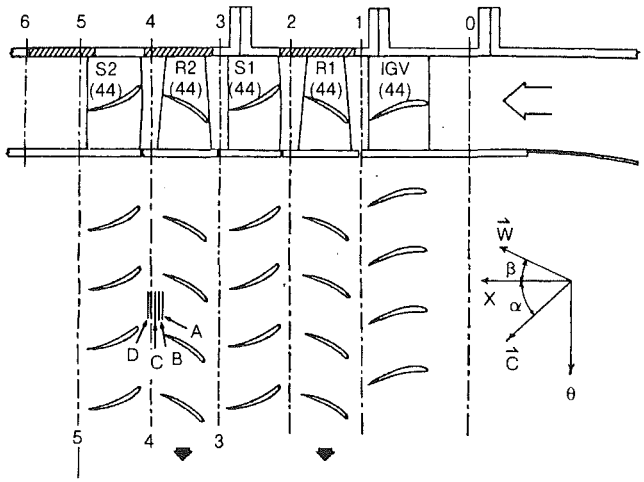

Fig. 1 Large-Scale Rotating Rig 2 flow geometry and measurement stations

Center Large-Scale Rotating Rig 2 (LSRR2). The two-stage model has previously been exhaustively studied with pneumatic pressure instrumentation including full-span airfoil pressure distributions and downstream traverse measurements for both the stators and the rotors, and also surface flow visualization. Hence, the LSRR2 is well documented and there exists a large database (Dring et al., 1982, 1983; Joslyn and Dring, 1985) against which to compare the time average of the data from the present time-accurate experiment.

The inlet flow to the LSRR2 is drawn from ambient air and the flow field throughout the facility is essentially incompressible. The two-stage compressor model has a 5 ft (1.52 m) tip diameter and a hub/tip ratio of 0.8. The midspan wheel speed (at $r/R = 0.9$) is $U_m = 153$ ft/sec (46.7 m/s) and the nominal design flow coefficient is $\bar{C}_x/U_m = 0.510$. The flow path, depicted in Fig. 1, consists of a row of inlet guide vanes (IGV) followed by two similar stages: Rotor 1, Stator 1, Rotor 2, and Stator 2. The only difference between the stages is that the Rotor 1 stagger angle is closed 3 deg more than that of Rotor 2. The IGV, rotor, and stator rows each consist of 44 airfoils.

The current measurement technique used a two-component laser-Doppler velocimeter (LDV) to measure the axial and circumferential velocity components on a cylindrical surface at midspan. In the LDV technique used, four beams are split off from an argon-ion laser (two blue beams for one velocity component and two green for the other) and are crossed at a point in space termed the probe volume. For the present experiment, this ellipsoidal volume was 0.024 in. long and 0.0033 in. in diameter (0.6 mm × 0.084 mm). The LDV configuration employed a Bragg cell on each channel to eliminate fringe bias. The Doppler shifts for the blue and green beam pairs due to the velocity of particles transiting the probe volume are measured, and the corresponding particle velocity is calculated from the geometry of the beam crossing. The LDV requires the presence of particles in the flow field from which laser light is scattered. Such particles must be small enough to follow the local flow aerodynamically, yet large enough to scatter sufficient light for detection. For this experiment the flow field was seeded with plastic microspheres (1.0 μm diameter, 1.05 specific gravity, and very uniformly sized). These were introduced into the flow field by creating an alcohol suspension and atomizing the suspension in front of the facility inlet. The alcohol evaporated, leaving the particles in the airstream. Dring (1982) has performed a Stokes drag analysis of particle motion for a cascade-type flow field. Such seedant particles have a Stokes number of less than 0.002, resulting in a maximum deviation of the particle velocity from the fluid velocity of 0.13 percent, and a flow angle error of less than 0.1 deg.

All particle velocity pairs (axial and circumferential velocity) were tagged with the instantaneous rotor position by means of a data word derived from an optical shaft encoder. The encoder hardware was configured so that there were 64 circumferential increments, or bins, across each rotor passage. As the data were acquired, they were placed into the appropriate bin corresponding to the rotor passage position at the instant of acquisition. The data samples acquired from all 44 rotor airfoil passages were overlaid into the same 64 bins resulting in the "average" rotor passage. It is "average" in the sense that it consisted of data acquired over many rotor revolutions and over 44 rotor passages; however, it is time accurate in that the data were phase-locked to the rotor position. The ensemble-average and rms velocities were calculated for each bin. Hence, the phase-locked-average velocity (time-accurate) of the average rotor passage was obtained for each LDV probe volume position.

This sorting and averaging procedure is different from that used by Sudar et al. (1987) in that their procedure maintained the identity of the rotor passage from which each data sample was acquired in addition to the bin position within the rotor passage. Only after computing the ensemble statistics was their "average" rotor passage flow field constructed. Because the present experiment involved equal numbers of airfoils in each row, the two procedures are essentially equivalent, assuming no passage-to-passage geometry variations or other flow field asymmetries that would preclude periodicity.

Throughout the course of this paper several other types of averages will be used. For the sake of clarity, they are defined now so that the significance and uniqueness of each average will be clear. The "phase-locked-average of the average rotor passage" is described immediately above. The "time average" in a given frame of reference (rotating or stationary) is what a slow-response probe affixed to that frame would measure. Temporal variations experienced by the probe are averaged out. For example, a time average in the frame of reference of an upstream airfoil row would show the wake (or other spatial variation) due to that airfoil row. A time average in the frame of reference of a downstream airfoil row would show the potential field (or other spatial variation) due to that airfoil row. Furthermore, the time average of data in frame of ref-

Nomenclature

B_x = airfoil axial chord
C = velocity in absolute frame
LE = leading edge
PS = pressure surface
r = radial coordinate, or rotor
s = stator
SS = suction surface
R = tip radius
TE = trailing edge
U_m = rotor wheel speed at midspan
W = velocity in relative frame
x = axial coordinate
α = flow angle in absolute frame from axial
β = flow angle in relative frame from axial
δ = wake parameter
δ_o = reference wake parameter
δ^* = δ/δ_o
η = $\Delta x/B_{xr}$
Θ = circumferential coordinate
$\Delta(\ )$ = increment in $(\ )$
$(\ )_\infty$ = undisturbed, or free-stream quantity
$\overline{(\ )}$ = averaged quantity

Table 1 Significant axial locations

Location	PP*	LDV	x (in)	$\Delta x/B_x$ (%)	$\eta = \Delta x/B_{xr}$
Rotor 2 TE			11.863	0.0 (B_{xr})	0.000
A		√	11.92	1.9	0.019
B		√	12.12	8.5	0.085
C		√	12.32	15.1	0.151
4	√	√	12.645	25.9	0.259
D		√	12.89	34.0	0.340
Stator 2 LE			13.310	47.9	0.479
Stator 2 TE			16.620	0.0 (B_{xs})	1.575
5	√	√	17.20	17.8	1.767

* Pneumatic Probe data

erence "A" results in the "spatial average" of frame "B" (i.e., spatial variations in frame "B" are averaged out), and vice versa.

Table 1 lists the six axial locations of the LDV measurement stations (A, B, C, 4, D, 5), as well as airfoil leading and trailing edge values, for the present experiment. Five locations are concentrated in a finely resolved array between the Rotor 2 trailing edge and the Stator 2 leading edge. The sixth location (Station 5) is aft of Stator 2. The axial stations labeled 3, 4, and 5 in Fig. 1 are those at which the flow field has been previously studied with pneumatic instrumentation. Thus, there are two axial locations (4 and 5) at which both pneumatic and LDV measurements have been made.

At each of the six axial locations indicated in Table 1, LDV data were acquired in an array of 25 circumferential locations. The circumferential array was arranged for a traverse of the probe volume across one stator passage (plus a circumferential overlap of three locations). The circumferential arrays were not of uniform density. There was a higher circumferential concentration of measurement locations clustered around the stator leading edge. At each measurement location approximately 25,000 data samples were acquired and sorted into the 64 bins across the "average" rotor airfoil passage. Then the probe volume was circumferentially traversed to the next location and the process repeated. Therefore, the data acquired describe the velocity as a function of both the rotor position and the stator position. Hence, the velocities can be time averaged and/or spatial averaged in either frame of reference. Because all the stationary and rotating rows have 44 airfoils, velocity data reflecting any flow field unsteadiness generated or modulated by the rotating hardware are phase locked to the rotor position. Likewise, flow field unsteadiness generated or modulated by the stationary hardware is locked to the stator position.

Results

The experiment yielded the axial and circumferential velocity components at midspan at five axial locations between Rotor 2 and Stator 2, and at one axial location aft of Stator 2. All data were acquired with the compressor operating at its nominal design flow coefficient of $\bar{C}_x/U_m = 0.51$. These data are both temporally resolved (rotor position relative to the probe volume) and spatially resolved (stator position relative to the probe volume). Hence, the velocity data can be considered as being functions of two independent variables: rotor pitch location and stator pitch location. They have been plotted as a surface against those variables in three-dimensional plots. The data from Station 4 are presented in Figs. 2(*a*) and 2(*b*) for the axial and circumferential velocity components, respectively. Figure 2(*a*) (the axial velocity component) has extensive annotation, particularly in the relation of stator to rotor, to assist the reader in the interpretation of this figure as well as the several related figures that follow. In these plots, all the velocity traces have been shifted to cause the wake to line up

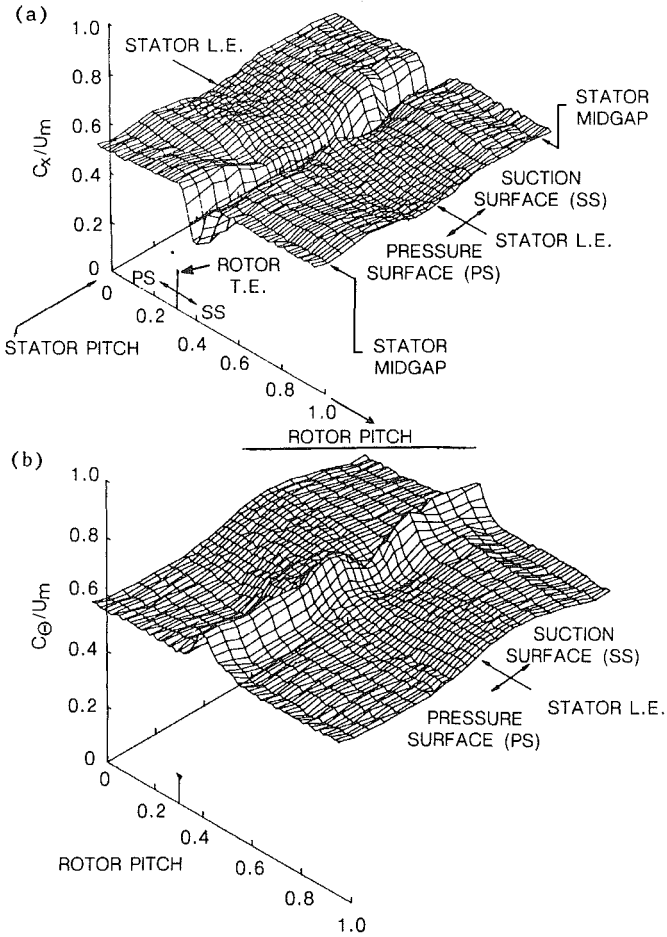

Fig. 2 (*a*) Axial velocity, C_x, and (*b*) circumferential velocity, C_Θ, at Station 4

at a single value on the rotor passage axis. This causes the data framework to be equivalent to circumferentially indexing the stators past the LDV probe volume rather than traversing the probe volume past the stators as was done. These data illustrate the interaction between the rotating and the stationary flow fields. This is particularly evident in the plot of the circumferential velocity (Fig. 2*b*), where the rotor wake appears as an excess in the absolute circumferential velocity; however, this excess is diminished significantly near the stator leading edge toward the suction surface.

The time-accurate LDV data between Rotor 2 and Stator 2 have been transformed to the rotor frame of reference. The carpet plot of the relative velocity vector, W, is presented in Fig. 3 (inverted to show wake detail). These data have also been time averaged to simulate a slow-response probe in the rotor frame. The time-averaging process in this frame involves averaging each individually ensemble-averaged velocity over the stator pitch for each constant value of rotor pitch position. This eliminates the dependence on stator position from the data. Hence, data reduced this way represent the stator-spatial-averaged rotor flow field, or equivalently, the rotor-time-averaged flow field, i.e., the unsteadiness experienced in the rotor frame due to stator effects has been averaged out.

The time-averaged rotor flow fields at the five measurement stations between Rotor 2 and Stator 2 can be compared to examine rotor wake decay. Figure 4(*a*) presents the five wake shapes as well as their circumferential displacement in the rotor frame of reference. As could be expected, the wake nearest the trailing edge (Station A) is initially sharp and deep, and it then decays and broadens out by nearly 50 percent of its original depth in less than a third of a rotor axial chord length

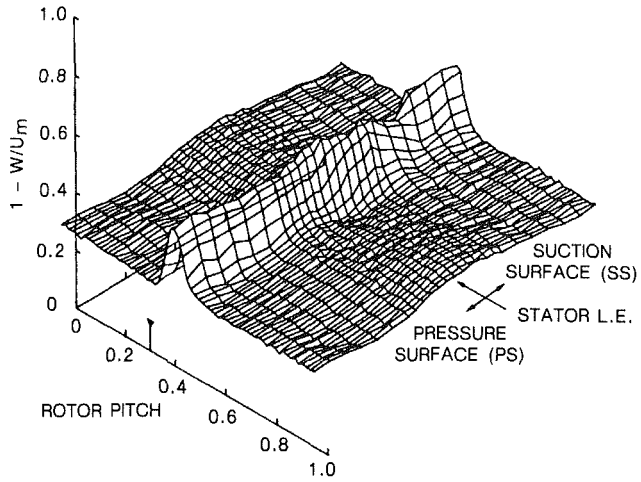

Fig. 3 Velocity vector, W, in rotating frame at Station 4

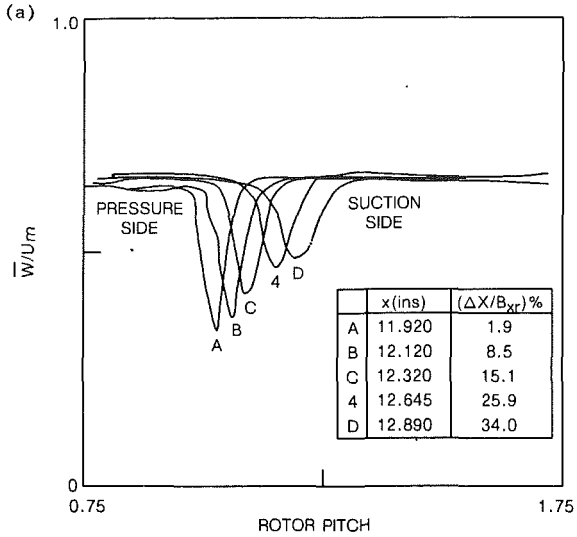

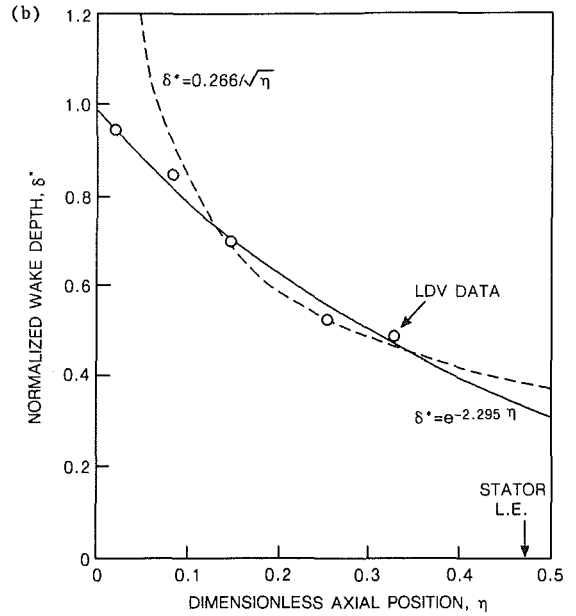

Fig. 4 (a) Rotor wake profiles between Rotor 2 and Stator 2; (b) rotor wake decay correlation

(B_{xr}). Nevertheless, a significant rotor wake probably still exists when it encounters the downstream stator leading edge at 48 percent B_{xr}.

In an effort to quantify the wake decay and examine this supposition, curve-fitting procedures were used to characterize the observed decay in wake depth. (No effort was made at this time to examine wake profiles.) At each axial location, the difference between the free-stream velocity and the minimum wake velocity was computed and defined as

$$\delta = (\overline{W}/U_m)_\infty - (\overline{W}/U_m)_{\min} = 0.65 - (\overline{W}/U_m)_{\min} \quad (1)$$

where 0.65 is the value of the undisturbed flow in Fig. 4(*a*). A dimensionless axial coordinate, η, was also defined, based on the axial distance aft from the Rotor 2 trailing edge, Δx, normalized by the rotor airfoil chord, B_{xr}, or

$$\eta = \Delta x/B_{xr} \quad (2)$$

(see Table 1). First, the difference parameter, δ, was plotted versus η on a semi-log scale, and it was found that the five measured values were distributed nearly linearly, implying an exponential wake decay. A least-squares fit yielded the expression

$$\delta^*(\eta) = \delta(\eta)/\delta_o = e^{-2.295\eta} \quad (3)$$

where $\delta_o = 0.342$ is the extrapolated value at $\eta = 0$. This is plotted as a solid line in Fig. 4(*b*). It is seen that the use of this exponential decay model appears adequate in the rotor wake near field, especially immediately behind the trailing edge. Next the Schlichting (1968) square root decay of a two-dimensional wake was matched to the normalized data over the range of $0.147 \leq \eta \leq 0.330$, yielding a proportionality constant of 0.266 and the equation

$$\delta^*(\eta) = 0.266(\eta)^{-1/2} \quad (4)$$

which is plotted as a dashed line. This also models most of the measured points but is obviously unbounded at the trailing edge. Furthermore, in the power law correlation as used here, the normalized wake parameter, δ^*, is based on the trailing edge reference value ($\delta_o = 0.342$), obtained above from the exponential extrapolation to $\eta = 0$, which, of course, is inconsistent with the unbounded functional behavior of the inverse power law near $\eta = 0$. Note also that this reference value of δ_o implies a wake depth at the rotor trailing edge of 52 percent of the free-stream velocity.

The question must be raised as to how these time-accurate data compare, when reduced to the time-average, to the corresponding time-average pneumatic data. Pneumatic measurements taken in one frame of reference with a slow-response pneumatic probe are unable to capture the time-varying aspects of the flow field due to the airfoils in the other frame sweeping past. For example, the previously acquired pneumatic data (cf. Dring et al., 1982, 1983; Joslyn and Dring, 1985) between Rotor 2 and Stator 2 at Station 4 were taken in the rotor frame of reference. A probe attached to the rotor hub was used and it was traversed circumferentially behind the rotor. Thus, the fluctuations in the flow due to the stationary field experienced by the probe sweeping past the stators were not captured; the measurement represented some average of these spatially dependent fluctuations, i.e., a stator-spatial-average value. Furthermore, the time-averaged velocities measured in this way are in the rotor frame of reference.

The rotor-transformed and time-averaged LDV data have been compared with the corresponding pneumatic probe data. As indicated above, treating the data in a time-averaged manner relative to the rotor ignores the flow field variations due to the stationary field. Upper and lower bounds on the average rotor wake signature (cf. Fig. 4*a*) due to such variations can be established by determining the maximum and minimum values of W over the stator pitch (cf. Fig. 3) for each location relative to the rotor. Of course, this process is analogous to

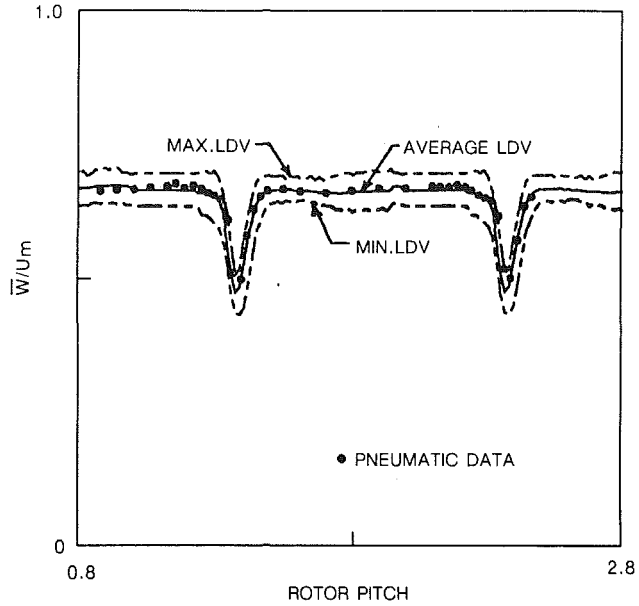

Fig. 5 Rotating-frame pneumatic probe data compared with rotor-time-averaged LDV data at Station 4; relative velocity vector $\overline{W}$

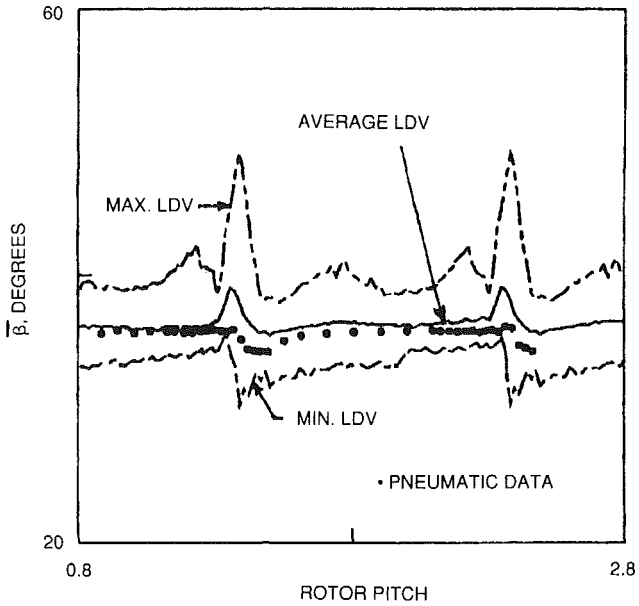

Fig. 6 Rotating-frame pneumatic probe data compared with rotor-time-averaged LDV data at Station 4; relative flow angle $\bar{\beta}$

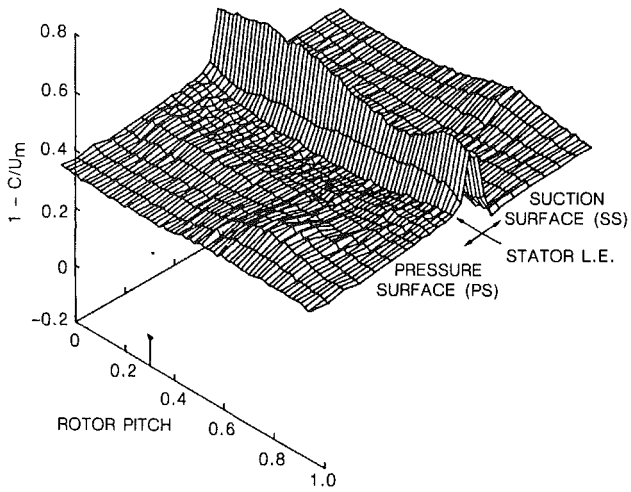

Fig. 7 Velocity vector, C, in stationary frame at Station 5

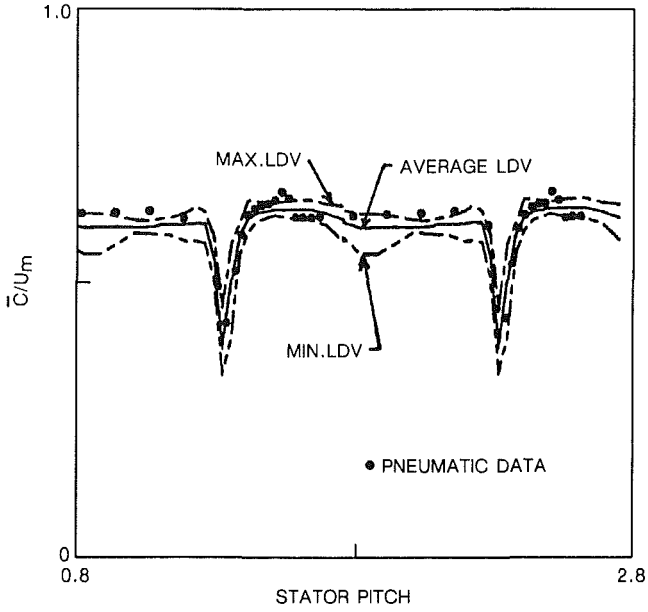

Fig. 8 Stationary-frame pneumatic probe data compared with stator-time-averaged LDV data at Station 5; absolute velocity vector C

the method used to obtain the time-average rotor wake signature, i.e., by averaging the W curves obtained for each location relative to the rotor. The results of this exercise are presented in Fig. 5 for Station 4 in which the LDV rotor exit velocity band (maximum, time-average, minimum) is plotted twice to cover two rotor passages while the pneumatic data, which were acquired in a traverse across nearly two rotor passages, are shown as symbols. Figure 6 presents corresponding results for the relative flow angle $\bar{\beta}$. It can be seen that the pneumatic data are remarkably close to the time-averaged LDV relative velocity profile ($\overline{W}/U_m$), but they are slightly low for the time-average relative angle profile ($\Delta\bar{\beta} \simeq 1$ deg). The difference is well within the combined uncertainties for the two experiments. The fluctuations in flow angle are significantly greater in the LDV data than in the pneumatic data. This may be partially due to the inability of an intrusive pneumatic probe of finite size to give an accurate flow angle reading in a wake shear flow. (The probe diameter was 2.3 percent of the rotor pitch.)

The absolute velocity aft of Stator 2 (Station 5 of Fig. 1) is presented in Fig. 7 (inverted to show wake detail). A similar maximum, minimum, and time-averaging process has been executed on these data, except in this case it was performed in the stator frame of reference. The resulting band is presented in Fig. 8, plotted twice to cover two stator passages. As before, the pneumatic data, which were acquired in the stationary frame in a traverse over two stator passages, are presented as symbols. Figure 9 presents the corresponding results for the absolute flow angle $\bar{\alpha}$. The pneumatic data for flow speed are in relatively good agreement with the LDV data. However, the flow angle data generally differ by about 3 deg ($\Delta\bar{\alpha} \simeq 3$ deg). Analysis of the pneumatic five-hole probe data has been ongoing since about 1984. It has been consistently observed that while the pneumatic probe data taken in the rotating frame (aft of Rotor 2) agreed closely with the measured inlet mass flow (error less than 1 percent), the probe data taken in the stationary frame (aft of Stators 1 and 2) were consistently higher than the measured inlet mass flow (error $\simeq$ 2–3 percent).

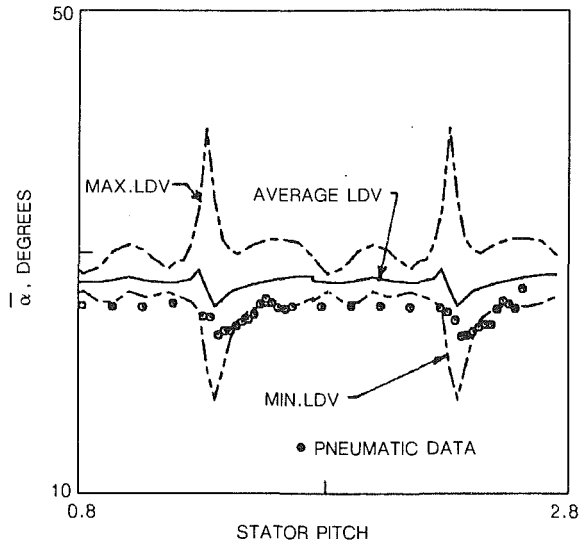

Fig. 9 Stationary-frame pneumatic probe data compared with stator-time-averaged LDV data at Station 5; absolute flow angle $\bar{\alpha}$

The observed difference between the averaged angles from the LDV and the pneumatic probe data (27.5 and 25.1 deg, respectively) comes very close to explaining this inconsistency in mass flow. For a fixed flow speed, the larger angle indicated by the LDV data suggests a decrease in mass flow of 2.1 percent, and this corresponds closely to the difference in measured flows. The pneumatic data exhibit little change in $\bar{\alpha}$ across the stator wake for the same reason as described for Fig. 6.

The extrapolations of both rotor wake correlations (cf. Fig. 4*b*, and equations (3) and (4)) to the Stator 2 leading edge, at $\eta = 0.479$, yield a wake defect that is still more than one-third of the defect nearest the rotor trailing edge ($\eta = 0.019$), which supports the earlier supposition of a significant wake encounter with the downstream stator leading edge. However, it should be noted that in a real machine of modern design, the axial gap spacing is likely to be less by a factor of two, so that there will likely be significantly stronger wakes impinging on the leading edges of the downstream airfoil row.

Extrapolating the rotor wake correlations further to Station 5 (aft of Stator 2 in Fig. 1) yields $\eta = 1.767$ and δ^* (1.767) $= 0.017$ for the exponential fit, and $= 0.20$ for the square-root fit; i.e., the exponential wake defect would decay to less than 2 percent of the δ_o value by the time it reaches Station 5, whereas the square-root defect would still retain as much as 20 percent of the δ_o value. On the basis of the measurements made at Station 5, which appear to show no remnants of the upstream rotor wake (except within the stator wake, which will be further discussed below), the exponential fit is more consistent with the data. However, further experimental results are needed before proposing this as a generalized model of wake decay.

Both Figs. 6 and 9 show that the LDV data have much larger maximum-minimum values in their respective wakes as compared to the regions between wakes. It was observed that, particularly in the LDV data aft of Stator 2 (e.g., Fig. 7), the presence of the stator airfoil seems to interfere with the decay of the wakes from the upstream rotor row, thus preserving the velocity fluctuations relative to the stator. This is consistent with the observations of Kerrebrock and Mikolajczak (1970). Hence, the large increase in the maximum-minimum values in the Stator 2 wake region (cf. Fig. 9) would represent Rotor 2 wake segments. Accordingly, the increase in the maximum-minimum values in the Rotor 2 wakes (cf. Fig. 6) would represent the Stator 1 wake. Why this effect appears so much

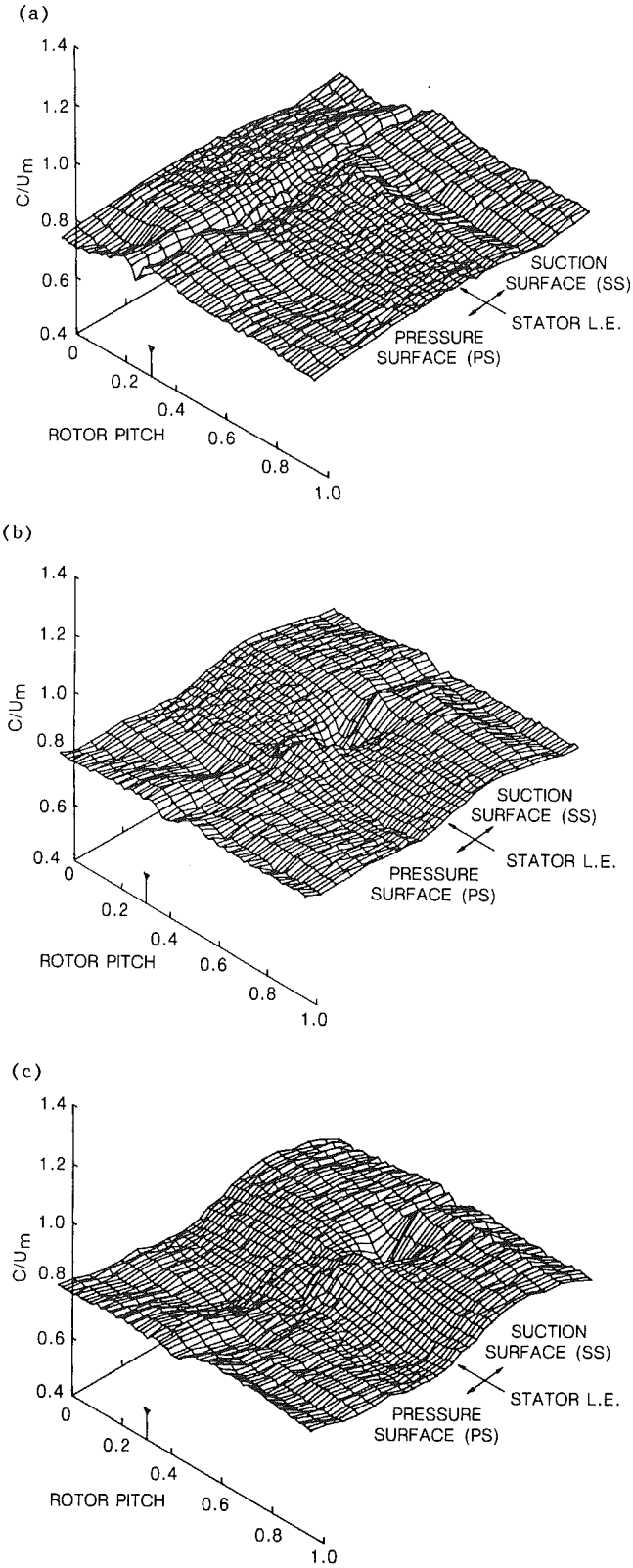

Fig. 10 Absolute velocity vector, *C*, between Rotor 2 and Stator 2 at (*a*) Station A, (*b*) Station 4, and (*c*) Station D

stronger in the flow angle data than in the flow speed data is not clear.

The effect of the Stator 2 upstream potential field was also investigated by examining both the time-resolved and the time-averaged velocity in the stationary frame. Figure 10 presents

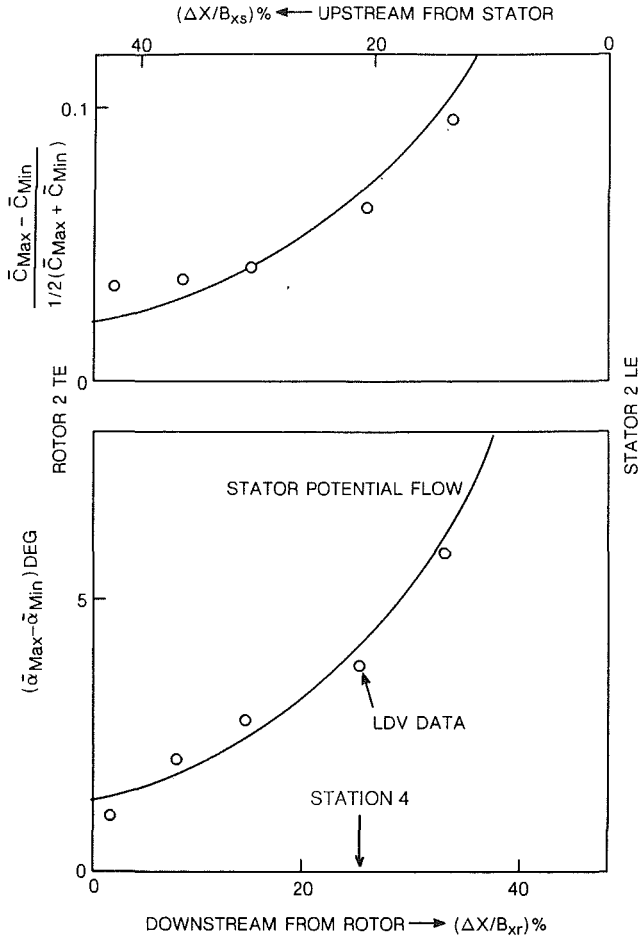

Fig. 11 LDV data compared with cascade potential analysis between Rotor 2 and Stator 2

the absolute velocity magnitude at three axial locations between Rotor 2 and Stator 2. Significant interactions between the rotating and stationary fields are seen in the neighborhood of the rotor wake and the stator leading edge. The question is raised as to whether the interaction effects shown in Fig. 10 represent the Stator 1 wake segments collecting at certain spatial locations in the Rotor 2 wake as suggested above, or if they are the result of the Stator 2 potential field affecting the Rotor 2 wakes (and the Stator 1 wake segments or any other upstream-generated unsteadiness). The absolute velocity magnitude just aft of the Rotor 2 trailing edge (Station A) is shown in Fig. 10(*a*), and ahead of the Stator 2 leading edge (Station D) in Fig. 10(*c*). It can be seen that the stationary field effect in the rotor wake region significantly increases as the Stator 2 leading edge is approached. This suggests a significant potential field effect.

To quantify the potential field effect further, these data were reduced to a single maximum-minimum quantity by first spatially averaging all the absolute velocities across the rotor passage at each constant stator position. The maximum and minimum values of the resulting rotor-spatial-averaged velocity versus stator pitch curve were calculated and compared with the values computed from an inviscid cascade potential flow analysis by Caspar et al. (1980). This exercise was also executed for the absolute flow angle. The comparisons are presented in Fig. 11. Note that two different sets of axial coordinates are used in these plots: percent rotor axial chord downstream from the rotor trailing edge (lower axis), and percent stator axial chord upstream from stator leading edge (upper axis). The agreement between the data and the computation is quite good.

Summary and Conclusion

Temporally and spatially resolved flow field data have been acquired with a two-component LDV in the flow field of a multistage, axial compressor model. These data exhibit the local effects of interaction between the stationary and the rotating fields, particularly in the region of the rotor wake (e.g., Figs. 2*b* and 10*c*), displaying many important time-dependent features of the rotor–stator flow field not captured by time-averaging pneumatic instrumentation. These time-accurate data have also been averaged in several ways to compare them with previously acquired pneumatic data, to examine wake decay, and to compare them with the potential field as computed from an inviscid cascade analysis.

The data have shown strong interaction between the rotating and stationary flow fields. The evidence suggests both viscous-potential interaction between the flow fields of adjacent airfoil rows, and viscous-viscous interaction with wake segments from an upstream row collecting within the wake of a downstream row. The rotor wakes have been successfully fitted to an exponential decay curve, implying a significant wake impinging on the leading edge of the downstream row. It should be noted that real machines with much smaller axial gaps will likely experience significantly greater interaction effects. Comparison demonstrates that the self-time-averaging of pneumatic data agrees very well with the appropriately averaged LDV data.

References

Adamczyk, J. J., 1985, "Model Equation for Simulating Flows in Multistage Turbomachinery," NASA TM-86869; ASME Paper No. 85-GT-226.

Adamczyk, J. J., Mulac, R. A., and Celestina, M. L., 1986, "A Model for Closing the Inviscid Form of the Average-Passage Equation," ASME JOURNAL OF TURBOMACHINERY, Vol. 108, No. 2, pp. 180–186.

Caspar, J. R., Hobbs, D. E., and Davis, R. L., 1980, "Calculation of Two-Dimensional Potential Cascade Flow Using Finite Area Methods," *AIAA Journal*, Vol. 18, No. 1, pp. 103–109.

Cyrus, V., 1986, "Experimental Study of the Flow in an Axial Compressor Stage," ASME Paper No. 86-GT-118.

Cyrus, V., 1988, "Effect of the Inlet Velocity Profile in the Three-Dimensional Flow in a Rear Axial Compressor Stage," ASME JOURNAL OF TURBOMACHINERY, Vol. 110, pp. 434–440.

Dong, Y., Gallimore, S. J., and Hodson, H. P., 1987, "Three-Dimensional Flows and Loss Reduction in Axial Compressors," ASME JOURNAL OF TURBOMACHINERY, Vol. 109, No. 3, pp. 354–361.

Dring, R. P., 1982, "Sizing Criteria for Laser Anemometry Particles," ASME *Journal of Fluids Engineering*, Vol. 104, No. 1, pp. 15–17.

Dring, R. P., Joslyn, H. D., and Hardin, L. W., 1982, "An Investigation of Compressor Rotor Aerodynamics," ASME *Journal of Engineering for Power*, Vol. 104, No. 1, pp. 84–96.

Dring, R. P., Joslyn, H. D., and Wagner, J. H., 1983, "Compressor Rotor Aerodynamics," *Viscous Flow Effects in Turbomachines*, AGARD-CP-351, Paper No. 24, Copenhagen, Denmark.

Gundy-Burlet, K. L., and Rai, M. M., 1989, "Two-Dimensional Computations of Multi-stage Compressor Flows Using a Zonal Approach," AIAA Paper No. 89-2452.

Gundy-Burlet, K. L., Rai, M. M., Stauter, R. C., and Dring, R. P., 1991, "Temporally and Spatially Resolved Flow in a Two-Stage Axial Compressor: Part 2—Computational Assessment," ASME JOURNAL OF TURBOMACHINERY, Vol. 113, this issue.

Joslyn, H. D., and Dring, R. P., 1985, "Compressor Stator Aerodynamics," ASME *Journal of Engineering for Gas Turbines and Power*, Vol. 107, No. 2, pp. 485–493.

Kerrebrock, J. L., and Mikolajczak, A. A., 1970, "Intra-stator Transport of Rotor Wakes and Its Effect on Compressor Performance," ASME *Journal of Engineering for Power*, Vol. 92, pp. 359–368.

Rai, M. M., 1987, "Navier-Stokes Simulations or Rotor/Stator Interactions Using Patched and Overlaid Grids," *Journal of Propulsion and Power*, Vol. 3, No. 5, pp. 387–396.

Rai, M. M., and Madavan, N. K., 1988, "Multi-airfoil Navier-Stokes Simulations of Turbine Rotor-Stator Interaction," AIAA Paper No. 88-0361.

Schlichting, H., 1968, *Boundary Layer Theory*, 6th ed., McGraw-Hill, New York.

Sudar, K. L., Hathaway, M. D., Okiishi, T. H., Strazisar, A. J., and Adamczyk, J. J., 1987, "Measurements of the Unsteady Flow Field Within the Stator Row of a Transonic Axial-Flow Fan: I—Measurement and Analysis Technique," ASME Paper No. 87-GT-226.

Wisler, D. C., Bauer, R. C., and Okiishi, T. H., 1987, "Secondary Flow, Turbulent Diffusion, and Mixing in Axial-Flow Compressors," ASME JOURNAL OF TURBOMACHINERY, Vol. 109, No. 4, pp. 455–482.

DISCUSSION

N. A. Cumpsty[1]

The unsteady flow inside compressors has been neglected in most investigations, probably because even the steady flow is sufficiently complicated that few people get near to understanding it. There are some real unsteady issues to be resolved and contributions are naturally welcome. I am nevertheless worried that this paper could give quite misleading results because the numbers of rotor and stator blades are equal.

When the numbers of rotor and stator blades are unequal, the interaction between the two can be visualized as a disturbance wave, which moves around the circumference so that the net flow, averaged around the circumference, is almost steady. The disturbance rotates with higher speed than the rotor. If the number of rotor and stator blades is equal all the blade interactions take place simultaneously around the circumference, and in this case the average flow around the circumference is not steady. What happens is that the mass flow (and the pressure rise) will vary in phase for all the blade passages and it seems likely that the unsteady flow measured in this case will be different in significant ways from the more typical case. The in-phase disturbances are a source of noise and vibratory excitation and for this reason equal numbers are generally not used for compressor or turbines; equal numbers are the basis of the design of a siren. In fact the difference in Figs. 5 and 6 between the maximum and minimum velocity midway between the wakes would seem evidence of this effect. Moreover the movie of the calculations shown at the presentation of Gundy-Burlet et al. (1991) showed clearly that there are axisymmetric waves propagating off downstream, just as one would expect from this very special choice of numbers.

It is possible that the data the authors have presented are not seriously compromised by the equal number of rotors and stators, but this must be confirmed. This could be done with a number of circumferentially spaced hot wires to see if there is strong correlation between them; if a substantial correlation exists ahead of the inlet guide vanes it will be evidence that there is good reason to mistrust the data.

[1]Whittle Laboratory, Cambridge, United Kingdom.

Authors' Closure

The authors would like to thank Professor Cumpsty for raising a valid and insightful concern in his discussion. There are several perspectives from which to address this concern.

The postulated axisymmetric waves would result in a periodic variation in the mass flow, or C_x. In order to examine the data for evidence of such axisymmetric waves, the axial velocity, C_x, was averaged circumferentially, i.e., across the stator pitch, at each time increment. The relation between the axial velocity, C_x, and time over one blade passing period was thus obtained. This temporal variation of the circumferentially averaged C_x is very nonsinusoidal and has an rms of $0.0025U_m$, or about 0.5 percent of the average C_x. The axial velocity, C_x, was also time averaged at each measurement location across the stator pitch, thus removing the temporal dependency. The result is a time-averaged C_x versus stator pitch relation. This is a nearly sinusoidal curve due to the stator potential field, with a period equal to one stator pitch and an rms of $0.0145U_m$, or about 2.9 percent of the average C_x. Comparing these two values, the variation due to the stator potential field is nearly six times the temporal variation in average mass flow. Thus, it can be said that airfoil-to-airfoil variations, typical of turbomachinery airfoil potential flow fields, are the dominant part of the difference seen between the maximum and minimum curves in Figs. 5 and 6.

Secondly, Fig. 11 shows that the maximum and minimum differences agree very well with predicted stator potential field variations. There is no indication of other significant variations, such as a temporal variation.

Lastly, it is not clear that such a phenomenon would affect the primary purpose for which these data were acquired, i.e., the assessment of time-accurate turbomachinery flow codes.

K. L. Gundy-Burlet

M. M. Rai
NASA Ames Research Center,
Moffett Field, CA 94035-1000

R. C. Stauter

R. P. Dring
United Technologies Research Center,
East Hartford, CT 06108

Temporally and Spatially Resolved Flow in a Two-Stage Axial Compressor: Part 2—Computational Assessment

Fluid dynamics of turbomachines are complicated because of aerodynamic interactions between rotors and stators. It is necessary to understand the aerodynamics associated with these interactions in order to design turbomachines that are both light and compact as well as reliable and efficient. The current study uses an unsteady, thin-layer Navier–Stokes zonal approach to investigate the unsteady aerodynamics of a multistage compressor. Relative motion between rotors and stators is made possible by the use of systems of patched and overlaid grids. Results have been computed for a 2½-stage compressor configuration. The numerical data compare well with experimental data for surface pressures and wakes. In addition, the effect of grid refinement on the solution is studied.

Introduction

Simulations of flows within turbomachines are challenging because of the complicated rotating geometries and unsteady flow structures. Designers are often required to place airfoils close together to minimize engine weight and size. This leads to aerodynamic interactions between rotor and stator airfoils. Part of the interaction is due to the inviscid potential effect between closely spaced rotor and stator airfoils. Viscous effects also contribute to the unsteady interactions. The angle of attack of an airfoil can vary widely as it passes through the wake of an upstream airfoil, because of the velocity deficit in the wake. Unsteady variations in angle of attack coupled with local adverse pressure gradients can cause unsteady separation. In addition, trailing-edge vortex shedding can increase the unsteadiness of the system. Simulation of the unsteady flow in a turbomachine can lead to an understanding of the aerodynamic interactions that occur.

Most methods used today to simulate flows in turbomachines are for either cascade flows or time-averaged flows through several airfoil rows. Simulations by Davis et al. (1988), Choi and Knight (1988), Subramanian et al. (1986), and Weinberg et al. (1986) are representative of these methods, but by no means make an exhaustive list of the methods available. Perturbation techniques can be applied to these simulations for an estimate of the unsteadiness for weak interactions. Distorting-grid techniques, described by Gibeling et al. (1986), can be used to investigate flows in which relative motion exists between rotors and stators. In these techniques, a single grid is wrapped about both airfoils and sheared as the airfoils move relative to one another. When the distortion in the grid exceeds a certain level, the solution is interpolated onto a new, undistorted grid. However, this method may produce inaccurate solutions because of the grid distortion if the airfoils are too closely spaced.

For this reason, Rai (1987) and Rai and Madavan (1988) used a system of patched and overlaid grids to compute the rotor–stator interaction problem in a single-stage turbine. Body-fitted "O" grids with fine-grid spacing at the airfoil surfaces were used to capture viscous effects near the airfoil surface. These "O" grids were overlaid on sheared Cartesian "H" grids, which were allowed to slip past each other to simulate the interaction problem. The ROTOR-2 code resulted from these efforts to simulate rotor–stator interaction for single-stage turbine configurations. The STAGE-2 code, used in the present study, is an extension of ROTOR-2 for multistage turbomachines. Results from STAGE-2 were compared with experimental data for both a multistage compressor and a single-stage turbine by Gundy-Burlet et al. (1989).

STAGE-2 is currently being used to investigate the flow in the multistage compressor further. The 2½-compressor geometry was chosen for the present analysis because a large body of experimental data is available for the multistage compressor. Much of the experimental data is summarized and tabulated by Dring and Joslyn (1985). This compressor is also part of the AGARD (1989) collection of test cases for computation of internal flows in aero-engine components. In addition, both steady and unsteady laser-Doppler velocimetry (LDV) data have been taken in the second stage of the compressor. These data are presented by Stauter et al. (1991) in Part 1 of this paper. Comparisons, in the present report, of STAGE-2 calculations with experimental data include time-averaged pressures and wake velocity profiles. The effect of grid refinement on the solution is studied, and instantaneous

Contributed by the International Gas Turbine Institute and presented at the 35th International Gas Turbine and Aeroengine Congress and Exposition, Brussels, Belgium, June 11–14, 1990. Manuscript received by the International Gas Turbine Institute January 1990. Paper No. 90-GT-299.

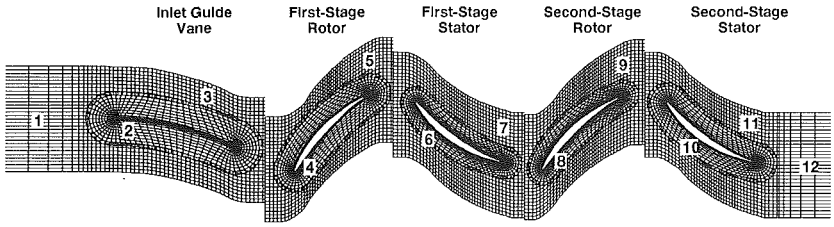

Fig. 1 Zonal grid system

entropy contours for the 2½-stage compressor are presented. The computed results are in good agreement with experimental data.

Approach

The current work is an extension of an algorithm developed by Rai and is discussed in detail by Rai and Chakravarthy (1986). The algorithm is discussed in brief here. The flow field is divided into two basic types of zone. The thin-layer Navier–Stokes equations are solved in inner zones near the airfoil where viscous effects are important. The Euler equations are used in outer zones where viscous effects are weak. These equations are cast in the strong conservative form. A fully implicit finite difference method is used to advance the solution of the nonlinear equations in time. At each time step, four Newton–Raphson iterations are used to reduce the factorization and linearization errors by an order of magnitude. The convective terms are evaluated using a third-order-accurate upwind-biased Osher scheme, and the viscous terms are evaluated using second-order central differences. The Baldwin–Lomax (1978) turbulence model is used to compute the turbulent eddy viscosity. Details of the turbulence model, zonal and natural boundary conditions, grid configuration, bookkeeping system, and database management systems are discussed by Gundy-Burlet et al. (1989).

Grid System

The grid system for the 2½-stage compressor geometry is shown in Fig. 1. The experimental compressor geometry consists of an inlet guide vane (IGV) followed by two nearly identical stages. The only difference between the stages is that the first-stage rotor is closed 3 deg relative to the second-stage rotor. The only deviation from the original design was that the axial gaps between the rotors and stators were increased slightly to permit the incorporation of a radial-circumferential traverse system. All airfoils are defined by NACA 65-series sections with circular-arc mean camber lines. There are 44 airfoils in each row. The hub and casing are at a constant radius along the axis of the compressor. These features make the compressor ideal for computational modeling.

The computation was performed using the midspan experimental geometry. It was assumed that the flow is periodic from airfoil to airfoil in the circumferential direction, so the flow through only one airfoil-to-airfoil passage was computed. In addition, the experimental IGV geometry was unavailable at the time this calculation was initiated, so a 0.8 percent thick parabolic arc airfoil was used. These assumptions are not expected to affect the comparison between the computation and the experiment significantly.

Two types of grids are used to discretize the flow about each of the airfoils, as seen in Fig. 1. An inner "O" grid, generated using an elliptical method, is used to resolve the viscous effects near the airfoil. The "O" grid is then overlaid on an algebraically generated, sheared Cartesian outer grid. The outer grids are allowed to slip past each other to model the relative motion between rotors and stators. Using this system, 12 grids are required to discretize the flow field fully through the 2½-stage compressor.

Two different grids were used to study the effect of grid refinement on the solution. Every other point in the coarse grid is displayed in Fig. 1. The inner grids have 151 × 31 grid points each, and the outer grids have 86 × 61 grid points each. The inlet and exit grids have 28 × 61 and 30 × 61 grid points each, respectively. The total number of points in all 12 zones of the coarse grid is 53,173.

Experimental data exist only for the second stage of the compressor. In order to reduce the computational time required for a grid refinement study, grid refinement was done only in the second stage of the compressor. The second-stage inner grids were refined to have 301 × 61 points each while the second-stage outer grids were refined to have 171 × 121 grid points each. The exit-grid size was increased to 59 × 121. Thus, the fine-grid cells are one quarter the area of the coarse-grid cells. The total number of points for the fine-grid system was 116,732.

Results

Results for the 2½-stage compressor configuration shown in Fig. 1 are presented in this section. For the 53,000-point coarse grid used in this study, 500 time steps are used for each blade-passing time. Each time step requires 3.9 CPU seconds on a Cray YMP. Time-averaged quantities converge within 10 blade passings, but the presence of multiple stages increases the time required to achieve a time-periodic solution, as compared to a single-stage system. Acoustic signals must travel a larger distance to exit from a multistage system. In addition, these signals reflect off airfoils and the reflections take time to exit the system. Depending on the level of convergence required of the time-periodic solution, between 5 and 40 hours of CPU time are needed for the calculations.

Several items must be taken into consideration when comparing these results with the experimental data. The experiment is inherently three dimensional, while the computations are two dimensional. Hub-corner separation, tip-leakage effects,

Nomenclature

C_p = pressure coefficient = $(P - P_{T_i})/\frac{1}{2}\rho_i U_m^2$
C_x = inlet axial velocity
F = airfoil force per unit span normalized by Q_{U_m} and τ
P = pressure
P_{T_i} = compressor inlet absolute total pressure
Q_{U_m} = dynamic pressure based on U_m
T = time normalized by airfoil passing period
t = tangential distance normalized by τ
U_m = wheel speed at midspan
W = relative flow speed
x = axial distance
ρ_i = compressor inlet density
τ = airfoil pitch
ϕ = flow coefficient = C_x/U_m

Subscripts

t = tangential component
x = axial component

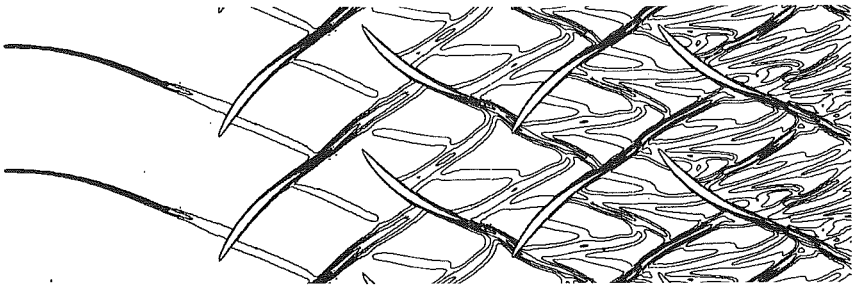

Fig. 2 Instantaneous entropy contours

and end-wall boundary-layer growth are not modeled. In the experiment, the end-wall boundary-layer growth generates a streamtube contraction that increases the axial velocity at midspan along the axis of the compressor; the midspan exit axial velocity is increased to 110 percent of the midspan inlet velocity. This increase is not reflected in the calculation because the streamtube contraction is currently not modeled.

The calculation was performed at an inlet Mach number of 0.07 and a Reynolds number of 100,000 per inch based on inlet conditions. These values were set to match the experimental operating conditions. The experimental flow coefficient is $\phi = 0.51$. The exit static-pressure coefficient for the experiment is $C_p = 1.11$. It is not possible to match the computational values with both the experimental pressure rise and the experimental flow coefficient because the streamtube contraction is not modeled.

The first comparison typically made between calculation and experiment is of the time-averaged pressures on the rotors and stators. As data are available only for the second stage of the compressor, setting the exit pressure equal to the experimental value and allowing the flow coefficient to float provide a reasonable comparison between computation and experiment. The mass flow rate in the calculation then adjusts itself to the pressure rise specified. Only the Riemann invariants (functions of velocity and speed of sound), total pressure, and flow angle are specified at the inlet, so the final time-averaged values of velocity and static pressure may vary from the initial condition. The flow coefficient in the calculation increased to $\phi = 0.524$ as the periodic steady state was reached. The flow coefficient for the experiment was $\phi = 0.51$.

In order to demonstrate the complexity of the flow field, instantaneous entropy contours are shown in Fig. 2. Entropy was chosen to display the viscous nature of the flow because, unlike total pressure, entropy is invariant with reference frame. These results were computed using refined grids in the second stage of the compressor. The entropy contours illustrate the depth and width of the wake for the inlet guide vane as well as for the rotors and stators. The wakes generated in the second stage of the compressor are better resolved than the wakes generated in the first stage of the compressor. Although it is difficult to see this in Fig. 2, the difference in resolution of the wakes becomes clear in subsequent figures (in particular, Fig. 5). The numerical dissipation associated with the coarse-grid resolution of the first stage of the compressor causes the wakes to diffuse more rapidly than they would have with a fine grid. Because the wakes from the first stage of the compressor are more diffuse, the general level of unsteadiness seen by the second stage of the compressor (especially the second-stage rotor) is expected to be underpredicted. All grids would have to be refined to get a more accurate estimate of the amplitude of the unsteady behavior in the compressor.

The field flow in the second stage of the compressor is complicated by the accumulation of the convected wakes. Wakes from the first-stage rotor and stator penetrate into the second stage of the compressor, despite the lack of grid resolution in the first stage. Both wake/wake interactions and

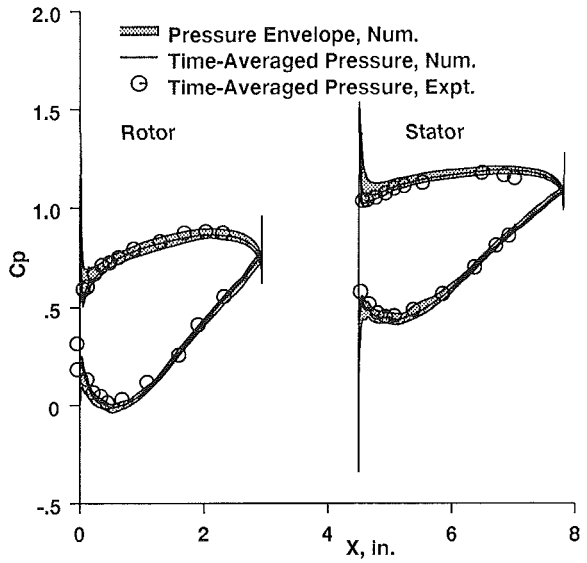

Fig. 3 Surface pressures in the second stage of the compressor

wake/airfoil interactions occur in the flow field. The impact of the difference in convection rate from the suction side of an airfoil to the pressure side of an airfoil is also evident, particularly on the second-stage rotor. The circulation around the airfoils produces a streamwise displacement of the wakes as they are convected along the suction and pressure surfaces. The circulation also causes a rotation of the chopped-wake segments as they are convected through the airfoil-to-airfoil passages. It is clear from Fig. 2 that wakes can be convected many chords downstream to interact with other airfoils. This causes unsteady variations in flow variables in the later stages of the compressor to be more complex than in the early stages.

As the downstream airfoils move through the wakes of the upstream airfoil rows, the wake/airfoil interaction causes the surface pressures to fluctuate. The airfoil surface pressures also fluctuate because of interactions with the potential flow fields of the upstream and downstream airfoil rows. The pressure distributions for the second-stage rotor and stator are presented in Fig. 3 in terms of the time-averaged surface pressures. The shaded band indicates the temporal maximum and minimum over a cycle caused by the fluctuations mentioned above. The time-averaged static pressure is arrived at by averaging the instantaneous static pressures over one cycle. A cycle is defined as the time it takes for the rotor to move from its position relative to one stator to the corresponding position with respect to the next stator. Pressure is plotted against axial position in the compressor. The axial distance between the rotor and stator results in the actual axial gap.

The symbols in Fig. 3 represent measured data for this compressor that had been reported previously by Joslyn and Dring (1989a). The data were acquired using long lengths of instrumentation tubing between the rotor and stator surface pressure taps and the rotating and stationary frame transducers, re-

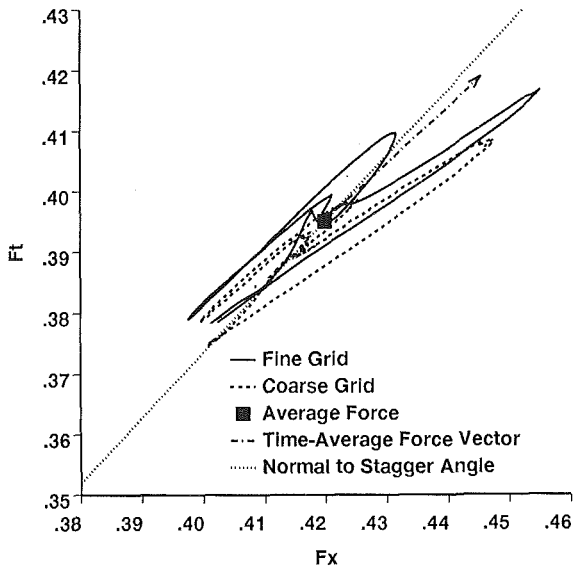

Fig. 4(*a*) Force polar plot for the second-stage rotor

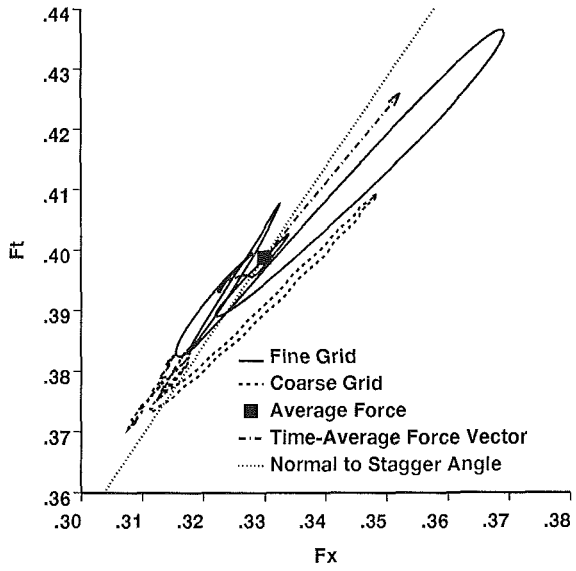

Fig. 4(*b*) Force polar plot for the second-stage stator

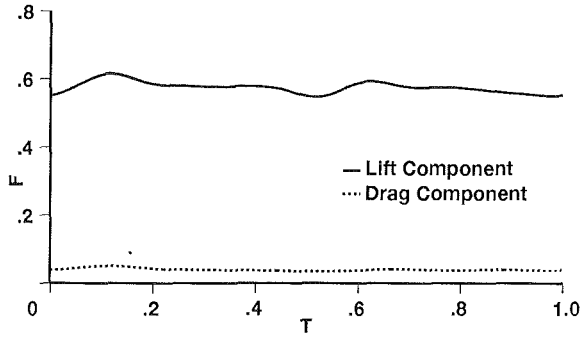

Fig. 4(*c*) Time variation of forces on the second-stage rotor

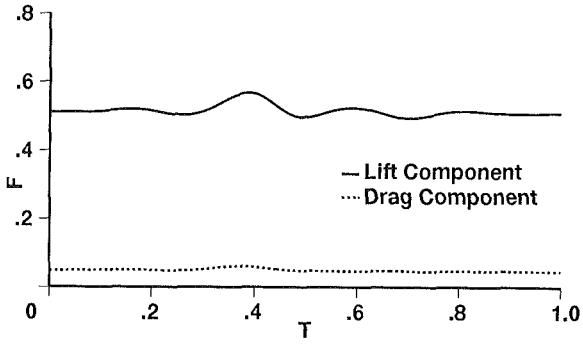

Fig. 4(*d*) Time variation of forces on the second-stage stator

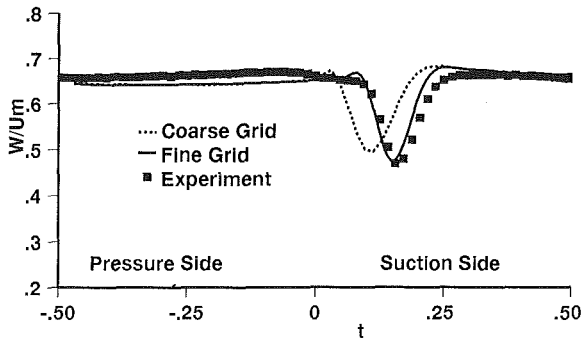

Fig. 5 Wake profiles 26 percent behind rotor for fine grid, coarse grid, and experiment

spectively. Thus, the measurements are presumed to be indicative of the time-averaged surface static pressure.

The agreement between the calculation and the experimental data is good. The small differences between them at the leading and trailing edges are due primarily to the mismatch in axial velocity. Although the flow coefficient in the experiment was 0.51 when averaged from hub to tip, a streamtube contraction caused the flow coefficient at the midspan to be 0.54 at the inlet to the second stage.

The band in Fig. 3 indicating the temporal maximum and minimum of the local surface static pressure on the rotor and stator is nearly uniform in width around both sides of both airfoils. The increase in this unsteady amplitude near the leading edges may be related to the wakes of the upstream airfoil. However, it may also be related to the large gradient in the time-averaged pressure at the leading edge. The amplitude of the unsteady static pressure is approximately 10 percent of the airfoil loading. The pressure amplitude is also evident in the pressure-force results presented in Fig. 4 and discussed below. Both the rotor and stator airfoils show a pressure spike at the trailing edge. The trailing-edge spikes in this fine-grid calculation are one-third the size of the trailing-edge spikes the coarse-grid calculation; this shows that the spikes are strongly dependent on grid resolution.

Close inspection of computed flow velocities at one instant in time near the second-stage stator shows the presence of a thin separation bubble from about 80 percent chord to the stator trailing edge. The separation bubble became apparent only under very high magnification of the results. It is undetectable at the scale of the results presented in Fig. 2 and does not appear strongly to affect the comparison with experiment in Fig. 3. The temporal behavior of the separation bubble has not yet been examined.

The existence of the separation bubble contrasts with previous flow visualization of the airfoils, which had indicated that at midspan both the rotor and stator suction-surface boundary layers are attached all the way to the trailing edge (Joslyn and Dring, 1989b). These two results are reconciled as follows. The turbulence model used in the present calculation is the fully turbulent Baldwin and Lomax (1978) model; Joslyn and Dring (1989b) showed that if the boundary layers were fully turbulent, both the rotor and stator would experience boundary layer separation at about the 80 percent chord location. They also demonstrated that the boundary layers had to be transitional to remain attached to the trailing edge. Tran-

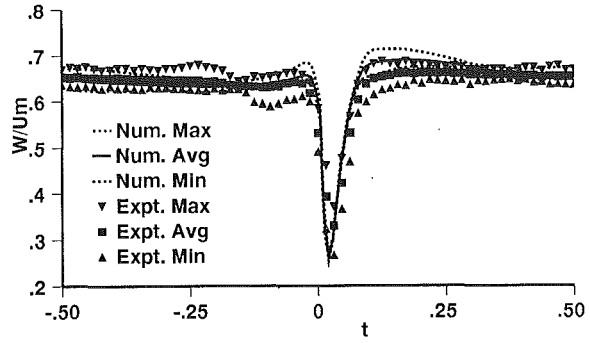

Fig. 6(*a*) Wake profiles 2 percent aft of the second-stage rotor

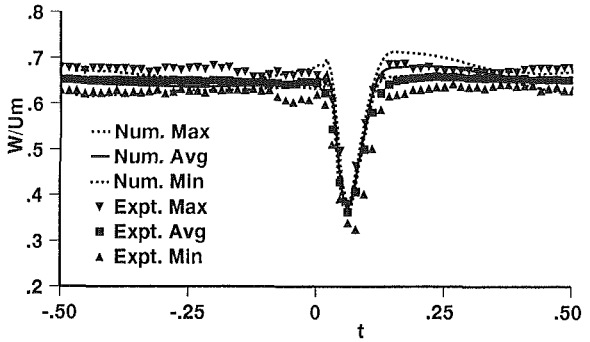

Fig. 6(*b*) Wake profiles 8 percent aft of the second-stage rotor

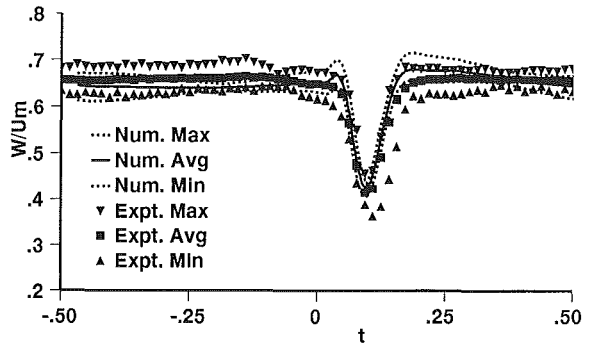

Fig. 6(*c*) Wake profiles 15 percent aft of the second-stage rotor

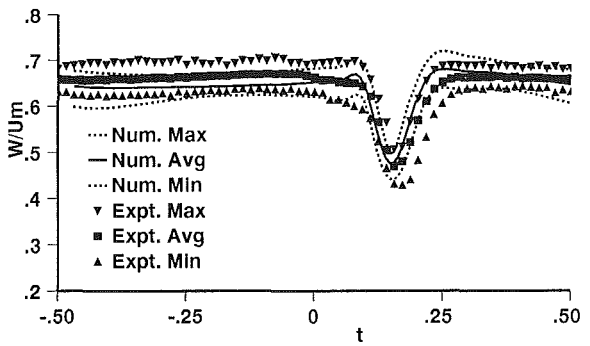

Fig. 6(*d*) Wake profiles 26 percent aft of the second-stage rotor

sitional modeling was beyond the scope of the present calculation.

In spite of the fact that the separation bubble on the stator did not seem to have any major impact on the pressure distribution, its presence should be kept in mind throughout the remainder of this assessment.

The instantaneous surface static pressures were integrated around the perimeter of the rotor and stator to produce the periodic variation of the pressure-force vector on each airfoil for both a coarse-grid and a fine-grid calculation. A similar integration for the skin-friction force has not been carried out yet. The instantaneous axial and circumferential components of the force are plotted as a polar curve for the second-stage rotor in Fig. 4(*a*) and for the second-stage stator in Fig. 4(*b*). The squares indicate the time-averaged values of the forces, computed with the fine grid. The direction of the time-averaged force and the normal to the stagger angle of each airfoil are included in the plots as reference.

These polar plots provide a good measure of the periodic convergence of the solution. At the periodic steady state, the force polar plot for one cycle should lie on top of the curve for the previous cycle. The coarse-grid results shown here are converged to this criterion. The fine-grid results show small variations from cycle to cycle, but are considered close to convergence. A time-accuracy study has been carried out for the coarse grid. Solutions were carried out at time steps of 500, 1000 and 2000 steps per cycle. Although not shown here, the force polar plots for each of these time steps compared well with those for the other time steps. This indicates that the periodic solution is independent of the time steps used in this study.

The coarse- and fine-grid solutions are qualitatively similar for the second-stage rotor shown in Fig. 4(*a*). Because only the grids in the second stage of the compressor were refined for the fine-grid calculation, the wakes for the airfoils upstream of the second-stage rotor are computed on identical grids for both the fine and coarse grids. There are larger differences between the coarse- and fine-grid solutions for the second-stage stator shown in Fig. 4(*b*), because of the difference in resolution of the second-stage rotor wake. The amplitude of the fine-grid force on the second-stage stator is approximately 40 percent larger than the amplitude of the coarse-grid force.

The unsteady forces are dominated by the variation in the lift component of the force. For brevity, "lift" is defined as the component of force normal to the stagger angle and "drag" as the component of force parallel to the stagger angle. The magnitude of the unsteady force is typically 10 percent of the time average for the relatively large rotor/stator axial gaps found in this compressor. These axial gaps are twice as large as those found in a typical modern engine.

The unsteadiness is largely contained in the lift component of the force. Figures 4(*c*) and 4(*d*) show the lift and drag components of the force plotted against time for the second-stage rotor and stator, respectively. The curves vary smoothly, indicating that the unsteadiness in the force is not due to a narrow wake, but is distributed more uniformly, as one might expect for a potential interaction. Had the axial gaps between airfoil rows been smaller, the wake contribution might have been more pronounced.

The effect of grid refinement on wake profiles can be seen in Fig. 5. Time-averaged relative velocities for the coarse grid, fine grid, and experiment (Stauter et al., 1991) are plotted against tangential displacement from the rotor trailing edge. This comparison is at an axial location 26 percent of the rotor axial chord downstream of the second-stage rotor trailing edge. The fine-grid calculation is in good agreement with the experimental data in terms of wake depth, width, and location. The wake depths for the coarse-grid results are shallower than for the experimental data and are visibly displaced. The fine-grid and experimental results have a displacement approximately 50 percent greater than those of the coarse grid. This is caused by the different computed rotor exit-flow angles, which resulted from the difference in airfoil loading between the coarse- and fine-grid solutions seen in Fig. 4(*a*); these results also suggest that solutions should be computed with several different grid densities in order to determine the asymptotic behavior of the solution with grid refinement. The remainder of the wake profile comparisons will be between the measured data (Stauter et al., 1991) and the fine-grid results.

A comparison of the fine-grid and the experimental data is

made at axial locations nominally 2, 8, 15, and 26 percent aft of the rotor trailing edge (Figs. 6*a–d*). Both the computed and the measured results are presented in terms of their temporal maximum, temporal minimum, and time average. The temporal fluctuation is caused by the interaction with the upstream stator wake (see Fig. 2), as well as by the potential field of the downstream stator.

Generally, at each axial location, the agreement is good between the measured and computed time-averaged results for wake depth, width, and tangential location. The greatest differences between the measured and computed results are in the regions between wakes, where there are systematic (albeit small) differences. This can be seen most clearly on the suction-surface side of the wake, where the wake merges with the "free stream." At all axial locations, the prediction at this tangential location is typically 5 percent greater than the measured results. These differences are probably related to the nature of the mixing of the wakes, the lack of resolution of the upstream wakes, and the inability to model three-dimensional effects with a two-dimensional calculation.

Flow-speed fluctuations are given, in Figs. 6(*a–d*), by the width of the band between the instantaneous maximum and minimum relative velocities. The agreement between the measured and computed fluctuations is reasonably good. While the maximum-to-minimum band width of the computation is generally smaller than that of the experiment, many of the features have been captured in the computation, most notably the increase in band width with distance aft of the rotor. As pointed out by Stauter et al. (1991), this increase is due to the potential field of the downstream stator.

Conclusions

A third-order-accurate upwind-biased Navier–Stokes zonal code (STAGE-2) has been developed to compute flows in multistage turbomachines. Systems of overlaid and patched grids are used to resolve viscous effects near airfoils allowing the rotor/stator interaction problem to be modeled. Flexible database and bookkeeping systems are used to allow flows to be computed in turbomachines with any number of stages.

Results from STAGE-2 compared well with experimental data for both surface pressures and wake profiles. Grid refinement substantially improved the agreement with experiment for the wake profiles, although static pressures were relatively insensitive to grid refinement. The temporal variation in airfoil force was 10 percent of the time-averaged force for the relatively large axial gaps found in this compressor. Strong viscous interactions were demonstrated by the use of entropy contours. The flow within the second stage of the compressor was highly complex, indicating the importance of unsteady-flow analysis in a multistage turbomachine.

With smaller axial gaps between the rotors and stators of modern engines, it can be anticipated that the interactions in general will be stronger and the unsteady forces in particular will be much larger than those for the compressor studied here.

References

AGARD, 1989, "Test Cases for Computation of Internal Flows in Aero Engine Components," AGARD Propulsion and Energetics Panel, Working Group 18, AGARD-AR-275.

Baldwin, B. S., and Lomax, H., 1978, "Thin Layer Approximation and Algebraic Model for Separated Turbulent Flow," AIAA Paper No. 78-257.

Choi, D., and Knight, C. J., 1988, "Computation of 3D Viscous Cascade Flows," AIAA Paper No. 88-0363.

Davis, R. L., Hobbs, D. E., and Weingold, H. D., 1988, "Prediction of Compressor Cascade Performance Using a Navier–Stokes Technique," ASME JOURNAL OF TURBOMACHINERY, Vol. 110, pp. 520–531.

Dring, R. P., and Joslyn, H. D., 1985, "An Assessment of Single- and Multi-Stage Compressor Flow Modeling," Final Report for Naval Air Systems Command contract No. N00014-84-C-0354, July, AD-B102 101.

Gibeling, H. J., Weinberg, B. C., Shamroth, S. J., and McDonald, H., 1986, "Flow Through a Compressor Stage," Report R86-910004-F, Scientific Research Associates, Inc., Glastonbury, CT, May.

Gundy-Burlet, K. L., Rai, M. M., and Dring, R. P., 1989, "Two-Dimensional Computations of Multi-stage Compressor Flows Using a Zonal Approach," AIAA Paper No. 89-2452.

Joslyn, H. D., and Dring, R. P., 1989a, "Multi-stage Compressor Airfoil Aerodynamics: Part I—Airfoil Potential Flow Analysis," *J. Propulsion Power*, Vol. 5, No. 4, July–Aug., pp. 457–462.

Joslyn, H. D., and Dring, R. P., 1989b, "Multi-stage Compressor Airfoil Aerodynamics: Part II—Airfoil Boundary-Layer Analysis," *J. Propulsion Power*, Vol. 5, No. 4, July–Aug., pp. 463–468.

Rai, M. M., and Chakravarthy, S. R., 1986, "An Implicit Form for the Osher Upwind Scheme," *AIAA J.*, Vol. 24, No. 5, May, pp. 735–743.

Rai, M. M., 1987, "Navier–Stokes Simulations of Rotor/Stator Interactions Using Patched and Overlaid Grids," *J. Propulsion Power*, Vol. 3, No. 5, Sept., pp. 387–396.

Rai, M. M., and Madavan, N. K., 1988, "Multi-airfoil Navier–Stokes Simulations of Turbine Rotor–Stator Interaction," AIAA Paper No. 88-0361.

Stauter, R. C., Dring, R. P., and Carta, F. O., 1991, "Temporally and Spatially Resolved Flow in a Two-Stage Axial Compressor: Part 1—Experiment," ASME JOURNAL OF TURBOMACHINERY, Vol. 113, this issue.

Subramanian, S. V., Bozzola, R., and Povinelli, L. A., 1986, "Computation of Three-Dimensional, Rotational Flow Through Turbomachinery Blade Rows for Improved Aerodynamic Design Studies," ASME Paper No. 86-GT-26.

Weinberg, B. C., Yang, R.-J., McDonald, H., and Shamroth, S. J., 1986, "Calculations of Two- and Three-Dimensional Transonic Cascade Flow Fields Using the Navier–Stokes Equations," ASME *Journal of Engineering for Gas Turbines and Power*, Vol. 108, pp. 93–102.

The Influence of Inlet Swirl Distortions on the Performance of a Jet Propulsion Two-Stage Axial Compressor

W. Pazur

L. Fottner

Universität der Bundeswehr München,
Institut für Strahlantriebe,
Neubiberg, Federal Republic of Germany

Aeroengine intakes containing S-shaped diffusers produce different types of inlet swirl distortions and essentially a combination of a twin swirl and a bulk swirl. The main object of this investigation was to assess the influence of inlet swirl distortions on the performance of a transonic two-stage axial compressor installed in a turbo jet bypass engine Larzac 04. A typical inlet swirl distortion was simulated by a delta-wing in front of the engine. An experimental method was investigated to measure the performance map of the installed low-pressure compressor for different engine operating lines. The influence of an inlet swirl distortion with different strengths on the performance map of the compressor was investigated experimentally. It is shown that the performance parameters decrease and a temperature distortion is generated behind the compressor. As the basis of the theoretical investigations of the performance map, including inlet swirl distortions, a computing model considering four compressors working in parallel was established. The model is based on the idea that an inlet swirl distortion can be substituted by two fundamental types of swirl components, i.e., a bulk swirl corotating, and a bulk swirl counterrotating to the revolution of the compressor. Computed performance maps of the compressor will be discussed and compared with the experimental data.

Introduction

In the past a distorted inlet flow was almost exclusively considered as a local nonuniform total temperature (e.g., Künkler and Tönskötter, 1979; Mehalic and Lottig, 1974) and total pressure distribution (e.g., Lecht, 1983; Hercock, 1982) over the inlet area or a nonuniform distribution with respect to time (e.g., Williams, 1986). In the scope of the development of new jet engines with even higher power density (i.e., RB 199) the loading of the compressors had to be increased. This resulted in a higher sensitivity to distortion of the flow angle (swirl) at the compressor inlet, which was found as a further configuration of flow distributions (Aulehla, 1982; Seddon and Goldsmith, 1985). This flow distortion is generated by an S-shaped inlet duct and is aggravated by extreme flight situations (high angle of attack, very high flight velocities).

In a feasibility study, Genssler et al. (1986) investigated possibilities to simulate a swirl distortion in front of a jet engine. Using the Larzac 04 engine as a demonstrator for testing the influence of swirl distortions on a jet engine, Meyer (1988) found that the engine's performance deteriorated extensively by decreasing the mass flow rate through the engine, the thrust, and, at the same time, increasing the specific fuel consumption.

In order to be able to explain the influence of the swirl distortions on the engine it will be the objective of this investigation to study the influence of swirl distortions on the low-pressure compressor of the Larzac 04 engine. In this investigation it will be found that a swirl distortion can be thought of as a superposition of a bulk swirl and a twin swirl. This leads to a highly unsteady inlet flow relative to the first rotor of the low-pressure compressor because the distortion is stationary and the flow in the rotating reference frame has to be observed. This physical phenomenon will be used in an analytical investigation. In order to compare the analytical results with experimental data, possibilities have to be investigated to measure a performance map of a compressor installed in an engine.

Test Rig and Measurement Techniques

All experimental tests were performed on a two-spool turbofan Larzac 04 engine because this engine is well suited for the investigation of the influence of swirl distortions on a jet engine due to the absence of an inlet guide vane. The test rig consists of the swirl generator, traversing equipment, and the engine with special test instrumentation (Fig. 1). In order to obtain data in the various planes the engine was equipped with

Contributed by the International Gas Turbine Institute and presented at the 35th International Gas Turbine and Aeroengine Congress and Exposition, Brussels, Belgium, June 11–14, 1990. Manuscript received by the International Gas Turbine Institute January 22, 1990. Paper No. 90-GT-147.

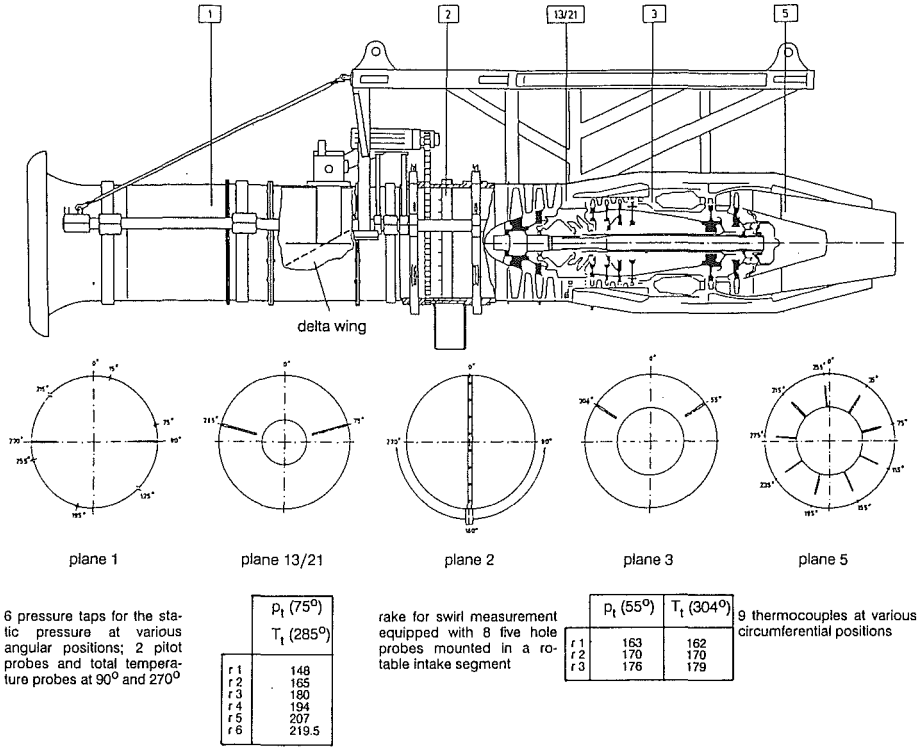

	p_t (75°)	T_t (285°)
r 1	148	
r 2	165	
r 3	180	
r 4	194	
r 5	207	
r 6	219.5	

	p_t (55°)	T_t (304°)
r 1	163	162
r 2	170	170
r 3	176	179

Fig. 1 Test arrangement of jet engine investigations with inlet swirl distortion

the appropriate sensors at the corresponding measurement locations. The traversing of the flow field was done with a rake for swirl measurements equipped with eight pyramidal five-hole probes. The rake is accommodated as a diagonal strut in a rotatable segment (Fig. 1, plane 2). The swirl generator consists of an adjustment mechanism (Fig. 2) and a delta wing swept by 60 deg (Fig. 3). It is mounted a distance of 1.5 times the diameter of the engine inlet in front of the entry of the compressor. This distance was found in the feasibility study to be optimal for the development of the swirl flow. The advantage of this test rig, compared to a fixed setup of the swirl generator, is the possibility that the swirl-generating delta wing could be returned to its horizontal position very quickly when strong engine instabilities required the removal of the swirl distortions. Angular adjustment of the delta wing and the traversing equipment was done by an electric motor, which could be set to certain preselected positions. Data acquisition and processing were performed on a PE 3220 computer located at the test facility.

Discussion of Experimental Results

A typical flow field with swirl distortions in the engine inlet plane 2 is shown in Fig. 4 for an angle of attack of the delta wing $\alpha_o = 23$ deg. For such a swirl distortion the DC 60 of a total pressure distortion at the compressor entry is only 0.09

Nomenclature

A = flow area
F,G = functions
La = Laval number
M = Mach number
R = gas constant
T = temperature
c = absolute velocity
c_u = circumferential component of the absolute velocity
c_{ax} = axial velocity
c_p = specific heat coefficient at constant pressure
h = enthalpy
l = blade chord
$\dot{m}$ = mass flow rate
n = speed of rotation
p = pressure
r = radius
t = time
u = circumferential velocity
w = relative velocity
w_u = circumferential component of the relative velocity
α_o = angle of attack of delta wing
α = angle of swirl in the circumferential direction
α_M = averaged value of the angle of swirl in the circumferential direction in a sector
β = angle between relative and axial velocity
γ = angle of swirl
ϵ = vertex angle
η_{is} = isentropic efficiency
θ = angle of circumferential position
θ = mass flow density
κ = ratio of specific heats
π = total pressure ratio
τ = time constant
φ = sector width of the distorted flow
φ_V = sweep angle of the leading edge

Subscripts

A = undistorted flow
eff = effective
F = sector without distorted flow
GD = counterrotational swirl
MD = corotational swirl
ND = low pressure
$R1$ = rotor entry of stage 1
$R2$ = rotor exit of stage 1
S = sector with distorted flow
SM = surge margin
t = total values
1 = plane of inlet entry
2 = entry of the compressor (measuring section)
21 = exit of the low pressure compressor

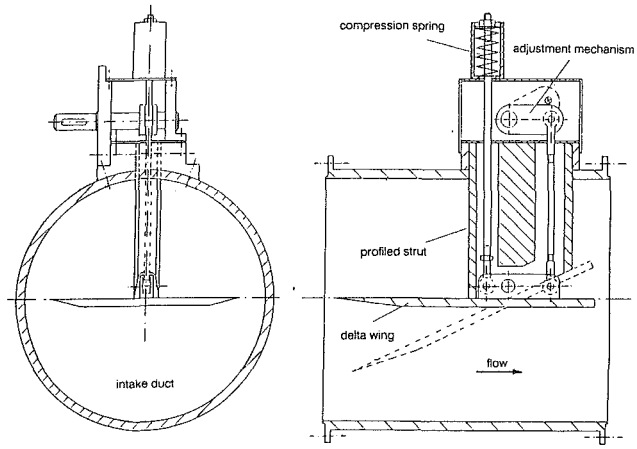

Fig. 2 Swirl generator (delta wing) between planes 1 and 2

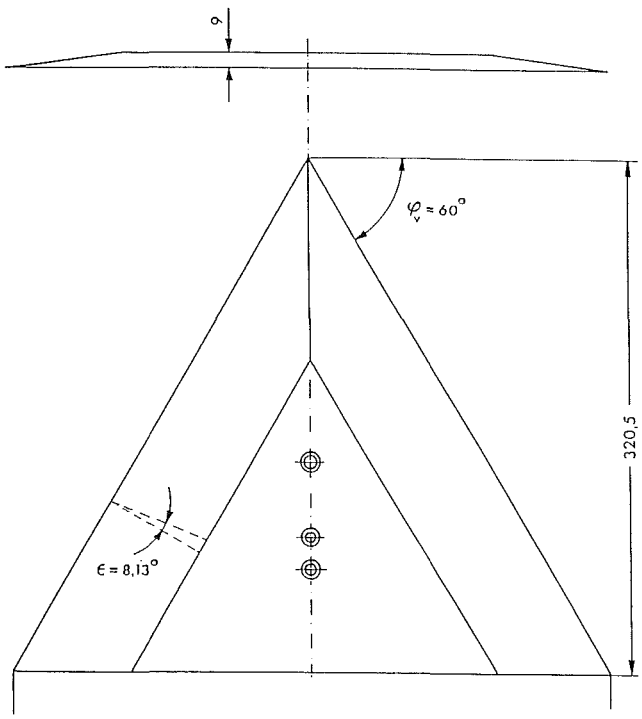

Fig. 3 Geometry of the delta wing

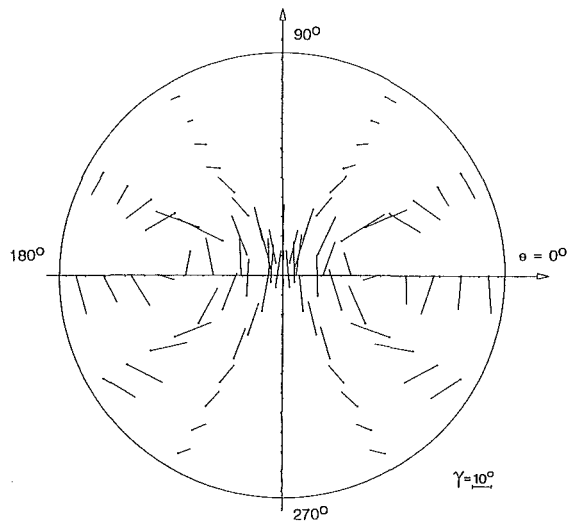

Fig. 4 Crossflow pattern behind the delta wing; angle of attack $\alpha_o = 23$ deg (γ in plane 2)

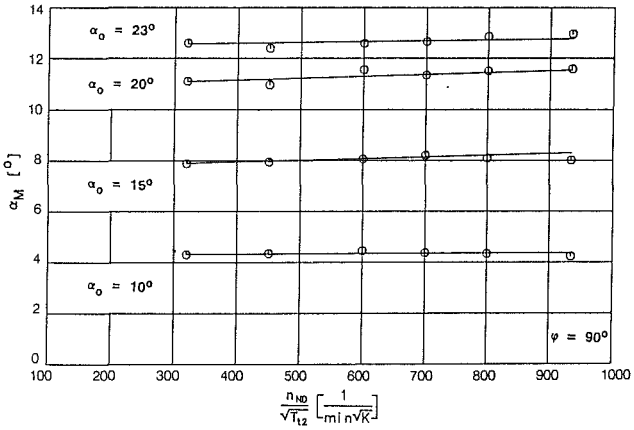

Fig. 5 Angle of swirl as a function of the corrected speed (plane 2)

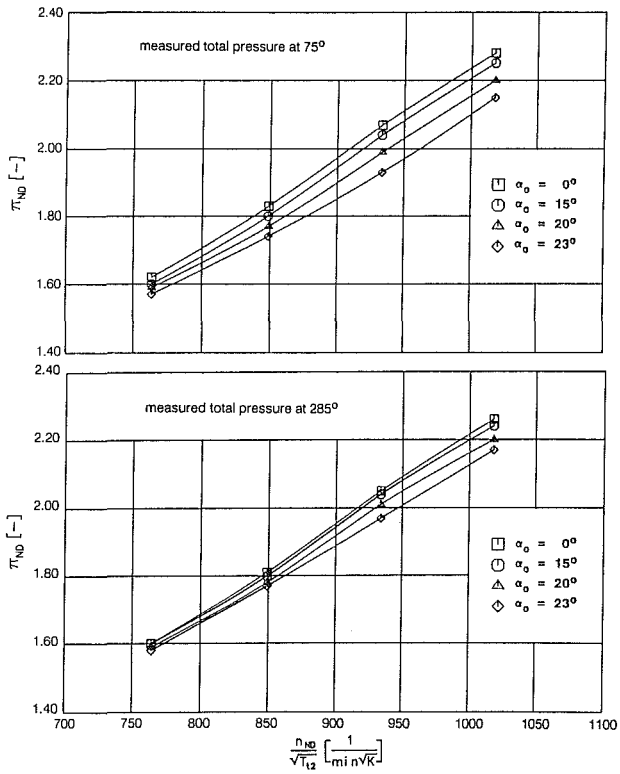

Fig. 6 Total pressure ratio as a function of the corrected speed

(Meyer, 1988). It is observed that the vortex pair emanating from the trailing edge of the delta wing develops to a stable twin vortex over a distance of 1.5 times the diameter of the engine inlet. By averaging the angle between the axis and the direction of the absolute velocity in a certain sector, and by neglecting the radial velocity component, an angle of swirl is obtained, defined as follows:

$$\alpha_M = \frac{\int_\varphi \int_r \alpha_i \cdot r \, dr d\theta}{\frac{1}{2} r^2 \cdot \varphi} \tag{1}$$

This average angle of swirl is shown in Fig. 5 for various angles of attack of the delta wing within the operating range of the compressor. It is noticed that the trace of the curves is almost horizontal, i.e., the average angle of swirl is nearly independent of the corrected compressor speed. This feature was used for the analytical calculations.

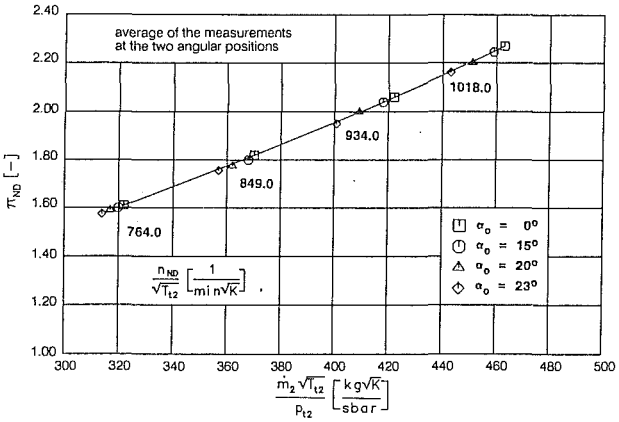

Fig. 7 Total pressure ratio as a function of the corrected mass flow rate

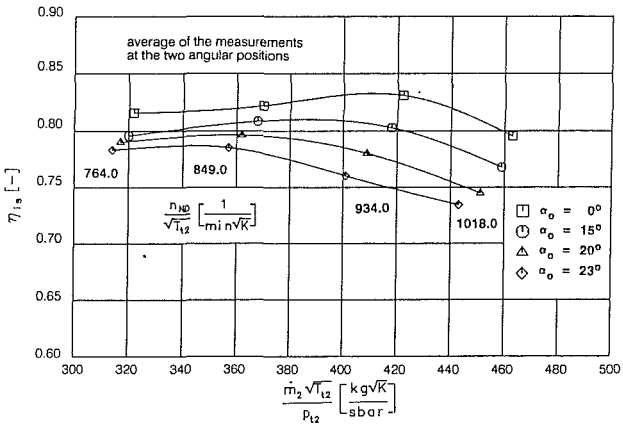

Fig. 9 Isentropic efficiency as a function of the corrected mass flow rate

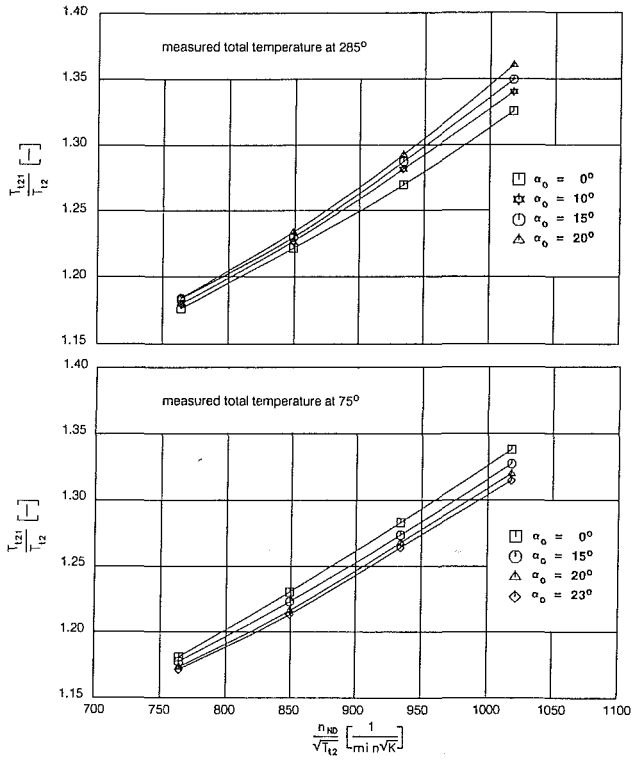

Fig. 8 Total temperature ratio as a function of the corrected speed

Area-related averages (Pianko and Wazelt, 1983) were computed from the traversed total pressure data at the entry of the compressor and the radial distributions of total pressure and total temperature at the exit of the low-pressure compressor. From these averaged values characteristic compressor parameters were obtained. The pressure ratio of the low-pressure compressor is shown in Fig. 6 for two different measuring locations in the circumferential direction at the exit of the compressor. It is observed from these two figures that the pressure ratio decreases with increasing angle of attack of the delta-wing simulator. It is also found that the decrease of the pressure ratio is nearly equal at both measuring locations for the same angle of attack of the delta wing, which leads to the conclusion that essentially no total pressure distortion exists at the exit of the compressor in circumferential direction. Thus averaging the values at the two positions in circumferential direction leads to values that are representative for the exit area of the compressor. Therefore it seems that there is no need to traverse the exit area in the circumferential direction, which would be very tough to accomplish in any case. Using the averaged values and computing the performance map of the compressor, it is shown in Fig. 7 that the constant speed lines in the performance map are shifted toward lower mass flow rate and total pressure ratio by the swirl distortion at the engine inlet plane.

The isentropic efficiency of the compressor computed from the measured data depends on the total pressure ratio and the power applied to the compressor, which is calculated from the temperature increase through the compressor. In order to investigate the influence of the temperature increase on the computed isentropic efficiency of the compressor, the total temperature ratio T_{t21}/T_{t2} was plotted versus the corrected speed in Fig. 8 for the two circumferential positions. Referring the measured temperature ratios to the measurement with undistorted inlet flow for the various angles of attack of the delta wing, it is found that on one location the temperature ratio increases with increasing strength of the swirl distortion; however, in the other location it decreases with increasing strength of the swirl distortion. This leads to the conclusion that a circumferential total temperature distortion exists at the exist of the low pressure compressor. This total temperature distortion becomes more and more severe with increasing intensity of the swirl distortion at the compressor inlet. It can be shown that this distortion is the result of a varying power input to the compressor in the circumferential direction, which will be investigated analytically later. Due to the varying total temperature at the exit of the compressor in the circumferential direction, an analysis of the isentropic efficiency shows that the isentropic efficiency is also varying along the circumference of the exit of the compressor. However, the increase in efficiency at one location is not as pronounced as the decrease at the other location due to the almost constant drop in pressure ratio in the circumferential direction. This leads to an average value of the computed isentropic efficiency, which decreases with increasing angle of attack of the delta wing and thus increasing intensity of the generated swirl distortion. This is shown in Fig. 9.

As a conclusion, the effect of a swirl distortion generated in the compressor inlet corresponds to the effect of a total pressure distortion, which leads to the observed phenomena: a decrease of the total pressure ratio, isentropic efficiency, and mass flow rate. However, a total temperature distortion is anticipated at the exit of the compressor, which is the result of a varying power input to the compressor in circumferential direction.

Methods of Measuring Performance Maps of an Installed Compressor

It was the objective of further investigations to find a method to obtain the performance map of the installed low-pressure

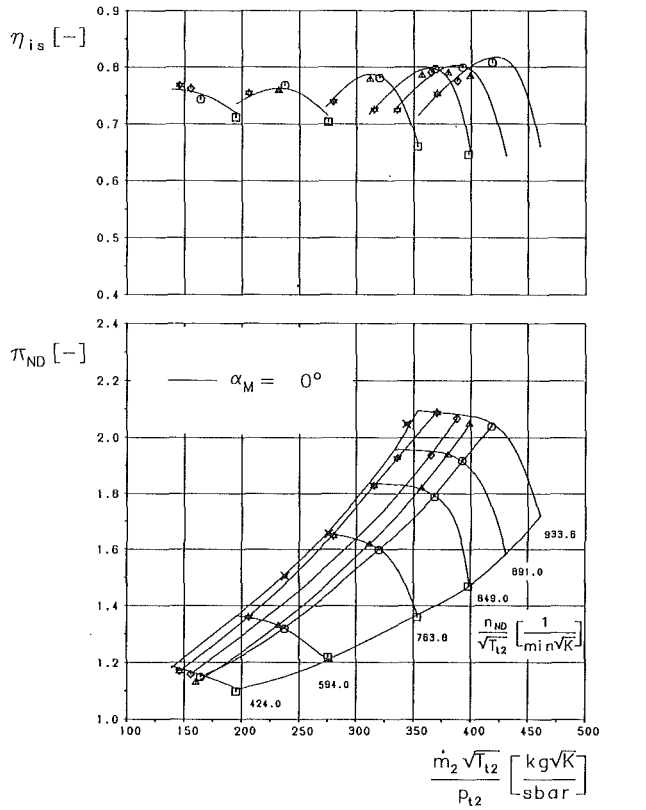

Fig. 10 Measured performance map of the low-pressure compressor

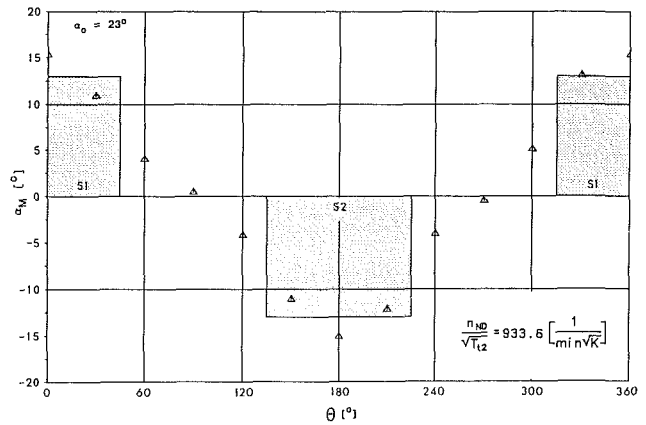

Fig. 11 Circumferential distribution of the swirl angle at the entry of the low-pressure compressor

compressor. However, there is no chance to throttle or unthrottle a compressor that is incorporated in an engine, compared with testing a compressor in a test rig, because the compressor can only follow the operating line of the engine. Thus a change of the operating line of the engine has to be accomplished. The following possibilities of changing the operating line exist on the Larzac 04 engine:

- A bleed from the high-pressure compressor into the fan duct. This bleed leads to a throttling of the low-pressure compressor over the whole operating range and is especially severe

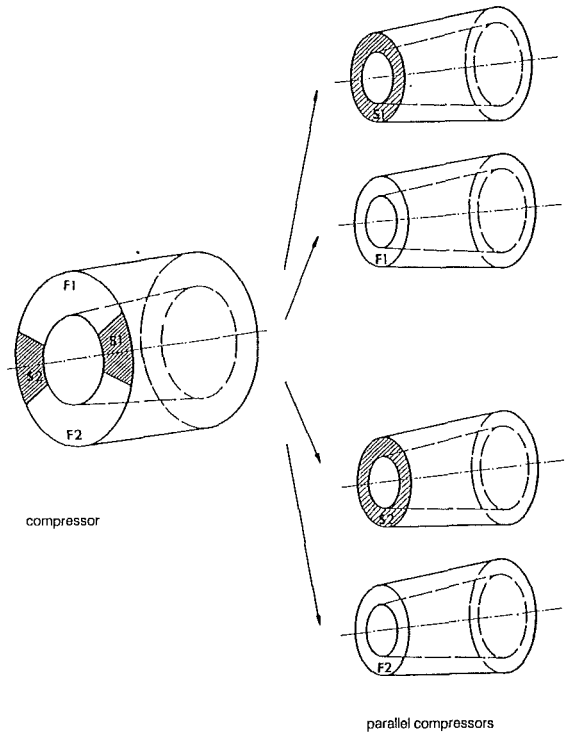

Fig. 12 Substitution of the compressor by four parallel compressors

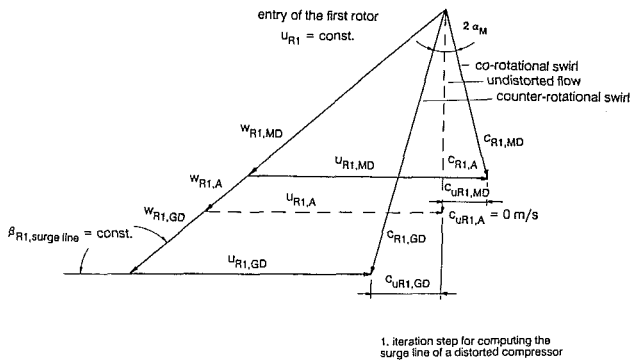

Fig. 13 Velocity triangles of the first iteration step for computing the surge line

in the upper partial power setting and at maximum power. The bleed valve is usually automatically opened below 80 percent high-pressure compressor speed in order to unthrottle the high-pressure compressor. During the test run the bleed valve could be opened or closed in an arbitrary manner.

- The bypass nozzle can be separated from the jet engine and tests can be run without the nozzle. This leads to a severe unthrottling of the low-pressure compressor. In addition, opening the bleed valves had no further influence on the operating line of the engine in the low-pressure compressor performance map. As a result a further unthrottling of this compressor is not possible.
- The bypass nozzle area was reduced up to a maximum of 28 percent of its standard area by fixing area restrictors at the exit of the nozzle. This leads to a throttling of the low-pressure compressor. Thus it is possible to obtain a surge point of the low-pressure compressor by decreasing the bypass nozzle area by a certain amount and opening the bleed valves at the same time. Varying the amount of the change of the nozzle area leads to the surge line of the compressor. This observed surge can only occur in the low-pressure compressor because throttling of the low-pressure compressor leads to an unthrottling

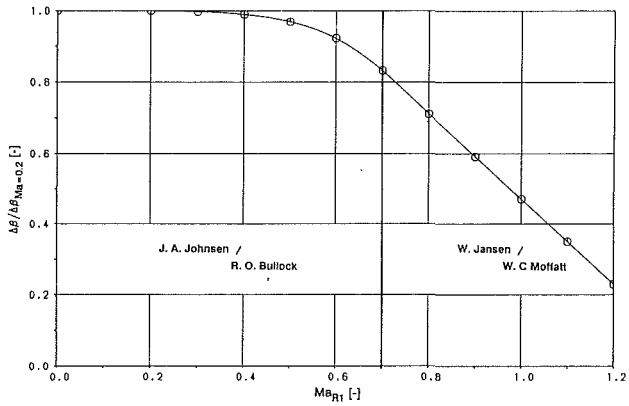

Fig. 14 Correction of the blade operating range

of the high-pressure compressor by changing the bypass ratio of the engine.

However, due to the action of the engine governor, it was not possible to run all the engine configurations mentioned before over the whole operating range of the compressor. This is a limitation for the measured performance map, and this limitation is especially prevalent when the compressor is unthrottled because the maximum exhaust gas temperature behind the low-pressure turbine set on the governor is reached already at the upper partial power setting. Figure 10 shows the performance map of the low-pressure compressor, which is obtained in the aforementioned way. This measured performance map will serve later as a basis for the computation of the performance map with distorted inlet flow.

Modeling of the Performance of a Swirl Distorted Compressor

When searching for a distortion model, it is a prerequisite that the distortion parameter can be displayed by a rectangular-coordinate sector distribution with respect to the circumferential direction as in Fig. 11. It is also desirable that the parameter be constant over the whole operating range of the compressor (Fig. 5). The rectangular distribution leads to a distortion model where the compressor is partitioned in independent parallel compressors according to the distributions of the distorted sectors. The flow at the inlet of one of these parallel compressors is undistorted, at one it contains a coswirl, and at one a counterswirl (Fig. 12).

Starting with the performance map of a compressor with undistorted inlet flow, the performance maps of the two compressors with co- and counterswirl at the inlet are to be computed: The mass flow density at the compressor inlet plane θ_2 is obtained from the corrected mass flow rate at surge of the compressor with undistorted flow

$$\theta_2 = \frac{\dot{m}_2 \cdot \sqrt{T_{t2}}}{p_{t2} \cdot A_2} \cdot \frac{1}{G(\kappa)} \tag{2a}$$

where

$$G(\kappa) = \sqrt{\frac{\kappa}{R} \cdot \left(\frac{2}{\kappa+1}\right)^{\frac{\kappa+1}{\kappa-1}}} \tag{2b}$$

Then the axial Laval number results: $La_2 = f(\theta_2)$. The flow angle of the relative flow to rotor 1 at surge condition is

$$\beta_{R1,SM,A} = \arctan\left(\frac{\pi}{30} \cdot r_2 \cdot \frac{n_{ND}}{\sqrt{T_{t2}}} \cdot \frac{1}{La_2 \cdot F(\kappa)}\right) \tag{3a}$$

where

$$F(\kappa) = \sqrt{2 \cdot \kappa \cdot R \cdot \frac{1}{\kappa+1}} \tag{3b}$$

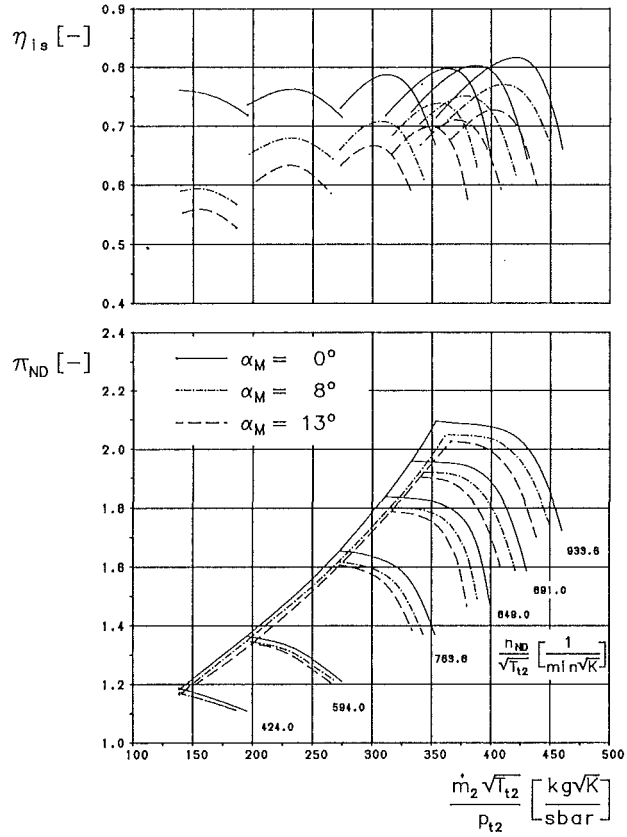

Fig. 15 Computed performance map with inlet swirl distortion (α_M = 13 deg/8 deg)

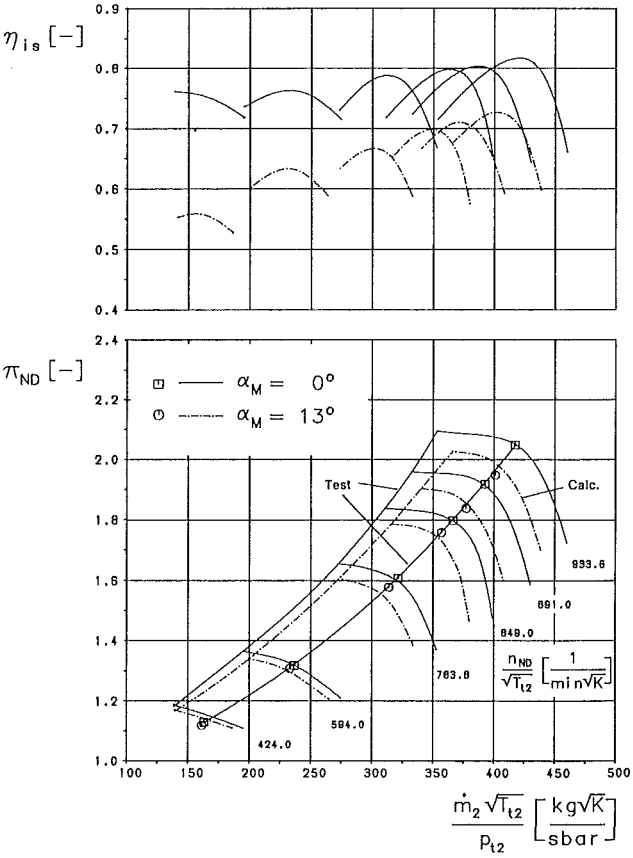

Fig. 16 Computed performance map (α_M = 13 deg) in comparison with a measured operating line

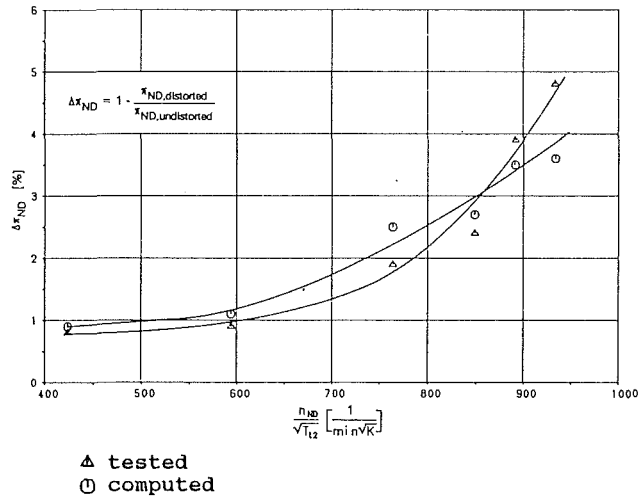

Fig. 17 Comparison between computed and measured total pressure ratio of the low-pressure compressor ($\alpha_o = 23$ deg, $\alpha_M = 13$ deg, see Fig. 5)

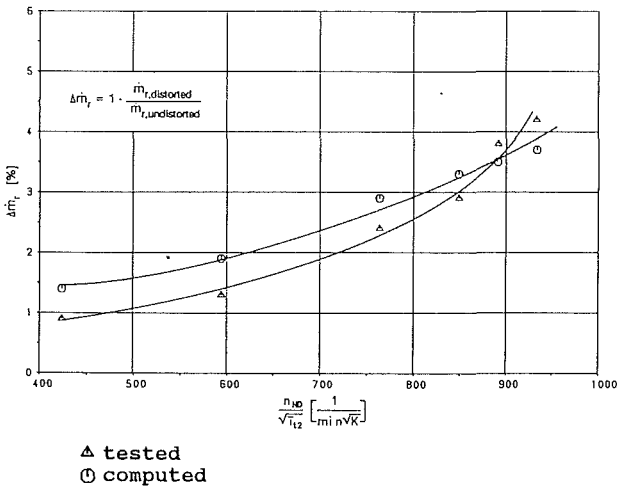

Fig. 18 Comparison between computed and measured mass flow rate of the low-pressure compressor ($\alpha_o = 23$ deg, $\alpha_M = 13$ deg, see Fig. 5)

and from this angle and the circumferential velocity u_{R1} the Mach number $M_{R1,A}$ is obtained. The iteration for the computation of the surge line with distorted flow is started with the assumption that the flow angle of the relative flow to rotor 1 at surge is the same with undistorted and distorted flow, $\beta_{R1,SM} = \text{const}$ (Fig. 13). Using the swirl angle α_M in the axial-velocity relation

$$c_{axR1,SM,MD/GD} = \frac{u_{R1}}{\tan(\beta_{R1,SM,MD/GD}) \pm \tan(\alpha_M)} \tag{4}$$

$M_{R1,MD/GD}$ is obtained. The blade operating range is corrected according to this Mach number, Fig. 14 (Johnsen and Bullock, 1965; Jansen and Moffat, 1966). Based on the theoretical models, it can now be assumed that the operating range of the blading is symmetric to the condition of lowest losses in the blading because the change of the Mach number due to the distortion is small compared to the Mach number operating range of the blading. This leads to an iteration process for the computation of $\beta_{R1,SM,MD/GD}$. It is assumed that the isentropic efficiency ratio of stage 1 for distorted and undistorted flow is the same for both stages, i.e., for the whole compressor. Comparing the power input to the compressor with distorted and undistorted flow and the resulting total enthalpy difference between entry and exit of stage 1 of the compressor, the following efficiency ratio is obtained:

$$\frac{\eta_{isND,MD/GD}}{\eta_{isND,A}} = \frac{u_{R2} \cdot c_{uR2,A}}{u_{R2} \cdot c_{uR2,MD/GD} - u_{R1} \cdot c_{uR1,MD/GD}} \cdot \frac{\Pi_{ND,MD/GD}^{\frac{\kappa-1}{\kappa}} - 1}{\Pi_{ND,A}^{\frac{\kappa-1}{\kappa}} - 1} \tag{5}$$

where

$$c_{uR1,MD/GD} = \pm c_{axR1,MD/GD} \cdot \tan \alpha_M \tag{6}$$

$$c_{uR2,A} = u_{R2} - \tan \beta_{R2,A} \cdot c_{axR2,A} = u_{R2} - w_{uR2,A} \tag{7}$$

$$c_{uR2,MD/GD} = u_{R2} - \frac{c_{axR2,MD/GD}}{c_{axR2,A}} \cdot (u_{R2} - c_{uR2,A}) \tag{8}$$

and

$$\frac{c_{axR2,MD/GD}}{c_{axR2,A}} = \frac{\dot{m}_{MD/GD}}{\dot{m}_A} \cdot \frac{p_{R2,A}}{p_{R2,MD/GD}} \cdot \frac{T_{R2,MD/GD}}{T_{R2,A}} \tag{9}$$

The efficiency can only be computed by an iterative process, because $p_{R2,MD/GD}$ and $T_{R2,MD/GD}$ are connected with $\eta_{isND,MD/GD}$ by the relation of isentropic changes of state. Furthermore, due to the resulting change of the pressure losses in the parallel compressors, an iterative process for the solution of the pressure ratio is necessary where, as an additional equation, the check of continuity for all parallel compressors is used

$$\theta_{21} = \theta_2 \cdot \frac{A_2}{A_{21}} \cdot \frac{\sqrt{T_{t21}/T_{t2}}}{\pi_{ND}} \tag{10}$$

Up to now only formulae are reported, which treat the steady-state flow phenomena in the parallel compressors resulting from the distortion at the inlet of the compressor. However, due to the mixing of the air flows from the parallel compressors, unsteady flow phenomena also have to be considered, since the inlet flow into the compressor contains on one revolution successively a sector of corotational swirl, an undistorted sector, a sector of counterrotational swirl, and again a sector with undistorted flow. The actual effective angle of attack of the relative flow at rotor 1, β_{Seff}, can be computed using a step function

$$\tau \cdot \frac{\delta \beta_{Seff}(t)}{\delta t} + \beta_{Seff}(t) = \beta_S(t) \tag{11}$$

and its general solution

$$\beta_{Seff} = e^{-\int \frac{1}{\tau} dt} \cdot \left[\int \left(\frac{1}{\tau} \cdot \beta_S \cdot e^{\int \frac{1}{\tau} dt} \right) dt + C \right] \tag{12}$$

With the initial condition $t = t_0$, $\beta_{Seff} = \beta_F$, according to Melick and Simpkin (1972), the following solution results:

$$\frac{\beta_{Seff}(\Delta t) - \beta_F}{\beta_S - \beta_F} = 1 - e^{-\frac{\Delta t}{\tau}} \tag{13}$$

where

$$\tau \approx 5.5 \frac{l}{w} \tag{14}$$

This solution serves as a basis to determine the actual operating range of the compressor with swirl distorted flow at the inlet. Behind the parallel compressors the flow is mixed. For the treatment of this mixing it is assumed in general that the static pressure in the mixing area is constant for all flows in and out of this area, i.e., the static pressures at the exit of all parallel compressors are equal

$$p_{21} = p_{21,GD} = p_{21,MD} = p_{21,A} \tag{15}$$

Using the rule of momentum

$$\dot{m} \cdot c_{ax21} = \dot{m}_A \cdot c_{ax21,A} + \dot{m}_{MD} \cdot c_{ax21,MD} + \dot{m}_{GD} \cdot c_{ax21,GD} \tag{16}$$

is obtained. The efficiency and the pressure ratio of the complete compressor are obtained iteratively with this formalism.

Comparison With Experimental Data

Figure 15 shows compressor performance maps with distorted flow computed on the basis of the measured performance map with the undistorted flow of Fig. 10. The average change of the angle of attack of the absolute flow at the inlet of the compressor α_M shown in Fig. 15 corresponds to a certain angle of attack of the delta wing, which can be obtained from Fig. 5. The comparison of the performance maps for distorted and undistorted flow indicates the following effects. The constant speed lines are shifted to lower pressure ratios as well as to lower mass flow rates. The surge line is shifted in such a way that the surge margin is smaller than with undistorted flow. The isentropic efficiency becomes smaller and especially at idle or low power settings further decrease in efficiency is computed. These result from the low level of the pressure ratio at low power settings because in this case small changes of the pressure ratio have a huge effect on the computed efficiency. The narrowing of the blade operating range due to the swirl distortion leads to a steeper speed line than without distorted flow. This steepening effect arises from the acceleration of the flow in the sector with counterswirl, which leads to a blocking of the blading already at low pressure ratios. The decrease of the efficiency results from the different increases of the total enthalpy in the various sectors

$$\Delta h_t = u_{R2} \cdot c_{uR2,MD/GD} - u_{R1} \cdot c_{uR1,MD/GD} = c_p(T_{tR2} - T_{tR1}) \quad (17)$$

because the change of $c_{uR1,MD/GD}$ is larger than the change of $c_{uR2,MD/GD}$. These differences of total enthalpy increase are responsible for a total temperature distortion, which arises at the exit of the compressor. A measured operating line of the engine in the low-pressure compressor performance map is plotted in Fig. 16 for undistorted and distorted flow, and it is observed that there is essentially no difference between the two operating lines as downstream throttling remains the same. Figures 17 and 18 show a comparison of the measured and the computed performance parameters of the low-pressure compressor for distorted flow, and it is found that measurement and calculation are in good agreement within the whole operating range of the compressor.

Conclusions

A test rig is described that simulates swirl distortions in the inlet of a jet engine. Furthermore, a method is shown to measure performance maps of a compressor incorporated in an engine and a formula is introduced to compute performance maps of a compressor with distorted flow by taking the measured performance map with undistorted flow as a basis. Selected measurements of the performance map of the low-pressure compressor with distorted swirl at the inlet show the mass flow rate, the pressure ratio, and the isentropic efficiency to decrease with increasing swirl intensity. In addition, a total temperature distortion could be demonstrated in the compressor exit, which arises from a variable total enthalpy increase along the circumference of the compressor. All these phenomena could be confirmed by the analytical formula presented in this paper.

Acknowledgments

The work reported herein was supported within research programs of the German Bundesministerium der Verteidigung and of the Bundesamt für Wehrtechnik und Beschafung. Permission to publish the results is greatly appreciated.

References

Aulehla, F., 1982, "Intake Swirl—A Major Disturbance Parameter in Engine/Intake Compatibility," ICAS/AIAA, ICAS-82-4.8.1.

Genssler, H. P., Meyer, W., and Fottner, L., 1986, "Development of Intake Swirl Generators for Turbo Jet Engine Testings," AGARD-CP-400.

Hercock, R. G., 1982, "Effect of Inlet Flow Distortion on Engine Stability," AGARD-CP-324.

Jansen, W., and Moffat, W. C., 1966, "The Off-Design Analysis of Axial Flow Compressors," ASME Paper No. 66-WA/GT-1.

Johnsen, J. A., and Bullock, R. O., 1965, "Aerodynamic Design of Axial Flow Compressors," NASA SP-36.

Künkler, H., and Tönskötter, H., 1979, "Zum Einfluss stationärer Temperatur- und Druckstörungen auf die Strömungsverhältnisse in einem installierten, vielstufigen Strahltriebwerk-Verdichter," *Z. Flugwiss. Weltraumforsch.*, Vol. 3, No. 6, pp. 360–378.

Lecht, M., 1983, "Beitrag zum Verhalten von Axialverdichterstufen bei stationärer Störung in der Zuströmung," DFVLR-FB83-39.

Mehalic, Ch. M., and Lottig, R. A., 1974, "Steady-State Inlet Temperature Distortion Effects on the Stall Limits of a J85-GE-13 Turbojet Engine," NASA TM X-2290.

Melick, H. C., and Simpkin, W. E., 1972, "A Unified Theory of Inlet/Engine Compatibility," AIAA Paper No. 72-1115.

Meyer, W., 1988, "Theoretische und experimentelle Untersuchungen über den Einfluss von Eintrittsdrallstörungen auf das Betriebsverhalten von Turbostrahltriebwerken," UniBw München, Institut für Strahlantriebe, Institutsbericht LRT-WE12-88/20.

Pianko, M., and Wazélt, F., 1983, "Propulsion and Energetics Panel Working Group 14 on Suitable Averaging Techniques in Non-uniform Internal Flows," AGARD-AR-182.

Seddon, J., and Goldsmith, E. L., 1985, "Intake Aerodynamics," William Collins Sons & Co. Ltd., London.

Williams, D. D., 1986, "Review of Current Knowledge on Engine Response to Distorted Inflow Conditions," AGARD-CP-400.

Three-Dimensional Flowfields Inside a Transonic Compressor With Swept Blades

C. Hah
GE Corporate Research and Development,
Schenectady, NY 12301

A. J. Wennerstrom
Aeropropulsion Laboratory,
Wright Patterson AFB, OH 45433

The concept of swept blades for a transonic or supersonic compressor was reconsidered by Wennerstrom in the early 1980s. Several transonic rotors designed with swept blades have shown very good aerodynamic efficiency. The improved performance of the rotor is believed to be due to reduced shock strength near the shroud and better distribution of secondary flows. A three-dimensional flowfield inside a transonic rotor with swept blades is analyzed in detail experimentally and numerically. A Reynolds-averaged Navier–Stokes equation is solved for the flow inside the rotor. The numerical solution is based on a high-order upwinding relaxation scheme, and a two-equation turbulence model with a low Reynolds number modification is used for the turbulence modeling. To predict flows near the shroud properly, the tip-clearance flow also must be properly calculated. The numerical results at three different operating conditions agree well with the available experimental data and reveal various interesting aspects of shock structure inside the rotor.

Introduction

Several years ago Prince (1980) observed that shock waves in low aspect ratio, low hub/tip radius ratio axial flow compressors were often quite three dimensional in shape. In particular, he noticed that even when a shock surface appeared almost normal to the relative flow in the cascade plane, the shock front was often quite oblique to the flow in the spanwise direction. He felt that this helped to explain why the efficiency of some of these stages was better than expected, and also why ensemble-averaged, high-frequency pressure measurements made over rotor tips often indicated a pressure rise across the shock that was considerably less than what one would expect from the apparent shock angle as seen in the cascade plane.

This observation led to the generation of the three-dimensional shock loss model of Wennerstrom and Puterbaugh (1984). It was immediately obvious that if a small amount of spanwise shock obliquity incorporated inadvertently could reduce shock losses, somewhat more added deliberately might lower shock losses even more. A rotor was subsequently designed incorporating more sweep but otherwise related to the rotor of the stage reported by Wennerstrom (1984). A computational analysis of this rotor is the subject of this paper.

A known weakness of the three-dimensional shock loss model is its treatment of the shock surface in the vicinity of the outer casing. The model assumes that the shock is normal to the oncoming flow as seen in the cascade plane on each stream surface. The three-dimensional surface created by these normals is swept or oblique in the spanwise direction. What the model ignores is that for subsonic relative flow downstream of the shock, the shock cannot intersect the outer casing obliquely in the spanwise direction. It must either turn normal to the casing or possibly bifurcate in a shock/boundary-layer interaction. One of the objectives of this paper is to examine the behavior of the shock near the outer casing to see what form this adjustment takes and how large a region it occupies.

Although significant progress has been made in recent years to predict flow inside turbomachinery (e.g., Hah, 1984; Moore and Moore, 1985; Weinberg et al., 1986; Dawes, 1987), accurate prediction of flow inside transonic compressor/fans remains one of the difficult problems in turbomachinery CFD. To apply a numerical solution of a transonic compressor/fan for a real design process, the numerical solution must be three dimensional and it must represent viscous flow effects correctly. In a modern, low aspect ratio transonic compressor, the three-dimensional effect on shock structure and the secondary flow field is dominant, and two-dimensional or quasi-three-dimensional methods do not represent the flow properly. The endwall and blade suction surface boundary layers develop very rapidly inside the low aspect ratio transonic compressor and shock-boundary layer interaction triggers boundary layer separation. In addition, the tip leakage flow interacts very strongly with the main flow. These complex viscous flow phenomena determine the location of shocks and the overall flow structure. Therefore, the viscous effects on flow development must be properly represented in the solution.

There have been two approaches to the prediction of flow inside a transonic compressor/fan. The first is the viscous–inviscid interaction method (Singh, 1982; Calvert, 1983; Meauze et al., 1989; etc.). In this approach, the boundary layer displacement effects are somehow coupled to the main inviscid solution of the flow. If a correct estimation of boundary layer

Contributed by the International Gas Turbine Institute and presented at the 35th International Gas Turbine and Aeroengine Congress and Exposition, Brussels, Belgium, June 11–14, 1990. Manuscript received by the International Gas Turbine Institute, January 16, 1990. Paper No. 90-GT-359.

growth is available, either through actual boundary layer calculation or through existing correlation information, this approach can give the correct shock location at moderate operating conditions. However, strong shock–boundary layer interaction and a detailed secondary flowfield cannot be adequately predicted with this approach. The second approach is the solution of a fully compressible Navier–Stokes equation (Thompkins, 1976; Dawes, 1986; Hah, 1987; etc.). Although obtaining good numerical solutions based on a full Navier–Stokes equation is relatively expensive compared with the first approach, the second approach has several advantages: There are no numerical problems matching viscous and inviscid regions, and shock–boundary layer interaction and resulting flow separation can be calculated naturally. Also, this approach can be applied to predict the flow at off-design conditions if the numerical scheme is robust and the turbulence modeling is properly handled.

In the present study, the viscous flowfields inside a low aspect ratio transonic compressor at various operating conditions are numerically calculated. The numerical results are analyzed and compared with the available measured data. Prospects for design applications (e.g., Karadimas, 1988) are also assessed.

The Experiment

The swept rotor was tested as a complete stage. The stage configuration and instrumentation were substantially as described by Wennerstrom (1984). The method used to design the new rotor was identical to that employed to design the referenced original except that the new three-dimensional shock loss model was used to predict the performance, and corrections for airfoil deflection under stress were carried out in three dimensions instead of only restaggering the airfoils as in the original.

In addition to all the instrumentation originally reported, this stage included a complement of 12 high-frequency Kulite pressure transducers mounted in the outer casing over the rotor blade tips. From these, ensemble-averaged static pressure distributions were measured; some of these measurements are included in this paper.

The performance achieved was better than the original design but did not achieve quite the efficiency of the design prediction. The discrepancy in the shock loss model was readily apparent and could be expected to increase at more extreme levels of blade sweep.

Numerical Procedure

Governing Equations and Turbulence Modeling. The following Reynolds-averaged Navier–Stokes equations are solved for the current problem:

$$\frac{\partial}{\partial x_i}(\rho U_i) = 0 \tag{1}$$

$$\frac{\partial}{\partial X_j}(\rho U_i U_j) + 2\rho\epsilon_{ijk}\Omega_j U_k = -\frac{\partial p}{\partial x_i} + \frac{\partial}{\partial x_j}\left[\mu\left(\frac{\partial U_i}{\partial x_j} + \frac{\partial U_j}{\partial x_i} - \frac{2}{3}\frac{\partial U_k}{\partial x_k}\delta_{ij}\right) - \rho\overline{u_i u_j}\right] + F_i \tag{2}$$

$$\frac{\partial}{\partial x_j}(\rho U_j e) = \frac{\partial}{\partial x_j}\left[\left(\frac{\mu}{\Pr}\right)_{\text{eff}}\frac{\partial T}{\partial x_j}\right] - \frac{\partial}{\partial x_j}(pU_j) + U_i F_i + \frac{\partial}{\partial x_j}\left[U_i u\left(\frac{\partial U_i}{\partial x_j} + \frac{\partial U_j}{\partial x_i} - \frac{2}{3}\frac{\partial U_k}{\partial x_k}\delta_{ij}\right)\right] \tag{3}$$

$$p = \rho RT \tag{4}$$

where U_i = mean velocity, u_i = fluctuating velocity, e = total energy, Ω_i = angular velocity,

$$\left(\frac{\mu}{\Pr}\right)_{\text{eff}} = \left(\frac{\mu}{\Pr}\right)_{\text{laminar}} + \left(\frac{\mu}{\Pr}\right)_{\text{turbulent}}$$

and

$$e = C_v T + \frac{1}{2}U_i U_i$$

It is well known that neither the conventional mixing length type turbulence model nor the standard two-equation turbulence model models turbulence stresses properly in the region behind a shock wave or when flow is separated because of shock-boundary layer interaction. Several recent studies (e.g., Goutines et al., 1989) indicate that significant improvement can be obtained when the standard two-equation model is modified to include the low Reynolds number effects. For the present study, a modified k–ϵ, two-equation model is used to estimate Reynolds stresses. The turbulence model is extended to the solid wall following the studies of Chien (1982). The following additional transport equations are solved to calculate turbulent stress terms:

$$\frac{\partial(\rho U_i k)}{\partial x_i} = \frac{\partial}{\partial x_i}\left(\frac{\mu_{\text{eff}}}{\sigma_k}\frac{\partial k}{\partial x_i}\right) - \rho\overline{u_i u_j}U_{i,j} - \rho\epsilon - \frac{2\mu k}{l^2} \tag{5}$$

Nomenclature

$C_1, C_2, C_3, C_4, C_u, \sigma_{dk}, \sigma_\epsilon$ = constants in turbulence closure models
CFD = computational fluid dynamics
C_m = total relative velocity
C_v = specific heat
F_i = additional body force in equation (2)
k = turbulence kinetic energy
k_c = thermal conductivity
$\dot{m}$ = mass flow rate
P = $-\overline{u_i u_j}U_{ij}$
p = static pressure
R = gas constant
S_V = specific heat
T = temperature
U_i = mean velocity vector
u_i = fluctuating velocity vector
β = coefficient of thermal expansion
δ_{ij} = Kronecker delta
ϵ_{ijk} = permutation tensor
ν = kinematic viscosity
ρ = density
Ω_i = angular velocity of impeller
PS = pressure side
SH = shroud
SS = suction side

Subscripts

t = total
w = value at wall
∞ = upstream condition
2 = downstream condition

Superscript

$(\bar{\ })$ = average value

$$\frac{\partial(\rho U_i \epsilon)}{\partial x_i} = \frac{\partial}{\partial x_i}\left(\frac{\mu_{\text{eff}}}{\sigma_\epsilon}\frac{\partial \epsilon}{\partial x_i}\right) + C_1 \frac{\rho\epsilon}{k}\left(\overline{u_i u_j} U_{i,j}\right)$$

$$-\frac{\rho\epsilon}{k}\left(C_2 f\epsilon + \frac{2\nu k e^{-C_4 u^* l/\nu}}{l^2}\right) \quad (6)$$

where

$$\mu_{\text{eff}} = \mu + C_\mu (k^2/\epsilon)\left(1 - e^{-C_3 u^* l/\nu}\right)$$

and

$$f = 1 - \frac{0.4}{1.8} e^{-(k^2/6\nu\epsilon)^2}$$

No attempt was made to optimize constants of the turbulence modeling equations for this study. Therefore, standard values of various constants of the turbulence model are used; the values are

$$C_\mu = 0.09,\ C_1 = 1.35,\ C_2 = 1.8,\ \sigma_k = 1.0,\ \sigma_\epsilon = 1.3,$$
$$C_3 = 0.0115,\ C_4 = 0.5$$

Numerical Scheme. Although significant progress has been made in numerical methods during the last decade, accurate numerical solution of equations (1)–(6) for the three-dimensional flow inside a transonic compressor remains one of the difficult problems. The additional body forces (centrifugal and Coriolis) from the system rotation and the inherent complexity in boundary conditions and difficulty in generating an optimum grid for the high turning blades make the overall numerical procedure very stiff.

For the current study, equations (1)–(6) are solved with an implicit relaxation method using a fully conservative control volume. With the current method, Cartesian components of momentum (ρU_i) are solved sequentially along with internal total energy (e), turbulence kinetic (k) energy, and energy dissipation rate (ϵ). As the governing equations are solved sequentially, each corresponding finite difference equation should be represented with a diagonally dominant matrix. To adjust sequentially solved Cartesian components of momentum for global conservation and to propagate local information, a correction equation is formed by combining the continuity equation and momentum equations. From this correction equation, a new pressure field is obtained and the density field is computed using equation (4).

The governing equations are solved on a general curvilinear coordinate. A third-order accurate interpolation scheme is used for the discretization of convection terms and central differencing is used for diffusion terms. The overall scheme is of second-order accuracy with smoothly varying grids. To apply the present relaxation scheme successfully to transonic flow, high-order upwinding should be consistently applied for all the Euler terms in momentum and correction equations. The detailed equations for the current method are given by Hah (1987) and applications for transonic and supersonic turbine blade rows are given by Hah (1989).

Computational Grid and Boundary Condition. Good grid generation is a primary part of obtaining a good numerical solution to the three-dimensional flow inside turbomachinery. Computation of the three-dimensional viscous flow inside blade rows with arbitrary endwalls requires many additional constraints for good grid generation.

An H-grid has been very widely used for inviscid and viscous flow computation in turbomachinery. Although the H-grid has been very good for field properties and is easy to apply for the periodicity condition, the grid tends to skew significantly when applied to transonic compressors/fans. A single O-grid or C-grid provides good grid resolution around the blade and in the wake (C-grid). However, the single O-grid or C-grid becomes very skewed at inflow and periodic boundaries and does not give good grid resolution for the description of endwall boundary layers.

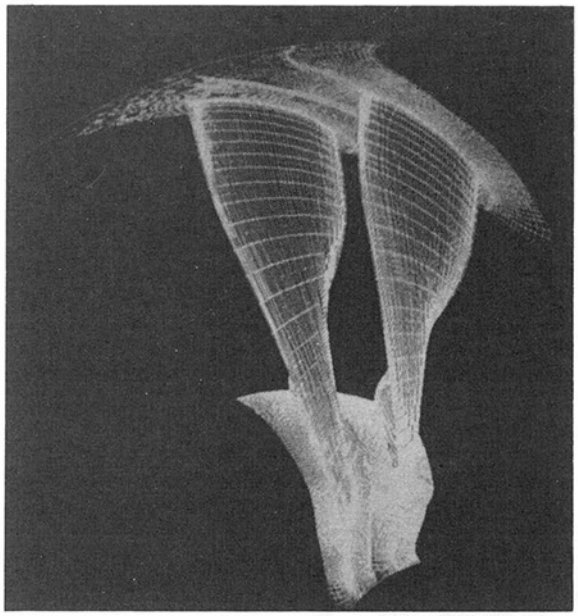

Fig. 1(*a*) Computational grid (41 × 35 × 111, 6 nodes inside tip clearance)

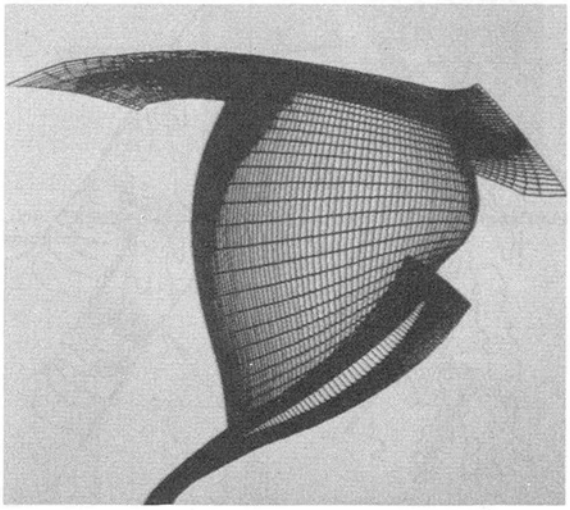

Fig. 1(*b*) Computational grid on blade surface and endwalls

An I-grid, which can be treated as a generalized H-grid, provides good grid resolution near the blade as well as at the far field. With the I-grid, spatial periodicity of the grid at the periodic surface is no longer enforced and the physical periodicity condition is handled inside the code. The I-grid for the current study is shown in Fig. 1. The grid consists of 41 nodes in the blade-to-blade direction, 35 nodes in the spanwise direction, and 111 nodes in the streamwise direction; 6 nodes in the spanwise direction describe the tip clearance of the compressor. The computational grid was generated with an elliptic grid generation method and good orthogonality is maintained across most of the computational domain.

At the inflow boundary surface, the distribution of total temperature, total pressure, and inlet flow angles is fixed. At the outflow boundary, which is located at the leading edge of the following stator, the static pressure at the tip is fixed and extrapolation is used for all unknown variables. Radial equilibrium is not valid at the outflow surface for this flow and is not applied for the current solution. For the turbulence boundary condition, the experimental value of turbulence kinetic energy is used at the inlet, and the equilibrium condition is

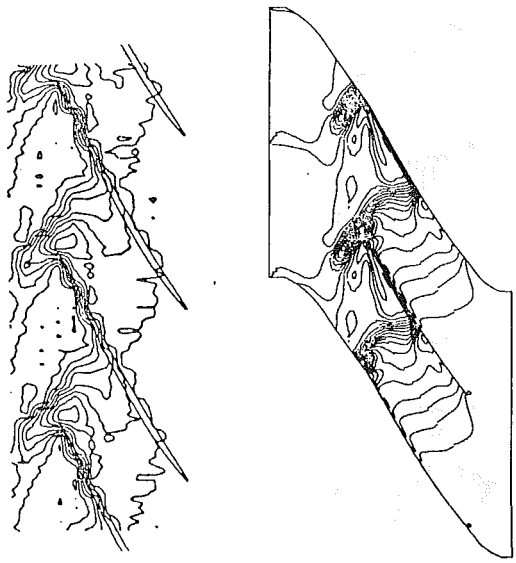

KULITE MEASUREMENT CALCULATION

Fig. 2(*a*) Comparison of shroud static pressure at stall condition

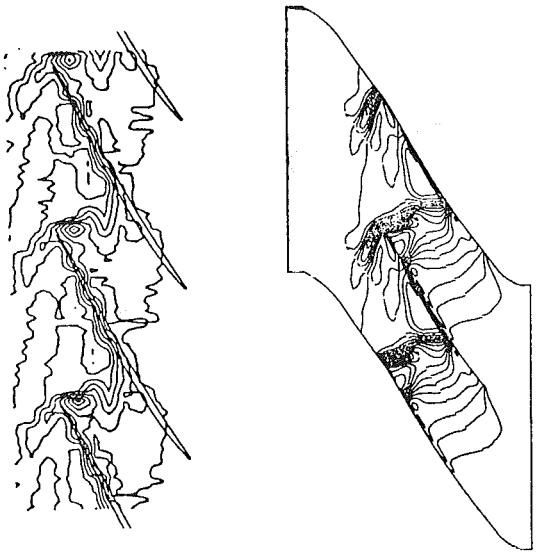

KULITE MEASUREMENT CALCULATION

Fig. 2(*b*) Comparison of shroud static pressure at design condition

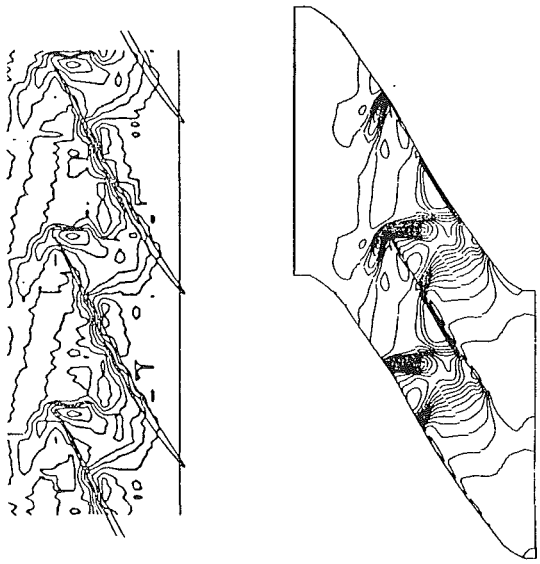

KULITE MEASUREMENT CALCULATION

Fig. 2(*c*) Comparison of shroud static pressure at choke condition

used to estimate the length scale for the turbulence dissipation rate. Residuals of each finite difference equation are integrated over the entire domain. When the integrated residuals of the equations are reduced by four orders of magnitude from their initial value, the solution is considered to be converged. The code was run on a Cray-XMP, and the required computing time with the current grid was about one hour, with a single processor for each case.

Results and Discussion

Flow Structures Near the Endwall. The numerical analyses were performed for three operating conditions (stall, design, and choke) at design rotor speed. The measured mass flow rate at the stall condition was about 3 percent lower than that at design condition, and the measured mass flow rate at the choke condition was 2 percent higher than at design condition. The calculated mass flow rates at the three operating conditions were slightly higher (less than 0.2 percent) than corresponding measured flow rates, but this is well within the measurement tolerance. In Fig. 2, the time-averaged static pressure contours on the compressor casing are compared with the Kulite measurements. At the stall condition, both the measured data and the numerical solution show that the shock is ahead of the leading edge, and the leading edge passage shock is not normal to the inlet relative flow angle. Also, a very strong interaction between the shock and the tip-leakage vortex is indicated by measurement and calculation.

At the design condition, the passage shock becomes nearly normal to the inlet relative flow angle and the suction surface shock moves toward the trailing edge (about 55 percent of chord). Again, the strong interaction between the passage shock and the tip-leakage vortex is clearly shown by calculation and by measurement. At the choke condition, the passage shock moves farther toward the trailing edge, and again the shock is more oblique to the inlet relative flow. Compared with both stall and design flow rates, a strong reflected shock is clearly present at the choke condition (both measurement and calculation). Comparisons in Fig. 2 show that the numerical solutions do correctly predict the shock structures on the casing at the different flow rates.

Various existing analytical models for shock loss assume that the passage shock is normal to the inlet relative flow direction. Both the measurements and the numerical results show that this assumption is valid only near the design flow condition. At all three flow rates, the interaction between the passage shock and the tip-leakage vortex is very strong. The velocity vectors inside the tip-clearance gap (50 percent of the tip gap) are shown in Fig. 3. These velocity vectors clearly illustrate the formation of the tip-leakage vortex near the suction side of the blade. In Fig. 4(*a*), the measured and calculated pressure contours and relative velocity vectors near the casing are compared at design flow rate. The influence of tip-leakage flow on the passage shock is shown near the tip-leakage vortex (the suction-side leg of the shock is moved farther downstream because of this interaction). Similar experimental observations and interpretations were reported by Kerrebrock (1980) and Freeman (1985).

A shadowgraph from a different transonic rotor with no blade sweep (Freeman, 1985) is shown in Fig. 4(*b*). Figure 4(*c*) shows the relative Mach number contours for the swept rotor. Similar structures for the tip-leakage vortex are observed for

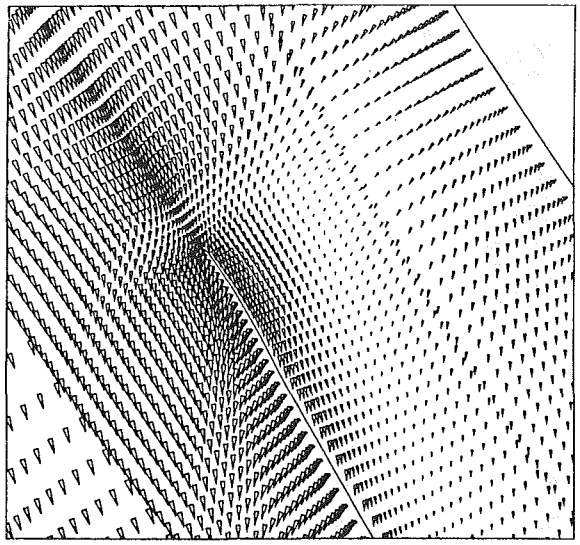

Fig. 3(*a*) Velocity vectors near leading edge inside tip clearance at stall condition

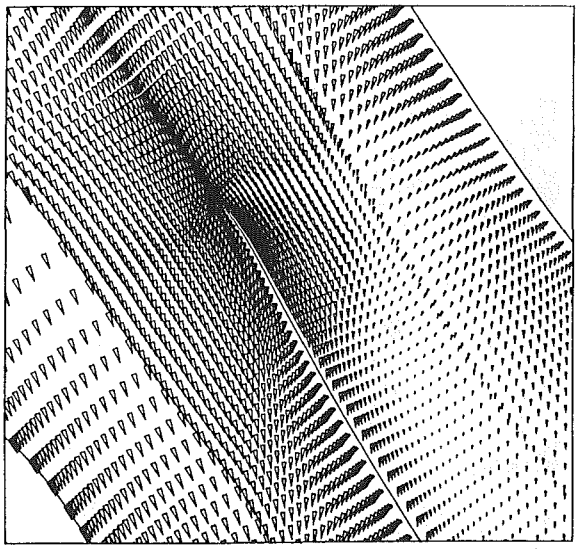

Fig. 3(*b*) Velocity vectors near leading edge inside tip clearance at design condition

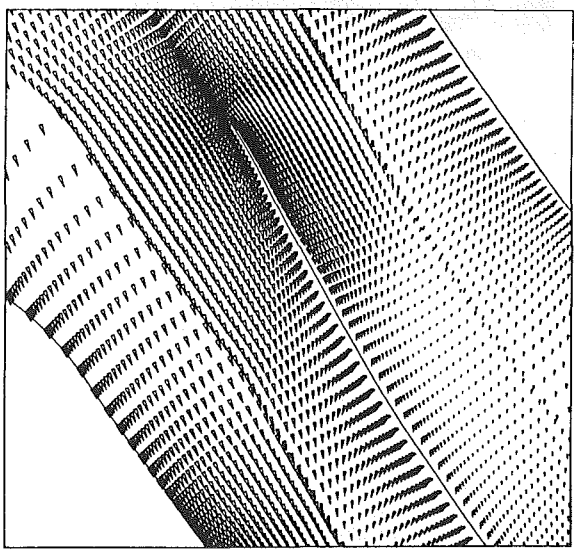

Fig. 3(*c*) Velocity vectors near leading edge inside tip clearance at choke condition

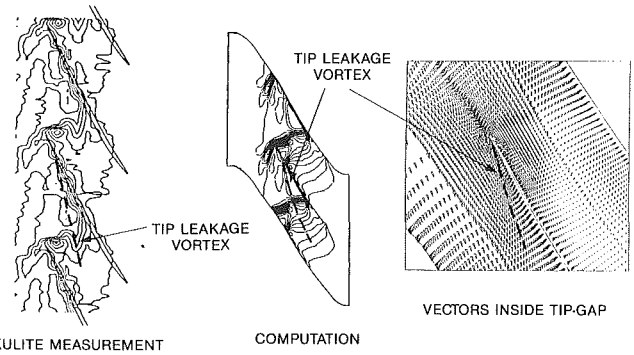

Fig. 4(*a*) Interaction between passage shock and tip leakage vortex at shroud

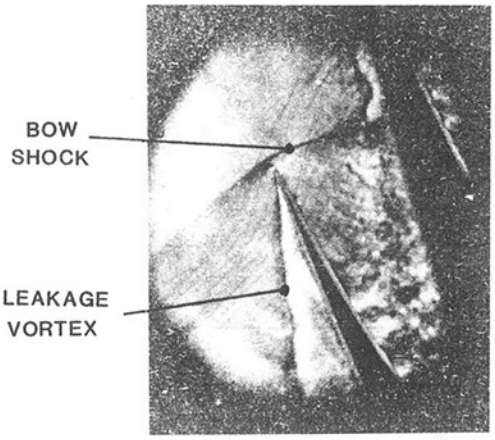

Fig. 4(*b*) Shadowgraph of tip-leakage vortex in a conventional transonic compressor

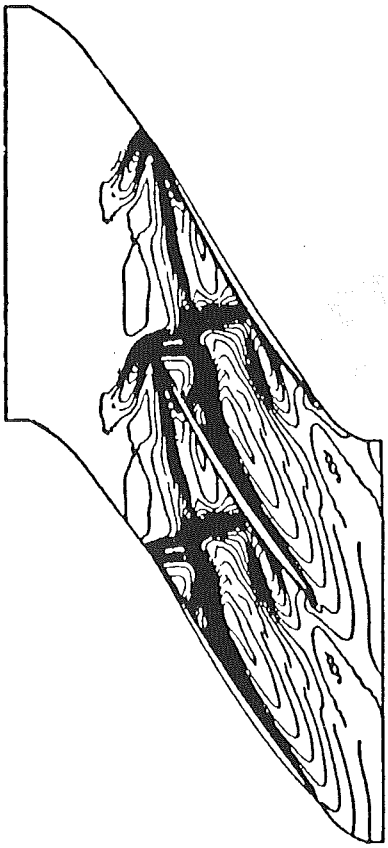

Fig. 4(*c*) Relative Mach number contours at 99.4 percent span

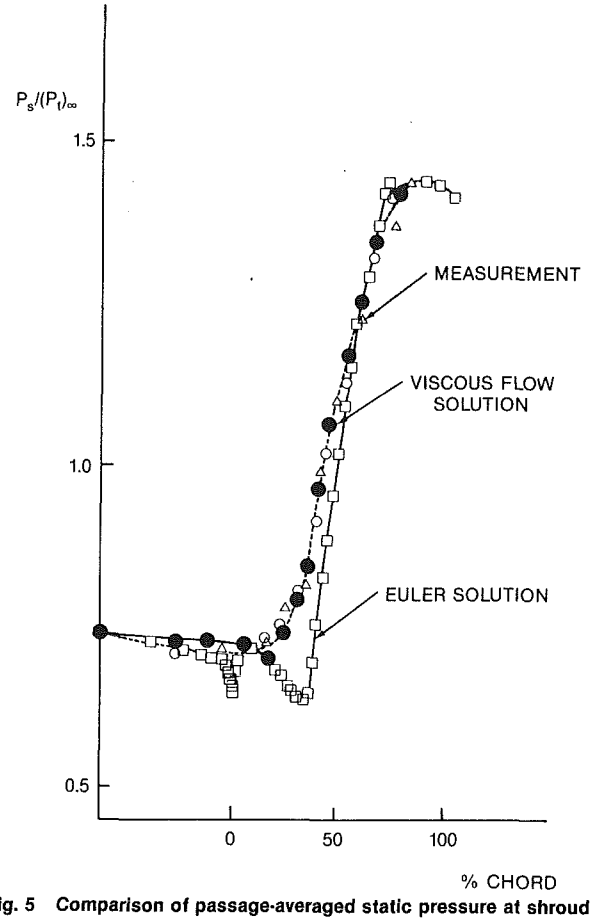

Fig. 5 Comparison of passage-averaged static pressure at shroud

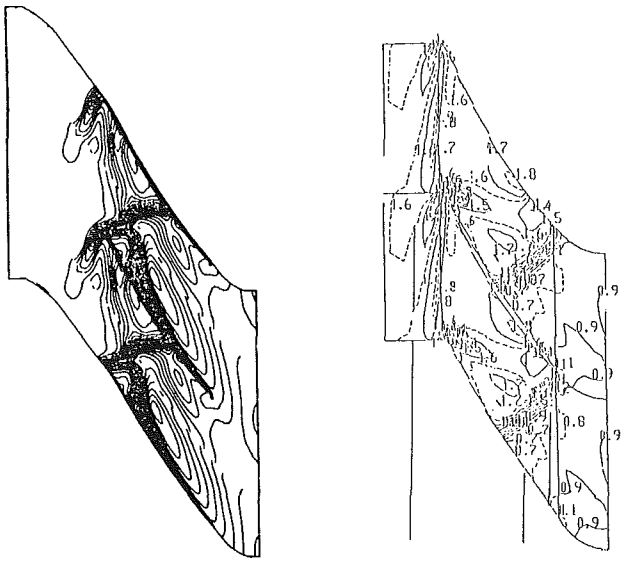

VISCOUS FLOW SOLUTION

EULER FLOW SOLUTION

Fig. 6 Comparison of relative Mach number at shroud

both rotors. Figure 5 compares measurement and calculation for the passage-averaged static pressure distribution on the shroud at the design condition. The corresponding Euler and viscous solutions at the tip are compared in Fig. 6. From Figs. 5 and 6, it is evident that the three-dimensional viscous effect must be properly modeled for a realistic solution in transonic compressors.

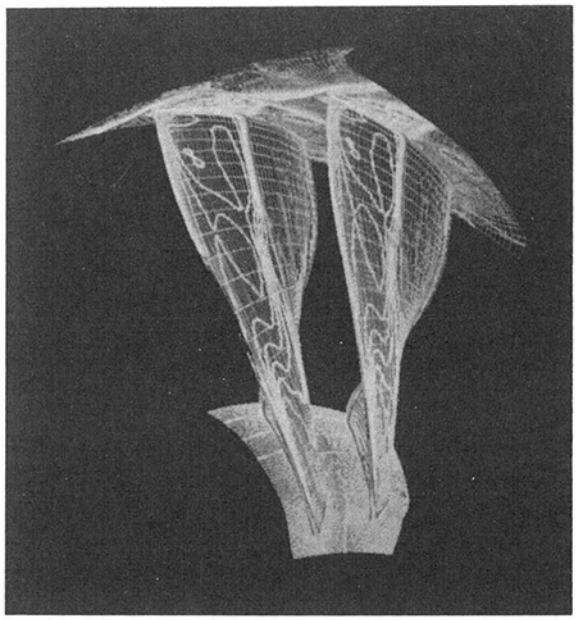

Fig. 7(*a*) Mach number contours on suction surface at stall condition

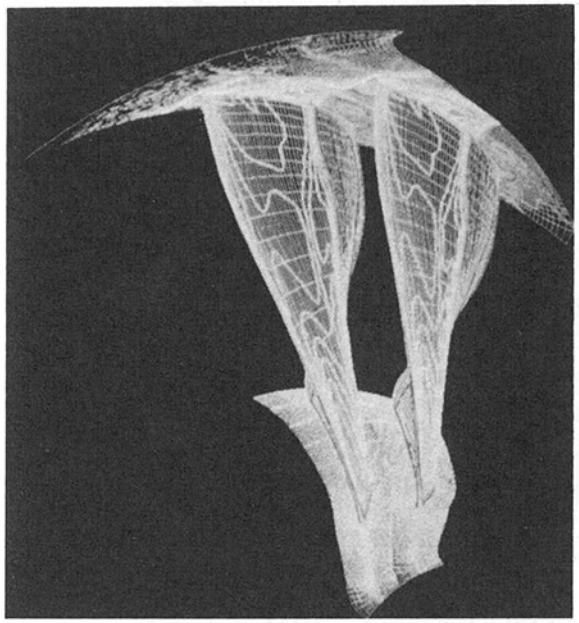

Fig. 7(*b*) Mach number contours on suction surface at design condition

Flow Structure Inside the Blade Passage. Relative Mach number contours on the shroud and on the suction surface are shown in Fig. 7. The numerical solution represents changes in the flow structure for the three operating conditions very well. With the increase in mass flow rate, the shock moves downstream. The contours on Fig. 7 show the very complex three-dimensional nature of the flowfield. At all three flow conditions, radial variation of the flow structure is very strong. The suction surface shock is oblique away from the endwall because of the sweep of the blade. However, the shock becomes nearly normal to the endwall as it approaches the endwall. This adjustment appears to occur in a very short distance. The strong shock extends from the tip up to 50 percent of the span. Below that radius, diffuse compression is observed for all cases. Figure 8 shows relative velocity vectors near the shock on the suction surface at the design condition. A strong radial outward

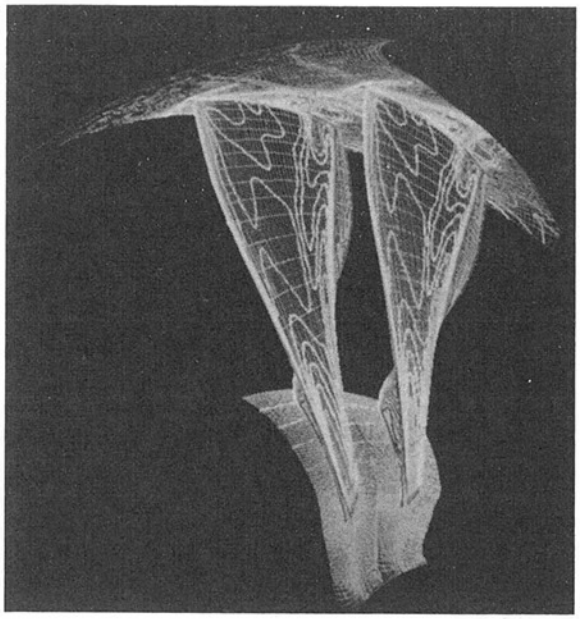

Fig. 7(*c*) Mach number contours on suction surface at choke condition

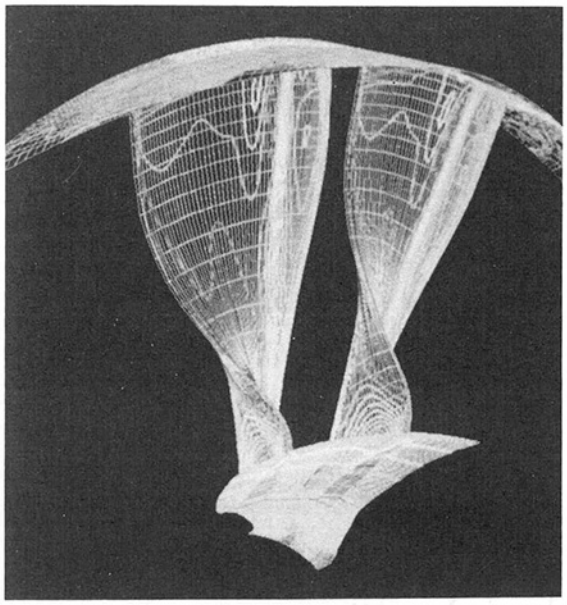

Fig. 9(*b*) Mach number contours on pressure surface at design condition

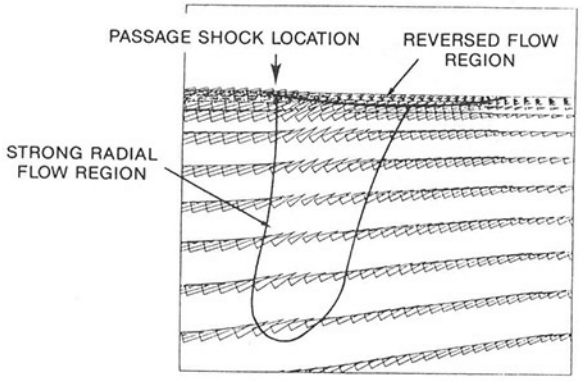

Fig. 8 Velocity vectors inside boundary layer on suction surface near passage shock

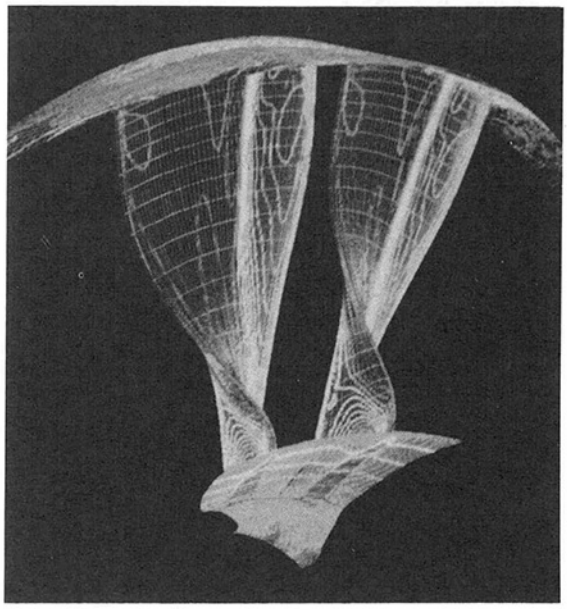

Fig. 9(*c*) Mach number contours on pressure surface at choke condition

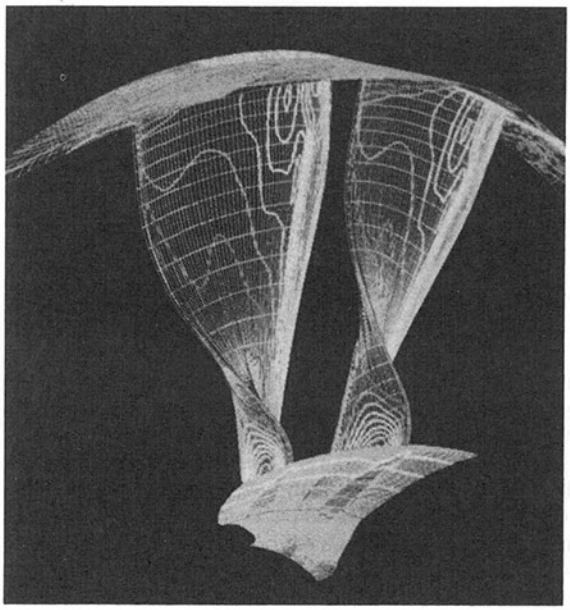

Fig. 9(*a*) Mach number contours on pressure surface at stall condition

flow is observed after the shock. This phenomenon, which is due to centrifugal effects, was also observed and discussed by Epstein et al. (1979). The strong radial components of velocity extend up to very near the casing, where reversed flow is present because of the complex interaction of shock, boundary layer, and tip-leakage flow.

Relative Mach number contours on the pressure surface are given in Fig. 9 (viewed from downstream of the trailing edge). The shock strength on the pressure side looks higher than on the suction side. This is due to the strong interaction with a thick boundary layer on the suction surface. The distribution of Mach number contours inside the blade passage at various radii is given in Fig. 10. The influence of tip-leakage flow on passage shock is clearly shown up to 20 percent of the span from the tip. Below 50 percent of the span, the strong passage shock is reduced to a weak diffuse compression.

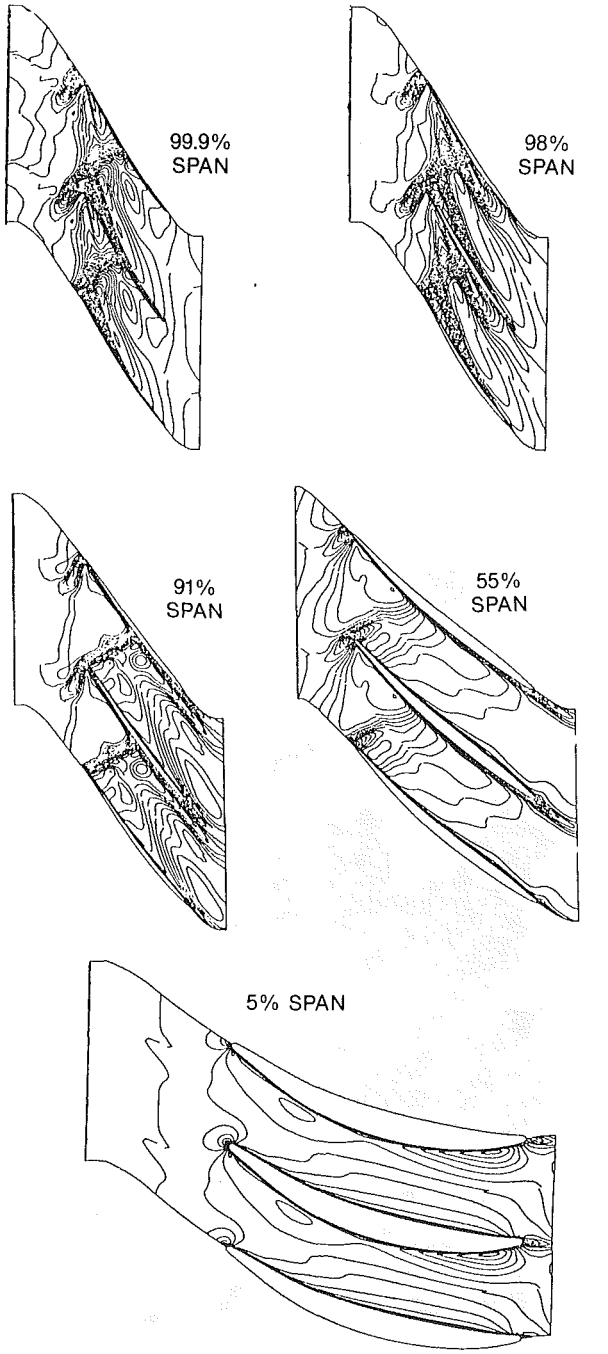

Fig. 10(*a*) Calculated relative Mach number contours at stall condition

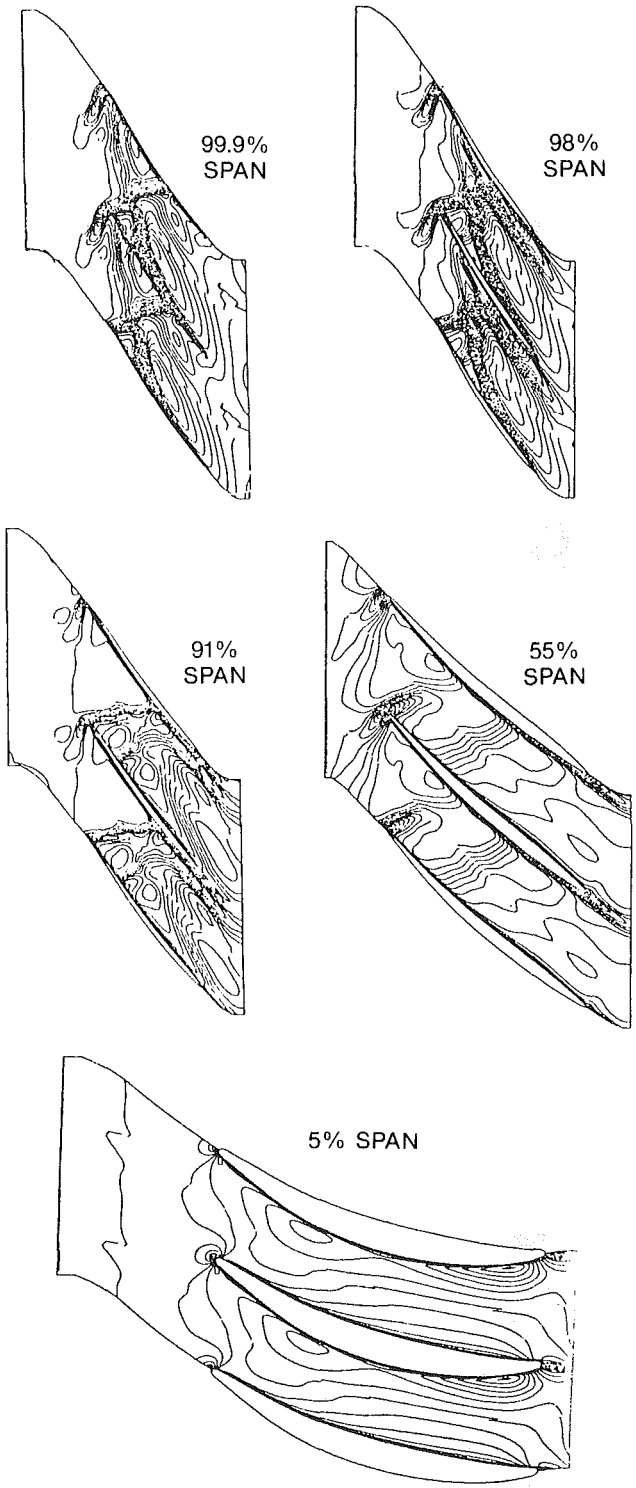

Fig. 10(*b*) Calculated relative Mach number contours at design condition

Based on the current numerical solution, the three-dimensional shock structure inside the rotor at the design condition is constructed and compared with the conventionally assumed shock structure in Fig. 11. The oblique shock from the current solution shows that the shock is swept back substantially at around 90 percent of the span. This is exactly what would have to occur for the shock to intersect the outer casing approximately normal to the casing and still appear normal to the relative flow direction at the outer casing. An improved three-dimensional shock model could be developed based on the current oblique shock system.

Overall Performance. The calculated inlet and exit relative angles are given in Fig. 12. Because no experimental data are available, direct comparisons cannot be made. However, the exit flow angle in Fig. 12 indicates that flow overturning caused by tip leakage extends more than 20 percent of the span from the tip. Again, this implies that three-dimensional viscous flow effects are very significant in the transonic compressor and some rational modification of the current design system probably should be made on further designs.

The distribution of total temperature at the rotor exit is compared with measurement in Fig. 13. In Fig. 14, the calculated distribution of nondimensional total pressure at the rotor exit is compared with the available experimental data at the stage exit. Considering the difficulty and the uncertainty

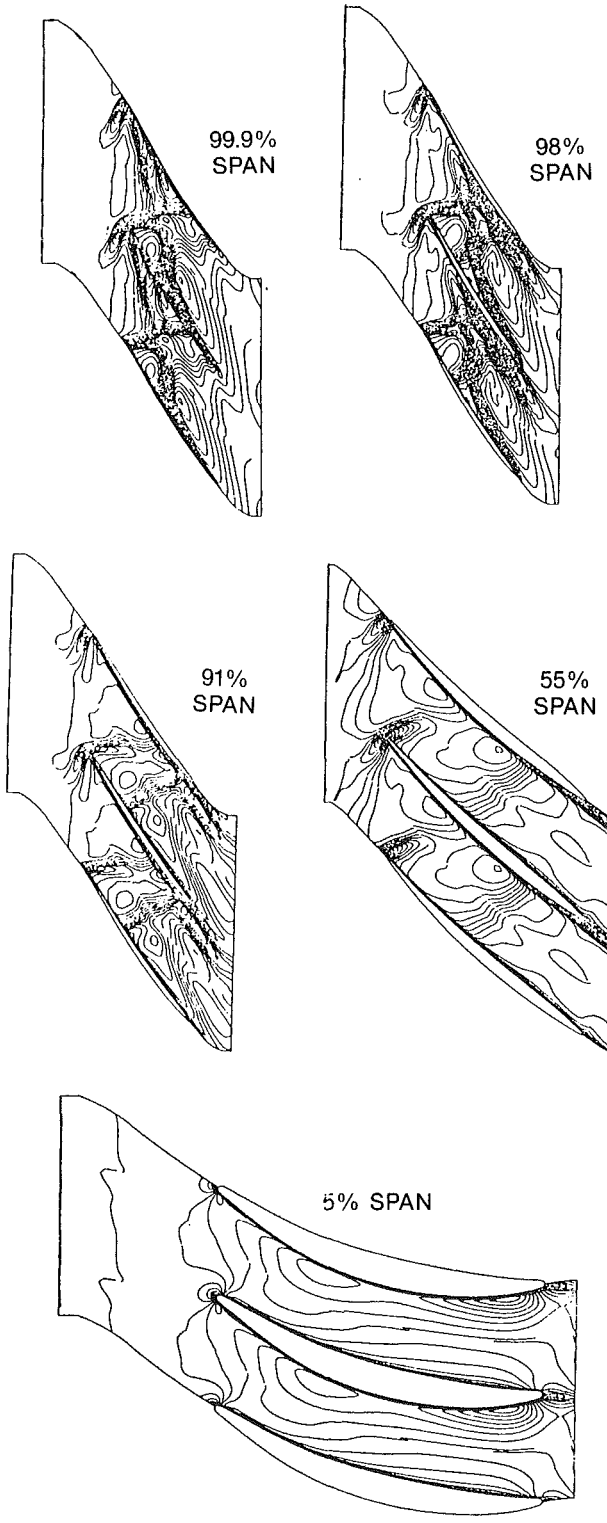

Fig. 10(*c*) Calculated relative Mach number contours at choke condition

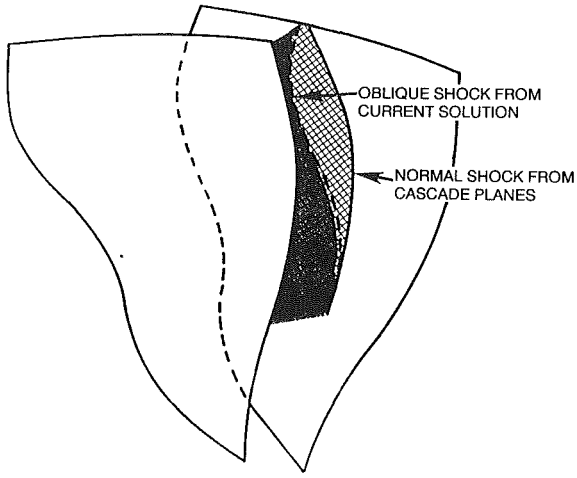

Fig. 11 Comparison of three-dimensional shock structure between current solution and conventional assumption

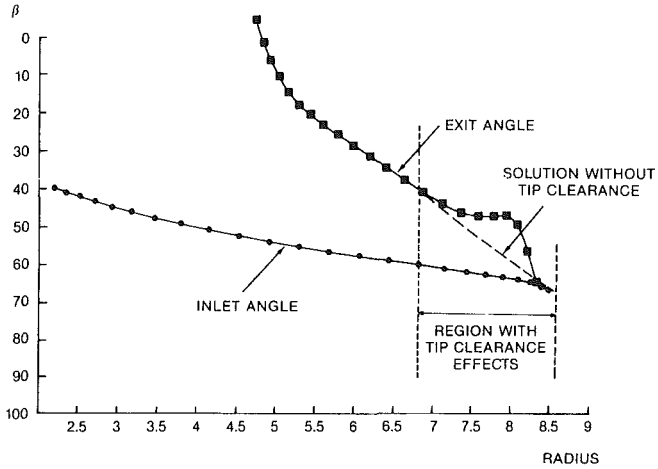

Fig. 12 Tip clearance effects on the relative flow angles

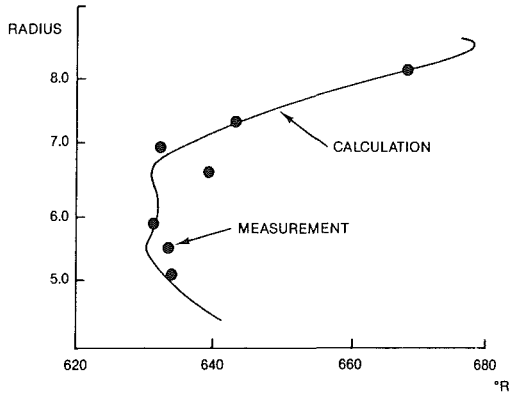

Fig. 13 Comparison of total temperature distribution at exit

of accuracy in the measured data, the comparison looks very reasonable. Table 1 compares calculated relative aerodynamic efficiencies of the current swept rotor and two conventional rotors.

Because the remaining experimental data (total pressure distribution at exit, aerodynamic efficiency) are restricted, we cannot present further comparisons here. However, calculated compressor efficiency is very close to the measured value, and the numerical solutions predict overall performance with an accuracy that is acceptable for engineering design guidance.

Conclusions

A detailed three-dimensional flowfield inside a modern transonic rotor with a swept blade has been studied using a three-dimensional viscous flow code.

The numerical solutions with about 130,000 computational nodes provide a detailed flowfield near the tip region as well as in the blade passage. Comparisons with limited experimental data are very good, and the accuracy of the numerical solution is acceptable for engineering design guidance. Several design

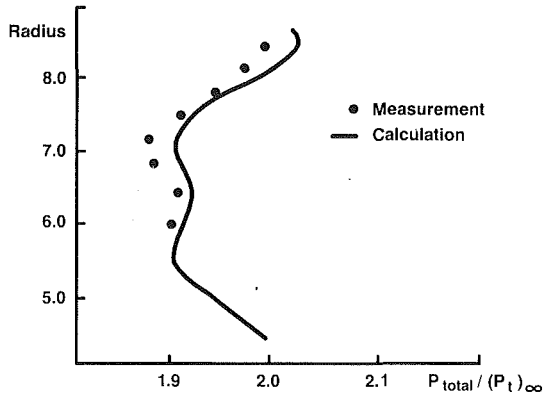

Fig. 14 Calculated distribution of nondimensional total pressure at rotor exit compared with available data at stage exit

Table 1 Aerodynamic efficiency comparison of swept and conventional rotors

Type	Ratio of Aerodynamic Efficiency
Swept Rotor	1.0
Conventional Rotor 1	0.98
Conventional Rotor 2	0.97

features of the swept compressor rotor are also confirmed with the numerical solution.

The results shown in Fig. 10(*b*) help to clarify the geometric shape of the shock as it approaches the outer casing. The simple three-dimensional shock loss theory presented by Wennerstrom and Puterbaugh (1984) assumed a shock normal to the incoming flow on each stream surface in the cascade plane. This is reasonably consistent with the Kulite measurements and the calculated pressure distribution shown in Fig. 2(*b*). However, the pressure distribution at 91 percent span in Fig. 10(*b*) shows a shock swept substantially back in the passage. This is exactly what would have to occur for the shock to intersect the outer casing approximately normally and still appear normal to the relative flow direction on the outer casing. Thus an improved three-dimensional shock loss model might be expected to include an oblique shock, possibly analogous to that of Koch and Smith (1976), coupled with some transition model that would cause the shock to become perpendicular to the outer casing at the outer casing.

The current study confirms that the apparent inefficiency in the supersonic flow zone of transonic compressor rotors is due to the strong interaction between passage shock, blade boundary layer, and tip-leakage flow. Based on this study, it appears to be possible to conduct a systematic study to improve the efficiency of transonic compressors by using the understanding gained from detailed numerical studies on the three-dimensional shock/viscous interaction to modify the passage geometry to minimize the effects of these interactions. This possibility can be best realized through widespread acceptance of these modern tools along with some creative ties to the detailed passage geometry generators.

Acknowledgments

The authors would like to acknowledge the contribution of D. Miller, who constructed the original computational grid for the rig.

References

Calvert, W. J., 1983, "Application of an Inviscid-Viscous Interaction Method to Transonic Compressor Cascades," NGTE Report R83001, Mar.

Chien, K. Y., 1982, "Predictions of Channel and Boundary-Layer Flows With a Low Reynolds Number Turbulence Model," *AIAA Journal*, Vol. 20, No. 1, pp. 33–38.

Dawes, W. N., 1986, "Development of a 3D Navier-Stokes Solver for Application to All Types of Turbomachinery," ASME Paper No. 86-GT-70.

Epstein, A. H., Kerrebrock, J. L., and Thompkins, W. T., Jr., 1979, "Shock Structure in Transonic Compressor Rotors," *AIAA Journal*, Vol. 17, No. 4, Apr.

Freeman, C., 1985, "Tip Clearance Effects in Axial Turbomachines," VKI Lecture Series LS-05.

Goutines, M., Hah, C., and Karadimas, G., 1989, "Mesh Generation for Flow Computation in Turbomachine," invited paper at AGARD Specialists' Meeting, May 1989; to appear as AGARD CP.

Hah, C., 1984, "A Navier-Stokes Analysis of Three-Dimensional Turbulent Flows Inside Turbine Blade Rows at Design and Off-design Conditions," ASME *Journal of Engineering for Gas Turbines and Power*, Vol. 106, pp. 421–429.

Hah, C., 1987, "Calculation of Three-Dimensional Viscous Flows in Turbomachinery With an Implicit Relaxation Method," AIAA *Journal of Propulsion and Power*, Vol. 3, No. 5, pp. 415–422.

Hah, C., 1989, "Generation and Decay of Secondary Flows and Their Impact on Aerodynamic Performance of Modern Turbomachinery Components," *Proceedings of AGARD 74th Specialists' Meeting on Secondary Flow in Turbomachinery*.

Karadimas, G., 1988, "Design of High-Performance Fans Using Advanced Aerodynamic Codes," ASME JOURNAL OF TURBOMACHINERY, Vol. 110, pp. 419–425.

Kerrebrock, J. L., 1980, "Flow in Transonic Compressors," *AIAA Journal*, Vol. 19, No. 4.

Koch, C. C., and Smith, L. H., Jr., 1976, "The Loss Sources and Magnitude in Axial Flow Compressors," ASME *Journal of Engineering for Power*, Vol. 98, pp. 411–424.

Meauze, G., Paulon, J., and Denhondt, D., 1989, "Numerical Simulation of Turbomachinery Flows With a Simple ONERA Model of Viscous Effects," *Proceedings of 9th ISABE Meeting*, Athens, Greece, Sept.

Moore, J., and Moore, J. G., 1985, "Performance Evaluation of Linear Turbine Cascades Using Three-Dimensional Viscous Flow Calculations," ASME *Journal of Engineering for Gas Turbines and Power*, Vol. 107, pp. 969–975.

Prince, D. C., Jr., 1980, "Three Dimensional Shock Structures for Transonic/Supersonic Compressor Rotors," *Journal of Aircraft*, Vol. 17, No. 1, pp. 28–37.

Singh, U. K., 1982, "A Computation and Comparison With Measurements of Transonic Flow in an Axial Compressor Stage With Shock and Boundary Layer Interaction," ASME *Journal of Engineering for Power*, Vol. 104.

Thompkins, W. T., Jr., 1976, "An Experimental and Computational Study of the Flow in a Transonic Compressor Rotor," PhD Thesis, Massachusetts Institute of Technology, June; also MIT Gas Turbine Lab. Rept. No. 129, May.

Weinberg, B. C., Yang, R.-J., McDonald, H., and Shamroth, S. J., 1986, "Calculation of Two- and Three-Dimensional Transonic Cascade Flow Fields Using the Navier-Stokes Equations," ASME *Journal of Engineering for Gas Turbines and Power*, Vol. 108, pp. 93–102.

Wennerstrom, A. J., 1984, "Experimental Study of a High-Through-Flow Transonic Axial Compressor Stage," ASME *Journal of Engineering for Gas Turbines and Power*, Vol. 106, No. 3, pp. 552–560.

Wennerstrom, A. J., and Puterbaugh, S. L., 1984, "A Three-Dimensional Model for the Prediction of Shock Losses in Compressor Blade Rows," ASME *Journal of Engineering for Gas Turbines and Power*, Vol. 106, No. 2, pp. 295–299.

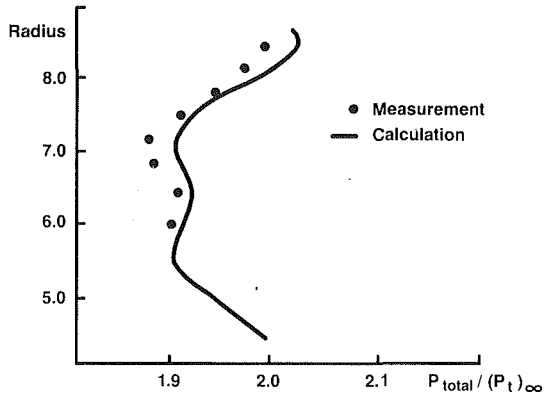

Fig. 14 Calculated distribution of nondimensional total pressure at rotor exit compared with available data at stage exit

Table 1 Aerodynamic efficiency comparison of swept and conventional rotors

Type	Ratio of Aerodynamic Efficiency
Swept Rotor	1.0
Conventional Rotor 1	0.98
Conventional Rotor 2	0.97

features of the swept compressor rotor are also confirmed with the numerical solution.

The results shown in Fig. 10(*b*) help to clarify the geometric shape of the shock as it approaches the outer casing. The simple three-dimensional shock loss theory presented by Wennerstrom and Puterbaugh (1984) assumed a shock normal to the incoming flow on each stream surface in the cascade plane. This is reasonably consistent with the Kulite measurements and the calculated pressure distribution shown in Fig. 2(*b*). However, the pressure distribution at 91 percent span in Fig. 10(*b*) shows a shock swept substantially back in the passage. This is exactly what would have to occur for the shock to intersect the outer casing approximately normally and still appear normal to the relative flow direction on the outer casing. Thus an improved three-dimensional shock loss model might be expected to include an oblique shock, possibly analogous to that of Koch and Smith (1976), coupled with some transition model that would cause the shock to become perpendicular to the outer casing at the outer casing.

The current study confirms that the apparent inefficiency in the supersonic flow zone of transonic compressor rotors is due to the strong interaction between passage shock, blade boundary layer, and tip-leakage flow. Based on this study, it appears to be possible to conduct a systematic study to improve the efficiency of transonic compressors by using the understanding gained from detailed numerical studies on the three-dimensional shock/viscous interaction to modify the passage geometry to minimize the effects of these interactions. This possibility can be best realized through widespread acceptance of these modern tools along with some creative ties to the detailed passage geometry generators.

Acknowledgments

The authors would like to acknowledge the contribution of D. Miller, who constructed the original computational grid for the rig.

References

Calvert, W. J., 1983, "Application of an Inviscid-Viscous Interaction Method to Transonic Compressor Cascades," NGTE Report R83001, Mar.

Chien, K. Y., 1982, "Predictions of Channel and Boundary-Layer Flows With a Low Reynolds Number Turbulence Model," *AIAA Journal*, Vol. 20, No. 1, pp. 33–38.

Dawes, W. N., 1986, "Development of a 3D Navier-Stokes Solver for Application to All Types of Turbomachinery," ASME Paper No. 86-GT-70.

Epstein, A. H., Kerrebrock, J. L., and Thompkins, W. T., Jr., 1979, "Shock Structure in Transonic Compressor Rotors," *AIAA Journal*, Vol. 17, No. 4, Apr.

Freeman, C., 1985, "Tip Clearance Effects in Axial Turbomachines," VKI Lecture Series LS-05.

Goutines, M., Hah, C., and Karadimas, G., 1989, "Mesh Generation for Flow Computation in Turbomachine," invited paper at AGARD Specialists' Meeting, May 1989; to appear as AGARD CP.

Hah, C., 1984, "A Navier-Stokes Analysis of Three-Dimensional Turbulent Flows Inside Turbine Blade Rows at Design and Off-design Conditions," ASME *Journal of Engineering for Gas Turbines and Power*, Vol. 106, pp. 421–429.

Hah, C., 1987, "Calculation of Three-Dimensional Viscous Flows in Turbomachinery With an Implicit Relaxation Method," AIAA *Journal of Propulsion and Power*, Vol. 3, No. 5, pp. 415–422.

Hah, C., 1989, "Generation and Decay of Secondary Flows and Their Impact on Aerodynamic Performance of Modern Turbomachinery Components," *Proceedings of AGARD 74th Specialists' Meeting on Secondary Flow in Turbomachinery*.

Karadimas, G., 1988, "Design of High-Performance Fans Using Advanced Aerodynamic Codes," ASME JOURNAL OF TURBOMACHINERY, Vol. 110, pp. 419–425.

Kerrebrock, J. L., 1980, "Flow in Transonic Compressors," *AIAA Journal*, Vol. 19, No. 4.

Koch, C. C., and Smith, L. H., Jr., 1976, "The Loss Sources and Magnitude in Axial Flow Compressors," ASME *Journal of Engineering for Power*, Vol. 98, pp. 411–424.

Meauze, G., Paulon, J., and Denhondt, D., 1989, "Numerical Simulation of Turbomachinery Flows With a Simple ONERA Model of Viscous Effects," *Proceedings of 9th ISABE Meeting*, Athens, Greece, Sept.

Moore, J., and Moore, J. G., 1985, "Performance Evaluation of Linear Turbine Cascades Using Three-Dimensional Viscous Flow Calculations," ASME *Journal of Engineering for Gas Turbines and Power*, Vol. 107, pp. 969–975.

Prince, D. C., Jr., 1980, "Three Dimensional Shock Structures for Transonic/Supersonic Compressor Rotors," *Journal of Aircraft*, Vol. 17, No. 1, pp. 28–37.

Singh, U. K., 1982, "A Computation and Comparison With Measurements of Transonic Flow in an Axial Compressor Stage With Shock and Boundary Layer Interaction," ASME *Journal of Engineering for Power*, Vol. 104.

Thompkins, W. T., Jr., 1976, "An Experimental and Computational Study of the Flow in a Transonic Compressor Rotor," PhD Thesis, Massachusetts Institute of Technology, June; also MIT Gas Turbine Lab. Rept. No. 129, May.

Weinberg, B. C., Yang, R.-J., McDonald, H., and Shamroth, S. J., 1986, "Calculation of Two- and Three-Dimensional Transonic Cascade Flow Fields Using the Navier-Stokes Equations," ASME *Journal of Engineering for Gas Turbines and Power*, Vol. 108, pp. 93–102.

Wennerstrom, A. J., 1984, "Experimental Study of a High-Through-Flow Transonic Axial Compressor Stage," ASME *Journal of Engineering for Gas Turbines and Power*, Vol. 106, No. 3, pp. 552–560.

Wennerstrom, A. J., and Puterbaugh, S. L., 1984, "A Three-Dimensional Model for the Prediction of Shock Losses in Compressor Blade Rows," ASME *Journal of Engineering for Gas Turbines and Power*, Vol. 106, No. 2, pp. 295–299.

DISCUSSION

N. A. Cumpsty[1]

This paper contains a number of very interesting ideas and results. It is particularly welcome to have set down in the conclusions that the inefficiency of supersonic regions of transonic compressors is associated primarily with shock boundary layer interactions and not with the loss of the shock itself.

I am no expert in the area of Navier–Stokes solvers, but I understand that the prediction of absolute levels of loss and efficiency is still very problematic. This is because in three dimensions an exceedingly large number of grid points would be needed to predict loss correctly since near solid surfaces it is necessary to have several mesh points inside the boundary

[1]Whittle Laboratory, University of Cambridge, Madingley Road, Cambridge CB3 0DY United Kingdom.

layer to define the loss due to shear work at all accurately. Where good agreement with measurement occurs using current grid sizes it should often be regarded as fortuitous. The methods are often better at predicting loss in flows where the loss generation is dominated by features with a relatively large scale—tip clearance flow and separated regions, for example—than in flows with fully attached flow and thin boundary layers.

Recently Freeman and Cumpsty (1989) described a method for estimating the profile loss from the forward region of supersonic blades where this loss is the result of shocks and shock boundary layer interactions. Although very simple (simple enough to be carried out by hand) the predictions of level and trends agreed well with measured values of loss for two conventional fan rotors, one a fan of the early 1970s, the other a recent one. It is asserted that this agreement is not coincidental, but is the consequence of conservation requirements for mass, enthalpy, and momentum; only if there are large spanwise flows should the approach be expected to be inaccurate. Would the authors care to show the comparison of their measured losses with the predictions of Freeman and Cumpsty?

References

Freeman, C., and Cumpsty, N. A., 1989, "A Method for the Prediction of Supersonic Compressor Blade Performance," ASME Paper No. 89-GT-326; to be published in the *AIAA Journal of Propulsion and Power*.

Authors' Closure

The authors would like to thank Professor Cumpsty for his detailed discussion. The following closure is prepared for the discussion.

1 The current work is to investigate detailed flow physics inside a transonic fan with a swept rotor. We are more interested in the three-dimensional effects on the detailed flow structure and the aerodynamic performance (three-dimensional shock system, shock-boundary layer-tip clearance flow interaction, etc.). The basic design goal of the swept rotor is to introduce favorable three-dimensional effects to the flow field for optimum aerodynamic efficiency. As Kerrebrock (1980) suggested, the details of the flow inside a transonic fan can be investigated with a three-dimensional viscous CFD analysis. The authors agree strongly with Professor Cumpsty that the study by Freeman and Cumpsty (1989) should complement the current CFD approach. The simple approach by Freeman and Cumpsty (1989) can explain certain aspects of flow physics inside a supersonic compressor.

2 One of the most important goals in applying three-dimensional Navier–Stokes CFD is to predict the aerodynamic loss accurately. To achieve this goal, the CFD approach must satisfy several criteria. The numerical procedure should be free of numerical diffusion. Also, the employed physical models (flow transition, turbulence models, etc.) should be as realistic as possible. With the recent development of large-scale computers and the advance of CFD technology, aerodynamic losses can be predicted very reasonably (within 10 percent of error from the measured values) for many important flows. Also, the difference in aerodynamic efficiency between various designs can be predicted with acceptable accuracy, although the absolute value of each configuration might not be calculated precisely.

To apply the method of Freeman and Cumpsty (1989) for the prediction of aerodynamic loss of the current swept rotor, additional study might be necessary. The one-dimensional method appears to underestimate the aerodynamic efficiency by about 2 percent at 90 percent span of the rotor. The prediction of the overall aerodynamic loss of the rotor seems quite dependent on which spanwise section of the rotor is used for the calculation. Although the method by Freeman and Cumpsty (1989) provides very useful guidance on the estimation of the aerodynamic loss, additional developments, which include the effects of the boundary layer, the tip-leakage flow, etc., might improve the loss prediction of the low-aspect-ratio compressor.

layer to define the loss due to shear work at all accurately. Where good agreement with measurement occurs using current grid sizes it should often be regarded as fortuitous. The methods are often better at predicting loss in flows where the loss generation is dominated by features with a relatively large scale—tip clearance flow and separated regions, for example—than in flows with fully attached flow and thin boundary layers.

Recently Freeman and Cumpsty (1989) described a method for estimating the profile loss from the forward region of supersonic blades where this loss is the result of shocks and shock boundary layer interactions. Although very simple (simple enough to be carried out by hand) the predictions of level and trends agreed well with measured values of loss for two conventional fan rotors, one a fan of the early 1970s, the other a recent one. It is asserted that this agreement is not coincidental, but is the consequence of conservation requirements for mass, enthalpy, and momentum; only if there are large spanwise flows should the approach be expected to be inaccurate. Would the authors care to show the comparison of their measured losses with the predictions of Freeman and Cumpsty?

References

Freeman, C., and Cumpsty, N. A., 1989, "A Method for the Prediction of Supersonic Compressor Blade Performance," ASME Paper No. 89-GT-326; to be published in the *AIAA Journal of Propulsion and Power*.

Authors' Closure

The authors would like to thank Professor Cumpsty for his detailed discussion. The following closure is prepared for the discussion.

1 The current work is to investigate detailed flow physics inside a transonic fan with a swept rotor. We are more interested in the three-dimensional effects on the detailed flow structure and the aerodynamic performance (three-dimensional shock system, shock-boundary layer-tip clearance flow interaction, etc.). The basic design goal of the swept rotor is to introduce favorable three-dimensional effects to the flow field for optimum aerodynamic efficiency. As Kerrebrock (1980) suggested, the details of the flow inside a transonic fan can be investigated with a three-dimensional viscous CFD analysis. The authors agree strongly with Professor Cumpsty that the study by Freeman and Cumpsty (1989) should complement the current CFD approach. The simple approach by Freeman and Cumpsty (1989) can explain certain aspects of flow physics inside a supersonic compressor.

2 One of the most important goals in applying three-dimensional Navier–Stokes CFD is to predict the aerodynamic loss accurately. To achieve this goal, the CFD approach must satisfy several criteria. The numerical procedure should be free of numerical diffusion. Also, the employed physical models (flow transition, turbulence models, etc.) should be as realistic as possible. With the recent development of large-scale computers and the advance of CFD technology, aerodynamic losses can be predicted very reasonably (within 10 percent of error from the measured values) for many important flows. Also, the difference in aerodynamic efficiency between various designs can be predicted with acceptable accuracy, although the absolute value of each configuration might not be calculated precisely.

To apply the method of Freeman and Cumpsty (1989) for the prediction of aerodynamic loss of the current swept rotor, additional study might be necessary. The one-dimensional method appears to underestimate the aerodynamic efficiency by about 2 percent at 90 percent span of the rotor. The prediction of the overall aerodynamic loss of the rotor seems quite dependent on which spanwise section of the rotor is used for the calculation. Although the method by Freeman and Cumpsty (1989) provides very useful guidance on the estimation of the aerodynamic loss, additional developments, which include the effects of the boundary layer, the tip-leakage flow, etc., might improve the loss prediction of the low-aspect-ratio compressor.

Tip Leakage Flow in Axial Compressors

J. A. Storer

N. A. Cumpsty

Whittle Laboratory,
University of Cambridge,
Cambridge, United Kingdom

Experimental measurements in a linear cascade with tip clearance are complemented by numerical solutions of the three-dimensional Navier–Stokes equations in an investigation of tip leakage flow. Measurements reveal that the clearance flow, which separates near the entry of the tip gap, remains unattached for the majority of the blade chord when the tip clearance is similar to that typical of a machine. The numerical predictions of leakage flow rate agree very well with measurements, and detailed comparisons show that the mechanism of tip leakage is primarily inviscid. It is demonstrated by simple calculation that it is the static pressure field near the end of the blade that controls chordwise distribution of the flow across the tip. Although the presence of a vortex caused by the roll-up of the leakage flow may affect the local pressure field, the overall magnitude of the tip leakage flow remains strongly related to the aerodynamic loading of the blades.

Introduction

Large tip clearance is recognized to be detrimental to both the efficiency and stability of axial compressors (Smith, 1970; Freeman, 1985). In most cases optimum performance is obtained at a clearance smaller than that dictated by mechanical constraints. Deliberate aerodynamic design to minimize the deleterious effects of tip leakage therefore remains the only option for further improvement, but such design cannot be fully effective without an appreciation of the factors governing tip leakage flow.

The work described in this paper is an investigation of tip leakage flow in a linear cascade using a combination of experimental measurements and three-dimensional numerical solutions of the Navier–Stokes equations. The calculations are used to explore aspects of tip leakage flow less accessible by experiment alone. Although the flowfield near the endwalls of a linear cascade is known to differ considerably from that in a compressor, this difference is of secondary importance to the present investigation because attention is directed to the leakage flow itself.

Experimental Methods

All the experimental results described in this paper were obtained in a linear cascade comprising five blades. Details of the aerodynamic design of the cascade are given in Table 1. The central blade was instrumented with pressure tappings on both surfaces at several spanwise positions near the tip. The blades were cantilevered so they could be moved relative to the endwalls to vary the clearance gap at the tip by adjusting the hub fixture.

The periodicity of the flow was controlled by adjustable flaps at the top and bottom of the cascade. This arrangement was adequate since it was only necessary to achieve the design flow conditions about the central aerofoil, around which the leakage flow measurements were to be taken. Comparison of the pressure distribution measured at midspan with a prediction by an inviscid (Martensen) calculation confirms the cascade was set up correctly (see Fig. 1).

Table 1 Summary of cascade aerodynamics

Chord	300.0 mm
Pitch	180.0 mm
Span	435.0 mm
Maximum thickness-to-chord ratio	0.05
Camber (circular arc)	45.5°
Stagger	22.2°
Inlet flow angle from axial	45.0°
Inlet Mach number	0.03
Reynolds' number based on chord	5.0×10^5
Inlet endwall boundary layer 140% chord upstream:	
Displacement thickness	2.9 mm
Momentum thickness	2.1 mm
Shape factor	1.4

Measurements of the static pressure on the endwall were made with a matrix of pressure tappings drilled in the endwall to span the two blade passages about the central blade. The distribution of pressure tappings on the endwall was nonuniform and reflected the anticipated pressure gradients. In total 522 tappings were arranged in a square mesh with the smallest spacing between adjacent tappings being 3 mm (1 percent of chord). The measurements were taken in blocks of 48 connected via a Scanivalve to a single pressure transducer.

Detailed measurements of the leakage flow were carried out at fixed positions along the blade chord for a variety of clearances. Traverses were made across the tip gap to an accuracy

Contributed by the International Gas Turbine Institute and presented at the 35th International Gas Turbine and Aeroengine Congress and Exposition, Brussels, Belgium, June 11–14, 1990. Manuscript received by the International Gas Turbine Institute February 10, 1990. Paper No. 90-GT-127.

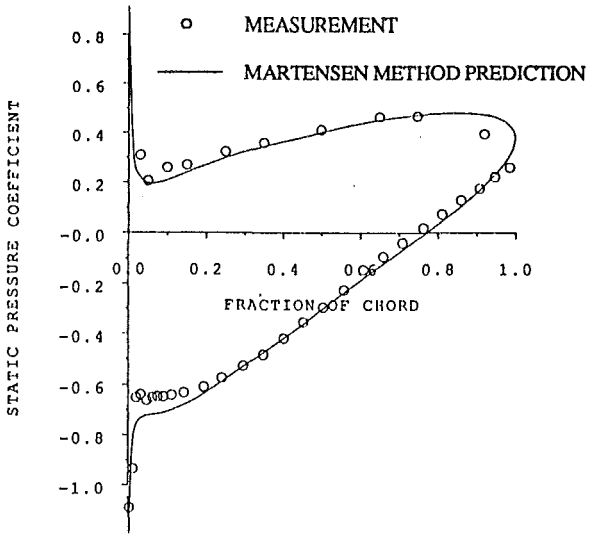

Fig. 1 Blade pressure distribution at midspan

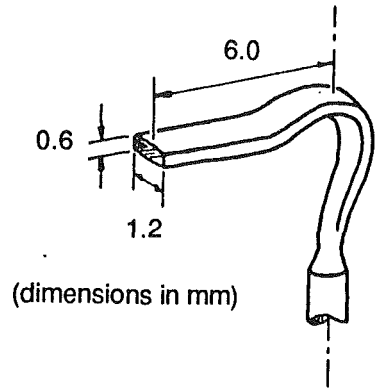

Fig. 2 External dimensions of pressure probe

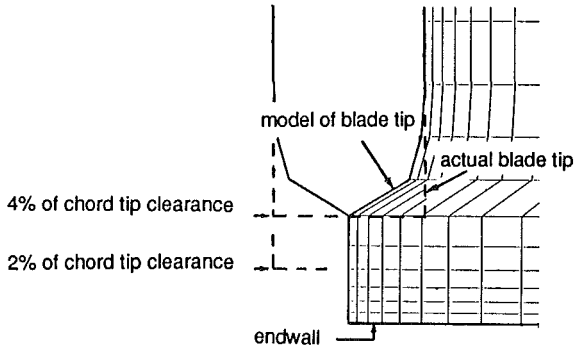

Fig. 3 Typical computation mesh at blade tip

in space of ±0.03 mm (±1 percent of the smallest clearance examined). Measurements were only made of the flow leaving the tip gap on the suction side of the blade where it was assumed the flow would be nearly parallel to the endwall and the static pressure would be effectively uniform across the height of the clearance gap. A flattened Pitot probe and a two-hole probe of the same external dimensions were used to give information on total pressure, flow speed, and direction. The size of the probes is indicated in Fig. 2. The combination of probes was equivalent to a single three-hole probe but was used in preference so as to keep probe blockage to a minimum and to improve the resolution of the measurements. The flow speed at the blade tip was obtained from a calibration of the two-hole probe assuming incompressible flow and has been nondimensionalized by the inlet velocity to the cascade. Flow direction was measured to ±0.5 deg by adjusting the yaw of the two-hole probe. Flow angles are quoted with reference to the notional axial direction of the cascade (the normal to the plane containing the leading edges).

All pressures were measured relative to the free-stream total pressure ahead of the cascade and were recorded automatically by a data logging system to an accuracy of within ±0.3 percent of the reading. The measurements of pressure are presented in two ways: static pressures are quoted as a static pressure coefficient, C_P, defined as

$$C_P = \frac{(p - p_1)}{(P_{01} - p_1)} \tag{1}$$

while total pressures are given as total pressure loss coefficient, ω, where

$$\omega = \frac{(P_{01} - P_0)}{(P_{01} - p_1)} \tag{2}$$

The inlet velocity was measured by a Pitot-static probe in the free stream ahead of the cascade and was maintained at 24 m/s giving an inlet Mach number to the cascade of 0.03.

Numerical Analysis Technique

Solutions of the three-dimensional Navier–Stokes equations for the flow in the cascade were obtained from the finite volume method of Dawes (1987). Closure is obtained in this code with a mixing length turbulence model patterned after Baldwin and Lomax (1978). The code is fully vectorized and executes on a single processor of an Alliant FX/8 computer at approximately 5×10^{-3} seconds per point per time step. Typically about 1500 time steps were needed for acceptible convergence on a $33 \times 61 \times 25$ mesh.

The code calculates tip leakage flow but does not attempt faithfully to model the conditions in the tip gap. Instead the computation mesh is rounded to a single point at the blade tip, above which a normal periodic boundary is assumed. An enlargement of the typical mesh around the blade tip with 4 percent clearance is shown in Fig. 3. The computation scheme is unsuited to flow of very low Mach number and it was necessary to assume an inlet Mach number of 0.3 for the present calculations. This value is sufficiently subsonic for the steady solution to resemble incompressible flow. The correct blade Reynolds number of 5.0×10^5 was maintained.

Results

Pressure on the Endwall. Static pressure on the endwall was measured with the tip clearance set to zero, 2 percent, and

Nomenclature

C_D = discharge coefficient (actual flow ÷ ideal flow rate)
C_P = static pressure coefficient = $(p - p_1)/1/2\rho V_1^2$
C_F = tangential blade force coefficient = $F_T/1/2\rho s V_x^2$
F_T = tangential blade force
p = static pressure
P_0 = total pressure
Re_C = Reynolds number based on blade chord
Re_δ = Reynolds number based on tip gap height
V = velocity
$\bar{V}$ = area mean velocity
ρ = density
ω = total pressure loss coefficient = $(P_{01} - P_0)/1/2\rho V_1^2$

Subscripts

0 = stagnation value
1 = reference in free stream ahead of cascade
L = in leakage direction
loc = local
p = pressure side
s = suction side
S = in streamwise direction

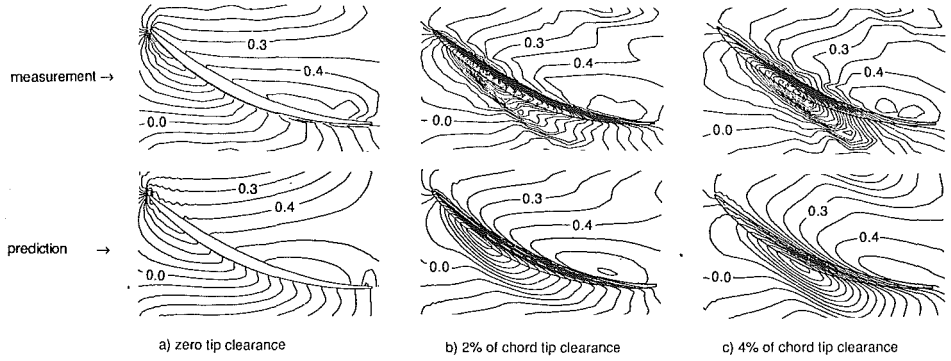

Fig. 4 Measured and predicted endwall static pressure distributions

4 percent of chord (clearances representative of those that can occur in a multistage machine). Contours of pressure measured on the endwall are shown in the upper part of Fig. 4; pressures calculated with the Navier–Stokes code are shown in the lower portion of the same figure for direct comparison. A contour interval of 5 percent inlet dynamic head is used throughout. The agreement between measurement and the prediction is very good.

With both 2 percent and 4 percent of chord tip clearance, visualization of the flow on the endwall by oil marked with fluorescent powder and tests with a wool tuft revealed the presence of a vortex in the passage near the blade tip. The trajectory of the vortex coincided with a trough of pressure measured on the endwall; a similar trough is evident in the numerical solution. The origin of the trough is close to the lowest pressure contour on the endwall, which is located close to the blade tip. The position of minimum pressure on the endwall moves progressively downstream of the leading edge as the tip clearance is increased. With 2 percent clearance the minimum pressure is located about 25 percent of chord from the leading edge; with 4 percent clearance it is near 42 percent of chord (see Fig. 4). The Navier–Stokes calculation predicts this change and is able to establish the correct location of the minimum pressure contour.

Blade Surface Pressure Distribution. Measurements were also made of the static pressures on the blade surfaces with tip clearances of zero, 2 percent, and 4 percent of chord.

With zero tip clearance the loading near the end of the blade was less than that near midspan (see Fig. 5). A contour plot of measured pressure on the suction surface without tip clearance (Fig. 6) reveals lines of constant pressure to be curved forward as a result of the blockage from the corner separation formed to the rear. This gives rise to a spanwise pressure gradient with generally higher pressure toward the tip, especially close to the leading edge. In spite of this the loading of the blade remains relatively high near the leading edge and resembles that at midspan.

When there is tip clearance, the pressure distribution near the tip may change significantly from that near midspan. The pressure distribution measured near the tip with 4 percent clearance is shown in Fig. 7, where it is compared with the distribution at midspan. In general tip clearance causes the pressure on the pressure side to be lower near the tip, especially near the leading edge. On the suction side the pressure near the tip tends to be higher near the leading edge. Toward the trailing edge a beneficial interaction of the tip leakage flow with the endwall flowfield prevents the corner separation found without tip clearance and locally the pressure on the suction side becomes similar to that at midspan. Near midchord, however, the pressure on the suction side tends to be reduced by the tip leakage vortex as discussed below.

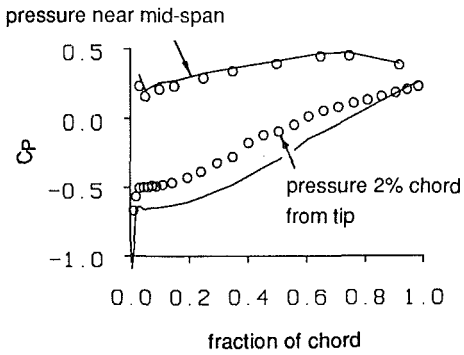

Fig. 5 Blade pressure distribution with zero tip clearance

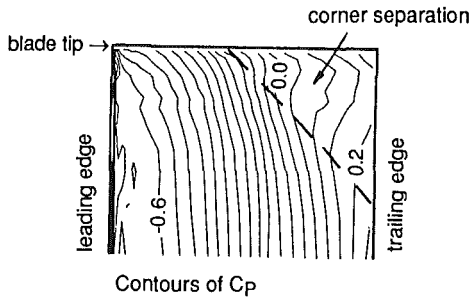

Fig. 6 Suction surface pressure distribution with zero clearance

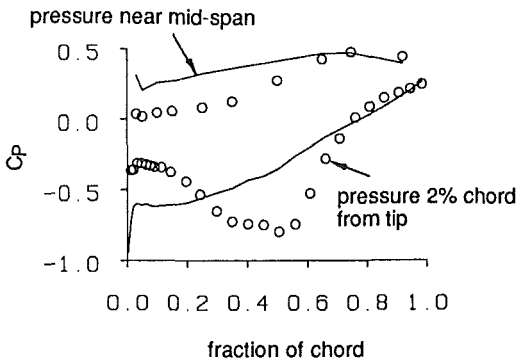

Fig. 7 Blade pressure distribution with 4 percent of chord tip clearance

Flow at Exit of Tip Gap. Detailed measurements of the leakage flow leaving the tip gap were made with the gap set to both 2 percent and 4 percent of chord. Measurements were made at 25 points across the gap at 10 chordwise locations. In general the pattern of the leakage flow was similar at both clearances and, to aid presentation, the salient features have been summarized by a selection of the measurements made at 4 percent clearance in Fig. 8. Shown in the figure are the

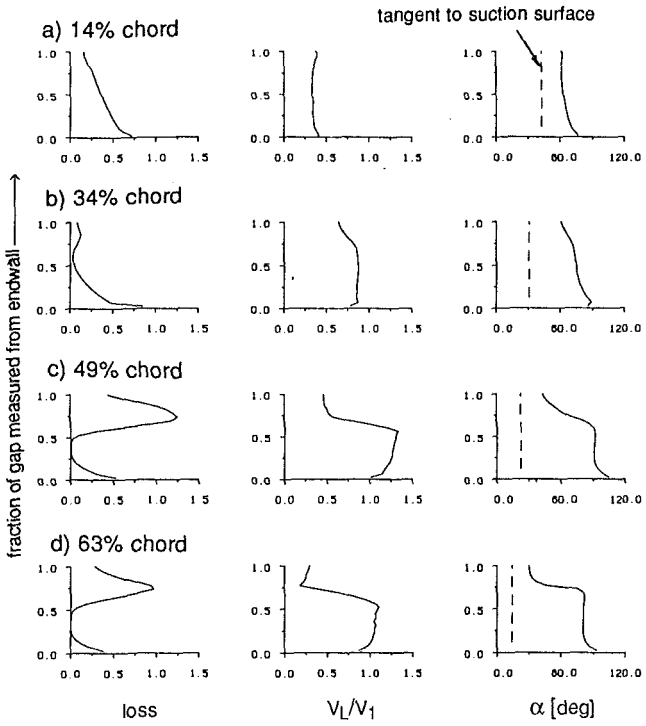

Fig. 8 Measurements of the flow leaving the tip gap on the suction side with 4 percent chord tip clearance

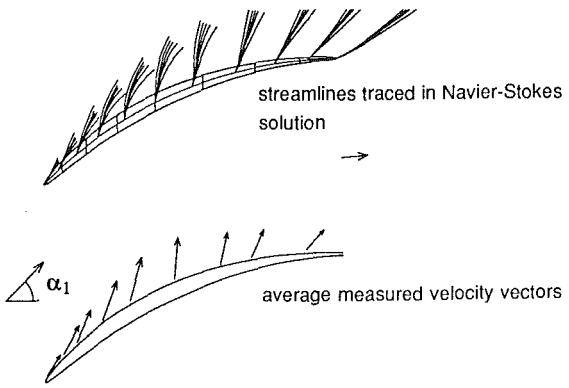

Fig. 9 Leakage flow direction with 4 percent of chord tip clearance

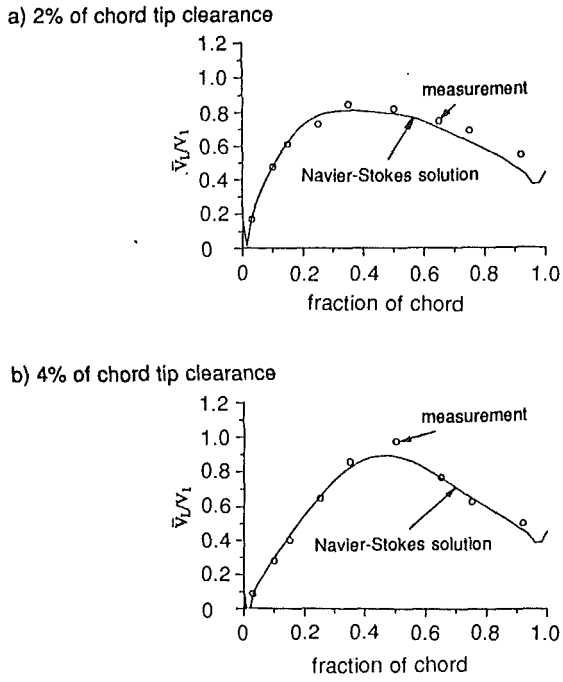

Fig. 10 Chordwise distribution of tip leakage flow averaged across the tip gap height

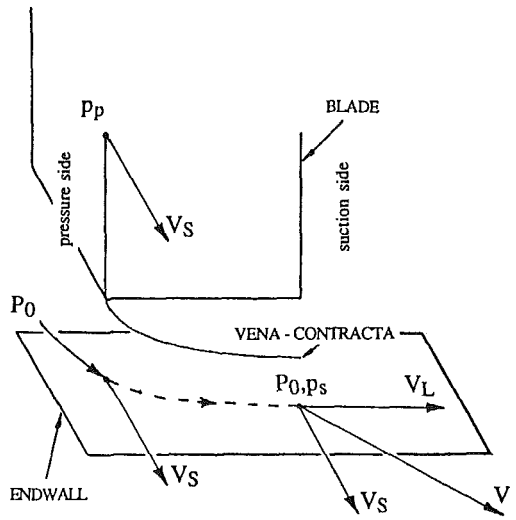

Fig. 11 The ideal flow model of Rains

nondimensional stagnation pressure loss relative to the inlet free stream, the leakage velocity nondimensionalized by the inlet velocity of the free stream, and the flow direction measured relative to the axial direction. Figure 9 shows mean absolute velocity vectors processed from the measurements with the vectors drawn from the position of the probe head used to make a measurement. The calculated trajectory of the leakage flow leaving the tip gap is also shown in Fig. 9. For present purposes the leakage velocity is defined as that component normal to the blade suction surface at the exit of the tip gap. (It is more conventional to follow Rains, 1954, and use the camberline as the reference for tip leakage flow, but since the blades are thin the choice is somewhat academic.)

With both 2 percent and 4 percent tip clearance the nature of the leakage flow was different on either side of the position of minimum pressure measured on the endwall. The difference is marked by the appearance of a distinct jet of fluid, which first emerges near the minimum pressure location and which is apparent at all the downstream measurement locations. The jet is evident in the measurements of total pressure at both 49 percent chord and 63 percent chord in Fig. 8, which show a core of very low loss fluid, bounded on the bottom by the endwall and on the top by a free shear layer at about 75 percent of the tip gap height. The flow direction remains almost constant in the core but changes by as much as 50 deg over the thickness of the shear layer (which is less than 13 percent of the tip gap height). As will be described in a future paper, the intense shearing that occurs across this thin layer between two high-speed streams of significantly different direction is the principal mechanism of the high loss associated with tip leakage flow in the cascade.

To condense the measurements of leakage flow into a more manageable form, the area-average leakage velocity, V_L, was calculated at each traverse location. This is shown in Fig. 10 plotted versus the chordwise location of the measurement for both 2 percent and 4 percent clearance. The numerical predictions of the tip leakage flow were also averaged across the blade tip and these too are presented in Fig. 10. The code predicts both the magnitude and chordwise distribution of the flow across the tip very well indeed and is sensitive to the changes in the distribution that occur when the clearance is increased.

Discussion

To understand the basic mechanisms of tip leakage it is helpful to consider a simple model owing much to Rains (1954).

A Simple Model for Tip Clearance Flow. The results in Fig. 8 show that the majority of the leakage flow with 4 percent of chord tip clearance is contained in a jet bounded by a very clearly defined free shear layer. As such the flow appears very different from the fully mixed-out flow observed by Moore and Tilton (1988) in a turbine cascade. The fact that very little mixing has taken place within the tip gap is clear from the measurement of almost zero loss of total pressure for the bulk of the flow leaving the tip gap between 49 percent chord and the trailing edge. (A similar result was obtained at 2 percent of chord clearance although this is not presented here.) The reason for less mixing across the blade tip in a compressor cascade is attributed to the much lower ratio of blade thickness to tip gap height: Measured perpendicular to the camberline the ratio in the present cascade is at most 2.5 with 2 percent of chord tip clearance, compared with a ratio of 7 in the results shown by Moore and Tilton. The observations of the flow in square-edged orifices by Ward-Smith (1971) suggest that the thickness-to-clearance ratio should characterize mixing and reattachment across a blade tip. It is important to make clear that this ratio is generally lower for compressors than for turbines because the thickness-to-chord ratio of the blades tends to be less while the running clearance as a proportion of chord is much the same.

The fact that there is negligible mixing across the blade tip causes the flow in the gap to resemble the ideal model proposed by Rains (1954) based on the solution for the potential flow into a sharp-edged orifice. Except for the stipulation that the flow separate from the corner at the entry to the tip gap, viscosity does not play a part in the model and the flow remains unattached, bounded by a free streamline along which the pressure is constant. Assuming that the contraction across the tip may be represented by a discharge coefficient (the theoretical value for a two-dimensional flow in a plane normal to the camberline and the endwall being 0.61), Rains proposed that incompressible tip leakage flow could be calculated by the simple application of the Bernoulli equation for a given pressure difference across the blade tip. The present measurements provide an opportunity to examine Rains' method and, in turn, use it to understand the mechanism controlling the flow.

A schematic diagram of the Rains' model is given in Fig. 11. It can be seen in this diagram that streamline curvature will tend to zero toward the exit of the tip gap, with the emerging jet nearly parallel to the endwall. Consequently the static pressure should be constant across the jet and, in the ideal case, so should the velocity. The absolute velocity of the leakage jet where it leaves the tip gap is therefore a function of its total pressure and the local static pressure on the suction side of the tip, viz.:

$$V = \sqrt{\frac{2\cdot(P_0 - p_s)}{\rho}} \tag{3}$$

Rains assumed that the leakage flow follows a trajectory across the blade tip such that the streamwise momentum possessed by the flow on the pressure side before it is drawn into the clearance gap is conserved. In the simple calculations described here this assumption has been retained.

As the flow accelerates into the tip gap the static pressure on the pressure side reduces toward the blade tip; this is readily shown by a solution of the two-dimensional potential flow in a plane normal to the endwall and the primary flow. The streamwise velocity of the fluid entering the tip gap cannot therefore be inferred from pressure measured *close* to the blade tip. Instead the static pressure on the pressure side of the blade outside the potential field of the inflow is a more reliable

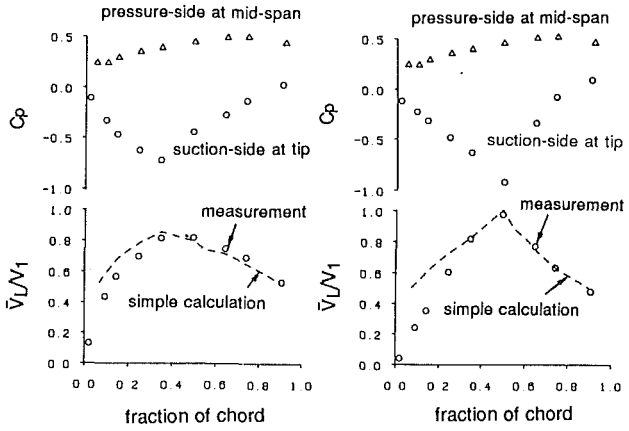

a) 2% of chord tip clearance

b) 4% of chord tip clearance

Fig. 12 Simple calculation of tip leakage flow

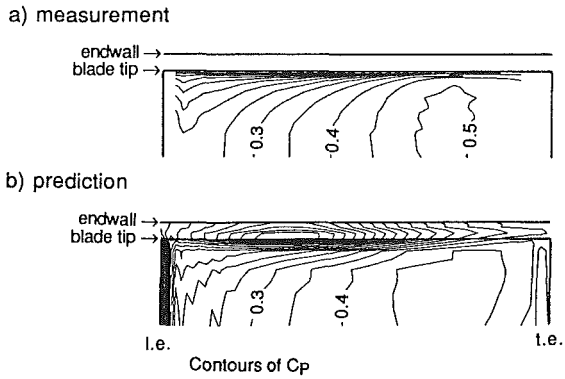

Fig. 13 Blade surface static pressure on pressure side near entry to tip gap with 4 percent of chord tip clearance

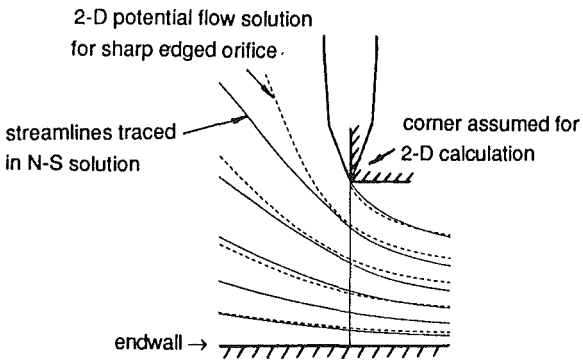

Fig. 14 Prediction of streamlines across blade tip at 97 percent of chord with 4 percent of chord tip clearance

indicator of the streamwise velocity. For present purposes the pressure is assumed to be the same as the midspan static pressure, although this is not valid near the leading edge as discussed below. The streamwise velocity entering the clearance gap at a particular chordwise location is now also obtained from the Bernoulli equation (see Fig. 9):

$$V_s = \sqrt{\frac{2\cdot(P_0 - p_p)}{\rho}} \tag{4}$$

where p_p is the static pressure at midspan on the pressure surface at the same location.

Using equations (3) and (4), an expression for leakage velocity normal to the *camberline* is obtained:

$$\frac{V_L}{V_1} = \sqrt{C_{Pp} - C_{Ps}} \tag{5}$$

The present calculation has been adjusted to give V_L as the component of velocity normal to the *suction surface* to be consistent with the presentation of the measurements.

Rains developed his method to account for resistance due to friction acting on the flow over the blade tip by incorporating a total pressure loss within the clearance space. The present measurements show that loss in the clearance gap itself is not significant and it has therefore been excluded from the calculation. A similar observation was made by Booth et al. (1981) who found that viscous effects at normal levels of clearance could be accounted for instead by small changes in the discharge coefficient.

The discharge coefficient, C_D, is used to obtain a value for the average flow rate across the tip from a prediction of actual leakage velocity according to the definition

$$\bar{V}_L = C_D \cdot V_L \tag{6}$$

A value of C_D other than the theoretical value of 0.61, which is derived from the two-dimensional analysis of the clearance flow, is essentially an empirical input to the calculation. In the present case a coefficient of 0.8 was chosen as it gave the "best fit" with experimental results. The same value was imposed at *all* chordwise locations for both 2 percent and 4 percent clearance.

The average tip leakage flow, $\bar{V}_L$, was calculated by the above method for tip clearances of 2 percent and 4 percent of chord using pressures measured in the cascade. The results are presented in Fig. 12 where they are compared directly with measured values. The upper diagram in each case shows the pressure distribution used for the calculation; it is a combination of the pressure at midspan on the pressure side (which was the same irrespective of the tip clearance) and the average static pressure measured by the two-hole probe across the exit of the tip gap on the suction side. The general level of agreement between the predictions of average leakage flow ($\bar{V}_L/V_1$) by the simple method and the measurements is good, especially over the rear 70 percent of the blade. In particular the change in the chordwise distribution of the flow across the tip that occurs with alteration of clearance is correctly indicated by the calculation.

Toward the leading edge there is a tendency for the simple method to overpredict the leakage flow, which can be seen in Fig. 12. The explanation for the discrepancy lies in the assumption of conservation of streamwise momentum across the blade tip. This is a good approximation as long as the gradient of pressure normal to the camberline is large compared to that along the blade, as Rains (1954) identified. Such a condition generally prevails downstream of the minimum pressure contour on the endwall (see Figs. 4*b* and *c*). In Fig. 13 the predicted static pressure near the tip with 4 percent clearance, obtained with the Navier–Stokes code, is compared with the corresponding measurements. Near the leading edge there is a substantial streamwise pressure gradient, comparable in magnitude to that across the tip, so that here the flow entering the tip gap experiences an appreciable acceleration in the streamwise direction. The simple model assumes that all the acceleration is produced by the pressure difference across the gap perpendicular to the camberline and therefore overestimates the flow in this direction.

The simple calculations show that, according to equation (5), it is the pressure difference across the blade tip that is the primary influence on the leakage flow. However, the pressure on the pressure side is held constant for the two cases examined and it is only the pressure on the suction side near the tip that changes with tip clearance. Therefore it is the latter that in practice controls the chordwise distribution of tip leakage flow.

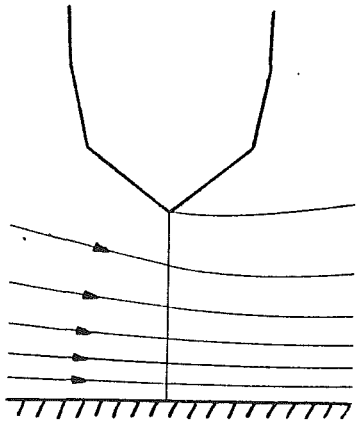

Fig. 15 Prediction of streamlines across blade tip at 14 percent chord with 4 percent of chord tip clearance

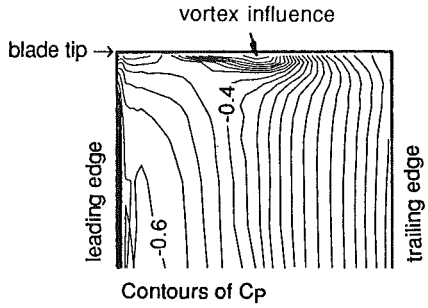

Fig. 16 Suction surface pressure distribution with 4 percent of chord tip clearance

Modeling of the Tip in the Navier–Stokes Code. The present Navier–Stokes code uses a very crude representation of the blade tip: The tip is assumed to be round so that a single point defines the tip gap height (see Fig. 3). As it stands the model of the tip does not attempt to resolve the flow in the clearance space and therefore precludes blade thickness as an important parameter in the calculation. Nevertheless the code demonstrates good overall agreement with the measurements of tip leakage flow (see, for instance, Fig. 10). This clearly suggests that tip leakage flow in the present cascade is insensitive to the tip geometry. Furthermore, since the prediction of the changes to the flowfield with tip clearance is satisfactory with an unsophisticated turbulence model, shear stresses can only play a small part in determining the flow.

When the majority of the clearance flow remains unattached across the blade tip, as in the present cascade with tip clearances greater than about 2 percent of chord, the leakage flow is in fact not influenced by blade thickness. To illustrate this point Fig. 14 shows streamlines traced across the tip at 93 percent chord in the Navier–Stokes solution for 4 percent tip clearance. Superimposed on this is the two-dimensional potential flow solution at the same clearance for comparison. It is evident that the flow approximates quite well that anticipated for a square-edged geometry without reattachment and therefore the error caused by rounding the blade tip to a single point in the computation mesh is not very large. Nearer the leading edge, for instance at 14 percent chord as shown in Fig. 13, three-dimensional calculation predicts the contraction of streamtubes across the tip to be much less.

The successful calculation of tip clearance effects by the Navier–Stokes code is determined by the prediction of the static pressure field, which is shown in Figs. 4 and 15 to be quite good. It would appear that the prediction of the static pressure field is relatively straightforward because viscous effects within the tip gap are of little significance. Instead tip leakage flow itself is responsible for large perturbations, which dominate

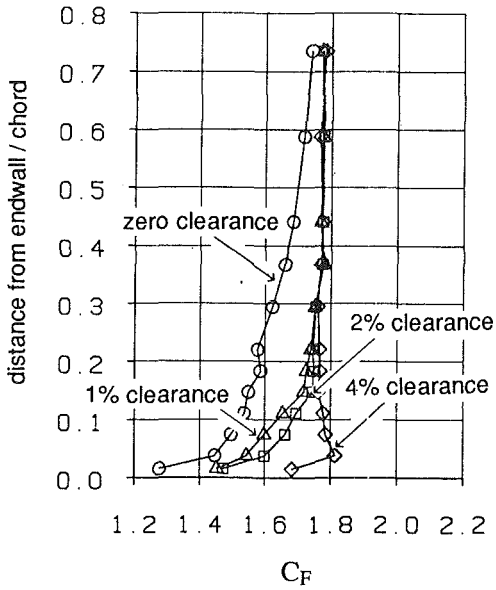

Fig. 17 Spanwise distribution of tangential blade force over a range of tip clearance

the endwall flowfield. The effects are of a scale comparable to the blade pitch and as such can be captured by a relatively coarse computation mesh.

Tip Leakage Vortex. It was not clear in the present experimental investigation whether the establishment of a leakage vortex was an inevitable consequence of tip clearance. With tip clearances less than 1 percent of chord, crude flow visualization with a wool tuft could provide no clear evidence of a vortex. With clearances upward of 2 percent of chord, a vortex could be traced to near the blade tip, which caused increasingly greater perturbation to the flowfield the greater the clearance.

The distribution of pressure near the blade tip is influenced by both the position and the strength of the leakage vortex. The blade pressure distribution for a tip clearance equal to 4 percent of chord is shown in Fig. 7, and it can be seen that the pressure distribution near the tip was affected to such an extent by the presence of a vortex that on the suction surface it hardly resembles the distribution at midspan. The influence of the vortex on blade pressure is also demonstrated by the suction-side contours shown in Fig. 16.

By producing lower pressure on the suction surface the vortex increases the local clearance volume flow. The leakage flow serves as a blockage to the primary flow in the passage and the resulting interaction as the primary flow is diverted causes pressure to rise near the leading edge. As a consequence the vortex tends to move further downstream as the tip clearance is increased, causing the minimum pressure near the blade tip to do likewise. The changes are large and it is not possible to consider the effects as simply additive, as they would be for small amplitude linear perturbations. Nevertheless it is demonstrated with the prediction of endwall pressures that the nonlinear Navier–Stokes solver is quite able to predict these effects.

Blade Force. Figure 17 shows the spanwise distribution of tangential blade force coefficient, C_F, obtained by integrating the pressure measurements over the blade surface. It can be seen that the blade force near the endwall in the present cascade tends to increase with tip clearance so that, even with a clearance of 4 percent of chord, the loading near the tip remains similar to that at midspan. Smith (1970) showed that the loss in blade force in the endwall regions, expressed as the force defect thickness, is small and is usually comparable in magnitude to the tip clearance. In the results of Smith, and of Hunter and Cumpsty (1984), there was considerable scatter in the tangential blade force defect thickness. Changes in position and strength of the clearance vortex may well be important in causing this scatter.

Relative Motion. The relative motion between rotor tips and the endwall introduces important effects (Hunter and Cumpsty, 1984; Inoue and Kuroumaru, 1989). There are two principal differences from the flow in cascades, both of which are well documented. Firstly the flow close to the endwall will be highly skewed relative to the free end of a rotor (or stator) blade, giving rise to a spanwise variation of incidence. The blade camber at rotor tips is normally small and therefore conventional secondary flow (produced by turning the flow) is generally less than that of the inlet skewing. This causes the high loss, low axial velocity fluid to collect near the pressure surface whereas in conventional cascade tests it collects near the suction surface. Secondly the flow in the endwall boundary layer possesses high relative velocity (and therefore also high relative total pressure and temperature). Some of the features of the present flowfield, for instance the effects of corner separation without tip clearance and the trajectory of the leakage vortex, may well differ in a machine, particularly in a rotor. Nevertheless the factors influencing leakage flow remain the same and it is within the capability of the present Navier–Stokes method to resolve tip leakage flow in a compressor blade row with a comparable level of agreement.

Conclusions

1 Measurements of tip leakage flow in a compressor cascade show that with a tip clearance typical of that in a machine the clearance flow separates from the blade tip and does not reattach along the majority of the chord.

2 Simple calculations based on Rains' method show that the magnitude and chordwise distribution of the tip leakage flow depend on the static pressure field near the end of the blade. Although the suction surface pressure changes with tip clearance, the pressure distribution outside the endwall boundary layer remains the primary aerodynamic input necessary to predict the overall magnitude of the flow.

3 A three-dimensional Navier–Stokes solver has shown very satisfactory predictions of many aspects of the tip clearance flow, including the static pressure field and the magnitude of the clearance flow rate along the entire chord. Since the computation mesh is relatively coarse, especially near the tip, and the turbulence modeling is unsophisticated, this shows that the tip leakage flow is controlled by a primarily inviscid mechanism.

4 The tip clearance vortex increases in size and strength as the clearance is increased. The tip clearance vortex is able substantially to alter the static pressure field near the tip on the suction side, moving the minimum pressure back along the chord as the clearance is increased. The position of the vortex relative to the suction surface is very important in determining the pressure distribution near the blade tip and the blade force.

5 Most of the clearance flow experiences very little loss within the clearance gap such that when the leakage jet emerges on the suction side its velocity is similar in magnitude to the local primary flow. Very high loss is produced in a thin layer separating the two high-speed flows near the exit of the tip gap where intense shearing is caused by the difference in flow direction.

Acknowledgments

The authors would like to thank Dr. W. N. Dawes for the use of his code. The authors are grateful for the assistance of the technical staff of the Whittle Laboratory, particularly Mr. P. Hunt for making the probes. The work was supported by

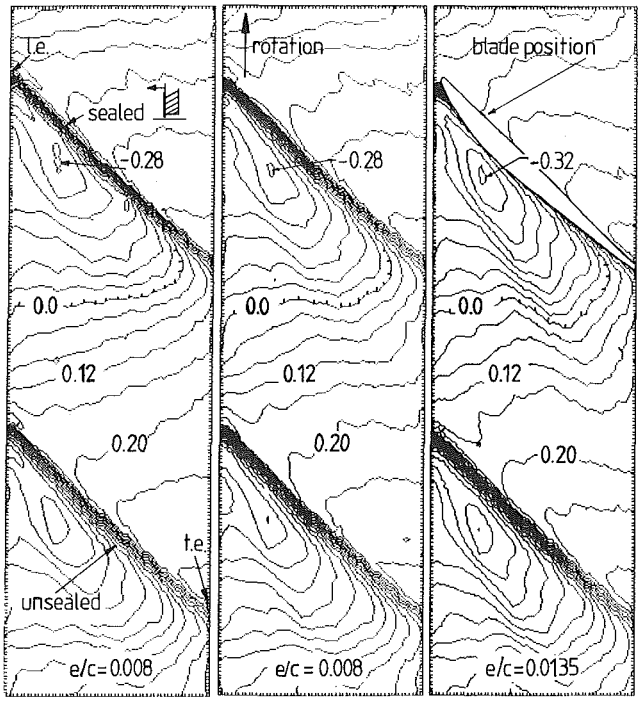

Fig. 18 Multistage rotor case wall pressure (C_p) distributions at tip clearances of 0 (sealed), 0.8, and 1.35 percent of chord showing a distinct low pressure region lying off the suction surface of the blade

Rolls-Royce plc. and the permission to publish the results is greatly appreciated.

References

Baldwin, B., and Lomax, H., 1978, "Thin Layer Approximation and Algebraic Model for Separated Turbulent Flows," AIAA Paper No. 78-257.

Dawes, W. N., 1987, "A Numerical Analysis of the Three-Dimensional Viscous Flow in a Transonic Compressor Rotor and Comparison With Experiment," ASME JOURNAL OF TURBOMACHINERY, Vol. 109, No. 1, pp. 83–90.

Freeman, C., 1985, "Effect of Tip Clearance on Compressor Stability and Engine Performance," *Tip Clearance Effects in Axial Turbomachines*, Von Karman Institute lecture series.

Hunter, I. H., and Cumpsty, N. A., 1984, "Casing Wall Boundary Layer Development Through an Isolated Compressor Rotor," ASME *Journal of Engineering for Gas Turbines and Power*, Vol. 106, No. 3, pp. 561–569.

Inoue, M., and Kuroumaru, M., 1989, "Structure of Tip Clearance Flow in an Isolated Axial Compressor Rotor," ASME JOURNAL OF TURBOMACHINERY, Vol. 111, pp. 250–256.

Moore, J., and Tilton, J. S., 1988, "Tip Leakage Flow in a Linear Turbine Cascade," ASME JOURNAL OF TURBOMACHINERY, Vol. 110, pp. 18–26.

Rains, D. A., 1954, "Tip Clearance Flows in Axial Flow Compressors and Pumps," California Institute of Technology, Hydrodynamics and Mechanical Engineering Laboratories, Report No. 5.

Smith, L. H., 1970, "Casing Boundary Layers in Multi-stage Axial Flow Compressors," *Brown Boveri: Flow Research in Blading*, L. S. Dzung, ed., Elsevier, Amsterdam.

Ward-Smith, A. J., 1971, *Pressure Losses in Ducted Flow*, Butterworths, London.

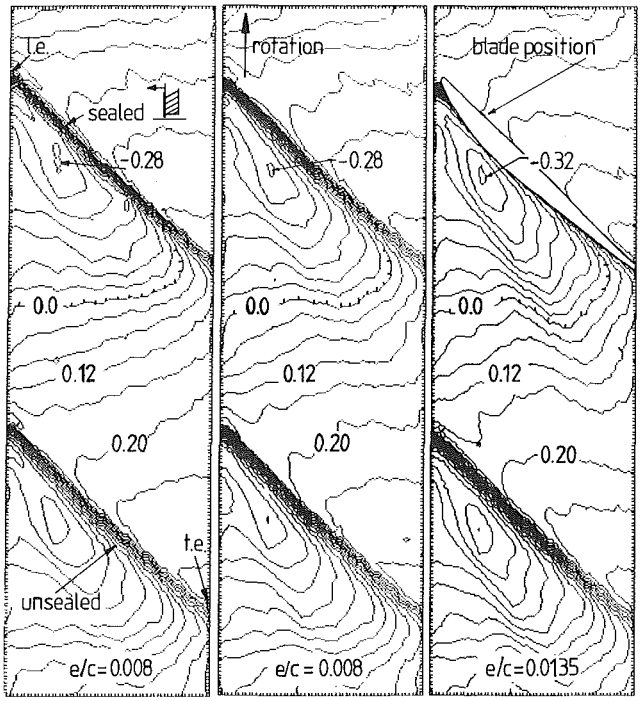

Fig. 18 Multistage rotor case wall pressure (C_p) distributions at tip clearances of 0 (sealed), 0.8, and 1.35 percent of chord showing a distinct low pressure region lying off the suction surface of the blade

Rolls-Royce plc. and the permission to publish the results is greatly appreciated.

References

Baldwin, B., and Lomax, H., 1978, "Thin Layer Approximation and Algebraic Model for Separated Turbulent Flows," AIAA Paper No. 78-257.

Dawes, W. N., 1987, "A Numerical Analysis of the Three-Dimensional Viscous Flow in a Transonic Compressor Rotor and Comparison With Experiment," ASME JOURNAL OF TURBOMACHINERY, Vol. 109, No. 1, pp. 83–90.

Freeman, C., 1985, "Effect of Tip Clearance on Compressor Stability and Engine Performance," *Tip Clearance Effects in Axial Turbomachines*, Von Karman Institute lecture series.

Hunter, I. H., and Cumpsty, N. A., 1984, "Casing Wall Boundary Layer Development Through an Isolated Compressor Rotor," ASME *Journal of Engineering for Gas Turbines and Power*, Vol. 106, No. 3, pp. 561–569.

Inoue, M., and Kuroumaru, M., 1989, "Structure of Tip Clearance Flow in an Isolated Axial Compressor Rotor," ASME JOURNAL OF TURBOMACHINERY, Vol. 111, pp. 250–256.

Moore, J., and Tilton, J. S., 1988, "Tip Leakage Flow in a Linear Turbine Cascade," ASME JOURNAL OF TURBOMACHINERY, Vol. 110, pp. 18–26.

Rains, D. A., 1954, "Tip Clearance Flows in Axial Flow Compressors and Pumps," California Institute of Technology, Hydrodynamics and Mechanical Engineering Laboratories, Report No. 5.

Smith, L. H., 1970, "Casing Boundary Layers in Multi-stage Axial Flow Compressors," *Brown Boveri: Flow Research in Blading*, L. S. Dzung, ed., Elsevier, Amsterdam.

Ward-Smith, A. J., 1971, *Pressure Losses in Ducted Flow*, Butterworths, London.

DISCUSSION

I. N. Moyle[1]

The authors are to be complimented on collecting some valuable information about the detailed nature of compressor tip leakage flow. Use of a large-scale cascade appears to have improved the resolution of measurements near the tip and captured some of the physical processes of interest. The authors also discussed how their results might be altered by relative motion in a rotor.

Their results reflect similar processes identified in measurements from a recent study of tip clearance flow in a multistage compressor at the Naval Postgraduate School. In that program measurements were made under the tip of a rotor. The rotor was located in the second stage of a two-stage axial flow compressor. The rotor had a tip radius of 457 mm (18 in.), a tip chord of 81 mm (3.2 in.) at 41 deg stagger, and a tip speed of 77 m/s (253 ft/s) in air.

Rotor case wall pressure distributions at tip clearances (e) of 0 (i.e., sealed), 0.8, and 1.35 percent of chord (c) are attached in Fig. 18. The C_P contour interval is 4 percent of a dynamic pressure based on tip speed. All the surveys shown were made between blades 2 and 3 of the rotor at the design flow condition for the stage. Note that only blade 2 was sealed on its pressure side in the test. The surveys were made along an axial line midway between the upstream stators' pitchwise spacing and reflect the flow at that stator relative location. However, the qualitative similarity of the data to those shown by the authors in Fig. 4 can be seen clearly.

If the *locations* of the low pressure regions of Fig. 4 of the paper are compared with the rotating situation of Fig. 18, it is clear there are major quantitative differences in the flows. The low-pressure features found under or near the blade suction edge in the authors' cascade are located sufficiently far away from the suction side, in the rotating case, that a different flow is produced near the blade. This "in-passage" location of the suction minimum is expected to alter the blade pressure distributions and loading near the tip.

Some projected effects of rotation and relative motion on the tip flow and vortex production were discussed by Moyle (1989) and have generally been supported by test data of the type attached in Fig. 18. However, if the relative motion effects are neglected, the authors' measurements have shown the same basic flow features observed in the rotating stage. The authors' confidence in the relevance of their cascade results to a rotating situation is well founded and it is encouraging to see their results can be reproduced by computational methods.

Reference

Moyle, I. N., 1989, "Influence of the Radial Component of Total Pressure Gradient on Tip Clearance Secondary Flow in Axial Compressors," ASME Paper No. 89-GT-19.

Authors' Closure

We are most grateful for these comments and for the inclusion of additional data. We are very conscious that there are important differences between endwall flows in cascades (for which the inlet flow is collateral) and flows in compressors (where it is generally not collateral). The difference was also brought out very clearly by the recent work of Chen et al. (1991) and was highlighted in the discussion of the paper: When there is a skewed inlet flow the vortex appears to spring from near the leading edge and not from further back, as in the cascade.

These differences between cascades and blade rows are now readily predictable by Navier–Stokes solvers. The cascade does make possible detailed measurements of, for example, the clearance flow itself and this can be used to enhance our understanding of the flow and the loss producing mechanisms, as well as to test the accuracy of the calculation methods.

Reference

Chen, G. T., Greitzer, E. M., Tan, C. S., and Marble, F. E., 1991, "Similarity Analysis of Compressor Tip Clearance Flow Structure," ASME JOURNAL OF TURBOMACHINERY, Vol. 113, this issue.

[1]Research Associate, Naval Postgraduate School, Monterey, CA 94943.

Similarity Analysis of Compressor Tip Clearance Flow Structure

G. T. Chen

E. M. Greitzer

C. S. Tan

Gas Turbine Laboratory,
Massachusetts Institute of Technology,
Cambridge, MA 02139

F. E. Marble

Jet Propulsion Center,
California Institute of Technology,
Pasadena, CA 91125

A new approach is presented for analyzing compressor tip clearance flow. The basic idea is that the clearance velocity field can be (approximately) decomposed into independent throughflow and crossflow, since chordwise pressure gradients are much smaller than normal pressure gradients in the clearance region. As in the slender body approximation in external aerodynamics, this description implies that the three-dimensional, steady, clearance flow can be viewed as a two-dimensional, unsteady flow. Using this approach, a similarity scaling for the crossflow in the clearance region is developed and a generalized description of the clearance vortex is derived. Calculations based on the similarity scaling agree well with a wide range of experimental data in regard to flow features such as crossflow velocity field, static pressure field, and tip clearance vortex trajectory. The scaling rules also provide a useful way of exploring the parametric dependence of the vortex trajectory and strength for a given blade row. The emphasis of the approach is on the vortical structure associated with the tip clearance because this appears to be a dominant feature of the endwall flow; it is also shown that this emphasis gives considerable physical insight into overall features seen in the data.

Introduction

There is little need to give a detailed background on the flow in turbomachinery endwall regions. It is well known that: (1) The fluid mechanics of the endwall region are critical in developing performance prediction methods (see, for example, Koch and Smith, 1976; Wisler, 1985; Senoo and Ishida, 1986; Cumpsty, 1989), and (2) in spite of over forty years of research on the topic, the flow in this region is not very well understood. An additional point is that, in much of the work that has been done, the problem has been cast into one or another simplified models in which the essential physical features were suppressed, an example being the attacks on the problem from the standpoint of pitch-averaged boundary layer type equations (e.g., Balsa and Mellor, 1975; De Ruyck and Hirsch, 1981). Approaches of this sort avoided dealing with the complex endwall flow structure by averaging, and thus aiming for a more global description, but there has been little success in developing general predictive procedures along such lines. The approach taken here is inherently different in that three dimensionality, and the role of the vortical structure associated with the tip clearance flow, are emphasized from the outset.

There have been many studies of compressor tip clearance flows, but the analyses carried out appear to fall into three main categories. The first is what might be termed leakage models. In these, the clearance flow is regarded as a jet driven by the pressure difference across a blade tip, with the kinetic energy of the jet subsequently lost through mixing (Rains, 1954; Moore and Tilton, 1988). Description on this level can give a useful measure of efficiency decrease due to tip clearance flow, but it provides no information on essential details of the passage flow field.

A second main approach makes use of lifting line analyses (Lakshminarayana and Horlock, 1965; Lakshminarayana, 1970) to compute the secondary velocity flow field as well as a loss in efficiency stemming from the induced drag of the trailing vortex system. A major drawback, however, is that empirical relations are needed (tip vortex circulation and core size) to close the problem and these are not universal.

The third category, which has appeared relatively recently, is numerical computation of the three-dimensional flow in a blade passage using the Reynolds-averaged Navier–Stokes equations (Hah, 1986; Dawes, 1987; Crook, 1989; Adamczyk et al., 1990). The present approach differs from all of the above, but it can be regarded as a strongly complementary adjunct to the computational procedures. In particular, a primary goal is to provide physical insight into the general features of the tip clearance flow field over a broad range of the parameters of interest. In developing the approach, we have focused on the structure of the vorticity field in the blade passage. Doing this enables one to obtain a useful "skeleton" to aid in inferring the behavior of complex three-dimensional flow fields (Perry and Tan, 1980). Although, as will be described, the focus on vorticity can lead to rapid and simple approximate computational procedures, we emphasize that it is the above-mentioned point, the possibility for enhancing physical insight, that is the main factor in our adoption of this approach.

The paper is organized as follows: First, the model formulation and basic assumptions are described, followed by the development of the similarity scaling for the clearance flow.

Contributed by the International Gas Turbine Institute and presented at the 35th International Gas Turbine and Aeroengine Congress and Exposition, Brussels, Belgium, June 11–14, 1990. Manuscript received by the International Gas Turbine Institute February 9, 1990. Paper No. 90-GT-153.

A brief description of the computational scheme used to obtain numerical results is also given. The available experimental data are then interrogated to assess the model adequacy; in doing this, emphasis is placed on elucidation of the physical concepts associated with the overall features and the parametric trends seen in both data and calculations.

Flow Model

The problem examined is the formation of a (tip clearance) vortex due to the flow through the clearance in a turbomachine rotor. Such vortices are clearly seen in experiments (Rains, 1954; Inoue et al., 1986; Inoue and Kuroumaru, 1989), as well as in recent three-dimensional computations (Crook, 1989; Adamczyk et al., 1990). A critical feature in the development of such structures is the "roll-up" process, which is a nonlinear effect, and this must be included in any realistic description of the endwall flow.

The flow field of interest is three dimensional and steady. As for slender bodies in external aerodynamics, however, one can model it from the point of view of a two-dimensional, but unsteady, flow. The central idea is that translation along the streamwise direction is analogous to moving in time, i.e., an observer moving with (some average) streamwise velocity is embedded in an unsteady flow field. This implies that the generation of the tip clearance flow, and the roll-up, can be treated as an unsteady process in successive crossflow planes (planes normal to the blade camber).

To illustrate the idea in more detail, consider crossflow planes A, B, C, and D at different chordwise locations a, b, c, and d, respectively, as shown in the top part of Fig. 1. Location a is at the leading edge and d is at the trailing edge. At station a, the tip clearance flow is initiated so that the flow in crossflow plane A might be as shown in the lower part of the figure. As one moves through the blade passage, the vortex sheet shed into the clearance rolls up so that subsequent cross sections might be as illustrated in planes B, C, and D.

The analogy proposed is that the flow pattern in different crossflow planes is similar to a two-dimensional unsteady flow. The velocities in the four crossflow planes of the top part of Fig. 1 are thus represented by the unsteady flow at the four different times shown in the lower part of the figure. If this analogy holds, it implies that evolution of the cross-plane flow structure (including tip clearance vortex strength and position) at different streamwise locations is similar to that at different times, when viewed from a moving reference frame. The transformation between time, t, and streamwise location, s, is $t = s/V(s)$, where $V(s)$ is the velocity of the moving frame.

A key argument for adoption of this (slender body type) approach to tip clearance flow is based on relative sizes of length scales in the streamwise and transverse directions. For

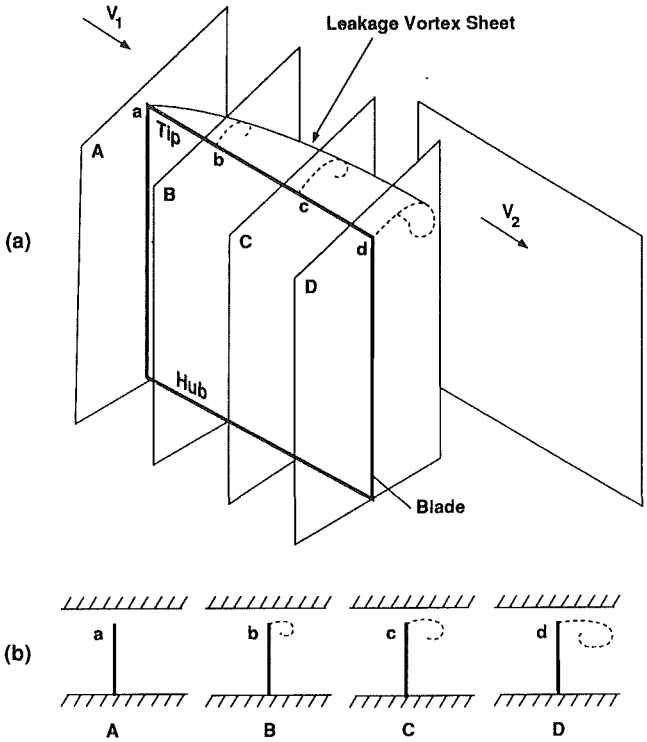

Fig. 1 Correspondence between three-dimensional steady tip clearance flow and unsteady two-dimensional flow

an inviscid flow, the relevant length scale in the two crossflow directions will be set by the size of (and on the order of) the tip clearance, whereas the streamwise length scale is the chord. For high-performance turbomachines, the former is much smaller than the latter. Since the pressure differences across the blade and along the blade are of the same order of magnitude, pressure gradients and acceleration components in the transverse directions are thus much larger than those in the streamwise direction.

In addition to the arguments concerning pressure gradients, in order to use a slender body type of approximation we must also be able to identify some (relatively uniform) mean streamwise reference velocity. If so, we can write the streamwise velocity component as a passage average value plus a deviation from the average, i.e.,

$$u(s, y, z) = \bar{u}(s) + u'(s, y, z)$$

where s is measured along the blade camber, y is normal to the camber, z is along the span, and we take $u'/\bar{u} \ll 1$. This

Nomenclature

b = span
c = chord
C_p = pressure coefficient = $\Delta P/0.5\ \rho U_t^2$
C_x = axial velocity
g = pitch
h = passage height = $b + \tau$
H = half-period of vortex system; see Appendix A
R_t = tip radius
s = distance along camber line or streamwise distance
t = time
t^* = similarity parameter; see equation (4)
$\bar{u}$ = average streamwise velocity
U_t = tip wheel speed
v, w = cross-plane velocities in y, z directions
V = velocity of "observer frame"
V_{inlet} = inlet relative velocity
x = axial coordinate
y = tangential or crossflow coordinate
y_c, z_c = coordinates of tip vortex core
y_c^*, z_c^* = nondimensional coordinates of tip vortex core = y_c/τ, z_c/τ
y_v, z_v = coordinates of vorticity centroid
y_v^*, z_v^* = nondimensional coordinates of vorticity centroid = y_v/τ, z_v/τ
z = spanwise coordinate
β_1 = inlet relative flow angle
β_2 = exit relative flow angle
β_m = vector mean relative flow angle
γ = vortex sheet strength; see Appendix B
ΔC_{pt} = blade pressure difference coefficient based on U_t
ΔP = pressure difference across blade
τ = tip clearance
ϕ = flow coefficient = C_x/U_t

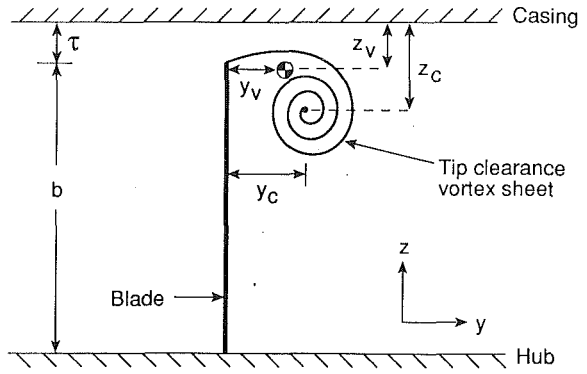

Fig. 2 Nomenclature and flow domain for tip clearance flow model

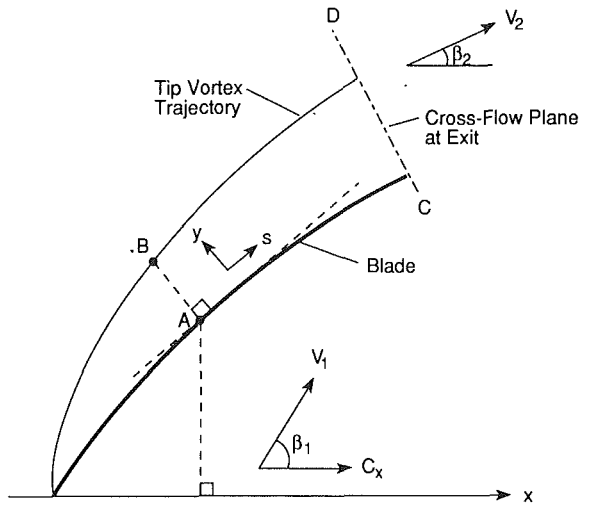

Fig. 3 Schematic of projection of vortex trajectory on constant radius surface (y_v or y_c)

strong inequality cannot be strictly true for highly loaded blades if applied all across a blade passage. Its use, however, is appropriate here since the primary interest is in the *local* regions of the flow domain where vorticity is shed and where roll-up occurs. Over this region, the normalized variation in streamwise velocity, $u'/\bar{u}$, can be small. As an example, if we take the mean blade pressure difference ΔP equal to $0.5 \times (1/2\rho V_{\text{inlet}}^2)$, and say that the region of interest is 25 percent pitch, the magnitude of $u'/\bar{u}$ over this region is less than 0.1. Arguments of this type imply, and the subsequent comparison with data will show, that the approximation $u'/\bar{u} \ll 1$ is indeed adequate for the present treatment.

Under the above two conditions, as shown in Appendix A, the (inviscid) equations describing flow in the transverse, or crossflow, plane are decoupled from the equations that describe flow in the streamwise direction. Within this approximation, s can be regarded as the streamwise direction and $V(s)$, the velocity of the moving frame, can be taken as $\bar{u}$. The relation between time and streamwise distance is thus

$$dt = \frac{ds}{\bar{u}} \tag{1}$$

The crossflow plane equations take the form (see Appendix A)

$$\frac{\partial v}{\partial y} + \frac{\partial w}{\partial z} = 0 \tag{2}$$

$$\frac{\partial v}{\partial t} + v\frac{\partial v}{\partial y} + w\frac{\partial v}{\partial z} = -\frac{1}{\rho}\frac{\partial p}{\partial y} \tag{3}$$

$$\frac{\partial w}{\partial t} + v\frac{\partial w}{\partial y} + w\frac{\partial w}{\partial z} = -\frac{1}{\rho}\frac{\partial p}{\partial z} \tag{4}$$

which are the equations describing two-dimensional unsteady flow.

In the preceding discussion, the flow has been taken as inviscid. This point has been examined in some detail by other investigators (e.g., Rains, 1954; Moore and Tilton, 1988; Storer and Cumpsty, 1991) and will not be elaborated upon here. These studies show that, while viscous effects do play a role, the dominant features of the flow due to tip clearance are inviscid, and useful descriptions can be developed on this basis.

Three other approximations are also implicit in the analysis. The first is that the effect of adjacent blades on the tip clearance flow is primarily important in setting up the overall pressure difference profile, which drives the flow through the tip clearance, rather than in determining the detailed structure of the tip flow. This implies that the latter can be analyzed as the unsteady flow through a single blade with clearance, rather than through an array of blades, if one uses the appropriate pressure difference. In addition, we represent the blade by its camber line only, with thickness neglected. As implied by Moore and Tilton (1988), the treatment is thus restricted to situations with thin blades (i.e., compressors) where the shear layer (vortex sheet) shed from the pressure surface does not reattach within the tip clearance. Finally, as mentioned in Appendix A, the blade camber is assumed such that the radius of curvature of the tip section camber line is much larger than the chord; this is generally a good approximation for compressors.

Fluid Dynamic Similarity

We have so far described the basic framework of the approach (the unsteady two-dimensional analysis of the velocity field on crossflow planes in the tip region) and the assumptions. We now examine the consequences of this model as far as overall flow features. In particular, we show that a similarity solution exists and that this in turn implies a generalized vortex trajectory independent of tip clearance.

The geometry and nomenclature to be used are given in Fig. 2, which shows the blade and flow domain at an arbitrary cross-sectional location. A schematic of the tip vortex sheet roll-up is also indicated. The vortex trajectory and further notation are as indicated in Fig. 3. Two quantities that will be used in what follows are the *centroid of the shed vorticity*, denoted by (y_v, z_v) and the *center of the tip vortex core*, denoted by (y_c, z_c). This latter is defined as the centroid of the "rolled-up" part of the vortex sheet.

Referring to Fig. 2, we note that, in almost all practical situations, the blade height (or blade span), b, is much larger than the tip clearance, τ. Because of this, the ratio of height/clearance would be expected to affect the local flow over the tip only slightly. If the blade span is not a significant parameter for the local details of the flow in the tip clearance region, the only relevant length is the tip clearance, and the physical variables that characterize the problem are tip clearance, τ, pressure difference across the blade, ΔP, density, ρ, and time, t. Considering a time increment, dt (as expressed in equation (1)), dimensional analysis shows that the only dimensionless variable that can be formed using the four quantities has the form

$$dt^* = \frac{dt}{\tau}\sqrt{\frac{\Delta P}{\rho}} \tag{5}$$

Equation (5) defines a nondimensional time increment in terms of local values of pressure difference, density, and tip clearance. In the most general situation, these will vary along the chord. As will be seen later, however, the use of an average loading, denoted as $\overline{\Delta P}$, gives good prediction of the tip vortex core trajectory. If the density and clearance are also taken as

constant, equation (5) can be integrated to given an expression for the nondimensional time corresponding to a given streamwise location:

$$t^* = \frac{t}{\tau}\sqrt{\frac{\overline{\Delta P}}{\rho}} \tag{6}$$

Two tip clearance flow fields will be similar if they correspond to the same t^*. The following quantities will thus all be functions of t^* only:

$$\left(y_c^* = \frac{y_c}{\tau},\ z_c^* = \frac{z_c}{\tau}\right); \qquad \text{vortex center coordinates}$$

$$\left(y_v^* = \frac{y_v}{\tau},\ z_v^* = \frac{z_v}{\tau}\right); \qquad \text{centroid of shed vorticity}$$

$$\left(\Gamma^* = \frac{\Gamma}{\tau\sqrt{\overline{\Delta P}/\rho}}\right); \qquad \text{(nondimensional) vortex circulation}$$

$$\left(v^* = \frac{v}{\sqrt{\overline{\Delta P}/\rho}},\ w^* = \frac{w}{\sqrt{\overline{\Delta P}/\rho}}\right); \qquad \text{crossflow plane velocity}$$

All of these variables can be expressed in the form $(\,)^* = f_i(t^*)$. The distances y_c^* (or z_c^*) are measured between the center of a tip vortex and the camber (or casing), and y_v^* (or z_v^*) is the distance between the centroid of the shed vorticity and the camber (or casing), measured from the mean camber line, in the direction of the local normal, as illustrated in Figs. 2 and 3.

The pressure difference across the blade varies along the span but evaluation of the loading at the mean radius appears to be adequate for good prediction of the tip vortex core trajectory. The nondimensional time, t^*, can be estimated as:

$$t^* = \frac{t}{\tau}\sqrt{\left(\frac{\overline{\Delta P}}{\rho}\right)_{\text{mean}}} \tag{7}$$

where

$$t = \int_0^s \frac{ds}{\overline{u}} = \frac{x}{C_x} \tag{8}$$

The combined equations (7) and (8) can be written in terms of flow angles at the mean radius using the expression for ideal pressure rise given in many texts (e.g., Horlock, 1973):

$$t^* = \frac{x}{\tau}\sqrt{\frac{g(\tan\beta_1 - \tan\beta_2)}{c\cos\beta_m}} \tag{9}$$

In equation (9), g is the blade spacing, c is the chord, β_1 and β_2 are the inlet and outlet flow angles (see Fig. 3), and β_m refers to the vector mean velocity direction.

Computational Procedure

The different functions $f_i(t^*)$, as well as any other information needed about the velocity or vorticity fields of the two-dimensional, unsteady flow, can be computed in a number of ways. The one used here is a vortex method. When applicable, these methods have the advantage that, if the locations of the vortex sheets are known, the velocities need to be calculated only on the sheets at each time step, rather than in the entire flow. Many such methods are available; a recent review of these is given by Sarpkaya (1989).

In essence, what is done is to track the vorticity shed (as a vortex sheet) from the tip of the blade. The evolution (in particular the roll-up) of this vortex sheet in time provides,

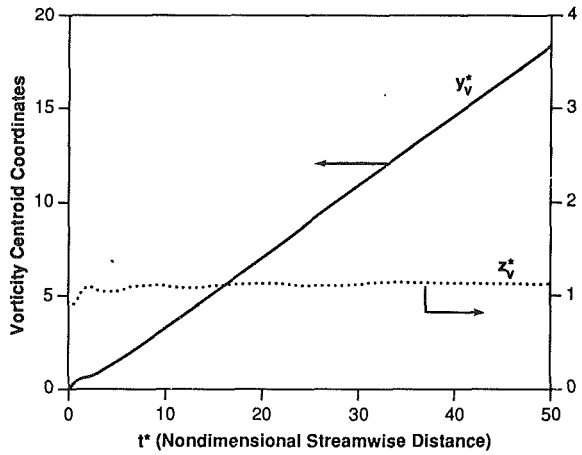

Fig. 4 Nondimensional coordinates of vorticity centroid for tip clearance vortex

using the relation that has been developed between time and the streamwise spatial variable, the three-dimensional structure of the tip leakage vortex. In-depth discussions of vortex methods are given, for example, in the papers by Leonard (1980) and Sarpkaya (1989), but several points should be commented on. First, as noted by Sarpkaya (1989), the fine structure of the computation depends critically on the number of vortices used, the time stepping procedure, and the smoothing techniques applied. More specifically, although quantities such as the circulation and the position of the centroid of vorticity (the sum and first moment of the shed vorticity) are essentially invariant to the type of scheme used, the details of the shape of the rolled-up vortex sheet are sensitive to the above factors.

To assess the degree to which the results depend on the computational parameters, we have carried out calculations using two different approaches, one involving a conformal transformation of the flow domain (Evans and Bloor, 1977) and the other an unsteady panel method. In the computations, several different time-stepping schemes, as well as substepping procedures, were examined with time steps (number of vortices) and number of substeps varied by factors of ten. The results show that the circulation and vorticity centroid are, as described by the above-mentioned review articles, not sensitive to these variations. For example, there is less than a 2 percent difference in the computed tip vortex position (y_c) for a factor of ten in time step. (The computations shown, however, are those with the smallest time step that was employed.) In summary, the central point is that the overall features of the vortical flow are of most interest here, and these are not dependent on the details associated with the computation.

Overall Similarity Results for Flow in the Blade Passage

Computations of the coordinates of the centroid of vorticity, y_v and z_v, are shown in Fig. 4. The computations have been carried out assuming ΔP is constant along the blade. While this is an oversimplification, computations with a varying ΔP show little difference from these results, at least for representative subsonic compressor blade pressure distributions. (A numerical example will be shown subsequently.)

A quantity that is more relevant than the centroid of vorticity is the position of the tip vortex, and the nondimensional tip vortex center position, y_c, is shown in Fig. 5. Included in the figure are data from the different tip clearance vortex experiments of Rains (1954), Smith (1980), Johnson (1985), Inoue and Kuroumaru (1989), and Takata (1988). Compressor parameters for these tests are given in Table 1. Where velocities were not measured directly in the experiments, the position of the tip vortex is taken as either the center of the low total

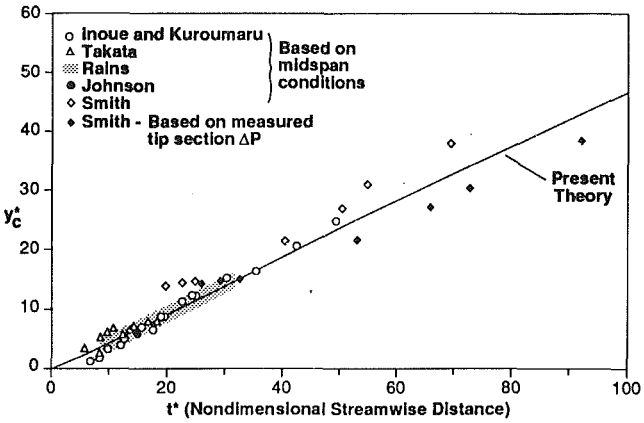

Fig. 5 Generalized tip clearance vortex core trajectory (projection on constant radius surface); references given in figure

pressure region (Takata, Smith)[1] or the center of the tip vortex cavitation bubble (Rains). The convection time is calculated based on mean axial velocity.

The experimental data cover a large range of clearances, loading, and flow coefficients (see Table 1). The conditions include moderate loading with large tip clearance (leading to generally low values of t^*) as well as near-stall loadings with small clearance (Smith, 1980) (which lead to large t^*).[2] The different vortex trajectories, however, are well described by the single similarity solution curve, in agreement with the dimensional analysis. In addition to providing a relevant dimensionless grouping, the theory thus gives a good absolute prediction of tip vortex location, even when applied at near-stall conditions. It can also be pointed out that the largest percentage deviations from theory are those for data near leading edges; for these the distances are small and the experimental results, taken from publications, are difficult to read precisely.

An observation from Fig. 5 is that the generalized tip vortex trajectory is nearly a straight line, which can be approximately (within ± 1 in units of y^* over the data range shown) represented by

$$y_c^* = 0.46t^* \tag{10}$$

Taking the pressure difference to be given by its value at the midspan location then yields an expression for the tip vortex trajectory as a function of axial position

$$\frac{y_c}{x} = 0.46\left[\sqrt{\frac{g(\tan(\beta_1)-\tan(\beta_2))}{c\cos(\beta_m)}}\right]_{\text{midspan}} \tag{11}$$

If the mean flow parameters are known, one can thus estimate the tip vortex trajectory from equation (11).

Equations (10) or (11) show that y_c, the (dimensional) locus of the tip vortex trajectory on a constant radius surface, does not depend on clearance. Varying clearance while keeping other parameters the same will not alter the projection of the tip vortex trajectory on this surface although, as will be seen, it will alter the crossflow pattern (Dean, 1954; Inoue et al., 1986; Zhang, 1988).

Table 1 Experimental data

Experiment	Flow Coefficient	Clearance/ Chord (%)
1. Inoue	.50	0.8
2. Inoue	.50	1.7
3. Inoue	.50	2.6
4. Inoue	.50	4.3
5. Rains	.45	1.3
6. Rains	.45	2.6
7. Rains	.45	5.2
8. Takata	.62	4.2
9. Takata	.56	4.2
10. Takata	.53	4.2
11. Takata	.50	4.2
12. Johnson	(stator or hub)	4.0
13. Smith	.29	1.0

Flow Downstream of the Blade Row

The discussion so far has been of the vorticity field in the blade passage, but the flow downstream of the blade row is also of interest. This can be calculated by representing the tip clearance vortices as an infinite periodic array of line vortices, plus the images needed to satisfy the kinematic boundary conditions at the wall. Formulae for the velocities associated with such arrays are given, for example, by Lamb (1932).[3] In line with the approximations made in the passage description, the procedure is to apply this vortex array description everywhere downstream of the crossflow plane corresponding to the blade trailing edge (plane CD in Fig. 3). The initial conditions for the computations in the downstream region are thus the computed vortex position and strength from the passage tip clearance flow analysis at plane CD.

Specific Applications of the Model

Figure 5 gives an overall illustration of the degree to which the model is able to describe tip clearance flows, but it is of interest to interrogate the results in more detail to see how the crossflow plane velocity field, the trajectory downstream of the passage, and the casing wall static pressure distribution are affected by overall flow parameters such as tip clearance and blade loading.

Velocity and Vorticity in the Exit Crossflow Plane. As a start on this examination, Fig. 6 shows the configuration of the vortex sheet in the crossflow plane passing through the trailing edge, for a clearance of 2.6 percent; similar behavior is seen at other clearances. The vorticity can be regarded as parceled into the tip clearance vortex and an umbilical stretching from the blade tip to the vortex. Although this structure is somewhat similar to that of the flow around a delta wing, there is an important difference because of the presence (and proximity) of the wall and hence of the image vortex system.

Figure 7 presents the crossflow plane velocity distribution at the trailing edge for four different clearances: 0.8, 1.7, 2.6, and 4.3 percent of chord. The velocity vectors shown are normalized with the blade tip speed and a reference velocity magnitude is indicated in the figure. The spanwise extent of the influence of the clearance flow is seen to increase as the tip clearance increases.

Figure 8 presents another view of the trailing edge flow field, showing computed and measured contours of the exit yaw and

[1]There is some small error involved in doing this, as pointed out by Crook (1989) and by Lee (1989). This, however, should be considerably less than the extent of the low total pressure region, and hence (at a given location) small compared to the values of y_c given in the figure.

[2]There are two sets of points plotted for the Smith (1980) compressor. The open symbols are based solely on conditions at the midspan. This rotor had a very low hub/tip radius ratio (0.4) and a consequent large twist, and it might be expected that midspan conditions do not adequately reflect tip section performance for this configuration. To examine this, we have also reduced the data based on the actual measurements of the "free-stream" tip section pressure difference (at a location 33 tip clearances, i.e., 0.33 chord, from the endwall). These points are plotted as the solid symbols in the figure.

[3]To some extent, the arguments made above that relate to only including the vorticity field of a single passage still apply. However, the influence of the other passages is stronger downstream of the trailing edge than in the passage, since the velocity field decay is dipole-like rather than quadrapole-like.

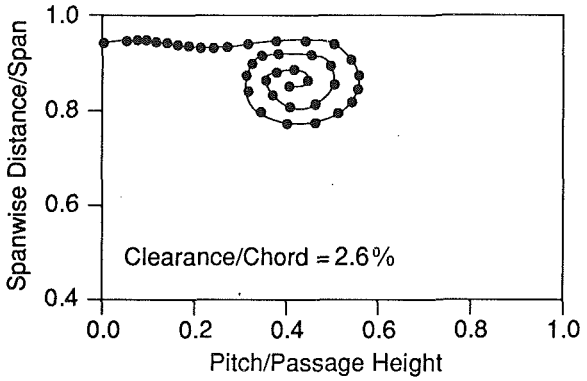

Fig. 6 Computed vorticity distribution at passage exit cross plane (points are at equal time intervals)

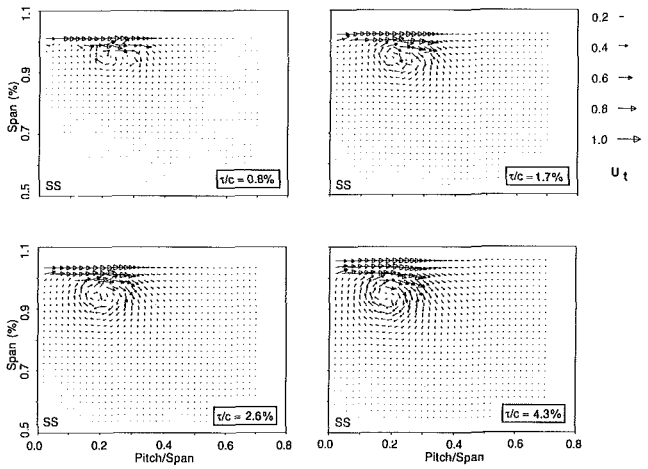

Fig. 7 Crossflow plane velocity at passage exit for different tip clearances

pitch angle deviations from the average, as well as the crossflow velocity field. The configuration has 2.6 percent clearance; this was chosen because the effects are most apparent. The velocity field associated with the tip clearance vortex can be seen to create significant velocities as far inboard as 10 percent span. The experimental measurements of Inoue et al. (1986) are shown so that the extent to which the general flow structure is captured can be assessed.

Other authors have shown that a good estimate of the crossflow plane vorticity distribution yields a reasonable picture of the velocity field. What is *different* in the present comparison is that the only information used is midspan inlet and exit flow angles, axial velocity parameter (or equivalently the overall operating point of the rotor), and camber line. *No* empirical input is given concerning vortex position and strength.

Vortex Core Trajectory. We now examine vortex core trajectories, both in the passage and downstream. Figure 9 shows results for different clearances using the data of Inoue et al. (1986) and Inoue and Kuroumaru (1989). The independence of the trajectory within the passage on the clearance (as discussed previously) can be seen in the figure, which encompasses a factor of five in the tip clearance.

Another feature seen in the calculations is the change in slope of the vortex trajectory at the exit crossflow plane. This can be explained with reference to the image system of the tip clearance vortex, drawn schematically in Fig. 10. The left-hand side of the figure shows a vortex (A) near a blade, with the three images needed to satisfy the relevant kinematic constraints (neglecting the nonzero velocity in the clearance region). On the right, the vortex is shown in the region

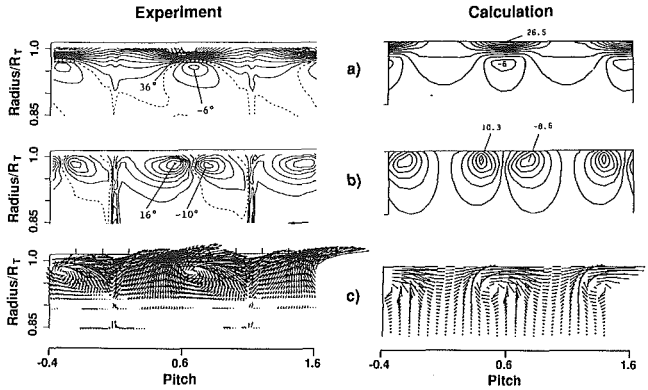

Fig. 8 Computed and measured exit velocity, yaw angle, and pitch angle deviations from axisymmetric mean; 2.6% clearance case (data of Inoue et al., 1986)

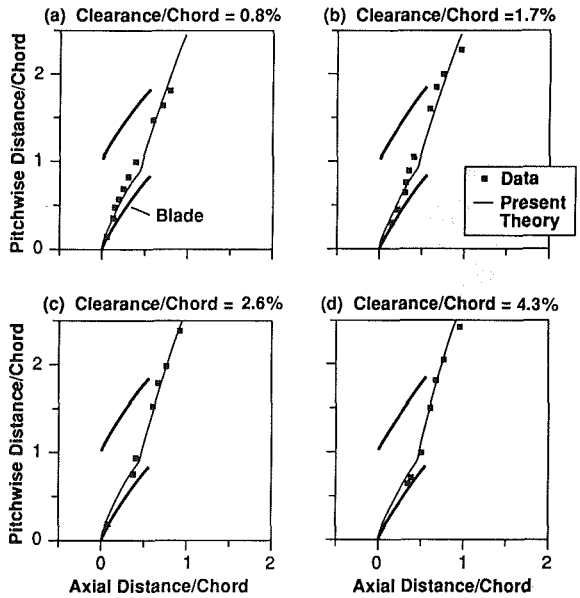

Fig. 9 Computed and measured vortex trajectory in passage and downstream for different clearances (data of Inoue et al., 1986, and Inoue and Kuroumaru, 1989)

downstream of the blade, where there is only one image vortex (B) needed to satisfy the boundary conditions. The horizontal velocity of vortex A due to B alone is greater than that due to B and C (D induces no horizontal velocity), so the crossflow plane velocity is larger downstream of the blade. For constant axial velocity, the slope of the trajectory will thus be larger in the downstream region. (There is also an effect due to the vorticity in the umbilical sheet between blade tip and vortex, but this is small compared to that associated with the image system.)

In the actual situation, there will not be a slope discontinuity since the influence of the blade drops off in a finite distance, rather than abruptly as in the model. However, the change in the slope of the vortex trajectory can still be rather sharp, as seen in Fig. 11, which is a photograph of tip vortex cavitation in an axial flow pump run in water (Rains, 1954). If the low pressure in the cavitation region is taken to correspond to the vortex core: (1) comparison can be made with the theory (which is plotted in the figure) and the two agree well; and (2) the change in slope near the passage exit can be noted.

We can also examine the radial motion of the tip clearance vortex in Fig. 12. The calculations show that the tip vortex center initially moves away from the wall as it travels from the leading edge to the trailing edge, but downstream of the

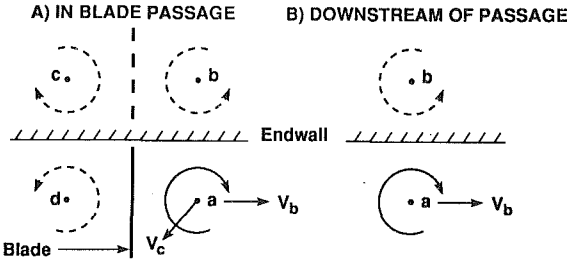

Fig. 10 Vortex and image system in passage and downstream

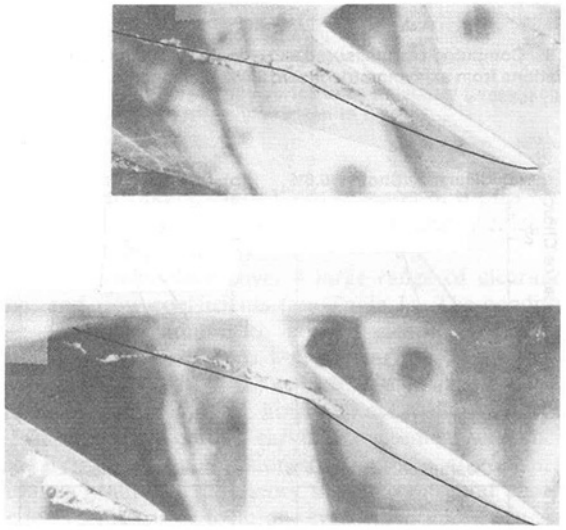

Fig. 11 Vortex trajectory shown by cavitation (data of Rains, 1954); solid line shows calculations based on present theory; (*a*) τ/c = 2.6 percent, (*b*) τ/c = 5.2 percent

trailing edge, the center of the vortex remains at a nearly constant radial location. This can be understood if we note that the centroid of vorticity and the center of the vortex are not very different and, within the description given by the model, the former will remain at a constant radial location. This behavior can be derived directly from the two statements of conservation of circulation and of impulse; the derivation is given in Appendix B.

Effect of Nonconstant Pressure Difference. To examine the influence of the assumption of constant pressure difference across the blade, calculations have also been carried out using a representative compressor pressure difference distribution (Cumpsty, 1989). The calculated tip vortex center using this pressure distribution is given in Fig. 13, where it is compared with the trajectory computed assuming a uniform pressure difference, with the mean pressure coefficient the same in the two cases. The detailed blade pressure distribution has little effect on the evolution of the tip vortex. This implies that the influence of blade loading on the trajectory is not a local effect but is rather determined by the global blade row parameters, at least to the approximation made here.

Endwall Static Pressure Field. Another quantity given by the theory is the variation in endwall pressure. The two-dimensional unsteady model includes no description of the variation in pressure level along the blade, because it deals only with the pressure difference. We therefore adopt the simplest hypothesis, namely that the pitch-averaged static pressure rises linearly from leading to trailing edge. The wall static pressure described is thus the predicted static pressure from the unsteady analysis, referred to this linear background increase.

The computed endwall static pressure is compared to the

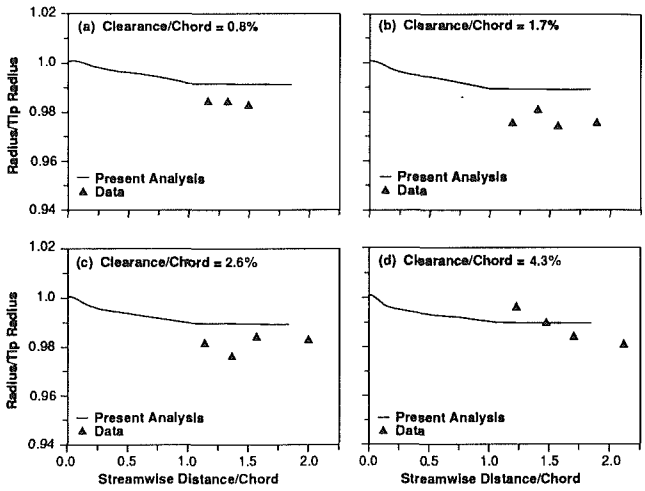

Fig. 12 Radial motion of tip clearance vortex for different clearances (data of Inoue et al., 1985)

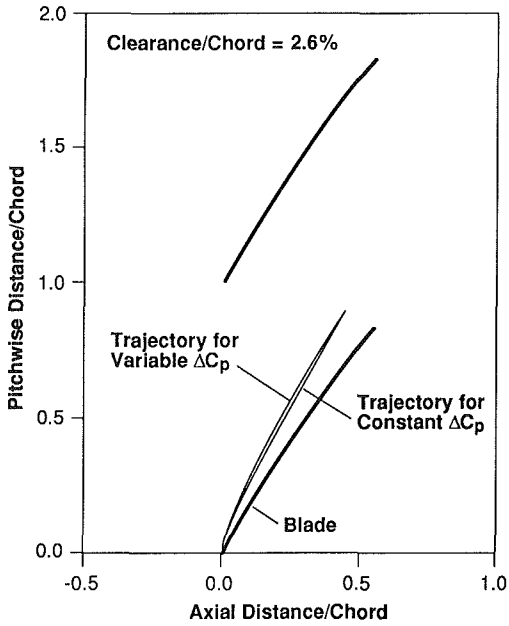

Fig. 13 Vortex trajectory computed based on constant blade pressure difference and on generic pressure distribution (pressure distribution from Cumpsty, 1989)

measurements in Fig. 14, which shows data from three different tip clearances. Two trends are seen in the experimental results. First, the magnitude of the dip in static pressure increases as the clearance decreases, because the tip vortex is closer to the endwall. Second, the location of the minimum static pressure tends to move downstream with increasing clearance. Both of these trends appear in the data and in the analysis.

Effect of Compressor Operating Point on Vortex Position. Takata (1988) has examined the effect of operating point on the vortex position by measuring the trajectory of the low total pressure region in the rotor tip endwall for different mass flows, from design point to stall. Calculations and data from this configuration are shown in Fig. 15 where the computed core trajectory and the regions of lowest total pressure are indicated. As might be expected, the tip vortex moves farther from the suction surface as mass flow decreases because the convection time and the shed vortex sheet strength both increase. The experimental results here also show the change in slope of the tip vortex trajectory near the trailing edge.

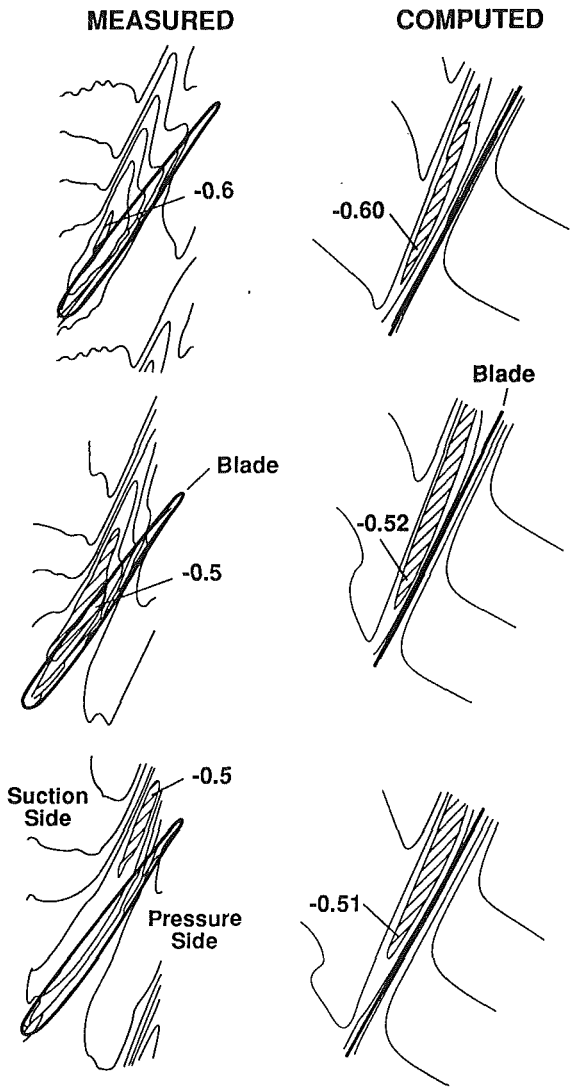

Fig. 14 Computed and measured endwall static pressure distribution (data of Inoue and Kuroumaru, 1989); top figure has clearance/chord ratio of 1.7 percent, middle 2.6 percent, and bottom, 4.3 percent

Application to High-Speed Machines. The analysis was formulated neglecting the effects of compressibility, so that comparison thus far has been with low-speed compressor data. It is of interest to see whether the analysis can be applied to describe the behavior of high-speed machines. There are considerably fewer published endwall flowfield measurements for these devices, and we have found only one data set with enough information so that comparisons can be made. This is a transonic fan whose performance was reported by Ware et al. (1973). The design tip speed was 489 m/s and the design pressure ratio was 1.5. Tip vortex trajectories were located using holography. (In contrast to the low-speed experiments, the trajectory could not be directly inferred from the shapes of the isobars on the casing.) Table 2 shows the flow parameters for the available data.

In Fig. 16 the experimental tip vortex trajectories are plotted on the similarity curve described in connection with Fig. 5. The theory does quite well at placing the vortex. While this may be surprising, examination of the data in the report indicates that the pressure differences across the blades are such that the Mach numbers associated with the crossflow plane velocities are subsonic. More specifically, based on the measured wall static pressure, the mean crossflow Mach number in the clearance region is less than 0.6. Thus, even for situations in which the relative Mach numbers are larger than unity, the basic ideas set forth concerning tip clearance vortex formation and evolution still can be applied.

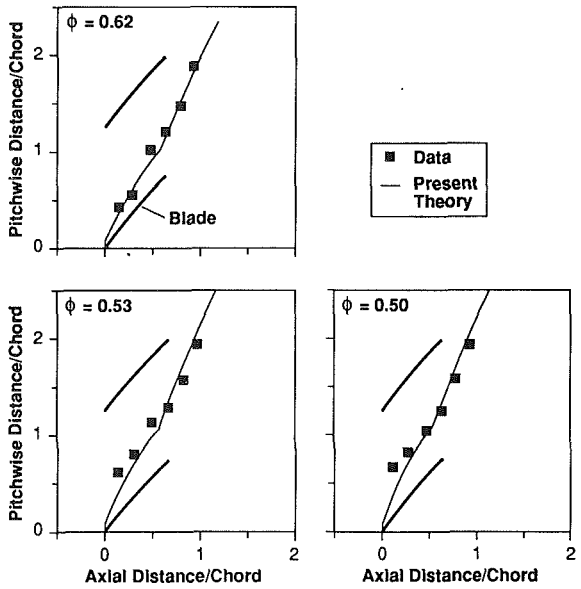

Fig. 15 Effect of operating point on clearance vortex trajectory (data of Takata, 1988)

Table 2 High-speed data

Case	% Design Speed	Pressure Ratio
1	90	1.32
2	90	1.52
3	95	1.60
4	100	1.37
5	100	1.51

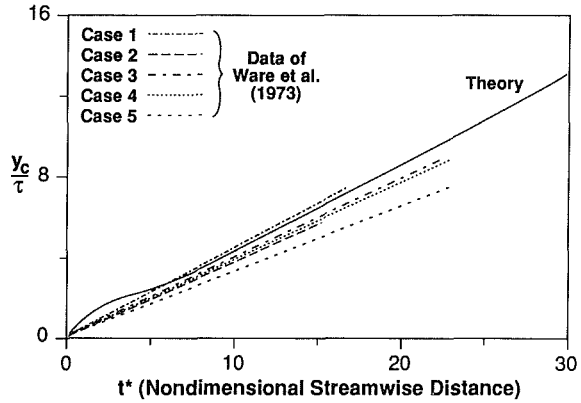

Fig. 16 Generalized tip clearance vortex core trajectory for a transonic fan

Discussion of the Model Limitations

Effects of Classical Secondary Flow. The analysis presented neglects any effects due to what could be termed "classical secondary flow," i.e., the crossflow plane velocities associated with streamwise vorticity due to inlet boundary layers. This streamwise vorticity can arise either from a noncollateral inlet boundary layer or from differential drift of particles on a vortex line, which tip vortex filaments that are initially normal to the stream into the streamwise direction (Lakshminarayana and Horlock, 1965; Horlock, 1973).

The approach taken here implies that the velocity field as-

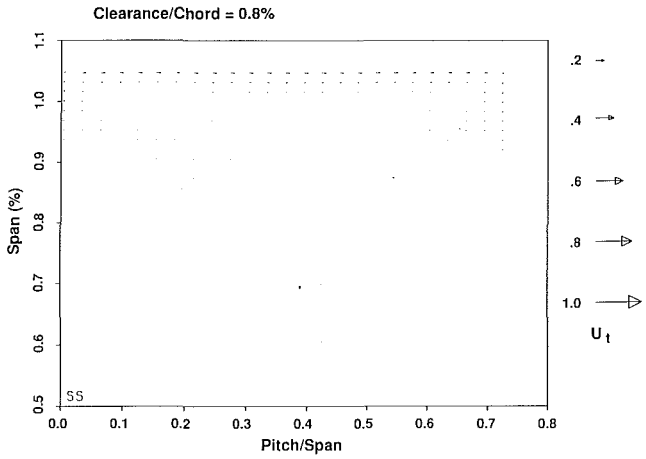

Fig. 17 "Classical" secondary flow due to inlet boundary layer

sociated with the tip clearance vortex dominates that due to classical secondary flow, and it is appropriate to examine this assumption. To do this, we have computed the secondary flow for the configuration of Inoue and Kuroumaru (1989), using the measured inlet boundary layer profiles. The inlet boundary layer is the same for all the different clearances, so that one figure represents his four cases. The crossflow plane velocity field at exit is plotted in Fig. 17 to the same scale as Fig. 7. Comparing the two figures, the velocities associated with the clearance vortex can be seen to be much larger than those due to classical secondary flow. Based on the data we have examined so far, this is generally true for rotor tip flows, which is the situation of greatest practical interest. (We have also done the computations based on the pitch-averaged *exit* boundary layer profiles; the crossflow plane velocities are larger than at inlet but are still small compared to those due to the tip clearance vortex.) When secondary flows do become comparable with the clearance flows, as in many *cascade* experiments, the predicted tip vortex core trajectories would need to be modified to include the secondary flow effects (Dean, 1954). We have not examined this question in any detail, however, since the interest here is in turbomachines.

Effect of Radial Nonuniformities. The data shown have been for situations in which the incoming boundary layers were relatively thin. More specifically, the axial velocity profile has been such that the tip clearance vortex could be considered to be embedded in a stream with velocity equal to the mean velocity. There are many situations in which this is not a valid approximation because the axial velocity changes substantially from the midspan station to the location of the vortex center.

If this occurs, the present analysis will be based on a convection time that is too short and will thus underpredict the distance of the vortex from the blade. Although not shown here, we have, in fact, examined this situation using data from Lakshminarayana and Murthy (1988). It is found that, if one makes a crude correction for this effect by using the inlet axial velocity at the blade tip, the trajectory is well predicted. In terms of the overall fluid mechanics, therefore, the basic analytical framework is still valid, but one must account for the mean flow nonuniformity, as one might expect.

Summary and Conclusions

A similarity analysis of compressor tip clearance flow, based on an inviscid slender body approach, is shown to agree well with a wide range of experimental data. The analysis, which provides a simple approximate description of the clearance flow, focuses on the vortical structure in the endwall region and requires only mean blade flow angles and camber line as input. A basic result of the analysis is a generalized trajectory for the tip clearance vortex. The agreement of this trajectory with the experiment, as well as of the computed velocities in the exit crossflow plane, implies that not only is the behavior of the clearance flow essentially inviscid, as noted by several other investigators, but that it is dominated by the vortical structure.

Features of the tip clearance vortex predicted by the analysis are: (1) Tip clearance does not influence the trajectory of the tip vortex core in the blade passage; (2) a change in the trajectory direction occurs at the blade row trailing edge; and (3) the centroid of vorticity in the vortex sheet shed from the blade tip remains at a constant radial position downstream of the trailing edge. Physical explanations are given for these results.

Acknowledgments

Primary support for this work is from NASA Lewis Research Center under Grant NSG-3208, F. A. Newman, Contract Monitor. Partial support has also been furnished by the General Electric Aircraft Engine Business Group. Both these sources are gratefully acknowledged. We would also like to thank M. B. Giles for helpful comments on the modeling, S. Tavares and Y. Qiu for useful discussions concerning the vortex method computations, N. A. Cumpsty for his usual constructively critical comments, and D. Park for exemplary forebearance in dealing with the authors.

References

Adamczyk, J. J., Celestina, M. L., Beach, T. A., and Barnett, M., 1990, "Simulation of Three-Dimensional Viscous Flow Within a Multistage Turbine," ASME JOURNAL OF TURBOMACHINERY, Vol. 112, pp. 370–376.

Balsa, T. F., and Mellor, G. L., 1975, "The Simulation of Axial Compressor Performance Using an Annulus Wall Boundary Layer Theory," ASME *Journal of Engineering for Power*, Vol. 97, pp. 305–318.

Crook, A. J., 1989, "Numerical Investigation of Endwall/Casing Treatment Flow Phenomena," M.S. Thesis, Department of Aeronautics and Astronautics, MIT, Cambridge, MA.

Cumpsty, N. A., 1989, *Compressors Aerodynamics*, Longman Scientific and Technical Publications, United Kingdom.

Dawes, W. N., 1987, "A Numerical Analysis of the Three-Dimensional Viscous Flow in a Transonic Compressor Rotor and Comparison With Experiment," ASME JOURNAL OF TURBOMACHINERY, Vol. 109, pp. 83–90.

Dean, R. C., Jr., 1954, "The Influence of Tip Clearance on Boundary-Layer Flow in a Rectilinear Cascade," MIT Gas Turbine Laboratory Report No. 27-3.

De Ruyck, J., and Hirsch, C., 1981, "Investigation of an Axial Compressor End-Wall Boundary Layer Prediction Method," ASME *Journal of Engineering for Power*, Vol. 103.

Evans, R. A., and Bloor, M. I. G., 1977, "The Starting Mechanism of Wave-Induced Flow Through a Sharp-Edged Orifice," *J. Fluid Mechanics*, Vol. 82, pp. 115–128.

Hah, C., 1986, "A Numerical Modelling of Endwall and Tip-Clearance Flow of an Isolated Compressor Rotor," ASME *Journal of Engineering for Power*, Vol. 108, pp. 15–21.

Horlock, J. H., 1973, *Axial Flow Compressors*, Robert E. Krieger Publishing Company, Huntington, NY.

Inoue, M., Kuroumaru, M., and Fukuhara, M., 1986, "Behavior of Tip Leakage Flow Behind an Axial Compressor Rotor," ASME *Journal of Engineering for Gas Turbines and Power*, Vol. 108, pp. 7–13.

Inoue, M., and Kuroumaru, M., 1989, "Structure of Tip Clearance Flow in an Isolated Axial Compressor Rotor," ASME JOURNAL OF TURBOMACHINERY, Vol. 111, pp. 250–256.

Johnson, M. C., 1985, "The Effects of Hub Treatment on Compressor Endwall Flowfields," M.S. Thesis, Department of Aeronautics and Astronautics, MIT, Cambridge, MA.

Koch, C. C., and Smith, L. H., Jr., 1976, "Loss Sources and Magnitude in Axial-Flow Compressors," ASME *Journal of Engineering for Power*, Vol. 98, pp. 411–424.

Lakshminarayana, B., 1970, "Method for Predicting the Tip Clearance Effects in Axial Flow Turbomachinery," ASME *Journal of Basic Engineering*, Vol. 92, pp. 467–481.

Lakshminarayana, B., and Horlock, J. H., 1965, "Leakage and Secondary Flows in Compressor Cascades," ARC R&M No. 3483.

Lakshminarayana, B., and Murthy, K. N. S., 1988, "Laser-Doppler Velocimeter Measurement of Annulus Wall Boundary Layer Development in a Compressor Rotor," ASME JOURNAL OF TURBOMACHINERY, Vol. 110, pp. 377–385.

Lamb, H., 1932, *Hydrodynamics*, 6th ed., Dover Publications, New York.

Lee, N. K. W., 1989, Private Communication.

Leonard, A., 1980, "Vortex Methods for Flow Simulation," *J. Computational Physics*, Vol. 37, pp. 289–335.

Moore, J., and Tilton, J. S., 1988, "Tip Leakage Flow in a Linear Turbine Cascade," ASME JOURNAL OF TURBOMACHINERY, Vol. 110, pp. 301–309.

Perry, A. E., and Tan, D. K. M., 1980, "Simple Three-Dimensional Vortex Motions in Co-Flowing Jets," *J. Fluid Mechanics*, Vol. 141, pp. 197–231.

Rains, D. A., 1954, "Tip Clearance Flow in Axial Flow Compressors and Pumps," California Institute of Technology, Hydrodynamics and Mechanical Engineering Laboratories Report No. 5.

Sarpkaya, T., 1989, "Computational Methods With Vortices—The 1988 Freeman Scholar Lecture," ASME *Journal of Fluids Engineering*, Vol. 111, pp. 5–52.

Senoo, Y., and Ishida, M., 1986, "Pressure Loss Due to the Tip Clearance of Impeller Blades in Centrifugal and Axial Blowers," ASME *Journal of Engineering for Gas Turbines and Power*, Vol. 108, pp. 32–37.

Smith, G. D. J., 1980, "Casing Treatment in Axial Compressors," Ph.D. Thesis, Engineering Department, University of Cambridge, UK.

Storer, J. A., and Cumpsty, N. A., 1991, "Tip Leakage Flow in Axial Compressors," ASME JOURNAL OF TURBOMACHINERY, Vol. 113, this issue.

Takata, H., 1988, Personal Communication. [See also Yanagida, M., Machida, Y., and Takata, H., 1989, "A Study on the Mechanism of Stall Margin Improvement of Casing Treatment (2nd Report: Result on Total Pressure Measurement and Discussion)," *Transactions of Japan Society of Mechanical Engineers*, Vol. 55, No. 518, Series B (in Japanese).]

Ware, T. C., Kobayashi, R. J., and Jackson, R. J., 1973, "High-Tip-Speed, Low Loading Transonic Fan Stage, Part II: Final Report," NASA CR-121263.

Wisler, D. C., 1985, "Aerodynamic Effects of Tip Clearance, Shrouds, Leakage Flow, Casing Treatment and Trenching in Compressor Design," Von Karman Institute Lecture Series 1985-05 on "Tip Clearance Effects in Axial Turbomachinery."

Zhang, J., 1988, "An Experimental, Analytical, and Computational Investigation of Turbomachinery Rotor Flow Fields," Ph.D. Thesis, Department of Aeronautical Engineering, Pennsylvania State University.

APPENDIX A

Equations of Motion for Clearance Flows

For a three-dimensional steady incompressible flow, the equations of mass and momentum conservation in curvilinear coordinates are given, respectively, by

$$\frac{R}{R+y}\frac{\partial u}{\partial s}+\frac{\partial v}{\partial y}+\frac{v}{R+y}+\frac{\partial w}{\partial z}=0$$

$$\frac{R}{R+y}u\frac{\partial u}{\partial s}+v\frac{\partial u}{\partial y}+w\frac{\partial u}{\partial z}+\frac{uv}{R+y}=-\frac{R}{R+y}\frac{1}{\rho}\frac{\partial p}{\partial s}$$

$$\frac{R}{R+y}u\frac{\partial v}{\partial s}+v\frac{\partial v}{\partial y}+w\frac{\partial v}{\partial z}-\frac{u^2}{R+y}=-\frac{1}{\rho}\frac{\partial p}{\partial y}$$

$$\frac{R}{R+y}u\frac{\partial w}{\partial s}+v\frac{\partial w}{\partial y}+w\frac{\partial w}{\partial z}=-\frac{1}{\rho}\frac{\partial p}{\partial z}$$

where s is measured along the camber, y is measured normal to the camber, and z is measured along the span. $R(s)$ is the radius of curvature of a blade camber line.

The streamwise component of velocity u can be written as

$$u(s, y, z) = \bar{u}(s) + u'(s, y, z)$$

where $\bar{u}(s)$ is the throughflow velocity. As discussed in the text, we assume that

$$\frac{u'(s, y, z)}{\bar{u}(s)} \ll 1$$

the governing equations then become

$$\frac{R}{R+y}\frac{d\bar{u}}{ds}+\frac{\partial v}{\partial y}+\frac{v}{R+y}+\frac{\partial w}{\partial z}=0$$

$$\frac{R}{R+y}\bar{u}\frac{d\bar{u}}{ds}+v\frac{\partial u}{\partial y}+w\frac{\partial u}{\partial z}+\frac{\bar{u}(s)v}{R+y}=-\frac{R}{R+y}\frac{1}{\rho}\frac{\partial p}{\partial s}$$

$$\frac{R}{R+y}\bar{u}\frac{\partial v}{\partial s}+v\frac{\partial v}{\partial y}+w\frac{\partial v}{\partial z}-\frac{\bar{u}^2}{R+y}=-\frac{1}{\rho}\frac{\partial p}{\partial y}$$

$$\frac{R}{R+y}\bar{u}\frac{\partial w}{\partial s}+v\frac{\partial w}{\partial y}+w\frac{\partial w}{\partial z}=-\frac{1}{\rho}\frac{\partial p}{\partial z}$$

For the clearance flow, the characteristic length in the s direction is the chord length, c. We taken that in the y and z directions as some multiple of the clearance, τ.

In compressor and fan applications, τ/c is of the order 10^{-2}, and the chord c is generally much less than the radius of curvature $R(s)$. The dominant terms in the equation of motion are thus

$$\frac{\partial v}{\partial y}+\frac{\partial w}{\partial z}=0 \tag{A1}$$

$$\frac{\partial v}{\partial t}+v\frac{\partial v}{\partial y}+w\frac{\partial v}{\partial z}=-\frac{1}{\rho}\frac{\partial p}{\partial y} \tag{A2}$$

$$\frac{\partial w}{\partial t}+v\frac{\partial w}{\partial y}+w\frac{\partial w}{\partial z}=-\frac{1}{\rho}\frac{\partial p}{\partial z} \tag{A3}$$

$$\bar{u}\frac{d\bar{u}}{ds}=-\frac{1}{\rho}\frac{\partial p}{\partial s} \tag{A4}$$

where we have made the substitution $ds = \bar{u}dt$. Equations (A1), (A2), and (A3) are the governing equations of a two-dimensional unsteady (cross) flow, and equation (A4) is the equation for the throughflow. The clearance flow can thus be decoupled into crossflow and throughflow.

APPENDIX B

Radial Motion of Tip Vortex After Trailing Edge

Consider a number of line vortices moving by their own induced velocities in a channel. This can be represented by a vortex system and its approximate images. Specifying the situation to be periodic with period $2H$, we examine only the vortices that lie between $z = \pm H$.

The Kelvin impulse of a vortex pair is given by

$$I_i=\rho\Gamma_i d_i \tag{B1}$$

where Γ_i is the circulation of the vortex and d_i is the distance between the centers of the vortex pair. The impulse of the N vortex pairs between $z = \pm H$ is

$$I=\sum_{i=1}^{N}\rho\Gamma_i d_i \tag{B2}$$

There is no force on the vortices so the total impulse is constant. Also in the region downstream of the trailing edge, the total circulation (of the vortices between $z = 0$ and $z = H$) is conserved, i.e.,

$$\Gamma=\sum_{i=1}^{N}\Gamma_i=\text{const} \tag{B3}$$

Combining equations (B1) and (B3), we have

$$\frac{\Sigma_{i=1}^{N}\Gamma_i d_i}{\Sigma_{i=1}^{N}\Gamma_i}=\text{const}=2z_c \tag{B4}$$

The content of equation (B4) is that the centroid of the vortices, z_c, remains at a fixed radial distance from the wall.

The conclusion also holds for a vortex sheet. The derivation is similar and the result is

$$\text{Radial distance of centroid}=\frac{\int_0^{\eta_{\max}} z\gamma d\eta}{\int_0^{\eta_{\max}}\gamma d\eta}=\text{const} \tag{B5}$$

where γ = strength of the vortex sheet, and η is the intrinsic coordinate along the sheet.

DISCUSSION

J. A. Storer[4]

This paper provides a very important contribution to the understanding of tip clearance effects in axial compressors. The paper demonstrates that tip leakage flow has an overwhelming effect on the endwall flowfield, but that the mechanism of the flow is not influenced significantly by viscosity or details of the inlet endwall boundary layer. The model of the roll-up of the leakage vortex developed by the authors highlights the importance of the blade loading outside the endwall region and indicates that the factors controlling tip leakage flow rate are substantially independent of the tip clearance itself. The observation of a generalized vortex trajectory for a variety of compressor rotors suggests that tip leakage flow in axial compressors is predominantly a pressure-driven phenomenon and that the motion of the wall over the blade tip is of secondary importance. The objective of the present discussion is primarily to demonstrate the correspondence between Navier–Stokes predictions of the tip leakage vortex and the model proposed by Chen et al. for rotors and stators. Calculations for a cascade, however, show a *weak* dependence of vortex trajectory on tip clearance, highlighting a difference between tip leakage flow in a cascade and in a machine. Although of minor importance to the conclusions drawn by the authors, I think the results help to clarify observations made in the paper.

The material for this discussion was obtained using the Navier–Stokes solver described by Storer and Cumpsty (1991). Further details of the calculations are given by Storer (1990). The first example is a calculation of the flow in a single-stage axial compressor with 2.3 percent of chord hub clearance, for which generally good agreement was obtained between measurements and Navier–Stokes predictions at the design flow coefficient. At this operating point the inlet boundary layer on the hub endwall was considerably skewed, although near midspan the blade operated with negative incidence. The conditions in the stator were therefore very different from those that may be recreated in a linear cascade with a stationary endwall and a collateral inlet boundary layer. The inlet condition for the Navier–Stokes calculation was the circumferential and time average of that measured downstream of the rotor, but the spanwise variation was maintained. The roll-up of the vortex predicted by the Navier–Stokes calculation is illustrated in Fig. 18. The figure shows particle paths integrated from the single line of points along the camberline that defined the blade tip in the calculation mesh (see Storer and Cumpsty, 1991). The vortex trajectory predicted by the model of Chen et al. is shown by a broken line in the figure and assumes the pressure difference across the end of the blade to be set up by the flow conditions at 10 percent span. Both methods predict a similar trajectory for the vortex in the blade passage, with the Navier–Stokes calculation also indicating a change of vortex trajectory downstream of the trailing edge, as explained by Chen et al.

The second example in Fig. 19 is taken from the measurements and Navier–Stokes calculations of the flow in a compressor cascade described by Storer and Cumpsty (1991). The tests and Navier–Stokes calculations showed that in a cascade the tip vortex tends to originate some distance along the blade chord, near the position of minimum pressure on the suction side of the tip. The Navier–Stokes calculations predicted the locus of the tip vortex core to change depending on tip clearance (see Fig. 19), the main differences arising from changes in the trajectory of the leakage flow near the leading edge. The basis of the Chen et al. model is the assumption made by Rains (1954) that flow perpendicular to the blade at the tip is effectively decoupled from flow in the streamwise direction. Simple calculations using the Rains model demonstrate that in a cascade this is generally a good approximation except near the leading edge, where the tip leakage flow locally experiences an acceleration in the streamwise direction comparable in magnitude with that across the tip (see Storer and Cumpsty, 1991). Hence the vortex trajectory predicted by the model of Chen et al. for the cascade did not agree very well with Navier–Stokes calculations. In machines, on the other hand, since the inlet boundary layer tends to be skewed in both the relative and stationary frames of reference, the flow incidence near the ends of both rotor and stator blades tends to be high. Consequently the minimum pressure on the suction side of the tip generally occurs nearer the leading edge than for a collateral inlet flow (see Storer, 1990). In these cases the leakage vortex also tends to originate from near the leading edge, as observed by Rains (1954), and the vortex position is predicted very well by the model of Chen et al.

Finally I would like to reaffirm the importance of the blade loading outside the endwall region as essentially providing the

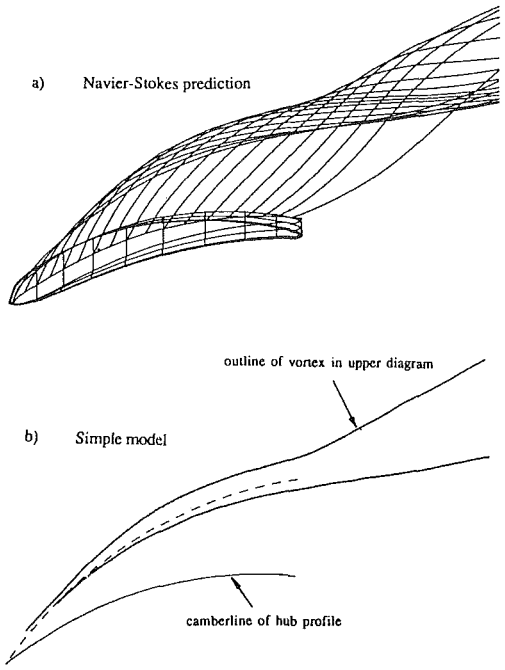

Fig. 18 Predictions of vortex trajectory in a stator hub

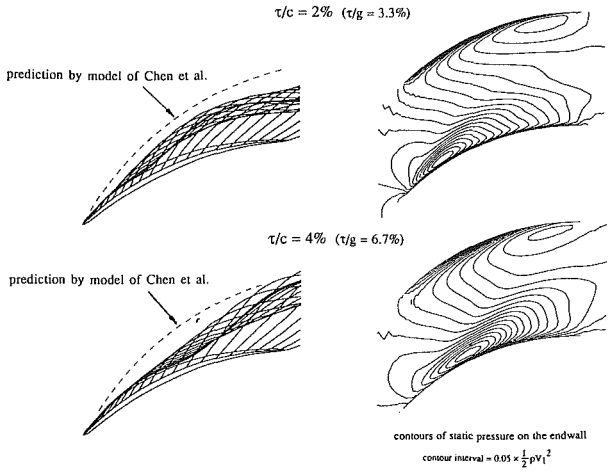

Fig. 19 Predicted relationship of the tip vortex trajectory to the pressure trough on the cascade endwall

[4]Rolls-Royce plc, Bristol BS17 7QE United Kingdom.

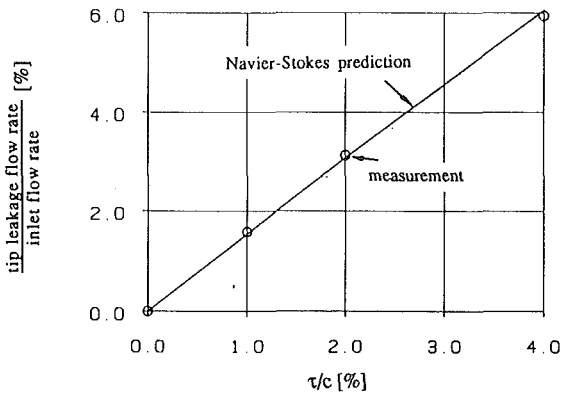

Fig. 20 Relationship of total tip leakage flow rate to tip clearance in a cascade

pressure difference to drive the tip leakage flow, as assumed by Chen et al. in the development of their model. It is shown by Storer and Cumpsty (1991) that the pressure distribution near the blade tip in a cascade changed due to the proximity of the tip vortex when the clearance was altered. The changes of pressure distribution gave rise to changes in the chordwise pattern of tip leakage flow, but nevertheless the *overall* tip leakage mass flow rate was not in fact changed by the vortex. (This can be seen since the flow rate increased linearly with respect to tip clearance, as shown in Fig. 3.) Therefore the average pressure difference driving the flow remained constant and a function of the flow conditions outside the endwall region, i.e., those at midspan.

References

Storer, J. A., 1990, "Tip Leakage Flow in Axial Compressors," Ph.D. Dissertation to be submitted, Cambridge University, United Kingdom.

Storer, J. A., and Cumpsty, N. A., 1991, "Tip Leakage Flow in Axial Compressors," ASME JOURNAL OF TURBOMACHINERY, Vol. 113, this issue.

Authors' Closure

The authors thank Mr. Storer for his discussion. We view it as a valuable addition to the paper, which represents one of the beneficial aspects of the ongoing collaboration between the Whittle Laboratory and the Gas Turbine Laboratory. Mr. Storer has brought out very clearly some of the differences that exist between clearance flows in turbomachines and in cascades; further components on the topic are given by Chen (1990).

We also have been using three-dimensional computations to examine the tip clearance flow, as a parallel effort to that in the paper. To restate a position given in the paper, it appears to us that the combination of well-chosen "numerical experiments," such as Mr. Storer has done (see also Crook, 1989) with analysis, is indeed useful for developing understanding, not only on a case-by-case basis, but for a broad class of fluid dynamic devices of practical interest.

Reference

Chen, G. T., 1990, "Vortical Structures in Turbomachinery Tip Clearance Flows," Ph.D. Thesis, Department of Aeronautics and Astronautics, MIT, Cambridge, MA.

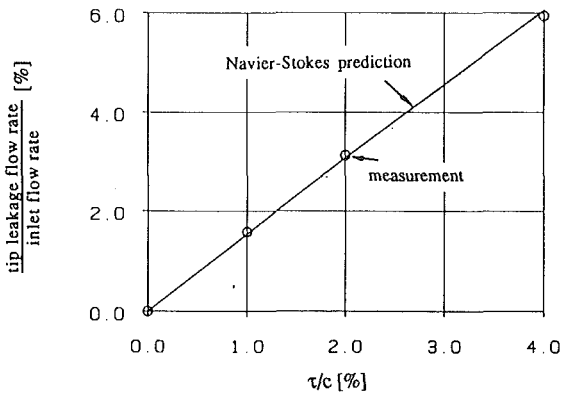

Fig. 20 Relationship of total tip leakage flow rate to tip clearance in a cascade

pressure difference to drive the tip leakage flow, as assumed by Chen et al. in the development of their model. It is shown by Storer and Cumpsty (1991) that the pressure distribution near the blade tip in a cascade changed due to the proximity of the tip vortex when the clearance was altered. The changes of pressure distribution gave rise to changes in the chordwise pattern of tip leakage flow, but nevertheless the *overall* tip leakage mass flow rate was not in fact changed by the vortex. (This can be seen since the flow rate increased linearly with respect to tip clearance, as shown in Fig. 3.) Therefore the average pressure difference driving the flow remained constant and a function of the flow conditions outside the endwall region, i.e., those at midspan.

References

Storer, J. A., 1990, "Tip Leakage Flow in Axial Compressors," Ph.D. Dissertation to be submitted, Cambridge University, United Kingdom.

Storer, J. A., and Cumpsty, N. A., 1991, "Tip Leakage Flow in Axial Compressors," ASME JOURNAL OF TURBOMACHINERY, Vol. 113, this issue.

Authors' Closure

The authors thank Mr. Storer for his discussion. We view it as a valuable addition to the paper, which represents one of the beneficial aspects of the ongoing collaboration between the Whittle Laboratory and the Gas Turbine Laboratory. Mr. Storer has brought out very clearly some of the differences that exist between clearance flows in turbomachines and in cascades; further components on the topic are given by Chen (1990).

We also have been using three-dimensional computations to examine the tip clearance flow, as a parallel effort to that in the paper. To restate a position given in the paper, it appears to us that the combination of well-chosen "numerical experiments," such as Mr. Storer has done (see also Crook, 1989) with analysis, is indeed useful for developing understanding, not only on a case-by-case basis, but for a broad class of fluid dynamic devices of practical interest.

Reference

Chen, G. T., 1990, "Vortical Structures in Turbomachinery Tip Clearance Flows," Ph.D. Thesis, Department of Aeronautics and Astronautics, MIT, Cambridge, MA.

Compressor Drum Aerodynamic Experiments and Analysis With Coolant Injected at Selected Locations

B. V. Johnson

W. A. Daniels

United Technologies Research Center,
East Hartford, CT 06108

E. J. Kawecki

Pratt & Whitney,
Government Products Division,
West Palm Beach, FL 33410

R. J. Martin

Wright Research and Development Center,
Wright-Patterson Air Force Base, OH 45433

Experiments were conducted to determine the pressure distributions within a multicavity compressor drum model for two coolant injection locations and a range of flow conditions. Flow was injected through the upstream conical wall or through the cylindrical wall of the rotating model. The coolant flow, the drum rotational rate, and the model pressure were varied to produce a range of tangential and coolant flow Reynolds numbers, typical of large aircraft engine high-pressure compressor drums. The experimental results were used to evaluate analytical procedures for predicting flow characteristics in rotating annular cavities with radially inward flow and for correlating flow characteristics in multiple-rotating annular cavities, which are not currently predicted. Swirling flows, radially inward between compressor disks and within rotating annular cavities with no net flow, were analyzed with a procedure that coupled a viscous solution for the rotating core flow with a momentum integral analysis for the boundary layers on the disks. Constant viscosity and variable turbulent viscosity models were used in the analysis. Results from the analysis and the experiments were used to estimate the tangential velocity distribution in trapped cavities for two coolant injection configurations and a range of flow rates.

Introduction

The prediction of flow in gas turbine compressor drum cavities and of the heat transfer to and from the disks and drums are important and complex problems in aircraft gas turbine, internal air systems technology. The durability of the engine disks is strongly influenced by the thermal stresses in the disks. These stresses are determined to a large extent by the heat transfer to and from the compressor disks during the gas turbine's acceleration and deceleration stages of flight. The performance of the compressor is determined in part by the blade tip clearances, which are a function of the disk temperatures. The disk cavity flow field is complex because the coolant is often injected into the cavity at one location and leaves the cavity near the center at the downstream end or at both ends of the compressor drum cavity. The flow in the coolant injection regions and the trapped cavity (i.e., a cavity with zero net throughflow) regions are usually governed by the angular momentum flux of the coolant, the secondary flow from the compressor disks, the turbulent mixing from flow adjacent to the disks, and the buoyancy-driven flows as the disks are heated or cooled.

The flow and heat transfer on rotor disks and on rotor–stator disk systems have been studied analytically and experimentally to a great extent, e.g., Dorfman (1963) and Owen and Rogers (1989). There has been a modest amount of research on flow in single rotating cavities with and without net radial flow, e.g., Yu et al. (1973), Gosman et al. (1976), Owen and Pincombe (1979), and Owen et al. (1985). However, there has been relatively little published research on flow in the geometric class of multiple cavities employed in the high-pressure compressors of aircraft gas turbines or large single-shaft stationary gas turbines. A limited amount of velocity data from a 1970s experiment with an eleven-cavity compressor drum model was presented by Bennett (1974) and Alberga et al. (1987).

Compressor drum cooling technology is one of the important technologies recognized in the United States DoD/NASA Integrated High Performance Turbine Engine Program. One emphasis in this program is the substantial reduction of cooling and leakage air to increase overall engine performance. Therefore, it is essential that the reduced cooling flows be used effectively and that the cooling technology be adequately understood so that new compressor drum cavity designs can adequately assessed. As previously noted, experimental and analytical studies of multiple-cavity flows have been limited in scope relative to the needs of the gas turbine designers for predicting the flow in compressor drum cavities and heat transfer to and from the compressor disks. Most gas turbine manufacturers have traditionally kept their internal air systems data proprietary. Therefore, the Turbine Engine Division/Aero Propulsion and Power Laboratory/U. S. Air Force recognized

Contributed by the International Gas Turbine Institute and presented at the 35th International Gas Turbine and Aeroengine Congress and Exposition, Brussels, Belgium, June 11–14, 1990. Manuscript received by the International Gas Turbine Institute January 16, 1990. Paper No. 90-GT-151.

that a publicly available data base would encourage the development of improved design technology for this aspect of compressor technology. The present paper is based on data obtained in one Air Force-sponsored study (Graber et al., 1987) of this technology.

In this paper, the air systems technology for flow in compressor drum cavities will be extended by (*a*) the presentation of pressure distribution results from a multiple cavity compressor drum model with two different coolant injection locations to show effects of angular momentum at injection on flow within the drum, (*b*) the use of results from an analytical study of flow in throughflow and trapped cavities to show the effects of core region turbulent viscosity on the pressure drop across those cavities, (*c*) the evaluation of a secondary flow parameter as a scaling parameter for flow in bleed and trapped cavities, and (*d*) the use of analytical results and the overall pressure drop across a trapped cavity to estimate the swirl at the bore radius and the velocity distribution within the cavity.

Background

The flows inside compressor drum assemblies can be represented by a system of corotating disk cavities, which rotate at the same angular velocity. Unlike rotor–stator disk systems, where the relative velocity between disks provides a means by which work can be input into the system, the only net angular momentum input into the compressor drum flow system is that due to the initial swirl of the coolant injected into the drum. As a result, the flow fields in the compressor drum are dominated by the conservation of the initial angular momentum of the coolant bled into the system. These flows have characteristically weak swirl and will be largely dependent upon the coolant flow rate and coolant injection location. In addition, the decay of the swirl can be significant reduced by wall friction in the trapped and bleed cavity until the cavity flows are primarily buoyancy driven. A comprehensive understanding of the rotating flows in the compressor drum is required to predict disk heat transfer and thermal response characteristics.

Three typical compressor drum bleed configurations are shown in Fig. 1. The disk cavity flow characteristics and disk heat transfer mechanisms in both the bleed and nonbleed cavities will differ significantly for each of these bleed configurations. For bleed Configuration 1, coolant enters the drum through the rim at a midcompressor stage with the same tangential velocity as the drum. Conservation of angular momentum for this situation requires that the tangential velocity of the fluid increase with decreasing radius. This is shown in

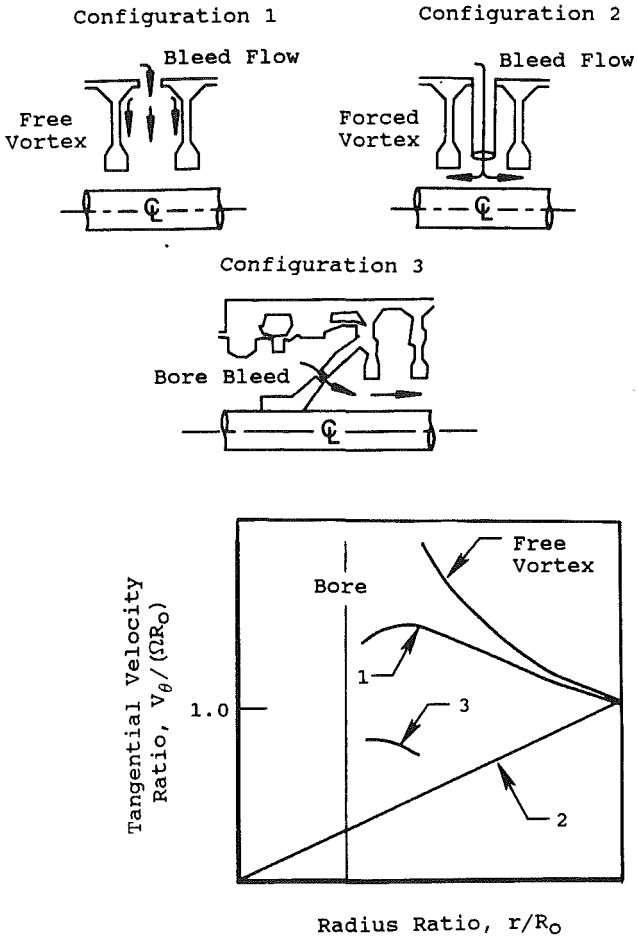

Fig. 1 Typical effects of bleed configuration on tangential velocity distribution in compressor drum

Fig. 1 as Curve 1 in the variation of the tangential velocity of the fluid in the cavity (normalized by its initial value) with the dimensionless radius ratio. For this bleed situation, Curve 1 indicates that the fluid in the bleed cavity rotates at a rate that is greater than that of the disks. Thus, a relative velocity exists between the fluid and the disks and a forced convective heat transfer process is possible for this bleed configuration. However, this heat transfer driving swirl can be expected to decay in the trapped cavities adjacent to the bleed cavity.

Nomenclature

K = coefficient for turbulent viscosity model
L = distance between disks, ft
m = coolant flow rate, lb/s
P = pressure, lb/ft^2
q = dynamic head of rotating flow, lb/ft^2
r = radius, ft
R = radial location, ft
Re_r = radial Reynolds number $= \rho_o V_{ro} R_o/\mu_o$
$\mathrm{Re}_{r,\mathrm{eff}}$ = effective radial Reynolds number $= \rho_o V_{ro} R_o/\mu_{\mathrm{eff}}$
Re_θ = tangential Reynolds number $= \rho_o \Omega R_o^2/\mu_o$
Re_z = coolant flow Reynolds number $= m/(2\pi\mu_o R_o)$
U = boundary layer velocity, ft/s
V = core flow velocity, ft/s
z = axial distance from wall, ft
δ = boundary layer thickness, ft
η = coolant flow parameter $= \mathrm{Re}_z/\mathrm{Re}_\theta^{0.8}$
θ = azimuthal distance, rad
μ = molecular dynamic viscosity, lb/(ft-s)
μ_t = turbulent dynamic viscosity, lb/(ft-s)
μ_{eff} = total dynamic viscosity, lb/(ft-s)
ν = kinematic viscosity, ft^2/s
ρ = density of fluid, lb/ft^3
σ = secondary flow parameter $= (m_s/2\pi\mu R_o)/\mathrm{Re}_\theta^{0.8}$
Ω = rotational rate, rad/s (rpm)

Subscripts

b = bore radius
c = core
i = bore tube radius
j = injection jet
o = outer radius of disk
r = radial component
s = boundary layer
t = total
z = axial component
θ = azimuthal component

Superscripts

$\bar{}$ = average value in boundary layer

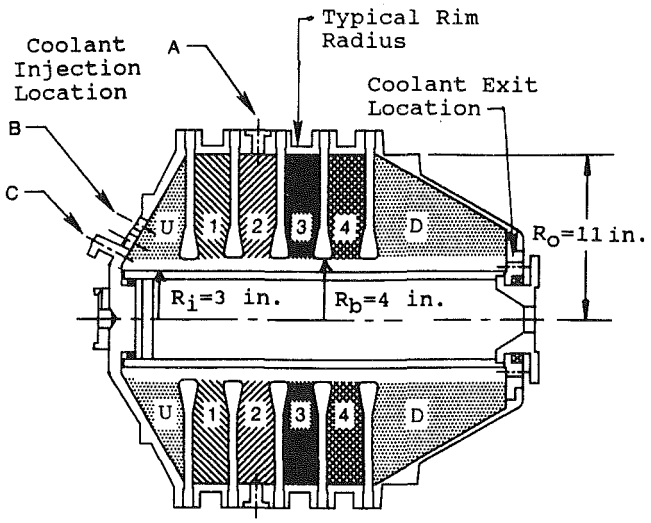

Fig. 2 Compressor drum model with cavity nomenclature

For bleed Configuration 2, coolant enters the drum from the same location as 1 but is constrained by a tube to move with the same angular velocity as the disk. The tangential velocity profile for this situation is shown in Fig. 1 as Curve 2. For this case, there is no relative velocity between the fluid and the disk. A heat transfer process that is predominantly buoyancy driven or "free" convection is probable here.

For injection Configuration 3, fluid enters the high-pressure compressor drum through the front endwall of the drum at a radius that is at or slightly greater than the compressor drum disk bore. Conservation of angular momentum for this case requires that the angular velocity of the fluid decrease with increasing radius in the cavity. Curve 3 for this injection configuration shows a tangential velocity profile that is somewhere in between that of injection Configurations 1 and 2. This indicates that a moderate amount of swirl is present and that a heat transfer process for this situation can be both free and forced convective in nature.

To quantify these effects, an experimental investigation was conducted to obtain compressor drum disk cavity aerodynamic data for a number of injection configurations and flow conditions. Pressure measurements at selected disk radii were obtained in a six-cavity compressor drum model (Fig. 2). Three injection configurations were investigated. One configuration (A) siumulated a high-pressure compressor midstage bleed configuration and the other two injection configurations (B and C) simulated two fan-bled compressor drum designs. All measurements were obtained at Reynolds numbers typical of current and advanced gas turbine engines using air as the working fluid. Results for configurations A and B are presented herein. The characteristics at all flow conditions for configuration C were essentially solid body rotation and are not discussed further.

The compressor drum test matrix for coolant injection location A is shown in Fig. 3. The operating range for axial flow aircraft gas turbines is shown for comparison. The coordinates for this matrix are the tangential Reynolds number (Re_θ) and the dimensionless mass flow Reynolds number (Re_z). These parameters are pertinent to the fluid mechanics of rotating disk wall friction problems. The tangential and mass flow Reynolds numbers are combined to form a dimensionless parameter for turbulent disk friction in rotating cavities (η). This parameter has the same relationships that were developed by Von Karman for turbulent flow on a free rotating disk (Schlichting, 1968). The parameter η will be shown to correlate the disk cavity radial pressure drop with flow conditions. Lines of constant η are shown in Fig. 3. Note that the test matrix

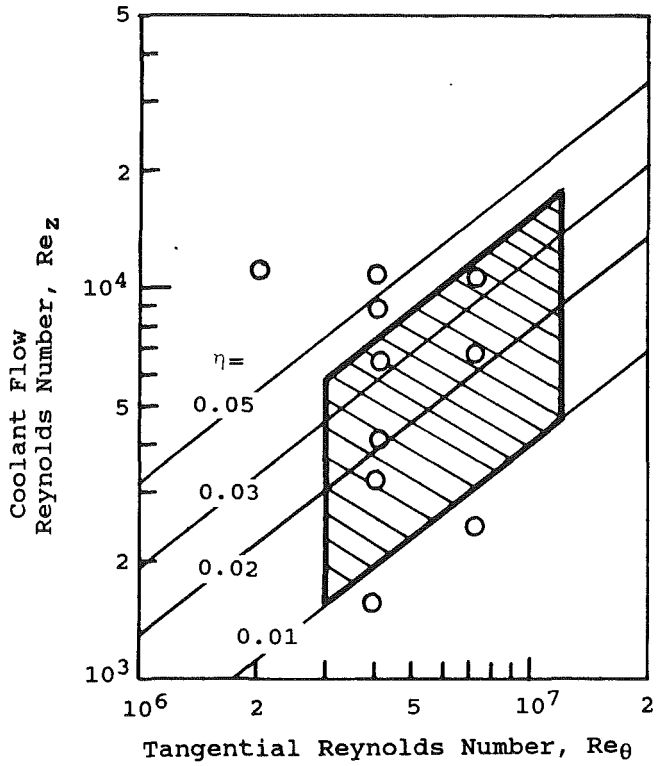

Fig. 3 Operating range for high-pressure compressor drums and model test conditions: o test flow conditions for injection configuration A; \\\\\ operating range for large aircraft gas turbine

covers a large portion of the operating range of current and advanced gas turbine engines.

Internal Air Systems Facility

The facility was designed for experimental investigation of aerodynamic and heat transfer characteristics of internal air flow system components, including compressor drums, turbine disks, turbine disk cavities, turbine rim cavity/seal systems, and rotating orifices. The facility has two independently operated drive systems, which provide capability for corotating and counterrotating disk experiments. Using air as the working fluid, the facility is capable of providing test conditions with dimensionless fluid parameters (e.g., Reynolds number) typical of current and advanced gas turbines (Fig. 3). A sketch of the facility is shown in Fig. 4.

The principal mechanical components of the facility include a pressure chamber, two drive systems, plumbing, flow control valves and meters, and two drive system control stations. The pressure chamber was designed to the American Society of Mechanical Engineers (ASME) boiler code specifications for pressure vessels and operates at pressures up to 150 psig. The vessel, approximately 3 ft in diameter and 6 ft in length, was designed so that the upper one-third of the vessel can be removed to facilitate model installation, modification, and checkout.

The pressure vessel and model air supply system receives compressed air at ambient temperature from the laboratory's 400 psi compressor facility. The air is regulated and the flow to the vessel and model is measured by two turbine flow meters. All of the flow going to the vessel and model is returned from the facility and is measured by two additional flow meters before being exhausted into the atmosphere. The air supply system provided a flow rate of up to 1 lb/s to the test model.

Each of the independently operated drive systems consisted of a 30-hp, d-c motor, a belt-driven drive shaft with air-cooled, high-speed bearing assemblies, drive pulleys, and a motor control station. The motors could be driven in either direction.

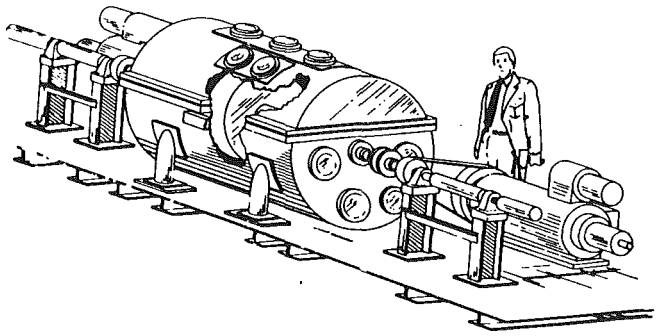

Fig. 4 Internal air systems facility

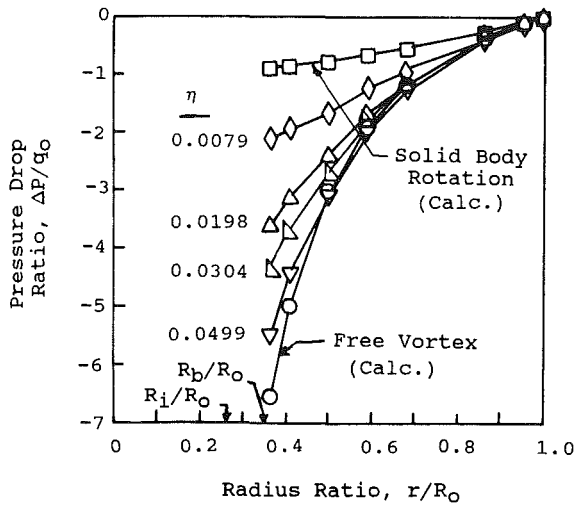

Fig. 5 Variation of measured pressure drop in cavity 2 with radius for selected flow conditions and coolant injection; Configuration A: $Re_\theta = 4 \times 10^6$

Facility instrumentation includes a data acquisition and control unit, flow and pressure measuring equipment, vibration sensors, safety circuits, slipring assemblies, and computers.

Compressor Drum Assembly

A compressor drum model was designed and built to conduct the compressor drum aerodynamic and heat transfer experiments. The model cross section is shown in Fig. 2. The model contains six cavities with tapered endwalls and compressor disk geometries. An independently driven bore tube simulated corotating and counterrotating bore tube designs. The bore tube was corotating at the drum rpm for all experiments described herein. The maximum design speed of the model is 2000 rpm. The compressor drum model has an overall length of 27.5 in. and a drum cavity and disk rim diameter of 22 in. The disk bore diameter is 8 in. and the bore tube has a diameter of 6 in. The upstream and downstream conical endwalls are tapered at included angles of 120 deg and 60 deg, respectively.

Coolant flow is injected into the model at several locations. Three injection locations are available on the 120-deg conical endwall for simulating coolant flow from a low-pressure compressor (LPC) into the high-pressure compressor (HPC) disk cavity. Each of the locations contain eight equally spaced bleed ports at 6, 5, and 4 in. radii, respectively. Locations B and C at radii of 6 and 4 in., respectively, are noted on Fig. 2. Injection of coolant from the high-pressure compressor gas path is modeled by injecting air through passage located at the o.d. of the cavity between disk 2 and 3 and is shown as coolant injection location A. The injectors at each coolant injection location are supplied air from a manifold attached to the 120-deg conical endwall. The manifold rotates with the model and is supplied by a stationary-to-rotating frame air transfer system that is incorporated in the bearing housing of the model. All coolant is exhausted from the model through 18 equally spaced holes located on the 60-deg conical endwall at a radius of 3.5 in.

Table 1 Flow parameters for tests with injection: Configuration A

	Dimensional Parameters					Dimensionless Parameters		
	Ω	P	m	T_o	V_j	$Re_\theta/10^6$	Re_z	η
Test	rpm	psia	lb/sec	°F	ft/sec			
A1	1500	142.9	0.495	78	30	7.6	6948	0.0216
A2	1500	142.1	0.180	88	11	7.3	2491	0.0080
A3	1500	147.7	0.740	72	43	8.1	10477	0.0312
A4	2000	60.7	0.234	76	34	4.3	3294	0.0161
A5	2000	58.5	0.110	87	16	4.0	1524	0.0079
A6	2000	63.6	0.465	67	65	4.7	6632	0.0304
A7	2000	62.8	0.620	67	90	4.7	8843	0.0410
A8	2000	64.2	0.766	70	112	4.7	10877	0.0499
A9	1000	59.2	0.794	69	113	2.2	11291	0.0959
A10	2000	60.9	0.290	73	42	4.4	4100	0.0198

The compressor drum model was instrumented with 68 static pressure taps (including 16 on the bore tube). Pressure taps were located at seven radii on one disk wall of each cavity, the drum o.d., and the bore i.d. of each disk. The pressure measurements were made in the rotating frame of reference using a 48-port Model 48J4-1 Scanivalve assembly and a ±25-psid Scanivalve pressure transducer mounted on the rotational centerline at each end of the drive systems. The local pressure at each radius was determined from the pressure measurements and the calculation of the pressure difference from $r=0$ assuming compressible constant temperature air in the tubing. Calibration of the pressure transducer with a dead weight tester before and after the investigation showed the transducer to be repeatable and accurate to within 0.04 psi. The electrical noise through the slipring increased the uncertainty of a particular measurement to 0.1 psi.

Typical Experimental Pressure Distributions in Cavity 2

Disk radial pressure measurements were obtained in Cavity 2 for the A bleed configuration and for a range of radial and tangential Reynolds numbers. The dimensional and dimensionless flow parameters for test with injection Configuration A are presented in Table 1. The results for a range of coolant flow parameters at one tangential Reynolds number are shown in Fig. 5 as the dimensionless pressure drop versus the dimensionless radius ratio. As the coolant flow rate m and therefore η is increased, the pressure drop profile in the bleed cavity approaches that of a free vortex. Increasing the flow rate increases the swirl level in the bleed cavity up to free vortex levels. The pressure drops for a solid body rotation flow ($V_\varphi \sim r$) and free vortex flow ($V_\varphi \sim r^{-1}$) are shown for comparison. The pressure drop ratios for all results presented herein are relative to the dynamic head of the fluid at the o.d. of the cavity.

Predicted Core Flow and Secondary Flow Characteristics for Cavity 2

The core (primary flow) and disk boundary layer (secondary flow) characteristics for flow between corotating disks were predicted using the analysis and assumptions outlined in the appendix. The characteristics predicted for five experimental flow conditions (including the four presented in Fig. 5) are presented in Fig. 6. These calculations were made for flow in Cavity 2 with the experimental flow conditions as boundary conditions (Table 1). The analytical model assumed the coolant

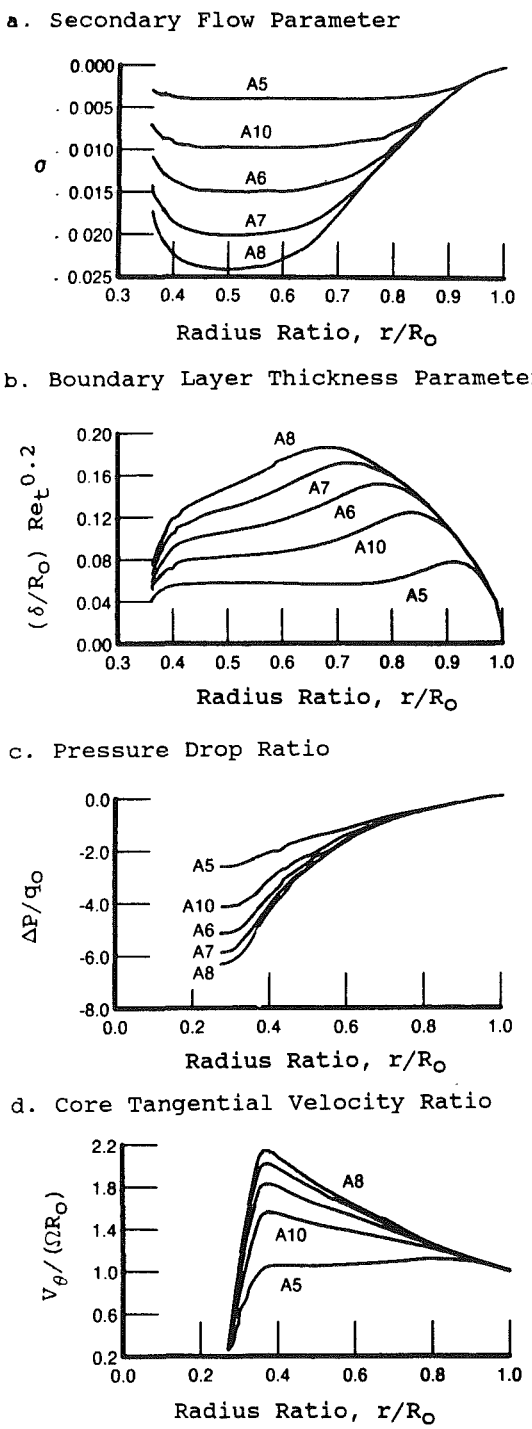

Fig. 6 Predicted primary and secondary flow in cavity 2 for injection Configuration A and constant velocity model: $\mu_{eff} = V_{ro}\,\rho_o R_o/200$

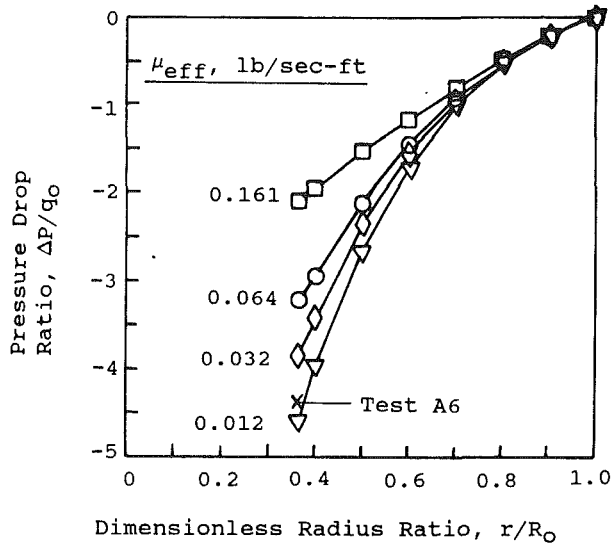

Fig. 7 Effect of core turbulent viscosity on predicted variation of pressure drop with radial location, test No. A6: $Re_t = 4.7 \times 10^6$; $Re_z = 3300$; $\eta = 0.0153$

core flow was only a function of radius. In the experiments, the coolant flow was injected through eight holes at location A (Fig. 2) as described. The core effective viscosity was assumed to be constant for a specific flow condition but was varied for each flow condition in a manner to be discussed.

The secondary flow parameter σ (Fig. 6*a*) is the dimensionless flow in one of the disk boundary layers. Thus, the maximum flow in one of the boundary layers is approximately $m/2$. When all the flow is in the boundary layers (i.e., $U_r = 0$), then $2\sigma = \eta$. Note that for flow conditions A5, A10, and A6, essentially all the flow is predicted to be in the disk boundary for a range of radius ratios from 0.45 to 0.65. Note also that a portion of the boundary layer flow is predicted to re-enter the core region before the bore radii. Although these predictions are a result of the assumptions in the coupling of the momentum integral equations and the core flow viscous flow solution, the same characteristics have been predicted by other analyses of swirling flow, e.g. Lewellen (1971), and have been observed for flows in vortex tubes, e.g., Travers and Johnson (1966) and Travers (1968).

The boundary layer thickness (Fig. 6*b*) is predicted to increase to a maximum thickness for all flow conditions and then decrease. Note that the solutions for all four parameters and ratios presented in Fig. 6 are identical near the o.d. wall. The pressure drop ratio and the velocity ratio vary as expected. Increasing the coolant flow (i.e., η) results in a larger tangential velocity ratio, $V_\theta/\Omega R_o$, thereby increasing the pressure drop.

Effects of Core Turbulent Viscosity

The effective core turbulent viscosity was varied in a parametric study to deduce an "ad hoc" turbulent viscosity relationship for the coolant injection at location A and for the range of flow conditions tested. The analysis was performed for a range of assumed constant core effective viscosities. The effect of core turbulent viscosity on the pressure distribution in Cavity 2 for flow condition A6 is shown in Fig. 7. Note that the measured pressure drop (marked with an *x*) is close to that which would be predicted for an effective core viscosity of 0.015 lb/sec-ft.

The effects of core turbulent viscosity on the predicted pressure drop across the cavity for five flow conditions are shown in Fig. 8. Note that as the core effective viscosity is increased, the pressure drop is lessened (in concert with the decreased tangential velocity). Note also from Fig. 7 that most of the variations, due to assumed core viscosity, occur at radii slightly larger than the disk bore radius, $R_b/R_o = 0.364$. The core flow effective radial Reynolds numbers at the disk o.d. are cross plotted on Fig. 8, $Re_{r,eff} = m/(2\pi\mu_{eff}\,L)$. From a comparison of the result from the experiments and the parametric study, it was determined that the selection of $Re_{r,eff} = 200$ produced the best predictions by the analysis. Thus $\mu_{eff} = m/(2\pi L)/200 = \rho_o V_{r,o} R_o/200$ was chosen as the "ad hoc" viscosity model for coolant injection configuration A and Cavity 2. The turbulent viscosity model, previously used by Alberga et al. (1987) for predictions in an eleven-cavity model with $R_b/R_o = 0.5$, was unsatisfactory because the pressure drops were consistently less than measured. The effective core viscosity model is com-

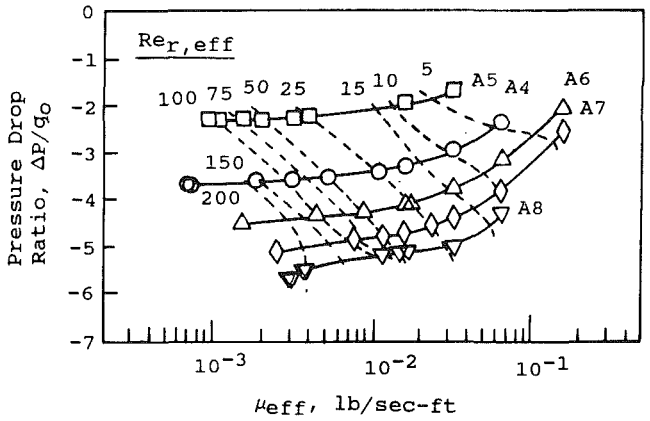

Fig. 8 Effect of core (- - - -) conditions: A4—η = 0.0161; A5—η = 0.0079; A6—η = 0.0304; A7—η = 0.0410; A8—η = 0.0499

a) Radial Pressure Distribution

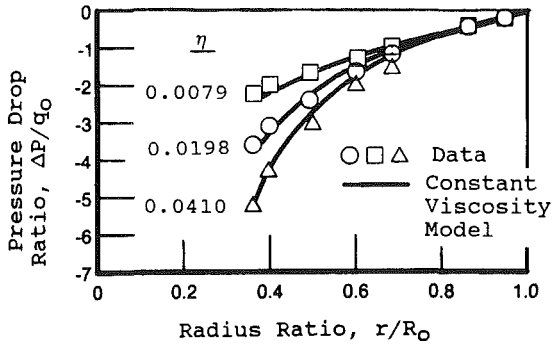

b) Pressure Drop From Bleed to Bore

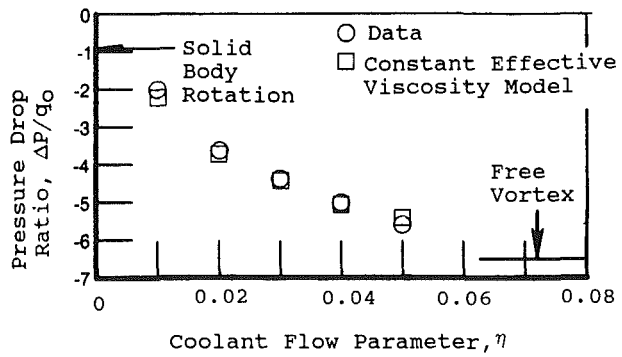

Fig. 9 Comparison of predicted and measured pressure distribution in cavity 2 for injection configuration A and constant viscosity model: $\mu_{eff} = \rho_o U_{r,o} R_o / 200$

patible with previous vortex tube experiments (Travers, 1968; Travers and Johnson, 1966), where the turbulent fluctuations in the core decreased significantly as the radial flow rate decreased.

Comparison of Predicted and Measured Pressure Drop for Cavity 2

The variation of pressure drop ratio $\Delta P/q_o$ across the cavity with the dimensionless flow parameter is shown in Fig. 9. Note that the limits on the pressure drop ratio for this configuration with coolant injected at the drum o.d., a radius ratio (R_b/R_o) equal to 0.364 and almost constant density fluid in the core are $\Delta P/q_o = 0.868$ for no coolant flow with solid body rotation and $\Delta P/q_o = 6.55$ for a free vortex with constant angular momentum in the core region from the o.d. to the core radius (Fig. 9*b*). Note that data lie in the allowed range and approach the limits as expected. Note also that the measured pressure drops are slightly less and more than predicted for the lowest and highest coolant flow conditions, respectively. Using the results of Fig. 9, it could be concluded that the core viscosity is higher than assumed for the lowest flow rate and higher than assumed for the highest flow rate. In spite of these small differences, the relationship of $\mu_{eff} = m/(200\ 2\pi L)$ appears to be appropriate for this configuration. Flow visualization studies of swirling flows in vortex tubes (Travers, 1968, and others), have shown that the scale and intensity of the radial velocity fluctuations in the core region vary in a manner compatible with the aforementioned assumption, i.e., decreasing fluctuations as the flow is decreased.

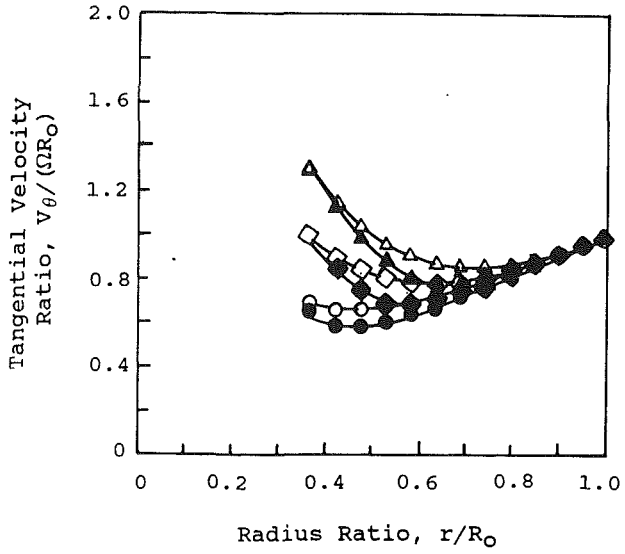

Fig. 10 Predicted tangential velocity distribution in trapped cavity for two core viscosity models: solid symbols, $\mu_{eff} = 3.2 \times 10^{-3}$ lb/ft-sec; open symbols, $\mu_{eff} = +0.002 \rho r V_\theta (R_o/r - 1)^2$

Predicted Flow Characteristics in Trapped Cavities

The core and secondary flow characteristics of trapped rotating annular cavities were predicted for the same flow conditions used to predict those in Cavity 2 except that no mass flow was added at the i.d. or o.d. of the cavity and the inner cylinder tangential velocity was varied. For these calculations, the bore tube or inner cylinder was located at a radius ratio of approximately 0.35. The core and flow boundary layer characteristics were determined for radii from the bore radius to the drum o.d. using the calculation procedure outlined in the appendix. The predictions were made using both a constant turbulent viscosity model and a core viscosity model presented by Alberga et al. (1987). Velocity distributions between the bore radius and the drum o.d. are presented in Fig. 10 for a constant turbulent viscosity of 3.2×10 lb/ft-sec (a value of approximately 250 times the dynamic viscosity of air at the test conditions). Note that the predicted tangential velocity distributions can be approximated as a free vortex from the bore radius until the free vortex approaches the solid body rotation at the local disk radius. There is a transitional region as the velocity profile transists to the solid body profile. A comparison of the tangential velocity profiles obtained for the constant turbulent viscosity condition and the turbulent viscosity, $\mu_{eff} = \mu_m + K\rho V_\theta r (R_o/r - 1)^2$, where $K = 0.002$ is also shown in Fig. 10 for inner bore velocity ratios approximately

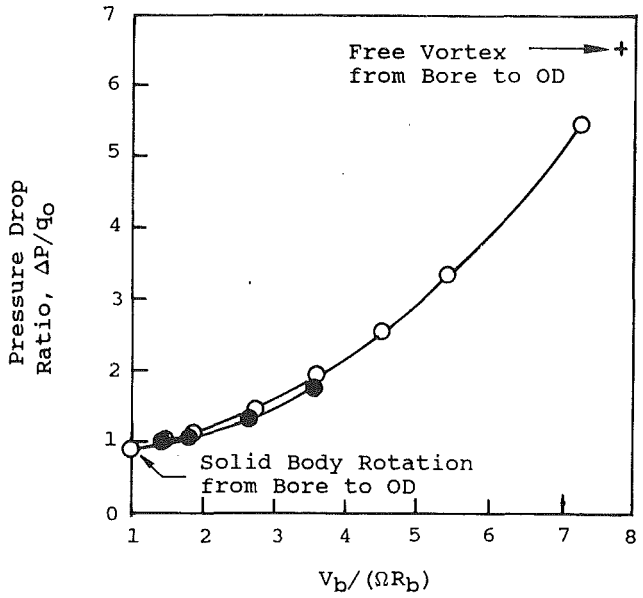

Fig. 11 Predicted pressure drop in trapped cavity with bore velocity ratio for two core viscosity models: solid symbols, $\mu_{eff} = 3.2 \times 10^{-3}$ lb/ft-sec; open symbols, $\mu_{eff} = +0.002\rho r V_\theta (R_o/r - 1)^2$

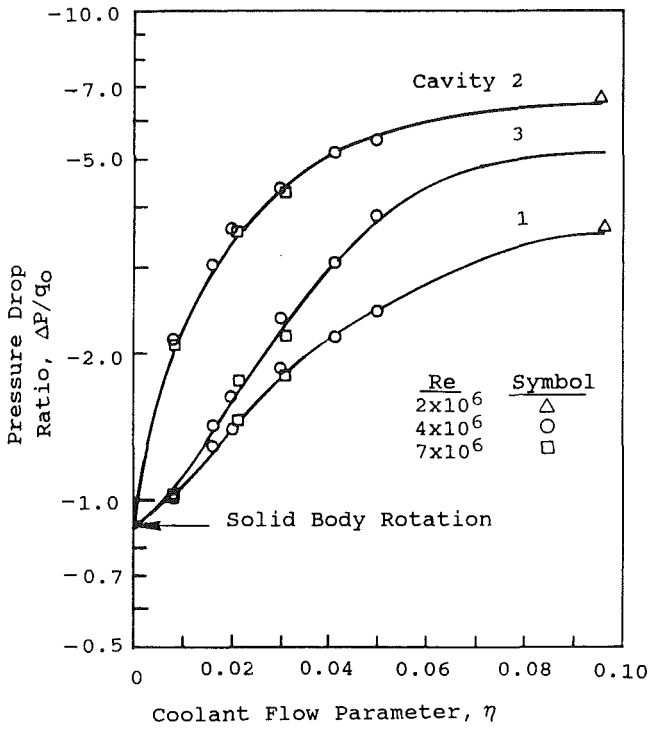

Fig. 12 Effect of coolant flow parameter on pressure drop ratio in bleed and trapped cavities for injection Configuration A

the same as the constant effective viscosity case. The tangential velocity profiles are determined by the effective core radial Reynolds number. Note that the velocity profiles for variable turbulent viscosity are higher than those for the lower constant turbulent viscosity. The lower effective radial Reynolds number with the higher viscosity has less of a tendency to "free vortex" outward than the lower viscosity case.

The predicted pressure drop, from the drum o.d. to the bore radius, is presented in Fig. 11 as the variation of $\Delta P/q_o$ with $V_{\theta,b}/\Omega R_b$, the ratio of the core flow tangential velocity to the disk tangential velocity at the bore. Predictions are presented

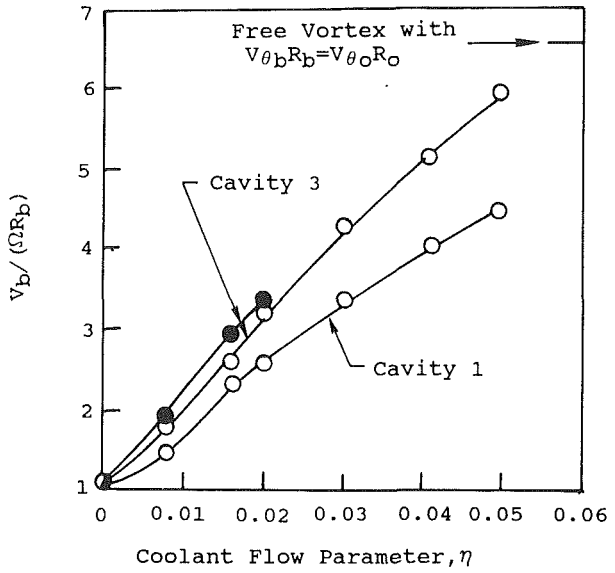

Fig. 13 Estimated values of $V_b/(\Omega R_b)$ at bores of trapped cavities for injection Configuration A; solid symbols, $\mu_{eff} = 3.2 \times 10^{-3}$ lb/ft-sec; open symbols, $\mu_{eff} = +0.002\rho r V_\theta (R_o/r - 1)^2$

for both viscosity models. These results will be used to estimate the variation of the bore velocity ratio with distance from the injection location and coolant flow rate.

Results for Trapped Cavities With Coolant Injection: Configuration A

The pressure drops across the injection cavity (Cavity 2), Cavity 1, and Cavity 3 are presented in Fig. 12 for a number of coolant flow rates, drum rotation rates, and pressures. The results are presented as the variation of pressure drop ratio ($\Delta P/q_o$) with the coolant flow parameter (η). The pressure drop ratios across the bleed cavity are the same as shown in Fig. 9. Although Cavity 1 and Cavity 3 are adjacent to Cavity 2 (the coolant injection location), the pressure drop across Cavity 3 is always greater than Cavity 1. This is believed to be caused by the preference of the fluid with a relatively high angular momentum to flow directly toward the coolant exit location rather than to proceed upstream and then double back to the coolant exit location. Previous experience with vortex tubes at UTRC and elsewhere, e.g., Lewellen (1971), showed that complex stream tubes can be formed in the exit radius regions of swirling flows.

The pressure drop measurements (Fig. 12) and the predicted pressure drops in trapped cavities (Fig. 11) are combined to obtain an estimate of core velocity ratio, $V_{\phi b}/(\Omega R_b)$, as a function of coolant flow parameter, η, and cavity location (Fig. 13). Additional effort will be required to obtain an angular momentum balance on the flows in the trapped cavities.

Results for Trapped Cavities With Coolant Injection: Configuration B

The pressure drops across Cavities 1, 2, and 4 with coolant injected at the B location (see Fig. 2 for model geometry) are presented (Fig. 14) as a variation of pressure drop ratio ($\Delta P/q_o$) with coolant flow parameter (η). Note that the pressure drop ratio increases with coolant flow ratio and decreases with distance from the injection location, as expected. The dimensional and dimensionless flow parameters for tests with injection Configuration B are presented in Table 2.

The measured pressure drop ratios (Fig. 14) and the predicted bore velocity ratio pressure drop relationship (Fig. 11) are again used to estimate the ratio of the core flow tangential velocity to the tangential velocity of the disk at the bore radius (Fig.

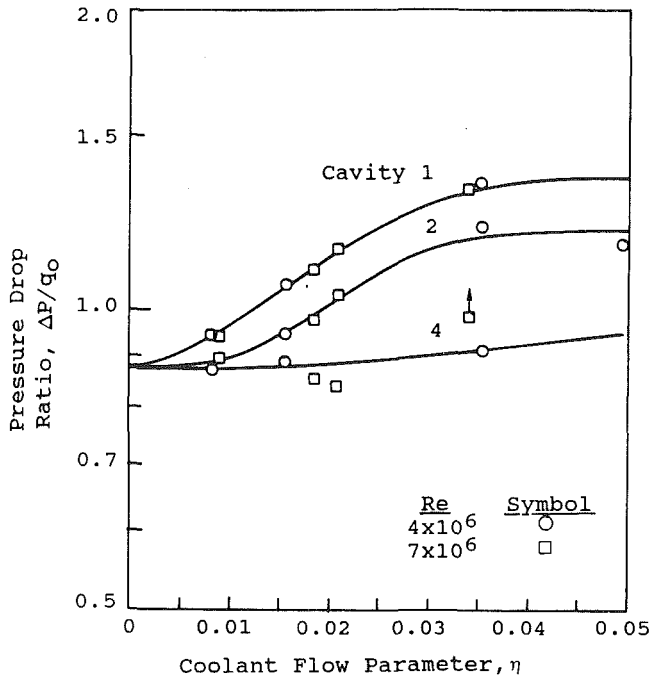

Fig. 14 Effect of coolant flow parameter on pressure drop ratio in trapped cavities

15). Note first that the ratios of the velocities are between 1 and 2.6, compared to the values of up to 3.5 to 4.5 obtained in cavities 1 and 3 for Injection Configuration A over the same coolant flow parameter range. These lower velocity ratios are expected because the coolant is injected with lower angular momentum at $R_i = 6$ in. for Configuration B compared to $R_j = 11$ in. for Configuration A. The maximum velocity ratio, $V_b/(\Omega R_b)$, expected for flow injected at Configuration B is 2.25. This velocity ratio is that obtained for conservation of injected angular momentum at a radius of 6.0 in. The estimated values of $V_b/(\Omega R_b)$ greater than 2.25 are attributed to the increase of angular momentum in Cavity A as the flow from the jets at a radius of 6 in. interacts with the rotating disks at radii greater than 6 in. and is accelerated.

The velocity ratio, $V_b/(\Omega R_b)$, decreases monotonically with distance from the injection location and increases with coolant flow parameter, η_c. However, the maximum velocity ratio is not expected significantly to exceed the value of 2.25 as discussed in the previous paragraph. For Cavity 1, the estimated value of $V_b/(\Omega R_b)$ shown on Fig. 15 for the variable turbulent viscosity model is likely to be more appropriate because of the high turbulence levels near the coolant injection location. For Cavity 4, the estimated values of $V_b/(\Omega R_b)$ are approximately the same for both core region turbulence models. Note that decrease in velocity ratio between cavity 2 and cavity 4 is greater than that between cavities 1 and 2 except for the lowest coolant flow rate.

Summary

1 The pressure distributions with the compressor drum model show that the angular momentum of the flow inside the drum cavity decreases with distance from the coolant injection location. Pressure drop distributions were quantified for two coolant injection configurations and a range of coolant flow parameters.

2 An analytical study showed the effects of core region viscosity on the core region tangential velocity distribution and hence pressure drop for rotating cavities with net flow radially inward and with zero net flow, i.e., trapped cavities. The effects of core viscosity on the tangential velocity distributions were greatest near the disk core radius.

Table 2 Flow parameters for tests with injection Configuration B

	Dimensional Parameters					Dimensionless Parameters		
	Ω	P	m	T_o	V_j	$Re_\theta/10^6$	Re_z	η
Test	rpm	psia	lb/sec	°F	ft/sec			
B1	1500	138.6	0.467	74	28	7.5	6593	0.0208
B2	1500	137.4	0.200	74	12	7.5	2824	0.0090
B3	1500	139.7	0.759	82	45	7.4	10593	0.0339
B4	1500	138.8	0.405	88	24	7.2	5605	0.0183
B5	2000	59.0	0.220	86	31	4.1	3053	0.0156
B6	2000	58.2	0.114	94	17	4.0	1565	0.0083
B7	2000	58.1	0.494	77	72	4.2	6944	0.0351
B8	2000	57.5	0.688	72	101	4.2	9741	0.0491
B9	1000	55.6	0.364	75	53	2.0	5131	0.0466

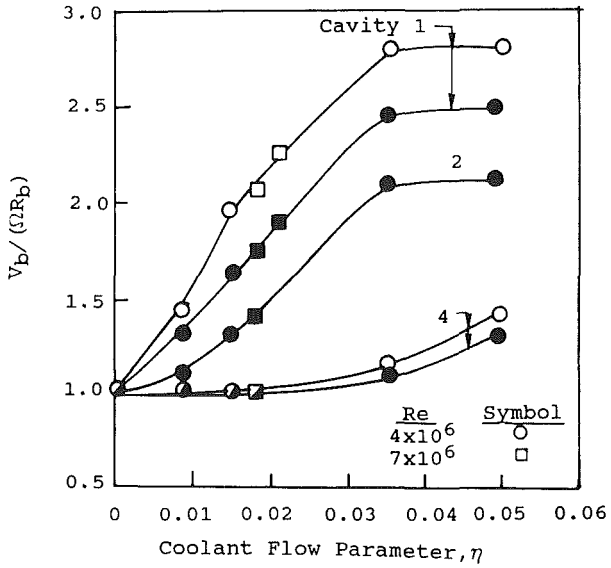

Fig. 15 Estimated values of $V_b/(\Omega R_b)$ at bores of trapped cavities for injection Configuration B; solid symbols, $\mu_{eff} = 3.2 \times 10^{-3}$ lb/ft-sec; open symbols, $\mu_{eff} = +0.002\rho r V_\theta (R_o/r - 1)^2$

3 The pressure drop ratios across cavities with zero net flow, i.e., trapped cavities, or with coolant flowing radially inward were well correlated by the coolant flow parameter, η.

4 A method was developed for estimating the tangential velocity distribution in trapped rotating cavities from the pressure drop between the disk o.d. and the disk bore. A parametric study showed that the pressure drop across the cavities was relatively insensitive to the assumed core viscosity distribution.

Acknowledgments

This work published in this paper was supported by the Aero Propulsion Laboratory, Air Force Wright Aeronautical Laboratories under Contract No. F33615-83-C-2331 to the Pratt & Whitney Government Products Division and by United Technologies Corporation under their independent research program. The computer code, used in the analyses, was developed by Dr. Olof L. Anderson (UTRC) and operated by Ms. S. L. Orr (UTRC).

References

Alberga, D. G., Stephens, G. E., and Johnson, B. V., 1987, "Comparison of Predicted and Measured Velocities in a Compressor Disk Drum Model," ASME Paper No. 87-GT-208.

Anderson, O. L., 1963, "Theoretical Effect of Mach Number and Temperature Gradient on Primary and Secondary Flow in a Jet Driven Vortex," Air Force Systems Command Report RTD-TDR-63-1098.

Bennett, J. C., 1974, "LDV Measurements in a Model Compressor Disk Cavity," *Proceedings of Second International Workshop on Laser Velocimetry*, Purdue University, W. Lafayette, IN.

Dorfman, L. A., 1963, *Hydrodynamic Resistance and the Heat Loss of Rotating Solids*, Oliver & Boyd, London.

Gosman, A. D., et al., 1976, "Transfer of Heat in Rotating Systems," ASME Paper No. 76-GT-25.

Graber, D. J., Daniels, W. A., and Johnson, B. V., 1987, "Disk Pumping Test," Final Report to Wright-Patterson Air Force Bae, OH, Report AFWAL-TR-87, 2050.

Lewellen, W. S., 1971, "A Review of Confined Vortex Flows," NASA Contractor Report CR-1772.

Owen, J. M., and Pincombe, J. R., 1979, "Vortex Breakdown in a Rotating Cylindrical Cavity," *J. Fluid Mech.*, Vol. 90, pp. 109–127.

Owen, J. M., Pincombe, J. R., and Rogers, R. H., 1985, "Source-Sink Flow Inside a Rotating Cylindrical Cavity," *J. Fluid Mech.*, Vol. 155, pp. 233–265.

Owen, J. M., and Rogers, R. H., 1989, *Flow and Heat Transfer in Rotating-Disc Systems, Vol. 1—Rotor-Stator Systems*, Wiley, New York.

Schlichting, H., 1968, *Boundary Layer Theory*, 6th ed., McGraw-Hill, New York, pp. 606–610.

Travers, A., 1968, "Experimental Investigation of Flow Patterns in Radial-Outflow Vortexes Using Rotating Peripheral Wall Water Vortex Tube," NASA CR991.

Travers, A., and Johnson, B. V., 1966, "Measurements at Flow Characteristics in a Basic Vortex Tube," NASA CR278.

Yu, J. P., Sparrow, E. M., and Eckert, E. R. G., 1973, "Experiments on a Shrouded, Parallel Disk System With Rotation and Coolant Throughflow," *Int. J. Heat Mass Transfer*, Vol. 16, pp. 311–328.

APPENDIX

Momentum integral analysis of the disk boundary layer flows coupled with a one-dimensional viscous analysis of the flow in the core regions of cavities have been used for over 30 years to analyze swirling flows in cavities. An excellent summary of the work to 1970 was presented by Lewellen (1971). A computer code for rotating flow with stationary walls, available at UTRC since 1960 (Anderson, 1963), was modified for use with rotating disks. Following is the description of the flow characteristics in the mathematical models contained in the code.

Although the flow in the bleed cavity is rather complex, previous investigations, e.g., Lewellen (1971), have shown that the flow can be divided into two principal regions: (1) a core flow with low radial velocities and tangential velocities, which are primarily functions of the radius, and (2) a turbulent boundary layer flow along the disk walls, which can have radial velocities on the same order of magnitude as the tangential velocities. These two regions can be highly interactive with flow into and out of the boundary layer depending upon the angular momentum and radial pressure balances in these two regions. The analytical formulation developed couples the flow in the core region with the disk boundary layer flows. The analysis combines a momentum integral analysis for the boundary layer flows, a one-dimensional viscous solution for the core flow, and a turbulent viscosity model. Since high pressure compressor drums operate at Reynolds numbers of 10^6 to 10^7, the flow in the bleed cavities is turbulent and therefore only turbulent models are used in the secondary flow analysis and for the core flow viscosity.

The analytical formulation is based on the following assumptions: (1) The flow is axisymmetric and time independent, (2) the radial velocities are independent of axial location in the core region, (3) the fluid density can be constant or can vary with the perfect gas law, and (4) the core fluid has a viscosity, μ_{eff}, which is assumed to be constant at all radii or which can be specified in terms of the core flow variables.

The core flow tangential momentum equation is (with nomenclature defined for this appendix)

$$\rho V_r \left(\frac{dV_\theta}{dr}+\frac{V_\theta}{r}\right)=\bar{\mu}\frac{d}{dr}\left[\frac{1}{r}\frac{d}{dr}(rV_\theta)\right] \tag{A1}$$

with solution

$$V_\theta = C_1 r^{\alpha-1}+C_2 r \tag{A2}$$

if a constant radial mass flow is assumed. Here,

$$\alpha = m_c/2\pi L\mu_{\text{eff}} \tag{A3}$$

where m_c = core radial flow rate; L = distance between the disks; C_1 and C_2 = constants.

The solution given by equation (A2) can be assumed for small radial domains (Δr) in which the local radial mass flow m_c is assumed to be constant. The solution for V_θ at the boundary of adjacent domains can be matched to obtain a piecewise continuous function for V_θ over values of the radius from the bore to the rim.. This results in a solution for C_1 and C_2 in each radial domain based on the domain inlet V_θ and the domain outlet V_θ. The error in assuming a constant radial core flow in each domain is small for small radial domains.

The core flow pressure gradient is obtained from the radial momentum equation. Assuming a constant core flow rate for each radial domain, the pressure gradient is given by

$$dP/dr = \rho V_\theta^2/r \tag{A4}$$

Here, the fluid density can be assumed to be constant or can be assumed to vary with the percent gas law.

The disk boundary layer tangential and radial momentum equations are given by

$$\frac{\partial}{\partial r}(rU_rU_\theta)+\frac{\partial}{\partial z}(rU_zU_\theta)=\nu r^2\frac{\partial^2 U_\theta}{\partial z^2} \tag{A5}$$

$$\frac{\partial}{\partial r}(rU_r^2)+\frac{\partial}{\partial z}(rU_rU_z)-U_\theta^2=-\frac{r}{\rho}\frac{\partial p}{\partial r}+\nu r\frac{\partial^2 U_r}{\partial z^2} \tag{A6}$$

Here, U is the velocity of the fluid in the boundary layer with r, θ, and z denoting the radial, tangential, and axial components, respectively.

The integral forms of these boundary layer equations are obtained by integrating from the disk wall ($z=0$) to edge of the boundary layer ($z=\delta$), which gives

$$\frac{d}{dr}\int_0^\delta (rU_rU_\theta)\,dz+V_\theta\frac{d}{dr}\int_0^\delta (rU_r)\,dz=\nu r^2\frac{dU_\theta}{dz}\Big|_0^\delta \tag{A7}$$

$$\frac{d}{dr}\int_0^\delta (rU_z^2)dz+\int_0^\delta (V_\theta^2-U_\theta^2)dz=\nu r\frac{dUr}{dz}\Big|_0^\delta \tag{A8}$$

The boundary layer radial and tangential velocity profiles are assumed to be given by

$$U_r(z/\delta)=\bar{U}_r\left(\frac{56}{13}\right)\left[\left(\frac{z}{\delta}\right)^{1/7}-\left(\frac{13}{7}\right)\left(\frac{z}{\delta}\right)+\left(\frac{6}{7}\right)\left(\frac{z}{\delta}\right)^2\right] \tag{A9}$$

and

$$U_\theta(z/\delta)=r\Omega+(V_\theta-r\Omega)+(z/\delta)^{1/7} \tag{A10}$$

The tangential velocity profile given by equation (A10) is similar to the 1/7th power law turbulent profile used by von Karman (Schlichting, 1968). The radial velocity profile given by equation (A9) also has a 1/7th power profile near the wall. The shape of the radial velocity profile in equation (A9) for the outer region of the boundary layer was first used by Anderson (1963). This profile shape is modestly different from that used by von Karman for secondary flow radially outward on rotating disks but was a closer approximation to the velocity profiles measured on vortex tube end walls for secondary flow radially inward.

In equation (A9), the quantity $\bar{U}_r$ is the average radial velocity in the boundary layer at radius r. The boundary layer flow and the core flow can be coupled in each of the radial domains (Δr) through the continuity equation given by

$$m_c = m_t - 2m_s \tag{A11}$$

where m_t is the total flow rate bled into the cavity. A solution is obtained when the mass balance in each radial domain has converged to a prescribed tolerance.

M. Inoue

M. Kuroumaru

T. Iwamoto

Y. Ando

Department of Mechanical Engineering
for Power,
Kyushu University,
Fukuoka, Japan

Detection of a Rotating Stall Precursor in Isolated Axial Flow Compressor Rotors

Statistical characteristics of pressure fluctuation on the casing wall of two axial flow compressor rotors have been investigated experimentally to find a precursor of rotating stall. Near stall, the casing wall pressure across a flow passage near the leading edge is characterized by a highly unsteady region where low-momentum fluid accumulates. The periodicity of the pressure fluctuation with blade spacing disappears and an alternative phenomenon comes into existence, which supports the disturbance propagating at a different speed from the rotor revolution. The precursor of rotating stall can be detected by monitoring collapse of the periodicity in the pressure fluctuation. To represent the periodicity qualitatively, a practical detection parameter has been proposed, which is easily obtained from signals of a single pressure sensor installed at an appropriate position on the casing wall during operation of a compressor.

Introduction

In aerodynamic research on axial flow compressors, an area of current interest is active control of stall and surge: aerodynamic instability suppression by application of an appropriate control action when rotating stall inception is imminent (Greitzer, 1987; Dugundji et al., 1989). Recognition of the rotating stall inception and suppression of the instability are major problems for implementing active control. Elucidating the mechanism for rotating stall inception is a key to its success.

After the classical explanation of rotating stall inception by Emmons et al. (1955), many theoretical and semi-empirical approaches have been made to predict a stall point or onset of instability. Although the onset of instability cannot be predicted accurately, there has been significant progress in the approaches. They include analyses based on blade row characteristics with nonlinear effect of time lag (Takata and Nagano, 1972), the concept of an equivalent diffuser (Koch, 1981; Zika, 1985) and the pressure rise versus flow rate characteristics of a compressor system (Greitzer, 1976; Stenning, 1980; Moore, 1984).

However, very little experimental work has been reported on the inception and development of the stall cell, while the details of fully developed stall cell have been the subject of many studies. Mathioudakis and Breugelmans (1985) reported the simultaneous existence of disturbances of different wavelength rotating at 82 to 86 percent of the rotor speed in the development of small rotating stall cells. Jackson (1987) observed the rotating speed and size of a developing stall cell by fixing the cell inception to a restaggered blade: A small cell initially traveled at near rotor speed and decelerated rapidly as it grew in size. According to the recent work by McDougall et al. (1990), prior to stall, disturbances rotated in concert with rotating variations in the endwall blockage at a speed similar to the fully developed stall cell speed. Garnier (1991) found small-amplitude disturbance waves propagating around the annulus, which can grow into the rotating stall. Many more experimental studies are desired to elucidate the mechanism of inception.

The purpose of this study was to recognize the precursor of rotating stall. Generally, the stall inception can be detected as a small cell whose wave shape is obtained from a low pass filtering signal of a hot wire or a high-frequency response pressure sensor. However, it is difficult to avoid stall when a control action is undertaken upon recognition of the small cell, because in many cases the small cell grows rapidly within a few revolutions of the rotor and sometimes precipitates surge. Once the stall cell is fully developed it takes considerable time to recover the operating conditions because of a hysteresis in the pressure rise–flow rate characteristics. Therefore, it is necessary to identify events occurring prior to the stall cell growth phase.

For this purpose, the experimental results of McDougall et al. (1989) are encouraging, because they show the existence of a low-order mode of disturbance for a considerable time prior to stall. This fact suggests the possibility of detection by high-frequency-response pressure sensors installed on the casing wall, which is more practical than the use of hot wires in the active control system.

In this study, the nature of the pressure fluctuation on the casing wall is investigated to find a rotating stall precursor. Two kinds of rotor with various tip clearances are tested. Static pressures on the casing wall are measured by a phase-locked data acquisition technique with high-frequency-response pressure sensors, and distributions of the mean pressure and the

Contributed by the International Gas Turbine Institute and presented at the 35th International Gas Turbine and Aeroengine Congress and Exposition, Brussels, Belgium, June 11–14, 1990. Manuscript received by the International Gas Turbine Institute February 7, 1990. Paper No. 90-GT-157.

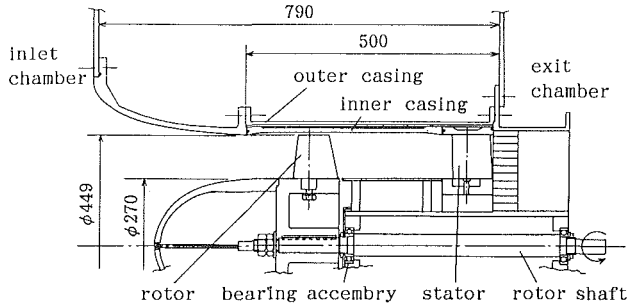

Fig. 1 Cross section of test facility

statistical values of the pressure fluctuation are obtained for various flow rates. Statistical processing is necessary to distinguish a substantial phenomenon from noisy data near stall condition. The data just before the rotating stall are obtained by a newly devised pretrigger data acquisition system, in which a sign of the stall inception is taken as a trigger and a required number of the data before the trigger are acquired in a microcomputer. The variations with flow rate in phase-locked patterns of mean, standard deviation, skewness, and pseudo-spatial correlation of the pressure fluctuation are discussed, and a detection parameter for the rotating stall precursor is presented.

Facility, Instrumentation, and Measurement

The experimental investigation was carried out in the low-speed rotating cascade facility described by Inoue et al. (1986). A cross section of the facility is shown in Fig. 1. Two rotors A and B with hub/tip ratios of 0.6, which were designed for free vortex flow with an axial inlet condition, have the same blade profile at the tip section but different solidity. The solidities at midspan are 1.25 and 1.67 for rotor A and B, respectively. For each rotor the tip clearance can be varied from $\tau = 0.5$ mm to 5 mm by changing the diameter of the casing wall. Details of the geometry and blading are given in the previous paper (Inoue and Kuroumaru, 1989).

The overall performances for both the rotors are shown in Figs. 2(*a*) and 2(*b*). The flow rate at which the rotor stalls is the minimum at a tip clearance of 1.0 mm (0.85 percent of chord length l_t) in the case of low solidity, while it increases with tip clearance in the case of high solidity. This reason is associated with the accumulation of low-energy fluid near the casing wall as will be presented by Inoue et al. (1990). In all cases, stall inception occurs at the tip. This was seen by examination of the kinetic energy defect behind the rotor as measured by a hot-wire anemometer using a periodic multi-sampling and averaging technique (Kuroumaru et al., 1982). The kinetic energy defect was defined as the difference of relative kinetic energy between the measured and the reference

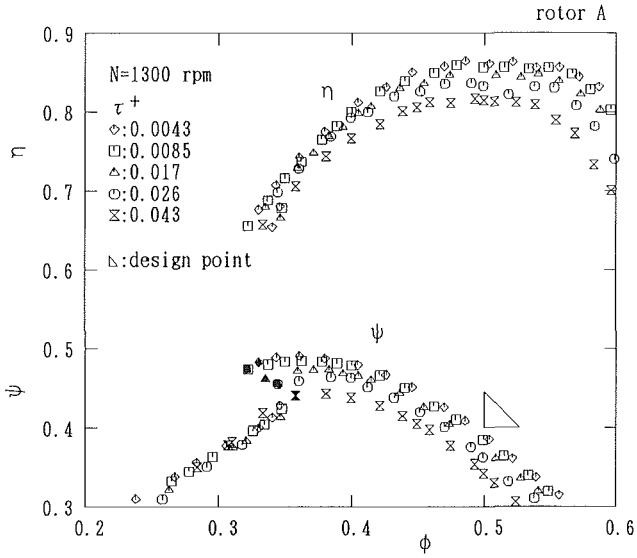

Fig. 2(*a*) Stage performance of rotor A

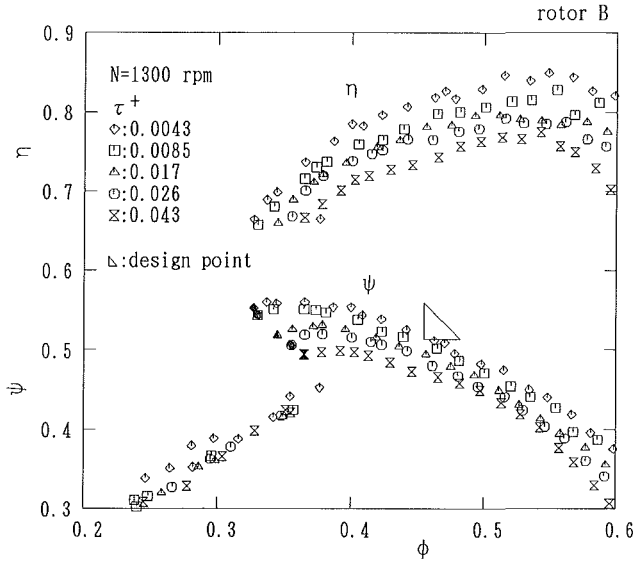

Fig. 2(*b*) Stage performance of rotor B

value divided by the reference kinetic energy defect. The reference values were calculated based on an axially symmetric flow assumption and two-dimensional cascade data. In Figs. 3(*a*) and 3(*b*) the kinetic energy defect behind rotor A with the minimum tip clearance near stall condition is compared with those at design flow rate. It is found that a region of low-

Nomenclature

C_p = nondimensional mean pressure (equation (A9))
$C_{p,i}$ = nondimensional instantaneous pressure
C_p' = nondimensional pressure fluctuation (standard deviation; equation (A10))
F_{sim} = similarity coefficient of periodic nature in pressure fluctuation (equation (1))
l_t = blade chord length at tip section
R = pseudo-spatial correlation (equation (A11))
R_z = circumferential cross correlation (equation (A12))
R_s = two-point cross correlation (equation (2))
r = radius
r_t = radius of rotor tip
s = blade spacing
S_p = skewness (equation (A8))
z = axial coordinate
η = efficiency
θ = circumferential coordinate in the relative reference frame
τ = tip clearance
τ^+ = nondimensional tip clearance ($=\tau/l_t$)
ϕ = flow rate coefficient (mean axial velocity divided by rotor tip speed)
ψ = total pressure rise coefficient (total pressure rise divided by dynamic pressure corresponding to rotor tip speed)

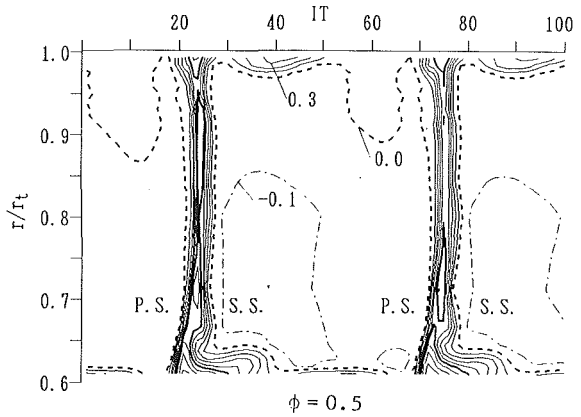

Fig. 3(*a*) Relative kinetic energy defect behind rotor A ($\tau^+ = 0.0043$) at design flow rate

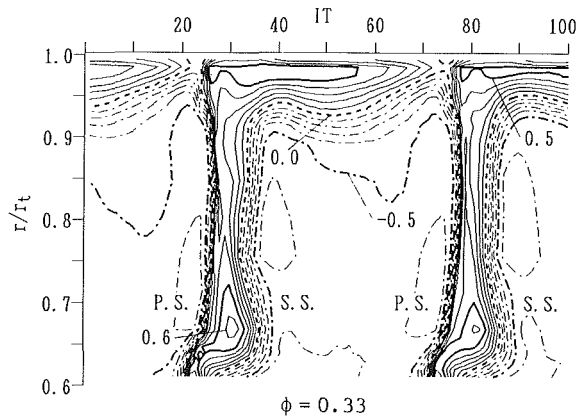

Fig. 3(*b*) Relative kinetic energy defect behind rotor A ($\tau^+ = 0.0043$) near stall

energy fluid becomes thicker at the casing and thinner at the hub near the stall condition.

For the rotors having the characteristics described above, the statistical characteristics of casing wall pressure were investigated. Phase-locked patterns of the casing wall pressure and the standard deviation and skewness of pressure fluctuation (equations (A6), (A7), and (A8) in the Appendix) were obtained by the periodic multisampling technique with a computerized data acquisition system. A Kulite sensor (model XCQ-080-1G) was installed on the casing wall in the same manner as described in the previous paper (Inoue et al., 1989). The measuring points relative to blades are indicated in Fig. 4. The circumferential and axial location of each point is identified by the numbers *IZ* and *IT*. To obtain the data at all the points, the axial location of the sensor was changed during the experiment by the sensor-setting device.

Cross correlation of the pressure fluctuations between a reference measuring point and any other point was also obtained using two Kulite sensors (equation (A11) in the Appendix). The cross correlation becomes a positive high value when the probability is high in which the two pressures are higher (or lower) than the mean value simultaneously, and a negative value means the probability in which higher and lower pressures are observed simultaneously between the two points. When the unsteadiness is uncorrelated between them, the absolute value becomes low. It is spatial correlation when two points are at the same circumferential location. It is time correlation when they are on the same axial location, since the data survey in the circumferential direction was made by one sensor with revolution of the rotor. Between any two points it would be spatial correlation in the relative reference frame if the fluctuating event were frozen during a blade passing across the measuring range. In this sense the phase-locked

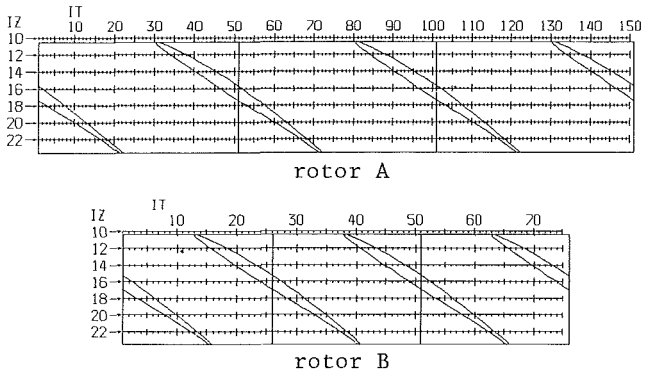

Fig. 4 Measuring points in the relative frame for rotors A and B

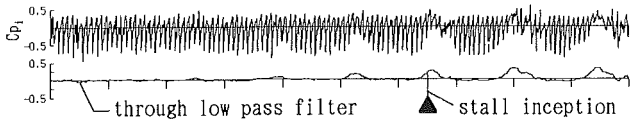

Fig. 5 Instantaneous traces of pressure sensor signal with and without low pass filter

pattern of the cross-correlation is called "pseudo-spatial correlation" in this paper.

The measurements were made mainly for the rotors with $\tau = 0.5$ mm ($\tau^+ = 0.0043$) and 2.0 mm ($\tau^+ = 0.017$) at various flow rates from the design point to the stall inception. The data just before the stall inception were gained by a newly devised pretrigger data acquisition system in the following manner. Very near stall inception the sensor outputs for the N circumferential sampling points (measuring points) are acquired every rotor revolution continuously until the stall is initiated naturally by careful handling of the throttle. They are overwritten on the looped memory of a microcomputer in which the M data can be included for each measuring point and the first data are renewed by the $(M+1)$th data. Therefore, the capacity of the data memory is N times M per transducer. When the required numbers of data are P just before the stall inception for each measuring point, the data acquisition is closed after writing the M-P data from a trigger pulse of the stall inception. The first P data are processed statistically to examine a rotating stall precursor and the second M-P data are used to investigate the development of the stall cell. The latter is not discussed in this paper. The trigger pulse of stall inception is taken by setting a threshold level for the low pass filtered signal of a pressure sensor installed just before the rotor, as shown in Fig. 5. To obtain the data at all the measuring points in Fig. 4, this technique was repeated by changing the axial location of the sensor. Reproducibility of the flow rate at stall inception was within $\pm$ 0.001 in ϕ in this experiment.

Experimental Results and Discussion

Typical phase-locked contour maps of the ensemble-average wall pressure and the pressure fluctuation (standard deviation) near the stall are compared with those at the design flow rate in Fig. 6. In the figure the phase-locked patterns of the relative velocity vectors in the tip clearance and the secondary flow maps just behind the rotor are also shown to help understanding of the phenomenon. The detailed description for the design condition is given by Inoue and Kuroumaru (1989). To describe briefly, an incoming and a leakage flow region are distinguishable at the tip. On the upstream side of the latter region, rolling-up of a tip clearance vortex appears along a pressure trough on the pressure contour, and the pressure fluctuation becomes high along the pressure trough. As the flow rate decreases, the

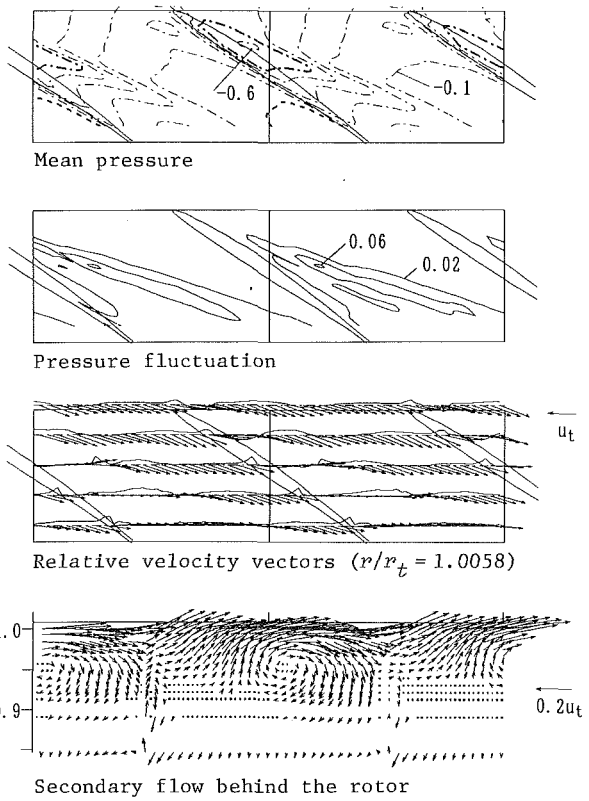

Fig. 6(*a*) Phase-locked patterns of mean pressure, fluctuation, relative velocity at tip clearance, and secondary flow behind rotor A ($\tau^+ = 0.017$) at design flow rate ($\phi = 0.5$)

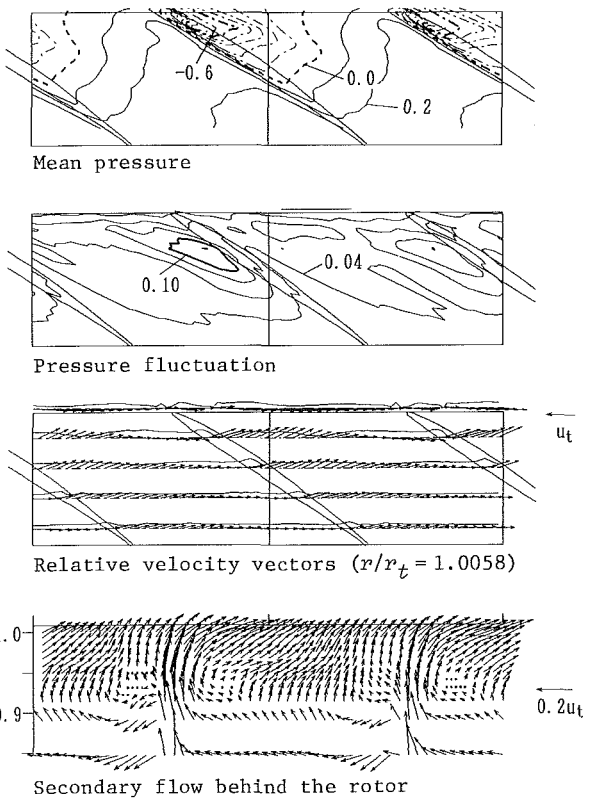

Fig. 6(*b*) Phase-locked patterns of mean pressure, fluctuation, relative velocity at tip clearance, and secondary flow behind rotor A ($\tau^+ = 0.017$) near stall ($\phi = 0.33$)

center of pressure trough (the rolling-up axis of the vortex) becomes more inclined toward the circumferential direction and the region of high-pressure fluctuation moves more upstream. Near the stall inception (Fig. 6(*b*)), the pressure trough following the minimum pressure location is shallow and short in comparison with the design condition, and the rolling-up vortex disappears in the secondary flow map just behind the rotor (that is collapse of the tip clearance vortex). At this flow rate, the casing wall pressure is characterized by a highly fluctuating region across a flow passage near the leading edge. As shown in the relative velocity vector map, the axial velocity component at clearance is very small in this region and a reverse flow appears downstream of it. This behavior suggests that low-momentum fluid accumulates here to block an incoming flow.

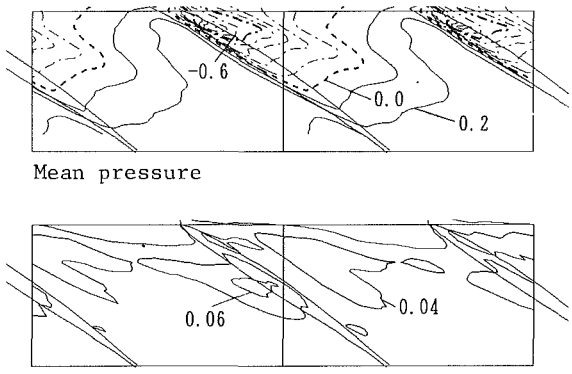

Fig. 7(*a*) Contour maps of mean pressure and fluctuation at flow rates with the maximum pressure rise (rotor A, $\tau^+ = 0.017$, $\phi = 0.35$)

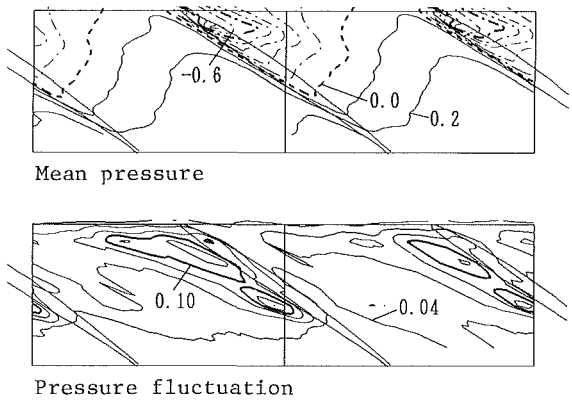

Fig. 7(*b*) Contour maps of mean pressure and fluctuation at flow rates just before stall inception (rotor A, $\tau^+ = 0.017$, $\phi = 0.324$)

Figures 7(*a*) and 7(*b*) show the contour maps of mean pressure and fluctuation at the flow rate with the maximum pressure rise ($\phi = 0.35$) and at the flow rate just before the stall inception ($\phi = 0.324$). In comparison with the case of $\phi = 0.33$ (Fig. 6), the mean pressure distributions are almost invariable, except the pressure trough becomes shallower and shorter with the flow rate decreasing. However, the pressure fluctuation increases noticeably as the flow rate draws near stall.

The nature of unsteadiness in this region is characterized in a frequency distribution of measured pressure at each point: It has an asymmetric distribution about the mean pressure. For example, the frequency distribution includes extremely low pressures near the pressure side, which makes the mean pressure lower than the pressure with the maximum frequency as shown in Fig. 8. In a statistical sense, a degree of asymmetry in the frequency distribution can be represented by a coefficient of skewness (see equation (8) in the Appendix): If the skewness is negative the frequency distribution includes pressure extremely lower than the mean value, and vice versa. In other words, the negative skewness indicates intermittent occurrence with extremely low pressure.

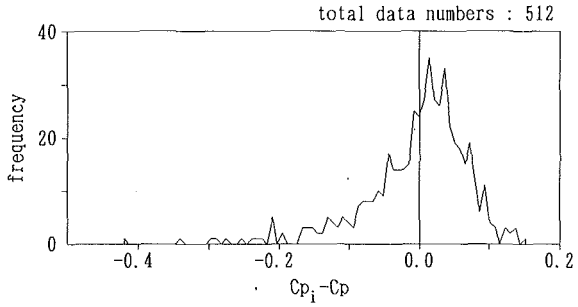

Fig. 8 Typical frequency distribution of pressure on pressure side in the upstream half of blade passage near stall

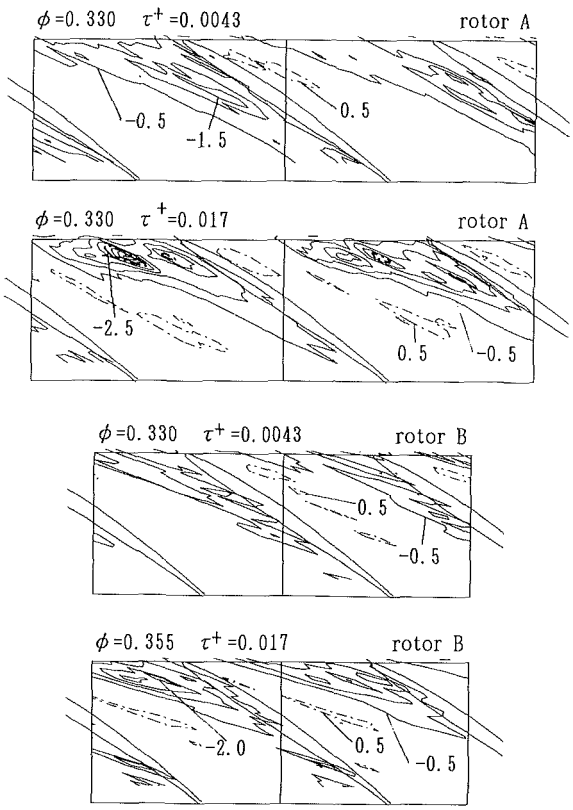

Fig. 9 Phase-locked patterns of skewness of pressure fluctuation near stall

Typical phase-locked patterns of the skewness near stall condition are shown in Fig. 9, where positive and negative values are represented by a dotted dash and solid lines, respectively. On the pressure side near the leading edge the skewness is negative. Its absolute value is larger as the tip clearance is larger and the solidity is lower. On the suction side in the upstream half of the blade passage, the skewness tends to be positive. It is highly probable that events with extremely lower pressure on the pressure side and events with higher pressure on the suction side occur at the same time due to intermittent local separation at the leading edge. It was supported by the instantaneous trace of direct signals of the pressure sensor.

Next, the nature of pressure fluctuation was investigated by the pseudo-spatial correlation as described earlier. Figure 10 shows the phase-locked patterns of the pseudo-spatial correlation for various flow rates. The coordinates of the reference point (θ^*, z^*), which are chosen on the location of relatively high pressure fluctuation, are denoted by the arrows on the upper and the right line. The solid and dotted lines denote positive and negative values, respectively. At the design condition (ϕ = 0.5) the correlation function indicates an opposite sign upstream and downstream of the rolling-up axis of tip

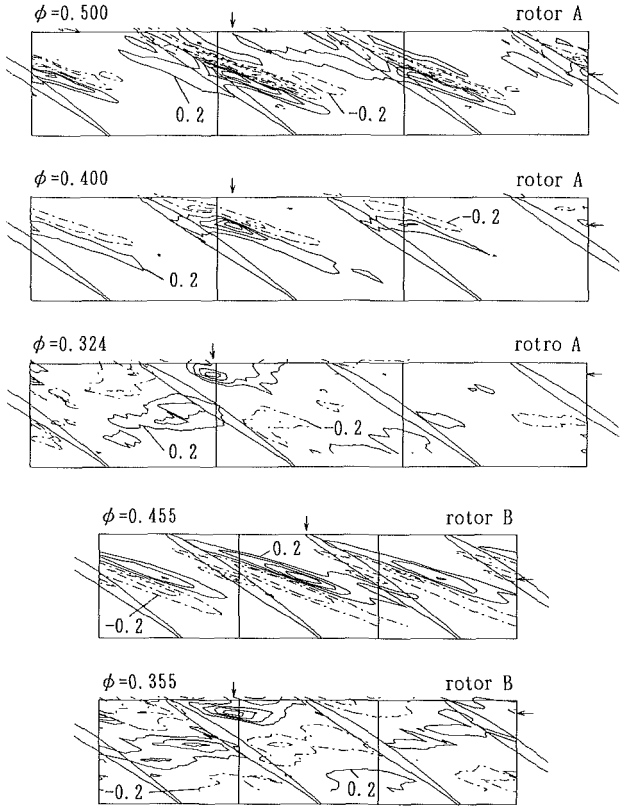

Fig. 10 Pseudo-spatial correlation of pressure fluctuation for various flow rates (τ^+ = 0.017)

clearance vortex. This is due to the tip clearance vortex fluctuating in the circumferential direction, as stated by Inoue and Kuroumaru (1984). The contour of the correlation in a blade passage is similar to that of adjacent passages. This fact shows that all the tip clearance vortices fluctuate at the same phase angle. As the flow rate decreases, however, the periodic nature with a blade spacing becomes weaker in the pseudo-spatial correlation. This may be caused either by occurrence of random disturbance or else by propagation of somewhat coherent disturbance at a different speed from the rotor revolution. Near the stall inception (ϕ = 0.323), the periodicity with blade spacing disappears completely in the pseudo-spatial correlation. Instead, the positive and negative regions of the correlation appear alternately in the nearly perpendicular to the relative flow. These are obviously at an interval different from blade spacing. Such a tendency is clearer as the solidity and the tip clearance increase. This phenomenon seems to support the existence of propagating of coherent disturbance.

It is possible to find the collapse of the periodic nature in the pressure fluctuation by the multisampling technique with a single pressure sensor mounted at an appropriate position on the casing wall. It can be seen in the circumferential cross-correlation function $R_z(\theta)$ as expressed by equation (A12). Figure 11 shows the variation in $R_z(\theta)$ for various flow rates. The numbers IZR and ITR represent the coordinates of the reference position. Similar wave shapes of the correlation function appear periodically at an interval of blade spacing near the design condition, and disappear near the stall. Namely, the similarity of $R_z(\theta)$ between adjacent blades indicates whether the unsteadiness between them is correlated. In order to represent the similarity quantitatively by one parameter, the following similarity coefficient is defined:

$$F_{\text{sim}} = \frac{\int_0^s R_z(\theta) R_z(\theta+s)\, d\theta}{\left\{ \int_0^s R_z^2(\theta)\, d\theta \cdot \int_0^s R_z^2(\theta+s)\, d\theta \right\}^{1/2}} \tag{1}$$

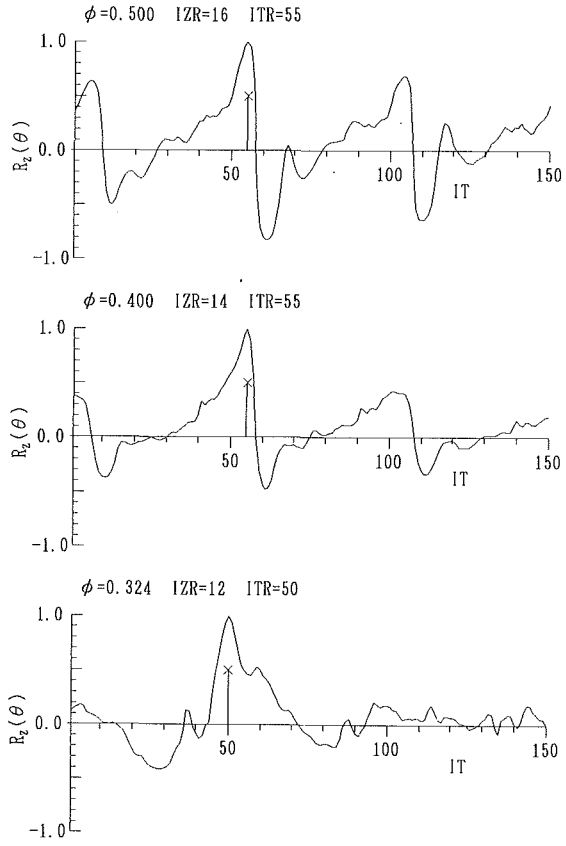

Fig. 11 Variation of cross correlation in the circumferential direction with flow rate (rotor A, $\tau^+ = 0.017$)

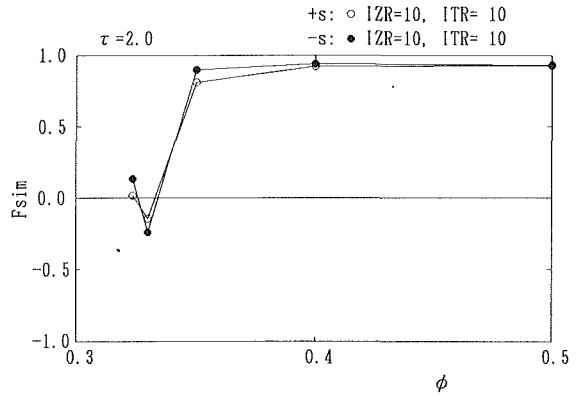

Fig. 12 Similarity coefficient of circumferential cross-correlation function (rotor A, $\tau^+ = 0.017$)

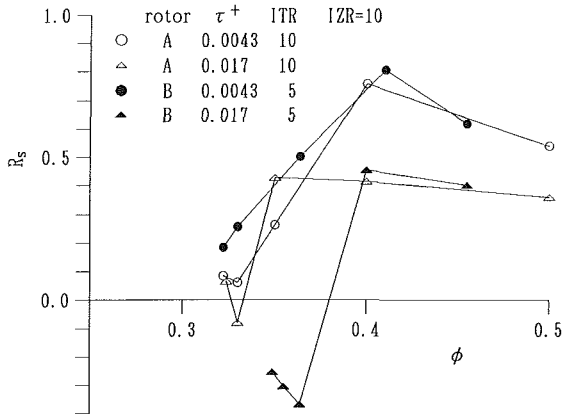

Fig. 13 Variations of two-point cross-correlation function with flow rate

where s = blade spacing. If $R_z(\theta)$ is similar to $R_z(\theta+s)$ exactly, this value becomes unity. The variation of the similarity coefficient with flow rate is shown in Fig. 12. Under a normal operating condition, the similarity coefficient keeps to nearly unity, but decreases rapidly as the flow rate draws near stall.

The nature of the disturbance may differ with geometry of a compressor rotor, as has been suggested by a few recent experimental studies. However, any kind of disturbance that rotates at a different speed from the rotor rotation must result in collapse of the pressure fluctuation essentially locked to rotor and periodic with blade spacing. Therefore, the similarity coefficient defined above can be used to warn of the imminence of rotating stall. However, this method is not practical because it is difficult to calculate the similarity coefficient quickly under operation of a compressor.

Alternatively, the two-point cross-correlation coefficient R_s of pressure fluctuation is taken as the detection parameter between the reference point and a point at a distance of one blade spacing in the relative reference frame. Namely, by replacing $\theta = \theta^* + s$ in equation (A12) in the Appendix,

$$R_s = R(\theta^* + s, z^*: \theta^*, z^*) \quad (2)$$

Figure 13 shows the variations of the two-point cross-correlation coefficient with flow rate for two rotors with different solidity and tip clearance. Although the correlation is not as high as the similarity coefficient under operating conditions, it decreases markedly near the stall point. This value is easily obtained from signals of a single pressure sensor mounted on an appropriate position of the casing wall, and can be renewed during the operation of compressor by dropping and adding the data one by one with an on-line microcomputer. Therefore, the rotating stall precursor can be seen by checking this detection parameter during the compressor operation provided that an appropriate threshold level is set beforehand for this parameter (patent applied for). It is recommended that the sensor be installed near the leading edge (IZ = 10 to 13 in this experiment). As the instantaneous pressure sensor signals are noisy essentially near stall condition, the statistical processing described above is available to avoid the noise. According to this investigation, more than M = 200 sampling data are required to get reproducible results, which means the detection parameter includes the data acquired over 200 or more rotor revolutions. As the decrease in R_s can be observed for some considerable time prior to stall inception, the requirement of 200 revolutions is not a severe limitation. When the flow rate is changing with time, however, sampling too many data results in deterioration of sensitivity for detecting the rotating stall precursor. In this case, it is necessary to increase the number of sampling points at each revolution. Although this detection method gives no information for the nature of disturbance prior to stall, it is practical in the active control of an axial compressor in the case where the control action is independent of the nature of disturbance.

Conclusion

In order to find a precursor of rotating stall in axial flow compressors, the variation in the statistical characteristics of pressure fluctuation on the casing wall with the flow rate has been investigated experimentally on two rotors with various tip clearances. The results are summarized as follows:

1 Near the inception of rotating stall, the casing wall pressure is characterized by a highly fluctuating region across a flow passage near the leading edge. The fluctuation becomes higher as the flow rate decreases.

2 In this region, the skewness of pressure fluctuation has a negative value on the pressure side and tends to be positive

on the suction side. This phenomenon is probably produced by intermittent local separation at the leading edge of the blade.

3 Periodicity of the pressure fluctuation can be examined by the phase-locked pattern of cross correlation between a reference point and other points in the relative reference frame. The periodicity with blade spacing disappears as the flow rate decreases. Near the stall, an alternative phenomenon comes into existence, which supports the disturbance propagating at a different speed from the rotor rotation.

4 A rotating stall precursor can be detected by observing collapse of the periodicity in the pressure fluctuation with blade spacing obtained from a single pressure sensor mounted on an appropriate position of the casing wall.

5 To represent the periodicity of pressure fluctuation qualitatively, a practical detection parameter has been presented, which is easily obtained during operation of a compressor.

This experimental study was made for the rotors with relatively small blade numbers (12 and 16) and low hub/tip ratio (0.6). It may be necessary to carry out many experiments for various rotor geometries to verify availability of the detection method for the rotating stall precursor. However, prior to stall the collapse of periodicity in the pressure fluctuation due to disturbance appears to be essential in any kind of turbomachinery. This method may have a potential for applying not only to an axial compressor but also to a centrifugal compressor. The authors hope that the statistical nature of wall pressure fluctuation will be investigated for many kinds of turbomachines.

References

Dugundji, J., Epstein, A. H., Garnier, V., Greitzer, E. M., Guenette, G. R., Paduano, J., Silcowski, P., Simon, J., and Valavani, L., 1989, "A Progress Report on Active Control of Flow Instabilities: Rotating Stall Stabilization in Axial Compressors," AIAA Paper No. 89-1008.

Emmons, H. W., Pearson, C. E., and Grant, H. P., 1955, "Compressor Surge and Stall Propagation," *Trans. ASME*, Vol. 79, pp. 455-469.

Garnier, V. H., Epstein, A. H., and Greitzer, E. M., 1991, "Rotating Stall Inception Indication in Axial Compressors," ASME JOURNAL OF TURBOMACHINERY, Vol. 113, this issue.

Greitzer, E. M., 1976, "Surge and Rotating Stall in Axial Flow Compressors: Parts I and II," ASME *Journal of Engineering for Power*, Vol. 98, No. 2, pp. 190-217.

Greitzer, E. M., 1987, "Unsteady Flow in Turbomachines: Recent Advances and Opportunities for Control," *Proceedings of the 1987 Tokyo Internationsl Gas Turbine Congress*, Vol. I, pp. 9-18.

Inoue, M., and Kuroumaru, M., 1984, "Three-Dimensional Structure and Decay of Vortices Behind an Axial Flow Rotating Blade Row," ASME *Journal of Engineering for Gas Turbines and Power*, Vol. 106, No. 3, pp. 561-569.

Inoue, M., Kuroumaru, M., and Fukuhara, M., 1986, "Behavior of Tip Leakage Flow Behind an Axial Flow Compressor Rotor," ASME *Journal of Engineering for Gas Turbines and Power*, Vol. 108, No. 1, pp. 7-13.

Inoue, M., and Kuroumaru, M., 1989, "Structure of Tip Clearance Flow in an Isolated Axial Compressor Rotor," ASME JOURNAL OF TURBOMACHINERY, Vol. 111, No. 3, pp. 250-256.

Inoue, M., Kuroumaru, M., and Ando, Y., 1990, "Behavior of Tip Clearance Flow in an Axial Flow Impeller at Low Flow Rate," to be presented at the 3rd China-Japan Joint Conference on Fluid Machinery.

Jackson, A. D., 1987, "Stall Cell Development in an Axial Compressor," ASME JOURNAL OF TURBOMACHINERY, Vol. 109, No. 4, pp. 492-498.

Koch, C. C., 1981, "Stalling Pressure Rise Capability of Axial Flow Compressor Stages," ASME *Journal of Engineering for Power*, Vol. 103, No. 4, pp. 645-656.

Kuroumaru, M., Inoue, M., Higaki, T., AbdElkhalek, F. A., and Ikui, T., 1982, "Measurements of Three-Dimensional Flow Field Behind an Impeller by Means of Periodic Multi-sampling of a Slanted Hot Wire," *Bulletin of the JSME*, Vol. 25, No. 209, pp. 1674-1681.

Mathioudakis, K., and Breugelmans, F. A. E., 1985, "Development of Small Rotating Stall in a Single Stage Axial Compressor," ASME Paper, 85-GT-227.

McDougall, N. M., Cumpsty, N. A., and Hynes, T. P., 1990, "Stall Inception in Axial Compressors," ASME JOURNAL OF TURBOMACHINERY, Vol. 112, pp. 116-125.

Moore, F. K., 1984, "A Theory of Rotating Stall of Multistage Axial Compressors: Part I—Small Disturbances," ASME *Journal of Engineering for Gas Turbines and Power*, Vol. 106, No. 2, pp. 313-320.

Stenning, A. H., 1980, "Rotating Stall and Surge," ASME *Journal of Fluids Engineering*, Vol. 102, No. 1, pp. 14-20.

Takata, H., and Nagano. S., 1972, "Nonlinear Analysis of Rotating Stall," ASME *Journal of Engineering for Power*, Vol. 94, No. 4, pp. 279-293.

Zika, V. J., 1985, "Correlation and Prediction of Rotating Stall Inception by Divergence Method," ASME *Journal of Fluids Engineering*, Vol. 107, No. 2, pp. 191-196.

APPENDIX

If $F(p)$ is the probability of an event in which pressure is larger than p, the probability density of $f(p)$ is $dF(p)/dp$. General representations of statistical characteristics of pressure p are the moment of order k

$$m_k = \int_{-\infty}^{\infty} p^k f(p)\, dp \tag{A1}$$

and the central moment of order k

$$\mu_k = \int_{-\infty}^{\infty} (p - m_1)^k f(p)\, dp \tag{A2}$$

By using these representations the mean pressure p_m, the standard deviation σ_p, and the skewness S_p are $p_m = m_1$, $\sigma_p = \sqrt{\mu_2}$, and $S_p = \mu_3/\sigma_p^3$.

On the other hand, according to the phase-locked averaging technique, an ensemble average of a physical value q at measuring point (θ, z) is obtained by

$$\bar{q} = \frac{1}{M} \sum_{i=0}^{M-1} q(\theta + iZ_b s, z) \tag{A3}$$

where θ = circumferential coordinate in the relative reference frame; z = axial coordinate; Z_b = blade numbers; and $\bar{}$ = phase-locked average.

Apart from the periodic component of pressure fluctuation due to the rotor revolution, m_k and μ_k can be replaced by

$$m_k = \lim_{M \to \infty} \overline{p^k} \tag{A4}$$

$$\mu_k = \lim_{M \to \infty} \overline{(p - p_m)^k} \tag{A5}$$

Therefore, the mean, standard deviation, and skewness are estimated by the following equations, provided that the sampling numbers M are sufficiently large:

$$p_m = \bar{p} \tag{A6}$$

$$\sigma_p = (\overline{p^2} - \bar{p}^2)^{1/2} \tag{A7}$$

$$S_p = (\overline{p^3} - \bar{p}^3)/\sigma_p^3 - 3\overline{p}/\sigma_p \tag{A8}$$

In this text, p_m and σ_p are normalized referring to the dynamic pressure corresponding to rotor tip speed

$$C_p = \bar{p} \Big/ \left(\frac{1}{2}\rho u_t^2\right) \tag{A9}$$

$$C_p' = \sigma_p \Big/ \left(\frac{1}{2}\rho u_t^2\right) \tag{A10}$$

where ρ = density; u_t = rotor tip speed.

The pseudo-spatial correlation was obtained by the periodic multisampling and averaging technique with multiplication of two pressure sensor outputs. Denoting the value at a reference point by an asterisk, the cross-correlation function between (θ^*, z^*) and (θ, z) is estimated by

$$\begin{aligned} R &= R(\theta, z; \theta^*, z^*) \\ &= (\overline{pp^*} - \bar{p}\,\overline{p^*})/(\sigma_p \sigma_p^*) \end{aligned} \tag{A11}$$

In the case of $z = z^*$, the above value can be obtained from outputs of a single pressure sensor. This is the circumferential cross correlation denoted by R_z

$$R_z = R(\theta, z^*; \theta^*, z^*) \tag{A12}$$

DISCUSSION

Y. N. Chen,[1] U. Haupt,[2] U. Seidel,[2] and M. Rautenberg[2]

The experimental results of this valuable paper reveal a series of very important features of the inception mechanism of rotating stall. They are as follows:

1 The leakage jet, which can be clearly seen from the flow patterns at the normal operating point of $\phi = 0.5$ in Figs. 3(*a*) and 6(*a*), practically ceases to exist at $\phi = 0.33$ near rotating stall; see Figs. 3(*b*) and 6(*b*). A reverse flow arises in the tip region; see the diagram for the relative velocity vectors at tip clearance ($r/r_t = 1.0058$), Fig. 6(*b*).

2 On the verge of rotating stall ($\phi = 0.33$) in Fig. 3(*b*), the region of low-energy fluid becomes thicker at the casing and thinner at the hub.

3 The higher the solidity of the cascade, the heavier the rotating stall in the form of a very steep pressure drop (Figs. 2(*a*) and 2(*b*)).

4 The narrower the tip clearance, the more severe the rotating stall (also see Figs. 2(*a*) and 2(*b*)).

5 A front can be detected between the forward and the reverse flow in the diagram of the relative velocity vectors in the tip clearance ($r/r_t = 1.0058$) near stall ($\theta = 0.33$) in Fig. 6(*b*).

These experimental results can be explained by means of the theory established by the discussers (1987, 1989), according to which rotating stall is introduced by secondary recirculations *r–f* and *m* in the meridional plane and around each of the blades (i.e., from the corner "pressure-side/hub" to the corner "suction-side/casing" of the neighboring blade channel); see Fig. 14. The reverse flow component *r* and the forward flow component *f* of the secondary recirculation in the meridional plane make the boundary layer on the casing thick due to deceleration, and the one on the hub thin due to acceleration. This explains the phenomenon in point 2 given above.

The reverse flow *r* then blocks the blade tip clearance and prevents generation of the leakage jet, as given in point 1. The narrower the tip clearance, the more severe the blocking. Therefore, a stronger rotating stall arises in the case of a narrow tip clearance, as shown in point 4.

In the diagram for the relative velocity vectors in the annular space of the tip clearance ($r/r_t = 1.0058$) in Fig. 6, the velocity vectors clearly show the leakage jet directed from the pressure side to the suction side of the blade at the normal operating point $\phi = 0.5$ in Fig. 6(*a*). Its strength increases from the inlet to the outlet because of the increasing pressure gradient across the blade tip. A strong forward flow prevails in the whole annular space from the inlet to the outlet region.

At the operating point of $\phi = 0.33$ near rotating stall in Fig. 6(*b*), however, the weak forward flow is still maintained at the inlet edge. But a little downstream at 1/5 of the blade chord, the flow becomes reverse on the suction side and is stagnated to practically zero on the pressure side of the blade. Farther downstream beyond 2/5 of the blade chord, the flow streams completely in the reverse direction. A front *p* between the forward and reverse flows, similar to the polar front at the midlatitude on the earth, can be drawn in the annular space between the inlet and 1/5 of the blade chord as given in Fig. 15(*b*). This front corresponds to the finding of the discussers (1987) by means of injecting colored dye through the casing into the flow. It is this front between two flows with different entropy (high entropy in the reverse flow and low entropy in the forward flow) that develops into a wavy motion because of the baroclinic instability.

The field of the maximum pressure fluctuation given in Fig. 6(*b*) is shown in Fig. 15(*a*) in addition to this wavy front. We can detect that its main region coincides with the reverse flow zone onto the front. The strong fluctuation appears to be caused by the activity of the baroclinic instability in combination with the separation of the reverse flow into vortex filaments (see the 1989 paper of the discussers). These two effects are thus especially strong on the pressure side of the blade. This special fact can therefore be evaluated from the experiment of the present paper. The low-pressure trough on the suction surface of the blade in the leading edge region (see Fig. 6(*b*)) is the nose bubble of the incoming flow. This nose bubble deflects the flow toward the tangential direction, inducing the secondary recirculations given in Fig. 14, according to the discussers (1989).

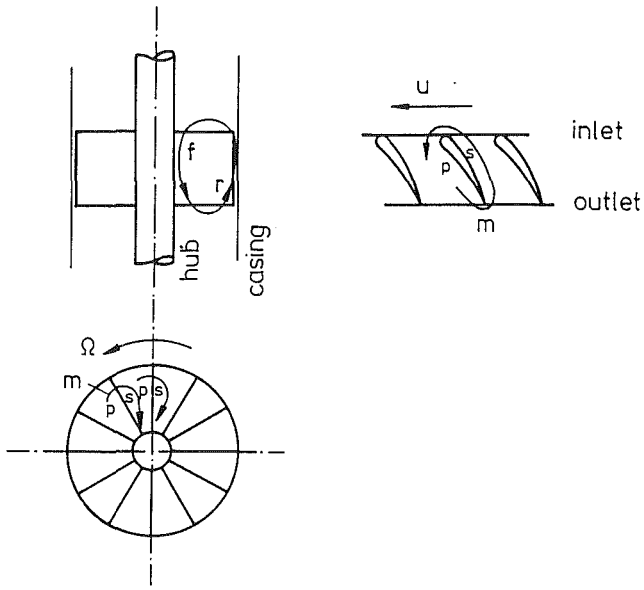

Fig. 14 Secondary recirculations in the meridional plane (*f–r*) and around each of the blades (*m*) on the verge of rotating stall

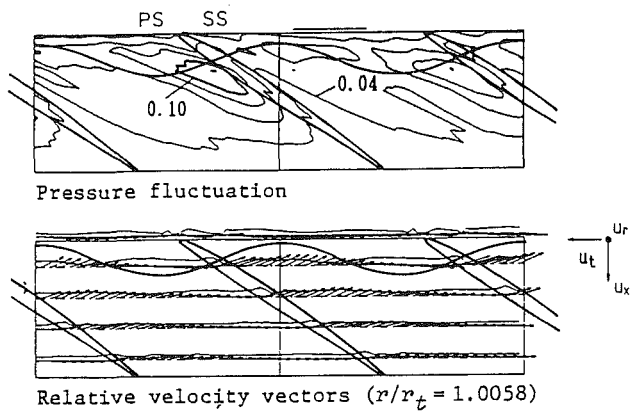

Fig. 15 Front between the forward and reverse flows in the annular space of the tip clearance (*b*) and in relationship with the pressure fluctuations (*a*), at the operating point of $\theta = 0.33$ near rotating stall

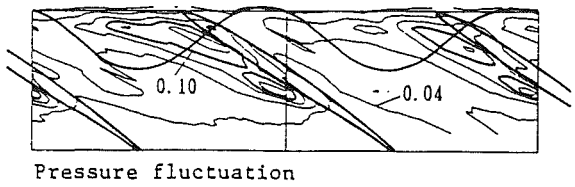

Fig. 16 Front between the forward and reverse flows in the annular space of the tip clearance in relationship with the pressure fluctuations on the verge of rotating stall ($\theta = 0.324$)

[1]Sulzer Brothers Ltd., Winterthur, Switzerland.

[2]Institute for Turbomachinery, University of Hannover, Hannover, Federal Republic of Germany.

When the flow rate is further decreased to the verge of rotating stall, the field of the maximum pressure fluctuation extends farther downstream; see Fig. 7(*b*). This indicates that the wavy front has grown to a larger amplitude to accommodate this field; see Fig. 16. This wavy front is finally developed into a very low-frequency wave (see Chen, 1990) guiding the rotating stall as shown in Fig. 10 for rotor A at $\phi = 0.324$. This low-frequency wave is the Rossby wave, as described in the papers of the discussers (1987, 1990a).

The secondary flow behind the rotor near rotating stall ($\phi = 0.33$) in Fig. 6(*b*) exhibits a vortex, which coincides with the main path of the reverse flow shown in the diagram of the relative velocity vectors in the tip clearance region ($r/r_t = 1.0058$), as referred to previously. Then, this vortex is a vortex sink as determined by the discussers in a recent paper (1990b). Therefore, the main reverse flow is guided by a longitudinal vortex, because of the vortex-filament nature of the reverse flow, according to the discussers (1989).

According to the investigation of the discussers (1990a), the rotating stall is associated with a circular von Karman vortex street rotating with the stall cell. The higher the solidity of the cascade, the stronger the von Karman vortex can be generated according to the experiment of Kriebel et al. (1960). Therefore, we have a very deep rotating stall in the case of a large solidity, which is manifested in point 3 given previously.

References

Chen, Y. N., Haupt, U., and Rautenberg, M., 1987, "On the Nature of Rotating Stall in Centrifugal Compressors With Vaned Diffusers, Part II: Karman Vortices as the Controlling Mechanism," *Proceedings of the 1987 Tokyo International Gas Turbine Congress*, pp. II 169–182.

Chen, Y. N., Haupt, U., and Rautenberg, M., 1989, "The Vortex-Filament Nature of Reverse Flow on the Verge of Rotating Stall," ASME JOURNAL OF TURBOMACHINERY, Vol. 111, pp. 450–461.

Chen, Y. N., 1990, "Rotating Stall in Radial Compressors and Pumps as Rossby Waves Associated With Transient Vortices," *Sulzer Technical Review*, No. 1, pp. 51–56.

Chen, Y. N., Haupt, U., and Rautenberg, M., 1990a, "Rossby Waves and Associated Transient Rotating Stall Vortices in Radial and Axial Turbo-compressors," *Zeitschrift für Flugwissenschaften und Weltraumforschung*, Vol. 14, No. 4, Aug.

Chen, Y. N., Haupt, U., and Rautenberg, M., 1990b, "Reverse Flow, Tip Leakage and Secondary Recirculations of Rotating Stall in Rotors/Impellers," *Proceedings of the 3rd International Congress of Fluid Mechanics*, Cairo, pp. 1549–1563.

Kriebel, A. R., Seidel, B. S., and Schwind, R. C., 1960, "Stall Propagation in a Cascade of Airfoils," NASA Report R-61.

Authors' Closure

The authors acknowledge Drs. Chen, Haupt, Seidel, and Rautenberg for giving a unique interpretation upon the present experimental results.

In the authors' opinion, the secondary recirculations in Fig. 14 do not bring about the flow phenomena in Figs. 3(*b*) and 6(*b*), but are produced as a result of the flow phenomena whose mechanism can be more physically explained by Inoue et al. (1990). However, this may be a which-came-first-the-chicken-or-the-egg question.

The authors also cannot make a hasty conclusion for the existence of wavy patterns in Figs. 15 and 16. If they exist, it will be necessary to find another mechanism to change from a short wave mode to a longer one. The rotating stall should be a long wave mode that covers several blade passages.

In any case, investigation to elucidate more clearly the mechanism of rotating stall inception should be continued by many researchers.

When the flow rate is further decreased to the verge of rotating stall, the field of the maximum pressure fluctuation extends farther downstream; see Fig. 7(*b*). This indicates that the wavy front has grown to a larger amplitude to accommodate this field; see Fig. 16. This wavy front is finally developed into a very low-frequency wave (see Chen, 1990) guiding the rotating stall as shown in Fig. 10 for rotor A at $\phi = 0.324$. This low-frequency wave is the Rossby wave, as described in the papers of the discussers (1987, 1990a).

The secondary flow behind the rotor near rotating stall ($\phi = 0.33$) in Fig. 6(*b*) exhibits a vortex, which coincides with the main path of the reverse flow shown in the diagram of the relative velocity vectors in the tip clearance region ($r/r_t = 1.0058$), as referred to previously. Then, this vortex is a vortex sink as determined by the discussers in a recent paper (1990b). Therefore, the main reverse flow is guided by a longitudinal vortex, because of the vortex-filament nature of the reverse flow, according to the discussers (1989).

According to the investigation of the discussers (1990a), the rotating stall is associated with a circular von Karman vortex street rotating with the stall cell. The higher the solidity of the cascade, the stronger the von Karman vortex can be generated according to the experiment of Kriebel et al. (1960). Therefore, we have a very deep rotating stall in the case of a large solidity, which is manifested in point 3 given previously.

References

Chen, Y. N., Haupt, U., and Rautenberg, M., 1987, "On the Nature of Rotating Stall in Centrifugal Compressors With Vaned Diffusers, Part II: Karman Vortices as the Controlling Mechanism," *Proceedings of the 1987 Tokyo International Gas Turbine Congress*, pp. II 169–182.

Chen, Y. N., Haupt, U., and Rautenberg, M., 1989, "The Vortex-Filament Nature of Reverse Flow on the Verge of Rotating Stall," ASME JOURNAL OF TURBOMACHINERY, Vol. 111, pp. 450–461.

Chen, Y. N., 1990, "Rotating Stall in Radial Compressors and Pumps as Rossby Waves Associated With Transient Vortices," *Sulzer Technical Review*, No. 1, pp. 51–56.

Chen, Y. N., Haupt, U., and Rautenberg, M., 1990a, "Rossby Waves and Associated Transient Rotating Stall Vortices in Radial and Axial Turbo-compressors," *Zeitschrift für Flugwissenschaften und Weltraumforschung*, Vol. 14, No. 4, Aug.

Chen, Y. N., Haupt, U., and Rautenberg, M., 1990b, "Reverse Flow, Tip Leakage and Secondary Recirculations of Rotating Stall in Rotors/Impellers," *Proceedings of the 3rd International Congress of Fluid Mechanics*, Cairo, pp. 1549–1563.

Kriebel, A. R., Seidel, B. S., and Schwind, R. C., 1960, "Stall Propagation in a Cascade of Airfoils," NASA Report R-61.

Authors' Closure

The authors acknowledge Drs. Chen, Haupt, Seidel, and Rautenberg for giving a unique interpretation upon the present experimental results.

In the authors' opinion, the secondary recirculations in Fig. 14 do not bring about the flow phenomena in Figs. 3(*b*) and 6(*b*), but are produced as a result of the flow phenomena whose mechanism can be more physically explained by Inoue et al. (1990). However, this may be a which-came-first-the-chicken-or-the-egg question.

The authors also cannot make a hasty conclusion for the existence of wavy patterns in Figs. 15 and 16. If they exist, it will be necessary to find another mechanism to change from a short wave mode to a longer one. The rotating stall should be a long wave mode that covers several blade passages.

In any case, investigation to elucidate more clearly the mechanism of rotating stall inception should be continued by many researchers.

Rotating Waves as a Stall Inception Indication in Axial Compressors

V. H. Garnier

A. H. Epstein

E. M. Greitzer

Gas Turbine Laboratory,
Massachusetts Institute of Technology,
Cambridge, MA 02139

Stall inception has been studied in two low-speed compressors (a single-stage and a three-stage) and in a high-speed three-stage compressor, using temporally and spatially resolved measurements. In all three machines, rotating stall was preceded by a period in which small-amplitude waves were observed traveling around the circumference of the machine at a speed slightly less than the fully developed rotating stall cell speed. The waves evolved smoothly into rotating stall without sharp changes in phase or amplitude, implying that, in the machines tested, the prestall waves and the fully developed rotating stall are two stages of the same phenomenon. The growth rate of these disturbances was in accord with that predicted by current analytical models. The prestall waves were observed both with uniform and with distorted inflow, but were most readily discerned with uniform inflow. Engineering uses and limitations of these waves are discussed.

Introduction

Axial compressors are subject to two distinct aerodynamic instabilities, rotating stall and surge, which can severely limit compressor performance. Rotating stall is characterized by a wave traveling about the circumference of the machine, surge by a basically one-dimensional fluctuation in mass flow through the machine. Whether these phenomena are viewed as distinct (rotating stall is local to the blade rows and dependent only on the compressor, while surge involves the entire pumping system: compressor, ducting, plenums, and throttle) or as related (both are eigenmodes of the compression system with surge being the zeroth order mode), they cannot be tolerated during compressor operation. Both rotating stall and surge reduce the pressure rise in the machine, cause rapid heating of the blades, and can induce severe mechanical distress.

The instabilities are commonly avoided by operating the compressor at a reduced pressure rise so as to leave a safety margin, the so-called "surge margin," between the operating point of the compressor and the point at which the machine surges. The requirement for surge margin reduces the available operating pressure rise from a given machine and often reduces the operating efficiency as well. Reduction of surge margin can then translate directly into compressor weight and efficiency improvement so that there is practical incentive to reducing the surge margin required. In the high-speed compressors common to aircraft engines, rotating stall and surge are closely coupled. As the machine moves along a constant speed operating line toward lower mass flow (Fig. 1), it generally first encounters rotating stall, which then (loosely) "triggers" the surge, often after only one or two rotor revolutions. Thus, surge and stall must both be considered; the compressor surge line could really be considered the rotating stall line, and the surge margin as stall margin.

We are aware of several alternate approaches under investigation for reducing the stall margin required. They can be considered to fall into one of two categories: those based on moving the operating point close to the stall line in situations

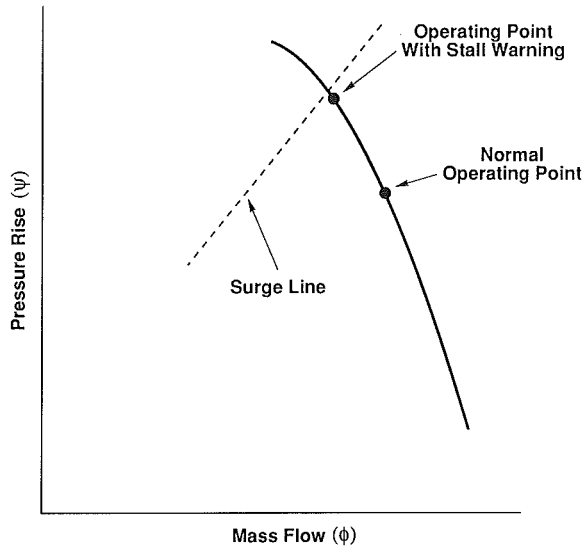

Fig. 1 Compressor performance is characterized by the constant speed line shown (solid line); the compressor cannot be safely operated to the left of the surge line

Contributed by the International Gas Turbine Institute and presented at the 35th International Gas Turbine and Aeroengine Congress and Exposition, Brussels, Belgium, June 11-14, 1990. Manuscript received by the International Gas Turbine Institute, February 7, 1990. Paper No. 90-GT-156.

when surge and stall do not threaten, and those based on moving the surge line itself and thus increasing the stable range of the compressor. Efforts in the former category include: (*a*) a real-time assessment of the stall margin by correlation of the instantaneous aircraft flight parameters with the measured compressor stall behavior; and (*b*) stall avoidance in which the control system detects rotating stall and then quickly moves the compressor operating point away from stall.

Dynamic compressor stabilization is based on an alternate approach. Here, the stall point is moved to lower mass flows by active feedback control. This scheme, and stall avoidance also, rely on the use of real-time measurements within the compressor to assess the machine stability. Clearly, the earlier a control system can detect a stall or even an incipient stall, the more effective (and less demanding) the control becomes.

This paper describes an experimental study of the rotating stall inception and growth process in three axial compressors. Its goals were both to illuminate the manner in which stall cells are born and develop, as well as to establish, as suggested by theory, whether real-time information can be extracted from the compressor, which would warn of an impending stall before the stall actually developed. This stall warning or "precursor" could have significant practical benefit if the warning is sufficiently in advance of the stall so as to permit time for control system response. The longer the warning, the greater the potential utility.

In the following sections, we review the relevant theoretical background on rotating stall development, describe the experimental arrangement, present data for three compressors under a variety of operating conditions, and finally comment on the generality of these findings and their usefulness.

Background

A large amount of experimental data taken over the last 20 years shows that, if measured at a single point in the compressor, rotating stall is seen as a sudden event with a growth period on the order of the stall cell period. Stall detection schemes based on this sort of measurement have thus not been successful in providing appreciable warning time. During the same period, however, a theoretical basis for the description of rotating stall has arisen based on the understanding of rotating stall as one class of the natural instabilities of the compression system. At its current state of development (e.g., Moore and Greitzer, 1986), the model describes the time evolution of surge and rotating stall in a compressor treated mathematically as a two-dimensional incompressible device (i.e., large hub-to-tip ratio), with three-dimensional phenomena represented only through empirical inputs. The results of a prediction by this model for a representative three-stage compressor (Fig. 2) show an instability evolving as a small-amplitude wave in axial velocity, which grows as it travels around the circumference of the compressor until, through nonlinear interaction, it causes a large-amplitude disturbance in annulus average axial velocity (surge). This type of model provides the background for the present work.

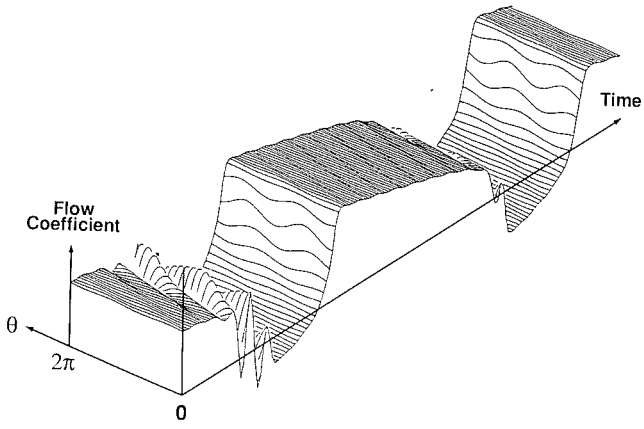

Fig. 2 The time evolution of the nondimensional axial velocity (C_x/U) distribution about the circumference ($0 \le \theta \le 2\pi$) of a three-stage compressor during compression system instability; mean level of C_x/U prior to instability is 0.5

As shown in the appendix, we can describe the stability of a compressor in terms of the time evolution of an asymmetric perturbation of the velocity potential, Φ, namely

$$\Phi = \sum_{|k| \neq 0} b_k \{e^{|k|\eta - \sigma_k \xi}\} \{e^{i(k\theta - \omega_k \xi)}\} \tag{1}$$

Each Fourier mode (k) is the product of two exponentials. The term $\exp(i[k\theta - \omega_k \xi])$ represents a traveling wave function of circumferential position (θ) and time (ξ); ω_k is the wave frequency. The term $\exp(|k|\eta - \sigma_k \xi)$ gives the dependence of the wave on axial position (η) and time; σ_k is the damping of the wave. Equation (1) can be viewed as analogous to the behavior of an oscillator rotating about the circumference of the compressor. The growth of the wave (i.e., the stability of the compressor) is determined by the instantaneous damping σ. When the damping is negative, oscillations grow and the flow in the compressor is unstable. Active control schemes aim to increase this damping. Here we make use of equation (1) in designing an experiment to detect the rotating waves and measure the instantaneous stability of the compressor.

McDougall (1988) and McDougall et al. (1990) were the first persons known to the authors to have made measurements of these rotating waves. Examining a single-stage, low-speed compressor, he found small disturbances rotating about the machine just prior to the onset of stall, in qualitative accord with the above theory. He included a good summary of previous experimental work.

To explore the use of the traveling waves as a stall precursor or warning, we pose the following questions:

- Do prestall waves exist in most (many, all) compressors?
- At what rate do these waves grow? How long do they persist?
- At what rate do they travel?
- How can they be observed?

Nomenclature

a_k, b_k = Fourier components of disturbance velocity potential
c_k = Fourier component of axial velocity disturbance
k = harmonic number
δP = pressure perturbation
R = compressor midspan radius
u = axial velocity perturbation (see Appendix)
U = rotor speed at midspan
V = measured axial velocity
η = nondimensional axial coordinate = axial distance/R
θ = circumferential coordinate
λ, μ = compressor inertia parameters
ξ = nondimensional time = (time • U)/R
σ = nondimensional damping ratio (see equation (1))
ϕ = compressor flow coefficient = axial velocity/U
Φ = nondimensional compressor velocity potential
ψ = compressor pressure rise = $P_{exit} - Pt_{inlet}/\frac{1}{2}\rho U^2$
ω = nondimensional frequency = frequency • (U/R)

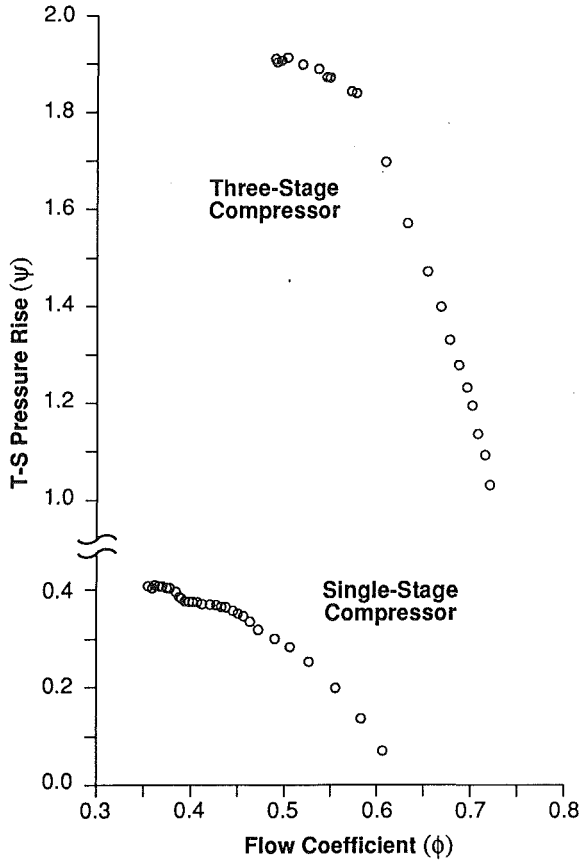

Fig. 3 Compressor characteristics of the two low-speed compressors examined in this study

- How is this behavior affected by inlet distortion and mass flow transients?
- Do high-speed (compressible) machines behave similarly?

In sum, these questions address both the basic assumptions inherent in the Moore/Greitzer model and its utility in providing real-time warning of an impending compressor stall. In the following, we experimentally examine these issues.

Experimental Apparatus

Prestall behavior of three compressors were examined: two low-speed and one high-speed machine. The low-speed, single-stage compressor consisted of IGV's, rotor, and stator. It is described in more detail by Johnson and Greitzer (1987) and Lee (1988). The low-speed, three-stage compressor is described by Gamache and Greitzer (1986) and Lavrich (1988). Nondimensional inlet total to exit static pressure compressor characteristics are shown for the two machines in Fig. 3. Both low-speed compressors were operated at tip speeds below 100 m/s, so that compressibility effects were negligible. The high-speed, three-stage compressor is a modern experimental design run at Pratt & Whitney Div., United Technologies Corp. This machine was equipped with fast-acting bleed valves, which quickly moved the operating point away from stall when it occurred to prevent mechanical damage. Experiments on that machine were conducted by Pratt & Whitney personnel and the raw data provided to the authors.

Instrumentation

All the compressors were outfitted with standard time-averaged instrumentation to provide the steady-state operating characteristics of the machines. Time-resolved instrumentation consisted of hot-wire anemometers in the low-speed compressors (oriented so as to measure axial velocity), and wall-mounted, high response, static pressure transducers in the high-speed compressor. The high-speed machine had eight transducers mounted about the circumference at each of four axial stations. The low-speed machines had either eight hot wires at a time at one axial station or three rows of four mounted at various stations. The low-speed data were digitized in real time (with suitable low pass anti-aliasing filters), while the high-speed data were first recorded on analog magnetic tape. All data were d-c coupled.

The hot wires were calibrated in place prior to each test to a velocity accuracy of ± 3 percent. The net resolution of the anemometers was 0.8 percent of the average prestall axial velocity. The pressure transducers in the high-speed experiment were calibrated by Pratt & Whitney personnel. One pressure transducer had significantly less amplitude than all its neighbors so that its gain was raised in post-test processing to yield the same level of rms fluctuations.

Signal Processing and Probe Placement Considerations

Experiments were conducted to look for small-amplitude traveling waves whose spatial and temporal structure was important. Probe placement and signal processing were therefore carefully considered. Also, because the measurements in both time and space were discrete, aliasing was of concern in both dimensions.

Probe number was determined by the number of spatial harmonics (N) to be examined. $2N+1$ measurement points are required about the circumference at each axial station. Eight were used in most cases, providing definition of the first three spatial harmonics. We expected most of the energy in the lowest order modes but were concerned about aliasing of the higher order modes and blade passing phenomena. Since small upstream disturbances due to the compressor are irrotational, they decay exponentially with upstream distance. Thus, the first measurements were made one-half compressor radius upstream so that high-order (short length scale) disturbances would be filtered out fluid dynamically. These disturbances appeared not to be a problem and measurements were subsequently made throughout the compressors.

We expect the waves to travel about the circumference at close to the rotating stall frequency, 20–50 percent of rotor shaft speed. Thus, the data was digitally band-pass filtered in the computer, with a passband 0.1 to 1.2 times rotor shaft frequency. These frequencies were determined by trial and error comparison to the unfiltered data.

The filtered time histories of the individual sensors can be used to calculate the modal information by taking a discrete Fourier transform in space about the circumference of the compressor at each point in time. Given N measurements about the machine, the complex Fourier coefficients for each mode k are given by

$$C_k = \frac{1}{N} \sum_{n=0}^{N-1} V_n \exp\left[- \frac{2ikn\pi}{N} \right] \tag{2}$$

where V_n is the measured axial velocity at angular position n. For most measurements described herein, eight sensors were used so that $N = 8$, $-3 \leq k \leq 4$, and, since V_n is real, C_k and C_{-k} are complex conjugates. The Fourier coefficients contain all the information on the wave position and amplitude as a function of time.

Low-Speed Compressor Experiments

The low-speed single-stage and three-stage compressors were used to explore the nature of the stall initiation process and the prestall traveling wave behavior, examine alternate sensor placements, establish the traveling wave statistical behavior,

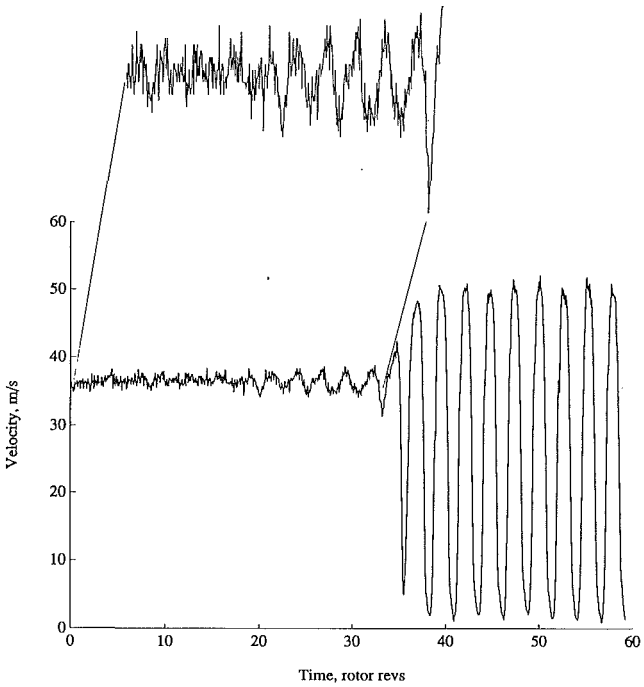

Fig. 4 Time history of axial velocity from a single hot wire positioned upstream of the single-stage compressor; the machine is in rotating stall after a time of 35 rotor revolutions

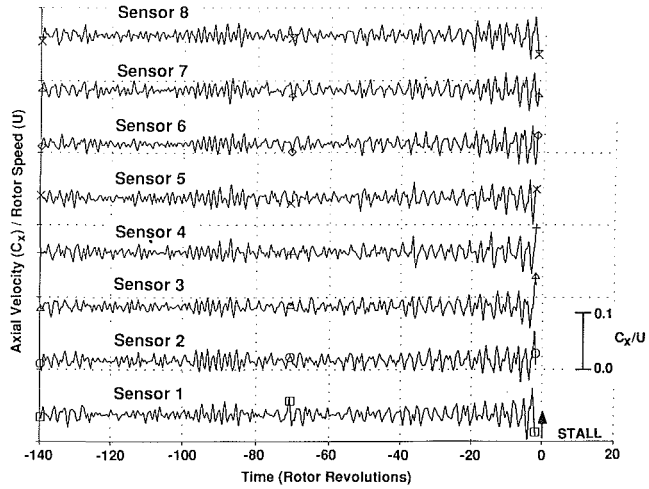

Fig. 5 Time history of axial velocity before stall as measured by eight hot wires equally spaced about the circumference 0.4 compressor radii upstream of the IGV's

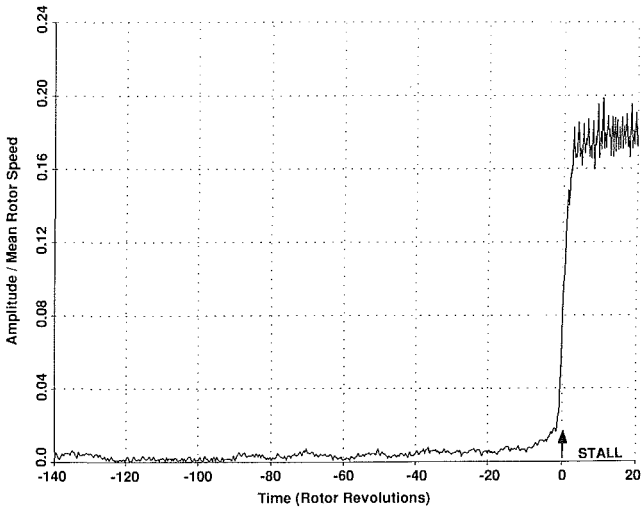

Fig. 6 Amplitude of the first Fourier harmonic ($|C_1|$) of the data in Fig. 5

and determine the influence of inlet distortion and throttle (mass flow) transients.

Quasi-Steady Stalling Behavior. During these experiments, the compressor operation was first stabilized very close to stall (within 0.005 in flow coefficient from the stall point in Fig. 3) and then the throttle closed very slowly so that machine would stall within 10 to 20 seconds. Data were taken during this entire period from the eight hot wires about the compressor annulus. Unless otherwise specified, the hot wires were positioned 0.5 compressor radii upstream of the IGV's.

Figure 4 shows the time history of the axial velocity as measured by a single sensor during the stalling transient. Here, time equal to zero has been defined, somewhat arbitrarily, as the time at which the velocity nonuniformity has grown to 50 percent of the fully stalled maximum value. The period of a rotor revolution is used as the unit of time since this is a characteristic time scale for the phenomena. As can be seen, the prestall fluctuations have a small amplitude compared to the rotating stall itself, during which the velocity fluctuations are greater than 100 percent of the prestall mean velocity. The time history of all eight sensors about the circumference is shown in Fig. 5 on a magnified scale, and regular disturbances can be observed here for a considerable time before the stall. The amplitude of the first Fourier component (the modulus of C_1), calculated from these data with equation (2), is shown in Fig. 6. This is a measure of the strength of the first mode of the rotating wave. Although small compared to the amplitude during fully developed rotating stall ($t > 0$), it is nonzero for a long period (90 revs) before the stall. The argument of C_1 is the phase angle of the traveling wave, and this is shown in Fig. 7 along with the phase of the second harmonic (arg C_2). The slopes of these lines are the speeds at which the harmonics of the waves travel around the compressor annulus (the annulus has been unwrapped in the figure so that 2π radians is one trip around). This coarse scale is used deliberately to show the overall trend. The key point from Fig. 7 is that phase speed of the first harmonic of the traveling waves is essentially constant and readily discernible for almost 90 rotor revolutions before the stall. There is a small shift in wave speed at the stall point, from 0.35 rotor speed before the stall to 0.38 rotor speed with fully developed stall. The curve marked "second harmonic" shows that, for this experiment, the second harmonic signal is too weak (i.e., the signal-to-noise ratio is too small with the instrumentation used) to give useful information.

A three-dimensional representation of the C_1 component during the last 20 revs before stall is shown in Fig. 8 in a format similar to that of the calculation shown in Fig. 2. The wave nature of the disturbance in this machine is evident.

The amplitude of the oscillations in the compressor flowfield (in this case the traveling waves about the circumference) reflects not only the operating point but also the level of disturbances in the system (the forcing). Near the neutral stability point (damping, σ, close to zero), the flowfield should behave like a narrow band system. Re-examining Fig. 7 we see that there is a stretch of constant phase speed between -140 and -125 revs, followed by a period of ill-defined speed to -95 revs, and then finally constant phase speed until stall at 0. In the context of the model, we interpret this to imply that the damping of the compressor (σ) is very close to zero, so that the traveling waves are very lightly damped. They can grow and then decay, depending upon the level of external disturbances. Thus, we might expect to see some test-to-test variation

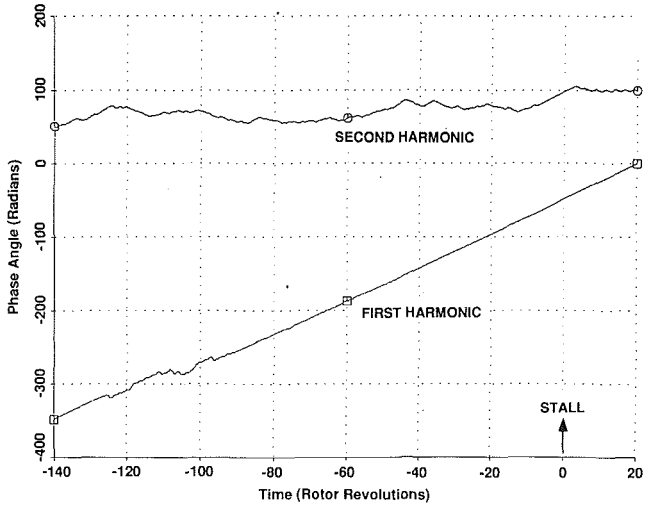

Fig. 7 The time history of the phase of the first and second Fourier coefficients measured upstream of the low-speed, three-stage compressor

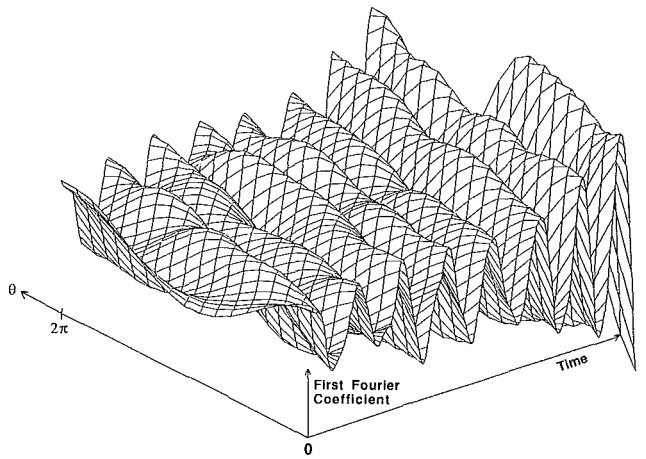

Fig. 8 Measured first harmonic behavior in a format comparable to that of Fig. 2

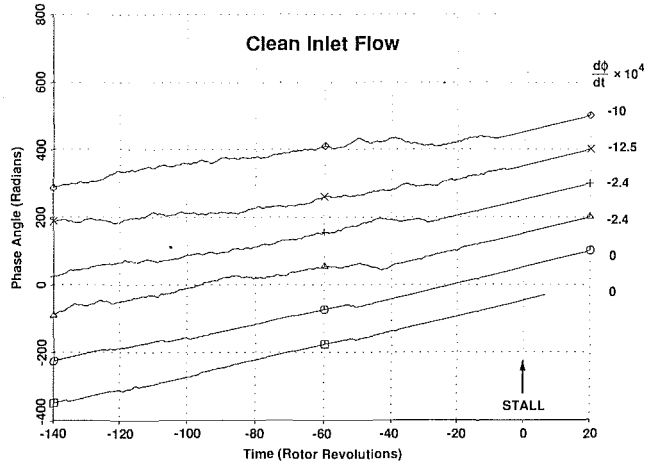

Fig. 9 Phase angle of first harmonic measured on the low-speed, three-stage compressor at different throttle rates

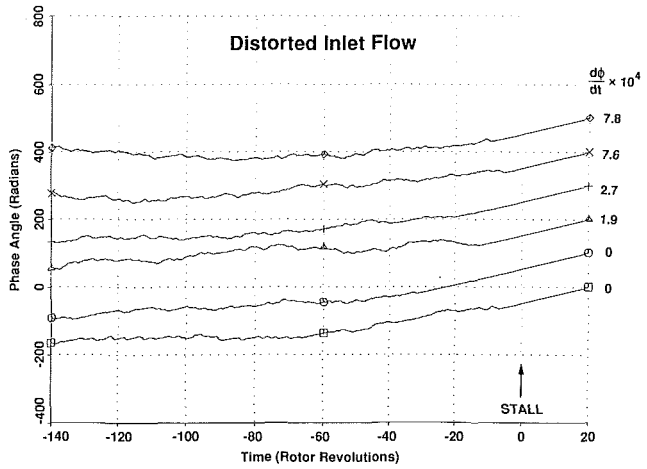

Fig. 10 As Fig. 9, but with inlet distortion

in the time during which the prestall waves propagate strongly enough to be evident. This was examined by carrying out nine tests on the three-stage compressor under nominally identical conditions. The mean prestall period of constant wave propagation was approximately 60 rotor revolutions with a high of 250 and a low of 30. (In all cases, the wave speed was 35 percent of rotor speed before stall and 38 percent during stall.) There is thus considerable statistical variation in the time during which the prestall waves were tracked. We have not characterized the source of these variations; they may be related to low-amplitude external disturbances (noise) convected into the compressor inlet. Overall, these data establish that rotating stall starts as a small amplitude travelling wave in the two low-speed compressors studied.

Throttle Transient and Inlet Distortion Effects. The influence of throttle (mass flow) transients and inlet distortion (spatially nonuniform inlet total pressure) is of interest since we know from engine experience that rotating stall is often associated with these phenomena. Experiments were conducted on both the one- and three-stage compressors with qualitatively similar findings.

The throttle transient experiments were conducted at three different throttle rates, which varied by a factor of 150 to 1, the fastest corresponding to a flow coefficient range of roughly 0.1 (Fig. 3) per 100 rotor revolutions. Distortion was generated by blocking off 180 deg of the annulus approximately one compressor diameter upstream of the IGVs, creating a roughly square wave total pressure distortion with an amplitude of 0.5 dynamic head, based on mean velocity. The time-resolved mass flow for these experiments was obtained using the average of the hot-wire measurements. The time derivative of the mass flow was obtained by a least-squares fit to the last second of data preceding stall. The absolute uncertainty of these measurements was estimated at 5 percent.

The prestall behavior of the three-stage compressor with a uniform (Fig. 9) and distorted (Fig. 10) inlet flow was measured at three throttle rates. In both cases, the rotating stall was always preceded by low-amplitude waves traveling at constant speed. The prestall duration of these waves is roughly inversely proportional to the throttle rate. This is consistent with the stability model in that the higher the throttle rate, the less time the machine spends at the low flow (ϕ) region of the speedline, which has low damping (σ) and, thus, the shorter the period during which the prestall waves can propagate for an appreciable time.

The flow coefficient (ϕ) at which prestall waves are first discerned is shown in Fig. 11 for the single-stage compressor as a function of nondimensional throttle rate ($d\phi/dt$), where t is measured in rotor revolutions, i.e., t = time/rotor revolution period. The waves appear at nearly the same value of ϕ independent of the throttle rate (over the rates examined, the waves appear slightly later as $d\phi/dt$ increases). The prestall

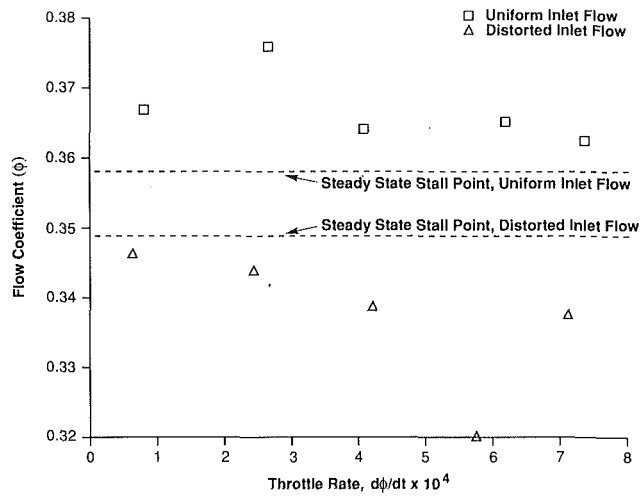

Fig. 11 Flow coefficient (ϕ) at which prestall waves are first discerned in the low-speed, single-stage compressor as a function of throttle rate

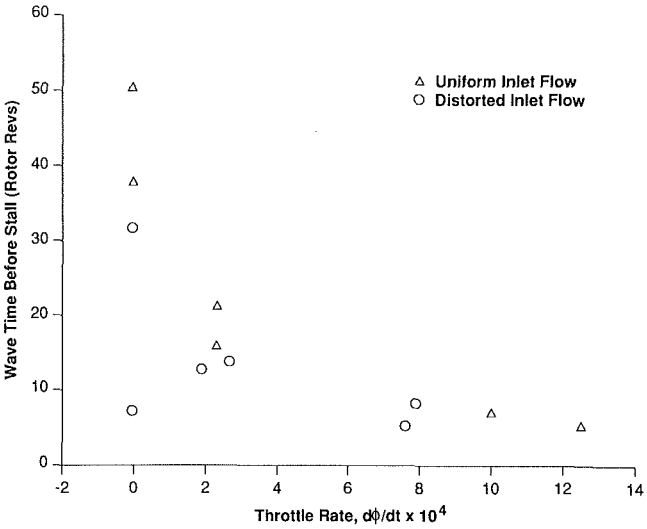

Fig. 12 Period during which the prestall wave is discerned as a function of throttle rate

period of constant traveling wave speed (the straight line segments in Figs. 9 and 10) is plotted in Fig. 12 as a function of the throttle rate and exhibits (roughly) a $1/(d\phi/dt)$ dependence.

The effects of inlet distortion are evident in Figs. 9–11. The prestall period at near-zero throttle rate is an order of magnitude smaller with the inlet distortion than without. This behavior is also consistent with a model such as that described by equation (1) if we consider that wave propagation velocity and amplitude are functions of the local flow conditions and thus will vary about the annulus in the case of distorted inflow. We infer that the signal processing technique used here (equation (2)), which looks only for *sinusoidal* waves, is not optimal with inlet distortion. Instead, a method based on the true eigenmodes of the system—and thus independent of wave shape—should be used. These could be calculated using the procedure outlined by Hynes and Greitzer (1987), but we have not yet taken this step.

Sensor Placement Influence. Data were taken with the circumferential array of sensors at five different axial stations upstream, downstream, and between the blade rows of the single-stage compressor to evaluate the influence of sensor placement on traveling wave detection. The waves were discernible at all axial stations. The amplitude increased as the sensors were moved downstream but so did the noise. This is

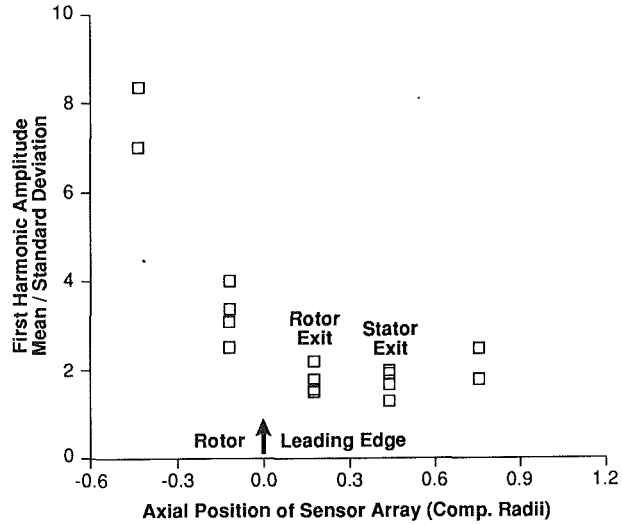

Fig. 13 Signal-to-noise ratio of first Fourier coefficient amplitude measured at various axial stations in the single-stage compressor

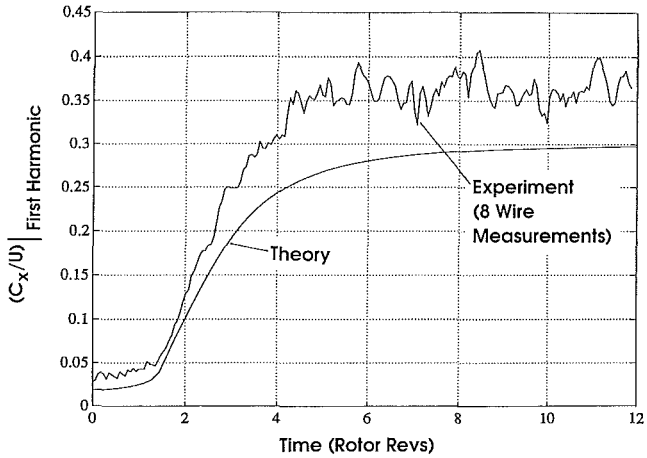

Fig. 14 Time evolution of the first harmonic of the axial velocity in the three-stage compressor during the inception of rotating stall

reflected in Fig. 13, which shows the signal-to-noise ratio, defined as the mean of the amplitude of the first harmonic ($|C_1|$) of the wave divided by the standard deviation. The signal is cleanest upstream of the IGVs.

Disturbance Growth Rate. The general nonlinear model that gives rise to equation (1) describes the evolution of the traveling wave system in the compressor and it should be capable of quantitatively predicting the growth of the waves. The inputs required for the calculation are the compressor geometry (lengths, blade stagger angles, etc.) and the steady-state compressor characteristic. Comparison of model prediction with experimental measurement for the three-stage low-speed compressor (Fig. 14) shows good agreement. (Note that, since the initial conditions for the model are not known, the zero time reference for the data and the calculation are arbitrary.) In our view, this agreement helps establish the validity of the model.

High-Speed Compressor Experiments

The wall static pressure history measured just upstream of the first stage stator in a three-stage high-speed compressor with uniform inlet flow during a slow throttle transient is shown in Fig. 15. The data are for eight circumferential locations. The phase speed of the first two spatial harmonics of these data as calculated using equation (2) shows that the second

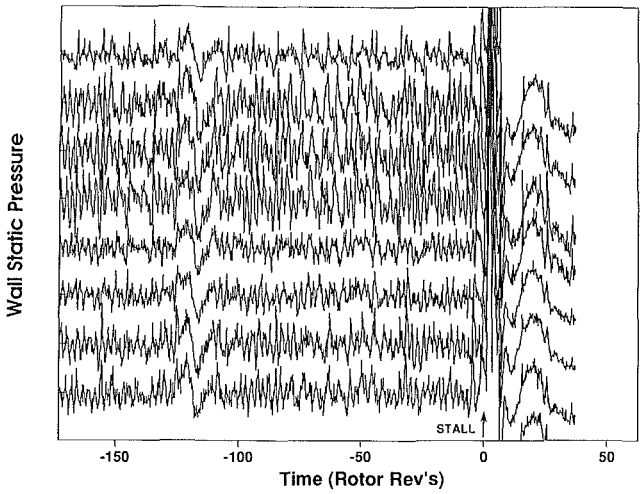

Fig. 15 Time history of eight wall static pressure transducers located about the circumference ahead of the first stator row in a high-speed, three-stage compressor

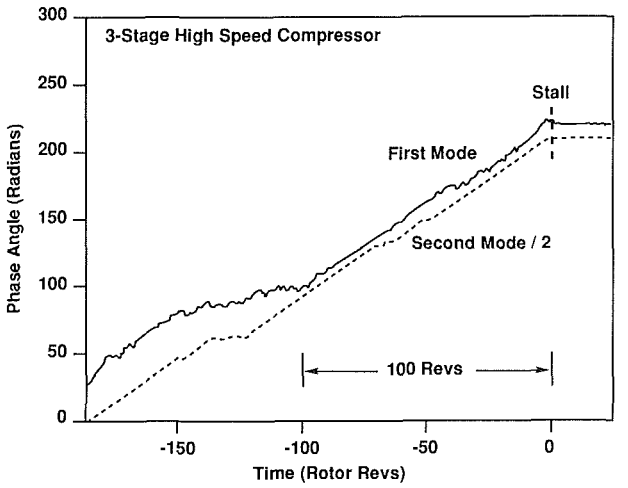

Fig. 16 The phase history of the first two spatial harmonics calculated from the high-speed compressor data of Fig. 15

harmonic is most readily discerned (Fig. 16). The prestall amplitude [$|C_N|$] is considerably higher for the second harmonic as well. The wave speed is constant for more than 100 rotor revolutions, showing a behavior similar to that of the low-speed compressors. Comparison of the phase speed of the second harmonic as measured at the leading edge of each of the three stator rows (Fig. 17) shows the signal to be the clearest at the first stage. Other measurements and calculations indicate that the first stage stalls first under these flow conditions.

Time history of the wall static pressure on the high-speed compressor with a 180 deg inlet distortion during a slow throttle transient is shown in Fig. 18. Here we see that the prestall disturbance level is not uniform about the circumference. The phase speeds of the first two spatial harmonics of this data are not readily discerned (Fig. 19) except for a short stretch of the second harmonic. The reason for this may be inferred from the time histories in Fig. 18, which show prestall disturbances of relatively high amplitude originating on sensor 7 (low flow region) being strongly attenuated as they move by sensors 6 and 5 (high flow region). Cross correlations of adjoining sensors were taken, which indicated a maximum at a time delay corresponding to 13 percent of rotor speed. A time history of the maximum value of the cross correlation between sensors 0 and 1 shows (Fig. 20) strong correlation for the period (-100 to -140 revs) during which constant phase speed of the second harmonic can be discerned. The correlation increases again as stall is approached.

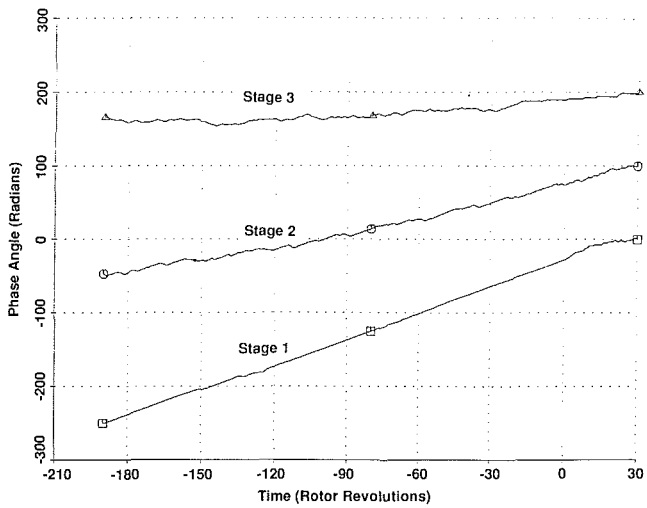

Fig. 17 Phase history of first spatial harmonic from measurements taken at the stator leading edges in a high-speed, three-stage compressor

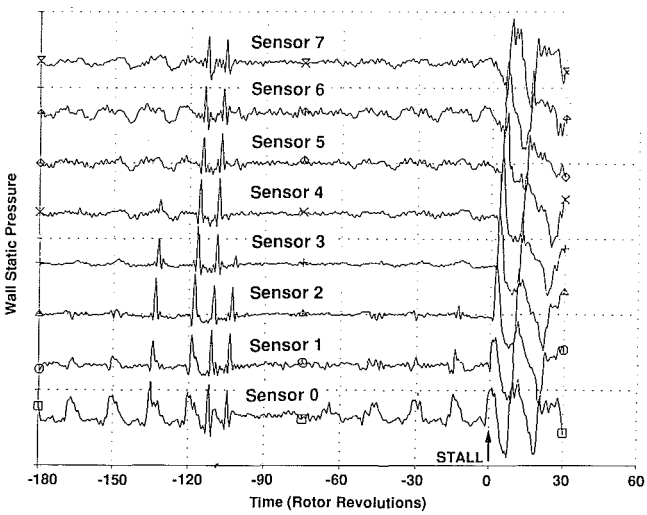

Fig. 18 As Fig. 15, but with inlet distortion

These high-speed data support the view that the distorted compressor acts (crudely) as parallel compressors with wave speed and damping varying about the circumference as a result of the locally varying flow field. The cross correlations of both high and low-speed compressor data show that there is local real-time information available on the instantaneous compressor stability, which may require more sophisticated data processing than represented by equation (2).

Application of Signal Processing to Compressor Stability Estimation

We believe that the experimental data presented have verified the applicability of the compressor stability model represented by equation (1), at least to the three machines studied. In this view, compressor stability is directly linked to the growth or decay of the traveling waves and rotating stall is simply the mature form of this wave evolution. The question of stall warning thus becomes one of identification of the waves and estimation of their growth rate. The practical implementation of this approach is complicated by two factors. The first is that, during transients, the growth of the disturbance may not be slow compared to its fundamental period, and this reduces the effectiveness of the more simple time spectra techniques such as fast Fourier transforms (FFT). The second is that the circumferentially uniform flowfield of a compressor with inlet

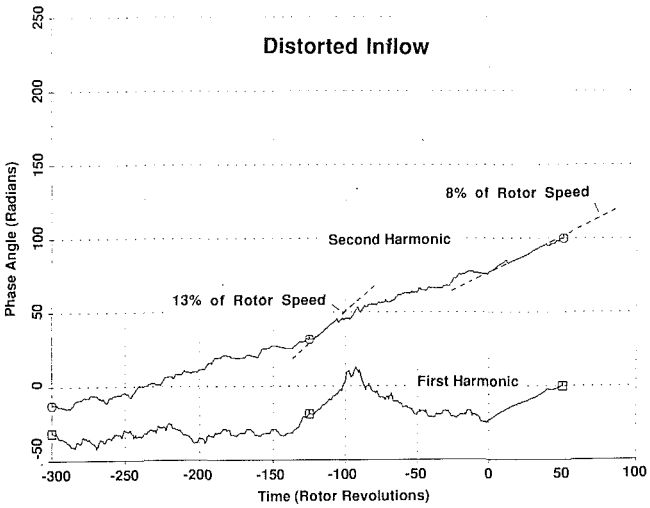

Fig. 19 Phase angle history of the first two spatial harmonics of the high-speed compressor with inlet distortion

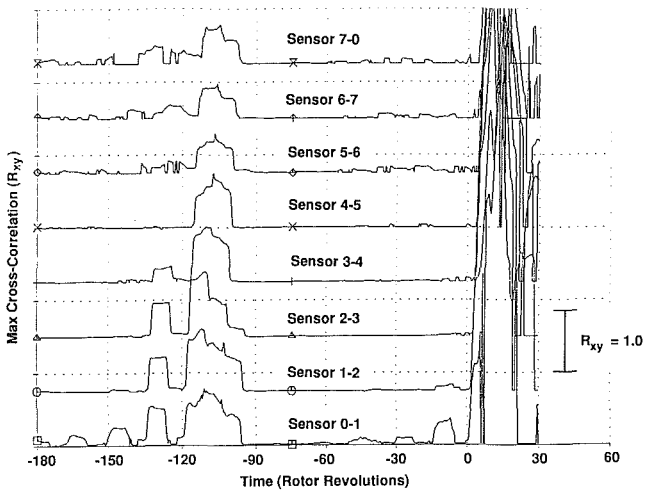

Fig. 20 The maximum value of the cross correlation of the adjacent transducers of Fig. 8 in a high-speed, three-stage compressor

distortion means that wave growth and propagation rates are nonuniform about the circumference, reducing the effectiveness of the simple spatial analysis approach of equation (2). To extract the maximum information available from the compression system, more sophisticated signal processing is thus required to cope with temporal and spatial variations. In the following sections, we address only the problem of temporal variability, leaving the spatial variation problem to a later time.

As sketched in the Appendix, the wave behavior of equation (1) is associated with the temporal behavior of the Fourier modes (a_k) of the velocity potential of the form

$$\frac{da_k}{d\xi}(\xi) = C_k a_k(\xi) \tag{3}$$

which is the description of a first-order system in which C is a constant that depends on geometry. Two interrelated approaches can be brought to bear on this system: spectral analysis and system identification techniques.

Spectral Analysis. In its simplest form, spectral analysis can be used to estimate the power spectral density (PSD) of each important spatial harmonic of the flowfield. A peak should be present at the frequency of the traveling waves (20–40 percent of rotor rotation) with its height being proportional to the power in the wave. Monitoring the time evolution of this

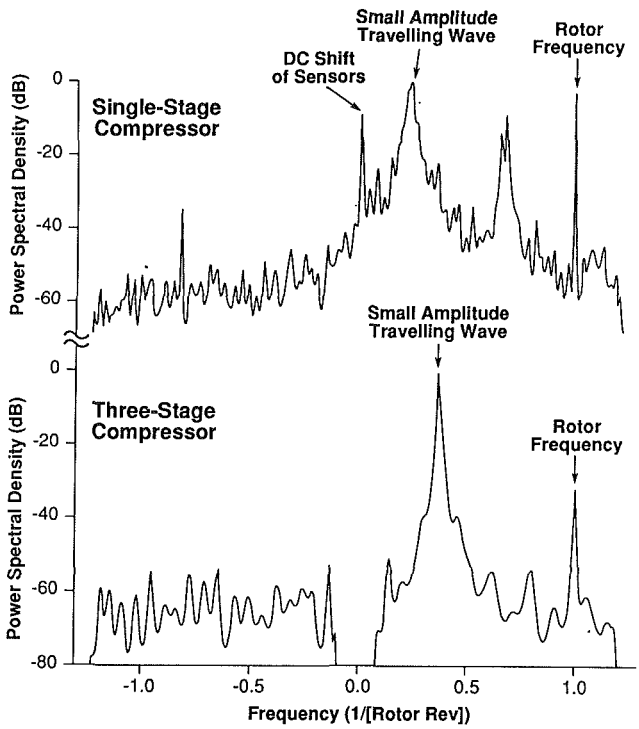

Fig. 21 Power spectral density (PSD) of first spatial harmonic of the axial velocity before stall in two low-speed compressors

peak yields information on the wave growth and thus the compressor stability. This should be a more discerning technique than the simple-phase speed plots (as in Figs. 7, 9, 10, and 15), since the phase is driven by the strongest frequency component present in the signal, which is not necessarily that of the traveling waves of interest, while the PSD will not be so affected.

The fast Fourier transform (FFT) is often used to calculate PSDs but has two limitations that are important in this application. The first is that the frequency resolution is proportional to the time interval available for analysis. The second is that the absence of information outside this interval distorts the spectral response. These problems can be particularly troublesome with very short data records and data with time varying spectral content, both of which are present in this application. Other techniques have been developed, however, which largely overcome these problems. The one adopted here is based on the fitting of a linear model to the data (Kay and Marple, 1981), which has the advantage of resolving sharp spectral features from short data records.

The power spectral densities of the first spatial harmonic of the axial velocity before stall in the single-stage and the three-stage low-speed compressors are shown in Fig. 21. The traveling wave is readily apparent in both compressors, at 0.24 of rotor frequency for the single-stage and 0.35 for the three-stage. (The three-stage data were low pass filtered to remove the d-c component; the single-stage data were not.) Figure 21 shows the power spectra at one flow coefficient at one instant of time. The power in the traveling wave (i.e., the height of the peak at the traveling wave frequency of Fig. 21) is plotted in Fig. 22 as a function of flow coefficient. The amplitude of this peak at the traveling wave frequency increases as the flow coefficient is decreased, implying that the power in the waves is related to the compressor stability. Note that the power in this first spatial harmonic is considerably reduced when inlet distortion is present. This is most likely a result of the signal processing technique used here, which was aimed at discerning sinusoidal waveforms traveling about the compressor circumference. The distorted inflow waveforms are not so simple,

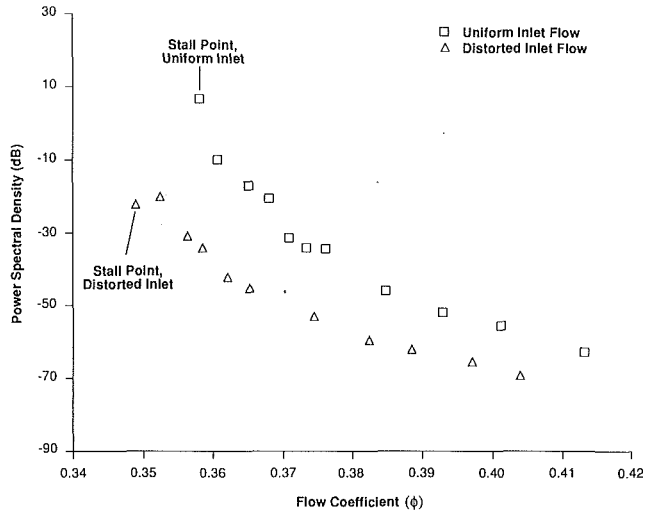

Fig. 22 The peak power of the first spatial harmonic as a function of flow coefficient (ϕ) on the single-stage, low-speed compressor

thus more sophisticated processing techniques may be required. The direct spectral approach lets us identify flow features but does not directly yield information on compressor stability, since the height of the peak is a function both of the damping of the system and the amplitude of the excitation. System identification techniques are of use in this respect.

System Identification. We have a model (equation (1)) that we believe to be a relevant description of the physical system, compressor stability. System identification is a technique that allows us to estimate the values of the physical parameters describing the compressor stability by fitting data to the model in real time. A discrete time series y_n can be modeled as the solution of a difference equation

$$y_n = b_1 y_{n-1} + \ldots + \mathbf{b}_p \mathbf{y}_{n-p} + \mathbf{v}_n \tag{4}$$

where v_n is a noise term (turbulence, electrical noise, convected disturbances, etc.). The p coefficients of b_i in equation (4) can be estimated by fitting a pth order linear model to the data. The advantage in this application is that only the parameters need be estimated since the form of the model has been established. Filtering can be used to enhance the results by removing unmodeled dynamics and correlated noise.

The model can be fitted to the data in either the time or frequency domain. The time domain was used here since it is well suited to real-time implementation. Least-squares techniques can be used recursively by updating the model parameter estimates for each new data point (Goodwin and Sin, 1984; Friedlander, 1984) and "forgetting" old data to track time varying parameters. We refer the reader to Garnier (1989) for further details.

We rewrite the wave model of equation (3) for each spatial harmonic in the form of equation (4) as an ordinary differential equation

$$\frac{dC_{-k}(\xi)}{d\xi} = (\sigma_k - i\omega_k) C_{-k}(\xi) + V(\xi) \tag{5}$$

where C_{-k} is the harmonic defined by equation (2), σ_k the traveling wave damping, ω_k the wave frequency, and $V(\xi)$ the driving noise. In fitting this model to the data at any instant in time, we have estimated the wave damping and frequency for each spatial harmonic. To the degree to which the model is valid, wave damping and compressor stability are equivalent. A real-time estimate of σ is thus an instantaneous measure of the compressor stability.

The fit of equation (5) to the power spectral density of the first spatial harmonic of the single-stage low-speed compressor is shown in Fig. 23 for undistorted flow and Fig. 24 for distorted inflow. In both cases, the model fits the general shape of the data well. The distorted data shows a peak frequency of -0.3, which is too close to traveling wave frequency to simply filter, so a second-order model was employed to account for this peak. All of the distorted inlet data subsequently used a second-order model.

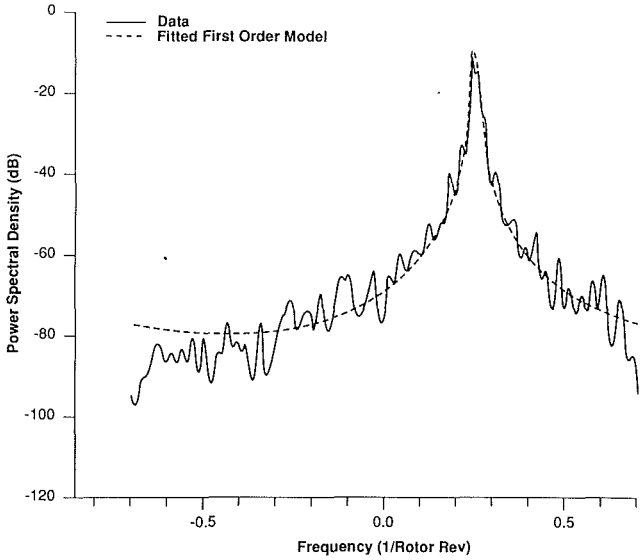

Fig. 23 Comparison of the linear model and measurement of the power spectral density of the first spatial harmonic on the low-speed, single-stage compressor

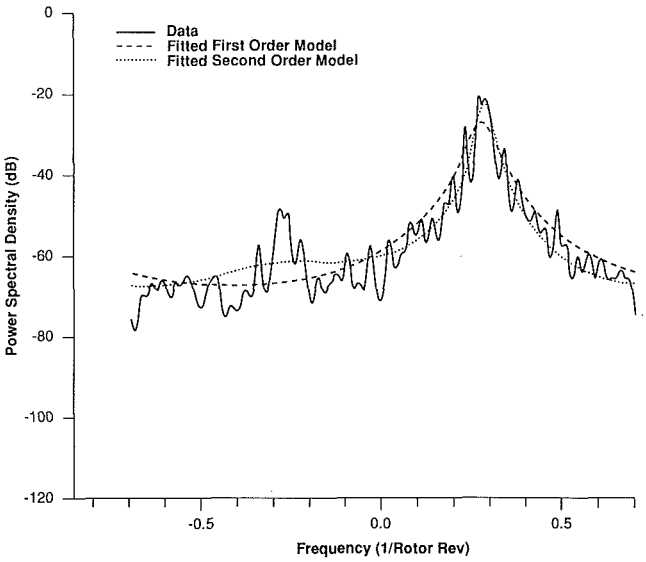

Fig. 24 As Fig. 23, but for second spatial harmonic

The damping coefficient (σ_1) of the first spatial harmonic estimated with this technique from the data is shown as a function of flow coefficient in Fig. 25, with and without inlet distortion. With undistorted inflow, the compressor is stable until the damping approaches zero. With inlet distortion, the damping is greater than for the undistorted case away from stall, but drops much faster with flow coefficient until the machine stalls at a somewhat higher value of σ. The frequency of the first spatial harmonic (ω_1) is the same with and without inlet distortion and independent of flow coefficient. The influence of throttle transients is apparently to steepen the drop in damping with flow coefficient as well as delay the stall to a somewhat lower flow coefficient (Fig. 26). How much of the delay is due to unmodeled inertia effects within the compressor and how much is due to time lags in the algorithm has not been determined.

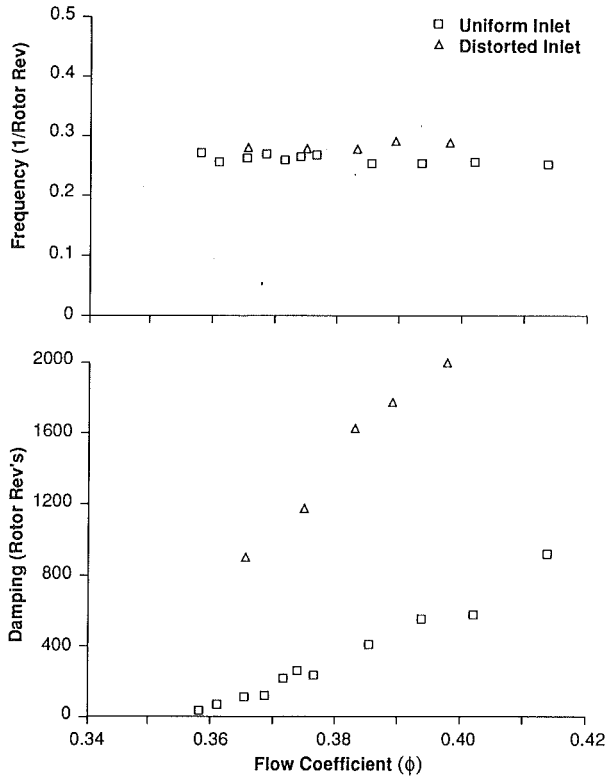

Fig. 25 First spatial harmonic wave damping (σ) and frequency (ω) estimated from the single-stage compressor measurements using parameter identifiation techniques

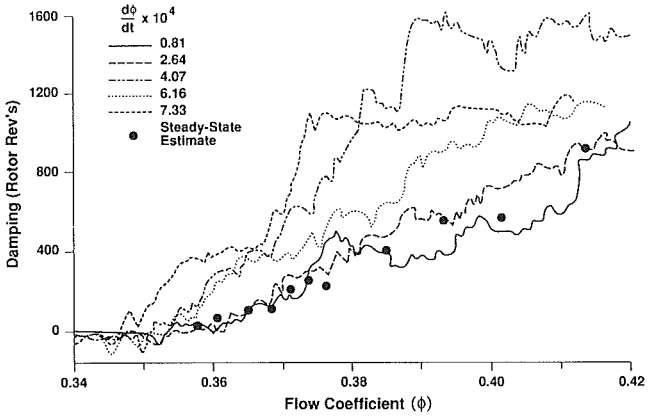

Fig. 26 First spatial harmonic damping, as in Fig. 25, but estimated for various throttle transient rates ($d\phi/dt$)

Discussion—Engineering Uses of Prestall Waves

As we have demonstrated, the compressor damping can be directly estimated on-line, given sufficient experimental data. The damping is a direct measure of the compressor stability over the period represented by the data and is thus an indication of the likelihood of stall. Whether a machine stalls at a given time is determined not just by the system damping, however, but also by the nature and level of the system forcing, which we have not addressed here. The damping by itself, though, is an indication of the susceptibility to the excitation and thus to stall.

One use of this information would be to establish the surge line of a new compressor on the test stand without the necessity of actually stalling the machine. This avoids the requirement to "dump" the compressor automatically to a higher mass flow each time surge is encountered (necessary to prevent mechanical damage), and can provide a savings in test time. A second possible use is to determine the location within a multistage compressor of the blade row in which the stall starts. The data from the high-speed compressor indicated that the waves are most clearly discerned at this axial station.

One of the most intriguing and challenging uses would be as a real-time prestall indicator in an operational engine. The limited data presented herein suggest that sufficient warning time may be available (tens to hundreds of rotor revolutions) for a more or less conventional engine control system to take corrective action (changing fuel flow, nozzle area, vane settings, etc.), thus reducing the surge margin required and the associated penalties. There are many questions that must be examined before the practicality of such a scheme could be established—not just ones of compressor dynamics as addressed here but also more applied ones such as sensor reliability, computational requirements, system complexity, overall dependability, and cost.

An even more challenging use of these prestall waves is as a control signal for an actively stabilized compressor, one in which external feedback control is used to increase the compressor stability by increasing the wave damping (σ). Epstein et al. (1989) first suggested this approach and an ongoing effort was described by Dugundji et al. (1989), where the inlet guide vanes of a single-stage low-speed compressor were being "wiggled" to suppress the traveling waves and thus increase the compressor stability.

For any of these applications to become practical, considerably more work than presented here must be done on the sensing and identification of these circumferentially traveling waves. In particular, the sinusoidal nature of the signal processing inherent in equation (2) must be relaxed in order to account for more complex flows, such as those with inlet distortion. Algorithm selection and adaptation to minimize the length of time data must be taken to identify the waves is another area where work is needed. We believe these extensions of the present work are straightforward, although not necessarily simple. Somewhat more complicated (or at least tedious) is the analytical inclusion of compressibility to model high-speed machines accurately (although the high-speed data examined to date are quite similar to that from low-speed machines).

An extremely fundamental question is how general are the results presented herein; do some, most, or all compressors exhibit this prestall wave behavior? We make no claims beyond the results for the compressors we have examined. All exhibit similar behavior, behavior in accord with the theoretical models of compression system stability.

We know of no reason why such waves should not exist in all compressors, although we would not be at all surprised if their strength and duration varied to such a degree as to render them very difficult to discern in some machines. Only more data can answer this question.

Conclusions and Summary

We have examined the flow in two low-speed and one high-speed compressor. The experiments in these machines show that:

1 Small-amplitude (less than 5 percent of the stall amplitude) waves can be discerned traveling about the compressor annulus at close to the rotating stall speed for 10–200 rotor revolutions prior to the onset of rotating stall.

2 These waves grow into a fully developed rotating stall without apparent sharp changes in either phase or amplitude.

3 The prestall period during which these waves were discerned varied by a factor of 5 at a single flow condition, apparently stochastically.

4 The behavior was similar in both the high and low-speed compressors, except that the first spatial harmonic was the strongest in the low-speed machines and the second in the high-speed.

5 In multistage compressors, the prestall waves are clearest in the stage that stalls first.

6 Inlet distortion reduces the period during which the prestall waves were discerned, using techniques based on the assumption of sinusoidal waves about the circumference.

7 The data fit the model of Moore and Greitzer, including both the qualitative behavior of the prestall waves and the quantitative prediction of the growth rates.

Overall, we believe that recognition of this wave behavior can be a useful tool in the study of compressor stability. Future work should encompass more sophisticated signal processing to account for distorted inflow, include the effects of compressibility, and extend the experimental work to a larger number of compressors.

Acknowledgments

The authors would like to acknowledge the assistance of Mr. James Paduano, Dr. G. R. Guenette, and Professor L. Valavani. We thank our colleagues Dr. I. J. Day and Dr. J. P. Longley for their stimulating discussions and thoughtful comments. The authors are grateful to Pratt & Whitney Government Engines Business for providing the high-speed compressor data and permission to publish it. This work was supported by the Office of Naval Research, Dr. R. J. Hansen technical monitor, and by the Air Force Office of Scientific Research, Captain H. Helin and Dr. J. McMichael technical monitors. We thank these gentlemen both for their support and active encouragement.

References

Dugundji, J., Epstein, A. H., Garnier, V., Greitzer, E. M., Guenette, G. R., Paduano, J., Silkowski, P., Simon, J., and Valavani, L., 1989, "A Progress Report on Active Control of Flow Instabilities: Rotating Stall Stabilization in Axial Compressors," AIAA Paper No. 89-1008.

Dunham, J., 1965, "Non-Axisymmetric Flows in Axial Compressors," Mech. Eng. Sci. Monograph No. 3, IMechE, Oct.

Epstein, A. H., Ffowcs Williams, J. E., and Greitzer, E. M., 1989, "Active Suppression of Aerodynamic Instabilities in Turbomachines," *Journal of Propulsion and Power*, Vol. 5, No. 2, pp. 204–211.

Friedlander, B., 1984, "The Overdetermined Recursive Instrumental Variable Method," IEEE *Transactions on Automatic Control*, Vol. AC-29, No. 4, pp. 353–356.

Gamache, R. N., and Greitzer, E. M., 1986, "Reverse Flow in Multistage Axial Compressors," AIAA Paper No. 86-1747, to appear in *Journal of Propulsion and Power*, 1990.

Garnier, V., 1989, "Experimental Investigation of Rotating Waves as a Rotating Stall Inception Indication in Compressors," M.S. Thesis, Dept. of Aeronautics and Astronautics, MIT, Cambridge, MA.

Goodwin, G. C., and Sin, K. S., 1984, *Adaptive Filtering, Prediction and Control*, Prentice-Hall, New Jersey.

Graupe, D., 1984, *Time Series Analysis, Identification and Adaptive Filtering*, Robert E. Krieger Publishing Company, Malabar, FL.

Greitzer, E. M., 1976, "Surge and Rotating Stall in Axial Compressors, Part I: Theoretical Compression System Model; Part II: Experimental Results and Comparison With Theory," ASME *Journal of Engineering for Gas Turbines and Power*, Vol. 98, pp. XX–XX.

Greitzer, E. M., and Moore, F. K., 1986, "A Theory of Post-Stall Transients in Axial Compressors: Part II—Applications," ASME *Journal of Engineering for Gas Turbines and Power*, Vol. 108, pp. 231–239.

Hynes, T. P., and Greitzer, E. M., 1987, "A Method for Assessing Effects of Circumferential Flow Distortion on Compressor Stability," ASME JOURNAL OF TURBOMACHINERY, Vol. 109, pp. XX–XX.

Johnson, M. C., and Greitzer, E. M., 1987, "Effects of Slotted Hub and Casing Treatments on Compressor Endwall Flowfields," ASME JOURNAL OF TURBOMACHINERY, Vol. 109, pp. 380–387.

Kay, S. M., and Marple, L. S., 1981, "Spectrum Analysis—A Modern Perspective," IEEE *Proceedings*, Vol. 69, No. 11, pp. 1380–1419.

Lavrich, P. L., 1988, "Time Resolved Measurements of Rotating Stall in Axial Flow Compressors," MIT Gas Turbine Laboratory Report #194.

Lee, N. K. W., 1988, "Effects of Compressor Endwall Suction and Blowing on Stability Enhancement," MIT Gas Turbine Laboratory Report #192.

Ljung, L., Morf, M., and Falconer, D., 1978, "Fast Calculations of Gain Matrices for Recursive Estimation Schemes," *International Journal of Control*, Vol. 27, No. 19, pp. 1–19.

Marple, L. S., 1980, "A New Autoregressive Spectrum Analysis Algorithm," IEEE *Transactions on Acoustics, Speech, and Signal Processing*, Vol. ASSP-28, No. 4, pp. 441–454.

McDougall, N. M., 1988, "Stall Inception in Axial Compressors," PhD Thesis, Cambridge University, United Kingdom.

McDougall, N. M., Cumpsty, N. A., and Hynes, T. P., 1990, "Stall Inception in Axial Compressors," ASME JOURNAL OF TURBOMACHINERY, Vol. 112, pp. 116–125.

Moore, F. K., 1983, "A Theory of Rotating Stall of Multistage Axial Compressors: Part I—Small Disturbances," ASME *Journal of Engineering for Power*, Vol. 105, pp. XX–XX.

Moore, F. K., and Greitzer, E. M., 1986, "A Theory of Post-Stall Transients in Axial Compressors: Part I—Developments of the Equations," ASME *Journal of Engineering for Gas Turbines and Power*, Vol. 108, pp. 68–76.

Stenning, A. H., 1980, "Rotating Stall and Surge," ASME *Journal of Fluids Engineering*, Vol. 102, pp. 14–20.

APPENDIX

Brief Description of the Basic Stall Inception Model

The underlying ideas of stall inception and the approach to the sensing are connected by a simple model, which provides a framework to view the phenomenon. Two points concerning rotating stall onset should be stressed at the outset. First, when one considers the actual flow, there are several disparate length scales involved. What is needed is a description of the interaction between flow on the blade element scale (length scales on the order of blade pitch or smaller) and the wave structure in the annulus (flow phenomena with length scale of the radius of the machine). Second, there is strong evidence that the "region" of the blade passage that is responsible for rotating stall is the endwall. Put another way, the mechanism of stall is generally *not* two dimensional, and the treatments that view it as such miss the essential fluid mechanics of the situation.

The model that we use was developed by Moore (1983) for rotating stall and later extended by Moore and Greitzer (1986) to encompass generalized disturbances, i.e., combined rotating stall and surge in multistage machines. Here we examine only onset of the former. In the model, the disturbances upstream and downstream of the compressor are viewed as two dimensional; this would be expected to be the case in compressors of high hub–tip radius ratio. The blade row description, however, makes use of the measured steady-state compressor pressure rise characteristic, with correction to account for unsteadiness. In a very real sense, then, three-dimensional effects *are* accounted for because the behavior at the endwalls, which can be a strong contributor to the "turnover" in the pressure rise versus flow curve, has been included. Although both the blade row modeling and the coupling between large scale disturbance field and blade element dynamics are crude, the model does appear to contain the necessary elements for a description of the stall process. It is this point, with the simplicity as a secondary issue, that suggests use of such a description in the sensing and control problem.

The derivations of the relevant equations have been given several times elsewhere, so that we will only sketch out the steps leading to the equations that we need. The flow fields considered are two dimensional, inviscid, and incompressible upstream and downstream of the compressor. The flow in these two regions is coupled by three matching conditions across the compressor, two kinematic and one dynamic. With these conditions, representing the modeling of the unsteady and nonaxisymmetric compressor performance, we describe the flow in each region as follows.

Upstream Flow Region. Upstream of the compressor the flow is irrotational, and a velocity potential can be used. We express the velocity as a uniform steady flow plus a small asymmetric perturbation, which is the gradient of a potential, Φ, satisfying the two-dimensional Laplace equation, with periodic boundary conditions and vanishing far upstream. Φ can thus be expressed in terms of its spatial Fourier coefficients as

$$\Phi(\eta, \theta, \xi) = \sum_{|k| \neq 0} a_k(\xi) e^{|k|\eta} e^{ik\theta} \qquad \text{(A1)}$$

The quantity η is the nondimensional axial coordinate x/R and ξ is a nondimensional time, where ξ = time $\cdot$ (U/R).

Across the Compressor. As stated, there are three matching conditions that are applied across the compressor. The first is that the local axial velocity distribution is the same at all *axial* stations through the compressor. This approximation is made on the basis of the small opportunity for circumferential redistribution within typical compressors. Order of magnitude arguments imply that it is most correct for disturbances with low order harmonic content, and these are precisely the ones of interest here. Discussion of the assumption can be found in the papers by Dunham (1965) or Stenning (1980).

Explicitly, the matching condition is

$$u_u(0, \theta, \xi) = u_d(0, \theta, \xi)$$

where the subscript u refers to just upstream and d to just downstream of the compressor.

The second matching condition is constant leaving angle at compressor exit. This is also an approximation, but it should be reasonable for the solidities of practical concern.

The last matching condition can be expressed in terms of a relation between the pressure difference across the compressor and the local axial velocity and its derivative. As developed by Moore (1983) (see also Moore and Greitzer, 1986) the matching condition can be written in a linearized form as

$$\left[\frac{\delta P_d - \delta P_{t_u}}{\rho U^2} = \left(\frac{d\psi}{d\phi}\right)\delta\phi - \lambda\frac{\partial\delta\phi}{\partial\theta} - \mu\frac{\partial\delta\phi}{\partial\xi}\right]_{(0,\theta,\xi)} \tag{A2}$$

The quantity $(d\psi/d\phi)$ is the slope of the steady-state compressor characteristic, and λ and μ are nondimensional parameters associated with the inertia of the fluid in the compressor blade passages. Their precise values are not critical here since what is of most interest is the general form of the solution, but for reference μ is roughly twice λ and is of order unity.

Downstream Flow Region. The linearized flow field in the downstream region is periodic and obeys the equation

$$\nabla^2\delta P_d = 0 \tag{A3}$$

with the boundary condition far downstream of constant static pressure. The downstream pressure field is thus of the form

$$\delta P_d = \Sigma P_{n_d}(\xi) e^{-|k|\eta + ik\theta} \tag{A4}$$

Using the linearized forms of the equations of motion in the upstream and downstream region equations, (A1), (A2), and (A4) may be combined into a single equation for $a_k(\xi)$, the Fourier component of the upstream velocity disturbance potential. This is

$$\frac{da_k(\xi)}{d\xi} = \frac{|k|\left|\left(\frac{d\psi_c}{d\phi}\right) - ik\lambda\right|}{(2 + |k|\mu)} a_k(\xi) \tag{A5}$$

If we define

$$\sigma_k = -\left(\frac{d\psi_c}{d\phi}\right)\frac{|k|}{2 + |k|\mu} \tag{A6}$$

$$\omega_k = k\lambda\frac{|k|}{2 + |k|\mu} \tag{A7}$$

The solution of equation (A5) can be written

$$a_k(\xi) = b_k e^{(-\sigma_k - i\omega_k)\xi} \tag{A8}$$

and thus

$$\Phi = \sum_{|k|\neq 0} b_k e^{(|k|\eta - \sigma_k\xi)} e^{i(k\theta - \omega_k\xi)} \tag{A9}$$

As stated in the main text, therefore, the Fourier mode is the product of two exponentials. The term $e^{i(k\theta - \omega_k\xi)}$ represents a traveling wave, with ω_k the wave frequency. The other exponential, $e^{|k|\eta - \sigma_k\xi}$, gives the dependence of the wave amplitude on axial position (η) and time; σ_k is the damping of the wave.

Across the Compressor. As stated, there are three matching conditions that are applied across the compressor. The first is that the local axial velocity distribution is the same at all *axial* stations through the compressor. This approximation is made on the basis of the small opportunity for circumferential redistribution within typical compressors. Order of magnitude arguments imply that it is most correct for disturbances with low order harmonic content, and these are precisely the ones of interest here. Discussion of the assumption can be found in the papers by Dunham (1965) or Stenning (1980).

Explicitly, the matching condition is

$$u_u(0, \theta, \xi) = u_d(0, \theta, \xi)$$

where the subscript u refers to just upstream and d to just downstream of the compressor.

The second matching condition is constant leaving angle at compressor exit. This is also an approximation, but it should be reasonable for the solidities of practical concern.

The last matching condition can be expressed in terms of a relation between the pressure difference across the compressor and the local axial velocity and its derivative. As developed by Moore (1983) (see also Moore and Greitzer, 1986) the matching condition can be written in a linearized form as

$$\left[\frac{\delta P_d - \delta P_{t_u}}{\rho U^2} = \left(\frac{d\psi}{d\phi}\right)\delta\phi - \lambda\frac{\partial\delta\phi}{\partial\theta} - \mu\frac{\partial\delta\phi}{\partial\xi}\right]_{(0,\theta,\xi)} \quad \text{(A2)}$$

The quantity $(d\psi/d\phi)$ is the slope of the steady-state compressor characteristic, and λ and μ are nondimensional parameters associated with the inertia of the fluid in the compressor blade passages. Their precise values are not critical here since what is of most interest is the general form of the solution, but for reference μ is roughly twice λ and is of order unity.

Downstream Flow Region. The linearized flow field in the downstream region is periodic and obeys the equation

$$\nabla^2\delta P_d = 0 \quad \text{(A3)}$$

with the boundary condition far downstream of constant static pressure. The downstream pressure field is thus of the form

$$\delta P_d = \Sigma P_{n_d}(\xi)e^{-|k|\eta + ik\theta} \quad \text{(A4)}$$

Using the linearized forms of the equations of motion in the upstream and downstream region equations, (A1), (A2), and (A4) may be combined into a single equation for $a_k(\xi)$, the Fourier component of the upstream velocity disturbance potential. This is

$$\frac{da_k(\xi)}{d\xi} = \frac{|k|\left|\left(\frac{d\psi_c}{d\phi}\right) - ik\lambda\right|}{(2 + |k|\mu)}a_k(\xi) \quad \text{(A5)}$$

If we define

$$\sigma_k = -\left(\frac{d\psi_c}{d\phi}\right)\frac{|k|}{2 + |k|\mu} \quad \text{(A6)}$$

$$\omega_k = k\lambda\frac{|k|}{2 + |k|\mu} \quad \text{(A7)}$$

The solution of equation (A5) can be written

$$a_k(\xi) = b_k e^{(-\sigma_k - i\omega_k)\xi} \quad \text{(A8)}$$

and thus

$$\Phi = \sum_{|k|\neq 0} b_k e^{(|k|\eta - \sigma_k\xi)}e^{i(k\theta - \omega_k\xi)} \quad \text{(A9)}$$

As stated in the main text, therefore, the Fourier mode is the product of two exponentials. The term $e^{i(k\theta - \omega_k\xi)}$ represents a traveling wave, with ω_k the wave frequency. The other exponential, $e^{|k|\eta - \sigma_k\xi}$, gives the dependence of the wave amplitude on axial position (η) and time; σ_k is the damping of the wave.

DISCUSSION

Y. N. Chen,[1] U. Haupt,[2] and M. Rautenberg[2]

The paper presents a series of interesting experimental results about the prestall wave. Figure 4 shows that this wave is amplified within about one cycle into the rotating stall wave of nearly the same frequency. The explanation of this extremely strong amplification is based on the two-dimensional theory of the velocity potential given in equation (1), as introduced by Moore and Greitzer (1986). This equation represents a traveling wave around the circumference of the rotor with dependence on the axial position. Equation (1) is viewed in the paper as analogous to the behavior of an oscillator rotating about the circumference of the compressor. The growth of the wave (i.e., the instability of the compressor) is determined by the instantaneous damping. When the damping is negative, oscillations grow and the flow in the compressor is unstable.

The prestall wave in the form of a stall precursor is thus considered in the paper as an axially transverse wave traveling around the circumference of the rotor. As the corresponding annular space is occupied by a lot of blades, it may be difficult to realize how such a traveling wave can cross the barrier in the form of these blades.

If the alignment of the stall cells of multistage axial compressors in the axial direction is considered, the waves associated with rotating stall of each of the stages are blocked in the axial direction. In other words, the waves penetrate through the whole depth of the compressor from the rotor of the first stage to the rotor of the last stage in the axial direction without changing in the global pattern. This depth-independent nature reveals that the waves of the different stages have the capability of blocking each other in the axial direction on one hand, and crossing the blade channels of the rotor on the other.

The writers of this discussion found in their previous publications (Chen, 1990; Chen et al., 1987, 1989, 1990a, 1990b, 1991; Haupt et al., 1987) that the baroclinic waves in combination with the Rossby waves and the associated transient vortices (a circular Karman vortex street) posses the capability required.

It was shown by the writers that on the verge of rotating stall the compressed reverse flow comes from the annular space behind the outlet of the rotor along the casing/shroud to meet the fresh forward flow on a ring-shaped front. Due to the different entropies and temperatures of the two opposite flows, a baroclinic instability deforms the ring into a wavy motion. This front was, in addition, confirmed by the measurements of Koch (1970) and Inoue et al. (1990) as cited in Chen et al. (1989, Fig. 14, and 1990a, Fig. 17). The wavy motion of the front is then developed into Rossby waves, the velocity field of which was detected from the measurement of Breugelmans and Sen (1982) on a centrifugal turbomachine (Chen, 1990, Fig. 10), and from the measurement of Lavrich (1988) on an axial compressor (Chen et al., 1990b, Fig. 20, and 1990a, Fig. 4).

There are two kinds of secondary recirculations in the rotor, which control the activity of the Rossby waves and the rotating stall.

The first kind of secondary recirculation, composed of the reverse flow along the casing/shroud and the forward flow along the hub, primarily promotes the Rossby waves and thus the rotating stall. There is a close analogy between the Rossby waves in the annular spaces in front of and behind the rotor of an axial compressor on one hand, and the Rossby waves (baroclinic waves) on the upper and bottom layers of a rotating

[1]Sulzer Brothers Ltd., Winterthur, Switzerland.
[2]Institute for Turbomachinery, University of Hannover, Federal Republic of Germany.

fluid annulus with an artificial recirculation between the outer and inner cylindrical walls found by Douglas et al. (1972) in their laboratory experiment (see Chen et al., 1987, Fig. 9) on the other hand. The pressure rise of the rotor corresponds to the gravity field in the experiment of the rotating annulus. The Rossby waves in the two annular spaces/layers are coupled with each other by their blocking effect.

In the case of the rotor, the communication of the activity of the Rossby waves between the blade channels is carried out by the second kind of secondary recirculation around each of the blades, as shown by Chen et al. (1990a, Figs. 14, 15, and 16).

Furthermore, each blade channel of the rotor of an axial compressor generates its own Rossby wave (see Chen et al., 1990b, Fig. 22), which serves as a communicating member between the Rossby waves in the two annular spaces in front of and behind the rotor. In this manner, the field of the Rossby waves around the entire rotor forms an ensemble, renewing from blade channel to blade channel under the guidance of the activity of the Rossby waves in the frontal and rear annular spaces.

The formation of the Rossby wave in each of the blade channels of centrifugal compressors can be also verified, as shown in a further paper of the writers (1991).

The Rossby waves in the turbocompressors and pumps are similar to those in the ocean and the middle atmosphere (e.g., 500 mbar height). In the latter case they guide the polar front on the earth's surface (i.e., between the warm westerly from the subtropical region and the cold easterly from the polar region, and thus subjected to the baroclinic instability for forming the meteorological vortices "low and high" of the unstable weather event), and the jet stream in the high atmospheric level (200 mbar).

The Rossby waves of the rotor have their velocity components primarily in the tangential and radial directions u and v. These two components correspond to the west–east direction of the zonal flow and its deflection to the north–south direction in the Rossby waves of the atmosphere. The axial velocity component w, which initiates the first and second kinds of secondary recirculations of the rotor mentioned above, is not directly involved in the Rossby waves. These tangential and radial components u and v of the Rossby waves are then capable of being communicated between the blade channels as stated previously.

The paper under discussion is based on the wave motion of the axial velocity component w around the rotor. This corresponds to a wave motion in the atmosphere in the direction normal to the earth's surface. Such a wave is observed as an internal wave in stratified flow on the earth, e.g., the lee wave downstream of a mountain as a barrier. This wave cannot cause a rotating disturbance around the earth. In other words, the axial disturbance in a rotor cannot stay in any direct connection with the rotating stall, which has the major property of a rotating disturbance.

The rotating stall of the axial compressor usually has one stall cell. The Rossby number of the accompanying Rossby wave was determined to be 0.083 by the writers (1990b). The rotating stall of the centrifugal compressor with its two-cell pattern has then a Rossby number of 0.17 (Chen, 1990). These values correspond well to those of the Rossby waves in nature.

The writers are quite aware that their Rossby-wave theory is still in a developing stage. It needs further mathematical and physical treatments. An advanced step for this will be carried out in the near future (Chen et al., 1991).

References

Chen, Y. N., Haupt, U., and Rautenberg, M., 1987, "On the Nature of Rotating Stall in Centrifugal Compressors With Vaned Diffuser, Part II: Karman Vortices as the Controlling Mechanism," *1987 Tokyo International Gas Turbine Congress*, Vol. II, pp. 169–182.

Chen, Y. N., Haupt, U., and Rautenberg, M., 1989, "The Vortex-Filament Nature of the Reverse Flow on the Verge of Rotating Stall," ASME JOURNAL OF TURBOMACHINERY, Vol. 111, pp. 450–461.

Chen, Y. N., Haupt, U., Seidel, U., Jin, D., and Rautenberg, M., 1990a, "The Behavior of the Rossby Waves of Rotating Stall in Turbocompressors," *Interfluid Dechema*, Druckhaus K. Schmitt Wwe, Frankfurt Main, pp. 403–416.

Chen, Y. N., Haupt, U., and Rautenberg, M., 1990b, "Rossby Waves and Associated Transient Rotating Stall Vortices in Radial and Axial Turbocompressors," *Zeitschrift für Flugwissenschaften und Weltraumforschung*, Vol. 14, No. 4.

Chen, Y. N., 1990, "Rotating Stall in Radial Compressors and Pumps as Rossby Waves Associated With Transient Vortices," *Sulzer Technical Review*, No. 1, pp. 51–56.

Chen, Y. N., Seidel, U., and Rautenberg, M., 1991, "The Rossby Waves of Rotating Stall in Impellers, Theory and Application," to be published.

Haupt, U., Chen, Y. N., and Rautenberg, M., 1987, "On the Nature of Rotating Stall in Centrifugal Compressors With Vaned Diffusers, Part I: Detection of Reverse Flow," *1987 Tokyo International Gas Turbine Congress*, Vol. II, pp. 161–168.

Authors' Closure

The authors thank Drs. Chen and Haupt and Profesor Rautenberg for their comments. We do not, however, agree with the points that are made. In particular, we do not see that any scientific evidence at all has been presented connecting rotating stall with either Rossby waves (which occur at high ratios of Coriolis to inertial forces) or baroclinic instability. To be more explicit, we have not seen, either in their discussion or in previous expositions, any clearly stated body of assumptions, a mathematical statement of the problem, calculations based on this statement, or predictions about the form of such waves in an axial compressor. We feel strongly that such a rational development is needed to demonstrate the appropriateness, let alone the correctness, of any proposed theory. Figure 14 of Garnier et al. is the result of such a process: a computation based on a clearly stated theory. Its agreement with experiment seems to us to show that the theory contains much of the essential physics of the stall cell wave evolution, but if this is disputed then there are specific statements that one examines to see the cause of any disagreement.

In addition to this overall view, there are clear errors of concept in the discussion. For example, baroclinic instability (which depends on density not being solely a function of pressure) in invoked by the discussers to explain some aspects of rotating stall. The flows examined by Garnier and predecessors, however, had low Mach numbers (on the order of 0.1 in some cases) and temperature rises much less than the ambient level. Under these conditions, the flow can be considered constant density, the entropy has no dynamic significance, and there is no role played by baroclinic instability. Further, in the theory presented in the paper, the propagation of the stall cell depends on a balance between inertial effects in the compressor and the upstream and downstream flow fields; there is no relationship to Rossby waves.

In summary, while some of the statements concerning Rossby waves made by the discussers may be correct, we have seen no factual trail leading to their connection with rotating stall. We would be pleased to consider such evidence if presented in a well-reasoned and unambiguous manner, rather than as the vague analogies that appear in the discussion.

fluid annulus with an artificial recirculation between the outer and inner cylindrical walls found by Douglas et al. (1972) in their laboratory experiment (see Chen et al., 1987, Fig. 9) on the other hand. The pressure rise of the rotor corresponds to the gravity field in the experiment of the rotating annulus. The Rossby waves in the two annular spaces/layers are coupled with each other by their blocking effect.

In the case of the rotor, the communication of the activity of the Rossby waves between the blade channels is carried out by the second kind of secondary recirculation around each of the blades, as shown by Chen et al. (1990a, Figs. 14, 15, and 16).

Furthermore, each blade channel of the rotor of an axial compressor generates its own Rossby wave (see Chen et al., 1990b, Fig. 22), which serves as a communicating member between the Rossby waves in the two annular spaces in front of and behind the rotor. In this manner, the field of the Rossby waves around the entire rotor forms an ensemble, renewing from blade channel to blade channel under the guidance of the activity of the Rossby waves in the frontal and rear annular spaces.

The formation of the Rossby wave in each of the blade channels of centrifugal compressors can be also verified, as shown in a further paper of the writers (1991).

The Rossby waves in the turbocompressors and pumps are similar to those in the ocean and the middle atmosphere (e.g., 500 mbar height). In the latter case they guide the polar front on the earth's surface (i.e., between the warm westerly from the subtropical region and the cold easterly from the polar region, and thus subjected to the baroclinic instability for forming the meteorological vortices "low and high" of the unstable weather event), and the jet stream in the high atmospheric level (200 mbar).

The Rossby waves of the rotor have their velocity components primarily in the tangential and radial directions u and v. These two components correspond to the west–east direction of the zonal flow and its deflection to the north–south direction in the Rossby waves of the atmosphere. The axial velocity component w, which initiates the first and second kinds of secondary recirculations of the rotor mentioned above, is not directly involved in the Rossby waves. These tangential and radial components u and v of the Rossby waves are then capable of being communicated between the blade channels as stated previously.

The paper under discussion is based on the wave motion of the axial velocity component w around the rotor. This corresponds to a wave motion in the atmosphere in the direction normal to the earth's surface. Such a wave is observed as an internal wave in stratified flow on the earth, e.g., the lee wave downstream of a mountain as a barrier. This wave cannot cause a rotating disturbance around the earth. In other words, the axial disturbance in a rotor cannot stay in any direct connection with the rotating stall, which has the major property of a rotating disturbance.

The rotating stall of the axial compressor usually has one stall cell. The Rossby number of the accompanying Rossby wave was determined to be 0.083 by the writers (1990b). The rotating stall of the centrifugal compressor with its two-cell pattern has then a Rossby number of 0.17 (Chen, 1990). These values correspond well to those of the Rossby waves in nature.

The writers are quite aware that their Rossby-wave theory is still in a developing stage. It needs further mathematical and physical treatments. An advanced step for this will be carried out in the near future (Chen et al., 1991).

References

Chen, Y. N., Haupt, U., and Rautenberg, M., 1987, "On the Nature of Rotating Stall in Centrifugal Compressors With Vaned Diffuser, Part II: Karman Vortices as the Controlling Mechanism," *1987 Tokyo International Gas Turbine Congress*, Vol. II, pp. 169–182.

Chen, Y. N., Haupt, U., and Rautenberg, M., 1989, "The Vortex-Filament Nature of the Reverse Flow on the Verge of Rotating Stall," ASME JOURNAL OF TURBOMACHINERY, Vol. 111, pp. 450–461.

Chen, Y. N., Haupt, U., Seidel, U., Jin, D., and Rautenberg, M., 1990a, "The Behavior of the Rossby Waves of Rotating Stall in Turbocompressors," *Interfluid Dechema*, Druckhaus K. Schmitt Wwe, Frankfurt Main, pp. 403–416.

Chen, Y. N., Haupt, U., and Rautenberg, M., 1990b, "Rossby Waves and Associated Transient Rotating Stall Vortices in Radial and Axial Turbocompressors," *Zeitschrift für Flugwissenschaften und Weltraumforschung*, Vol. 14, No. 4.

Chen, Y. N., 1990, "Rotating Stall in Radial Compressors and Pumps as Rossby Waves Associated With Transient Vortices," *Sulzer Technical Review*, No. 1, pp. 51–56.

Chen, Y. N., Seidel, U., and Rautenberg, M., 1991, "The Rossby Waves of Rotating Stall in Impellers, Theory and Application," to be published.

Haupt, U., Chen, Y. N., and Rautenberg, M., 1987, "On the Nature of Rotating Stall in Centrifugal Compressors With Vaned Diffusers, Part I: Detection of Reverse Flow," *1987 Tokyo International Gas Turbine Congress*, Vol. II, pp. 161–168.

Authors' Closure

The authors thank Drs. Chen and Haupt and Profesor Rautenberg for their comments. We do not, however, agree with the points that are made. In particular, we do not see that any scientific evidence at all has been presented connecting rotating stall with either Rossby waves (which occur at high ratios of Coriolis to inertial forces) or baroclinic instability. To be more explicit, we have not seen, either in their discussion or in previous expositions, any clearly stated body of assumptions, a mathematical statement of the problem, calculations based on this statement, or predictions about the form of such waves in an axial compressor. We feel strongly that such a rational development is needed to demonstrate the appropriateness, let alone the correctness, of any proposed theory. Figure 14 of Garnier et al. is the result of such a process: a computation based on a clearly stated theory. Its agreement with experiment seems to us to show that the theory contains much of the essential physics of the stall cell wave evolution, but if this is disputed then there are specific statements that one examines to see the cause of any disagreement.

In addition to this overall view, there are clear errors of concept in the discussion. For example, baroclinic instability (which depends on density not being solely a function of pressure) in invoked by the discussers to explain some aspects of rotating stall. The flows examined by Garnier and predecessors, however, had low Mach numbers (on the order of 0.1 in some cases) and temperature rises much less than the ambient level. Under these conditions, the flow can be considered constant density, the entropy has no dynamic significance, and there is no role played by baroclinic instability. Further, in the theory presented in the paper, the propagation of the stall cell depends on a balance between inertial effects in the compressor and the upstream and downstream flow fields; there is no relationship to Rossby waves.

In summary, while some of the statements concerning Rossby waves made by the discussers may be correct, we have seen no factual trail leading to their connection with rotating stall. We would be pleased to consider such evidence if presented in a well-reasoned and unambiguous manner, rather than as the vague analogies that appear in the discussion.

High-Speed Compressor Surge With Application to Active Control

A. M. Cargill

C. Freeman

Rolls-Royce plc,
Derby DE2 8BJ United Kingdom

This paper discusses the mechanics of surge as observed on the high-speed axial compressors of modern aero-engines. It argues that the initial stage of the instability consists of a high-amplitude blast wave that develops nonlinearly from a small-scale disturbance and is thus not correctly described by traditional small perturbation stability theories. It follows from this that active control schemes of the global type may be inappropriate, since to be effective, control would have to be applied in a short time and in a very detailed manner, requiring a large number of transducers and actuators. Active control may, though, be effective in controlling the disturbances that grow into the above blast wave and in the control of other phenomena such as rotating stall, given an adequate number of transducers.

Introduction

As the flow in an axial compressor is reduced while the speed is held constant, a point will be reached at which some or all of the blades begin to stall and one (or more) of a number of instabilities may develop. The most violent of these is surge, which for a high-speed compressor can result in periodically reversed flow and mechanical damage, but which on lower speed machines is a more gentle pulsing of the whole flow. The other phenomenon of great significance on an aero-engine is rotating stall. In its large-scale fully developed form, it can result in a region of blocked flow covering half the annulus and rotating at half the rotor speed. The practical consequence is that unless suitable measures are taken, the engine may not be able to accelerate out of this "locked-in-stall" condition. Rotating stall can also exist as a number of stall cells, which rotate around the machine. This is usually associated with low-speed running of a compressor, where only the front stages are stalled. A general review of these phenomena has been given by Greitzer (1980). Other phenomena that can occur when isolated parts of a compressor are stalled are acoustic resonance and stall flutter. These are mainly of significance during the development of a compressor, where they can result in blade failure. The purpose of the present paper is to discuss high-speed surge and simple conceptual models thereof, showing up inadequacies in the currently accepted simple models of the phenomena. The motivation for the work lies in the assessment of various recently proposed schemes for the active control of surge and stall and the analysis casts doubt on the effectiveness of those schemes in the particular context of high-speed surge.

The scientific understanding of the surge phenomenon starts with the work of Emmons et al. (1955), who showed that on a relatively low-speed machine, surge can be considered as a Helmholtz resonator type of oscillation in which the compressor forms the neck of the resonator and the plenum its volume. The system is unstable when the slope of the compressor pressure rise–flow characteristic becomes positive. This simple theory was expanded to a fully nonlinear version by Greitzer (1976) and can explain many observed features of compressor instabilities. In particular, he highlighted the importance of the B parameter, a ratio of the pressure forces to the inertia forces on the system. At small values of this B parameter, the dominant instability of the system is rotating stall and the dynamics of the system are dominated by the response of the compressor. At large values of B, the overall dynamics are governed by the emptying and filling time of the plenum and the mode of instability is a large amplitude relaxation oscillation. It is with that large B region that this paper is mainly concerned.

This simple "lumped parameter" type of model was later shown to apply to the large-scale rotating stall by Moore (1984) and finally Moore and Greitzer (1986) and Greitzer and Moore (1986) combined the rotating stall and surge modeling to show how the two phenomena are linked. In particular, rotating stall can trigger surge and can be responsible for the sharp drop in the compressor pressure rise characteristic often observed as the flow is reduced. This type of model was later applied to the interaction of the compressor with flow distortions (Moore, 1986) and formed the basis of the distorted flow stability calculations give by Hynes and Greitzer (1987). In many respects, these models are the best we have for understanding the overall dynamics of the compressor, but it is the opinion of the present authors that they are deficient for the important case of high-speed surge and in particular, for the initial part of that motion that takes place on a very short time scale.

One of the defects of the lumped parameter type of model discussed above is that it ignores the possibility that in a long high-speed machine, disturbances take a finite time to propagate from the front to the back (or vice versa) and that the stage characteristics vary considerably along the machine. These phenomena have been included by a number of authors (Tesch and Steenken, 1976; Elder and Gill, 1984; Davis and O'Brien,

Contributed by the International Gas Turbine Institute and presented at the 35th International Gas Turbine and Aeroengine Congress and Exposition, Brussels, Belgium, June 11–14, 1990. Manuscript received by the International Gas Turbine Institute February 15, 1990. Paper No. 90-GT-354.

1987) who split the compression system up into a number of elements, which then interact. These models are claimed to predict many of the observed features of engine operation correctly, in particular, whether the engine goes into nonrecoverable stall. They are probably deficient in two respects, though. First, the initial stage of high-speed surge probably happens too quickly for it to be modeled correctly, and second, because they are one-dimensional, these models do not handle the coupling of surge and rotating stall in a meaningful way. They can only allow for it by assuming that the compressor characteristics drop suddenly when the flow stalls and rotating stall is present. In some sense, this is tantamount to assuming the answer!

An entirely different approach to modeling high-speed surge has been taken by Mazzawy (1979). He notes that experimentally, surge begins with a high-amplitude wave traveling down the compressor. This "blast wave" is the cause of the large impulsive loads that are produced during surge and are sufficient to bend blades and shafts. His modeling is concerned with this initial stage, which he models as a propagating shock wave. This process is apparently ignored by most workers in the field of compressor instabilities, but is the basis for calculations used for many years at the design stage of a compressor to ensure that surge does not result in mechanical failure. A discussion of recent developments in this field using sophisticated computer models has been presented by Birch et al. (1988). This paper will show how this process can be connected to the other types of instability model.

Recently, various schemes have been put forward for the "active control" of these instability phenomena (Epstein et al., 1986, is the first reference in the open literature). It is argued that if the instabilities are described by linear dynamics, they are susceptible to feedback control. In this, the state of the system is measured by suitable sensors and the resulting signal is used to drive an actuator that stabilizes the system. The main point is that the feedback loop alters the dynamics of the system as a whole, so that it can operate in a region where it was otherwise unstable. It is argued that since, in its controlled state, the oscillations can be kept small, the power and weight of the controller will be correspondingly small. Initial experiments at MIT (Pinsley, 1988) and at Cambridge University (Huang, 1988; Ffowcs Williams and Huang, 1989) have been most encouraging. These experiments were on the type of low-speed machine with one dominant instability mode for which the prospect of success is greatest. It is argued here, however, that for a high-speed machine, the likelihood of success is very much less for a number of fundamental reasons.

The main motivation for the work described in this paper was the belief that if compressor surge takes the form described by Mazzawy (1979), then the claims for the prospect of active control are not credible for a high-speed, high-pressure-ratio machine. To support this, the paper begins by examining the standard lumped parameter model of surge, developing it in ways that show where it is deficient in the case of a high-speed multistage machine, both in a general sense and as applied to active control. It turns out that the major defect lies in the neglect of wave propagation effects in the body of the compressor during the "fast" phase of the high B parameter high-speed surge. To overcome this, a different model is proposed, which includes what are believed to be the essential physics of this part of the problem. Throughout, the emphasis is on relatively simple conceptual models that give understanding rather than exact calculations. It is argued that at the present time, this is more useful than any of the complex computer models, particularly as they are all, in the final analysis, limited by an inability to describe events on the scale of a blade chord.

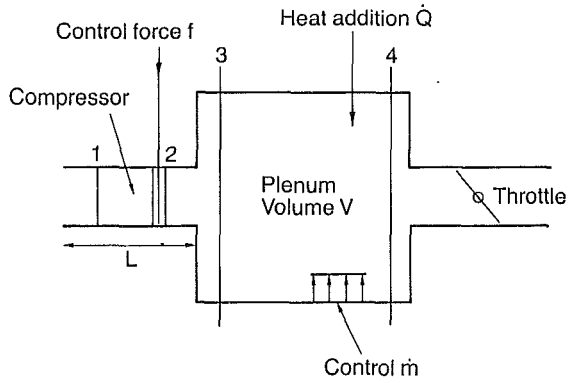

Fig. 1 Lumped parameter model of compressor surge

The purpose of this section is to examine the conventional lumped parameter model of compressor surge with respect to the issues of what happens for a high-speed machine and active control. The basic model of the compressor (cf. Greitzer, 1976) is illustrated in Fig. 1 and comprises a compression element and a plenum or combustion chamber. It is assumed that the compressor has an effective length L and is described by the following dynamic equation:

$$\rho L \frac{du}{dt} + p_2 - p_\alpha = \Delta p(u) + f \tag{1}$$

where f is a notional control force and Δp is the axial force per unit area due to the compression system. It will be assumed that for an N stage machine, this can be sensibly scaled as

$$\Delta p(u) = N\rho U^2 \Psi(u/U) \tag{2}$$

where U is the blade speed, Ψ is the pressure rise coefficient per stage and is a function of the flow coefficient, the ratio

Nomenclature

A = flow area
B = parameter
c = sound speed
C_p = specific heat
e = internal energy
f = force (control)
h = enthalpy
k = constant
L = length of compressor
M = Mach number based on blade speed
M_x = axial Mach number
$\dot{m}$ = mass flow rate (control)
N = number of stages
p = pressure
$\dot{Q}$ = heat addition rate
s = entropy
t = time
T = temperature, time constant
T_H = Time scale for Helmholtz resonator oscillations
U = blade speed
u = axial velocity
V = volume
x = axial distance
γ = specific heat ratio
δ, Δ = differences
ρ = density
τ = nondimensional time
Φ = flow coefficient
Ψ = pressure rise coefficient
ω = angular frequency

Superscripts

$\bar{}$ = mean quantity
$'$ = fluctuation

Subscripts

c = control
e = equilibrium
s = stall
α = atmospheric

of axial velocity to blade speed. This is obviously a gross oversimplification of what really happens, but is probably as complex as is necessary for the present purposes. In particular, it neglects the consequences of the change in mean flow conditions along the compressor. For this section, equation (1) will be linearized to give

$$\rho L \frac{du'}{dt} + p' = N\rho U \Psi' u' + f' \tag{3}$$

where Ψ' is the slope of the compressor characteristic.

To derive a simple equation for the plenum, it is probably better to start with the energy equation rather than the continuity equation as is more usual. Ignoring the kinetic energy of the fluid, this gives

$$\frac{d}{dt}(\int \rho e dV) + \int \rho u h dA = \dot{Q} \tag{4}$$

with e and h the internal energy and enthalpy and $\dot{Q}$ the heat addition rate. Substituting for the energy quantities gives

$$\frac{d}{dt}(pV) = [\gamma p u A]_3^4 = (\gamma - 1)\dot{Q} + \gamma p A_c u_c \tag{5}$$

In this equation, the last term is a representation of a control, which for the sake of argument, is taken to be an oscillation of a region of the wall of area A_c with velocity u_c. The analysis proceeds by linearizing equation (5). At the inlet, it is assumed that the flow is effectively isentropic, while at the exit there is assumed to be a short choked nozzle (the turbine nozzle guide vanes on an engine) such that the ratio $u/\sqrt{T}$ is constant. The pressure is assumed to be the same throughout the chamber and the temperature fluctuations can be related to the pressure and entropy fluctuations resulting in

$$\frac{V dp'}{dt} - u_3' A_3 \gamma p + p' \gamma A_3 \bar{u}_3 \left(\left(\frac{T_4}{T_3} - 1 \right) + \frac{\gamma - 1}{2\gamma} \cdot \frac{T_4}{T_3} \right) = [(\gamma - 1)\dot{Q} - \bar{u}_4 A_4 \gamma \bar{p} (s'/C_p)] + \gamma A_c \bar{p} u_c \tag{6}$$

The terms in square brackets may be combined to give an effective heat release rate $(\gamma - 1)Q_{\text{eff}}$. The value of Q_{eff} can only be obtained by employing a specific model of the combustion process. That is beyond the scope of the present work. The last term, the control, can be written as the rate of mass addition multiplied by the sound speed squared. Additionally, the volume flux at stations 2 and 3 is the same (ignoring compressibility). Introducing a factor K for the temperature ratio terms on the left-hand side, the equation for the plenum becomes

$$\left(\frac{V_2}{c_2^2} \frac{d}{dt} + \frac{\bar{u}_2 A_2 K}{c_2^2} \right) p_2 = \rho_2 A_2 u' + \frac{d\dot{m}^*}{dt} \tag{7}$$

where m^* is the combined effect of the control and the heat addition (which could itself be used as a control).

In the following analysis, it will be assumed that the mean flow conditions can be taken as the same along the length of the compressor, so that we can drop the suffix 2. Equations (7) and (3) can then be combined to give the following equation for the pressure as affected by the controls:

$$\left(\frac{\rho L V}{c^2} \frac{d^2}{dt^2} - \left(\frac{V \rho U_2 \Psi' N}{c^2} - \frac{\rho L \bar{u} A K}{c^2} \right) \frac{d}{dt} + \left(\rho A - \frac{\rho U \bar{u} K A \Psi' N}{c^2} \right) \right) p = \rho A f' + \left(\rho L \frac{d}{dt} - \rho U \Psi' N \right) \frac{d\dot{m}^*}{dt} \tag{8}$$

At this point, the equations are nondimensionalized by scaling the time by T_H, $1/2\pi$ times the Helmholtz resonator period.

$$T_H = (VL/Ac^2)^{1/2} \tag{9}$$

and introducing the B parameter (see Greitzer, 1976)

$$B = UT_H/2L, \tag{10}$$

giving

$$\left(\frac{d^2}{d\tau^2} - 2NB \left(\Psi' - \frac{AL}{V} \cdot \frac{1}{N} \cdot K\Psi' \right) \frac{d}{d\tau} + (1 - M^2 \Phi N \Psi') \right) \frac{p}{N\rho U^2} = \frac{f'}{N\rho U^2} + \left(\frac{1}{2NB} \cdot \frac{d}{d\tau} - \Psi' \right) \left(\frac{1}{\rho \bar{u} A} \cdot \frac{d\dot{m}^*}{d\tau} \right). \tag{11}$$

A large number of conclusions can be drawn from this equation regarding high-speed surge, even without allowing for nonlinear effects of wave propagation. First, the important parameter governing the dynamics is not the B parameter, but the B parameter multiplied by the number of stages (cf. Greitzer, 1980). This is equivalent to basing the B parameter not on the total length but on the length per stage, or equivalently, to saying that it is the time scale based on the stalling of an individual stage relative to the frequency that is important, rather than the time scale based on the overall inertia. Second, it is of interest, from the point of view of the overall dynamics, to note that T_H can be written in the form

$$T_H^2 = (VL/Ac^2) = (L/\bar{u}) \cdot (V/KA\bar{u}_2) \cdot (\bar{u}/c)^2 \cdot K \tag{12}$$

which is the time scale based on the inertia of the compressor and the plenum emptying time multiplied together and by the Mach number squared, or equivalently, the time for a blade to stall multiplied by the time for the plenum to empty multiplied by the square of the Mach number and the number of stages. Thus T_H becomes relatively large for a high-speed multistage compressor.

The (well-known) stability characteristics of the uncontrolled system are governed by the slope of the characteristic. The system becomes unstable at a point where the slope is slightly positive by an amount dependent on the ratio of the compressor and plenum volumes. Very close to the instability point, the system behaves as an unstable oscillatory system. Note, though, that these oscillations only occur for a decreasingly small margin on either side of this point when NB is large. Elsewhere, the system is divergent if it is unstable.

The potential for control can be understood by asserting that if we have neutral stability in a regime that was unstable in the absence of the control, then in the case where the system is being controlled by the force f, that force must just balance the negative damping force on the left-hand side of the equation, so that

$$\frac{f}{\rho U^2 N} \sim \frac{d}{d\tau} \left(\frac{p}{\rho U^2 N} \right) \cdot 2NB\Psi' \tag{13}$$

If it is assumed that Ψ_2 is quadratic near its peak (i.e., $\Psi \sim (u - u_p)^2/2\Delta u^2$, then with a given level of force available and with a given level of pressure fluctuation against which the system must be stabilized, the improvement in flow at the instability point can be estimated as

$$\frac{\delta(\bar{u} - u^p)}{U} = \left(\frac{\Delta u}{U} \right)^2 \frac{(f/\rho U^2 N)}{d(p'/\rho U^2 N)/d\tau} \cdot \frac{1}{2NB} \tag{14}$$

The available force and the pressure are both likely to scale as implied by this equation, so that it is clear that the practical improvement available is likely to be small for high-speed multistage machines, for which NB is necessarily large.

Similar arguments can be produced for control in the plenum (or combustion chamber) and the improvement there is

$$\frac{\delta(\bar{u} - u_p)}{U} = \left(\frac{\Delta u}{U} \right)^2 \cdot \frac{d((d\dot{m}^*/d\tau)/\rho \bar{u} A)/d\tau}{d(p'/\rho U^2 N)} \tag{15}$$

Additionally, if the system is unstable and subject to an impulse, the response will grow as $\exp[\Psi' NBt/T_H]$. If the control has a time delay associated with it, then as NB increases, this

time delay must decrease if the disturbance level is to be kept low to prevent a nonlinear response.

The final issue in the linear theory is where compressibility effects, in the sense of wave propagation along the compressor, are likely to be important. This is likely to be when the length of the compressor is greater than the wavelength of sound based on the cycle time, or when

$$(L/cT) = \sqrt{((L^2Ac^2)/(c^2VL))} = \sqrt{(AL/V)} > > 1 \quad (16)$$

That is when the volume of the compressor becomes comparable to the plenum volume. This is rarely the case on low-speed laboratory scale experiments but is likely to be the case on modern aero-engine compressors, where there are many stages and the combustion chamber volume has been minimized. A somewhat different impression, though, is created if one writes

$$(L/cT) = MN \cdot (L/NUT_H) = MN/2NB \quad (17)$$

showing that this ratio is also the Mach number times the number of stages divided by the effective B parameter.

The important points of this section, then, are that even on a linear theory, active control looks increasingly difficult as the B parameter is increased and the number of stages is large and that if the plenum volume is sufficiently small relative to the compressor, wave propagation along the compressor is likely to become important. There are, of course, many ways in which the analysis could be extended, such as by allowing for realistic changes in the mean flow conditions along the compressor and by allowing for time lags in the generation of unsteady blade forces. Important though these effects are for numerically exact calculations, it is difficult to believe that they are significant as far as major trends are concerned.

Nonlinear Lumped Parameter Analysis

This section considers the nonlinear version of the analysis of the previous section. For this, the two basic equations are written in the form

$$\rho L \frac{du}{dt} = N\rho U^2 \Psi(u/U) - (p - p_\alpha) + f \quad (18)$$

$$\frac{V}{c^2}\frac{dp}{dt} = \rho A(u - \bar{u}) - \frac{uAK(p - \bar{p})}{c^2} + \frac{d\dot{m}^*}{dt} \quad (19)$$

Note that these include the slight restriction that the effective throttle line is linear. Equations (18) and (19) can be combined to give the following nonlinear equations for the flow function $\varphi = u/U$

$$\frac{d^2\varphi}{d\tau^2} - 2NB\left[\Psi'(\varphi) - K\bar{\varphi}\left(\frac{AL}{VN}\right)\right]\frac{d\varphi}{d\tau} + (\varphi - K\Psi(\varphi)\mathrm{MM}_x N)$$
$$= (\bar{\varphi} - K\Psi(\bar{\varphi})\mathrm{MM}_x N) - \frac{1}{\rho AU}\cdot\frac{d\dot{m}^*}{d\tau} + \left(2B\frac{d}{d\tau} + K\mathrm{MM}_x\right)\frac{(p_\alpha + f)}{\rho U^2} \quad (20)$$

The important feature of this equation is that it is now a nonlinear second-order differential equation (if the controls are set to zero) with a nonlinear damping term. This means that when NB is large, the system can exhibit limit cycle oscillations, which take on the character of relaxation oscillations (first pointed out in the present context by Greitzer, 1976). When NB is sufficiently large, this limit cycle consists of fast and slow elements (see Kervorkian and Cole, 1981, for an account of the asymptotic structure of these types of nonlinear oscillations). During the fast legs of the motion AB and CD (Fig. 2), the pressure ratio remains effectively constant and the dynamics are governed by the inertia of the compressor. In the limit of large NB, the time scale set by this is necessarily much shorter than that set by the plenum, so that the pressure in the plenum remains relatively constant. If that is so, it

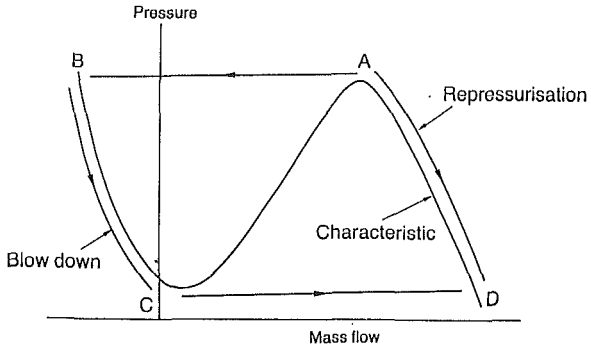

Fig. 2 Surge cycle for high-pressure-ratio high-pressure compressor

follows from equation (18) that these fast parts of the motion must take place on a time scale

$$\Delta t \sim L/NU \quad (21)$$

which is equivalent to the time taken to stall or unstall a compressor blade. What is interesting is to examine the ratio of this time to the time taken for waves to propagate down the compressor. If the latter behaves as a simple pipe with Mach number M_x, then for the discharge phase of the motion, that time is $\sim L/c(1 - M_x)$. It follows that compressibility is likely to be important if

$$NM/(1 - M_x) > 1 \quad (22)$$

This is likely to be the case for any high-speed multistage machine, but probably not for the low-speed devices used in laboratory scale experiments. This implies that the the dynamics of the fast phase of any limit cycle of this type will not be described by any lumped parameter model. The significance of this for the initial stages of surge will become clear shortly.

The slow phases of the motion are those during which the compressor variously discharges (along BC) and repressurizes (along DA). This occurs on a time scale set by the discharge of the plenum and sets the time scale for the overall motion. If this process is determined by the flow through the throttle, then that time is

$$\Delta t \sim V/KAu \quad (23)$$

so that

$$(\Delta t/T_H) \sim 2B/M_x M \quad (24)$$

For large values of B, this is much larger than one and is the reason that the surge frequency can be as low as 7 Hz on a large engine.

An alternative way of looking at this nonlinear system is to employ what is essentially a phase plane approach, in which equations (18) and (19) are combined to give (in the absence of controls)

$$\frac{V}{\rho Lc^2}\cdot\frac{dp}{du} = \frac{\rho A(u - \bar{u}) - \bar{u}AK(p - \bar{p})/c^2}{\rho U^2 N\Psi(u/U) - (p - p_\alpha)} \quad (25)$$

Nondimensionalizing, this can be written

$$\frac{d(p/N\rho U^2)}{d\varphi} = \frac{(\varphi - \bar{\varphi} - \varphi KNM^2(p - \bar{p})/N\rho U^2)}{(\Psi(\varphi) - (p - p_\alpha)/N\rho U^2)}\cdot\frac{1}{(2NB)^2} \quad (26)$$

The key points here are that there is a unique trajectory from any point in the (p, u) plane and that when NB is large, these trajectories have special characteristics. That is, they are vertical for any point on the characteristic and nearly horizontal elsewhere, as sketched on Fig. 3. It may be of interest to note the similarity of this to concepts that have been employed in the study of the human heart and the action of pacemakers (see Jones and Sleeman, 1983). This phase plane result also implies that if the system is in a stable condition and its operating point is suddenly moved to a point above the characteristic as a result of some random disturbance, then the

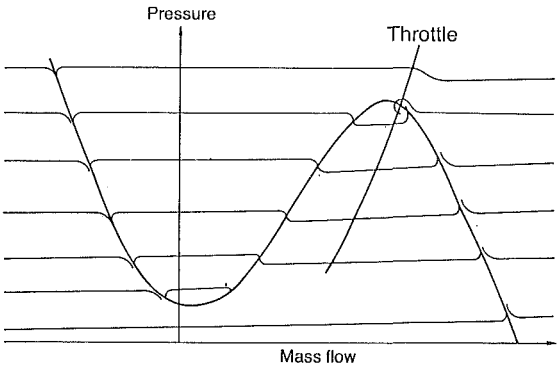

Fig. 3 Phase plane representation of flow trajectories for lumped parameter compressor

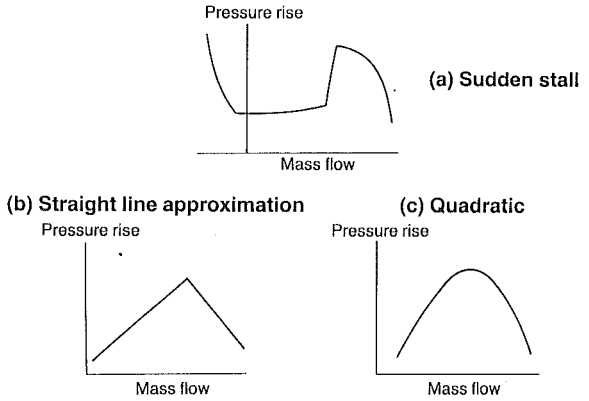

Fig. 4 Approximate representation of compressor characteristics

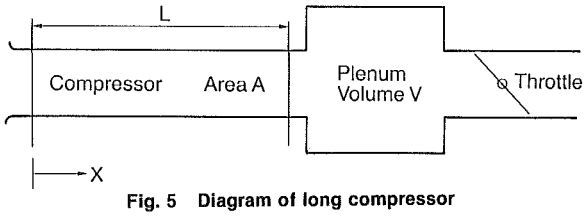

Fig. 5 Diagram of long compressor

trajectory goes to the left-hand side of the picture and the system executes a surge cycle before coming to rest. Putting this another way, an isolated surge can be triggered by a sufficiently large disturbance and there is a threshold level above which surge can be so triggered. If surge starts in this way, then the first event is a sudden decrease in the mass flow, which takes place, for the reasons given below, on the short time scale. It therefore follows from the above arguments that it is highly likely that none of the initial stages of surge on a high-speed compressor are adequately described by either linear dynamics or by a lumped parameter model.

Keeping to the lumped parameter model, the threshold required to trigger surge will depend in detail on the slope of the compressor characteristics. Analysis of this process can be done for different types of characteristic, such as those in Fig. 4. These are one in which there is a sudden decrease in the pressure rise available at stall, either due to the presence of rotating stall or due to blades that stall suddenly, (*a*), one in which the characteristics are linear on either side of the peak, (*b*), and one in which the shape is quadratic at the peak, (*c*). These will feature in the analysis of the next section, which will present conceptual models for what happens along the length of the compressor, i.e., abandoning the lumped parameter approach.

Finally, if the process referred to above of a sudden surge triggered by a disturbance is correct, it implies that the currently envisaged notions of active control may be irrelevant and that the process must be modeled in another way.

Linear Stability Theory—Long Compressor

In the previous two sections, it was established that it is highly likely that the lumped parameter models that are commonly used for the analysis of surge phenomena are conceptually wrong and that the propagation of waves along the compressor must be allowed for. In this section, an alternative conceptual model of the flow is proposed and is used to look at the linear stability of the flow—the finite length counterpart of the simple linear stability theory using the lumped parameter model. The next section then used this model to examine the initial stages of surge , which were discussed in the last section, and for which the lumped parameter type of model is inadequate.

For a conceptual model of a long compressor, it is suggested that the compressor is treated as a one-dimensional medium along which waves can propagate (Fig. 5). Specifically, it is described by continuity and axial momentum equations of the following form:

$$\frac{1}{\rho c^2}\left(\frac{\partial p}{\partial t}+\frac{u\partial p}{\partial x}\right)+\frac{\partial u}{\partial x}=0 \tag{27}$$

$$\rho\left(\frac{\partial u}{\partial t}+\frac{u\partial u}{\partial x}\right)+\frac{\partial}{\partial x}(p-p_e)=\frac{N\rho U^2}{L}(\Psi(u/U)-\Psi_e) \tag{28}$$

The first equation is simply the usual unsteady flow continuity equation in one dimension with the mean flow properties taken as constant. This is, of course, strictly inaccurate, since the mean pressure must increase along the compressor. It also ignores the generation of losses and the possibility that the presence of the blades will impede any propagating waves. However, it should be good enough to understand what is happening in a conceptual sense. In the momentum equation, the left-hand side is simply the usual one-dimensional momentum equation with the equilibrium pressure gradient subtracted, while the right-hand side represents the axial forces due to the blades relative to some equilibrium value. Note that in the equilibrium case, the term on the right-hand side, $N\rho U^2\Psi_e L$, is the average axial force per unit distance and is equal to the mean pressure gradient. For this conceptual level of modeling, the axial forces are regarded as smeared out and distributed uniformly along the compressor. The momentum equation may then be linearized as

$$\rho\left(\frac{\partial u'}{\partial t}+\frac{\bar{u}\partial u'}{\partial x}\right)+\frac{\partial p'}{\partial x}=\frac{N}{L}\rho U\Psi' u' \tag{29}$$

Equations (27) and (28) can be combined to give a wave equation for the pressure

$$\left(\frac{D^2}{Dt^2}-c^2\frac{\partial^2}{\partial x^2}\right)p'=-\frac{\rho U\Psi' N}{L}\frac{Dp}{Dt};\quad \frac{D}{Dt}=\frac{\partial}{\partial t}+\frac{\bar{u}\partial}{\partial x} \tag{30}$$

This is a damped wave equation with the amount of damping being dependent on the local slope of the characteristic. Its solutions are best approached by assuming that the right-hand side is small so that the waves are solutions of the basic linear wave equation modified by the presence of damping. Taking the basic acoustic wave solution and perturbing leads to solutions of the form

$$p=p^{\pm}\exp[i\omega t\pm i\omega^* x/(1\pm M_x)c] \tag{31}$$

where the modified frequency ω^* is given by

$$\omega^*=\omega-iNU\Psi'/L \tag{32}$$

showing that the waves grow or decay as the local slope of the compressor characteristic is positive or negative. The slope of the compressor characteristic is thus the critical factor governing the stability just as it is in the lumped parameter models. The difference here is that (if the slope varies axially) the local properties of the wave are dependent on the local slope and not on the overall compressor characteristic.

The above ideas can be used to examine the stability of the compressor. To do this, the forward and backward traveling waves are combined to form an impedance condition for the compressor exit plane. This is given by

$$(p_2'/\rho c u_2) = -i \tan(\omega^* L/(1-M_x^2)c) \tag{33}$$

This must be matched to the corresponding condition for the plenum, which in the absence of controls and unsteady heat addition, is

$$(p_2'/\rho c u_2) = ((i\omega V/Ac) + KM_x)^{-1} \tag{34}$$

Thus the stability of the system is governed by

$$-i \tan\left(\frac{\omega^* L}{c(1-M_x^2)}\right)\left(\frac{i\omega L}{c}\cdot\frac{V}{AL} + KM_x\right) = 1 \tag{35}$$

it can be seen that if the volume of the compressor is much less than that of the plenum ($AL \ll V$), this reduces to the previous lumped parameter model. If that is not the case, then wave propagation effects are important and the lumped parameter modeling is inappropriate. Once again, it should be emphasized that the main value of this type of model is conceptual and it should not be interpreted too literally as a representation of what happens, but taken as an indication of the broad trend.

The Initial Stages of Surge

In one of the previous sections, it was argued that critical examination of the lumped parameter model led to the idea that the initial stage of surge consisted of a sudden stall of the compressor followed by a large-amplitude excursion from the steady state of equilibrium condition. In this section, a plausible model of how this can occur is examined. The analysis begins with the equations of motion of the last section: equations (27) and (28). It will be assumed that except for the terms representing the blade force, the rest of the equation can be taken as linear and any nonlinear wave propagation phenomena can be added later, using established techniques (see Whitham, 1974). The details depend on the assumptions made about the poststall compressor characteristic. If we have a characteristic that is locally of the type shown as Fig. 4(*b*), then as soon as a part of the compressor is made to operate on the unstable positively sloped part of the characteristic, then the waves will amplify with distance as described in the last section and rapidly reach a large amplitude. A similar thing will happen when the characteristic is quadratic and the disturbances exceed a critical threshold level beyond which any waves can grow. The most dramatic type of phenomenon is one that can occur if the characteristics are shown in Fig. 4(*a*), where stall results in a sudden drop in the effective blade force.

Ignoring, for the moment, any time lags in the stalling response of the blades, that last possibility can be modeled by considering the equations of motion

$$\frac{1}{\rho c^2}\cdot\frac{Dp'}{Dt} + \frac{\partial u'}{\partial x} = 0 \tag{36}$$

$$\rho\frac{Du'}{Dt} + \frac{\partial p'}{\partial x} = -\frac{\Delta\Psi N\rho U^2}{L} \tag{37}$$

in which $\Delta\Psi$ is the drop in the value of Ψ when stall occurs and the left-hand side is zero in those regions to which the stall has not propagated. For a stall that begins at an initial site x_s, this will be the region where $|x-x_s| > (1 \pm M_x)ct$, with the upper and lower signs taken for downstream and upstream propagation. These equations can be most easily solved by converting them into a single wave equation for the pressure and then working in the characteristic coordinates $t_{1,2} = t \pm (x-x_s)/(1 \pm M_x)c$. The result is that within the regions to which the waves have propagated, the pressure and velocity are given by

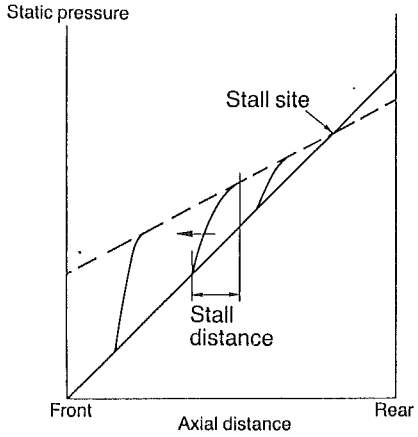

Fig. 6 Propagation of pressure wave along compressor at different times

$$p' = -\frac{N\rho U^2\Delta\Psi}{2}\cdot\frac{(x-x_s-ut)}{L}, \quad u' = -\frac{N\rho U^2\Delta\Psi t}{2L} \tag{38}$$

The sudden stall at x_s results in a wave of positive amplitude traveling downstream and growing as it does so. The amplitude at the head of the wave is half the change in pressure rise due to the stall. Within the stalled region, the velocity is spatially constant and growing in time. When this pressure wave is superimposed on a mean pressure that grows with the distance downstream, the effect is as shown in Fig. 6. This is precisely the type of phenomenon described by Mazzawy (1979). It may be argued that by linearizing the motion, we have ignored certain phenomena. However, the general characteristics must be the same in the nonlinear case. This is shown if we consider the exact nonlinear equations

$$\frac{\partial}{\partial t}(\rho A) + \frac{\partial}{\partial x}(\rho u A) = 0 \tag{39}$$

$$\frac{\partial}{\partial t}(\rho u) + \frac{\partial}{\partial x}(\rho u^2 + p) = F \tag{40}$$

and integrate over the region including the wave, say from $x_1(t)$ to $x_2(t)$. It is then found that subtracting the equilibrium values from these equations

$$\frac{\partial}{\partial t}\int_{x_1(t)}^{x_2(t)}(\rho - \rho_e)A\,dx = 0 \tag{41}$$

and

$$\frac{\partial}{\partial t}\int_{x_1(t)}^{x_2(t)}((\rho u) - (\rho u)_e) = \int_{x_1(t)}^{x_2(t)}(F - F_e)dx \tag{42}$$

The first equation implies that the density and hence pressure variations average out over a length of the wave and the second that the velocity defect must grow with time. These are just as in the linear model.

Two things must be added to complete the picture. First, the stall of the blades must take some time to develop. This can be modeled by changing equation (37) to

$$\left(\frac{Td}{dt} + 1\right)\left(\rho\frac{Du}{Dt} + \frac{\partial p}{\partial x}\right) = -\frac{\Delta\Psi N\rho U^2}{L} \tag{43}$$

The practical consequence is that the head of the wave is rounded off over a time T and hence over a distance $cT(1-M_x)$. The second issue is that of nonlinear propagation. This means that the wave will propagate forward at a speed greater than the linear value by an amount (treating it as a simple nonlinear wave)

$$\delta\frac{dx}{dt} = \frac{(\gamma+1)}{2}\cdot\frac{\delta p}{\rho c} \tag{44}$$

where δp is the wave amplitude. Now from the above analysis, the amplitude at the head of the wave is $-\Delta pct/2L$, where Δp is the drop in the level of the characteristic due to stall. Integrating, it follows that in a given time, t, the wave will have advanced an extra distance

$$\delta x_{NL} \sim -\frac{\Delta p}{\rho c^2}\frac{ct^2}{2}\cdot\frac{(\gamma+1)}{2}\cdot\frac{1}{\rho c} \tag{45}$$

For the whole compressor, this gives a total advance of

$$\delta x_{NL} \sim -\frac{\Delta p}{\rho c^2}\cdot\frac{(\gamma+1)}{8}\cdot\frac{L}{(1-M_x)^2} \tag{46}$$

This may be compared with the opposite effect due to the stall delay time, $cT(1-M_x)=\delta x_s$. Now for an N-stage machine, T will be of the order L/NU so that substituting for Δp in terms of $\Delta\Psi$

$$\frac{\delta x}{\delta x_s}NL \sim \frac{N^2M^2}{(1-M_x)^3}\cdot\frac{(\gamma+1)}{8}\cdot\Delta\Psi \tag{47}$$

This will be greater than one for any high-speed multistage machine even if there is only a small step change in the axial force at stall. When this happens, the rounding off of the wave due to the stall response time is extinguished and (at least in this simplified analysis) a shock wave forms. This then propagates at the acoustic velocity plus half of the increment given by equation (44). This is the process deduced by Mazzawy (1979) and the present analysis further establishes the reasonableness of his conclusions. In practice, it should be noted that the detail of the motion on the scale of the blade chord is likely to be considerably more complicated than this. There is, though, no satisfactory method of analyzing this for a multistage compressor.

The negative (expansion) wave that propagates rearward can be treated in a similar manner, but this has little importance since it will be considerably attenuated on its interaction with the combustor. The positions of the various waves can be displayed on an (x, t) diagram as shown in Fig. 7. There, AB is the stall delay time, the shock forms at C and any waves generated at B can only interact with the forward propagating wave at a later time, G, say.

If surge does start with the type of process described above, there are some important implications for the prospects of applying active control. Suppose, to begin with, that one attempts to control the initial surge wave with a controlling signal generated at the rear of the compressor. Now the control system (sensors, electronics, and actuators) inevitably imposes a time delay between the start of surge and the generation of the control. But the control wave must be able to catch the surge wave in order to affect it and this can only happen if that time delay is very small. The reason for this is that the control wave travels at the speed of wave propagation appropriate to the gas behind the shock wave. This speed is only slightly greater than the shock wave speed and the result is that if the control wave is to catch the surge wave, the allowable time delay is very small, of the order of a millisecond. Moreover, even if one were able to catch the surge wave, the amplitude of the catching wave would have to be very large to make a significant impact on it. If the surge blast wave cannot be caught with a control applied at the rear of the annulus, it might, of course, be controlled in other ways. The only one that seems physically reasonable is to have a scheme in which the surge is sensed at the point at which it starts and to apply the control as close to this as possible. This would be feasible in the sense that it could be achieved with a small control action, but not feasible in the sense that a very large number of actuators and sensors would be required. The reason for this is that in reality, the wave is at least two, rather than one-dimensional as we have assumed here and will start at a particular point on the circumference. This point will be determined by the circumferential distortion to the mean flow going through the machine and the local irregularities in the blading. As a result, this starting position is not known in advance and all possibilities must be allowed for in designing the control system. These two-dimensional aspects of surge are discussed in more detail below.

To make some preliminary estimates of the times involved in the various phenomena, estimates have been made of the propagation of waves in a typical modern ten-stage high-pressure compressor. The method used is based on that given by Mazzawy (1979) rather than the approximate method discussed above. This is because that method does not allow for the changes in mean flow conditions along the compressor. These are given in Fig. 8.

Following Mazzawy, and consistent with the calculation given above, the pressure behind the shock is estimated as shown on Fig. 9. Using these values, the speeds of propagation of the shock wave and the other waves have been calculated, giving the wave trajectories shown on Fig. 10. The time for the blade to stall has been estimated from a brief study of the available data on aerofoil stalling characteristics to be the time taken for the air flowing past the blade to travel a distance of five chord lengths. This time has been estimated as 0.4 ms at the stall site close to the rear of the compressor. The shock forms at point C and propagates along DC reaching the rear of the compressor 2 ms after the stall begins. This wave can only be caught by a wave that is initiated from the rear of the compressor less than half a millisecond after stall is initiated. It is very difficult to imagine a control system that could respond this quickly and supply a large enough control signal. Other items shown on the diagram are the line BC, which is

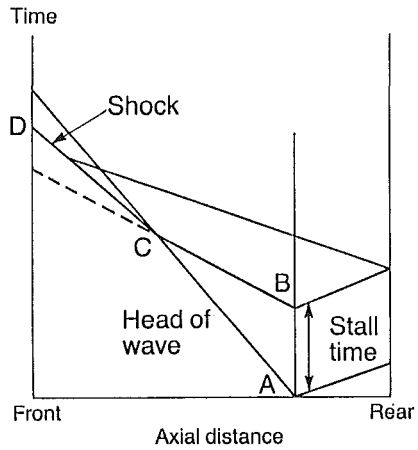

Fig. 7 Schematic of compressor wave trajectories in time and space

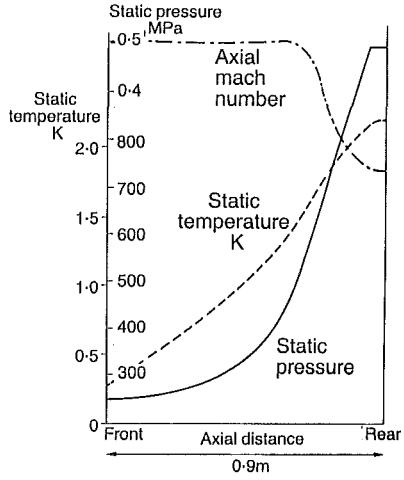

Fig. 8 Assumed variation in mean flow properties along compressor

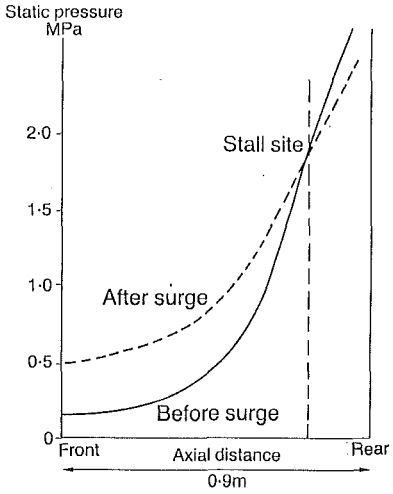

Fig. 9 Assumed variation in pressure along the compressor

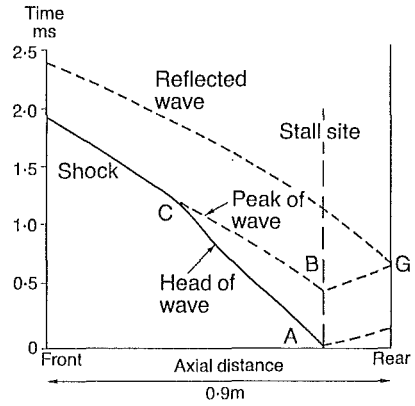

Fig. 10 Calculated wave trajectories for typical compressor

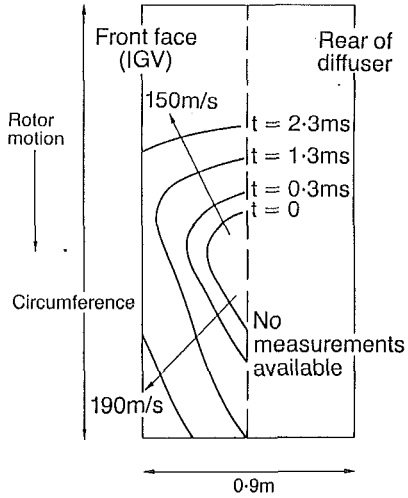

Fig. 11 Developed view of compressor annulus showing wave propagation at different times as deduced from experimental measurements

the position of the peak of the pressure that intersects the path of the head of the wave at the shock formation point C and the propagation path of the reflected wave. Strictly speaking, nonlinear spreading of the rearward-propagating expansion wave should have been allowed for, but this effect appears insignificant over the short propagation distance involved.

The preceding discussion in this paper has been conducted on the basis of the phenomenon being one-dimensional. In fact, it is, of course, well known (see, e.g., Mazzawy, 1979) that surge of the type that has been described is actually two-dimensional in character and probably starts at a point on the annulus determined by the local distortion level and the irregularities in the blading. What Mazzawy's paper shows is a wave that starts at a point and travels in a spiral fashion along the compressor. This is responsible for the large impulsive side loads that are exerted on the compressor rotor and casing during this initial stage of surge. Other data show similar phenomena. Schaffler and Miatt (1985) present data from the three-shaft compression system of an RB199 engine, showing how surge is preceded by rotating stall. The surge itself actually takes the form of a sudden pulse lasting around a millisecond. Despite the large number of measurements made on engines, there are very few that are available and are directly useful for drawing inferences about the initial stages of surge. This is mainly due to the measurements being made with a-c rather than d-c coupled transducers and the fact that measurements are only made at a small number of positions. Nonetheless, it has been possible to infer wave propagation characteristics from some limited data on the same compressor, as was used for the propagation calculations presented earlier. These are shown in Fig. 11 and indicate waves that are initiated at a point on the circumference and spread out forward in a skewed manner. The speed of propagation is approximately half that given by the one-dimensional calculation. This is probably due to the retarding action of the scattering of the wave by the individual blades.

The two-dimensional influences on the surge wave propagation probably affect the fundamental mechanism in the following way. First, suppose that there were no gaps between the blade rows. Then one would expect that the motion of the rotor blades would transport the wave in a circumferential direction at a speed roughly half the blade speed. When gaps are present, the same sort of thing is likely to happen except that the wave will additionally propagate sideways as it does in other examples of two dimensional wave propagation. This spreading will cause the amplitude to decrease. However, if the wave starts with a finite circumferential width, it is likely that it will propagate initially as a quasi-one-dimensional beam. This is the same type of effect as is experienced with acoustic waves (to which we have argued the present situation is analogous). There, a beam of waves of wavelength λ and width a remains as a beam over the Rayleigh distance a^2/λ. An alternative explanation emerges if one thinks of a sharp wavefront propagating through two blade passages with an axial gap between them. As the gap is increased, it is clear that any wave can leak out sideways to a greater extent as the gap is increased.

In the present context, one can therefore imagine that for a surge wave to develop, there must be a critical circumferential extent to the region of stalled flow. What happens is that a certain level of distortion can trigger surge if it is greater than a certain amplitude and of greater than a critical circumferential extent. This is broadly consistent with data on the initiation of surge by inlet distortion and may be a better explanation of what really happens than arguments based on stability theory (e.g., Hynes and Greitzer, 1987). It suggests that if surge starts in the manner that has just been described and at the rear of the compressor, then the process depends on the local character of the flow and not on the circumferential average as suggested by Hynes and Greitzer. As a function of the characteristics of the applied distortion, the overall change in the surge margin is possibly the same, though. It would also explain how the surge wave can be generated when the compressor is stable overall and the compressor characteristics have a strongly negative slope. Furthermore, it is consistent with the observations by Reid (1969) of a "last-stage effect" in the response of compressors to distortions, whereby a different correlation was obtained if the rear of the compressor stalled rather than the whole machine.

Conclusions

1 For an axial compression system of sufficient length and pressure ratio,[1] surge can begin with a high-amplitude blast wave propagating forward along the compressor. This wave is initiated by a region of stalled flow at the rear of the compressor and need not be preceded by any large-scale oscillation corresponding to a linear instability of the system. The process can be simply described as the condition where the axial force exerted by the blades drops below the level necessary to balance the static pressure at the compressor outlet. If the blade force falls as the flow decreases, the flow breaks down catastrophically. The conditions under which this will occur are likely to be met on modern aero-engine compressors running at full speed and with stall tending to occur toward the rear of the machine.

2 If the above mechanism is the cause of surge, then it is unlikely that any of the recently proposed active control schemes will be effective. If they are to control the motion while its amplitude is low, then the control must be applied close to the point at which the waves are generated. Since this point cannot be known in advance, this would require a very large number of sensors and actuators to effect the control. In addition, any control of this sort would have to act very rapidly to suppress the wave before it escaped from its region of inception and had grown to a large amplitude. If the wave cannot be controlled on a local basis and one tries to control it by an actuator placed elsewhere, at the rear of the compressor, for example, this is also likely to be ineffective. If a controlling wave is generated at the rear of the compressor, it must catch the blast wave before the latter reaches the front face of the compressor. This means that the control wave must be generated with a very short time delay and with a very large amplitude. Alternatively, if one tries to control the wave at the front of the compressor, impractically large control amplitudes are required. Even if the wave mechanism for surge does not apply, the more conventional type of lumped parameter analysis strongly points to conclusions in the same direction.

3 Overall, this form of instability does not require the compressor to have positively sloping characteristics. All that is required is that the stages at the rear of the compressor be close to stall and that any wave that starts off there can progressively stall the front stages of the compressor as it propagates forward. This is consistent with the observed behavior of high-pressure-ratio compressors.

4 In the presence of distorted flow, the instability can be triggered by a local reduction in the mass flow. This type of instability depends on local conditions and not on the average around the circumference. This appears to be consistent with the observed behavior of compressors that stall at the rear first.

5 The results of low-speed laboratory-scale (i.e., low speed, low pressure ratio, small number of stages) experiments on compressor surge must be seriously questioned when extrapolated to high-speed machines. This is particularly likely to be the case for experiments specifically directed at active control.

6 The modeling of surge that has been given here is phenomenological in character and is believed to bridge the gap between lumped parameter models of the phenomena and models in which all the blade rows are represented individually. Despite this, there is a great deal of work that needs to be done if the initial stages of surge are to be modeled in such a manner as to capture properly the two-dimensional character of the surge wave and its propagation through the blade rows of the compressor.

7 While the modeling presented here is broadly consistent with the known behavior of high-speed axial compressors during surge, its further development is greatly handicapped by the lack of detailed experimental measurements of the phenomenon. To develop the subject further, there is a considerable need for measurements made throughout the compressor with suitably high response instrumentation.

8 While Conclusion 2 is certainly pessimistic with regard to the active control of compressor surge, it should not be taken to imply that the overall concept of active control is inapplicable. There is every reason to believe that active control may be of benefit in the context of large-scale rotating stall and that by controlling it, we may reduce the constraints on compressor design enabling higher performance to be achieved. Even in the present context of high-speed surge, there is some hope that active control might be of use in controlling the disturbances that would otherwise develop into surge and that it will thus be of some benefit even though it is not controlling surge directly. Furthermore, since many compromises are required in the design of a modern high-speed axial compressor to produce satisfactory high-speed performance and adequate low-speed stability, any improvements in stability active control could produce would indirectly improve the stability margin at other speeds.

[1]Strictly speaking, the condition where this type of surge is present should be expressed in terms of the parameters NB and L, but the practical consequence is as written here.

Acknowledgments

The authors would like to thank the Directors of Rolls-Royce plc for their permission to publish this paper.

References

Birch, N. T., Brownell, J. B., Cargill, A. M., Lawson, M. R., Parker, R. J., and Tillen, K., 1988, "Structural Loads Due to Surge in an Axial Compressor," presented at the 4th Int. Conf. on Vibrations in Rotating Machinery, Heriot-Watt University, Edinburgh.

Davis, M. W., and O'Brien, W. F., 1987, "A Stage-by-Stage Post Stall Compression System Modelling Technique," AIAA Paper No. 87-2088.

Elder, R. L., and Gill, M. E., 1984, "A Surge Prediction Method for Multistage Axial Flow Compressors," IMechE Paper No. C74/84.

Emmons, H. W., Pearson, C. E., and Grant, H. P., 1955, "Compressor Surge and Stall Propagation," *Trans. ASME*, Vol. 77, pp. 455–469.

Epstein, A. H., Ffowcs Williams, J. E., and Greitzer, E. M., 1986, "Active Suppression of Aerodynamic Instabilities in Turbomachines," AIAA Paper No. 86-1994; also *J. Propulsion*, Vol. 5 (2), pp. 204–211.

Ffowcs Williams, J. E., and Huang, X. Y., 1989, "Active Stabilization of Compressor Surge," *J. Fluid Mech.*, Vol. 204, pp. 245–269.

Greitzer, E. M., 1976, "Surge and Rotating Stall in Axial Flow Compressors. Part I: Theoretical Compression System Model," ASME *Journal of Engineering for Power*, Vol. 98, pp. 190–198.

Greitzer, E. M., 1980, "Review—Axial Compressor Stall Phenomena," ASME *Journal of Fluids Engineering*, Vol. 102, pp. 134–151.

Greitzer, E. M., and Moore, F. K., 1986, "A Theory of Post-stall Transients in Axial Compression Systems: Part II—Application," ASME *Journal of Engineering for Gas Turbines and Power*, Vol. 108, pp. 231–239.

Huang, X. Y., 1988, "Active Controls of Aerodynamic Instabilities," PhD Thesis, Cambridge University, United Kingdom.

Hynes, T. P., and Greitzer, E. M., 1987, "A Method for Assessing Effects of Circumferential Flow Distortion on Compressor Stability," ASME JOURNAL OF TURBOMACHINERY, Vol. 109, pp. xx–00.

Jones, D. S., and Sleeman, B. D., 1983, *Differential Equations and Mathematical Biology, Chap. 5: Mathematics of Heart Physiology*, George Allen and Unwin, London, United Kingdom.

Kervorkian, J., and Cole, J. D., 1981, *Perturbation Methods in Applied Mathematics*, Springer-Verlag, New York.

Mazzawy, R. S., 1979, "Surge-Induced Loads in Gas Turbines," ASME *Journal of Engineering for Power*, Vol. 101, pp. xx–00.

Moore, F. K., 1984, "A Theory of Rotating Stall in Multistage Axial Flow Compressors: Parts I, II, and III," ASME *Journal of Engineering for Gas Turbines and Power*, Vol. 106, pp. 313–336.

Moore, F. K., 1986, "Stall Transients in Axial Compression Systems With Inlet Distortion," *J. Propulsion*, Vol. 2 (6), pp. 552–561.

Moore, F. K., and Greitzer, E. M. K, 1986, "A Theory of Post-Stall Transients in Axial Compression Systems: Part I—Development of Equations," ASME *Journal of Engineering for Gas Turbines and Power*, Vol. 108, pp. 68–76.

Pinsley, J., 1988, "Active Control of Centrifugal Compressor Surge," M. S. Thesis, MIT, Cambridge, MA.

Reid, C., 1969, "The Response of Axial Flow Compressor to Inlet Flow Distortion," ASME Paper No. 69-GT-29.

Schaffler, A., and Miatt, D. C., 1985, "Experimental Evaluation of Heavy-Fan–High-Pressure Compressor Interaction in a Three-Shaft Engine: Part I—Experimental Setup and Results," ASME *Journal of Engineering for Gas Turbines and Power*, Vol. 107, pp. 828–832.

Tesch, W. A., and Steenken, W. G., 1976, "Dynamic Blade Row Compression Component Model for Stability Studies," AIAA Paper No. 76-203.

Whitham, G. B., 1974, *Linear and Nonlinear Waves*, Wiley, New York.

Forcing Function Effects on Rotor Periodic Aerodynamic Response

S. R. Manwaring

S. Fleeter

Thermal Sciences and Propulsion Center,
School of Mechanical Engineering,
Purdue University,
West Lafayette, IN 47907

A series of experiments are performed in an extensively instrumented axial flow research compressor to investigate the effects of different low reduced frequency aerodynamic forcing functions and steady loading level on the gust-generated unsteady aerodynamics of a first-stage rotor blade row. Two different two-per-rev forcing functions are considered: (1) the velocity deficit from two 90 deg circumferential inlet flow distortions, and (2) the wakes from two upstream obstructions, which are characteristic of airfoil or probe excitations. The data show that the wake-generated rotor row first harmonic response is much greater than that generated by the inlet distortion, with the difference decreasing with increased steady loading.

Introduction

Periodic aerodynamic excitations generate unsteady aerodynamic forces and moments on turbomachinery blading. At the resonance conditions where the aerodynamic excitation frequency matches a blade natural frequency, catastrophic vibrational responses of the blading may occur. In the design process, Campbell diagrams are utilized to predict the occurrence of the resonant conditions in the operating range of the engine. Unfortunately, accurate predictions of the amplitude of the blade vibration at these resonances cannot currently be made due to the inability of mathematical models to predict the unsteady aerodynamics accurately, i.e., the aerodynamic forcing function to the blade row and the resulting unsteady aerodynamics acting on the blading. As a result, empirical correlations are currently used to indicate the blade row response to the various excitations with varying degrees of success. However, the applicability of these correlations to advanced blade designs has been in question for some time; see for example Mikolajczak et al. (1975).

Nonuniform inlet flow to a rotor represents the most common aerodynamic excitation source for aerodynamically forced vibrations. These nonuniformities are broadly categorized as wake excitations or inlet distortions, with two-per-rev schematic depictions of each shown in Fig. 1. They are generated by a variety of sources including support struts, inlet guide vanes, stator vanes, engine inlet designs, and aircraft maneuvers. In addition to the degradation in performance associated with the various nonuniform inlet flows, they can also result in detrimental aeromechanical effects. Namely, the distortion and wakes both represent unsteady aerodynamic forcing functions to downstream rotor blade rows, thereby resulting in the possibility of aerodynamically induced blade vibrations. This impacts the fatigue life of the blading and, thus, has an adverse effect on overall engine durability.

Distortions and wakes are both high-energy aerodynamic forcing functions characterized by low to moderate values of the reduced frequency. On a first principles basis, they are analyzed by first defining the unsteady aerodynamic forcing function in terms of harmonics. The periodic response of an airfoil row to each harmonic is then assumed to be comprised of two components. One is due to the harmonic components of the unsteady aerodynamic forcing function being swept past the nonresponding airfoil row, termed the streamwise and transverse gust responses. The second, the self-induced unsteady aerodynamics, arises when a vibrational response of the airfoil row is generated.

Current state-of-the-art unsteady aerodynamic models for the prediction of forced response do not consider differences in the various types of aerodynamic forcing functions, i.e., distortion or wake-generated aerodynamic response. Also, the gust and motion-induced unsteady aerodynamic models involve many physical and numerical assumptions. Therefore, experimental modeling of the fundamental distortion and wake-generated blade row periodic unsteady aerodynamic response,

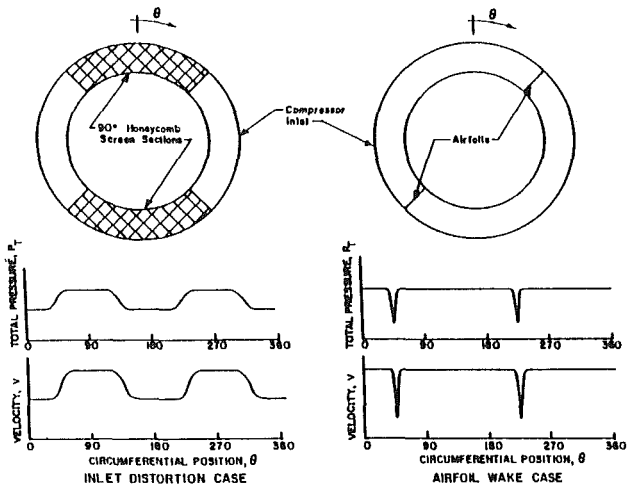

Fig. 1 Two-per-rev aerodynamic forcing functions

Contributed by the International Gas Turbine Institute and presented at the 35th International Gas Turbine and Aeroengine Congress and Exposition, Brussels, Belgium, June 11–14, 1990. Manuscript received by the International Gas Turbine Institute January 15, 1990. Paper No. 90-GT-109.

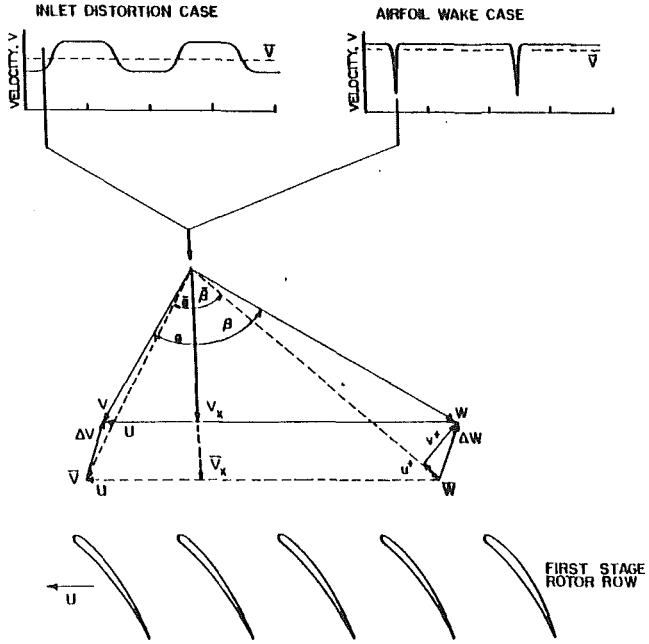

Fig. 2 Aerodynamic forcing function decomposition

including both the forcing function and the resulting blade row unsteady aerodynamics, is needed for validation and enhancement of theoretical and numerical models.

Unsteady aerodynamic gust experiments of direct interest to turbomachines have been performed in low-speed research compressors. Utilizing the stationary vane rows of both single and multistage compressors, with the aerodynamic forcing function being the high reduced frequency wakes shed by the upstream rotor blades, the effects of airfoil camber, rotor–stator axial spacing, and the waveform of the aerodynamic forcing function on the first harmonic vane row response have been investigated (Fleeter et al., 1978, 1980; Capece et al., 1986; Capece and Fleeter, 1987). Gallus et al. (1980) utilized five transducers embedded in each vane surface to quantify the unsteady lift coefficients corresponding to the first five harmonics of rotor blade passing frequency.

With regard to inlet flow distortions, O'Brien et al. (1980) used six dynamic pressure transducers embedded on each rotor blade surface to measure the unsteady aerodynamic response to a distorted inlet flow field. However, the periodic rotor blade row inlet flow field was not measured and, thus, the unsteady aerodynamic gust forcing function was not quantified. Manwaring and Fleeter (1990) investigated the effect of inlet distortion waveform shape on the unsteady pressure response of a first-stage rotor row in a multistage compressor. Hardin et al. (1987) measured low reduced frequency oscillating airfoil aerodynamics on a rotor of a single-stage compressor and also stated that they performed similar distortion

Table 1 Overall airfoil and compressor characteristics

	ROTOR	STATOR	IGV
Airfoil type	C4	C4	C4
Number of Airfoils	43	31	36
Chord, C (mm)	30	30	30
Solidity, C/S	1.14	1.09	0.96
Camber, θ	28.0	27.7	36.9
Stagger Angle, γ	36.0	-36.0	21.0
Aspect Ratio	2.0	2.0	2.0
Thickness/Chord (%)	10.0	10.0	10.0
Flow Rate (kg/s)		2.03	
Design Axial Velocity (m/s)		24.4	
Design Rotational Speed (RPM)		2250	
Number of Stages		3	
Design Stage Pressure Ratio		1.0	
Inlet Tip Diameter (mm)		420	
Hub/Tip Radius Ratio		0.714	
Stage Efficiency (%)		85	

experiments, although the results were not presented. In the high-speed flow regime, Datko and O'Hara (1987) measured the forced vibratory response of an advanced transonic compressor first-stage integrally bladed disk (a blisk) generated by seven different inlet total pressure distortion screens. These experiments found that the blisk was susceptible to excessive resonant stresses generated by the inlet distortions, with complex inlet distortions exciting the lower natural frequencies at a number of engine orders. Although the distorted inlet flow field was measured with a total pressure probe, the harmonic content of the distortion was not always discernible. Also, the detailed forcing function, i.e., the streamwise and transverse gusts, and the rotor blade surface unsteady pressure and pressure differences were not quantified.

In this paper, the fundamental flow physics of disturbance-generated periodic rotor blade row unsteady aerodynamics, including the effect of different unsteady aerodynamic forcing functions, are experimentally investigated for the first time. This is accomplished by means of a series of experiments performed in an extensively instrumented axial flow research compressor directed at the investigation of the effects of both the aerodynamic forcing function and steady aerodynamic loading level on the gust-generated unsteady aerodynamics of a first stage rotor blade.

As schematically depicted in Fig. 1, two different two-per-rev aerodynamic forcing functions are considered: (1) the velocity deficit from two 90 deg circumferential inlet flow distortions, and (2) the wakes from two upstream obstructions, which are characteristic of airfoil or probe excitations. These aerodynamic forcing functions to the first-stage rotor blade row are measured with a rotating cross hot wire probe, with these data then analyzed to determine the streamwise and trans-

Nomenclature

b = rotor blade semichord
$\bar{C}_l$ = rotor blade steady loading = $\int_0^c (\bar{C}_{p,\text{pressure}} - \bar{C}_{p,\text{suction}})dx$
$\bar{C}_p$ = rotor blade steady pressure coefficient
C_{pi} = rotor blade harmonic unsteady pressure coefficient
$C_{\Delta pi}$ = rotor blade harmonic unsteady pressure difference coefficient
$\bar{i}$ = rotor blade mean incidence angle
k = reduced frequency = $\omega b/\bar{V}_x$
p = rotor blade surface unsteady pressure
P_{exit} = rotor drum steady pressure
$\bar{P}_s$ = rotor blade surface steady pressure
$\hat{p}_i$ = harmonic unsteady pressure
U_t = rotor blade tip speed
u^+ = streamwise unsteady velocity component
$\hat{u}_i$ = streamwise gust harmonic component
v^+ = transverse unsteady velocity component
$\hat{v}_i^+$ = transverse gust harmonic component
$\bar{V}_x$ = mean axial velocity
ρ = density of air
σ = interblade phase angle
ω = two-per-rev forcing function frequency, rad

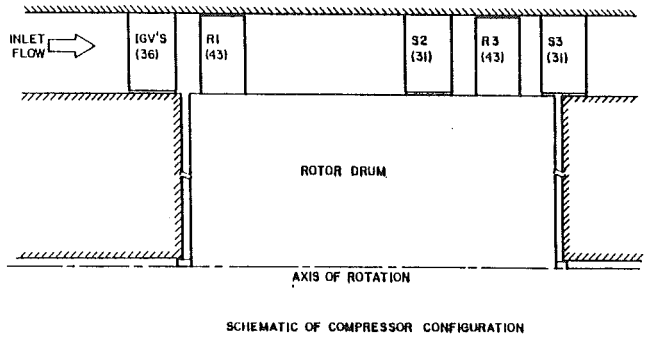

Fig. 3 Research compressor configuration

verse velocity components, u^+ and v^+, shown in Fig. 2. The resulting unsteady aerodynamic gust-generated rotor blade surface unsteady pressure chordwise distributions are measured with embedded ultraminiature high response dynamic pressure transducers.

Research Compressor

The Purdue Axial Flow Research Compressor experimentally models the fundamental turbomachinery unsteady aerodynamic multistage interaction phenomena including the incidence angle, the velocity and pressure variations, the aerodynamic forcing function, the reduced frequency, and the unsteady blade row interactions. The compressor is driven by a 15 hp d-c electric motor and is operated at a speed of 2250 rpm. Each identical stage of the baseline compressor contains 43 rotor blades and 31 stator vanes having a British C4 profile, with the first-stage rotor inlet flow field established by a row of 36 variable setting inlet guide vanes. The overall airfoil and compressor characteristics are presented in Table 1. For these experiments, the first-stage rotor blade row was extensively instrumented. Due to the large gap between the IGV row and the first-stage rotor row, approximately 75 percent vane chord, the potential flow effects are negligible compared to the viscous wakes. To eliminate any potential flow effects from the downstream stator row on the instrumented first-stage rotor blades, the first-stage stators and second-stage rotors were removed, as schematically depicted in Fig. 3.

Instrumentation

Both steady and unsteady first-stage rotor blade row data are required. The steady data quantify the rotor mean inlet flow field and midspan steady loading distribution. The unsteady data define the periodic aerodynamic forcing function and the resulting midspan blade surface periodic pressure distributions.

The inlet flow field, both steady and unsteady, is measured with a rotating cross hot-wire probe mounted 30 percent of blade chord upstream of the rotor row. The cross hot-wire probe is calibrated and linearized for velocities from 18.3 m/s to 53.4 m/s and $+/-35$ deg angular variation, with the accuracy of the velocity magnitude and flow angle determined to be 4 percent and $+/-1.0$ deg, respectively. Centrifugal loading effects on the rotating hot-wire sensor resistances and, thus, responses were found to be negligible.

The detailed steady aerodynamic loading on the rotor blade surfaces is measured with a chordwise distribution of 20 midspan static pressure taps, 10 on each surface. The static pressure at the rotor exit plane, measured with a rotor drum static tap, is used as the blade surface static pressure reference. These static pressure measurements are made using a rotor based 48 port constant speed drive Scanivalve system located in the rotor drum. To determine the accuracy of the steady pressure measurements, a 95 percent confidence internal, root-mean-square error analysis of 20 samples is performed.

The measurement of the midspan rotor blade surface unsteady pressures is accomplished with 20 ultraminiature, high response transducers embedded in the rotor blades at the same chordwise locations as the static pressure taps. To minimize the possibility of flow disturbances associated with the inability of the transducer diaphragm to maintain the surface curvature of the blade exactly, a reverse mounting technique is utilized. The pressure surface of one blade and the suction surface of the adjacent blade are instrumented, with transducers embedded in the nonmeasurement surface and connected to the measurement surface by a static tap. The embedded dynamic transducers were both statically and dynamically calibrated. The static calibrations showed good linearity and no discernible hysteresis. The dynamic calibrations demonstrated that the frequency response, in terms of gain attenuation and phase shift, were not affected by the reverse mounting technique. The accuracy of the unsteady pressure measurements, determined from the calibrations, is $+/-4$ percent.

The rotor-based static pressure Scanivalve transducer, rotating hot-wire probe, and 20 blade surface dynamic pressure transducers are interfaced to the stationary frame of reference through a 40 channel slip ring assembly. Onboard signal conditioning of the transducer output signals is performed to maintain a good signal-to-noise ratio through the slip ring. The remaining 17 channels of the slip-ring assembly are used to provide excitation to the transducers and on/off switching excitations to the Scanivalve DC Motor.

Data Acquisition and Analysis

Steady Data. The rotor blade surface static pressure data, measured with the rotor-based Scanivalve system, are defined by a root-mean-square error analysis of 20 samples with a 95 percent confidence interval. The reference for these midspan blade pressure measurements is the static pressure at the exit of the rotor measured on the rotor drum. Thus, the blade surface and the reference static pressures are measured at different radii. Hence, a correction for the resulting difference in the radial acceleration is derived and applied in calculating the blade surface static pressure coefficient defined in equation (1).

$$\bar{C}_p = \frac{\bar{P}_s - \bar{P}_{\text{exit}}}{1/2\rho U_t^2} \tag{1}$$

where U_t is the rotor blade tip speed.

Periodic Data. The periodic data of interest are the harmonic components of the aerodynamic forcing function to the first-stage rotor blade row together with the resulting rotor blade surface unsteady pressures and unsteady pressure differences. These are determined by defining a digitized ensemble averaged unsteady aerodynamic data set consisting of the rotating cross hot-wire probe and blade surface dynamic pressure transducer signals at each steady operating point. In particular, these time-variant signals are digitized with a high-speed A-D system at a rate of 20 kHz and then ensemble averaged. The key to this averaging technique is the ability to sample data at a preset time, accomplished by an optical encoder mounted on the rotor shaft. The microsecond range step voltage signal from the encoder is the data initiation time reference and triggers the high speed A-D multiplexer system. To significantly reduce the random fluctuations superimposed on the periodic signals of interest, 200 averages are used. A Fast Fourier Transform (FFT) algorithm is then applied to these ensemble-averaged signals to determine the harmonic components of the unsteady aerodynamic forcing function and the resulting rotor blade surface harmonic unsteady pressures and pressure differences.

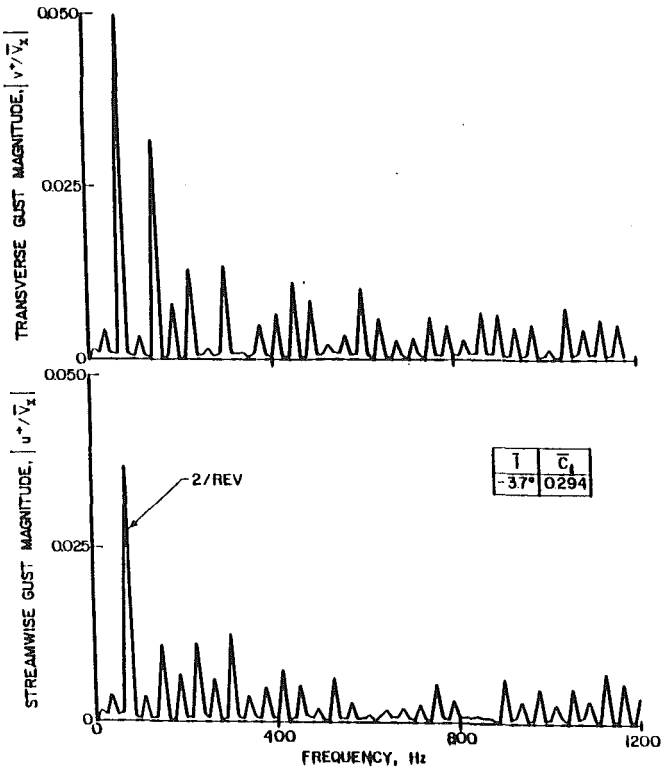

Fig. 4 Fourier decomposition of inlet distortion forcing function for low steady loading

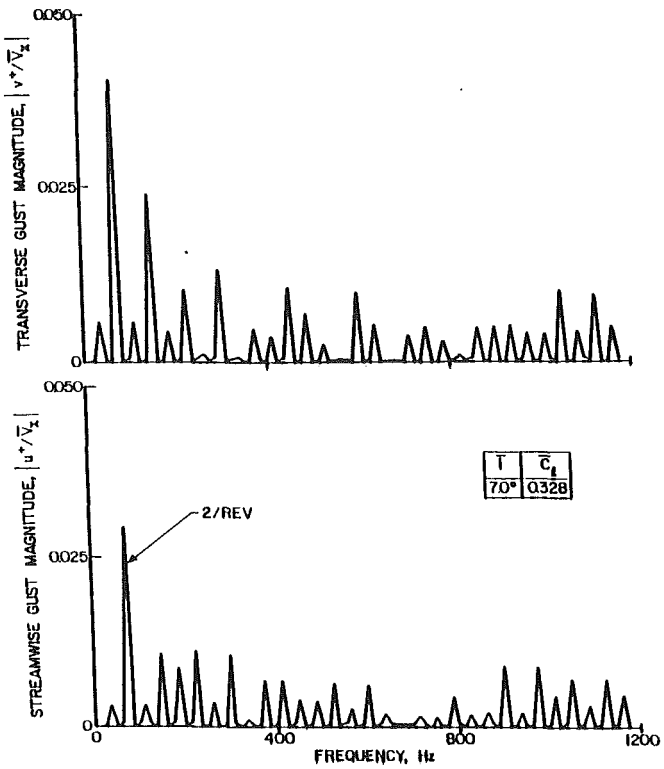

Fig. 6 Fourier decomposition of inlet distortion forcing function for high steady loading

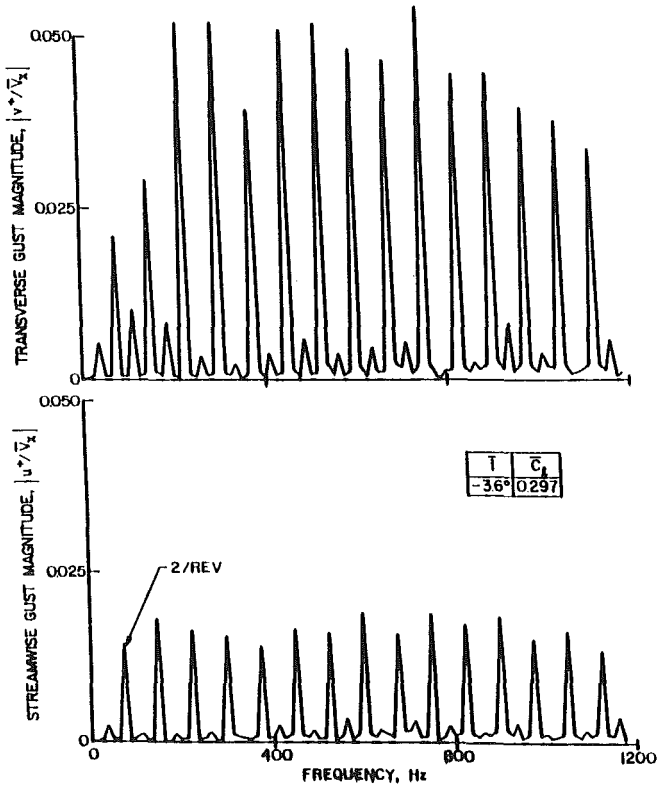

Fig. 5 Fourier decomposition of wake forcing function for low steady loading

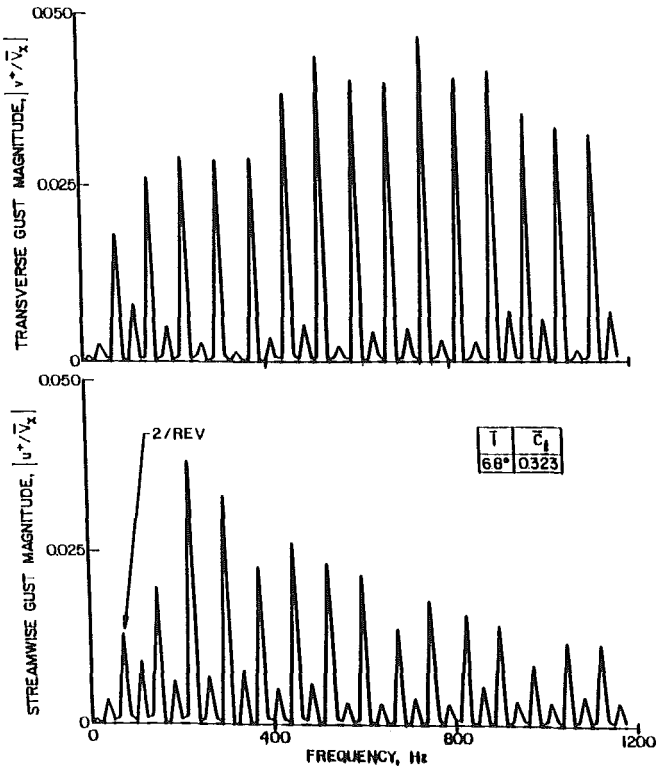

Fig. 7 Fourier decomposition of wake forcing function for high steady loading

The unsteady inlet flow field to the rotor row, measured with the rotating cross hot-wire probe, is quantified by the inlet relative velocity and flow angle. The velocity triangle relations depicted in Fig. 2 are then used to determine the detailed unsteady velocity into the rotor row, in particular, the streamwise and transverse velocity components, u^+ and v^+, respectively. These are then Fourier decomposed to determine their harmonic components, $\hat{u}_i^+$ and $\hat{v}_i^+$.

The various unsteady aerodynamic gust mathematical models reference the gust-generated airfoil aerodynamic response to a transverse gust at the leading edge of the airfoil. However, in the experiments described herein, the time-variant data are

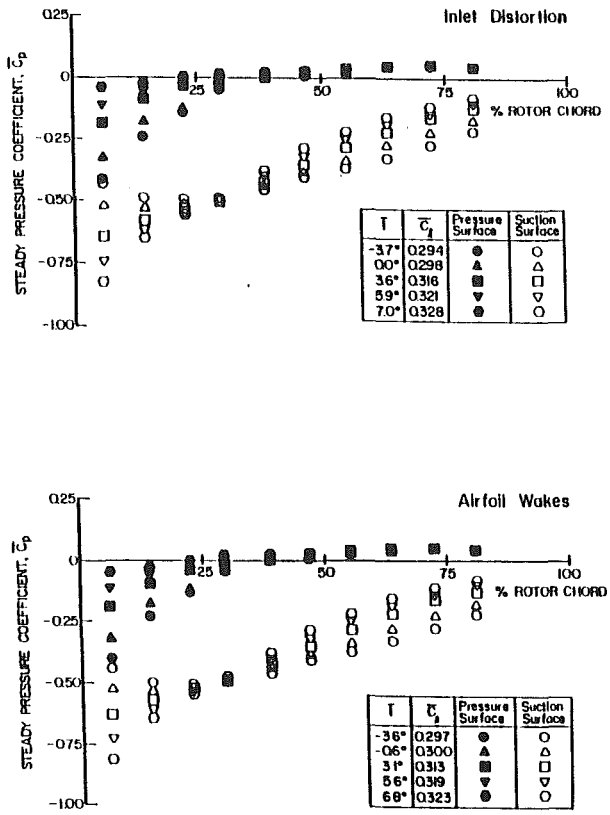

Fig. 8 Forcing function and steady loading effects on surface static pressure coefficient

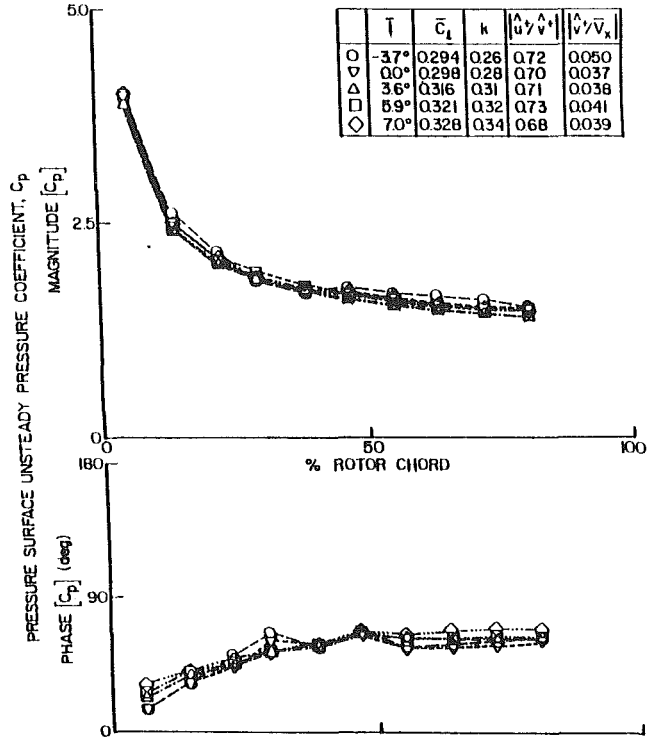

Fig. 9 Pressure surface steady loading effect on unsteady pressure with inlet distortion forcing function

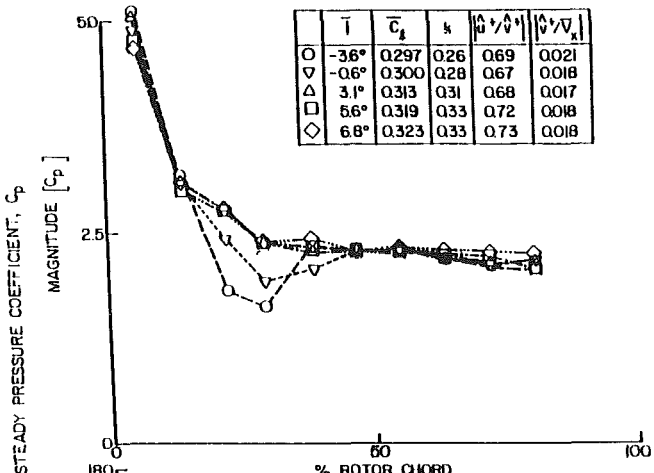

Fig. 10 Pressure surface steady loading effect on unsteady pressure with wake forcing function

referenced to the initiation of the data acquisition shaft trigger pulse. Thus, for consistency with the models, the periodic data are further analyzed and referenced to a transverse gust at the leading edge of the first stage rotor blade. This is accomplished by assuming that: (1) The aerodynamic forcing function remains fixed in the stationary reference frame; and (2) the forcing function does not change from the rotating hot-wire probe axial location to the rotor row leading edge plane.

The rotor blade surface unsteady pressure data, measured with the embedded high response pressure transducers, are analyzed to determine the harmonics of the chordwise distribution of the unsteady pressure coefficient, C_{pi}, and the unsteady pressure difference coefficient, $C_{\Delta pi}$. These are defined in equation (2) and are specified from the Fourier coefficients of the digitized unsteady pressure transducer signals. The nondimensionalization term, $\bar{\beta}$, is used in addition to the standard terms to collapse the steady loading effects associated with mean incidence angle as will be shown later.

$$C_{pi} = \frac{\hat{p}_i}{\rho \bar{V}_x^2 \left(\frac{\hat{v}_i^+}{\bar{V}_x}\right) \bar{\beta}} \tag{2a}$$

$$C_{\Delta pi} = C_{pi,\text{pressure}} - C_{pi,\text{suction}} \tag{2b}$$

where $\hat{v}_i^+$ is the harmonic transverse gust component, $\bar{V}_x$ is the mean axial velocity, and $\bar{\beta}$ is the relative mean flow angle.

The final form of the gust-generated rotor blade row unsteady aerodynamics is the chordwise distribution of the harmonic complex unsteady pressure and pressure difference coefficients. Also included as a reference where appropriate are predictions from the transverse gust analysis of Smith (1971). This model analyzes the unsteady aerodynamics generated on a flat plate airfoil cascade at zero incidence by a transverse gust convected with an inviscid, subsonic, compressible flow.

Results

A series of experiments are performed to investigate and quantify the effects of different aerodynamic forcing functions and the level of steady aerodynamic loading on periodic gust unsteady aerodynamics of a first stage rotor blade. Two different types of two-per-rev forcing functions are considered:

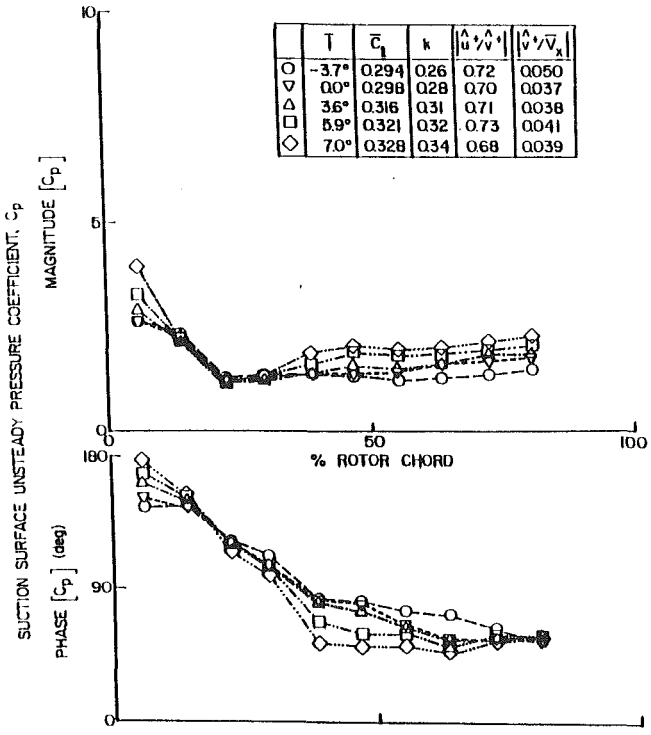

Fig. 11 Suction surface steady loading effect on unsteady pressure with inlet distortion forcing function

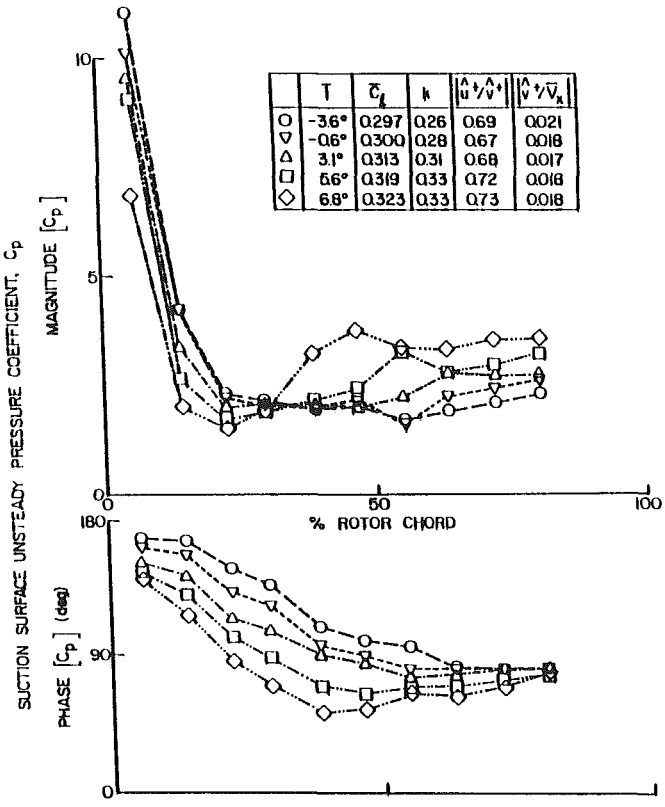

Fig. 12 Suction surface steady loading effect on unsteady pressure with wake forcing function

(1) a circumferential inlet flow distortion, and (2) upstream airfoil wakes. In these experiments, the two two-per-rev forcing functions are equivalent in terms of aerodynamically forced response as each has approximately the same nominal value for the first harmonic streamwise-to-transverse gust amplitude ratio, 0.72 for the inlet distortion and 0.70 for the wakes.

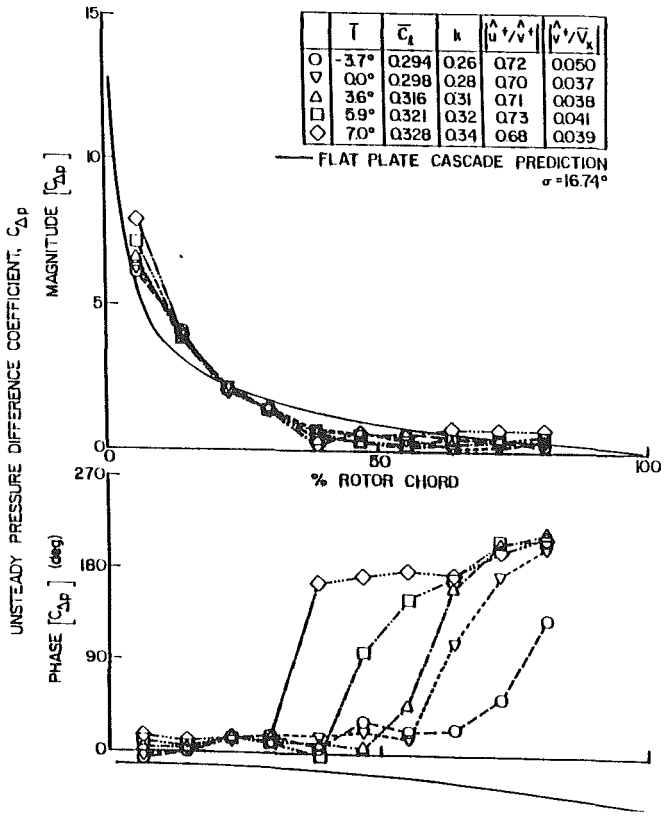

Fig. 13 Steady loading effect on unsteady pressure difference with inlet distortion forcing function

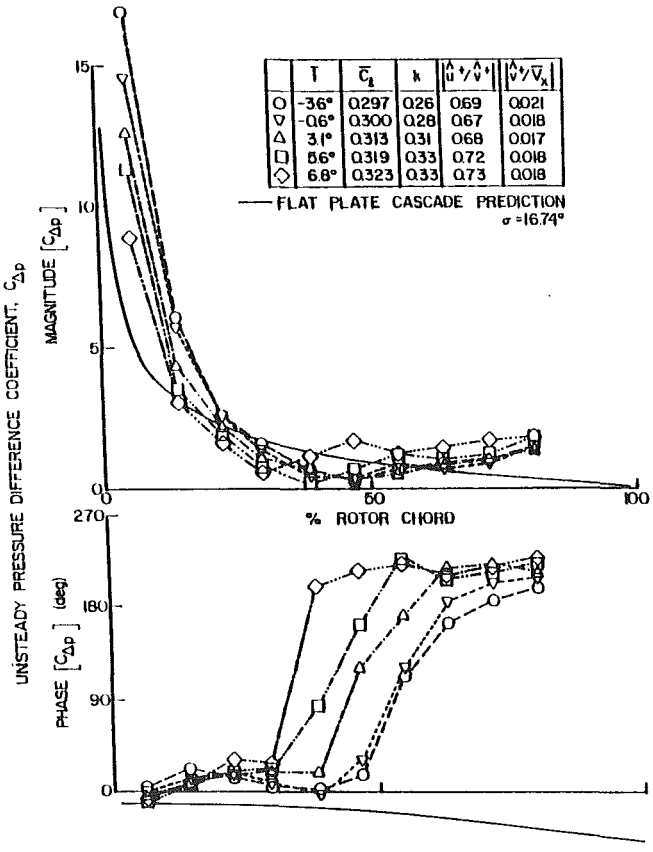

Fig. 14 Steady loading effect on unsteady pressure difference with wake forcing function

Periodic Aerodynamic Forcing Functions. The Fourier decompositions of the inlet distortion and wake aerodynamic forcing functions to the first-stage rotor in terms of the gust components are presented in Figs. 4 and 5 for the lowest steady loading level. The inlet distortion results in a dominant two-per-rev excitation with smaller higher harmonics. With the wake forcing function, a strong two-per-rev signal is again present. However, the higher harmonic amplitudes are approximately the same magnitude as the generating wake two-per-rev fundamental for the streamwise gust components and are larger for the transverse gust component.

The inlet distortion and wake aerodynamic forcing functions for the highest steady loading level are shown in Figs. 6 and 7. The effect of steady loading on the inlet distortion forcing function is minimal, with both the transverse and streamwise harmonic gust components having relatively the same magnitudes as the low steady loading level. However, for the wake forcing function, while the first harmonic streamwise and transverse gust amplitudes are relatively unchanged from the low steady loading level results, the higher harmonic gust component magnitudes differ considerably. For this higher steady loading level, the larger higher harmonics imply that the wake deficit and flow angle changes through the airfoil wake are increased.

Blade Surface Static Pressures. The effect of steady aerodynamic loading, characterized by the mean incidence angle, on the rotor blade surface static pressure coefficient for both the inlet distortion and the obstruction wake forcing function are shown in Fig. 8. The level of steady loading only affects the static pressure distribution on the pressure surface over the front 40 percent of the chord. On the suction surface, the steady loading variation has a large effect on the static pressure distribution over the entire suction surface. Also, these data exhibit no indication of flow separation. Of particular interest to the unsteady experiments, these data clearly show that these different aerodynamic forcing functions have no effect on the steady aerodynamic performance of the rotor, i.e., the airfoil steady surface static pressures are independent of the unsteady aerodynamic forcing function.

Rotor Periodic Aerodynamic Response. The unsteady aerodynamic response of the first-stage rotor blade row to the first harmonic of the inlet distortion and wake forcing functions, including the effect of steady aerodynamic loading, are presented in Figs. 9–14. In particular, these figures present the chordwise distributions of the complex unsteady pressure coefficient on the individual rotor blade surfaces as well as the corresponding complex unsteady pressure difference coefficients generated by these equivalent first harmonic two-per-rev aerodynamic forcing functions.

Pressure Surface Unsteady Pressures. The effect of steady aerodynamic loading level on the first harmonic of the complex unsteady pressure distribution on the rotor blade pressure surface for the inlet distortion and the wake forcing functions is shown in Figs. 9 and 10, respectively.

For the inlet distortion, the unsteady pressure magnitude decreases monotonically with increasing chord for all steady loading levels. This form of the dimensionless unsteady pressure coefficient, equation (2*a*), results in the compression of these magnitude data for all mean flow incidence angle values. Thus, the magnitude of the unsteady pressure response on the blade pressure surface, i.e., the low camber airfoil surface, is primarily due to the level of steady loading as characterized by the mean flow incidence angle.

With the wake forcing function, the unsteady pressure magnitude also decreases monotonically with increasing chord for the three highest steady loading levels, with the data collapsed for these loadings. For the lowest steady loading levels, the data are also collapsed in the aft half of the surface but exhibit

Table 2 Summary of unsteady aerodynamic experimental results

PRESSURE SURFACE UNSTEADY PRESSURE

	DISTORTION	WAKE
MAGNITUDE	decreases monotonically with chord	decreases monotonically with chord for higher loadings
	compressed distributions with respect to mean incidence	decreased between 15% and 40% chord at lowest loadings
PHASE	increases from 0% to 50% chord	increases over entire chord
	independent of steady loading	dependent on steady loading, decreasing with increased loading

SUCTION SURFACE UNSTEADY PRESSURE

	DISTORTION	WAKE
MAGNITUDE	*decreases to a minimum* and then increases with chord	*decreases to a minimum* and then increases with chord
	dependent on steady loading, increasing with increased steady loading	dependent on steady loading, decreasing forward of 30% chord and increasing aft with increased loading
PHASE	decreases over chord	decreases over chord
	dependent on steady loading, with different trends forward and aft of 25% chord	dependent on steady loading

UNSTEADY PRESSURE DIFFERENCE

	DISTORTION	WAKE
MAGNITUDE	decreases with increasing chord	decreases with increasing chord
	increases with increased incidence	*decreases forward of 40% chord* and increases aft with increased incidence
PHASE	nearly constant and independent of loading forward of 40% chord	nearly constant and independent of loading forward of 40% chord
	sharp increase in midchord region, with the onset location moving forward with increasing incidence	sharp increase in midchord region, with the onset location moving forward with increasing incidence

a significant decreased magnitude region between 15 and 40 percent of the chord. This is attributed to the acceleration of the mean flow around the pressure surface leading edge region at these two negative mean incidence angles. As this effect was not seen in the inlet distortion case, this indicates that the first harmonic gust generated by the wake has a much larger interaction with the accelerated mean flow field than the corresponding inlet distortion-generated gust.

The effects of steady loading on the unsteady pressure phase data are also dependent on the specific forcing function. With the inlet distortion, these phase data are essentially independent of the steady loading level. However, with the wake forcing function, the phase of the unsteady pressure is a function of the level of steady loading, with the phase decreasing as the incidence angle increases. Another difference in the effect of the two forcing functions is that with the inlet distortion, the unsteady pressure phase increases over the front half of the surface and remains constant over the aft half, whereas the corresponding phase data increase in value along the entire pressure surface with the wake forcing function.

Suction Surface Unsteady Pressures. The effect of steady aerodynamic loading on the first harmonic complex unsteady pressure on the rotor blade suction surface is shown in Fig. 11 for the inlet distortion and in Fig. 12 for the wake forcing function.

In contrast to the pressure surface, the form of the dimensionless unsteady pressure coefficient, equation (2*a*), does not compress the suction surface magnitude data with mean flow incidence angle, the exception being between 13 and 20 percent of the chord for the inlet distortion. For both forcing functions, the unsteady pressure magnitude data decrease to a minimum and then increase as the chord is traversed. Also, the magnitude data exhibit the same steady loading trends aft of the minimum magnitude chordwise position for the two forcing functions, with the unsteady pressure magnitude increasing with increasing steady loading. In the front chord region, however, the unsteady pressure magnitudes generated by the wake decrease with increasing steady loading, whereas the corresponding inlet distortion-generated magnitudes increase with increasing steady loading. Another difference associated with the forcing functions is that the wake-generated unsteady pressure magnitude

data are significantly larger in value than the corresponding inlet distortion-generated magnitudes for all steady loading levels, particularly in the front chord region, with the differences decreasing with increasing steady loading.

The forcing function has a significant influence on the effect of steady loading level on the unsteady pressure phase data. For the inlet distortion at approximately 25 percent chord and for the wake forcing function over the entire suction surface, the phase data decrease as the incidence angle is increased. However, there is a much larger steady loading effect apparent with the wake forcing function, particularly over the front 75 percent of the chord. Other differences in the effects of the two forcing functions on the suction surface phase data are that with the inlet distortion: (1) The variation with steady loading in the leading edge region changes, increasing with the increasing incidence angle; and (2) these data are nearly independent of the loading level from approximately 15 to 25 percent chord, the vicinity of the minimum unsteady pressure magnitude data. Neither of these effects are found in the wake-generated phase data.

Unsteady Pressure Differences. The effects of steady loading on the first harmonic complex unsteady pressure difference across the rotor blade are shown for the inlet distortion and for the wake forcing functions in Figs. 13 and 14. Also presented in these figures as a reference are the flat plate cascade predictions.

The unsteady pressure difference magnitude data for both forcing functions generally decrease with increasing chord, in trendwise agreement with the predictions. The wake-generated magnitude data are of greater amplitude than the corresponding distortion data in the front chord region, with the distortion data increasing and the wake data decreasing with increasing steady loading. The unsteady pressure difference data generated by the two forcing functions are greatly decreased in magnitude and are in better agreement with one another in the mid to aft chord region, with both increasing slightly with increased loading. Thus, the unsteady lift response of the rotor blade is much greater for the wake forcing function than for the inlet distortion, with the differences decreasing with increasing steady loading.

The unsteady pressure difference phase data are nearly independent of the forcing function. Over the front part of the blade, the phase is nearly constant and is independent of the steady loading level. There is a sharp increase in the phase data in the midchord region, with the phase increasing to an aft chord value, which is slightly greater for the wake forcing function than for the inlet distortion for all steady loading levels. The chordwise location of the onset of this rapid phase increase moves forward with increasing steady loading level.

Summary and Conclusions

The fundamental flow physics of wake and distortion-generated periodic rotor blade row unsteady aerodynamics, including the effect of different unsteady aerodynamic forcing functions, were experimentally investigated. This was accomplished through a series of experiments performed in an extensively instrumented axial flow research compressor, which quantified the effects of the aerodynamic forcing function and the steady aerodynamic loading level on the wake and distortion-generated gust unsteady aerodynamics of a first-stage rotor blade. Two different two-per-rev forcing functions were considered: (1) the velocity deficit from two 90 deg circumferential inlet flow distortions, and (2) the wakes from two upstream obstructions, which are characteristics of airfoil or probe excitations. General experimental results are noted in the following with detailed unsteady aerodynamic results summarized in Table 2.

- The rotor steady aerodynamic performance is independent of the aerodynamic forcing function.
- The inlet distortion forcing function shows a dominant two-per-rev, with much small higher harmonic content. In contrast, the wake forcing function shows a strong two-per-rev with higher harmonics of larger amplitudes.
- On both the suction and pressure surfaces, the first harmonic complex unsteady pressure distributions are dependent on the particular forcing function.
- The unsteady pressure difference magnitude data generally decrease with increasing chordwise distance for both forcing functions, in trendwise agreement with the flat plate cascade predictions.
- The wake-generated rotor row unsteady first harmonic response is much greater than that generated by the inlet distortion, with the difference decreasing with increased steady loading.

Acknowledgments

This research was sponsored by the Air Force Office of Scientific Research (AFSC) under Contract No. F49620-88-C-0022. The United States Government is authorized to reproduce and distribute reprints for governmental purposes notwithstanding any copyright notation hereon.

References

Capece, V. R., Manwaring, S. R., and Fleeter, S., 1986, "Unsteady Blade Row Interactions in a Multi-stage Compressor," *AIAA Journal of Propulsion and Power*, Vol. 2, No. 2, pp. 168–174.

Capece, V. R., and Fleeter, S., 1987, "Unsteady Aerodynamic Interactions in a Multi-stage Compressor," ASME JOURNAL OF TURBOMACHINERY, Vol. 109, No. 3, pp. 420–428.

Datko, F. T., Jr., and O'Hara, J. A., 1987, "The Aeromechanical Response of an Advanced Transonic Compressor to Inlet Distortion," ASME Paper No. 87-GT-189.

Fleeter, S., Jay, R. L., and Bennett, W. A., 1978, "Rotor Wake Generated Unsteady Aerodynamic Response of a Compressor Stator," ASME *Journal of Engineering for Power*, Vol. 100, No. 4, pp. 664–675.

Fleeter, S., Bennett, W. A., and Jay, R. L., 1980, "The Time Variant Aerodynamic Response of a Stator Row Including the Effects of Airfoil Camber," ASME *Journal of Engineering for Power*, Vol. 102, No. 2, pp. 334–343.

Gallus, H. E., Lambertz, J., and Wallman, Th., 1980, "Blade-Row Interaction in an Axial-Flow Subsonic Compressor Stage," ASME *Journal of Engineering for Power*, Vol. 102, No. 1, pp. 169–177.

Hardin, L. W., Carta, F. O., and Verdon, J. M., 1987, "Unsteady Aerodynamic Measurements on a Rotating Compressor Blade Row at Low Mach Number," ASME JOURNAL OF TURBOMACHINERY, Vol. 109, No. 4, pp. 499–507.

Manwaring, S. R., and Fleeter, S. 1990, "Inlet Disortion Generated Periodic Aerodynamic Rotor Response," ASME JOURNAL OF TURBOMACHINERY, Vol. 112, pp. 298–307.

Mikolajczak, A., Arnoldi, R., Snyder, L., and Stargardter, H., 1975, "Advanced Fan and Compressor Blade Flutter Analysis Predictions," *AIAA Journal*, Vol. 12, No. 4, pp. 325–332.

O'Brien, W. F., Cousins, W. T., and Sexton, M. R., 1980, "Unsteady Pressure Measurements and Data Analysis Techniques in Axial-Flow Compressors," *ASME Measurement Methods in Rotating Components of Turbomachinery*, pp. 195–201.

Smith, S. N., 1971, "Discrete Frequency Sound Generation in Axial Flow Turbomachines," ARC R&M 3709.